



HAL
open science

Anilate-based Functional Molecular Materials with Conducting and Magnetic Properties

Matteo Atzori

► **To cite this version:**

Matteo Atzori. Anilate-based Functional Molecular Materials with Conducting and Magnetic Properties. Other. Université d'Angers; Univerità di Cagliari (ITALY), 2015. English. NNT: 2015ANGE0009 . tel-01266640

HAL Id: tel-01266640

<https://theses.hal.science/tel-01266640>

Submitted on 3 Feb 2016

HAL is a multi-disciplinary open access archive for the deposit and dissemination of scientific research documents, whether they are published or not. The documents may come from teaching and research institutions in France or abroad, or from public or private research centers.

L'archive ouverte pluridisciplinaire **HAL**, est destinée au dépôt et à la diffusion de documents scientifiques de niveau recherche, publiés ou non, émanant des établissements d'enseignement et de recherche français ou étrangers, des laboratoires publics ou privés.



Thèse de Doctorat

Matteo ATZORI

*Mémoire présenté en vue de l'obtention du
grade de Docteur de l'Université d'Angers
sous le label de L'Université Nantes Angers Le Mans, et du
grade de Dottore di Ricerca de l'Università di Cagliari*

École doctorale : Matière, Matériaux et Molécules en Pays de la Loire

Discipline : Chimie des Matériaux

Spécialité : Chimie Inorganique Moléculaire

Unité de recherche : Laboratoire MOLTECH-Anjou, Université d'Angers
Dipartimento di Scienze Chimiche e Geologiche, Università di Cagliari

Soutenue le 19/03/2015

Thèse N° : 1463

Anilate-based Functional Molecular Materials with Conducting and Magnetic Properties

JURY

Rapporteurs :	Marc FOURMIGUÉ , Directeur de recherche, Université de Rennes 1 (France) Giuseppe BRUNO , Professeur, Università di Messina (Italy)
Examineurs :	Miguel JULVE , Professeur, Universitat de València (Spain) Anna MUSINU , Professeur, Università di Cagliari (Italy) Nicolas MERCIER , Professeur, Université d'Angers (France) Maria Laura MERCURI , Professeur, Università di Cagliari (Italy) Narcis AVARVARI , Directeur de recherche, Université d'Angers (France)
Directeurs de Thèse :	Maria Laura MERCURI , Professeur, Università di Cagliari (Italy) Narcis AVARVARI , Directeur de recherche, Université d'Angers (France)



Università degli Studi di Cagliari

Facoltà di Scienze

Dipartimento di Scienze Chimiche e Geologiche

Dottorato di Ricerca in Scienze e Tecnologie Chimiche

Settore Scientifico Disciplinare CHIM/03

XXVII Ciclo

Anilate-based Functional Molecular Materials with Conducting and Magnetic Properties

PhD Thesis of:

Matteo Atzori

Supervisors:

Prof. Maria Laura Mercuri

Dr. Narcis Avarvari

Coordinator:

Prof. Mariano Casu

Esame finale Anno Accademico 2013-2014

Alla mia nonna Piera

Poche cose mi rendono felice quanto l'emozione provata per una nuova scoperta

This work has been performed in the frame of a conjoint PhD thesis between the Chemical and Geological Sciences Department of the Cagliari University (Italy) and the Moltech Anjou Laboratory of the Angers University (France).

Abstract

This work reports on the design, synthesis and characterization of novel anilate-based functional molecular materials showing magnetic and conducting properties.

The family of anilate ligands comprises several derivatives obtained by introducing various substituents (H, F, Cl, Br, I, CN, Me, NO₂, etc.) at the 3 and 6 positions of a common 2,5-dihydroxy-1,4-benzoquinone framework. Their electronic/structural features, coordination modes and ability to mediate magnetic exchange interactions between coordinated metal centers make them suitable candidates for the preparation of the above-mentioned materials.

In Chapter 1, the syntheses of novel anilate-based ligands (anilate = An) having thiophene (Th), 3,4-ethylenedioxy-thiophene (EDOT), or Cl/CN as substituents are presented, along with their crystal structures, the investigation of the emission (Cl/CN derivative) or charge-transfer (Th, EDOT derivatives) properties and preliminary coordination chemistry studies.

Chapter 2 reports on a general synthetic strategy to achieve rationally designed tris-chelated octahedral paramagnetic metal complexes, based on the combination of Cr^{III} and Fe^{III} as metal ions with chloranilate, bromanilate, iodanilate, hydranilate and chlorcyananilate as ligands. The crystal structure analyses, spectroscopical and electrochemical features, density functional theory calculations, and the magnetic properties of these metal complexes of general formula [A]₃[M^{III}(X₂An)₃] (A = (*n*-Bu)₄N⁺, (Ph)₄P⁺; M^{III} = Cr, Fe; X = Cl, Br, I, H, Cl/CN) are described.

In Chapter 3 a novel class of molecule-based ferrimagnets formulated as [A][Mn^{II}M^{III}(X₂An)₃] (A = [H₃O(phz)₃]⁺, (*n*-Bu)₄N⁺; M^{III} = Cr, Fe; X = Cl, Br, I, H), obtained according to the “complex-as-ligand” approach by combining Mn^{II} metal ions with the [M(X₂An)₃]³⁻ molecular building blocks described in Chapter 2, is reported. The crystal structures and the magnetic properties for these compounds are described, and the structure/properties correlation observed between the ordering temperature values and the electron density on the ligand ring, associated with the electron withdrawing properties of the X substituents, is particularly highlighted.

Chapter 4 reports on the structural diversity and the physical properties of three new paramagnetic molecular conductors obtained combining the BEDT-TTF organic donor and the [Fe(Cl₂An)₃]³⁻ metal complex as conducting and magnetic building blocks, respectively. The correlation between the crystal structure and conductivity behavior is reported.

Finally, in Chapter 5, the crystal structures and the physical properties of a complete series of isostructural chiral molecular conductors obtained by combining the TM-BEDT-TTF organic donor in its (*S,S,S,S*) and (*R,R,R,R*) enantiopure forms, or their racemic mixture (*rac*), with 2D heterobimetallic anionic layers obtained *in situ* by association of tris(chloranilato)ferrate(III) metal complexes and potassium cations are described.

As far as the framework of the thesis is concerned, this work is organized as follows. Part I contains a general introduction on molecular materials, the state of the art and the aim of the work. Part II contains the obtained results and their discussion divided in 5 Chapters whose content has been summarized above. Part III contains the conclusions and the perspectives for this work. Finally, Part IV contains 5 Appendixes where additional information (basic principles of conductivity and magnetism, details on the electrocrystallization technique, etc.) are given.

Sommario

Questo lavoro di tesi è focalizzato sulla progettazione, la sintesi e la caratterizzazione di nuovi materiali molecolari funzionali con proprietà magnetiche e di conduzione elettrica.

Per l'ottenimento di questi materiali, sono stati selezionati come leganti i derivati del 2,5-diidrossi-1,4-benzoquinone variamente sostituiti nelle posizioni 3 e 6 (H, F, Cl, Br, I, CN, Me, NO₂, etc.), chiamati tradizionalmente anilati. Le loro caratteristiche elettroniche e strutturali, le loro modalità di coordinazione e la capacità di mediare interazioni di superscambio magnetico li rendono degli ottimi leganti per la preparazione di questi materiali.

Nel Capitolo 1 viene presentata la sintesi di nuovi leganti anilato aventi come sostituenti il tiofene (Th), l'etilendiossiofene (EDOT), o gruppi funzionali misti Cl/CN, la loro caratterizzazione strutturale e lo studio delle proprietà di trasferimento di carica (derivati di Th e EDOT) e di emissione (derivato Cl/CN).

Nel Capitolo 2 viene descritta la strategia di sintesi generale che è stata sviluppata per l'ottenimento di complessi paramagnetici ottaedrici tris-chelati. Questa si basa sulla combinazione degli ioni metallici Cr^{III} e Fe^{III} con i leganti cloranilato, bromanilato, iodanilato, idranilato e clorociananilato. In questo Capitolo sono riportate inoltre l'analisi strutturale, le caratteristiche spettroscopiche ed elettrochimiche, i calcoli teorici DFT e le proprietà magnetiche di questi complessi metallici aventi formula generale [A]₃[M^{III}(X₂An)₃] (A = (n-Bu)₄N⁺, (Ph)₄P⁺; M^{III} = Cr, Fe; X = Cl, Br, I, H, Cl/CN).

Nel Capitolo 3 è descritta una nuova classe di ferrimagneti molecolari avente formula generale [A][Mn^{II}M^{III}(X₂An)₃] (A = [H₃O(phz)₃]⁺, (n-Bu)₄N⁺; M^{III} = Cr, Fe; X = Cl, Br, I, H), ottenuta combinando lo ione metallico paramagnetico Mn^{II} con i complessi metallici descritti nel Capitolo 2. In questo Capitolo sono inoltre riportate la caratterizzazione strutturale e magnetica di questi composti e la correlazione tra la struttura e le proprietà fisiche osservate.

Nel Capitolo 4 sono riportate la caratterizzazione strutturale, le proprietà fisiche e la correlazione struttura/proprietà di tre nuovi conduttori paramagnetici molecolari, ottenuti combinando il donatore organico BEDT-TTF e il complesso metallico [Fe(Cl₂An)₃]³⁻, impiegati rispettivamente come carriers di conduttività e di magnetismo.

Infine, nel Capitolo 5 viene riportata la sintesi, la caratterizzazione strutturale e le proprietà fisiche di una serie di conduttori molecolari chirali ottenuta combinando il donatore organico TM-BEDT-TTF nelle sue forme enantiopure (S,S,S,S) e (R,R,R,R), o come miscela racemica (*rac*), con layer eterobimetallici anionici ottenuti per associazione *in situ* del complesso tris(cloranilato)ferrato(III) e ioni potassio.

La tesi è strutturata come segue. Nella Parte I è riportata un'introduzione generale sui materiali molecolari, lo stato dell'arte e lo scopo del lavoro. La Parte II contiene i risultati ottenuti e la loro discussione suddivisa in 5 Capitoli il cui contenuto è stato riassunto sopra. La Parte III contiene le conclusioni generali e le prospettive di questo lavoro. Infine, la Parte IV contiene 5 Appendici dove sono riportate informazioni aggiuntive utili alla lettura della tesi (fondamenti di conduttività e di magnetismo, dettagli sulla tecnica di elettrocristallizzazione, etc.).

Résumé

Ce mémoire de thèse est focalisé sur le design, la synthèse et la caractérisation de nouveaux matériaux moléculaires fonctionnels avec des propriétés magnétiques et de conduction électrique. Pour la préparation de ces matériaux on a sélectionné comme ligands les dérivés du 2,5-dihydroxy-1,4-benzoquinone diversement substitués sur les positions 3 et 6 (H, F, Cl, Br, I, CN, Me, NO₂, etc.), qui sont traditionnellement appelés anilates. Leurs caractéristiques électroniques et structurales, leurs modalités de coordination et leur capacité de médiation des interactions de superéchange magnétique en font d'excellents ligands pour la préparation de ces matériaux.

Dans le Chapitre 1 est présenté la synthèse de nouveaux ligands anilate qui ont comme substituants le thiophène (Th), l'éthylènedithio-thiophène (EDOT), ou des groupes fonctionnels mixtes Cl/CN, leur caractérisation structurale, et leurs propriétés de transfert de charge (pour les dérivés de Th et EDOT) et d'émission (pour le dérivé Cl/CN).

Dans le Chapitre 2 est décrite une stratégie synthétique générale développée pour l'obtention de complexes paramagnétiques octaédriques tris-chélates. Cette stratégie se base sur la combinaison des ions métalliques Cr^{III} et Fe^{III} avec les ligands chloranilate, bromanilate, iodanilate et chlorocycanoanilate. Dans ce Chapitre, l'analyse structurale, les caractéristiques spectroscopiques et électrochimiques, les calculs DFT, et les propriétés magnétiques de ces complexes métalliques de formule générale [A]₃[M^{III}(X₂An)₃] (A = (n-Bu)₄N⁺, (Ph)₄P⁺; M^{III} = Cr, Fe; X = Cl, Br, I, H, Cl/CN), sont aussi reportées.

Dans le Chapitre 3 est décrite une nouvelle classe de ferriaimants moléculaires de formule générale [A][Mn^{II}M^{III}(X₂An)₃] (A = [H₃O(phz)₃]⁺, (n-Bu)₄N⁺; M^{III} = Cr, Fe; X = Cl, Br, I, H), obtenue par combinaison du ion métallique Mn^{II} avec les complexes métalliques présentés dans le Chapitre 2. Dans ce Chapitre sont aussi reportés la caractérisation structurale et magnétique de ces composés, et la corrélation entre la structure et les propriétés physique discutées.

Dans le Chapitre 4 sont reportées la caractérisation structurale, les propriétés physiques et la corrélation entre la structure et les propriétés de trois nouveaux conducteurs paramagnétique moléculaires obtenus par combinaison du donneur organique BEDT-TTF et le complexe métallique [Fe(Cl₂An)₃]³⁻, comme porteurs de conductivité et de magnétisme, respectivement.

Enfin, dans le Chapitre 5 sont reportées la synthèse, la caractérisation structurale et les propriétés physiques d'une série de conducteurs moléculaires chiraux obtenus par combinaison du donneur organique TM-BEDT-TTF sous forme énantiopure (S,S,S,S) et (R,R,R,R), ou comme mélange racémique (*rac*), avec des couches hétérobimétalliques anioniques obtenues par association *in situ* du complexe tris(chloranilate)ferrate(III) et des ions potassium. La structure de la thèse est la suivante. Dans la Partie I est reporté une introduction générale sur les matériaux moléculaires, l'état de l'art, et l'objectif du travail. La Partie II contient les résultats obtenus et leur discussion. La Partie III contient les conclusions générales et les perspectives pour ce travail. Enfin, la Partie IV contient 5 Annexes où sont reportées des informations additionnelles utiles pour la lecture de la thèse (les principes de conductivité et magnétisme, la technique d'électrocristallisation, etc.).

Publication List

Part of the results of this thesis have been published as follows:

- I. **M. Atzori**, S. Benmansour, G. Mínguez-Espallargas, M. Clemente-León, A. Abhervé, P. Gómez-Claramunt, E. Coronado, F. Artizzu, E. Sessini, P. Deplano, A. Serpe, M. Laura Mercuri, and C. J. Gómez-García. A Family of Layered Chiral Porous Magnets Exhibiting Tunable Ordering Temperatures. *Inorganic Chemistry*, **2013**, *52*, 10031–10040.
- II. **M. Atzori**, F. Artizzu, E. Sessini, L. Marchiò, D. Loche, A. Serpe, P. Deplano, G. Concas, F. Pop, N. Avarvari, and M. L. Mercuri. Halogen-bonding in a new family of tris(haloanilato)metallate(III) magnetic molecular building blocks. *Dalton Transactions*, **2014**, *43*, 7006–7019.
- III. **M. Atzori**, F. Pop, P. Auban-Senzier, C. J. Gómez-García, E. Canadell, F. Artizzu, A. Serpe, P. Deplano, N. Avarvari, and M. L. Mercuri. Structural Diversity and Physical Properties of Paramagnetic Molecular Conductors Based on Bis(ethylenedithio)tetrathiafulvalene (BEDT-TTF) and the Tris(chloranilato)ferrate(III) Complex. *Inorganic Chemistry*, **2014**, *53*, 7028–7039.
- IV. **M. Atzori**, F. Pop, T. Cauchy, M. L. Mercuri, and N. Avarvari. Thiophene-benzoquinones: synthesis, crystal structures and preliminary coordination chemistry of derived anilate ligands. *Organic and Biomolecular Chemistry*, **2014**, *12*, 8752–8763.
- V. **M. Atzori**, L. Marchiò, R. Clérac, A. Serpe, P. Deplano, N. Avarvari, and M. L. Mercuri. Hydrogen-Bonded Supramolecular Architectures Based on Tris(Hydranilato)Metallate(III) (M = Fe, Cr) Metallotectons. *Crystal Growth & Design*, **2014**, *14*, 5938–5948.

Symbol List

A	Ampère
B	magnetic induction
C	Curie constant
D	zero field splitting parameter
δ	bending vibrational mode
χ_m	molar magnetic susceptibility
M	magnetization
ε	absorption extinction coefficient
E_a	activation energy
E_g	energy gap
$e.m.f.$	electromotive force
F_0	electrostatic Coulomb force
g	Landé factor
G	gauss
H	magnetic field
J	magnetic exchange constant
k_0	Coulomb constant
k_B	Boltzmann constant
λ	wavelength
m	magnetic moment
N_A	Avogadro number
Oe	Oersted
ρ	pole strength
Pa	Pascal
θ	Weiss constant
Φ	emission quantum yield
q	electrical charge
r	radius
ρ	electrical resistivity
σ	electrical conductivity
S	Siemens
T	Tesla
T	temperature
T_c	critical or ordering temperature
μ	magnetic permeability
μ_B	Bohr magneton
ν	stretching vibrational mode
Wb	Weber

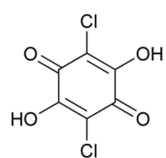
Abbreviation List

A	acceptor
AC	alternate current
An	anilate
BEDO-TTF	bis-(ethylenedioxy)-tetrathiafulvalene
BEDS-TTF	bis-(ethylenediselena)-tetrathiafulvalene
BEDT-TTF	bis-(ethylenedithio)-tetrathiafulvalene
BETS	bis-(ethylenedithio)-tetraselenafulvalene
C	complex
CD	circular dichroism
CT	charge transfer
1D	mono-dimensional
2D	bi-dimensional
3D	tri-dimensional
D	donor
DC	direct current
DM-EDT-TTF	dimethyl-ethylenedithio-tetrathiafulvalene
DR	diffuse reflectance
dmit	2-thioxo-1,3-dithiole-4,5-dithiolate
DFT	density functional theory
EC	excited state
EDOT	3,4-ethylenedioxy-thiophene
EDT-TTF	ethylenedithio-tetrathiafulvalene
eMChA	electrical magneto-chiral anisotropy
EP	electrostatic potential
EPR	electron paramagnetic resonance
ES	excited state
Et	ethyl
FT-IR	FourierTransform-InfraRed
FWHM	full width at half maximum
GS	ground state
H	hybrid system
HB	hydrogen bonding
hfac	hexafluoroacetylacetonate
HOMO	highest occupied molecular orbital
HS	Hirshfeld Surface
L	ligand
LMCT	ligand to metal charge transfer
LUMO	lowest occupied molecular orbitals
M	Molecule-based magnets

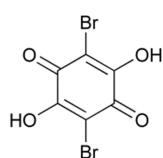
Me	methyl
MO	molecular orbital
MIR	Middle InfraRed
mnt	maleonitriledithiolate
<i>n</i> -Bu	normal-Butyl
NPA	natural population analysis
NIT- <i>i</i> -Pr	2-isopropyl-4,4,5,5-tetramethyl-4,5-dihydro-1 <i>H</i> -imidazolyl-1-oxyl 3-oxide
ox	oxalate
Ph	phenyl
phz	phenazine
PL	photoluminescence
Pr	Propyl
PXRD	powder X-ray diffraction
r.t.	room temperature
SCE	saturated calomel electrode
tbbpy	4,4'-bis(<i>tert</i> -butyl)-2,2'-bipyridine
TCNE	tetracyanoethylene
TCNQ	7,7,8,8-tetracyano- <i>p</i> -quinodimethane
TD-DFT	Time Dependent Density Functional Theory
TGA	thermogravimetric analysis
Th	thiophene
TM-BEDT-TTF	tetramethyl-bis-(ethylenedithio)-tetrathiafulvalene
TM-TSF	tetramethyl-tetraselenafulvalene
TTF	tetrathiafulvalene
UV-Vis	Ultraviolet-Visible
WAPXRD	wide-angle powder X-ray diffraction
X	halogen
XB	halogen bonding
XRD	X-ray diffraction
ZFS	zero field splitting

Chart 1

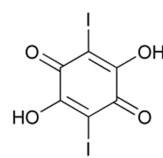
Ligands



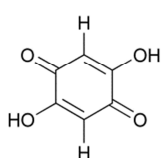
L1
 H_2Cl_2An



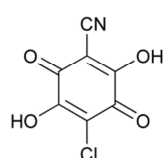
L2
 H_2Br_2An



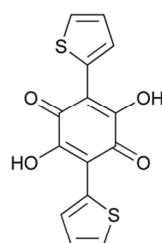
L3
 H_2I_2An



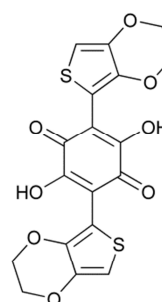
L4
 H_2H_2An



L5
 $H_2ClCNAn$



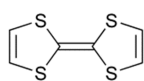
L6
 H_2Th_2An



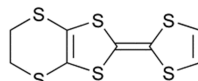
L7
 H_2EDOT_2An

Chart 2

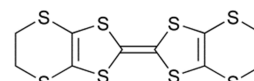
Donors



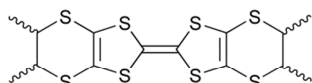
D1
TTF



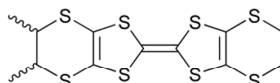
D2
EDT-TTF



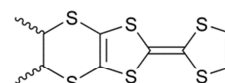
D3
BEDT-TTF



D4
TM-BEDT-TTF



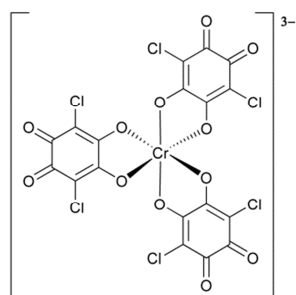
D5
DM-BEDT-TTF



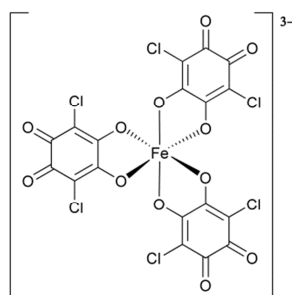
D6
DM-EDT-TTF

Chart 3

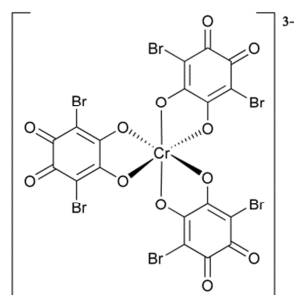
Complexes



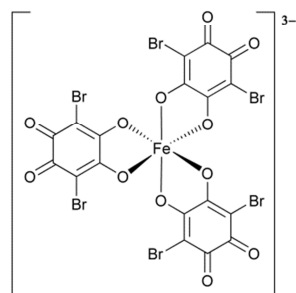
C1
 $[\text{Cr}(\text{Cl}_2\text{An})_3]^{3-}$



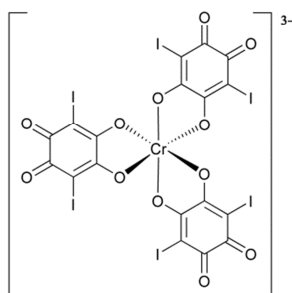
C2
 $[\text{Fe}(\text{Cl}_2\text{An})_3]^{3-}$



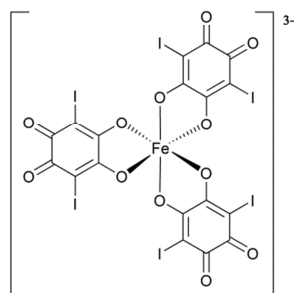
C3
 $[\text{Cr}(\text{Br}_2\text{An})_3]^{3-}$



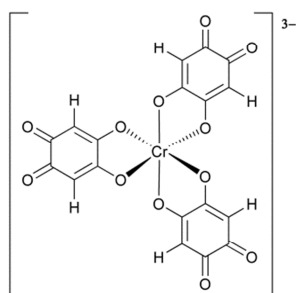
C4
 $[\text{Fe}(\text{Br}_2\text{An})_3]^{3-}$



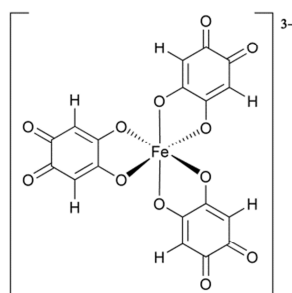
C5
 $[\text{Cr}(\text{I}_2\text{An})_3]^{3-}$



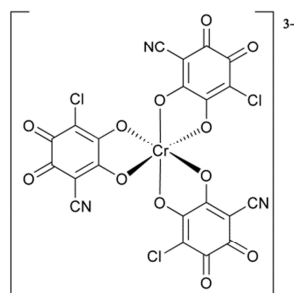
C6
 $[\text{Fe}(\text{I}_2\text{An})_3]^{3-}$



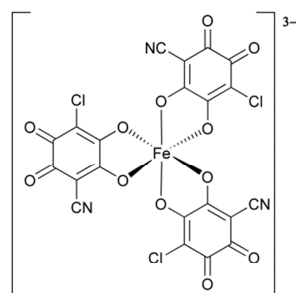
C7
 $[\text{Cr}(\text{H}_2\text{An})_3]^{3-}$



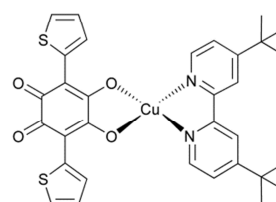
C8
 $[\text{Fe}(\text{H}_2\text{An})_3]^{3-}$



C9
 $[\text{Cr}(\text{ClCNAn})_3]^{3-}$



C10
 $[\text{Fe}(\text{ClCNAn})_3]^{3-}$



C11
 $[\text{Cu}(\text{Th}_2\text{An})(\text{tbbpy})]$

Table of Contents

Part I

Introduction

1.1	Introduction	2
1.2	State of the Art	3
1.3	Aim of the Work	10
	References	11

Part II

Results and Discussion

Chapter 1. Anilate-based Ligands

1.1	Introduction	18
1.1.1	Synthesis of Anilic Acids and their Molecular Structures	19
1.1.2	Coordination modes of the anilate dianions	22
1.1.3	Selected and Novel Anilate Ligands	23
1.2	Results and Discussion	24
1.2.1	Synthesis	24
1.2.2	Crystal Structure Description	26
1.2.3	Emission Properties	30
1.2.4	UV-Vis Absorption Properties and TD-DFT Calculations	32
1.2.5	Electrochemical Studies	36
1.2.6	Preliminary Coordination Chemistry Studies	37
1.3	Conclusions	41
1.4	Experimental	42
1.4.1	General Remarks	42
1.4.2	Syntheses and Analytical Data	42
1.4.3	Equipment and Measurements Details	45
	References	47

Chapter 2. Anilate-based Metal Complexes as Molecular Building Blocks

2.1	Introduction	52
2.2	Results and Discussion	54
2.2.1	Synthetic Strategy	54
2.2.2	Crystal Structure Description	54
2.2.3	Hirshfeld Surface Analysis	64
2.2.4	DFT Calculations	66
2.2.5	Spectroscopical Studies	69
2.2.5.1	FT-IR Spectroscopy	69
2.2.5.2	UV-Vis Spectroscopy	72
2.2.6	Electrochemical Studies	73
2.2.7	Magnetic Properties	74
2.3	Conclusions	82
2.4	Experimental	83
2.4.1	Syntheses and Analytical Data	83
2.4.2	Equipment and Measurements Details	87
	References	91

Chapter 3. Molecule-based Magnets

3.1	Introduction	96
3.2	Results and Discussion	98
3.2.1	Synthetic Strategy	98
3.2.2	Crystal Structure Description	98
3.2.3	Thermogravimetric Analysis	103
3.2.4	Vibrational Spectroscopy	103
3.2.5	Magnetic Properties	104
3.3	Conclusions	108
3.4	Experimental	109
3.4.1	General Remarks	109
3.4.2	Syntheses and Analytical Data	109
3.4.3	Equipment and Measurements Details	110
	References	113

Chapter 4. Magnetic Molecular Conductors

4.1	Introduction	118
4.2	Results and Discussion	119
4.2.1	Synthetic Strategy	119
4.2.2	Crystal Structure Description	120
4.2.3	Conducting Properties	127
4.2.4	Band Structure Calculations	129
4.2.5	Magnetic Properties	133
4.2.6	Electron Paramagnetic Resonance	134
4.3	Conclusions	136
4.4	Experimental	136
4.4.1	General Remarks	136
4.4.2	Syntheses	137
4.4.3	Equipment and Measurements Details	137
	References	139

Chapter 5. Chiral Molecular Conductors

5.1	Introduction	144
5.2	Results and Discussion	145
5.2.1	Synthetic Strategy	145
5.2.2	Crystal Structure Description	146
5.2.3	Conducting Properties	153
5.2.4	Band Structure Calculations	154
5.2.5	Magnetic Properties	157
5.3	Conclusions	158
5.4	Experimental	159
5.4.1	General Remarks	159
5.4.2	Synthesis	159
5.4.3	Equipment and Measurement Details	159
	References	161

Part III

Conclusions and Perspectives

1.1	Conclusions	166
1.2	Perspectives	167

Part IV

Appendices

Appendix 1. Electrical Conductivity of Molecular Materials 173

Appendix 2. Fundamentals of Magnetism and Magnetochemistry 181

Appendix 3. The Electrocrystallization Technique 215

Appendix 3. Supplementary Material 219

Appendix 5. Supplementary Crystallographic Data 241

Acknowledgements 271

Part I

Introduction

1.1 Introduction

The miniaturization of silicon-based electronic devices has nowadays reached its physical limits, and molecular electronics, *i.e.* the use of molecular chemistry to realize electronic circuits and then electronic devices by means of predesigned molecular building blocks, represents the current frontier of electron-based technology.

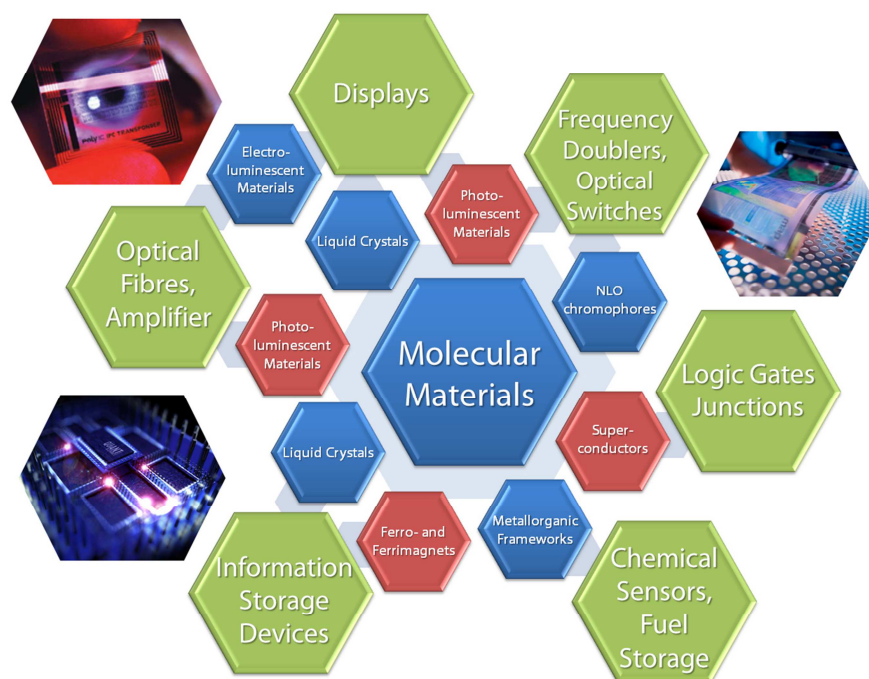
Since 1980s, the unceasing miniaturization of electronic circuits led to the idea that the “top-down approach”, *i.e.* the miniaturization of bulk materials for preparing electronic circuits, was not able to satisfy the upcoming technological demand, and a novel approach for designing and preparing new materials, able to provide smaller devices, was required. Today, the most employed method to reach this goal is the “bottom-up approach”. This approach consists in build perfectly chemically and physically controlled molecular building blocks, and then combine these units to realize circuits at the molecular scale. This provides smaller and more performing devices than the previously obtained by bulk miniaturization.

The technological interest of molecular electronics takes advantage of the richness of molecular chemistry, *i.e.* organic, coordination and supramolecular chemistry, compared to the relatively poor chemistry of conventional inorganic materials used in microelectronics, such as silicon, germanium, III-V semiconductors, *etc.* In fact, the physical properties of molecule-based materials can be easily tuned by conventional synthetic methods based on soft routes (room temperature, atmospheric pressure, *etc.*) in an almost infinite way. This opens unprecedented possibilities to designing molecules with the desired size, shape, charge, polarity, and electronic properties. In this context, molecular materials represent nowadays a well-established class of materials for the preparation of electronic devices, since they exhibit many technologically relevant properties (*e.g.* magnetic ordering, conductivity, superconductivity, *etc.*) traditionally considered to be solely available for classic atom-based inorganic solids such as metals, alloys or oxides.

The area of molecular materials with interesting technological properties started almost 50 years ago with the discovery of the first metal complex showing spin transition $[\text{Fe}(\text{S}_2\text{CNET}_2)_2\text{Cl}]$.¹⁻⁴ Since then, the field of molecular materials has been enlarged with systems exhibiting spin crossover transition,⁵⁻⁸ semiconductors, metals and superconductors,⁹⁻¹³ ferrimagnets, ferromagnets, single-molecule magnets,¹⁴ chromophores for non-linear optics,¹⁵⁻¹⁶ and Vis-NIR emitters based on lanthanide complexes.¹⁷⁻²⁰ A summary of their most appealing technological applications in electronic, magnetic and photonic devices, ranging from data storage to telecommunication/information technology (switches, sensors, *etc.*) is reported in Scheme 1.1.

In addition to mono-functional materials, a more recent and appealing goal in the field of molecule-based materials is the search for multifunctionality. In these systems, the proper selection of the molecular building blocks allows for the combination (or even the interplay) in the same crystal lattice of two or more physical properties, such as magnetism and conductivity or magnetism and optical properties, that are difficult or impossible to achieve in conventional inorganic solids.²¹ In this aspect the possibilities offered by the molecular

bottom-up approach are unprecedented and many interesting and challenging combinations of physical properties can be envisaged.



Scheme 1.1, Some examples of molecule-based materials and their technological applications.

1.2 State of the Art

Certain organic molecules, when partially oxidized and properly organized in the crystal lattice, can behave as metal-like conductors and, in some cases, they can also behave as superconductors below a certain critical temperature. These materials are called organic conductors and their discovery represented a real revolution in material science because, since then, these properties were considered to be available only for classic inorganic solids.

The pioneering work of Knop, which synthesized in 1842 the first molecular metal based on the tetracyanoplatinate anion,²² may be considered as the origin of this research field.²² Actually, the stoichiometry of this systems was determined, and its conducting properties were investigated, only in 1968.²³ This system consists in a partially oxidized salt of formula $K_2[Pt(CN)_4]Br_{0.3} \cdot 3H_2O$, whose structure is formed by stacks of $[Pt(CN)_4]$ units extended along the overlapping direction of the $Pt^{II} d_z^2$ orbitals (Figure 1.1a). This high structural anisotropy reflects the mono-dimensional nature of the conductivity that shows its maximum value along the stacking direction ($\sigma_{||,RT} = 300 \text{ S cm}^{-1}$), whereas it is negligible perpendicularly to the stacks ($\sigma_{\perp,RT} \approx 10^{-5} \text{ S cm}^{-1}$).

In 1973 the discovery of the first organic metal, the TTF-TCNQ system (Figure 1.1b), gave a strong input to this field of research. This compound is a charge transfer salt formed by combining the TTF donor and the TCNQ acceptor (see Appendix 1), showing a r.t. electrical

conductivity, σ_{RT} , of 500 S cm^{-1} and a metallic state down to ca. 55 K.^{24,25} Subsequently, in 1980 the first organic superconductor, the $[\text{TMTSF}]_2[\text{PF}_6]$ system (Figure 1.1c), was discovered. This system shows a metal-superconductor transition at 1.2 K under the pressure of 10 kbar.²⁶

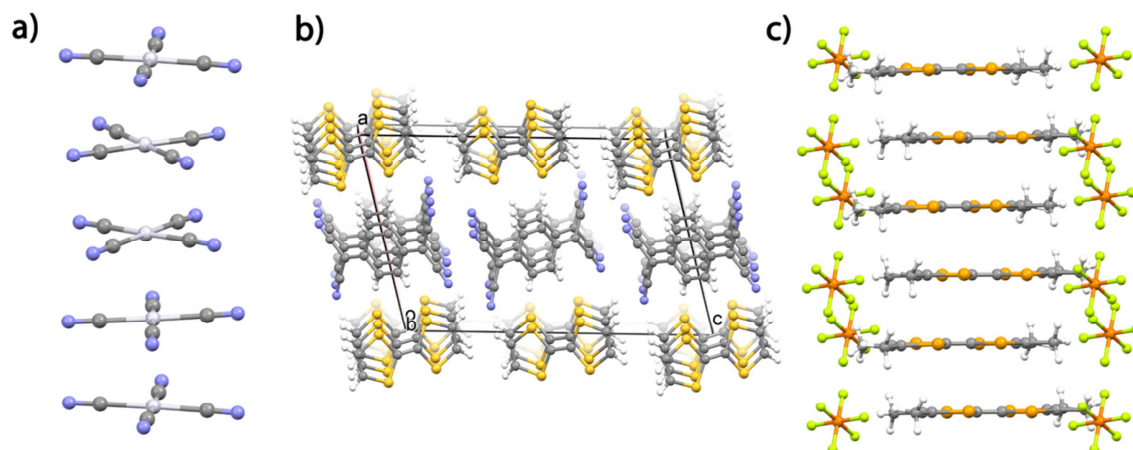


Figure 1.1. a) Stacks of the $[\text{Pt}(\text{CN})_4]$ units in $\text{K}_2[\text{Pt}(\text{CN})_4]\text{Br}_{0.3}\cdot 3\text{H}_2\text{O}$, b) Segregated stacks of TTF and TCNQ in the TTF-TCNQ systems, c) Segregated stacks of the TMTSF donors and PF_6^- anions in $[\text{TMTSF}]_2[\text{PF}_6]$.

After the discovery of these two systems, many scientific efforts were devoted to the search for various derivatives of the TTF molecule, with the aim of increasing the intermolecular interactions between different units, that are, in turn, responsible for the conducting properties (see Appendix 1). Among its derivatives, the BEDT-TTF molecule has been demonstrate the most successful donor, affording the largest number of molecular conductors and the majority of the known molecular superconductors. In particular, the κ - $[\text{BEDT-TTF}]_2[\text{CuN}(\text{CN})_2\text{Br}]$ system shows a metal-superconductor transition temperature of ca. 11.6 K, and represents the highest T_c value for this class of compounds.²⁷

The discovery of molecular conductors based on metal-dithiolenes complexes gave also a great contribution to this field. Among them, the $[(\text{H}_3\text{O})_{0.33}\text{Li}_{0.8}][\text{Pt}(\text{mnt})_2](\text{H}_2\text{O})_{1.67}$ system represents the first metal-like conductor,²⁸ whereas the $[\text{TTF}][\text{Ni}(\text{dmit})_2]_2$ system is the first superconductor (T_c of 1.62 K under a pressure of 7 kbar).²⁹

Another field of relevant interest in material science is molecular magnetism. The discovery in 1967, by Wickman *et al.*, of $[\text{Fe}(\text{S}_2\text{CNET}_2)_2\text{Cl}]$, where the Fe^{III} ion is found in a $S = 2/3$ spin state, intermediate between the high spin ($S = 5/2$) and the low spin ($S = 1/2$) states, showing a magnetic ordering temperature (see Appendix 2) of ca. 2.5 K,¹⁻⁴ marked the start of this field. In 1968, Ito, Suenaga and Ono, described the system $\text{Fe}^{\text{II}}_4[\text{Fe}^{\text{I}}(\text{CN})_6]_3\cdot x\text{H}_2\text{O}$, also known as “Prussian Blue” (Figure 1.2), exhibiting ferromagnetic ordering with a T_c of 5.5 K.³⁰ This system can be considered the parent member of a series of molecular magnets, based on its structural motif, commonly called prussian-blue analogues, showing the highest critical temperature values ($> 300 \text{ K}$) observed in this field.³¹

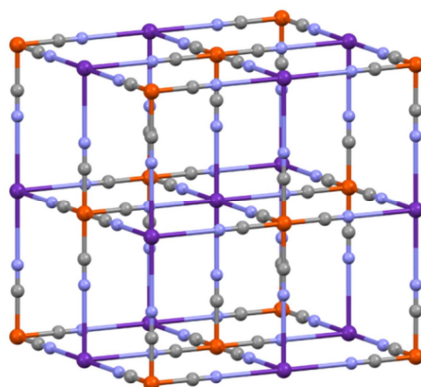


Figure 1.2, View of the crystal structure for a generic “Prussian Blue” analogue. Colour codes: C = gray, N = nitrogen, M = orange and violet.

In 1979 Miller *et al.* reported on the $[\text{Fe}^{\text{III}}(\text{C}_5\text{Me}_5)_2]^+[\text{TCNQ}]^-$ system, the first example of a molecular metamagnet. This system shows an antiferromagnetic ground state which undergoes a ferromagnetic transition under a critical magnetic field of 1.5 kOe at 2.55 K.³² Subsequently, in 1985 the same group obtained the ferromagnetic system $[\text{Fe}^{\text{III}}(\text{C}_5\text{Me}_5)_2]^+[\text{TCNE}]^-$, showing a T_c of 4.8 K and a coercive field of 1 kOe at 2 K. This system is analog to the previously reported one, but with the TCNQ acceptor replaced by the TCNE. The major spin density of TCNE when compared to TCNQ allows for the stabilization of a ferromagnetic ground state instead of an antiferromagnetic one (Figure 1.3).³³⁻³⁵

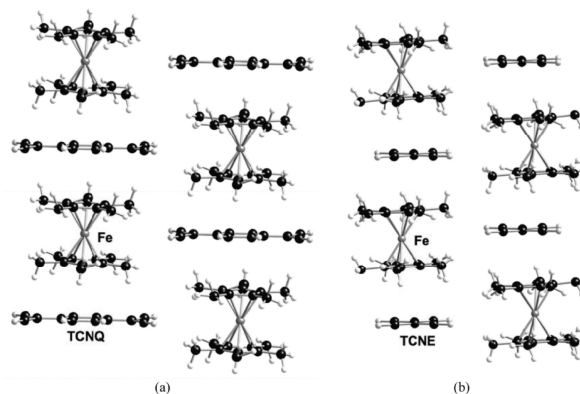


Figure1.3, View of the crystal structure for the donor-acceptor systems $[\text{Fe}^{\text{III}}(\text{C}_5\text{Me}_5)_2]^+[\text{TCNQ}]^-$ (a) and $[\text{Fe}^{\text{III}}(\text{C}_5\text{Me}_5)_2]^+[\text{TCNE}]^-$ (b). Reprinted with permission of ref. 35. Copyright 2006 Indian Academy of Science.

In 1985-86 Reiff and Carlin reported the $[\text{Cr}^{\text{III}}(\text{NH}_3)_6][\text{Cr}^{\text{III}}(\text{CN})_6]$ and $[\text{Cr}^{\text{III}}(\text{NH}_3)_6][\text{Fe}^{\text{III}}\text{Cl}_6]$ bimetallic systems showing ferromagnetic ($T_c = 0.66$ K) and ferrimagnetic ordering ($T_c = 2.85$ K), respectively.^{36,37} These systems can be considered pioneering since most of the molecular magnets subsequently obtained have been designed on their model, *i.e.* by means of superexchange magnetic interactions mediated by bridging ligands connected between paramagnetic *d* metal centers.

Other two classes of molecular magnets who represent pioneering systems are the Mn^{II} -nitronyl nitroxide systems obtained by Gatteschi and Ray in 1989,³⁸ and the Mn^{II} - Cu^{II} chain compounds obtained by Kahn (Figure 1.4).³⁹

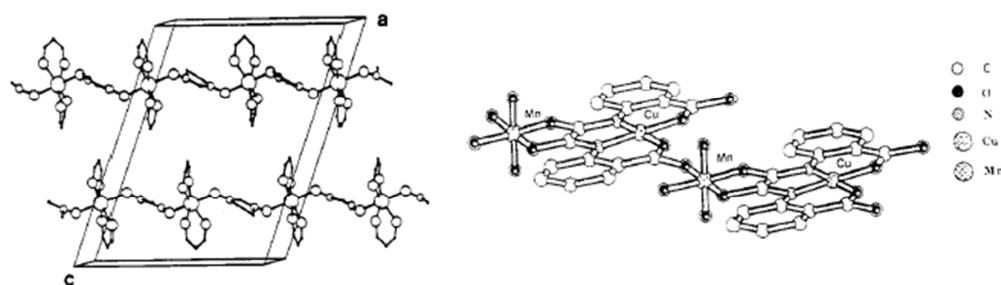


Figure 1.4. Left, View of the crystal structure of the Mn-(hfac)₂NIT-*i*-Pr system. Right, Proposed structure for the Mn^{II}-Cu^{II} chain compounds of O. Kahn. Adapted with permission of ref. 38,39. Copyright 1989 American Chemical Society.

In 1992, Verdaguer *et al.* reported a molecular ferromagnet based on the “Prussian Blue” structure, the CsNi^{II}[Cr^{III}(CN)₆]₂·2H₂O system, having a T_c of 90 K.⁴⁰ As an extension of this work, in 1995 the mixed valence system V^{II}_{0.42}V^{III}_{0.58}[Cr(CN)₆]_{0.86}·2.8H₂O was prepared, showing ferrimagnetic ordering at 315 K.⁴¹ Subsequent studies led to analogous systems having even higher critical temperatures (373 K).⁴²

In 1992 Okawa *et al.* reported on a novel class of molecular ferromagnets; the heterobimetallic polymeric compounds of general formula [N(Bu)₄][M^{II}Cr^{III}(ox)₃].⁴³ In these systems the oxalate ligand behaves as a bridging ligand between two paramagnetic metal Cr^{III} and M^{II} (M^{II} = Mn, Fe, Co, Ni, Cu, Zn) and it is able to mediate superexchange magnetic interactions, leading to long range ferromagnetic ordering with T_c between 6 and 15 K as a function of the coordinated metal ions. The chiral structure (Δ , Λ) of the mononuclear anionic building block [Cr^{III}(ox)₃]³⁻ allows to obtain different polymeric systems whose dimensionality varies as a function of the stereochemical configuration. If both enantiomers crystallize, a 2D honeycomb type structure is obtained, whereas, if only one enantiomer self-assembles, a 3D chiral structure is achieved (Figure 1.5).⁴⁴

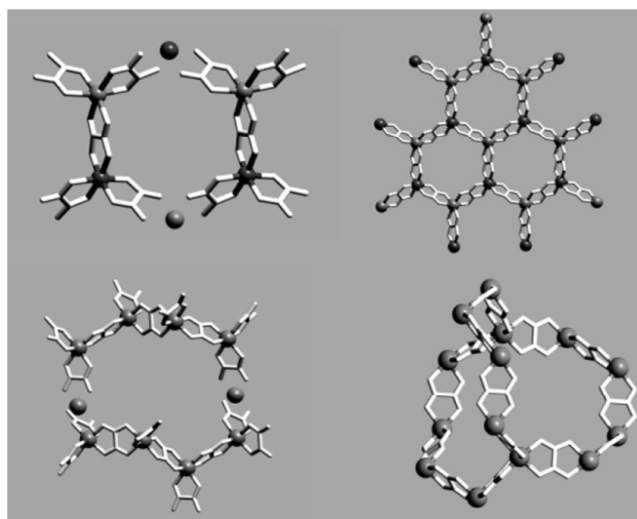


Figure 1.5. Top left, Two dimeric units formed by enantiomers of opposite chirality needed to obtain an hexagonal moiety. Top right, A portion of the resulting honeycomb 2D layers. Down left, Two tetrameric units formed by enantiomers having the same chirality needed to obtain a dodecagon. Down right, A portion of the resulting 3D structure. Adapted with permission of ref. 44. Copyright 2002 Wiley-VCH.

In 1993, Sessoli *et al.* reported on the first example of a new class of molecular magnets commonly called single-molecule magnets.⁴⁵ The Mn_{12} ($S = 10$) cluster reported in Figure 1.6, presents a 0D atomic scale structure whose dimensions, absence of any intramolecular interaction with the surrounding molecules, and strong magnetic coupling between paramagnetic centers in a highly anisotropic environment induced unprecedented magnetic properties in this field. In these systems the magnetization relaxes through quantum tunneling phenomena giving rise to a magnetic bistability.

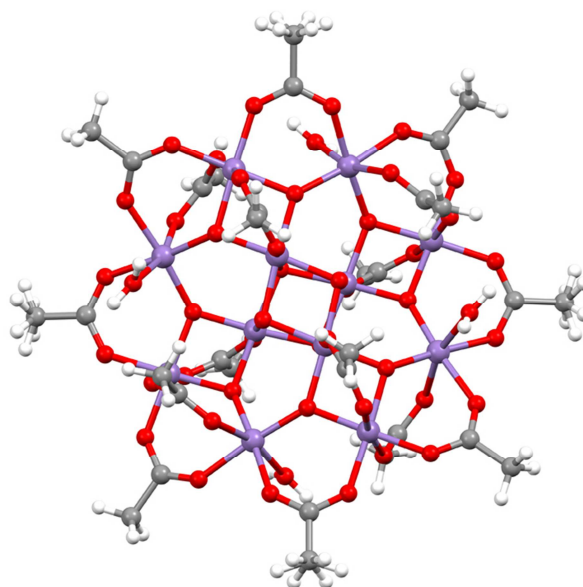


Figure 1.6, Molecular structure of the Mn_{12} cluster of the $[Mn^{III}_9Mn^{IV}_3O_{12}(O_2CH_3)_{16}(H_2O)_4] \cdot 4H_2O \cdot 2CH_3COOH$ system.

Since '90, in addition to the interest devoted to materials exhibiting a single physical property, relevant interest was also addressed to introduce multifunctionality in molecular materials. The most effective strategy to achieve these materials consists in combining two different organic or inorganic molecular networks, each one carrying a specific physical property. As far as the magnetic and conducting properties are concerned, the first example of such materials showing coexistence of two different physical properties, is the $[perilene]_2[M(mnt)_2]$ system.⁴⁶ In 1995, Day *et al.* reported the first paramagnetic superconductor, the radical cation salt $[BEDT-TTF]_4[(H_2O)Fe(ox)_3] \cdot C_6H_5CN$,⁴⁷ whereas the first ferromagnetic metal-like conductor, the $[BEDT-TTF]_3[MnCr(ox)_3]$ systems, has been obtained in 2000 by Coronado *et al.*⁴⁸ The latter consists in single layers of the heterobimetallic anionic polymer $[MnCr(ox)_3]^-$, responsible for the ferromagnetic properties, and layers of the partially oxidized BEDT-TTF, responsible for the conducting properties (Figure 1.7). Interactions between the conducting and magnetic properties were observed in 2001 by Kobayashi *et al.* in the λ - $[BETS]_2[FeCl_4]$ system.⁴⁹ In this system the interactions between the delocalized π -electrons of the BETS molecules and the magnetic moments generated by the d -electrons of the Fe^{III} metal ions are likely responsible for the induced superconductivity at low temperature ($T_c = 0.1$ K) under high magnetic fields (> 17 T) parallel to the direction of the conducting layers (Figure 1.7).

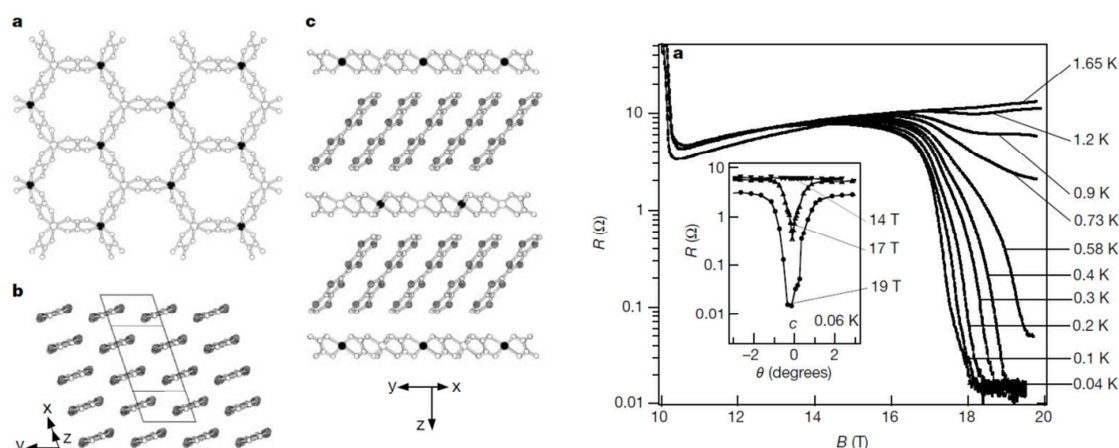


Figure 1.7, Left: View of the (a) inorganic, and (b) organic networks of $[\text{BEDT-TTF}]_3[\text{MnCr}(\text{C}_2\text{O}_4)_3]$, and (c) global view of its crystal structure. Right: conductivity measurements as a function of the magnetic field at different temperatures for λ - $[\text{BETS}]_2[\text{FeCl}_4]$. Inset shows the influence of magnetic fields higher than 17 T on the electrical conductivity. Adapted with permission from ref. 48,49. Copyright 2000 and 2001 Macmillan Magazines Ltd.

Of recent interest in the field of functional molecular materials is the introduction of chirality. Chirality can reduce the structural disorder that can be observed in achiral systems improving the conducting properties, as demonstrate in 2005 by Fourmigué, Avarvari *et al.* with the (*S*)-, (*R*)- or (*rac*)- $[\text{EDT-TTF-methyl-oxazoline}]_2\text{AsF}_6$ systems.^{50,51} In this family of radical cation salts, the enantiopure forms show electrical conductivity one order of magnitude higher than the racemic one (Figure 1.8).

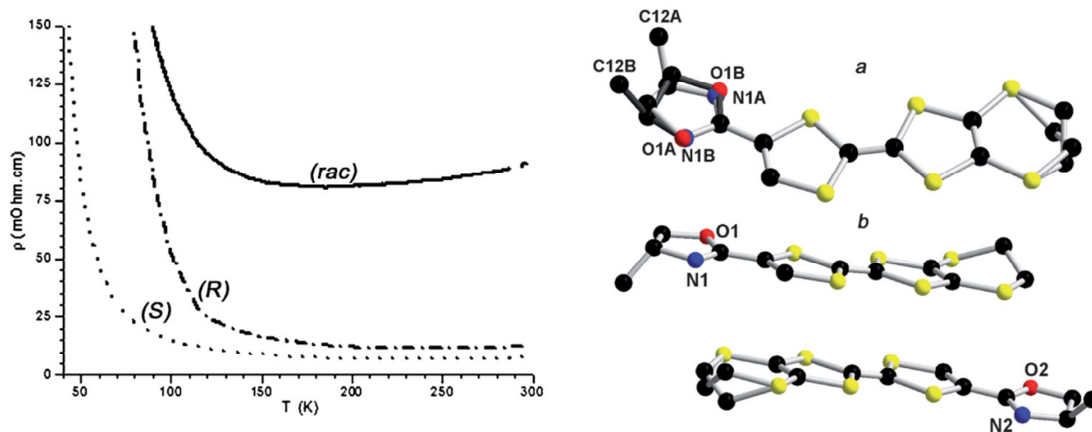


Figure 1.8, Left, Conductivity measurements for the (*R*)-, (*S*)-, and (*rac*)- $[\text{EDT-TTF-methyl-oxazoline}]_2\text{AsF}_6$ systems where the difference in the conductivity values is highlighted. Right, Molecular structures for the (*R*)-, (*S*)- and (*rac*)- $[\text{EDT-TTF-methyl-oxazoline}]_2\text{AsF}_6$. Adapted with permission from ref. 41. Copyright 2009 Royal Chemical Society.

Among the chiral systems, of special interest is also the $[(S,S,S)\text{-TM-BEDT-TTF}]_x[\text{MnCr}(\text{ox})_3] \cdot \text{CH}_2\text{Cl}_2$ system reported in 2010 by Coronado *et al.* (Figure 1.9), where coexistence of metal-like conductivity and chirality, due to the presence of layers of the (*S,S,S*)-TM-BEDT-TTF chiral donor showing metal-like conductivity, and ferromagnetism, due to the presence of heterobimetallic $[\text{MnCr}(\text{ox})_3]^-$ layers, has been observed for the first time in a multifunctional material.⁵²

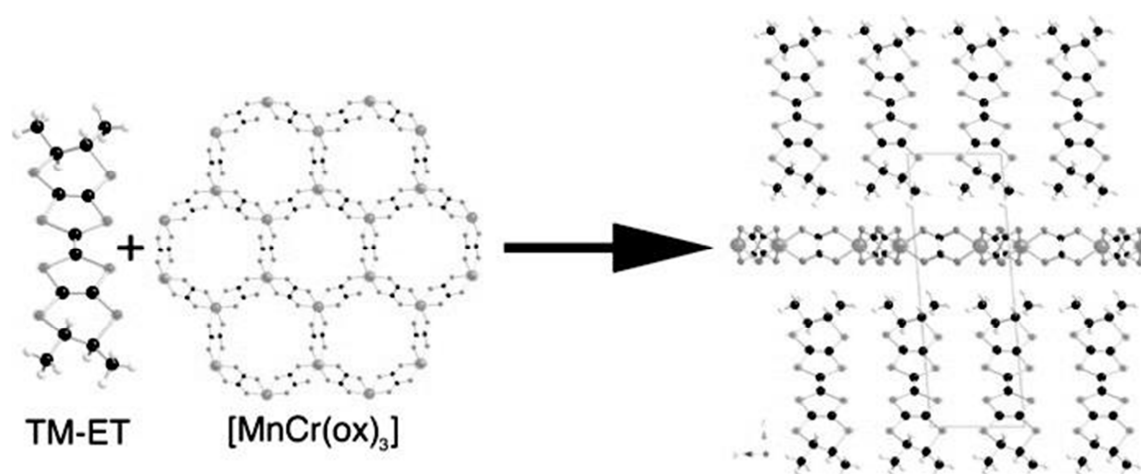


Figure 1.9, Schematic representation of the molecular building blocks (left) and the hypothesized crystal structure (right) for the $[(S,S,S,S)\text{-TM-BEDT-TTF}]_x[\text{MnCr}(\text{C}_2\text{O}_4)_3]\cdot\text{CH}_2\text{Cl}_2$ system. Reprinted with permission of ref. 52. Copyright 2010 American Chemical Society.

Introducing chirality in such systems is also very challenging since it can affect the electromagnetic properties of the resulting materials. The first evidence of the influence of chirality on the electromagnetic properties of a nanomaterial has been established by Rikken^{53,55} who predicted and demonstrated electrical magneto-chiral anisotropy in chiral carbon nanotubes, *i.e.* a difference in the resistance of the two enantiomers was observed when the magnetic field was coaxial with the nanotube. Since recently, this was the only known example of this effect at the molecular scale. In 2014, Avarvari, Rikken *et al.* succeeded in demonstrating, for the first time, this effect in the (S,S) - or (R,R) -[DM-EDT-TTF]₂ClO₄ molecular material. This system, where the two enantiomers show eMChA effect with anisotropy factors opposite in sign, but equal in magnitude, field, and current dependencies (Figure 1.10), represents the most recent and significant advance in this field.⁵⁶

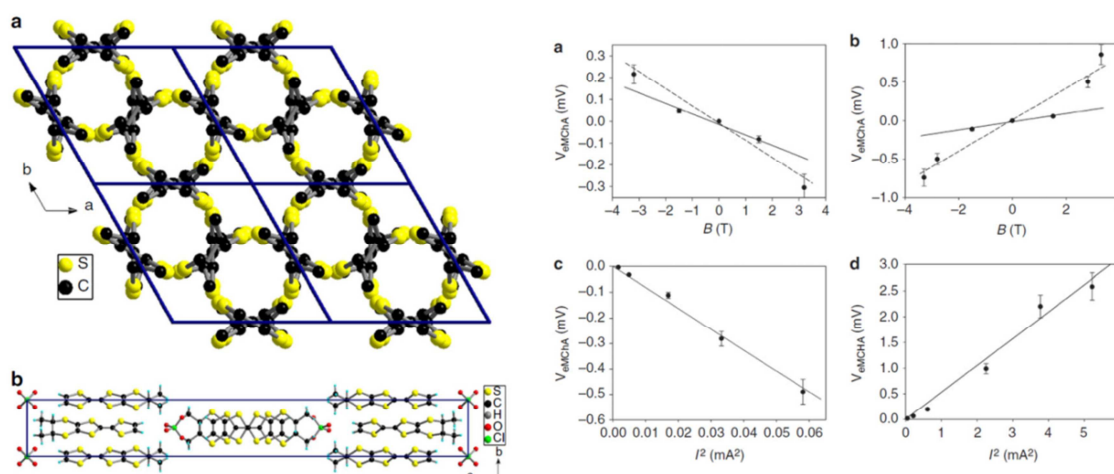


Figure 1.10, Views of the crystal structure (right) and eMChA results (left) for compounds (S,S) - and (R,R) -[DM-EDT-TTF]₂[ClO₄]. Adapted with permission from ref. 56. Copyright 2014 Macmillan Publishers Limited.

1.3 Aim of the Work

In view of the important perspectives in both fundamental science and applications of molecular materials in molecular electronics, the aim of the present work is to explore the potential of anilate-based ligands in the synthesis of new rational designed functional molecular materials exhibiting improved magnetic and conducting properties.

This family of ligands comprises several derivatives obtained by introducing various substituents (H, F, Cl, Br, I, CN, Me, NO₂, etc.) at the 3 and 6 positions of a common 2,5-dihydroxy-1,4-benzoquinone framework. Among the several classes of organic and inorganic molecular building blocks whose molecular materials are based, anilates have been selected as ligands since their electronic/structural features, coordination modes and ability to mediate magnetic exchange interactions between coordinated metal centers make them potential candidates for the preparation of the above-mentioned materials. In fact, despite they are well-known ligands in coordination chemistry, their ability to work as components of molecular materials with appealing magnetic and/or conducting properties is still unexplored and worth to be investigated.

The research has been particularly addressed to:

- select suitable anilate ligands, among those already known in the literature, as promising ligands for the design and the preparation of novel paramagnetic tris-chelated octahedral mononuclear metal complexes as molecular building blocks;
- functionalize the anilate moiety with various substituents with the aim to introduce new properties on the ligands and the resulting metal complexes;
- use the obtained anilate-based molecular building blocks for the preparation of new molecule-based magnets showing chemical and structural features suitable for obtaining multifunctional molecular materials;
- combine the above-mentioned magnetic building blocks with TTF-based organic donors, such as BEDT-TTF or its chiral derivatives, as conductivity carriers, to achieve hybrid multifunctional materials where magnetic and conducting properties coexist or interact in the same material.

Specific attention has been devoted to investigate structure/properties relationships in the obtained materials with the support of theoretical calculation analyses. Moreover, the influence of the chirality on the conducting properties, as well as the role of supramolecular non-covalent interactions on the physical properties of such materials, as topics of current special interest, have been also investigated. All these aspects are of fundamental importance in drawing up the guidelines for designing new anilate-based functional materials with improved physical properties.

References

1. Wickmann, H. H.; Trozzolo, A. M. M.; Hull, G. W.; Merritt, F. R. *Phys. Rev.* **1967**, *155*, 563.
2. Wickmann, H. H. *J. Chem. Phys.* **1972**, *56*, 976.
3. Defotis, G. C.; Palacio, F.; O' Connor, C. J.; Bhaatia, S. N.; Carlin, R. L. *J. Am. Chem. Soc.* **1977**, *99*, 8314–8315.
4. Arai, N.; Sorai, M.; Suga, H.; Seki, S. *J. Phys. Chem. Solids* **1977**, *36*, 1231.
5. Bousseksou, A.; Molnár, G.; Salmon, L.; Nicolazzi, W. *Chem. Soc. Rev.* **2011**, *40*, 3313–3335.
6. Halcrow, A. M. *Chem. Soc. Rev.* **2011**, *40*, 4119–4142.
7. Nihei, M.; Shiga, T.; Maeda, Y.; Oshio, H. *Coord. Chem. Rev.* **2007**, *251*, 2606–2621.
8. Gütlich, P.; Ksenofontov, V.; Gaspar, A. B. *Coord. Chem. Rev.* **2005**, *249*, 1811–1829.
9. Williams, J. M.; Ferraro, J. R.; Thorn, R. J.; Carlson, K. D.; Geiser, U.; Wang, H. H.; Kini, A. M.; Whangbo, M. H. *Organic Superconductors* **1992**. Englewood Cliffs: Prentice Hall.
10. Coronado, E.; Day, P. *Chem. Rev.* **2004**, *104*, 5419–5448.
11. Enoki, T.; Miyazaki, A. *Chem. Rev.* **2004**, *104*, 5449–5478.
12. Kobayashi, H.; Cui, H. B.; Kobayashi, A. *Chem. Rev.* **2004**, *104*, 5265–5288.
13. Mercuri, M. L.; Deplano, P.; Serpe, A.; Artizzu, F. Chapter 7 in *Handbook of Multifunctional Molecular Materials, Multifunctional Nanomaterials of interest in Electronics* **2013**, 219–280; Ouahab, L., Ed.; Pan Stanford Publishing: Singapore.
14. Miller, J. S.; Drillon, M. *Magnetism: Molecules to Materials* **2004**, Wiley-VCH, Weinheim, Vol. 1–5.
15. Prasad, P. N.; Williams, D. J.; *Introduction of Nonlinear Optical Effects in Molecules and Polymers* **1991**, J. Wiley and Sons, New York.
16. Chemla, D. S.; Zyss, J.; *Nonlinear Optical Properties of Organic Molecules and Crystals* **1987**, Academic Press, New York, Vol. 1,2.
17. Curry, R. J.; Gillin, W. P. *Appl. Phys. Lett.* **1999**, *75*, 1380–1382.
18. Gillin, W. P.; Curry, R. J. *Appl. Phys. Lett.* **1999**, *74*, 798–799.
19. Mitscke, U.; Bauerle, P. *J. Mater. Chem.* **2000**, *10*, 1471–1507.
20. Kelley, T. W.; Baude, P.F.; Gerlach, C.; Ender, D. E.; Muyres, D.; Haase, M. A.; Vogel, D. E.; Theiss, S. D. *Chem. Mater.* **2004**, *16*, 4413–4422.
21. Clemente-León, M.; Coronado, E.; Martí-Gastaldo, C.; Romero, F. M. *Chem. Soc. Rev.* **2011**, *40*, 473–497.
22. Knop, W. *Justus Liebig's Ann. Chem.* **1842**, *43*, 111.
23. Krogmann, K.; Hausen, H. D. Z., *Anorg. Allg. Chem.* **1968**, *358*, 67.
24. Coleman, L. B.; Cohen, M. J.; Sandman, D. J.; Yamagishi, F. G.; Garito, A. F.; Ferris, A. J. *Solid State Commun.* **1973**, *12*, 1125–1202.
25. Farris, A. J.; Cowan, D. O.; Walatka Jr., V.; Perlstein, J. H. *J. Am. Chem. Soc.* **1973**, *95*, 948–949.
26. Jerome, D.; Mazaud, M.; Ribault, M.; Bechgaard, K. *J. Phys. Lett.* **1980**, *L95*, 1416.
27. Kini, A. M.; Geiser, U.; Wang, H. H.; Carlson, K. D.; Williams, J. M.; Kwok, W. K.; Vandervoort, K. G.; Thompson, J. E.; Stupka, D. L.; Jung, D.; Whangbo, M. H. *Inorg. Chem.* **1990**, *29*, 2555–2557.

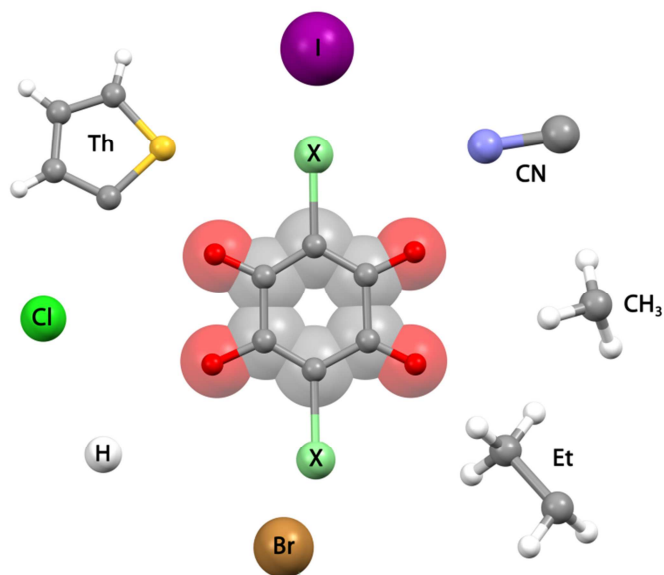
28. Underhill, A. E.; Ahmad, M. M. *J. Chem. Soc. Chem. Commun.* **1981**, 67–68.
29. Brossard, L.; Ribault, M.; Bousseau, M.; Valade, L.; Cassoux, P. *C. R. Acad. Sci. Paris, Série II* **1986**, 302, 205.
30. Ito, A.; Suenaga, M.; Ono, K. *J. Chem. Phys.* **1968**, 48, 3597.
31. Verdaguer, M.; Girolami, G. S. *Magnetic Prussian Blue Analogues*, Chapter 9 in *Magnetism: Molecules to Materials* **2005**, Wiley-VCH, Weinheim, Vol. 5. Edited by J. S. Miller and M. Drillon.
32. Candela, G. A.; Swartzendruber, L. J.; Miller, J. S.; Rice, M. J. *J. Am. Chem. Soc.* **1979**, 101, 2755–2756.
33. Miller, J. S.; Epstein, A. J.; Reiff, W. M. *Mol. Cryst. Liq. Cryst.* **1985**, 120, 27.
34. Miller, J. S.; Calabrese, J. C.; Epstein, A. J.; Bigelow, R. W.; Zhang, J. H.; Reiff, W. M. *J. Chem. Soc., Chem. Commun.* **1986**, 1026.
35. Miller, J. S. *Organic and Molecule-based Magnets* **2006**, 67, 1–16.
36. Helms, J. H.; Hatfield, W. E.; Kwiecien, M. J.; Reiff, W. M. *J. Chem. Phys.* **1986**, 84, 3994.
37. Burriel, R.; Casabo, J.; Pons, J.; Carnegie, D. E.; Carlin, R. L. *Physica* **1986**, 132B, 185.
38. Caneschi, A.; Gatteschi, D.; Renard, J. P.; Rey, P.; Sessoli, R. *Inorg. Chem.* **1989**, 28, 1976–1980.
39. Nakatani, K.; Carriat, J. Y.; Journaux, Y.; Khan, O.; Lloret, F.; Renard, J. P.; Pei, Y.; Slettern, J.; Verdaguer, M. *J. Am. Chem. Soc.* **1989**, 111, 5739–5748.
40. Gadet, V.; Mallah, T.; Castro, I.; Verdaguer, M. *J. Am. Chem. Soc.* **1992**, 114, 9213–9214.
41. Ferlay, S.; Mallah, T.; Ouahes, R.; Veillet, P.; Verdaguer, M. *Nature* **1995**, 378, 701–703.
42. Buschmann, W. E.; Zhang, J.; Manson, J. L.; Miller, J. S. *Adv. Mater.* **1999**, 121, 5593–5594.
43. Tamaki, H.; Zhong, Z. J.; Matsumoto, N.; Kida, S.; Koikawa, M.; Achiwa, N.; Hashimoto, Y.; Okawa, H. *J. Am. Chem. Soc.* **1992**, 114, 6974–6979.
44. Pilkington, M.; Decurtins, S. *Oxalate-based 2D and 3D Magnets*, Chapter 10 in *Magnetism: Molecules to Materials* **2002**, Wiley-VCH, Weinheim, Vol. 2. Edited by J. S. Miller and M. Drillon.
45. Sessoli, R.; Gatteschi, D.; Caneschi, A.; Novak, M. A. *Nature* **1993**, 365, 141–143.
46. Almeida, M.; Henriques, R. *Handbook of Organic Conductive Molecules and Polymers* **1997**, Vol. 1, 87, Ed. H. S. Nalwa, J. Eiley, New York.
47. Kurmoo, M.; Graham, A. W.; Day, P.; Coles, S. J.; Hursthouse, M. B.; Caulfield, J. L.; Singleton, J.; Pratt, F. L.; Hayes, W.; Ducasse, L.; Guionneau, P. *J. Am. Chem. Soc.* **1995**, 117, 12209–12217.
48. Coronado, E.; Galán-Mascarós, J. R.; Gómez-García, C. J.; Laukhin, V. *Nature* **2000**, 408, 447–449.
49. Uji, S.; Shinagawa, H.; Terashima, T.; Yakabe, T.; Terai, Y.; Tokumoto, M.; Kobayashi, A.; Tanaka, H.; Kobayashi, H. *Nature* **2001**, 410, 908–910.
50. Réthoré, C.; Fourmigué, M.; Avarvari, N. *Tetrahedron* **2005**, 61, 10935–10942.
51. 10935.Avarvari, N.; Wallis, J. D. *J. Mater. Chem.* **2009**, 19, 4061–4076.
52. Galán-Mascarós, J. R.; Coronado, E.; Goddard, P. A.; Singleton, J.; Coldea, A. I.; Wallis, J. D.; Coles, S. J.; Alberola, A. *J. Am. Chem. Soc.* **2010**, 132, 9271–9273.
53. Krstic, V.; Roth, S.; Burghard, M.; Kern, K.; Rikken, G. L. J. A. *J. Chem. Phys.* **2002**, 117, 11315–11319.
54. Krstic, V.; Rikken, G. L. J. A. *Chem. Phys. Lett.* **2002**, 364, 51.
55. Rikken, G. L. J. A.; Folling, J.; Wyder, P. *Phys. Rev. Lett.* **2001**, 87, 236602.
56. Pop, F.; Auban-Senzier, P.; Canadell, E.; Rikken, G. L. J. A.; Avarvari, N. *Nature Commun.* **2014**, 5, 3757.

Part II

Results and Discussion

Chapter 1

Anilate-based Ligands



In this Chapter a brief introduction on the chemistry of anilate-based ligands is reported, along with the synthesis of novel anilate derivatives having thiophene (Th), 3,4-ethylenedioxy-thiophene (EDOT), or Cl/CN substituents connected to the anilate moiety. The crystal structures, the investigation of the emission (Cl/CN derivative) or charge-transfer (Th and EDOT derivatives) properties, and the electrochemical and preliminary coordination chemistry studies of these derivatives are also presented here.

1.1 Introduction

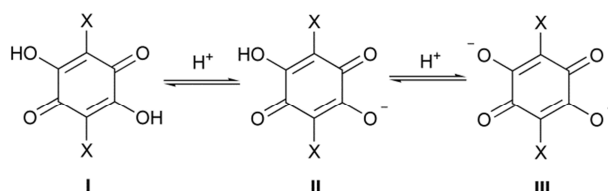
Derivatives of the 2,5-dioxy-1,4-benzoquinone framework containing various substituents at the positions 3 and 6 constitute a well-known motif present in many natural products showing important biological activities such as anticoagulant,¹ antidiabetic,² antioxidative,³ anticancer,⁴ etc. Structural modifications of the natural products afforded related compounds of relevant interest in medicinal chemistry.^{5,6} Furthermore, the 2,5-dihydroxy-1,4-benzoquinone (DHBQ) represents the parent member of a family of organic compounds traditionally called anilic acids that, in their deprotonated dianionic form, act as valuable ditopic ligands towards transition metal ions.⁷

Anilic acids are obtained when the hydrogens on the 3 and 6 positions of the DHBQ are replaced by halogen atoms or functional groups. Their molecular formula can be represented as $H_2X_2C_6O_4$ (H_2X_2An) where X indicates the substituent and C_6O_4 indicates the anilate moiety (An) (Table 1.1).

Table 1.1, Names, molecular formulas and acronyms of the anilic acids reported in the literature to date.

Substituent, X	Formula	Anilic Acid Name	Acronyms	Anilate Dianion Name	Acronyms	Ref.
H	$H_4C_6O_4$	Hydranilic acid	H_2H_2An	Hydranilate	H_2An^{2-}	8-10
F	$H_2F_2C_6O_4$	Fluoranilic acid	H_2F_2An	Fluoranilate	F_2An^{2-}	11
Cl	$H_2Cl_2C_6O_4$	Chloranilic acid	H_2Cl_2An	Chloranilate	Cl_2An^{2-}	12
Br	$H_2Br_2C_6O_4$	Bromanilic acid	H_2Br_2An	Bromanilate	Br_2An^{2-}	13
I	$H_2I_2C_6O_4$	Iodanilic acid	H_2I_2An	Iodanilate	I_2An^{2-}	13
NO_2	$H_2N_2C_6O_8$	Nitranilic acid	$H_2(NO_2)_2An$	Nitranilate	$(NO_2)_2An^{2-}$	14
OH	$H_4C_6O_6$	Hydroxyanilic acid	$H_2(OH)_2An$	Hydroxyanilate	$(OH)_2An^{2-}$	15-19
CN	$H_2N_2C_8O_4$	Cyananilic acid	$H_2(CN)_2An$	Cyananilate	$(CN)_2An^{2-}$	20,21
Cl/CN	$H_2ClNC_7O_4$	Chlorocyananilic acid	$H_2ClCNAn$	Chlorocyananilate	$ClCNAn^{2-}$	22
NH_2	$H_6N_2C_6O_4$	Aminanilic acid	$H_2(NH_2)_2An$	Aminanilate	$(NH_2)_2An^{2-}$	23
CH_3	$H_8C_8O_4$	Methylanilic acid	H_2Me_2An	Methylanilate	Me_2An^{2-}	24
CH_2CH_3	$H_{12}C_{10}O_4$	Ethylanilic acid	H_2Et_2An	Ethylanilate	Et_2An^{2-}	24
<i>iso-C</i> ₃ H ₇	$H_{16}C_{12}O_4$	Isopropylanilic acid	$H_2iso-Pr_2An$	Isopropylanilate	<i>iso-Pr</i> ₂ An^{2-}	25
C_6H_5	$H_{12}C_{18}O_4$	Phenylanilic acid	H_2Ph_2An	Phenylanilate	Ph_2An^{2-}	9,26

Anilic acids (I) undergo a mono and double deprotonation process of the two hydroxyl groups giving rise to the monoanionic (II) and dianionic (III) forms shown in Scheme 1.1.



Scheme 1.1, Protonation equilibria for a generic anilic acid.

The form III prevails in aqueous media due to the strong resonance stabilization of the negative charge (*vide infra*).

The coordination chemistry of the anilic acids in their dianionic form (anilate ligands) is described in the literature with particular attention to the DHBQ²⁻ (H₂An²⁻) and its chloro derivative, chloranilate (Cl₂An²⁻).⁷ Due to their versatile coordination modes, several types of metal complexes ranging from discrete mononuclear systems to extended polymeric systems, showing a large variety of peculiar crystal structures and properties, were obtained so far.⁷

The physical properties of the molecular materials that stem from these anilate-based derivatives are dominated by (i) the presence of various substituents in the anilate moiety that furnish diverse intermolecular interactions (H-Bonding, Halogen-Bonding, π - π stacking and dipolar interactions) in the resulting material, (ii) their interesting redox properties,²⁷ (iii) their ability of mediating magnetic superexchange interactions when the ligand coordinates two metals ions in the 1,2-bis-bidentate coordination mode, and (iv) the possibility of modulating the strength of this magnetic superexchange interaction by varying the nature of the substituents (X) on the 3,6 positions of the anilate-ring.²⁸ These features provide an effective tool for engineering a great variety of new anilate-based materials showing peculiar physical properties. Furthermore, uncoordinated anilic acid have been also used as molecular building blocks for obtaining different types of functional materials such as organic ferroelectrics or as a component of charge transfer salts.²⁹⁻³³

1.1.1 Synthesis of Anilic Acids and their Molecular Structures

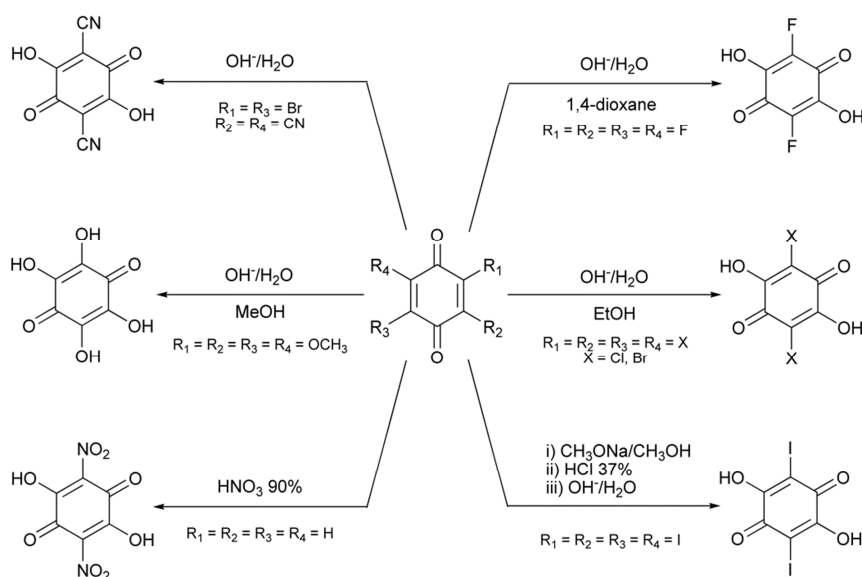
Despite the remarkable similarity in their molecular structure (*vide infra*), the various substituted anilic acids cannot be prepared by a common synthetic procedure. In the following, an overview of the synthetic methods reported in the literature to achieve the anilic acids described in Table 1.1 is reported (Schemes 1.2 and 1.3).

H₂H₂An can be obtained in good yields (70–80%) by treatment of hydroquinone in concentrated sodium hydroxide solution with 30% hydrogen peroxide.^{8,9} Alternatively, it can be also obtained by treatment of resorcinol in acetic acid with 11% peracetic acid (70% yield).¹⁰ H₂X₂An (X = F, Cl, Br) can be synthesized following a common synthetic method consisting in the treatment of the corresponding 2,3,5,6-tetrahalo-1,4-benzoquinone, C₆X₄O₂ (X = F, fluoranil; Cl, chloranil; Br, bromanil), in ethanolic (X = Cl, Br) or dioxane solution (X = F) with concentrated sodium or potassium hydroxide solutions.^{11,12} H₂I₂An cannot be obtained by simple basic hydrolysis of iodanil as described for the other haloanilic acids. The synthesis of H₂I₂An consists in the preparation of the sodium salt of the diiodo-dimethoxy-dimethylhemiacetal by treatment of iodanil with sodium methoxide, then the hemiacetal is isolated by acidification and then treated with sodium hydroxide. This generates the sodium salt of the iodanilate dianion and the corresponding iodanilic acid can be isolated by acidification.¹³

H₂(NO₂)₂An is obtained by treatment of 1,4-benzoquinone with fuming nitric acid,¹⁴ whereas H₂(NH₂)₂An can be obtained by treatment of 2,3,5,6-tetrahydroxy-1,4-phenylene-diammonium chloride in a EtOH/H₂O 1:1 mixture with 2,4-dinitrophenolate or sodium picrate.²³

Among the synthetic methods used to prepare $H_2(OH)_2An$, also known as tetrahydroxy-1,4-benzoquinone, there seems to be a lot of confusion arising from the contradictory results published in the past. The first method used to obtain this product consists in the oxidation of inositol with fuming nitric acid, a reaction difficult to control that leads to a mixture of several products difficult to separate.¹⁵⁻¹⁷ Moreover, the various obtained products, including $H_2(OH)_2An$, are not very stable in aqueous media and are reactive toward oxygen. In particular, $H_2(OH)_2An$ can undergo a cyclic rearrangement leading to the croconate dianion ($C_5O_5^{2-}$).^{15,34} Two alternative methods for the synthesis of $H_2(OH)_2An$ consist in the self-condensation of the glyoxal in an aqueous solution of sodium sulphite and sodium bicarbonate in the presence of oxygen (10% yield),¹⁸ or in the basic hydrolysis of tetramethoxy-1,4-benzoquinone obtained from chloranil.¹⁹

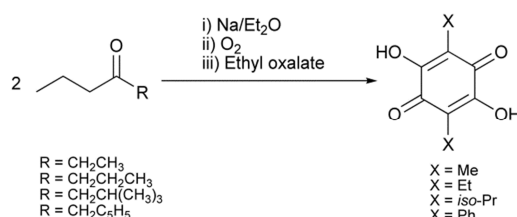
The first report on the synthesis of $H_2(CN)_2An$ claims that this compound can be prepared by treatment of chloranil with potassium cyanide in a 80% methanol solution in water.³⁵ The product obtained through this reaction is instead the 2,3-dicyano-5,6-dichloro-1,4-dihydroxybenzene as successively demonstrated by Wallenfels *et al.*, which also proposed a mechanistic pathway for the above mentioned reaction.²⁰ Wallenfels described an alternative synthesis for obtaining $H_2(CN)_2An$ based on the basic hydrolysis of 2,5-dicyano-3,6-dibromo-1,4-benzoquinone.²⁰ An alternative synthesis of 2,5-dicyano-3,6-dibromo-1,4-benzoquinone, the precursor for the synthesis of $H_2(CN)_2An$, was more recently reported.²¹



Scheme 1.2. Overview of the synthetic procedures for the preparation of the H_2X_2An ($X = F, Cl, Br, I, NO_2, OH, CN$) anilic acids. The corresponding anilate dianions, generated in solution, afford the protonated forms by simple acidification.

The syntheses of H_2X_2An ($X = Me, Et$) consist in an acyloin condensation between ethyl propionate ($X = Me$) or ethyl butyrate ($X = Et$) followed by cyclization with ethyl oxalate.²⁴ H_2X_2An ($X = iso-Pr, Ph$) were synthesized by a different author using a similar method as the one described for the Me and Et derivatives. This method consists in using ethyl isovalerate and ethyl phenylacetate as starting materials for the acyloin condensation in presence of ethyl oxalate, for the preparation of $H_2iso-Pr_2An$ and H_2Ph_2An , respectively (Scheme 1.3).^{25,26} The

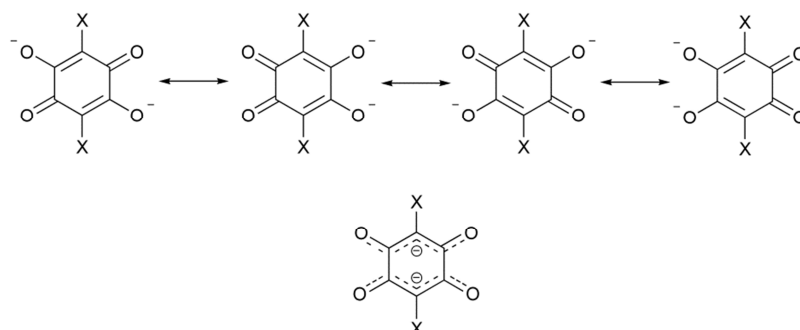
synthesis of H_2Ph_2An has been more recently described by using a synthetic strategy based on a Suzuki-Miyaura coupling reaction between 2,5-dimethoxy-3,6-dibromo-1,4-benzoquinone and phenylboronic acid.⁹



Scheme 1.3. Overview of the synthetic procedure for the preparation of the H_2X_2An ($X = Me, Et, iso-Pr, Ph$) anilic acids.

The molecular and crystal structures of the anilic acids reported in Table 1.1 have been described.^{23,36-44} All structures of protonated anilic acids are characterized by similar features (i) a centrosymmetric quasi-quinonoid structure with $C=O$ and $C=C$ distances in the 1.215–1.235 Å and 1.332–1.355 Å ranges, respectively, (ii) a planar structure of the benzoquinone ring, and (iii) moderate-strong H-bonding and π -stacking interactions in the crystal structure.^{36-38,41-42} It should be noted that the crystal structures of $H_2(NO_2)_2An$ hexahydrate and $H_2(CN)_2An$ hexahydrate reveal the presence of hydronium nitranilates and hydronium cyananilates, respectively,^{39,40} as a result of their strong acidity (pK_a values for $H_2(NO_2)_2An$: -3.0 and -0.5).¹¹ The structure of the nitranilic acid hexahydrate is characterized by the presence of the Zundel cation, $(H_5O_2)_2^+$, whose proton dynamics has been recently studied by a multi-technique approach.⁴⁵ Interestingly, the structure of $H_2(NH_2)_2An$ reveals the presence of an highly polarized zwitterionic structure with the protons located on the amino groups.²³

The molecular and crystal structures of alkali metal salts of some anilic acids have also been reported.⁴⁶⁻⁵³ The X-ray analysis reveals that the carbon ring system for the anilates in their dianionic form assumes planar conformation but is not in a quinoidal form, having four $C-C$ bonds of equal length (1.404–1.435 Å range) and two considerably longer $C-C$ bonds (1.535–1.551 Å range) whose bond distances vary as a function of the substituents. Moreover, the four $C-O$ bonds are of equal length (1.220–1.248 Å range). This description can be represented with four resonance structures that, in turn, can be combined in one form with delocalized π -electrons along the $O-C(-X)-C-O$ bonds (Scheme 1.4).^{39,40,46,47}



Scheme 1.4. Resonance structures for a generic anilate dianion. The π -electron delocalization over the $O-C(-X)-C-O$ bonds is highlighted.

The crystal structures of the anilate anions are dominated by π -stacking interactions between quinoid rings. Since the dianions are characterized by (i) π -electron delocalization on the O–C–C(–X)–C–O bonds and (ii) strong repulsion due to double negative charges, their crystal structures are dominated by parallel offset π – π stacking arrangement, similarly to what found in aromatic systems.^{49,50} Monoanionic alkali salts are, instead, able to stack in a perfect face-to-face parallel arrangement with no offset, where single bonds are sandwiched between double bonds and *vice versa*, with short distances of the ring centroids (3.25–3.30 Å), as thoroughly described by Molčanov *et al.* (Figure 1.1).^{49,50,53} This arrangement minimizes π -electrons repulsions while maximizes σ – π and dipolar attractions.⁵⁰

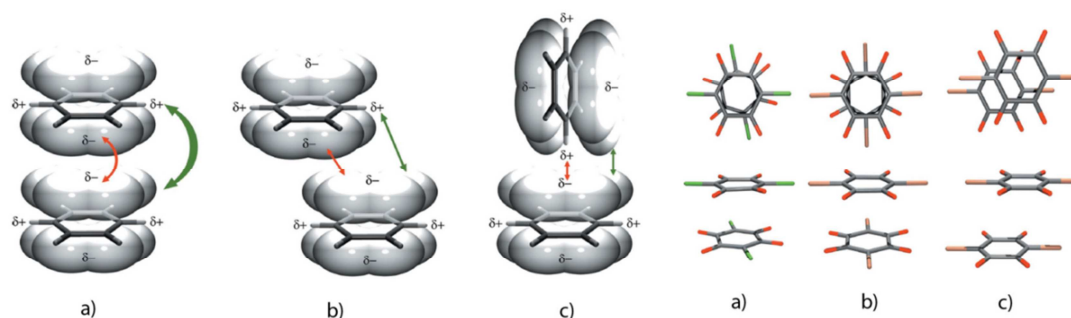


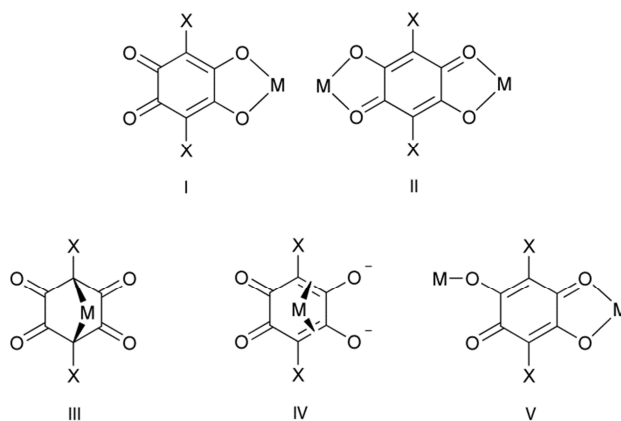
Figure 1.1. Left, Attractive $s \cdots p$ (green) and repulsive $p \cdots p$ (red) interactions between two generic aromatic rings in three different π -stacking arrangements: a) parallel face-to-face with no offset, b) parallel face-to-face with offset, c) T-shaped. Right, Top-down (upper row) and side view (lower row) of pairs of quinoid rings: a) HClAn[–] anions in KHClAn·2H₂O⁵³ stacked in a nearly eclipsed fashion, b) HBrAn[–] anions in RbHBrAn·3H₂O⁵⁰ in a staggered arrangement, c) Br₂An^{2–} dianions in K₂Br₂An·2H₂O⁵⁰ in an offset stack geometry similar to aromatic π -interactions. Adapted with permission from ref. 35. Copyright 2009 Royal Society of Chemistry.

It should be highlighted that the alkali salts of the H₂An^{2–} dianion do not follow the stacking arrangement observed in their halo-derivatives (X = Cl, Br). In fact, they stack in a parallel face-to-face π -stacking with no offset as observed for the monoanionic forms of chloranilate and bromanilate alkali salts.⁵¹ The eclipsed orientation of the H₂An^{2–} rings can be due to the additional attraction between antiparallel dipoles of the C–O and C–H bonds, not present in the halo-derivatives, whereas the repulsions are minimised by larger ring separations.⁵¹

1.1.2 Coordination modes of the anilate dianions

The wide variety of crystal structures obtained so far using anilate dianions is mainly due to the different coordination modes exhibited by these ligands. Anilates dianions can coordinate in the (i) 1,2-bidentate coordination mode (I) where the ligand assumes the *o*-quinone-like form with coordinating C–O bonds that are considerably longer than the peripheral uncoordinated C–O bonds, (ii) bis-1,2-bidentate coordination mode (II) where the ligand acts as bridging ligand and assumes the localized *p*-quinone-like form or the delocalized form represented in Scheme 1.4, depending on the coordinated metals and the nature of the additional co-ligands when they are present, (iii) 1,4-bidentate coordination mode (III) where the ligand coordinates by means of the carbon atoms in the 1,4-positions assuming the bis-carbanion form, (iv) π -

bonding coordination mode (**IV**) where the ligand assumes the *o*-quinone-like form and coordinates the metal through localized π -electrons, (v) 1,2-bidentate/monodentate coordination mode (**V**) where the ligand acts as a bridging ligand between two metals binding a metal in a 1,2-bidentate mode and the other metal on the opposite side of the ring in a monodentate fashion (Scheme 1.5).⁷



Scheme 1.5. Coordination modes exhibited by the anilate dianions: 1,2-bidentate (**I**), bis-1,2-bidentate (**II**), 1,4-bidentate (**III**), π -bonding (**IV**), 1,2-bidentate/monodentate (**V**).

It should be pointed out that among the described coordination modes, **I** and **II** are the most common, whereas **III**, **IV** and **V** have been only rarely observed.

1.1.3 Selected and Novel Anilate Ligands

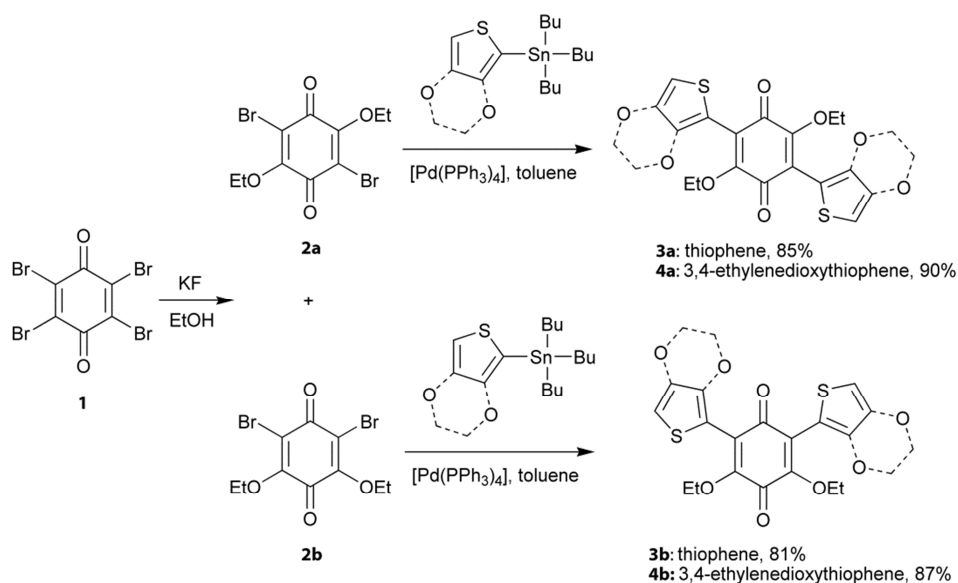
As already stated in the Aim of the Work Section, the goal of the present work is to explore the potential of anilate-based ligands to afford new molecular building blocks for constructing functional molecular materials with new or improved physical properties. Among the various anilic acids already known in the literature, the H_2X_2An derivatives with $X = Cl, Br, I,$ and H , were selected as suitable ligands for the preparation of such materials. H_2Cl_2An (**L1**) and H_2H_2An (**L4**) are commercially available and were purchased and used without further purification, whereas H_2Br_2An (**L2**) and H_2I_2An (**L3**) were synthesized according to the literature methods.^{12,13} Furthermore, since the X substituents of the X_2An^{2-} anilate ligands currently employed in coordination chemistry are only electron withdrawing groups, part of this work was addressed to introduce at the 3,6 positions of the 2,5-dioxybenzoquinone ring electron rich substituents; this may provide additional properties to the ligands and the corresponding metal complexes. In particular, the thiophene and ethylenedioxy-thiophene (EDOT) motifs were selected due to their planar conjugated structure, prone to promote intramolecular charge transfer (CT) towards the electron poor benzoquinone acceptor, and to provide an access to electroactive metal complexes. Moreover, the possibility to introduce luminescence properties into this family was investigated by replacing a chloro substituent on the chloranilate ligand with a cyano group. This rare example of asymmetric anilate ligand, the chlorocyananilate, was briefly described in the past without a detailed synthesis and analytical data.²² Moreover, neither its crystal structure was reported nor its luminescence properties were mentioned.

In this Chapter, synthesis, crystal structures, spectroscopic and electrochemical characterization of 3,6-bis(thiophene) or EDOT derivatives of 2,5-diethoxybenzoquinone, as well as those of their 3,5-substituted-2,6-diethoxybenzoquinone isomers are reported. Theoretical calculations at DFT level explain the differences observed in the absorption properties, and the synthesis of 3,6-bis(thiophene) (**L6**) and EDOT-anilate (**L7**) ligands is also described together with preliminary coordination chemistry studies. Moreover, a revised synthesis of the chlorocyananilate ligand (**L5**) is reported, along with its crystal structure, UV-Vis absorption and emission properties.

1.2 Results and Discussion

1.2.1 Synthesis

The 1,4-benzoquinone derivatives **3a,b** and **4a,b** were synthesized by palladium catalyzed Stille type coupling reaction between (*n*-Bu)₃Sn-R (**3a,b**, R = 2-thiophenyl; **4a,b**, R = 3,4-ethylenedioxy-2-thiophenyl) and either 2,5-dibromo-3,6-diethoxy-1,4-benzoquinone **2a** or 2,6-dibromo-3,5-diethoxy-1,4-benzoquinone **2b**, respectively (Scheme 1.6).



Scheme 1.6, Synthesis of thiophenyl (**3a,b**) and 3,4-ethylenedioxythiophenyl (**4a,b**) derivatives of 1,4-benzoquinone.

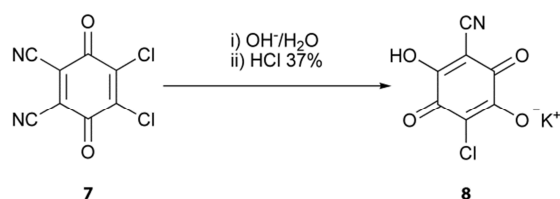
The dibromo derivatives **2a,b** used as starting materials for the coupling reactions were synthesized according to the synthetic procedure described by Wallenfels and Draber, originally reported for the preparation of **2a** as the only isomer.⁵⁴ In our case, by treating 2,3,5,6-tetrabromo-1,4-benzoquinone **1** (bromanil) with KF in EtOH (Scheme 1.6), the formation of two isomers, the 2,5-dibromo-3,6-diethoxy-1,4-benzoquinone **2a** and the 2,6-dibromo-3,5-diethoxy-1,4-benzoquinone **2b**, in a ca. 50:50 ratio (89% as total yield) was observed, in contrast with what was previously reported.⁵⁴ Although compounds **2a** and **2b**

have very close retention factors, they can be separated by column chromatography with the proper elution system (see Experimental Section). It is noteworthy that similar results were reported for the synthesis of 2,2,6,6-tetramethyl-1-piperidinyloxy (TEMPO) bis-substituted dibromobenzoquinone *para* and *meta* derivatives.^{55,56}

The final assignment as *para* (**2a**) and *meta* (**2b**) isomers was provided by single crystal X-ray analysis. Suitable crystals of **2a** were obtained by slow evaporation of a solution of **2a** in CH₂Cl₂. An ORTEP drawing and a summary of crystallographic data for **2a** are reported as Supplementary Material in Appendix 5 (Figure S1.1 and Table S1.1). Although initially the main objective was to access electron rich substituted *para*-anilates as precursors for anilate ligands, the substitution with both *para* and *meta* isomers was investigated in order to estimate the influence of the substituents position on the CT properties. Accordingly, the bis-Stille coupling reactions with **2a,b** and the tin based precursors of thiophene and EDOT provided the bis functionalized diethoxy-benzoquinones **3** and **4** in good yields as orange (**3a**), red (**4a**) or deep purple (**3b** and **4b**) crystalline solids. Stille type functionalization of the substrate **2a** has been previously described for the preparation of bis(indole) derivatives belonging to the family of fungal natural products astringinones,⁵⁷ while Suzuki-Miyaura coupling has been reported for the mono or bis-functionalization of the dimethoxy analogue of **2a** with phenyl-boronic acids.^{9,58}

The synthesis of the asymmetrically substituted chlorocyananilate (CICNAn²⁻) was briefly described in 1966,²² but, surprisingly, no metal complexes with this ligands have been reported to date, although its reactivity towards metal ions it is expected to be very similar to the symmetrically substituted chloranilate. Since the presence of cyano substituents directly connected to the benzoquinone moiety in its reduced form, 1,4-dihydroxybenzene, is known to induce highly luminescent properties,³⁵ this ligand was investigated in order to explore this aspect and the synthesis was revisited and supported by crystallographic structural data.

Chlorocyananilic acid can be easily obtained by treating 2,3-dicyano-5,6-dichloro-1,4-benzoquinone **7** with a concentrate water solution of potassium hydroxide, followed by acidification with concentrate acid (Scheme 1.7).



Scheme 1.7, Synthesis of the monoprotonated form of chlorocyananilic acid.

This method provides in good yield **L5** in its monoprotonated form HKCICNAn (**8**) as orange crystalline solid, representing the first example of an asymmetrically substituted anilate ligand. All attempts to isolate and crystallize the bis-protonated chlorocyananilic acid (H₂CICNAn) were unsuccessful. This is not surprising given the strong acidity of this ligand due to the presence of the cyano group (pK_a value for H₂(CN)₂An: -0.5),¹¹ which favors the anionic forms.

1.2.2 Crystal Structure Description

Single crystals for compounds **3a,b** and **4a,b** were obtained by slow evaporation of CH_2Cl_2 or $\text{CH}_2\text{Cl}_2/\text{MeOH}$ solutions. Compound **3a** crystallizes in the triclinic system, space group $P\bar{1}$, with one half independent molecule in the unit cell. The thiophene units are coplanar with the benzoquinone ring (Figure 1.1), very likely as a result of the conjugation between the aromatic thiophene substituents and the benzoquinone moiety, but also thanks to the establishment of intramolecular 1,5-nonbonded $\text{S}\cdots\text{O}$ interactions.⁵⁹⁻⁶⁴ Indeed, a very short $\text{S}\cdots\text{O}$ distance of 2.66 Å is observed. The preference for the $\text{S}\cdots\text{O}=\text{C}_{\text{quinone}}$ rather than $\text{S}\cdots\text{O}-\text{C}_{\text{alkoxy}}$ interactions is in agreement with previous theoretical calculations.⁶¹

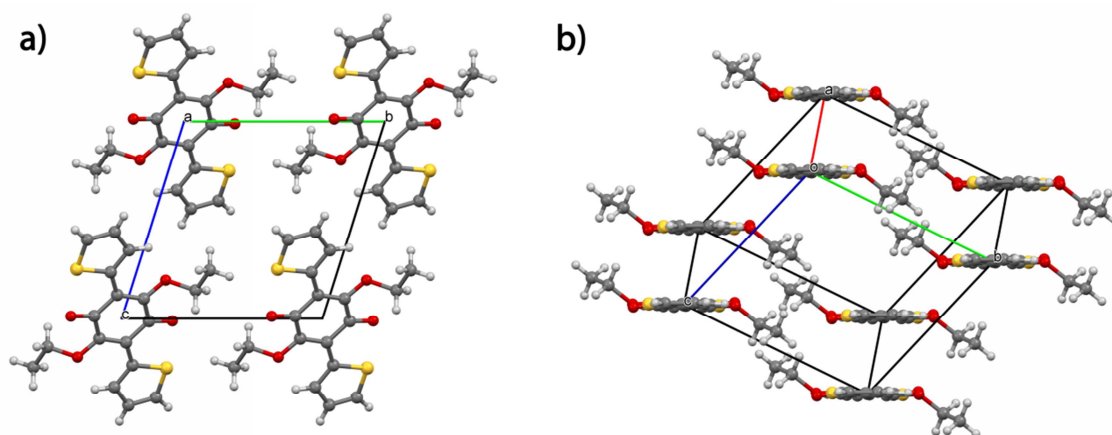


Figure 1.1, a) View of the crystal packing of **3a** in the bc plane; b) stacking of **3a** along the a axis.

Compound **3b** crystallizes in the monoclinic space group $P2_1/a$ with two independent molecules in the unit cell. Both independent molecules of the *meta*-substituted isomer do not show fully planar structures, as found in the *para* isomer **3a**, but they are slightly twisted, with dihedral angles between the plane formed by each thiophene and the benzoquinone ring of ca. 173° and 165°, and ca. 173° and 161° for the **A** and **B** molecules, respectively. Moreover, one of the thiophenes in molecule **A** is disordered with two different orientations presenting 0.64 and 0.36 site occupancy factors (Figure 1.2). Now, both types of possible intermolecular $\text{S}\cdots\text{O}$ nonbonded interactions occur in the structure, with the $\text{S}\cdots\text{O}=\text{C}$ distances, amounting at 2.63 Å in **A** and 2.62 Å in **B**, being shorter than the $\text{S}\cdots\text{O}-\text{C}$ contacts of 2.71 Å in **A** and 2.76 Å in **B**.

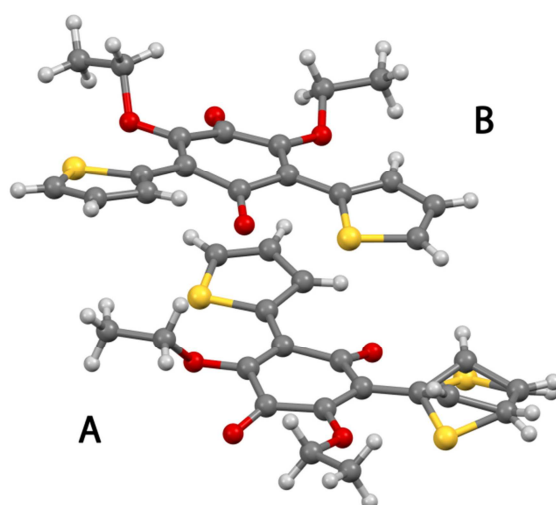


Figure 1.2. Two crystallographically independent molecules in the structure of **3b**; the disorder on the orientation of the thiophene substituent in molecule **A** is shown.

Compound **4a** crystallizes in the monoclinic $C2/c$ space group with one half of independent molecule in the unit cell. The EDOT moieties do not lie in the plane of the benzoquinone ring, as found for the analogous thiophene derivative **3a**, but show symmetry related dihedral angles of ca. 130° . This non-planar conformation can be due either to the steric hindrance between the 3,4-ethylenedioxy group and the oxygen atoms of the benzoquinone moiety (Figure S1.2) or to the stacking interactions between the EDOT substituents in the molecular packing of **4a** (*vide infra*). The crystal packing of **4a** is dominated by the parallel head-to-tail arrangement of EDOT substituents along the c axis (Figure 1.3) that, in turn, do not allow for any type of short contacts between the benzoquinone moieties, as found in **3a**.

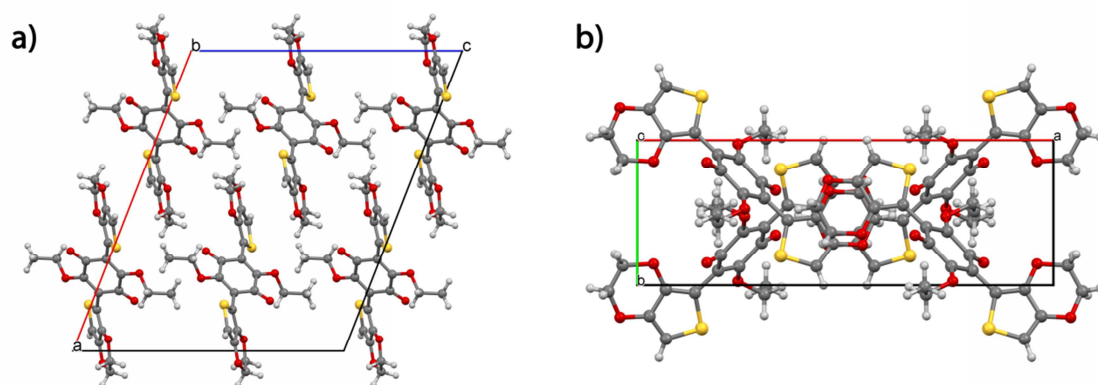


Figure 1.3. Portion of the crystal packing of **4a** a) in the ac plane and b) in the ab plane; the stacking of the EDOT substituents along the c axis is highlighted.

Compound **4b** crystallizes in the monoclinic $P2_1/c$ space group with one independent molecule in the unit cell. Once again, compound **4b** does not show planar conformation, as the EDOT substituents form dihedral angles of ca. 131° and 129° with respect to the plane of the benzoquinone (Figure 1.4).

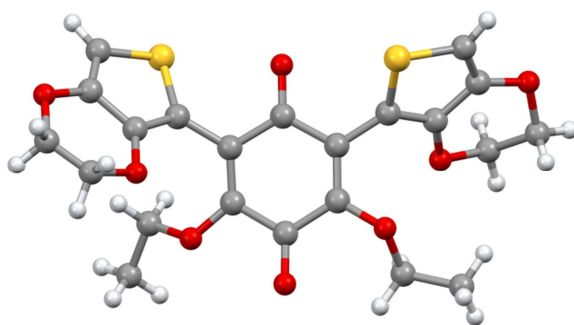


Figure 1.4. Molecular structure of **4b**.

This is very likely due to the steric hindrance (Figure S1.3). However, unlike the structure of **3b**, now both thiophene units are oriented towards the C=O group. Some short intermolecular contacts between ethylenedioxy and benzoquinone fragments can be observed in the packing (Figure S1.3).

Single crystals of compound **8** suitable for X-ray studies were obtained by recrystallization in a hydrochloric acidified water solution. Compound **8** crystallizes in the monoclinic $P2_1/a$ space group with one independent HCICNAN⁻ anionic molecule in the unit cell and a potassium cation. An ORTEP drawing for **8** with atoms labeling scheme is reported in Figure 1.5a.

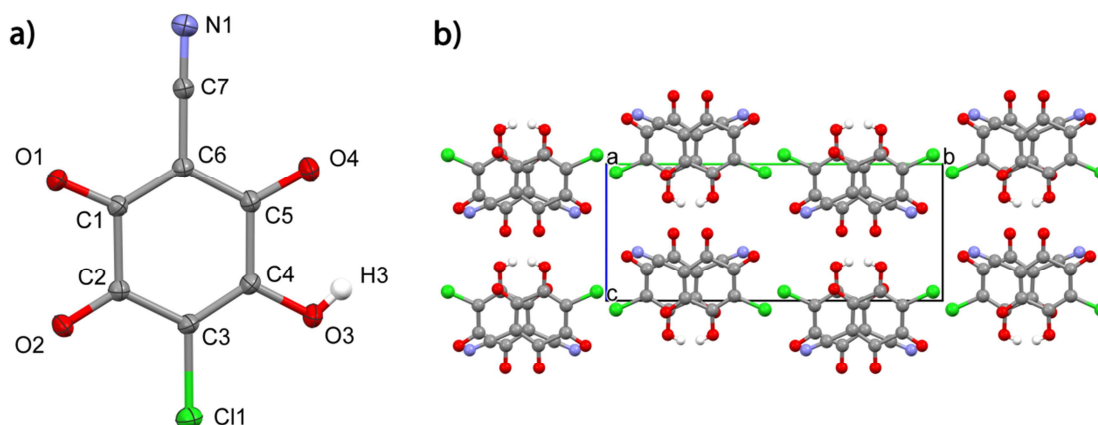


Figure 1.5. a) Ortep drawing of **8** with thermal ellipsoids at 30% probability level. Selected bond distances: C(1)–O(1) 1.247 Å, C(2)–O(2) 1.216 Å, C(5)–O(4) 1.234 Å, C(4)–O(3) 1.327 Å. b) View of the crystal structure of **8** where the stacked columns of HCICNAN⁻ along the *a* crystallographic axis are highlighted. Potassium cations were omitted for clarity.

The molecular structure of the benzoquinone ring shows intermediate features with respect to the centrosymmetric quinoidal form typical of the bis-protonated anilic acids and the non quinoidal form of the dianions (*vide supra*). In fact, it shows three C–O bond in the 1.216–1.248 Å distance range, slightly longer than pure C=O bonds, and one C–O distance of 1.327 Å typical of single C–O bonds (associated to the protonated oxygen). Moreover, four C–C distances associated to the O–C(–X)–C–O bonds fall in a narrow range (1.345–1.455 Å), and the two other C–C bonds are slightly longer (1.507 Å and 1.548 Å).

The crystal structure of **8** shows parallel columns of monoprotanated acid stacked along the *a* crystallographic axis (Figure 1.5b). The columns are separated by potassium cations exhibiting a nona-coordinated tri-capped trigonal prism coordination geometry (Figure 1.6a) by four O atoms, two Cl atoms and two N atoms of the hydrogen chlorocyananilate (Figure 1.6b).

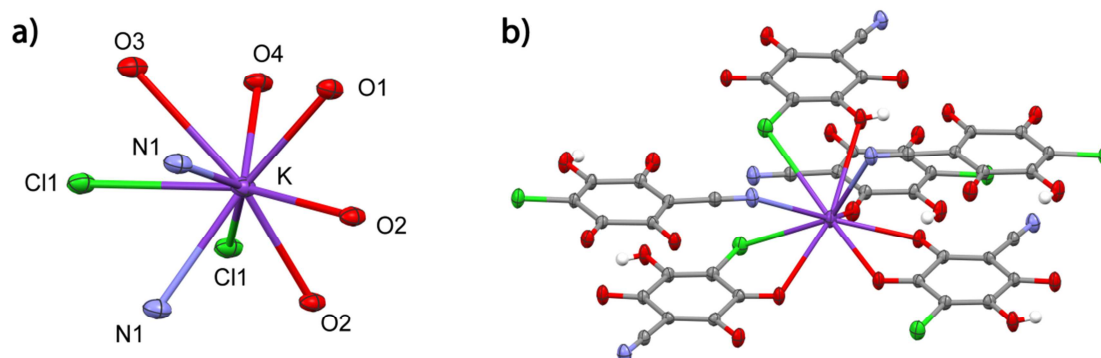


Figure 1.6. Coordination environment around the potassium cations for **8** where a) the tri-capped trigonal prism geometry and b) the coordinating molecules are highlighted.

The $K^+ \cdots O$ and $K^+ \cdots Cl$ distances, ranging from 2.722 to 3.311 Å, and from 3.369 to 3.449 Å, respectively, and the coordination environment exhibited by the potassium cations are close to those already observed for the analogous compound $KHCl_2An \cdot H_2O$.⁵³

The chlorocyananilate dianion was obtained instead as $(Ph)P^+$ salt, by recrystallizing **8** in a basic aqueous solution containing $(Ph)_4PBr$. Single crystals of $[(Ph)_4P]_2[CICNAn] \cdot 2H_2O$ (**9**), suitable for X-ray diffraction studies, were successfully obtained. Compound **9** crystallizes in the triclinic centrosymmetric space group $P\bar{1}$ with one half $CICNAn^{2-}$ molecule, one $(Ph)_4P^+$ cation and one water molecule as independent units in the unit cell. The chloro and cyano substituents on the $CICNAn^{2-}$ anion were found disordered in two equivalent positions (0.50 and 0.50 site occupancy factors) related to two possible orientations of the ligand along an ideal plane formed by the planar benzoquinone ring.

The molecular structure of **9** shows the typical features of the anilate dianions, (i) a planar structure of the benzoquinone moiety, (ii) four C–O bonds of similar length (1.232–1.243 Å), and (iii) four C–C bonds of similar length (1.414–1.424 Å), and two considerably longer C–C bonds (1.542 Å). The crystal structure of **9** consists of chlorocyananilate anions connected through a HB in supramolecular chains. This HB involves the O1w water molecule and the O(2) and N(1) (or Cl(1)) atoms of two adjacent ligands (Figure 1.7a). No interactions between the chains were observed being separated by the bulky $(Ph)_4P^+$ cations (Figure 1.7b).

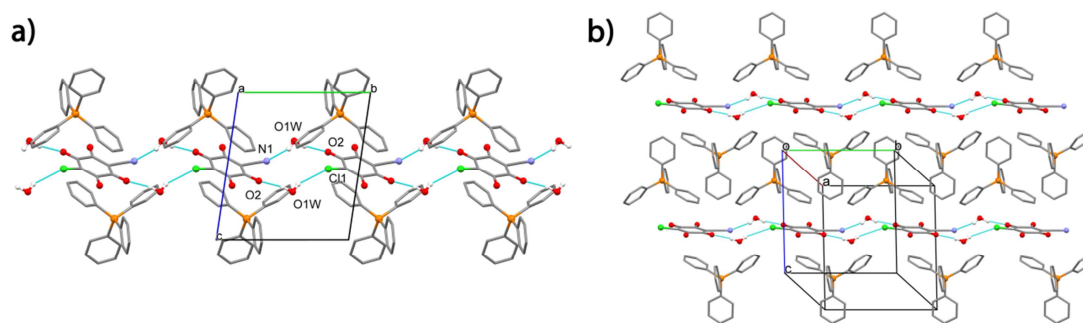


Figure 1.7, View of the crystal structure of **9**. a) ClCNAn²⁻ anions connected in supramolecular chains through HB interactions along the *b* crystallographic axis, b) two chains separated by (Ph)₄P⁺ cations. Selected distances and angles: N(1)···O1w 2.991 Å, O1w···O(2) 2.870 Å, O1w–H1A···O(2) 2.013 Å, O1w–H2A···O(2) 166.51°.

1.2.3 Emission Properties

The UV-Vis absorption spectra of **8** and **9** show, in the 230–800 nm region, three absorption bands (Figure 1.8). The absorption spectrum of **9**, recorded in CH₃CN, shows two bands in the UV region centered at $\lambda_{\text{max}} = 268$ nm and 318 nm, both with high extinction coefficients, $\epsilon = 19718$ dm³ mol⁻¹ cm⁻¹ and 23262 dm³ mol⁻¹ cm⁻¹, respectively, and one band in the Vis region centered at $\lambda_{\text{max}} = 460$ nm, having a very low extinction coefficient ($\epsilon = 526$ dm³ mol⁻¹ cm⁻¹). The same features are observed in the UV-Vis absorption spectra of **8**, recorded in H₂O, in its protonated and dianionic forms (red and blue lines in Figure 1.8, respectively), obtained by adding an excess of concentrated HCl or Et₃N to the corresponding solutions. These bands are present at $\lambda_{\text{max}} = 251$ nm ($\epsilon = 10405$ dm³ mol⁻¹ cm⁻¹), 305 nm ($\epsilon = 16036$ dm³ mol⁻¹ cm⁻¹), and 464 nm ($\epsilon = 512$ dm³ mol⁻¹ cm⁻¹), and at $\lambda_{\text{max}} = 261$ nm ($\epsilon = 13361$ dm³ mol⁻¹ cm⁻¹), 316 nm ($\epsilon = 19973$ dm³ mol⁻¹ cm⁻¹), and 487 nm ($\epsilon = 438$ dm³ mol⁻¹ cm⁻¹), for the protonated and dianionic forms, respectively (Figure 1.8).

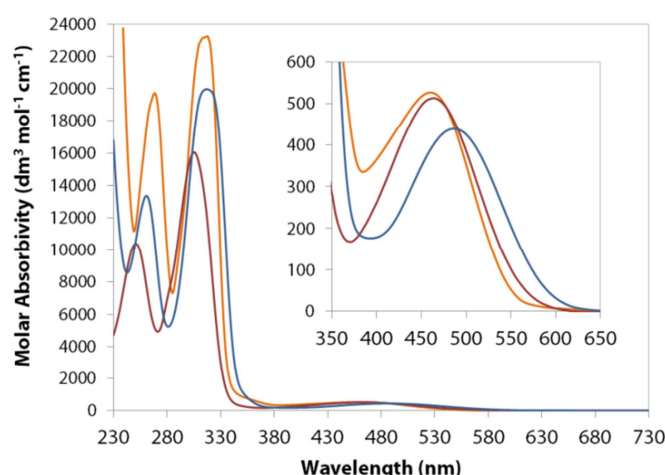


Figure 1.8, UV-Vis spectra (230–730 nm) for **9** in CH₃CN solution (orange line), and **8** in H₂O solution in its protonated (red line) and dianionic (blue line) forms. Inset shows the Vis region characterized by a band with a low extinction coefficient.

The UV-Vis spectrum of **8** in its dianionic form is red-shifted when compared to that of its protonated form. This is very likely due to the energy stabilization of the anion in water. Comparing the spectra of the dianionic chlorocyananilate ligand in CH₃CN (orange line) and H₂O (blue line) solutions, a red-shift of the spectrum is observed as the polarity of the solvent increases (Figure 1.8).

In Figure 1.9 the photoluminescence spectra of **8** and **9** are reported.

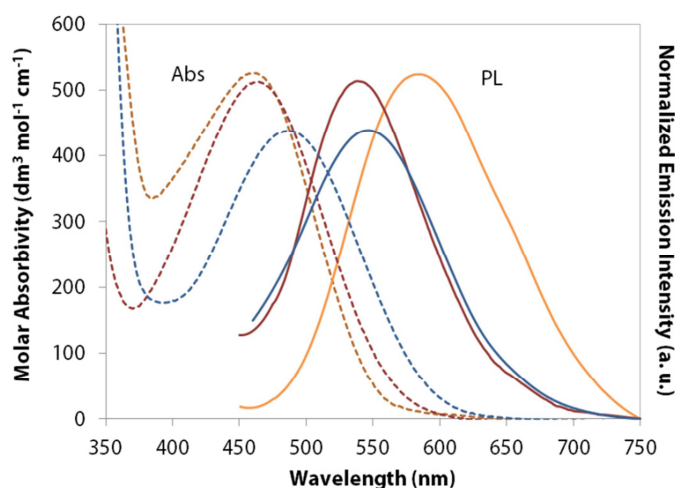


Figure 1.9, UV-Vis (dashed lines) and PL (solid lines) spectra (350–750 nm) for **9** in CH₃CN solution (orange line), and **8** in H₂O solution in its protonated (red line) and dianionic (blue line) forms.

When a CH₃CN solution of **9** is excited at 400 nm, an emission band centered ca. $\lambda_{\max} = 585$ nm is observed. A basic aqueous solution of **8** shows an emission band centered at ca. $\lambda_{\max} = 550$ nm when excited at 400 nm. Interestingly, when going from CH₃CN to H₂O, the absorption band of the dianion is red-shifted, whereas the emission band is blue-shifted. PL measurements were also performed on an acidic aqueous solution of **8**. In this case, the most effective excitation wavelength was found at $\lambda_{\text{exc}} = 370$ nm, in agreement with the blue-shifted absorption spectrum of the protonated form of the chlorocyananilate ligand when compared to the absorption band of the dianion in the same solvent, and in agreement with the excitation spectra (Figure S1.4). Interestingly, the position of the emission band of the protonated form is almost unchanged ($\lambda_{\max} = 540$) when compared to that of the dianion. Emission quantum yields were estimated with the relative method (see Experimental Section) and their values for **8** in the dianionic and protonated forms, and **9** are summarized in Table 1.2.

Table 1.2, Excitation (λ_{exc}) and emission (λ_{em}) wavelengths, and emission quantum yield values (Φ) for compounds **8** and **9**.

Compound	λ_{exc} (nm)	λ_{em} (nm)	Φ (%)
8 (acid)	370	540	5.5(1)
8 (dianion)	400	550	5.5(1)
9	400	585	1.4(1)

The comparable quantum yields values of **8** in the protonated and deprotonated forms, suggest that the electrons located on oxygen atoms are not predominantly involved in the electronic transition responsible for the luminescent properties. It should be also pointed out that the lower value of the quantum yield for **9** is affected by a higher absorption value at the excitation wavelength. This can be related to the fact that the observed band may be considered as a convolution of the band of interest with an additional absorption band. Theoretical calculations are currently underway for assigning the observed Vis absorption band to a specific electronic transition, that, in turn, is responsible for the radiative decay and the light emission properties of this ligand.

1.2.4 UV-Vis Absorption Properties and TD-DFT Calculation

An interesting feature of the thiophene and EDOT derivatives is the possibility to show charge transfer from the thiophene or EDOT units to the benzoquinone ring. Interestingly, a solution of **3a** in acetonitrile has yellow colour, while that one of **3b** is violet. Indeed, the UV-Vis spectra show the presence of a tail at ca. $\lambda_{\text{max}} = 525$ nm for **3a**, with a very low extinction coefficient $\epsilon = 407$ $\text{dm}^3 \text{mol}^{-1} \text{cm}^{-1}$, and an absorption band centered at $\lambda_{\text{max}} = 536$ nm for **3b**, with a much higher value for the extinction coefficient ($\epsilon = 1896$ $\text{dm}^3 \text{mol}^{-1} \text{cm}^{-1}$) (Figure 1.10). These intriguing spectral features have an explanation related to symmetry selection rules for the electronic transitions (*vide infra*), since the molecule **3a** has an inversion center while **3b** is not centrosymmetric. Both compounds show a band centered at ca. $\lambda_{\text{max}} = 390$ nm with very similar extinction coefficients (5905 and 6036 $\text{dm}^3 \text{mol}^{-1} \text{cm}^{-1}$ for **3a** and **3b**, respectively) and one absorption band in the UV region with comparable extinction coefficients and wavelengths: $\lambda_{\text{max}} = 302$ nm ($\epsilon = 18300$ $\text{dm}^3 \text{mol}^{-1} \text{cm}^{-1}$) and $\lambda_{\text{max}} = 278$ nm ($\epsilon = 16680$ $\text{dm}^3 \text{mol}^{-1} \text{cm}^{-1}$) for **3a** and **3b**, respectively, which can be related to a $\pi \rightarrow \pi^*$ transition involving the benzoquinone ring.

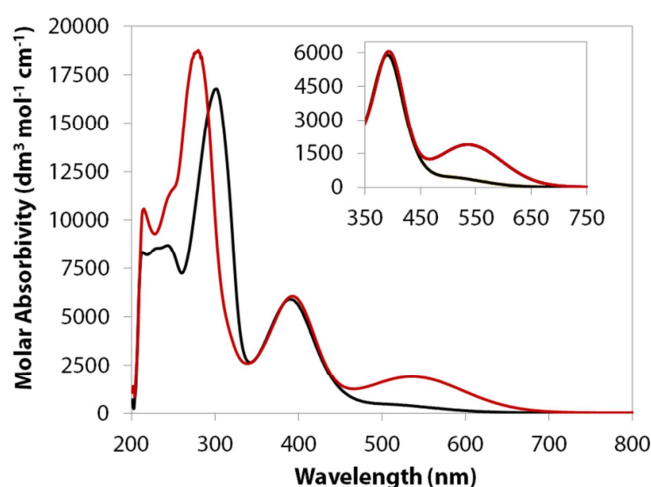


Figure 1.10, UV-Vis spectra (200–800 nm) for **3a** (black line) and **3b** (red line) in CH_3CN solution; the inset shows the charge transfer band region.

DFT and TD-DFT calculations were performed in order to rationalize the electronic spectra of compounds **3a** and **3b** and to understand the difference in the charge transfer properties. The equilibrium ground state geometries have been optimized for both isomers. There is no significant change with respect to the starting geometries taken from the X-ray data. The isomer **3a** converged to a C_i point group symmetry structure. The frontier molecular orbital plots clearly show that the HOMO, of π type, is delocalized over the thiophene–(C=C)_{quinone} fragments, with some contribution from the oxygen atoms of the ethoxy groups, while the LUMO, also of π symmetry, is largely based on the electron poor C=O groups (Figure 1.11 and Table S1.3), both of the orbitals being symmetric (g) with respect to the inversion center. In the *meta* isomer **3b**, which does not present any symmetry element since the thiophene rings point in opposite directions, the HOMO and LUMO are delocalized over the same fragments as in **3a**. It is then clear that, independently of any symmetry considerations, charge transfer from the thiophene units to the central benzoquinone ring might occur as HOMO→LUMO excitations.

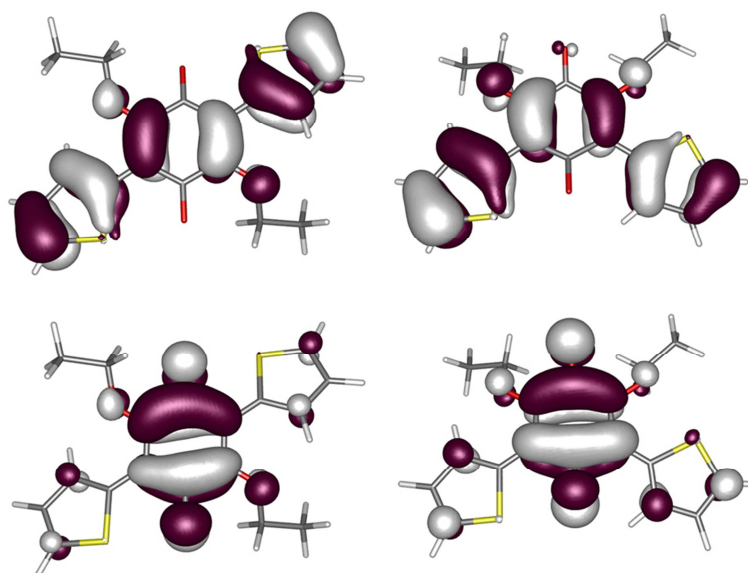


Figure 1.11, Frontier orbitals for **3a** (HOMO top left and LUMO bottom left) and **3b** (HOMO top right and LUMO bottom right) with an isovalue chosen to represent 35% of the function.

Then, TD-DFT calculations, which are very well adapted for such organic systems,^{65,66} have been performed to rationalize the UV-Vis absorption spectra. The hybrid functional PBE0^{67,68} with a large basis set has been used (see Experimental Section for details). Such methodology reproduces almost exactly all local $\pi \rightarrow \pi^*$ transitions whereas a relatively large error (0.2 to 1 eV) has been observed for charge transfer and Rydberg type transitions.⁶⁹ Therefore the diagnostic tool proposed by Peach and Tozer, who have shown that, for a hybrid functional, if the spatial overlap (noted Λ) between the ground state and excited state wavefunction is below 0.3 eV, the calculated excitation energy is likely to be inaccurate, has been used for every transition in order to evidence any possible issue.^{70,71} An excellent agreement has been found between the experimental and calculated transitions in the high energy region (Figure 1.12). Tables 1.3 and 1.4 give details, energies and spatial overlap about the calculated excitations for both isomers **3a** and **3b**.

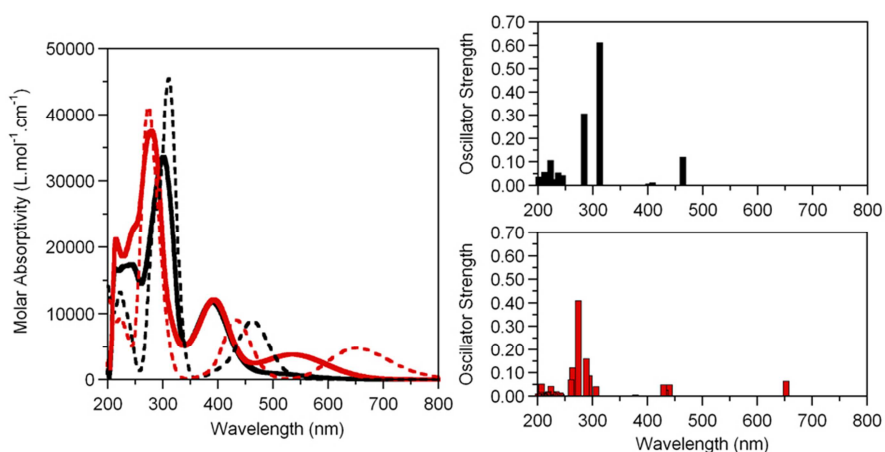


Figure 1.12, Left, Experimental (solid lines) and simulated (dashed lines) absorption spectra of isomers **3a** (in black) and **3b** (in red). Right, Electronic transitions calculated for the isomers **3a** (in black, up) and **3b** (in red, bottom).

Nevertheless, for the first excitation of **3b**, calculated at 652 nm and observed at 536 nm, corresponding to a charge transfer, a difference in energy of 0.4 eV, which is not improved using calculations in solutions (Figure S1.5), is observed. Hence, the color is not accurately reproduced by this method.^{65,66} However, the difference between the absorption properties of both isomers is clearly in agreement with the calculations. Indeed, the S_0 to S_1 excitation is forbidden by symmetry in the case of the *para* substituted isomer **3a**, whereas higher energy excitations are related. The resemblance between both S_0 to S_1 excitations can be better seen with the density difference plots. The thiophene moieties lose density whereas the π^* of the carbonyl groups are populated (Table 1.4 and Table S1.4).

Table 1.3, TD-DFT calculated energies, spatial overlap and assignment of the most pertinent low-lying singlet to singlet electronic excitations of **3a**.

Excitation	λ (nm)	Wavenumber (cm^{-1})	Energy (eV)	Oscillator Strength	Λ
$S_0 \rightarrow S_1$	676	14800	1.83	0.000	0.58
$S_0 \rightarrow S_2$	463	21587	2.68	0.122	0.65
$S_0 \rightarrow S_8$	312	32067	3.98	0.612	0.77
$S_0 \rightarrow S_9$	284	35244	4.37	0.304	0.68

Table 1.4, TD-DFT calculated energies, spatial overlap and assignment of the most pertinent low-lying singlet to singlet electronic excitations of **3b**.

Excitation	λ (nm)	Wavenumber (cm^{-1})	Energy (eV)	Oscillator Strength	Λ
$S_0 \rightarrow S_1$	652	15333	1.90	0.066	0.62
$S_0 \rightarrow S_2$	440	22739	2.82	0.050	0.39
$S_0 \rightarrow S_4$	429	23297	2.89	0.050	0.40
$S_0 \rightarrow S_8$	293	34094	4.23	0.088	0.58
$S_0 \rightarrow S_9$	299	34673	4.30	0.161	0.40
$S_0 \rightarrow S_{10}$	274	36514	4.53	0.410	0.62
$S_0 \rightarrow S_{11}$	263	37995	4.71	0.122	0.33
$S_0 \rightarrow S_{12}$	284	38366	4.76	0.071	0.60

Table 1.5. One-electron density difference between the ES and GS. The isocontour value is set to represent 75% of the electron. The solid turquoise (white grid) zones indicate increase (decrease) of density upon electronic transition.

Excitation (Osc. Str.)	3a	Excitation (Osc. Str.)	3b
$S_0 \rightarrow S_1$ (0.000)		$S_0 \rightarrow S_1$ (0.066)	
$S_0 \rightarrow S_2$ (0.122)		$S_0 \rightarrow S_2$ (0.050) + $S_0 \rightarrow S_4$ (0.050)	

UV-Vis spectra of the corresponding EDOT derivatives **4a** and **4b** show similar features when compared to the thiophene analogues. However, solutions of **4b** in acetonitrile are deep red, while those of **3b** are violet, very likely because of the less efficient conjugation in the former than in the latter, and hence the weaker charge transfer. Compound **4a** shows a weak tail-like absorption at around $\lambda_{\max} = 540 \text{ nm}$ ($\epsilon = 720 \text{ dm}^3 \text{ mol}^{-1} \text{ cm}^{-1}$), which correspond to the charge transfer from EDOT to the benzoquinone ring, whereas the *meta* isomer **4b** shows the charge transfer band as a shoulder at around $\lambda_{\max} = 520 \text{ nm}$ ($\epsilon = 1812 \text{ dm}^3 \text{ mol}^{-1} \text{ cm}^{-1}$), hence blue-shifted with respect to **3b**, in agreement with the observed difference in color between the two compounds. As for **3b** this transition should be allowed since there is no inversion center in the molecule. Both **4a** and **4b** show two absorption bands centered at $\lambda_{\max} = 418 \text{ nm}$ ($\epsilon = 4005 \text{ dm}^3 \text{ mol}^{-1} \text{ cm}^{-1}$) and $\lambda_{\max} = 275 \text{ nm}$ ($\epsilon = 28300 \text{ dm}^3 \text{ mol}^{-1} \text{ cm}^{-1}$) (for **4a**) and $\lambda_{\max} = 414 \text{ nm}$ ($\epsilon = 3121 \text{ dm}^3 \text{ mol}^{-1} \text{ cm}^{-1}$) and $\lambda_{\max} = 267 \text{ nm}$ ($\epsilon = 26595 \text{ dm}^3 \text{ mol}^{-1} \text{ cm}^{-1}$) (for **4b**), with similar λ_{\max} and extinction coefficients (Figure 1.13).

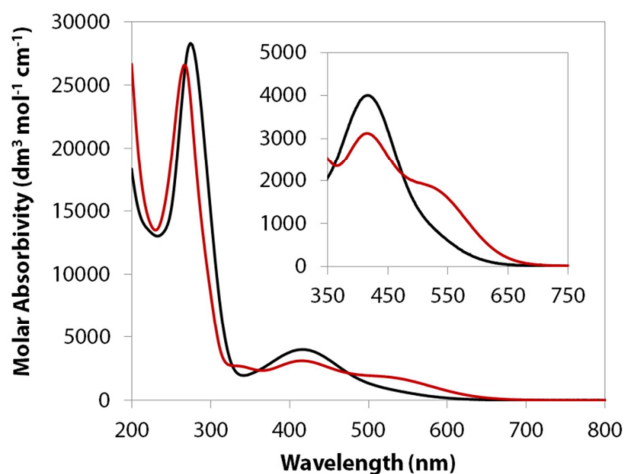


Figure 1.13, UV-Vis spectra (200–800 nm) for **4a** (black line) and **4b** (red line) in CH₃CN solution; Inset shows the charge transfer band region.

1.2.5 Electrochemical Studies

Compounds **3a,b** and **4a,b** were studied by cyclic voltammetry in order to get insight on their electrochemical properties. Cyclic voltammograms for **3a** and **3b** show for both compounds one irreversible oxidation peak at ca. +1.46 V and one reversible reduction peak at ca. –0.50 V (Table 1.6).

The oxidation peak may be associated to the oxidation of the thiophene moiety; its position at lower values with respect to the oxidation potential of the unsubstituted thiophene (ca. 2.0–2.1 V vs SCE) is in the normal range for substituted thiophenes.⁷² The reduction peak may be, instead, associated to a reversible reducing process involving the benzoquinone moiety (Figure 1.14).

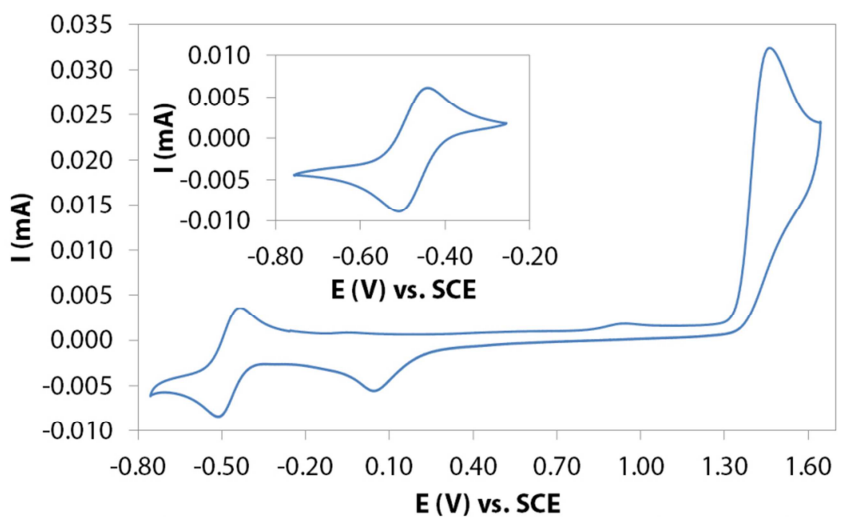
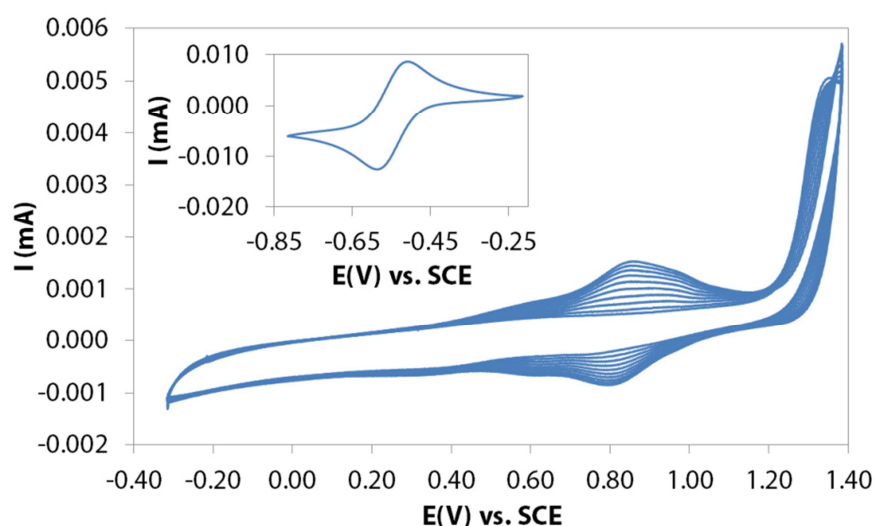


Figure 1.14, Cyclic voltammogram (–0.80–1.60 V) for **3a** (CH₃CN, 0.1 mol dm⁻³ [(*n*-Bu)₄N]PF₆, 100 mV s⁻¹). Inset shows the reversible reduction peak.

Table 1.6, Cyclic voltammometry data for compounds **3a,b** and **4a,b**.

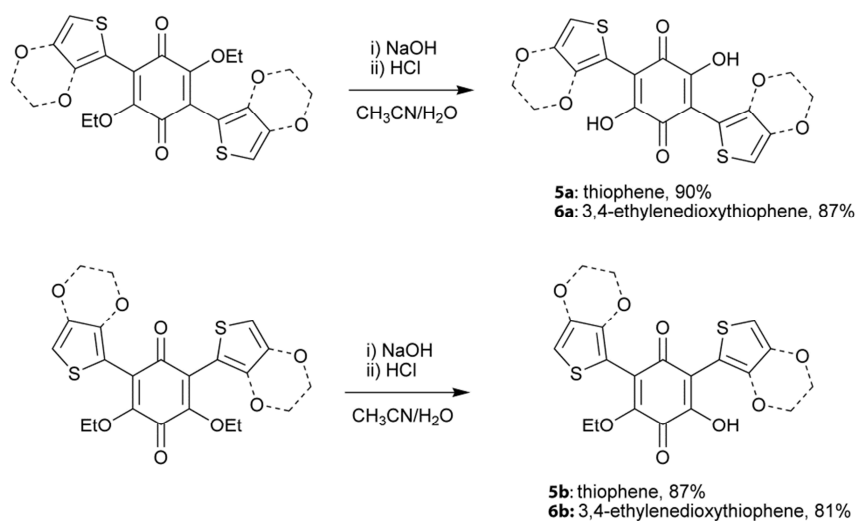
Redox Potential (vs SCE)	3a	3b	4a	4b
E_{ox}	+1.46	+1.47	+1.37	+1.32
$E_{1/2,red}$	-0.47	-0.48	-0.55	-0.54

Cyclic voltammograms for **4a** and **4b** show similar features with respect to those for their thiophene analogues. An irreversible oxidation potential centered at ca. +1.34 V associated to the oxidation of the EDOT units, thus occurring at a slightly more cathodic potential than the one for the unsubstituted EDOT (ca. +1.5 V vs SCE),⁷³ and a reversible reduction peak centered at ca. -0.55 V associated to the reduction of the benzoquinone ring are present for both isomers (Table 1.6). In addition, the EDOT derivatives **4a** and **4b**, when compared to **3a** and **3b**, undergo electropolymerization generating a polymeric redox system characterized by a reversible oxidation peak at ca. +0.80 V, for which the intensity increases upon repetitive cycling (Figure 1.15).

**Figure 1.15**, Cyclic voltammogram (-0.40–1.40 V) for **4a** (CH_3CN , 0.1 mol dm^{-3} $[(n\text{-Bu})_4\text{N}]\text{PF}_6$, 100 mV s^{-1}). Inset shows the reversible reduction peak.

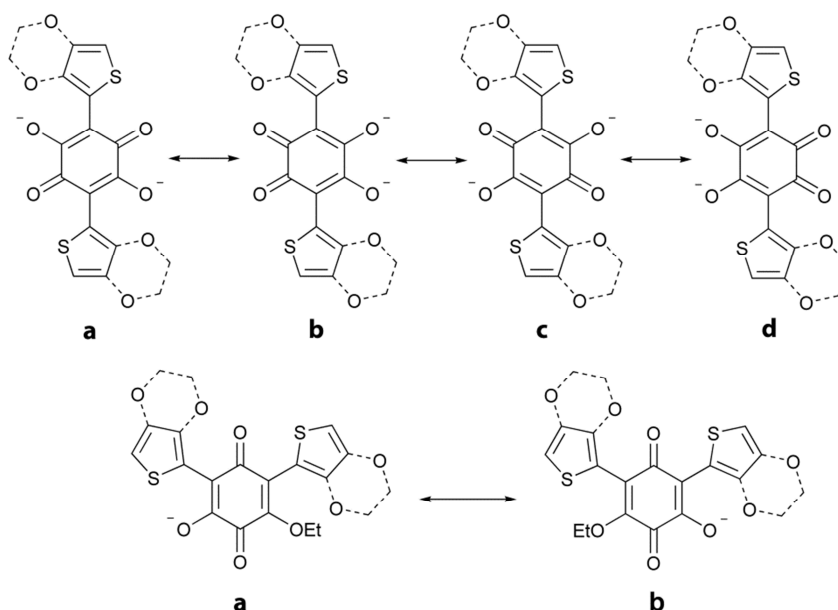
1.2.6 Preliminary Coordination Chemistry Studies

Hydrolysis in basic conditions of compounds **3a** and **4a** followed by acidification with concentrate acid affords the expected 2,5-di(thiophen-2-yl)-3,6-dihydroxy-1,4-benzoquinone **5a** and 2,5-di(3,4-ethylenedioxythiophen-2-yl)-3,6-dihydroxy-1,4-benzoquinone **6a** products, whereas compounds **3b** and **4b**, under the same conditions, give rise to the mono-protected compounds 2,6-di(thiophen-2-yl)-3-hydroxy-5-ethoxy-1,4-benzoquinone **5b** and 2,6-di(3,4-ethylenedioxythiophen-2-yl)-3-hydroxy-5-ethoxy-1,4-benzoquinone **6b** (Scheme 1.8).



Scheme 1.8, Synthesis of compounds **5a,b** and **6a,b**.

These results can be explained on the basis of the stability of the corresponding anions. For the *para*-substituted derivatives **5a** and **6a** the deprotection of the ethoxy groups takes easily place on both positions 3 and 6 because of the stability of the generated dianionic structure (Scheme 1.9). Instead, for the *meta*-substituted derivatives **5b** and **6b** only one of the two ethoxy groups is removed, generating the monoanions. The deprotection of the second ethoxy group does not take place probably because of the limited conjugation possibilities of the monoanions, in contrast with the dianions generated from the *para* isomer (Scheme 1.9).



Scheme 1.9, Resonance structures for the dianionic forms of **5a** and **6a** (above) and the monoanionic forms of **5b** and **6b** (below); note that **a** and **c** are the prevailing forms for **5a** and **6a** while **a** is the prevailing form for **5b** and **6b**.

Compounds **5a** and **6a** in their deprotonated form (indicated as **L6** and **L7**, respectively) can thus behave as suitable ligands towards transition metal ions, in analogy with what described

in the literature for the electron withdrawing substituted analogues. It should be pointed out that **L6** and **L7** are the first anilate ligands containing electron rich substituents. To prove their coordinating abilities, **L6**, hereafter thiophene-anilate ($\text{Th}_2\text{An}^{2-}$), has been reacted with the Cu^{II} complex $[\text{Cu}(\text{tbbpy})\text{Cl}_2]$,⁷⁴ affording the heteroleptic square-planar complex $[\text{Cu}(\text{Th}_2\text{An})(\text{tbbpy})]\cdot 2\text{H}_2\text{O}$ (**C11**) (Figure 1.16).

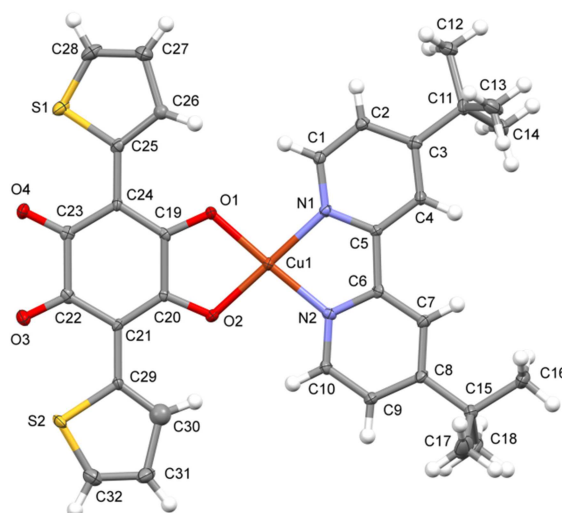


Figure 1.16, ORTEP drawing for **C11** with thermal ellipsoids at 30% probability level.

Single crystal X-ray analysis shows that **C11** crystallizes in the monoclinic space group $P2_1/n$ with one independent molecule of the complex and two crystallization water molecules in general positions in the asymmetric unit. The complex shows an overall planar structure with thiophene substituents that are practically coplanar with the benzoquinone ring (dihedral angles of ca. 170°), with short 1,5-nonbonded $\text{S}\cdots\text{O}$ interactions (2.76–2.77 Å) between the sulfur atoms of the thiophenes and the peripheral oxygen atoms of the ligand (Figure 1.17).

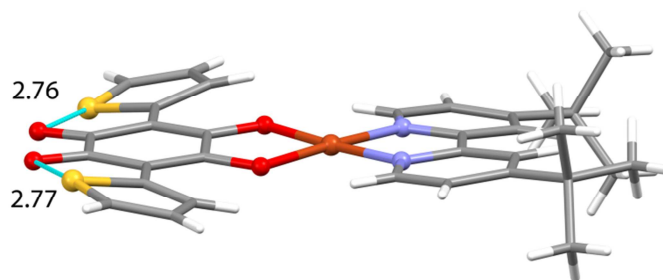


Figure 1.17, Molecular structure of **C11** with 1,5-nonbonded $\text{S}\cdots\text{O}$ interactions highlighted.

The thiophene units were found disordered in two different orientations presenting 0.57 and 0.43 site occupancy factors. One of the two orientation is the one described above (Figure 1.17) where the sulfur atoms of the thiophenes interact with the peripheral oxygen atoms of the ligand, while the other one presents the thiophene units ca. 180° rotated, with sulfur atoms interacting with the coordinating oxygen atoms through 1,5-nonbonded $\text{S}\cdots\text{O}$ interactions (2.74 and 2.77 Å). The metal centre exhibits a square-planar coordination geometry with the thiophene-anilate and tbbpy ligands coordinated to the Cu^{II} ion in the 1,2-

bidentate coordination mode, with the O and N atoms respectively. The metal-oxygen and metal-nitrogen bond distances are 1.911(3)–1.914(3) and 1.954(4)–1.961(4), respectively (Table 1.7), in the normal range for heteroleptic Cu^{II} complexes containing chloranilate and 2,2'-bipyridine ligands.⁷⁵ The C–O bond distances are influenced by the coordination to the metal center. The oxygen atoms coordinated to the metal have C–O distances, on average, 0.06 Å longer than those of the peripheral oxygen atoms which show a major double bond character (Table 1.7), suggesting that the thiophene-anilate ligand is likely present in the well-known o-quinone-like resonance structure (**b** and **d** forms in Scheme 1.9).⁷

Table 1.7, Selected bond distances (Å) for **C11**.

Bonds	C1c
Cu–O(1)	1.911(3)
Cu–O(2)	1.914(3)
Cu–N(1)	1.954(4)
Cu–N(2)	1.961(4)
C(19)–O(1)	1.285(5)
C(20)–O(2)	1.302(5)
C(22)–O(3)	1.236(5)
C(23)–O(4)	1.238(5)

The crystal packing of **C11** is dominated by alternated head-to-tail stacking interactions between the molecules of complex that run parallel to the *a* crystallographic axis (Figure 1.18), with C...S and some C...C distances lower than the sum of the van der Waals radii (S(1)...C(10) 3.47 Å, S(2)...C(2) 3.49 Å, C(1)...C(22) 3.33 Å, C(1)...C(21) 3.39 Å).

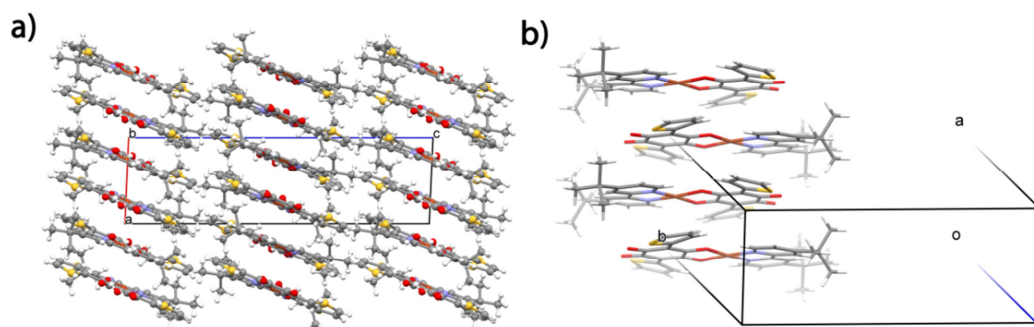


Figure 1.18, a) View of the crystal packing of **C11** in the *ac* plane; b) Detailed view of the alternated head-to-tail disposition along the *a* crystallographic axis.

Interestingly, the crystallization water molecules present in the structure connect pairs of metal complexes of adjacent parallel columns *via* HB interactions with the peripheral oxygen atoms of the thiophene-anilate ligands (Figure 1.19).

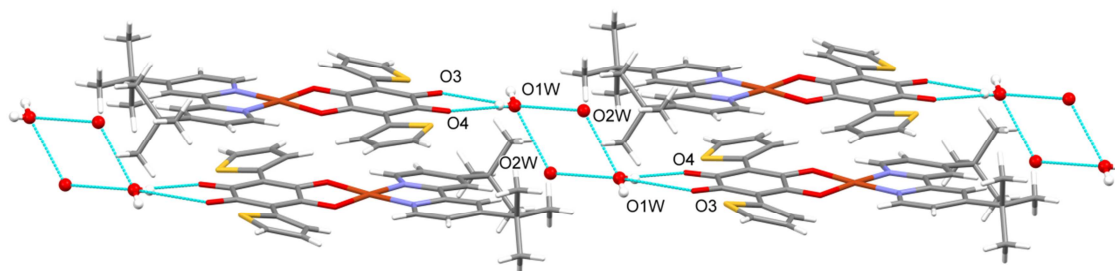


Figure 1.19, HB intermolecular interactions between crystallization water molecules and pairs of metal complexes. (Å): O(3)···O1w 3.04, O(4)···O1w 2.79, O1w···O2w 2.84, O1w···O2w 2.86.

1.3 Conclusions

An elegant synthesis of thiophene and EDOT 2,5-disubstituted anilate derivatives through Stille coupling is described, together with the simultaneous preparation of the corresponding 2,6-disubstituted derivatives. The four compounds have been characterized by single crystal X-ray diffraction, which emphasized the planar conformation of the thiophene derivatives with the establishment of S···O 1,5-nonbonded interactions. Moreover, the synthesis of the first example of an asymmetrical substituted anilate ligand, the chlorocyananilate, has been revisited and the ligand fully characterized. Very interestingly, theoretical calculations at the TD-DFT level show that in the 2,5-bis(thiophene) derivatives (*para* isomers) the intramolecular charge transfer from the thiophene units to the benzoquinone ring is symmetry forbidden, while it is allowed in the 2,6-derivatives (*meta* isomers), in agreement with the different colours of the respective solutions. The 2,5-derivatives are potential precursors for the preparation of thiophene or EDOT-anilate ligands by further deprotection of the ethoxy groups and deprotonation. Among the anilate ligands, these are the first containing electron rich, electroactive, substituents. Their binding ability has been proved in a preliminary coordination chemistry study through the preparation and structural characterization of a square planar Cu^{II} complex containing one thiophene-anilate ligand and one 4,4'-bis(*tert*-butyl)-2,2'-bipyridine ligand. The synthetic strategy described herein is very challenging and opens the way to the preparation of a large variety of *d*- and *f*-metal complexes based on these new electroactive anilate ligands. Moreover, the Cl/CN substituted anilate ligand, which shows luminescent properties, is also very challenging since it can be a potential candidate for the preparation of luminescent molecular building blocks, emitting multidimensional chlorocyananilate-based coordination polymers or supramolecular architectures showing a combination of luminescent and magnetic properties.

1.4 Experimental

1.4.1 General Remarks

Chemical shifts are expressed in parts per million (ppm, δ), downfield from TMS as an external reference. The following abbreviations are used: singlet (s), doublet (d), triplet (t), quartet (q), doublet of doublets (dd). Palladium catalyzed reactions were carried out under argon atmosphere in toluene (HPLC grade). Bromanil (**1**) was synthesized according to the literature.¹² 2-(tributylstannyl)thiophene was purchased from Sigma-Aldrich and 2-(tributylstannyl)-3,4-ethylenedioxythiophene was synthesized according to the literature.⁷⁶ [Cu(tbbpy)Cl₂] was synthesized according to the literature method.⁷⁴

1.4.2 Syntheses and Analytical Data

2,5-dibromo-3,6-diethoxy-1,4-benzoquinone (2a) and 2,6-dibromo-3,5-diethoxy-1,4-benzoquinone (2b). **1** (12 g, 28.4 mmol) was partially dissolved in anhydrous ethanol (800 mL) and KF (16 g, 275.4 mmol) was added under stirring at room temperature. After 1.5 h the white solid was filtered off and the solution evaporated. The orange solid was redissolved in ca. 400 mL of CCl₄ and heated until reflux. The black impurities were filtered off and the orange solution evaporated to give a mixture of **2a** and **2b** in a ca. 50:50 ratio (9 g, 89% yield). **2a** and **2b** can be separated by column chromatography on silica gel (pentane/CH₂Cl₂, 2:1, Rf **2a** = 0.53, Rf **2b** = 0.48; then CH₂Cl₂). Single crystals suitable for X-ray analysis were obtained by slow evaporation from a solution of **2a** in CH₂Cl₂. **2a**: ¹H NMR (300 MHz, CDCl₃): δ = 4.57 (q, 4H, ³J 6.9), 1.43 (t, 6H, ³J 6.9); ¹³C NMR (125 MHz, CDCl₃): δ = 174.9, 156.3, 116.0, 71.4, 16.0; MS (MALDI-TOF): m/z calcd for C₁₀H₁₀Br₂O₄: 354.0; found: 353.7; Elemental analysis calcd. (%) for C₁₀H₁₀Br₂O₄: C 33.93, H 2.85; found: C 34.02, H 2.77. **2b**: ¹H NMR (300 MHz, CDCl₃): δ = 4.46 (q, 4H, ³J 6.9), 1.43 (t, 6H, ³J 6.9); ¹³C NMR (125 MHz, CDCl₃): δ = 173.8, 155.5, 118.8, 70.8, 15.9; MS (MALDI-TOF): m/z calcd for C₁₀H₁₀Br₂O₄: 354.0; found: 353.7; Elemental analysis calcd. (%) for C₁₀H₁₀Br₂O₄: C 33.93, H 2.85; found: C 33.92, H 2.79.

2,5-di(thiophen-2-yl)-3,6-diethoxy-1,4-benzoquinone (3a). **2a** (50 mg, 0.14 mmol), 2-(tributylstannyl)thiophene (135 mg, 0.36 mmol), and [Pd(PPh₃)₄] as catalyst (63 mg, 15% mmol) were mixed in dry toluene (50 mL) and heated at reflux for 12 h under argon atmosphere. The mixture was filtered through Celite and silica gel, washed with toluene and then CH₂Cl₂. The combined organic phases were evaporated and purified by column chromatography on silica gel (pentane/CH₂Cl₂, 1:1) to give **3a** as yellow crystals (yield 85%). Single crystals suitable for X-ray analysis were obtained by slow evaporation from a solution of **3a** in CH₂Cl₂. ¹H NMR (300 MHz, CDCl₃): δ = 8.10 (dd, 2H, ³J 3.9, ⁴J 1.2), 7.53 (dd, 2H), 7.15 (dd, 2H, ³J 5.4, ⁴J 3.9), 4.47 (q, 4H, ³J 7.2), 1.50 (t, 6H, ³J 7.2); ¹³C NMR (125 MHz, CDCl₃): δ = 182.5, 151.8, 131.9, 130.6, 129.7, 126.8, 121.9, 70.3, 16.0; MS (MALDI-TOF): m/z calcd for C₁₈H₁₆O₄S₂: 360.5; found: 360.8; elemental analysis calcd. (%) for C₁₈H₁₆O₄S₂: C 59.98, H 4.47, S 17.79; found: C 58.74, H 4.37, S 17.18.

2,6-di(thiophen-2-yl)-3,5-diethoxy-1,4-benzoquinone (3b). **3b** was obtained as violet shiny crystals according to the procedure described for **3a** using **2b** (50 mg, 0.14 mmol), 2-(tributylstannyl)thiophene (135 mg, 0.36 mmol), and [Pd(PPh₃)₄] as catalyst (63 mg, 15% mmol) (yield 81%). Single crystals suitable for X-ray analysis were obtained by slow evaporation from a solution of **3b** in CH₂Cl₂. ¹H NMR (300 MHz, CDCl₃): δ = 8.05 (dd, 2H, ³J 3.9, ⁴J 1.2), 7.56 (dd, 2H, ³J 5.1, ⁴J 1.2), 7.15 (dd, 2H, ³J 5.1, ⁴J 3.9), 4.42 (q, 4H, ³J 7.2), 1.48 (t, 6H, ³J 7.2); ¹³C NMR (125 MHz, CDCl₃): δ = 182.5, 151.8, 131.9, 130.6, 129.7, 126.8, 121.9, 70.3,

16.0; MS (MALDI-TOF): m/z calcd for $C_{18}H_{16}O_4S_2$: 360.5; found: 360.8; Elemental analysis calcd. (%) for $C_{18}H_{16}O_4S_2$: C 59.98, H 4.47, S 17.79; found: C 59.41, H 4.41, S 17.77.

2,5-di(3,4-ethylenedioxythiophen-2-yl)-3,6-diethoxy-1,4-benzoquinone (4a). **2a** (100 mg, 0.28 mmol), 2-(tributylstannyl)-3,4-ethylenedioxythiophene (151 mg, 0.36 mmol), and $[Pd(PPh_3)_4]$ as catalyst (63 mg, 7.5% mmol) were mixed in dry toluene (40 mL) and heated at reflux for 24 h under argon atmosphere. Then, 2-(tributylstannyl)-3,4-ethylenedioxythiophene (101 mg, 0.36 mmol), and fresh $[Pd(PPh_3)_4]$ (63 mg, 7.5% mmol) in dry toluene (10 mL) were added to the reaction mixture and heated at reflux for other 16 h. The mixture was filtered through Celite and silica gel, washed with toluene and then CH_2Cl_2 . The combined organic phases were evaporated and purified by column chromatography on silica gel (CH_2Cl_2 , then $CH_2Cl_2/EtOAc$, 99%/1%) to give **4a** as yellow-orange crystals (yield 90%). Single crystals suitable for X-ray analysis were obtained by slow evaporation from a solution of **8** in a $CH_2Cl_2/MeOH$ mixture. 1H NMR (300 MHz, $CDCl_3$): δ = 6.54 (s, 2H), 4.31 (q, 4H, 3J 7.0), 4.22 (m, 8H), 1.33 (t, 6H, 3J 7.0); ^{13}C NMR (125 MHz, $CDCl_3$): δ = 181.4, 154.8, 141.0, 140.7, 119.1, 105.3, 102.5, 69.7, 64.7, 64.4, 15.8; MS (MALDI-TOF): m/z calcd for $C_{22}H_{20}O_8S_2$: 476.5; found: 477.2; Elemental analysis calcd. (%) for $C_{22}H_{20}O_8S_2$: C 55.45, H 4.23, S 13.46; found: C 55.05, H 4.13, S 13.23.

2,6-di(3,4-ethylenedioxythiophen-2-yl)-3,5-diethoxy-1,4-benzoquinone (4b). **4b** was obtained as violet-red crystals according to the procedure described above for **4a** using **2b** (100 mg, 0.28 mmol), 2-(tributylstannyl)-3,4-ethylenedioxythiophene (302 mg, 0.72 mmol), and $[Pd(PPh_3)_4]$ as catalyst (121 mg, 15% mmol) (yield 87%). Single crystals suitable for X-ray analysis were obtained by slow evaporation from a solution of **4b** in a $CH_2Cl_2/MeOH$ mixture. 1H NMR (300 MHz, $CDCl_3$): δ = 6.57 (s, 2H), 4.21 (q, 4H, 3J 7.0), 4.20 (m, 8H), 1.32 (t, 6H, 3J 7.0); ^{13}C NMR (125 MHz, $CDCl_3$): δ = 179.1, 153.5, 141.1, 140.9, 120.7, 105.8, 103.5, 69.2, 64.7, 64.4, 15.7; MS (MALDI-TOF): m/z calcd for $C_{22}H_{20}O_8S_2$: 476.5; found: 477.2; Elemental analysis calcd. (%) for $C_{22}H_{20}O_8S_2$: C 55.45, H 4.23, S 13.46; found: C 55.45, H 4.14, S 13.15.

2,5-di(thiophen-2-yl)-3,6-dihydroxy-1,4-benzoquinone (5a). **3a** (50 mg, 0.14 mmol) was dissolved in CH_3CN (30 mL). NaOH (11 mg, 0.28 mmol) dissolved in H_2O (10 mL) were added to the CH_3CN solution and the resulting mixture stirred and heated at reflux temperature for 1.5 h. The violet solution was filtered and acidified using concentrate HCl. **5a** precipitates by concentration of the CH_3CN/H_2O solution as brown-yellow solid together with some colourless impurities. The product can be purified by dissolution in a mixture of $MeOH:CH_2Cl_2$ (80:20) and filtration of the insoluble product (yield 90%). 1H NMR (300 MHz, CH_3COCH_3): δ = 8.10 (dd, 2H, 3J 3.6, 4J 0.9), 7.62 (dd, 2H, 3J 5.2, 4J 0.9), 7.18 (dd, 2H, 3J 5.2, 4J 3.6); MS (MALDI-TOF): m/z calcd for $C_{14}H_8O_4S_2$: 304.3; found: 304.4; Elemental analysis calcd. (%) for $C_{14}H_8O_4S_2$: C 55.25, H 2.65, S 21.07; found: C 54.81, H 2.51, S 21.06.

2,6-di(thiophen-2-yl)-3-hydroxy-5-ethoxy-1,4-benzoquinone (5b). **5b** was obtained as brown solid according to the procedure described for **5a** using **3b** (50 mg, 0.14 mmol) instead of **3a**, and NaOH (11 mg, 0.28 mmol) (yield 87%). 1H NMR (300 MHz, CH_3COCH_3): δ = 8.12 (dd, 1H, 3J 3.9, 4J 0.9), 8.08 (dd, 1H, 3J 3.9, 4J 1.2), 7.76 (dd, 1H, 3J 5.1, 4J 1.2), 7.66 (dd, 1H, 3J 5.1, 4J 1.2), 7.20 (dd, 1H, 3J 5.4, 4J 4.2), 7.17 (dd, 1H, 3J 5.4, 4J 4.2), 4.50 (q, 2H, 3J 7.2), 1.45 (t, 3H, 3J 7.2); ^{13}C NMR (125 MHz, CH_3COCH_3): δ = 188.2, 180.7, 151.4, 151.0, 134.8, 133.6, 133.2, 133.1, 132.8, 131.4, 128.6, 128.2, 126.1, 114.7, 71.5, 17.1; MS (MALDI-TOF): m/z calcd for $C_{16}H_{12}O_4S_2$: 332.4; found: 332.8; Elemental analysis calcd. (%) for $C_{16}H_{12}O_4S_2$: C 57.81, H 3.64, S 19.29; found: C 57.67, H 3.45, S 19.52.

2,5-di(3,4-ethylenedioxythiophen-2-yl)-3,6-dihydroxy-1,4-benzoquinone (6a). **4a** (50 mg, 0.10 mmol) was dissolved in CH_3CN (30 mL). NaOH (8.5 mg, 0.20 mmol) dissolved in H_2O (10 mL) were added to the CH_3CN solution and the resulting mixture stirred and heated at reflux temperature for 24 h. The violet-reddish solution was filtered and acidified using concentrate HCl. **6a** precipitates by

concentration of the CH₃CN/H₂O solution as yellow-brown solid together with some colourless impurities. The product can be purified by several washing with fresh water. (yield 83%). ¹H NMR (300 MHz, CD₃COCD₃): δ = 6.61 (s, 2H), 4.22 (m, 8H); MS (MALDI-TOF): m/z calcd for C₁₈H₁₂O₈S₂: 420.0; found: 419.5; Elemental analysis calcd. (%) for C₁₄H₈O₄S₂: C 51.42, H 2.88, S 15.25; found: C 50.91, H 2.86, S 14.68.

2,6-di(3,4-ethylenedioxythiophen-2-yl)-3-hydroxy-5-ethoxy-1,4-benzoquinone (6b). **6b** was obtained as dark violet solid according to the procedure described for **6a** using **4b** (50 mg, 0.10 mmol) and NaOH (8.5 mg, 0.20 mmol) (yield 81%). ¹H NMR (300 MHz, CD₃COCD₃): δ = 6.71 (s, 1H), 6.63 (s, 1H), 4.28 (q, 2H, ³J 7.2), 4.24 (m, 4H), 4.22 (m, 4H), 1.30 (t, 3H, ³J 7.2); ¹³C NMR (125 MHz, CH₃COCH₃): δ = 185.3, 180.6, 154.3, 153.1, 143.5, 143.1, 143.0, 142.5, 133.7, 133.6, 130.3, 124.3, 105.0, 103.7, 70.6, 66.6, 66.5, 66.2, 66.1, 17.0; MS (MALDI-TOF): m/z calcd for C₂₀H₁₆O₈S₂: 448.4; found: 449.2; elemental analysis calcd. (%) for C₂₀H₁₆O₈S₂: C 53.56, H 3.60, S 14.30; found: C 52.93, H 3.52, S 13.96.

KHCiNAn (8). **7** (5 g, 0.022 mol) was suspended in H₂O (150 mL) and the mixture was stirred and heated at ca. 60 °C. A 6 M KOH aqueous solution (30 mL) was slowly added to the orange solution that became deep-red. After 30 min under stirring at 60 °C, **7** was completely dissolved, and the solution was concentrated to half of the initial volume and kept in cold for one night to induce the precipitation of **L5** as potassium salt. The dark-red needle-like crystals were filtered and washed several time with a 3 M KOH aqueous solution, then with acetone, and dried in air. The sodium salt (3 g) were dissolved in H₂O (100 mL) by heating, then the solution filtered and acidified with concentrate HCl. The deep-red solution was concentrated by rota-evaporation until the incipient precipitation of **8** (ca. 50 mL) as red-orange shiny crystals suitable for X-ray analysis. (yield 40%). ¹³C NMR (125 MHz, D₂O): δ = 177.1, 169.0, 117.8, 112.5, 92.2, 86.5. FT-IR (ν_{max}/cm⁻¹, KBr pellets): 3462(w, broad), 3069(m, broad), 2236(vs), 2207(s), 1676(m), 1636(m), 1625(m), 1578(vs), 1400(m), 1361(w), 1300(m), 1271(m), 1184(m), 1004(m), 863(m), 801(m), 779(m), 752(w), 653(w), 607(m), 550(w), 479(w). ESI-MS, m/z found (calcd) = 197.75 (197.96) [CICNAn-H]⁻; UV-Vis (H₂O solution, λ_{max}/nm (ε/dm³ mol⁻¹ cm⁻¹)): 269 (20020), 316 (23520), 459 (526). Elemental analysis calcd. (%) for C₇HCiNO₄K: C 37.95, H 0.45, N 6.32; found: C 37.58, H 0.39, N 6.25.

[(Ph)₄P]₂[CICNAn]·2H₂O (9). **8** (50 mg, 0.20 mmol) was dissolved under heating in a H₂O solution (100 mL) containing NaOH (20 mg, 0.50 mmol) and (Ph)₄PBr (210 mg, 0.50 mmol). By slow cooling of the solution, **9** precipitates as orange shiny single crystal suitable for X-ray analysis. FT-IR (ν_{max}/cm⁻¹, KBr pellets): 3479(m, broad), 3057(w), 2208(w), 2188(m), 1624(m), 1586(w), 1558(s), 1530(vs), 1484(m), 1435(s), 1376(w), 1340(w), 1314(w), 1196(w), 1109(s), 997(m), 827(w), 763(m), 725(s), 694(m), 609(m), 530(vs), 461(w). ESI-MS, m/z found (calcd) = 197.75 (197.96) [CICNAn-H]⁻; 535.88 (536.08) [(Ph)₄P][CICNAn]⁻. UV-Vis (CHCN₃ solution, λ_{max}/nm (ε/dm³ mol⁻¹ cm⁻¹)): 263 (13478), 318 (20800), 486 (438). Elemental analysis calcd. (%) for C₅₅H₄₄CiNO₆P₂: C 72.41, H 4.86, N 1.54; found: C 72.35, H 4.73, N 1.59.

[Cu(Th₂An)(tbbpy)]·2H₂O (C11). NaOH (22 mg, 0.56 mmol) was dissolved in H₂O (15 mL) and added drop-wise to a CH₃CN (60 mL) solution of **3a** (100 mg, 0.28 mmol). The mixture was stirred and heated at reflux temperature for 1.5 h. [Cu(tbbpy)Cl₂] (113 mg, 0.28 mmol) was dissolved in H₂O (15 mL) and added drop-wise to the blue solution containing the dianionic form of **5a**. **C11** precipitates immediately as green solid. The mixture was filtered and the precipitate washed several times with CH₃CN, then Et₂O (yield 87%). Single crystals suitable for X-ray analysis were obtained by slow diffusion of MeOH in a solution of **7** in DMF. ESI-MS, m/z found (calcd) = 634.27 (634.10) [[Cu(Th₂An)(tbbpy)]-H]⁺; UV-Vis (CHCl₃ solution, λ_{max}/nm (ε/dm³ mol⁻¹ cm⁻¹)): 305 (25920), 333 (18720), 347 (16174), 394 (6034), 634 (1634). Elemental analysis calcd. (%) for C₃₂H₃₄CuN₂O₆S₂: C 57.34, H 5.11, N 4.18; found: C 57.16, H 4.60, N 4.15.

1.4.3 Equipment and Measurements Details

Elemental Analyses. C, H, N, and S measurements were performed with a Thermo Electron Analyser CHNS Flash 2000 analyser.

NMR Spectroscopy. NMR spectra were recorded on a Bruker Advance DRX 300 spectrometer (300 MHz for ^1H , 75 MHz for ^{13}C).

UV-Vis Spectroscopy. UV-Vis absorption spectra (800–200 nm) were recorded in CH_3CN on a Varian Cary 5 spectrophotometer.

MS Analyses. MS (MALDI-TOF) spectra were recorded on a Bruker Biflex-IIIITM equipped with a 337 nm N_2 laser.

Cyclic Voltammetry. Cyclic voltammetry was carried out with a BioLogic potentiostat model SP-150, using a three-electrode cell equipped with a platinum working millielectrode with a surface area of 0.126 cm^2 , an Ag/Ag^+ pseudoreference and a platinum-wire as counterelectrode. The experiments were performed at room temperature ($25\text{ }^\circ\text{C}$), in dry and Nitrogen-degassed CH_3CN solution containing 0.1 mol dm^{-3} $[(n\text{-Bu})_4\text{N}]\text{PF}_6$ as supporting electrolyte, at 100 mV s^{-1} scan rate. All the voltamograms were corrected for the half-wave potential of the ferrocene-ferrocenium couple as internal standard ($+0.42\text{ V}$ under these conditions).

Single Crystal X-ray Crystallography. X-ray diffraction measurements were performed on a Bruker Nonius Kappa CCD diffractometer, using graphite-monochromated $\text{MoK}\alpha$ radiation ($\lambda = 0.71073\text{ \AA}$). The structures were solved by direct methods (SHELXS-97⁷⁷ or SIR2004⁷⁸) and refined on F^2 with full-matrix least squares (SHELXL-97),⁷⁷ using the Wingx software package.⁷⁹ The non-H atoms were refined with anisotropic displacement parameters. A summary of the crystallographic data and the structure refinement for **3a**, **3b**, **4a**, **4b**, **8**, **9**, and **C11** is reported in Table 1.8.

Table 1.8. Summary of X-ray crystallographic data for **3a**, **3b**, **4a**, **4b**, **8**, **9**, and **C11**.

	3a	3b	4a	4b
Empirical formula	$\text{C}_{18}\text{H}_{16}\text{O}_4\text{S}_2$	$\text{C}_{36}\text{H}_{32}\text{Cl}_6\text{O}_8\text{S}_4$	$\text{C}_{22}\text{H}_{20}\text{O}_8\text{S}_2$	$\text{C}_{22}\text{H}_{20}\text{O}_8\text{S}_2$
Formula weight	360.43	720.86	476.50	476.50
Crystal size, mm	$0.40 \times 0.10 \times 0.05$	$0.50 \times 0.20 \times 0.20$	$0.60 \times 0.20 \times 0.20$	$0.26 \times 0.24 \times 0.04$
Crystal system	Triclinic	Monoclinic	Monoclinic	Monoclinic
Space group	$P-1$	$P2_1/a$	$C2/c$	$P2_1/c$
a , \AA	4.891(1)	7.6923(7)	20.441(2)	9.782(1)
b , \AA	9.361(2)	46.482(6)	6.614(1)	14.556(1)
c , \AA	9.693(4)	9.938(2)	17.168(2)	15.493(1)
α , deg.	104.639(2)	90	90	90
β , deg.	101.792(2)	112.20(1)	111.534(6)	98.14(1)
γ , deg.	100.598(2)	90	90	90
V , \AA^3	407.06(2)	3290.1(8)	2158.9(4)	2183.9(3)
Z	1	4	4	4
T , K	293(2)	293(2)	293(2)	293(2)
ρ (calc), Mg/m^3	1.470	1.455	1.468	1.449
μ , mm^{-1}	0.347	0.343	0.282	0.291
θ range, deg.	4.38–26.49	2.21–25.00	3.36–30.50	2.99–27.50
GooF	1.022	1.040	1.051	1.038

	8	9	C11
R1	0.0588	0.0589	0.0494
wR2	0.1092	0.1564	0.1259
Empirical formula	C ₇ HClKNO ₄	C ₅₅ H ₄₄ ClNO ₆ P ₂	C ₃₂ H ₃₂ CuN ₂ O ₆ S ₂
Formula weight	237.64	912.30	668.26
Crystal size, mm	0.60×0.09×0.03	0.50×0.30×0.10	0.40×0.05×0.05
Crystal system	Monoclinic	Triclinic	Monoclinic
Space group	<i>P</i> 2 ₁ / <i>a</i>	<i>P</i> -1	<i>P</i> 2 ₁ / <i>n</i>
<i>a</i> , Å	7.039(1)	9.987(1)	6.878(2)
<i>b</i> , Å	17.051(3)	11.087(1)	17.926(8)
<i>c</i> , Å	7.106(1)	12.249(1)	24.286(8)
α, deg.	90	88.863(8)	90
β, deg.	102.389(15)	68.550(6)	92.51(2)
γ, deg.	90	66.460(7)	90
<i>V</i> , Å ³	833.0(2)	1144.6(1)	2991.5(5)
<i>Z</i>	4	1	4
<i>T</i> , K	293(2)	293(2)	150(2)
ρ (calc), Mg/m ³	1.895	1.324	1.484
μ, mm ⁻¹	0.941	0.207	0.918
θ range, deg.	3.19–26.99	1.81–28.79	2.42–24.20
Goof	1.063	1.022	1.042
R1	0.0446	0.0583	0.0599
wR2	0.1041	0.1327	0.1169

$$R1 = \frac{\sum ||F_o| - |F_c||}{\sum |F_o|}, wR2 = \frac{[\sum (w(F_o^2 - F_c^2)^2)] / \sum (w(F_o^2)^2)]^{1/2}}, w = 1 / [\sigma^2(F_o^2) + (aP)^2 + bP], \text{ where } P = [\max(F_o^2, 0) + 2F_c^2] / 3.$$

Computational Details. All calculations were performed with the Gaussian09 program.⁸⁰ Starting from the X-ray data and without forcing any symmetry, the gas phase ground state geometries were optimized by a DFT method with the hybrid PBE0 functional (with 25% of exact exchange)^{67,68} and the augmented and polarized Pople type basis set 6-311++G(3df,2pd). The gas phase excited states energies have been determined at the same level by a linear response Time-Dependent DFT method. To evaluate the error committed by ignoring the solvent, the *meta* isomer ground state geometry and excited state energies were also computed by a polarizable continuum model (LR-PCM-TD-DFT).⁸¹ The calculated absorption spectra have been enlarged with a gaussian shape (FWHM = 3000 cm⁻¹) with GaussSum to compare with experiment.⁸² The Tozer diagnostic parameter^{70,71} and the molecular orbitals and density difference plots have been calculated and represented by the ABSICC program.⁸³

Photoluminescence Spectroscopy. PL emission spectra (450–750 nm) were collected in CH₃CN or H₂O solutions with a Horiba-Jobin Yvon Fluoromax-4 spectrofluorimeter using a DC Xenon lamp. All spectra were spectrally corrected for detector response. Bandpass was set as 5 nm slit width for each measurement. Emission quantum yields (Φ) were evaluated using the relative method⁸⁴ by means of the following equation

$$\Phi = \Phi_R \frac{1 - 10^{-A_R} I n^2}{1 - 10^{-A} I_R n_R^2}$$

where A_R and A are the absorbance of the reference and the sample, respectively, at the excitation wavelength, I_R and I indicate the integrated emission signal of the reference and the sample, respectively, and n_R and n indicate the refractive index of the solvent for the reference and the sample, respectively. [Ru(bpy)₃]Cl₂ ($\Phi_R = 0.063$) was used as reference.

References

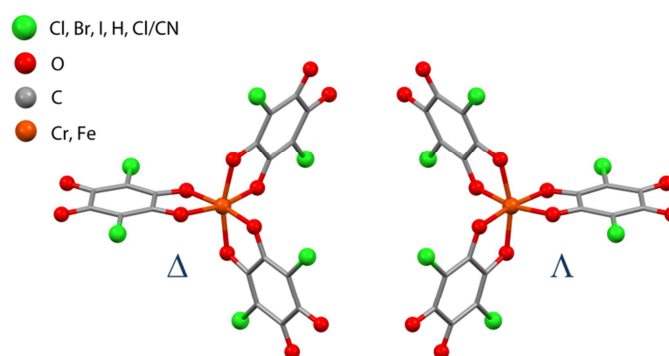
1. Khanna, J. M.; Malone, M. H.; Euler, K. L.; Brady, L. R. *J. Pharm. Sci.* **1965**, *54*, 1016–1020.
2. Zhang, B.; Salituro, G.; Szalkowski, D.; Li, Z.; Zhang, Y.; Royo, I.; Vilella, D.; Diez, M. T.; Pelaez, F.; Ruby, C.; Kendall, R. L.; Mao, X.; Griffin, P.; Calaycay, J.; Zierath, J. R.; Heck, A. V.; Smith, R. G.; Moller, D. E. *Science* **1999**, *284*, 974–977.
3. Tsukamoto, S.; Macabalong, A. D.; Abe, T.; Hirota, H.; Ohta, T. *Tetrahedron* **2002**, *58*, 1103–1105.
4. Puder, C.; Wagner, K.; Vettermann, R.; Hauptmann, R.; Potterat, O. *J. Nat. Prod.* **2005**, *68*, 323–326.
5. Wood, H. B. Jr.; Black, R.; Salituro, G.; Szalkowski, D.; Li, Z.; Zhang, Y.; Moller, D. E.; Zhang, B.; Jones, A. B. *Bioorg. Med. Chem. Lett.* **2000**, *10*, 1189–1192.
6. Liu, K.; Xu, L.; Szalkowski, D.; Li, Z.; Ding, V.; Kwei, G.; Huskey, S.; Moller, D. E.; Heck, J. V.; Zhang, B. B.; Jones, A. B. *J. Med. Chem.* **2000**, *43*, 3487–3494.
7. Kitagawa, S.; Kawata, S. *Coord. Chem. Rev.* **2002**, *224*, 11–34.
8. Jones, R. G.; Shonle, H. A. *J. Am. Chem. Soc.* **1945**, *67*, 1034–1035.
9. Viault, G.; Grée, D.; Das, S.; Yadav, J. S.; Grée, R. *Eur. J. Org. Chem.* **2011**, *7*, 1233–1244.
10. Barltrop, J. A.; Burstall, M. L. *J. Chem. Soc. (Resumed)* **1959**, 2183–2186.
11. Wallenfels, K.; Friedrich, K. *Chem. Ber.* **1960**, *93*, 3070–3082.
12. Stenhouse, J. J. *J. Chem. Soc.* **1870**, *23*, 6–14.
13. Torrey, H. A.; Hunter, W. H. *J. Am. Chem. Soc.* **1912**, *34*, 702–716.
14. Meyer, H. O. *Berichte der deutschen chemischen Gesellschaft (A and B Series)* **1924**, *57*, 326–328.
15. Gelormini, O.; Artz, N. E. *J. Am. Chem. Soc.* **1930**, *52*, 2483–2494.
16. Hoglan, F. A.; Bartow, E. J. *J. Am. Chem. Soc.* **1940**, *62*, 2397–2400.
17. Preisler, P. W.; Berger, L. *J. Am. Chem. Soc.* **1942**, *64*, 67–69.
18. Fatiadi, A. J.; Sager, W. F. *Org. Syn.* **1962**, *42*, 90–91.
19. Junek, H.; Unterweger, B.; Peltzmann, R. *Z. Naturforsch. B Chem. Sci.* **1978**, *33B*, 1201–1203.
20. Wallenfels, K.; Bachmann, G.; Hofmann, D.; Kern, R. *Tetrahedron* **1965**, *21*, 2239–2256.
21. Zaman, B.; Morita, Y.; Toyoda, J.; Yamochi, H.; Sekizaki, S.; Nakasuji, K. *Mol. Cryst. Liq. Cryst.* **1996**, *287*, 249–254.
22. Rehwoldt, R. E.; Chasen, B. L.; Li, J. B. *Anal. Chem.* **1966**, *8*, 1018–1019.
23. Akutagawa, T.; Nakamura, T. *Cryst. Growth Des.* **2005**, *6*, 70–74.
24. Kögl, F.; Lang, A. *Ber. d. deutsch. chem. Ges.* **1926**, *59*, 910–913.
25. Fichter, F.; Willmann, A. *Ber. d. deutsch. chem. Ges.* **1904**, *37*, 2384–2390.
26. Fichter, F. *Justus Liebigs Annalen der Chemie* **1908**, *361*, 363–402.
27. Ward, M. D.; McCleverty, J. A. *J. Chem. Soc., Dalton Trans.* **2002**, *3*, 275–288.
28. Tinti, F.; Verdaguer, M.; Kahn, O.; Savariault, J. M. *Inorg. Chem.* **1987**, *26*, 2380–2384.
29. Horiuchi, S.; Kumai, R.; Tokura, Y. *J. Am. Chem. Soc.* **2013**, *135*, 4492–4500.
30. Kagawa, F.; Horiuchi, S.; Minami, N.; Ishibashi, S.; Kobayashi, K.; Kumai, R.; Murakami, Y.; Tokura, Y. *Nano Lett.* **2014**, *14*, 239–243.

31. Murata, T.; Yakiyama, Y.; Nakasuji, K.; Morita, Y. *CrystEngComm* **2011**, *13*, 3689–3691.
32. Horiuchi, S.; Kumai, R.; Tokunaga, Y.; Tokura, Y. *J. Am. Chem. Soc.* **2008**, *130*, 13382–13391.
33. Horiuchi, S.; Kumai, R.; Tokura, Y. *J. Am. Chem. Soc.* **2005**, *127*, 5010–5011.
34. Reinoso, S.; Vitoria, P.; San Felices, L.; Montero, A.; Lezama, L.; Gutiérrez-Zorrilla, J. M. *Inorg. Chem.* **2007**, *46*, 1237.
35. Richter, M. M. *Ber. d. deutsch. chem. Ges.* **1911**, *44*, 3469–3477.
36. Klug, A. *Acta Cryst.* **1965**, *19*, 983–992.
37. Andersen, E. K. *Acta Cryst.* **1967**, *22*, 188–191.
38. Andersen, E. K. *Acta Cryst.* **1967**, *22*, 191–196.
39. Andersen, E. K. *Acta Cryst.* **1967**, *22*, 204–208.
40. Andersen, E. K.; Andersen, I. G. K. *Acta Cryst. B* **1975**, *31*, 379–383.
41. Andersen, E. K.; Andersen, I. G. K. *Acta Cryst. B* **1975**, *31*, 384–387.
42. Semmingsen, D. *Acta Chem. Scand. B* **1977**, *31*, 11–14.
43. Robl, C. *Zeitschrift für Kristallographie* **1988**, *184*, 289.
44. Munakata, M.; Wu, L. P.; Kuroda-Sowa, T.; Yamamoto, M.; Maekawa, M.; Moriwaki, K. *Inorg. Chim. Acta* **1998**, *268*, 317–321.
45. Molcanov, K.; Stare, J.; Vener, M. V.; Kojic-Prodic, B.; Mali, G.; Grdadolnik, J.; Mohacek-Grosev, V. *Phys. Chem. Chem. Phys.* **2014**, *16*, 998–1007.
46. Andersen, E. K. *Acta Cryst.* **1967**, *22*, 196–201.
47. Andersen, E. K. *Acta Cryst.* **1967**, *22*, 201–203.
48. Biliskov, N.; Kojic-Prodic, B.; Mali, G.; Molcanov, K.; Stare, J. *J. Phys. Chem. A* **2011**, *115*, 3154–3166.
49. Molcanov, K.; Sabljic, I.; Kojic-Prodic, B. *CrystEngComm* **2011**, *13*, 4211–4217.
50. Molcanov, K.; Kojic-Prodic, B. *Acta Cryst. B* **2012**, *68*, 57–65.
51. Molcanov, K.; Kojic-Prodic, B.; Babic, D.; Stare, J. *CrystEngComm* **2013**, *15*, 135–143.
52. Robl, C. *Mater. Res. Bull.* **1987**, *22*, 1395–1403.
53. Molcanov, K.; Kojic-Prodic, B.; Meden, A. *CrystEngComm* **2009**, *11*, 1407–1415.
54. Wellenfels, K.; Draber, W. *Chem. Ber.* **1957**, *90*, 2819–2832.
55. Nobusawa, M.; Akutsu, H.; Yamada, J.; Nakatsuji, S. *Chem. Lett.* **2008**, *37*, 788–789.
56. Nakatsuji, S.; Nobusawa, M.; Suzuki, H.; Akutsu, H.; Yamada, J. *J. Org. Chem.*, **2009**, *74*, 9345–9350.
57. Pirrung, M. C.; Li, Z.; Park, K.; Zhu, J. *J. Org. Chem.* **2002**, *67*, 7919–7926.
58. Gan, X.; Jiang, W.; Wang, W.; Hu, L. *Org. Lett.* **2009**, *11*, 589–592.
59. Ángyán, J.; Poirier, R. A.; Kucsman, Á.; Csizmadia, I. G. *J. Am. Chem. Soc.* **1987**, *109*, 2237–2245.
60. Iwaoka, M.; Takemoto, S.; Tomoda, S. *J. Am. Chem. Soc.* **2002**, *124*, 10613–10620.
61. Nakanishi, W.; Nakamoto, T.; Hayashi, S.; Sasamori, T.; Tokitoh, N. *Chem. Eur. J.* **2007**, *13*, 255–268.
62. Réthoré, C.; Madalan, A.; Fourmigué, M.; Canadell, E.; Lopes, E. B.; Almeida, M.; Clérac, R.; Avarvari, N. *New J. Chem.* **2007**, *31*, 1468–1483.
63. Nakanishi, W.; Hayashi, S.; Narahara, K. *J. Phys. Chem. A*, **2008**, *112*, 13593–13599.

64. Brezgunova, M. E.; Lieffrig, J.; Aubert, E.; Dahaoui, S.; Fertey, P.; Lebegue, S.; Angyan, J. G.; Fourmigué, M.; Espinosa, E. *Cryst. Growth Des.* **2013**, *13*, 3283–3289.
65. Adamo, C.; Jacquemin, D. *Chem. Soc. Rev.* **2013**, *42*, 845–856.
66. Kantchev, E. A. B.; Norsten, T. B.; Sullivan, M. B. *Org. Biomol. Chem.* **2012**, *10*, 6682–6692.
67. Adamo, C.; Barone, V. *J. Chem. Phys.* **1999**, *110*, 6158–6170.
68. Perdew, P.; Kurth, S.; Zupan, A.; Blaha, P. *Phys. Rev. Lett.* **1999**, *82*, 2544–2547.
69. Laurent, A. D.; Jacquemin, D. *Int. J. Quantum Chem.* **2013**, *113*, 2019–2039.
70. Peach, M. J. G.; Benfield, P.; Helgaker, T.; Tozer, D. J. *J. Chem. Phys.* **2008**, *128*, 044118.
71. Peach, M. J. G.; Tozer, D. J. *J. Mol. Struct. (Theochem)* **2009**, *914*, 110–114.
72. Roncali, J. *Chem. Rev.* **1992**, *92*, 711–738.
73. Akoudad, S.; Roncali, J. *Synth. Met.* **1998**, *93*, 111–114.
74. Awad, D. J.; Schilde, U.; Strauch, P. *Inorg. Chim. Acta* **2011**, *365*, 127–132.
75. Molčanov, K.; Jurić, M.; Kojić-Prodić, B. *Dalton Trans.* **2013**, *42*, 15756–15765.
76. Zhu, S. S.; Swager, T. M. *J. Am. Chem. Soc.* **1997**, *119*, 12568–12577.
77. Sheldrick, G. M. *SHELX97. Programs for Crystal Structure Analysis (1997)* (Release 97-2). University of Göttingen, Germany.
78. Burla, M. C.; Caliendo, R.; Camalli, M.; Carrozzin, B.; Cascarano, G. L.; De Caro, L.; Giacovazzo, C.; Polidori, G.; Spagna, R. *J. App. Cryst.* **2005**, *38*, 381–388.
79. Farrugia, L. J. *J. App. Cryst.* **1999**, *32*, 837–838.
80. Gaussian 03, Revision C.02, Frisch, M. J.; Trucks, G. W.; Schlegel, H. B.; Scuseria, G. E.; Robb, M. A.; Cheeseman, J. R.; Montgomery, Jr. J. A.; Vreven, T.; Kudin, K. N.; Burant, J. C.; Millam, J. M.; Iyengar, S. S.; Tomasi, J.; Barone, V.; Mennucci, B.; Cossi, M.; Scalmani, G.; Rega, N.; Petersson, G. A.; Nakatsuji, H.; Hada, M.; Ehara, M.; Toyota, K.; Fukuda, R.; Hasegawa, J.; Ishida, M.; Nakajima, T.; Honda, Y.; Kitao, O.; Nakai, H.; Klene, M.; Li, X.; Knox, J. E.; Hratchian, H. P.; Cross, J. B.; Bakken, V.; Adamo, C.; Jaramillo, J.; Gomperts, R.; Stratmann, R. E.; Yazyev, O.; Austin, A. J.; Cammi, R.; Pomelli, C.; Ochterski, J. W.; Ayala, P. Y.; Morokuma, K.; Voth, G. A.; Salvador, P.; Dannenberg, J. J.; Zakrzewski, V. G.; Dapprich, S.; Daniels, A. D.; Strain, M. C.; Farkas, O.; Malick, D. K.; Rabuck, A. D.; Raghavachari, K.; Foresman, J. B.; Ortiz, J. V.; Cui, Q.; Baboul, A. G.; Clifford, S.; Cioslowski, J.; Stefanov, B. B.; Liu, G.; Liashenko, A.; Piskorz, P.; Komaromi, I.; Martin, R. L.; Fox, D. J.; Keith, T.; Al-Laham, M. A.; Peng, C. Y.; Nanayakkara, A.; Challacombe, M.; Gill, P. M.; Johnson, W.; Chen, B. W.; Wong, M. W.; Gonzalez, C.; Pople, J. A. *Gaussian, Inc.*, Wallingford CT, **2004**.
81. Tomasi, J.; Mennucci, B.; Cammi, R. *Chem. Rev.* **2005**, *105*, 2999–3094.
82. O'boyle, N. M.; Tenderholt, A. L.; Langner, K. M. *J. Comput. Chem.* **2008**, *29*, 839–845.
83. ABSiCC, *automating boring stuffs in computational chemistry*, is designed by T. Cauchy and written by Y. Morille, Angers University.
84. Brouwer, A. M., *Pure Appl. Chem.* **2011**, *12*, 213–2228.

Chapter 2

Anilate-based Metal Complexes as Molecular Building Blocks



tris(anilato)metallate(III) $[M^{III}(X_2An)_3]^{3-}$

This Chapter reports on the synthesis, crystal structure, DFT calculations and magnetic properties of a novel family of versatile paramagnetic molecular building blocks formulated as $[M^{III}(X_2An)_3]^{3-}$ ($M^{III} = Cr, Fe; X = Cl, Br, I, H, Cl/CN$).

2.1 Introduction

The interest in molecule-based materials, namely materials built from predesigned molecular building blocks, has increased in recent years since they are known to exhibit many technologically important properties (*e.g.* magnetic ordering, electrical conductivity, superconductivity, ferroelectricity, *etc.*) traditionally considered to belong solely to the realm of classic inorganic solids such as metals, alloys or oxides.¹

The vast potential of molecular chemistry opens extraordinary possibilities for designing molecules with desired size, shape, charge, polarity, and electronic properties. Molecular materials are, in fact, built by combining such molecules in the solid state through “soft”, frequently solution-based, routes, involving coordination and/or supramolecular chemistry. Intermolecular interactions play a key role in assembling these molecular bricks into 1-, 2- and 3-D arrays with a desired structure and functionality. These non-covalent supramolecular interactions include hydrogen- and halogen-bonds, cation–anion electrostatic, π – π , dipole-dipole and van der Waals interactions. A given solid may involve any combination of them, with their strength and directionality determining the supramolecular architecture of the materials and their physical properties.¹ In this context, crystal engineering, the art of designing synthetic crystalline materials through the knowledge of the electronic, steric, topological and intermolecular interactions between the functional groups of their constituent building blocks,^{2–5} offers a powerful tool for preparing novel molecular materials with appealing physical properties. One of the most powerful strategies to design such materials is based on the use of tectons,^{2–5} in particular metallotectons which are metal complexes able to be involved in well identified intermolecular interactions through peripheral groups present in the ligand (tecton) coordinated to the metal. As such, they can work as building blocks for the rational construction of crystals. There are several advantages of employing metallotectons to construct supramolecular architectures or coordination polymers. In particular it is possible to tune both the coordination geometry around the metal centre, the bonding capability at the complex’s periphery, and the metallotecton shape by varying the metal, its oxidation state, and/or the organic ligands used.

With this view, anilate-based ligands have been selected as suitable ligands for the preparation of octahedral tris-chelated molecular building blocks for the construction of supramolecular architectures, coordination polymers or as paramagnetic components of hybrid organic-inorganic systems. These ligands have been selected since they exhibit the following features: (i) ability to coordinate metal centers in the 1,2-bidentate coordination mode, (ii) ability to bridge two different metal ions through peripheral coordinating C–O groups, (iii) presence of four oxygens as donors atoms that favour the coordination to paramagnetic hard metal ions (*e.g.* Cr^{III}, Fe^{III}, Mn^{II}, *etc.*), (iv) high stability of the –2 charged dianionic form, able to afford tris-chelated metal complexes by reaction with trivalent metal ions, (v) wide range of derivatives having various substituents on the 3 and 6 positions (see Chapter 1) whose nature do not affect the 1,2-bidentate coordination mode, (vi) ability to mediate magnetic exchange interactions between coordinated metal ions whose strength is modulated by the nature of the substituents, (vii) ability of the substituent groups on the

ligand to be involved in various supramolecular interactions affecting the dimensionality of the obtained material, (viii) non-innocent redox properties and easy reduction process to a radical-anion form, (ix) possibility to introduce additional properties by playing with the various substituent groups connected to the anilate moiety (see Chapter 1). All these features make them appealing ligands for the preparation of the above-mentioned molecular materials.

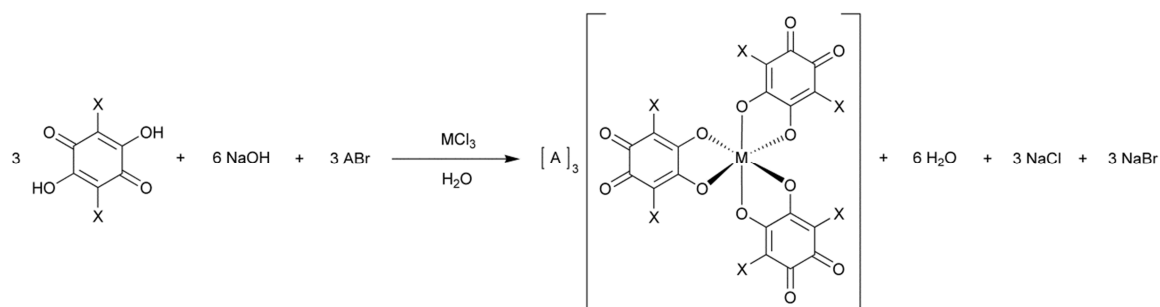
The coordination chemistry of these ligands is described in the literature with particular attention for chloranilate⁶ and hydranilate,⁷⁻¹⁰ whereas the other derivatives have been rarely used. Among the anilate-based metal complexes, some dinuclear^{9,11,12} and several *n*-D (*n* = 1, 2, 3) polymeric systems have been reported,¹¹⁻²⁰ but only few examples of mononuclear complexes have been obtained so far.^{11,18,21-24} Moreover, except the tris(chloranilato)ferrate(III) complex obtained by Miller *et al.* as counteranion of a cationic dimeric Fe^{II} complex,²⁵ no reports on the synthesis and characterization of tris-chelated homoleptic mononuclear complexes with the previously mentioned ligands are available in the literature so far.

With the aim to investigate the ability of such ligands to provide tris-chelated octahedral paramagnetic metal complexes as suitable molecular building blocks for the preparation of molecule-based materials exhibiting magnetic and conducting properties, a general synthetic strategy to achieve a family of tris(anilato)metallate(III) complexes with general formula $[A]_3[M^{\text{III}}(X_2An)_3]$ ($M^{\text{III}} = \text{Cr}$, $X = \text{Cl}$ (**C1**), Br (**C3**), I (**C5**), H (**C7**), Cl/CN (**C9**); $M^{\text{III}} = \text{Fe}$, $X = \text{Cl}$ (**C2**), Br (**C4**), I (**C6**), H (**C8**), Cl/CN (**C10**); $A = (n\text{-Bu})_4\text{N}^+$ (**C1a-6a** and **C9a-10a**), $(\text{Ph})_4\text{P}^+$ (**C1b-10b**), $(\text{Et})_3\text{N}^+$ (**C1c-2c**)) (see Chart 3) is reported in this Chapter. Their full characterization, consisting in the X-ray crystal structures, also supported by PXRD, Hirshfeld surface analysis, DFT calculations, spectroscopical studies through UV-Vis and FT-IR spectroscopy, electrochemical studies and magnetic properties, is also given here to provide a thorough knowledge of the structure and the properties of these systems. This is of fundamental importance to get deeper insight into the structure/properties relationships of all functional materials based on these molecular building units (see Chapters 3-5).

2.2 Results and Discussion

2.2.1 Synthetic Strategy

The tris(anilato)metallate(III) complexes were obtained, as described in detail in the Experimental Section, according to the general synthetic strategy illustrated in Scheme 2.1.



Scheme 2.1. General reaction scheme for the synthesis of the $[A]_3[M^{III}(X_2An)_3]$ ($A = (n\text{-Bu})_4N^+$, $(Ph)_4P^+$; $M = Cr, Fe$; $X = Cl, Br, I, H, Cl/CN$) complexes.

A one-pot reaction between an aqueous solution of the trivalent metal ion ($M = Cr$ or Fe) and an aqueous solution of the anilate dianion generated *in situ* allows to obtain compounds **C1-10** in high yields ranging from 70 to 90%.

2.2.2 Crystal Structure Description

The crystal structures of the Cr^{III} and Fe^{III} anilate complexes consist of homoleptic tris-chelated complex anions of formula $[M^{III}(X_2An)_3]^{3-}$ ($M^{III} = Cr$ or Fe ; $X = Cl, Br, I, H, Cl/CN$) and $(n\text{-Bu})_4N^+$, $(Ph)_4P^+$, or $(Et)_3NH^+$ cations. The complexes exhibit octahedral geometry with the metal bound by six oxygen atoms from three chelating ligands. According to the metal coordination of three bidentate ligands, the metal complexes are chiral, and in the crystal lattice both Λ and Δ enantiomers are present since all the space groups are centrosymmetric. The molecular structure of the complex anions for **C6b**, **C8b** and **C9b** are reported in Figure 2.1.

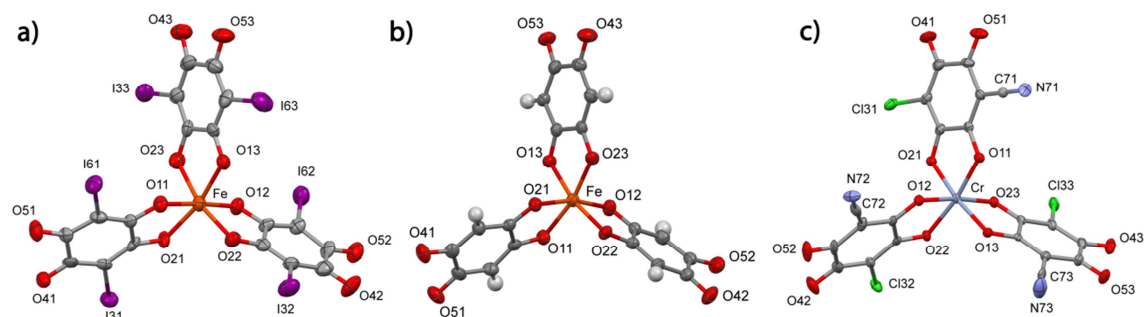


Figure 2.1. ORTEP drawing for the anionic complexes (Λ enantiomers) for **C6b** (a), **C8b** (b), and **C9b** (c) with thermal ellipsoids at the 30% probability level, along with principal atoms labelling scheme.

The metal-oxygen bond distances range from 1.951(4)–1.987(4) Å and 1.994(7)–2.028(7) Å for the Cr^{III} and Fe^{III} complexes, respectively, and are in agreement with the high spin character of these systems (*vide infra*) (Table 2.1).

Table 2.1. M–O bond distances (Å) for the structurally characterized metal complexes.

Bonds	C1c	C2c	C5a	C2b	C4b
M–O(11)	1.951(4)	1.999(2)	1.968(5)	2.002(6)	2.012(7)
M–O(21)	1.972(4)	2.013(2)	1.971(4)	2.008(6)	2.020(7)
M–O(12)	1.974(4)	2.003(3)	1.978(5)	2.001(6)	1.999(7)
M–O(22)	1.987(4)	-	1.971(5)	2.017(6)	2.028(7)
M–O(13)	1.968(4)	-	1.966(5)	2.013(6)	2.018(7)
M–O(23)	1.959(4)	-	1.962(5)	1.999(6)	1.994(7)
	C6b	C8b	C9a	C9b	C10a
M–O(11)	2.01(1)	1.998(3)	1.961(4)	1.966(3)	1.998(3)
M–O(21)	2.006(9)	1.995(2)	1.966(4)	1.968(3)	2.018(3)
M–O(12)	1.99(1)	1.997(3)	1.975(4)	1.968(3)	2.008(3)
M–O(22)	2.00(1)	2.000(3)	1.977(4)	1.977(3)	2.017(3)
M–O(13)	2.04(1)	2.036(3)	1.975(4)	1.982(3)	2.021(3)
M–O(23)	2.01(1)	1.990(3)	1.978(4)	1.973(3)	2.019(3)

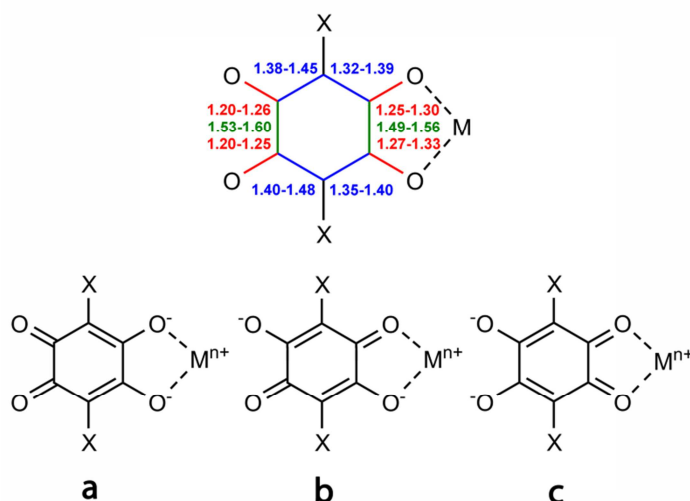
The C–O bond distances are influenced by the metal coordination since the oxygen atoms bound to the metal lead to C–O distances that are, on average, 0.06 Å longer than those of the peripheral oxygen atoms (Table 2.2).

Table 2.2. C–O bond distances (Å) for the structurally characterized metal complexes.

Bonds	C1c	C2c	C5a	C2b	C4b
C(11)–O(11)	1.296(6)	1.275(3)	1.298(8)	1.28(1)	1.30(1)
C(21)–O(21)	1.307(6)	1.279(3)	1.292(8)	1.29(1)	1.27(1)
C(41)–O(41)	1.223(7)	1.216(4)	1.226(8)	1.20(1)	1.25(1)
C(51)–O(51)	1.228(7)	1.229(4)	1.222(9)	1.22(1)	1.22(1)
C(12)–O(12)	1.295(6)	1.280(3)	1.284(8)	1.29(1)	1.30(1)
C(22)–O(22)	1.280(6)	1.227(4)	1.280(8)	1.290(9)	1.27(1)
C(42)–O(42)	1.498(8)	1.519(4)	1.51(1)	1.51(1)	1.49(1)
C(52)–O(52)	1.514(8)	-	1.52(1)	1.50(1)	1.51(1)
C(13)–O(13)	1.230(7)	-	1.225(9)	1.23(1)	1.23(1)
C(23)–O(23)	1.224(7)	-	1.207(9)	1.214(9)	1.24(1)
C(43)–O(43)	1.288(6)	-	1.279(8)	1.25(2)	1.25(1)
C(53)–O(53)	1.324(6)	-	1.284(8)	1.31(2)	1.30(2)
	C6b	C8b	C9a	C9b	C10a
C(11)–O(11)	1.30(2)	1.301(5)	1.292(7)	1.275(7)	1.282(6)
C(21)–O(21)	1.29(2)	1.294(5)	1.293(7)	1.215(6)	1.282(6)
C(41)–O(41)	1.22(2)	1.228(5)	1.222(8)	1.229(8)	1.226(7)
C(51)–O(51)	1.20(2)	1.234(5)	1.227(8)	1.204(9)	1.226(7)
C(12)–O(12)	1.33(2)	1.298(5)	1.281(7)	1.287(4)	1.293(6)

C(22)–O(22)	1.30(2)	1.293(5)	1.279(7)	1.286(4)	1.281(6)
C(42)–O(42)	1.56(2)	1.230(6)	1.232(8)	1.233(5)	1.242(7)
C(52)–O(52)	1.51(2)	1.231(6)	1.220(8)	1.222(5)	1.234(7)
C(13)–O(13)	1.23(2)	1.288(6)	1.296(7)	1.290(4)	1.281(6)
C(23)–O(23)	1.26(2)	1.297(5)	1.287(7)	1.280(4)	1.281(6)
C(43)–O(43)	1.33(2)	1.227(5)	1.230(7)	1.229(5)	1.216(7)
C(53)–O(53)	1.24(2)	1.244(5)	1.231(7)	1.222(5)	1.229(7)

The C–O distances of the peripheral C–O moieties are, thus, in agreement with a double bond character, whereas the OC–CO bond distances are in agreement with the presence of a single bond for all complexes. According to the intra-ligand bond distances, the electronic structure of the ligand can be described as a mixture of the three limit resonance structures (**a**, **b** and **c** in Scheme 2.2), with the *o*-quinone-like resonance structure (**a** form) prevailing.



Scheme 2.2, Top, Summary of intra-ligand bond distances (Å) ranges for compounds **C1-10** (red: C–O, green: OC–CO, and blue OC–CX distances, respectively). Bottom, Limit resonance structures of the ligands (M = Cr, Fe; X = Cl, Br, I, H, Cl/CN).

The X-ray analysis reveals that **C2c** crystallizes in the orthorhombic *Pbcn* space group with half of one $[\text{Fe}(\text{Cl}_2\text{An})_3]^{3-}$ complex anion, half of three $(\text{Et})_3\text{NH}^+$ cations and half water molecule in the asymmetric unit. The complex molecules engage in two types of interactions with the surrounding complexes. In particular, the ligand comprising the Cl(22) atom is involved in a partial stack with symmetry-related ligands, with shortest distance occurring between Cl(22) and C(32) atoms (3.325(3) Å). On the other hand, the ligand with Cl(61) interacts with the C(31) atom of an adjacent complex molecule (3.448(4) Å). These interactions determine the formation of irregular layers that are parallel to the *bc* crystallographic plane, and are separated by layers of $(\text{Et})_3\text{NH}^+$ cations (Figure 2.2).

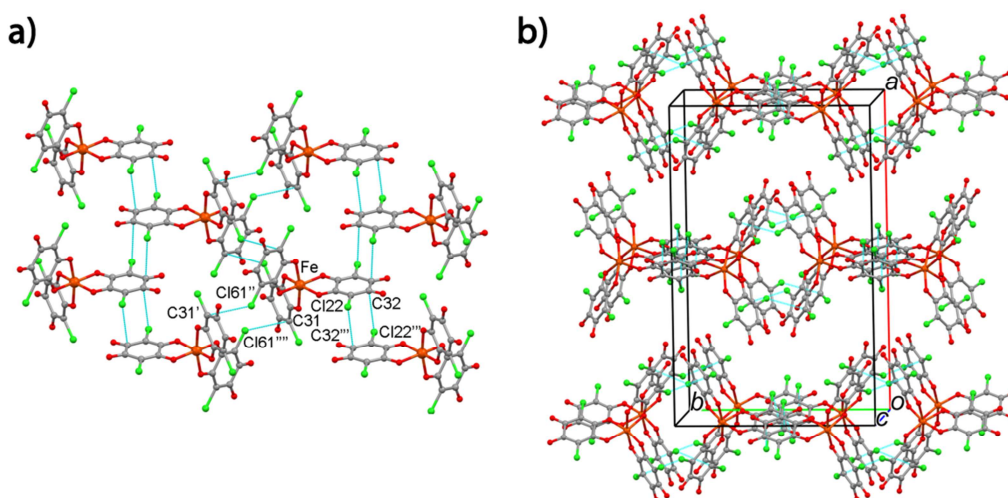


Figure 2.2. Portion of the molecular packing of **C2c** showing the two types of interactions occurring between the complex anions. $(\text{Et})_3\text{NH}^+$ cations and crystallization water molecules are omitted for clarity. Symmetry codes ' = -x; -y; -z, '' = -x; y; $1/2-z$, ''' = -x; 1-y; -z, '''' = x; -y; z-1/2.

Interestingly, each complex anion interacts with the three $(\text{Et})_3\text{NH}^+$ cations through bifurcated HBs, involving the peripheral oxygen atoms of the complex and the N–H hydrogens of the cation (Figure 2.3).

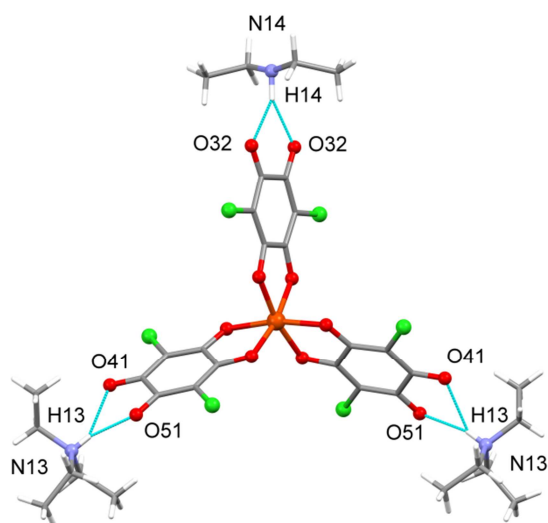


Figure 2.3. Anionic complex for **C2c** showing the bifurcated HB interactions between the peripheral oxygen atoms of the complex and the $(\text{Et})_3\text{NH}^+$ cations. Selected bond lengths (Å) and angles (°): N(13)–O(41) 2.991, N(13)–O(51) 2.812, N(14)–O(32) 2.989, N(13)–H(13)–O(41) 134.24, N(13)–H(13)–O(51) 153.08, N(14)–H(14)–O(32) 141.84.

It should be pointed out that despite **C1c** crystallizes in the monoclinic $P2_1/n$ space group, its crystal packing is very similar to that of **C2c** described above.

C5a crystallizes in the orthorhombic $Pbca$ space group with one $[\text{Cr}(\text{I}_2\text{An})_3]^{3-}$ complex anion and three $(n\text{-Bu})_4\text{N}^+$ cations in the asymmetric unit. Its crystal packing shows metal complexes held together in supramolecular dimers by two symmetry related I...O interactions (3.092(8) Å)

considerably shorter than the sum of the iodine and oxygen van der Waals radii (3.50 Å) (Figure 2.4).

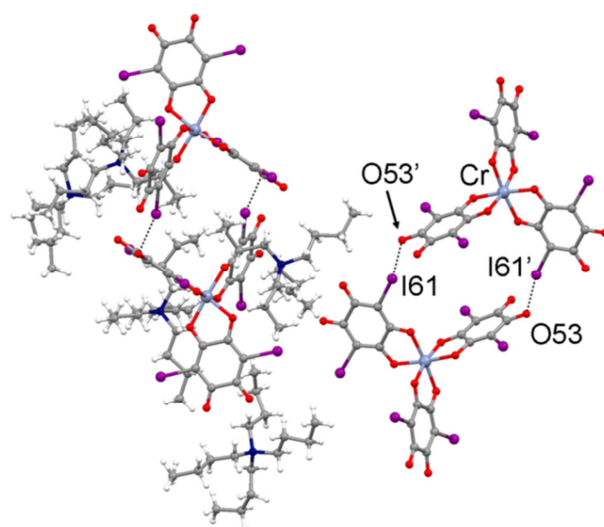


Figure 2.4, Portion of the molecular packing of **C5a** where four complex anions arranged in two supramolecular dimers are shown. Symmetry code ' = 1-x; 1-y; 1-z.

The I...O interaction can be regarded as a XB, where the iodine behaves as XB donor and the oxygen atom as the XB acceptor. This is in agreement with the properties of the electrostatic potential for $[\text{Cr}(\text{I}_2\text{An})_3]^{3-}$ that predicts a negative charge accumulation on the peripheral oxygen atoms and a positive charge accumulation on the iodine (*vide infra*). Given the charge distribution on the halogen atoms, which is mainly located on the portion of the iodine surface opposite to the C–I bond, this interaction is expected to be linear. In fact, the C(61)–I(61)···O(53)' angle is 165°. The dinuclear entity held together by two XB is then extensively enveloped by $(n\text{-Bu}_4)\text{N}^+$ cations. Remarkably, these XB interactions may be responsible for the weak antiferromagnetic interactions among paramagnetic centers at low temperature observed for this compound (*vide infra*).

Compounds **C9a** and **C10a** are isostructural, therefore, their crystal structures can be described together. These compounds crystallize in the monoclinic $P2_1/a$ space group with one $[\text{M}^{\text{III}}(\text{ClCNA})_3]^{3-}$ ($\text{M}^{\text{III}} = \text{Cr}, \text{Fe}$) complex anion and three $(n\text{-Bu})_4\text{N}^+$ cations in the asymmetric unit. The main feature of their crystal packing is the presence of C–N···Cl interactions between complex anions having opposite stereochemical configuration, that lead to the formation of infinite 1D supramolecular chains parallel to the a crystallographic axis (Figure 2.5). The C–N···Cl interaction is characterized by a Cl···N distance of 3.121 Å, shorter than the sum of chlorine and nitrogen van der Waals radii (3.30 Å), and a C–Cl···N angle of ca. 153.5°. Therefore, the Cl···N interaction may be regarded as an XB where the chlorine behaves as XB donor and the nitrogen atom as the XB acceptor. No close contacts between the chains were observed since they are well separated by the presence of $(n\text{-Bu})_4\text{N}^+$ (omitted for clarity in Figure 2.5b).

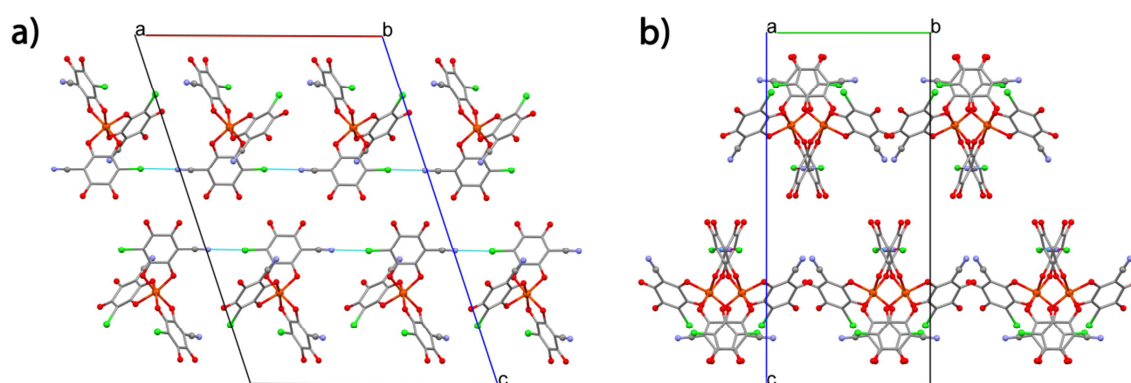


Figure 2.5. (a) Portion of the molecular packing of **C10a** showing the Cl...N interactions occurring between the complex anions; (b) View of the supramolecular chains along the *a* axis. (*n*-Bu)₄N⁺ cations are omitted for clarity.

Compounds **C2b**, **C4b** and **C9b** are isostructural, therefore, their crystal structures can be described together. Moreover, PXRD measurements performed on polycrystalline samples of **C1b**, **C3b** (Cr^{III} complexes) and **C10b** (Fe^{III} complex) show that these compounds are isostructural to their Fe^{III} (**C2b**, **C4b**) or Cr^{III} (**C9b**) analogues. The PXRD patterns are reported as Supplementary Material in Appendix 4 (Figures S2.1–S2.3).

These compounds crystallize in the monoclinic *P2₁/n* space group with one [M^{III}(X₂An)₃]³⁻ (M^{III} = Cr, Fe; X = Cl, Br, Cl/CN) complex anion, three (Ph)₄P⁺ cations and one water molecule in the asymmetric unit. In these structures, the presence of the (Ph)₄P⁺ cations opens the possibility to the formation of π - π interactions between the aromatic rings of the cations and the quinoid ring of the three anilate ligands. In fact, the complex anions are embedded in a pocket formed by several (Ph)₄P⁺ cations where each ligand engage in π - π interactions with a phenyl ring (Figure 2.6). These interactions preclude a close contact between the complex anions for which the smallest intermolecular M...M distances are of ca. 13.50 Å.

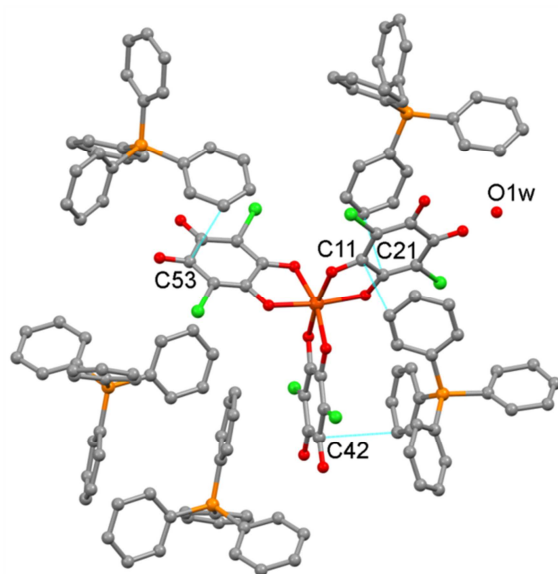


Figure 2.6. Portion of the crystal packing of **C2b** showing the interactions occurring between the complex anion and the surrounding (Ph)₄P⁺ cations. Hydrogen atoms are omitted for clarity.

The X-ray analysis reveals that **C6b** crystallizes in the monoclinic $C2/c$ space group with one $[\text{Fe}(\text{I}_2\text{An})_3]^{3-}$ complex anion, three $(\text{Ph})_4\text{P}^+$ cations, and four water molecules in the asymmetric unit. PXRD measurements performed on a microcrystalline sample of **C5b** (Cr^{III} complex) show that this compound is isostructural to its Fe^{III} analogue (**C6b**) (Figure S2.4).

Despite the presence of the $(\text{Ph})_4\text{P}^+$ counterion, as in compounds **C2b** and **C4b**, the iodine substituent changes considerably the crystal packing of **C6b**. In fact, a series of interactions involving the iodine atoms, the oxygen atoms, and the phenyl rings of the $(\text{Ph})_4\text{P}^+$ cation are observed (Figure 2.7).

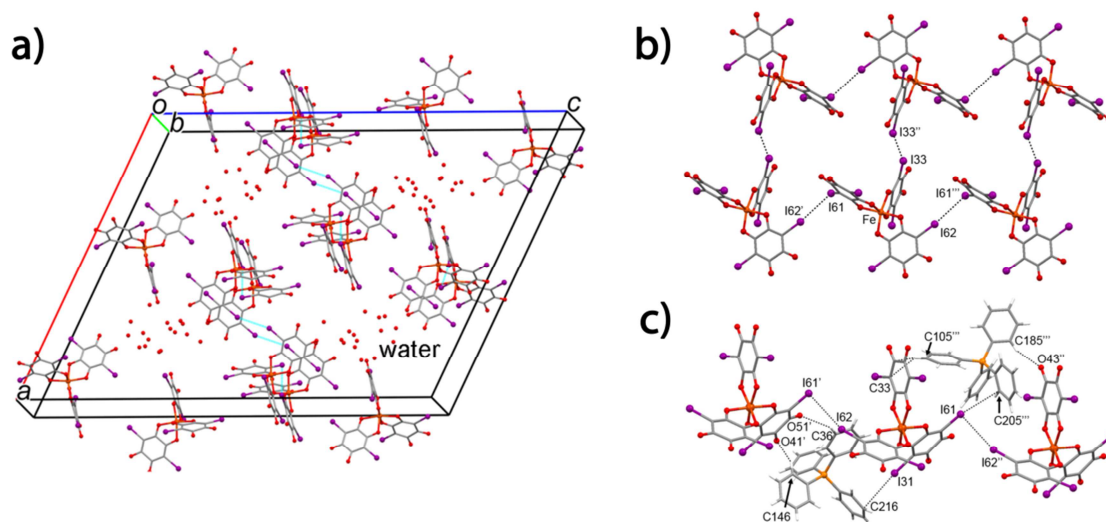


Figure 2.7. (a) Portion of the molecular packing of **C6b** where $(\text{Ph})_4\text{P}^+$ cations are omitted for clarity. (b) Halogen bonds between the complex anions. (c) Interactions occurring between the complex anions and the surrounding $(\text{Ph})_4\text{P}^+$ cations. Symmetry codes $' = x; y-1; z$; $'' = x; y+1; z$; $''' = 3/2-x; 5/2-y; 1-z$.

In particular, each $[\text{Fe}(\text{I}_2\text{An})_3]^{3-}$ shows three $\text{I}\cdots\text{I}$ XBs with the surrounding complex anions. According to the geometry of the $\text{C}\cdots\text{I}\cdots\text{I}$ interaction, in the $\text{I}(62)\cdots\text{I}(61)'''$ contact (3.882(2) Å), the $\text{I}(62)$ atom behaves as a XB donor and the $\text{I}(61)'''$ as a XB acceptor ($\text{I}(62)$ is the Lewis acid and $\text{I}(61)'''$ is the Lewis base), with an almost linear geometry (162°). The opposite situation is present for the $\text{I}(62)'$ and $\text{I}(61)$ couple. These $\text{I}\cdots\text{I}$ interactions lead to the formation of supramolecular chains parallel to the b axis that are arranged in a supramolecular layer by means of an additional $\text{I}\cdots\text{I}$ interaction with symmetry-related $\text{I}(33)$ atoms (3.886(2) Å). This latter interaction is less directional than the previously described ones, and seems that each $\text{I}(33)$ atom may behave at the same time as a XB donor and acceptor. Additional XB interaction can be observed by the inspection of the crystal packing of **C6b**. In particular, $\text{I}(31)$ interacts with $\text{C}(216)$ (3.589(1) Å) and $\text{I}(61)$ interacts with $\text{C}(205)'''$ (3.493(1) Å). Interestingly, $\text{I}(61)$ behaves as a XB acceptor (Lewis base) with respect to a symmetry related $\text{I}(62)$ and as XB donor (Lewis acid) with respect to $\text{C}(205)'''$. Within each unit cell four pockets surrounded by oxygen atoms of the iodanilate ligands host several crystallization water molecules (Figure 2.7a).

C8b crystallizes in the centrosymmetric triclinic space group $P\bar{1}$ and its crystal structure consists of $[\text{Fe}(\text{H}_2\text{An})_3]^{3-}$ complex anions surrounded by crystallization water molecules (indicated as O1w–O6w) and $(\text{Ph})_4\text{P}^+$ cations (Figure 2.8).

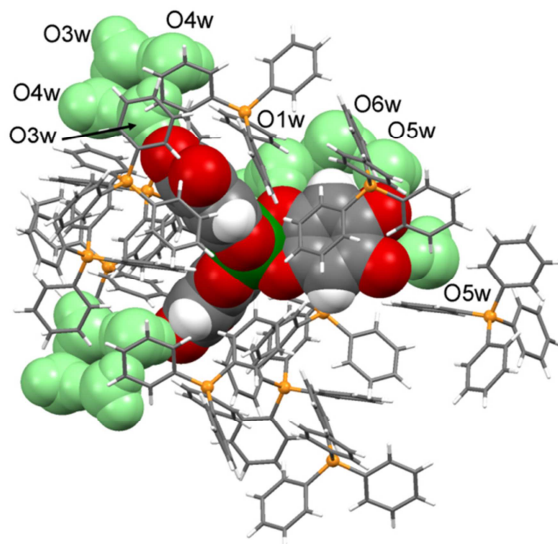


Figure 2.8, Picture of the $[\text{Fe}(\text{H}_2\text{An})_3]^{3-}$ anion in colored spacefill model, together with crystallization water molecules (light green spacefill mode), and $(\text{Ph})_4\text{P}^+$ cations.

The metal complexes are arranged in two different types of rectangular lattices having $\text{Fe}\cdots\text{Fe}$ intermolecular distances of ca. $13.2 \times 13.7 \text{ \AA}$ and ca. $13.7 \times 15.4 \text{ \AA}$, and are surrounded by several $(\text{Ph})_4\text{P}^+$ cations and crystallization water molecules. The water molecules establish an extended network of HBs (Figures 2.9) that promotes the formation of supramolecular layers, based on complex anions and water molecules, that run parallel to the a crystallographic axis (Figures 2.10 and 2.11).

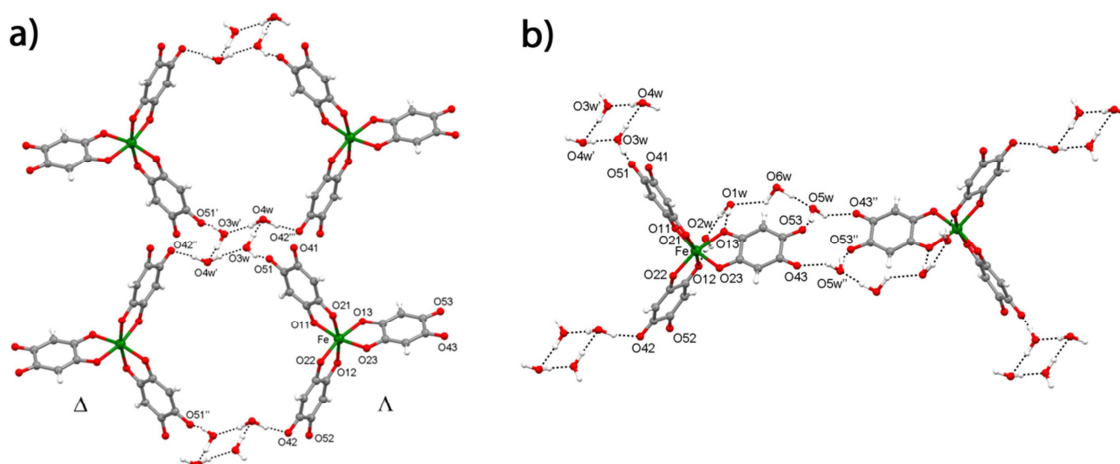


Figure 2.9, (a) View of the crystal structure of **C8b** where four complexes are indicated with one of the HB networks running along the a axis. (b) Two molecular complexes of opposite chirality are indicated showing one of the HB networks linking two complexes. The $(\text{Ph})_4\text{P}^+$ cations are omitted for clarity. Symmetry codes ' = $-x$; $-y$; $-z$, '' = $-x$; $1-y$; $1-z$, ''' = $x-1$; y ; z .

In particular, the O3w and O4w water molecules, arranged in a square fashion with two symmetry-related molecules, link together four complex anions by interacting with their peripheral O(42) and O(51) oxygen atoms, favouring the extension of the layer along the *a* axis (Figure 2.9). Moreover, the O5w water molecule establishes a HB with the O(43) oxygen atom of a symmetry-related complex molecule, favouring the extension of the layer along the [011] direction (Figures 2.10-2.12).

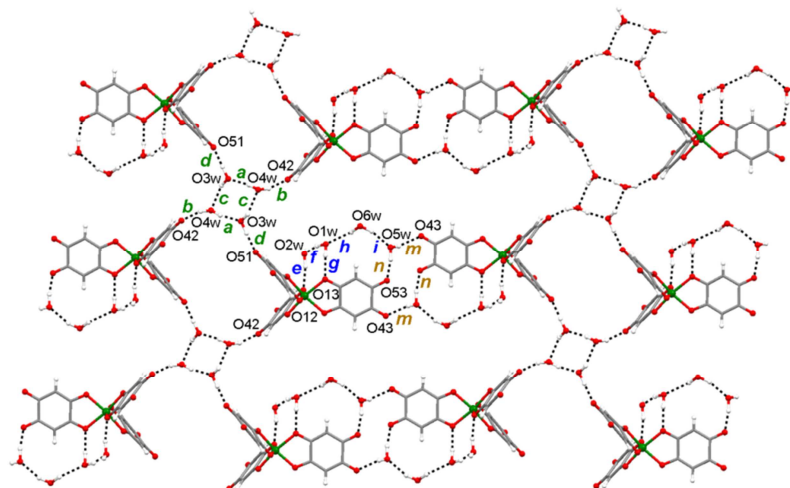


Figure 2.10, View of the crystal packing of **C8b** where the HB interactions occurring between the water molecules and the metal complexes are highlighted. The eleven HBs are indicated with coloured letters. HB donors and acceptor are also indicated.

The O1w, O2w and O6w water molecules do not contribute to the formation of the supramolecular layer, but instead, they form a chain of HBs that runs from the O(12) to the O(53) oxygen atoms of $[\text{Fe}(\text{H}_2\text{An})_3]^{3-}$ (Figures 2.9b and 2.10). On the account of the differences between the interactions established by the water molecules, the HBs can be conveniently divided into three groups, **a–d**, **e–i** and **m–n** (see Figure 2.10). According to the HB donor and acceptor distances, the strongest interaction is exhibited by the **a–d** system (Table 2.3).

Table 2.3, Distances (Å) and angles (°) between the HB donors and HB acceptors for the three groups of HBs shown in Figure 2.10.

HB type	distance	angle
a	2.756(7)	164.3(5)
b	2.816(6)	163.0(5)
c	2.739(6)	130.5(5)
d	2.685(6)	159.0(5)
e	2.887(5)	163.0(5)
f	2.850(8)	165.0(5)
g	2.860(4)	172.0(5)
h	2.934(6)	114.4(5)
i	2.808(8)	150.0(5)
m	2.901(5)	150.0(5)
n	2.861(4)	155.0(5)

The described HB network between the water molecules and the $[\text{Fe}(\text{H}_2\text{An})_3]^{3-}$ complex anions give rise to a resulting supramolecular architecture showing two types of cavities. One cavity shows a distorted hexagonal symmetry, driven by the presence of metal complexes having opposite absolute configuration (Λ and Δ), and is formed by two complex anions connected through the **a**, **b** and **d** HB types (Figures 2.9a and 2.11). The other cavity shows a hexagonal prism-like symmetry and is formed by four metal complexes connected by the **m** and **n** HB types along the long side, and by the **b**, **c**, **d** HB types along the short side (Figures 2.10 and 2.11). The overall topology of the resulting supramolecular architecture can be described as a 1:1 hybrid between the well-known hexagonal honeycomb and the PtS-related topologies (Figure 2.11).¹⁹

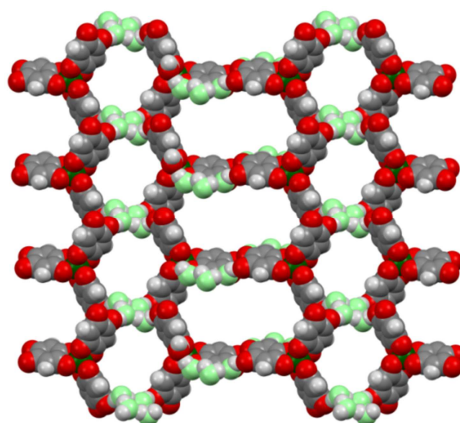


Figure 2.11, View of the crystal packing of **C8b** with metal complexes and water molecules in spacefill model highlighting the supramolecular topology.

Inside the hexagonal prism-like cavity two symmetry related $(\text{Ph})_4\text{P}^+$ cations are present. They interact with each other through π - π interplanar interactions with offset, as typically observed in aromatic systems,²⁶⁻³¹ in a double phenyl embrace (Figure 2.12a).³² Moreover, each one interacts with the quinoid ring of one coordinated H_2An^{2-} ligand in a face-to-face alignment and in an almost eclipsed way, with shorter interplanar separation (Figure 2.12b).³³

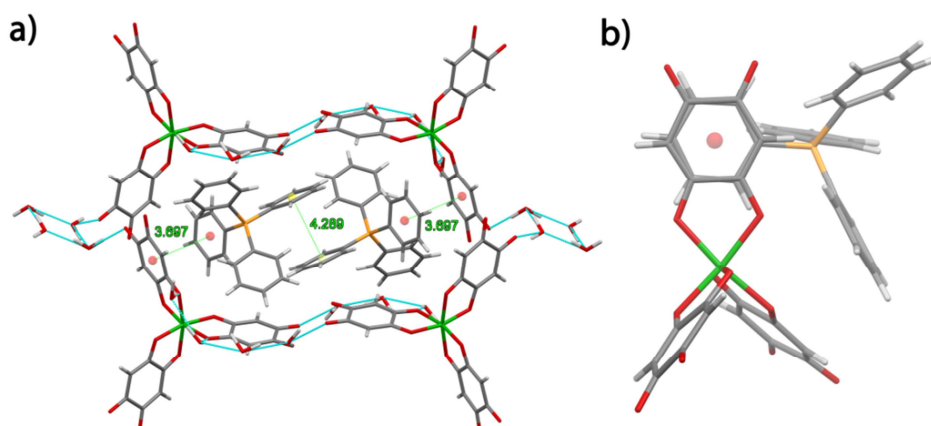


Figure 2.12, (a) $(\text{Ph})_4\text{P}^+$ cations inside the hexagonal prism-like cavity where the interplanar distances are highlighted. (b) eclipsed face-to-face arrangement between the quinoid ring of the ligand and the aromatic ring of the cation.

The hexagonal-like cavity is too small to host a $(\text{Ph})_4\text{P}^+$ cation so that the other counterions are placed between the 2D supramolecular layers of the structure, that are arranged in an alternated disposition (Figure 2.13).

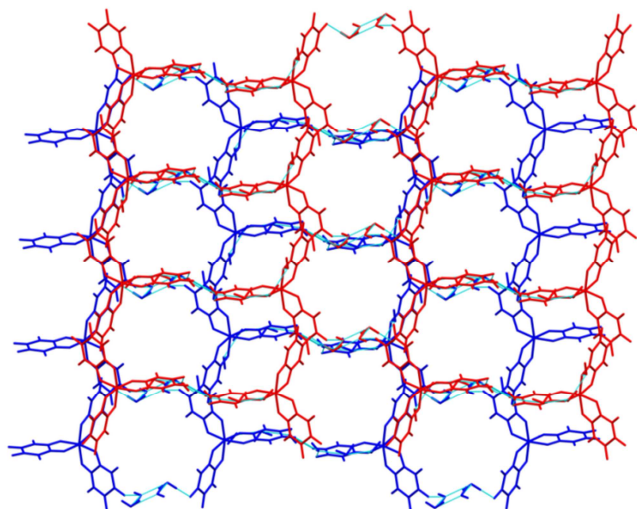


Figure 2.13, Two supramolecular layers of the structure of **C8b** showing the alternated disposition of the layers that precludes the formation of hexagonal channels.

PXRD measurements performed on a polycrystalline sample of **C7b** clearly show that the Cr^{III} complex is isostructural to its Fe^{III} analogue **C8b** (Figure S2.5). Therefore, the crystal packing of **C7b** can be considered the same as **C8b** except for small deviations on the bond distances related to the coordination to the different metal center.

2.2.3 Hirshfeld Surface Analysis

The Hirshfeld Surface (HS) defines the volume of space in a crystal where the sum of the electron density of the spherical atoms for the molecule (pro-molecule) exceeds that for the crystal (pro-crystal). In particular the HS contains a region of space where the pro-molecule electron density is greater than that of the surrounding molecules. Various properties of the HS can be computed and visualized, in particular d_e and d_i , which represent the distance from a point on the surface to the nearest nucleus outside or inside the surface, respectively. The d_{norm} is the normalized contact distance and is defined by taking into account d_e and d_i and the van der Waals radii of the atoms

$$d_{\text{norm}} = \frac{d_i - r_i^{\text{vdW}}}{r_i^{\text{vdW}}} + \frac{d_e - r_e^{\text{vdW}}}{r_e^{\text{vdW}}}$$

Mapping d_{norm} on the HS gives a clear-cut and thorough picture of the interactions occurring between adjacent molecule or molecular fragments that are shorter than the sum of van der Waals radii (visualized as red spots on the HS). In addition, 2D diagrams reporting the correlation between d_e and d_i (fingerprint plots) are particularly useful to highlight the types of interactions that occurs between molecular fragments.

The HS properties of **C8b** were investigated in order to have a thorough description of the various interactions occurring between the complex anion $[\text{Fe}(\text{H}_2\text{An})_3]^{3-}$ and the surrounding environment.³⁴ As previously described, the complex anion is surrounded by different $(\text{Ph})_4\text{P}^+$ cations and by water molecules responsible of the formation of supramolecular layers. The strongest interactions exhibited by the $[\text{Fe}(\text{H}_2\text{An})_3]^{3-}$ complex are those involving the water molecules, in agreement with the presence of moderately strong HBs. Moreover, the complex anion exchanges different type of contact with the surrounding $(\text{Ph})_4\text{P}^+$ cations and these can be categorized as follows: (i) $\pi-\pi$, between one H_2An^{2-} ligand and a phenyl ring of the cation, (ii) $\text{C}-\text{H}\cdots\pi$, between a $\text{C}-\text{H}$ of a phenyl ring of the cation and the carbon atom of one H_2An^{2-} ligand that is linked to the hydrogen atom (according to DFT calculations (*vide infra*) this carbon atom is characterized by a partial negative charge, which favours the interaction with the phenyl residue), (iii) $\text{C}-\text{H}\cdots\text{O}$, between the $\text{C}-\text{H}$ of the phenyl rings of the cation and the peripheral oxygen atoms of H_2An^{2-} ligands. All these interactions are visualized as red spots on the HS that correspond to the mapping of d_{norm} on the HS (Figure 2.14).

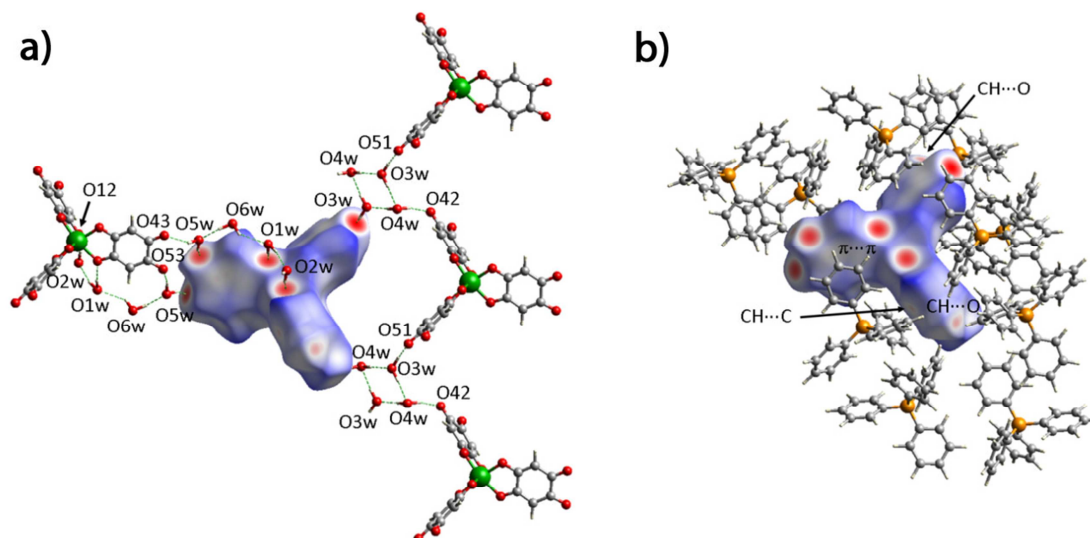


Figure 2.14, View of the d_{norm} mapped on the Hirshfeld surface (blue) for the complex anion $[\text{Fe}(\text{H}_2\text{An})_3]^{3-}$. (a) interactions occurring through the HBs network, (b) interactions occurring with the $(\text{Ph})_4\text{P}^+$ cations.

From the red spots on Figure 2.14 it can be appreciated how the HBs are particularly important for the construction of the overall supramolecular arrangement.

A more detailed representation of the interaction exchanged by the $[\text{Fe}(\text{H}_2\text{An})_3]^{3-}$ complex and the surrounding moieties can be obtained by the fingerprint plots (Figure 2.15), confirming the importance of the HBs as the strongest type of interaction in the crystal packing. This is evidenced by the presence of a pronounced cusp for the $\text{O}_{\text{IN}}\cdots\text{H}_{\text{OUT}}$ interaction.

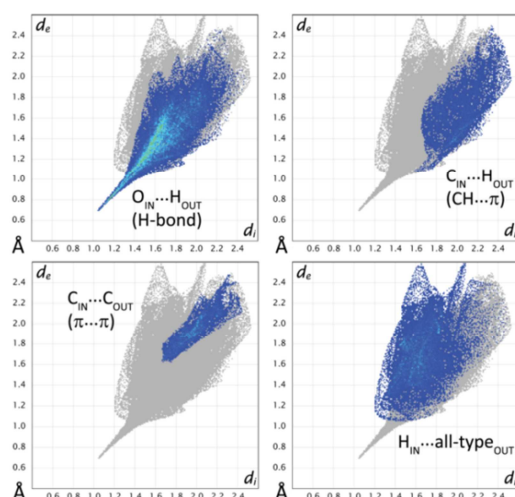


Figure 2.15, Fingerprint plots for **C10b** highlighting the major interactions occurring between the complex anion and the surrounding environment, water molecules and $(\text{Ph})_4\text{P}^+$ cations. IN and OUT refers to atoms/fragments belonging to the $[\text{Fe}(\text{H}_2\text{An})_3]^{3-}$ anion or the surrounding molecules, respectively. The fingerprint plot of the indicated interaction is depicted as a coloured area, which is overlaid over the full fingerprint plot (in gray).

2.2.4 DFT Calculations

DFT calculations were performed to gain insight into the electronic structures of the $[\text{M}^{\text{III}}(\text{X}_2\text{An})_3]^{3-}$ ($\text{M}^{\text{III}} = \text{Cr}, \text{Fe}$; $\text{X} = \text{Cl}, \text{Br}, \text{I}, \text{H}$) complexes, as well as to characterize the spin and charge distribution of the metal centers and to compare the electronic properties of the free and coordinated $\text{Cl}_2\text{An}^{2-}$, $\text{Br}_2\text{An}^{2-}$, I_2An^{2-} and H_2An^{2-} ligands. According to the presence of six oxygen atoms in the coordination sphere of the metals, and in agreement with magnetic measurements (*vide infra*), the calculations were performed in the high spin states for all systems ($S = 3/2$ and $S = 5/2$ for Cr^{III} and Fe^{III} complexes, respectively). Two different computational schemes were employed in order to represent the atomic charges of the anionic complexes, namely Mulliken and NPA, to provide a more complete description of the charge distribution on the different structural fragments.³⁵ By inspecting the Mulliken and NPA charges of the isolated ligands, it is evident that the negative charge is localized on the four oxygen atoms, whereas there is a slight negative charge accumulation on the halogen atoms, that decreases in the following order $\text{Cl} > \text{Br} > \text{I}$ (Figure 2.16).

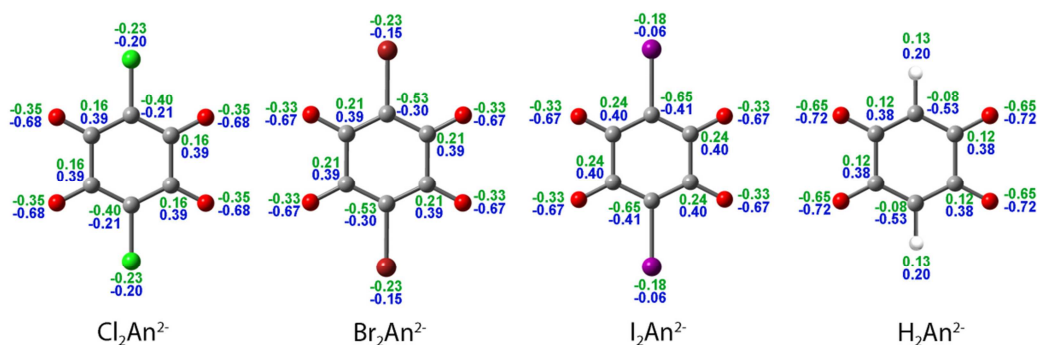


Figure 2.16, Mulliken (green) and NPA (blue) charges for $\text{Cl}_2\text{An}^{2-}$, $\text{Br}_2\text{An}^{2-}$, I_2An^{2-} and H_2An^{2-} (B3LYP/6-31+G(d) or B3LYP/SDD with SDD pseudopotentials on Br and I atoms).

As far as the H_2An^{2-} ligand is concerned, there is a negative charge accumulation on the carbon atom linked to the hydrogen, whereas the remaining carbon and the hydrogen atoms present a positive charge. These charge distributions on the ligands are qualitatively similar in both Mulliken and NPA schemes (Figure 2.16).

According to the NPA charges, when the ligands are coordinated to the metal centers, there is a slight negative charge depletion on the two oxygen atoms that are bound to the metal and also a negative charge depletion on the two peripheral oxygen atoms, which, however, retain a considerable negative charge (ca. -0.6) (Figure 2.17).

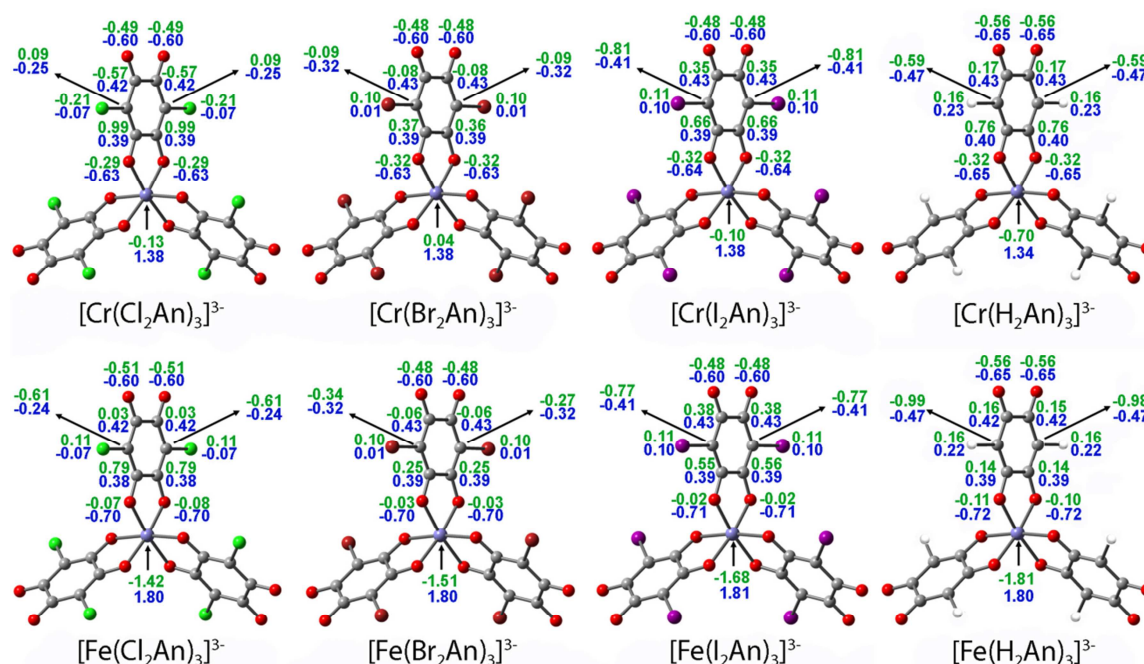


Figure 2.17, Mulliken (green) and NPA (blue) charges for **C1-8**. (B3LYP/6-31+G(d)-lan12dz). The charges of only one ligand are depicted for clarity.

On the other hand, the Mulliken analysis predicts that there is a certain degree of negative charge accumulation on the peripheral oxygen atoms (Figure 2.17). In addition, as observed in the free ligands, the negative charge on the halogen atoms tends to vary in the following order $\text{Cl} > \text{Br} > \text{I}$, becoming slightly positive in the case of bromine and iodine, whereas the carbon atom linked to the hydrogen in H_2An^{2-} still presents a considerably negative charge, either with Mulliken or NPA schemes. This scenario is identical for both Cr^{III} and Fe^{III} complexes.

A thorough depiction of the charge distribution can be obtained by visualizing the Electrostatic Potential (EP) of the metal complexes.^{35,36} The isodensity surfaces mapped with the EP are shown in Figure 2.18. It can be appreciated that the oxygen atoms are regions where there is a marked negative charge accumulation, whereas the metal are the main source of the positive charge. The carbon atoms attached directly to the halogen atoms present a slightly more negative charge than the remaining four carbon atoms of the quinoid ring, whereas the carbon atoms linked directly to the hydrogen atoms in the hydranilate complexes present the highest negative charge accumulation. As predicted by the Mulliken or

NPA charges, on-going from the $\text{Cl}_2\text{An}^{2-}$ to the I_2An^{2-} ligands there is a positive charge accumulation on the halogen atoms. According to these calculations, it appears that the iodine atoms of I_2An^{2-} in the Cr^{III} or Fe^{III} complexes can behave as XB donors (Lewis acids) whereas the peripheral oxygen atoms can act as XB acceptor (Lewis bases). The observed supramolecular interactions in the previously described structures of **C5a** and **C6b** are in agreement with this description. As far as the structure of **C8b** is concerned, the hydrogen atoms on the ligand play a crucial role in increasing the electron density on the carbon atoms where they are directly connected, favouring the electron delocalization toward the peripheral oxygen atoms of the ligand that act, in turn, as suitable HB-acceptors.

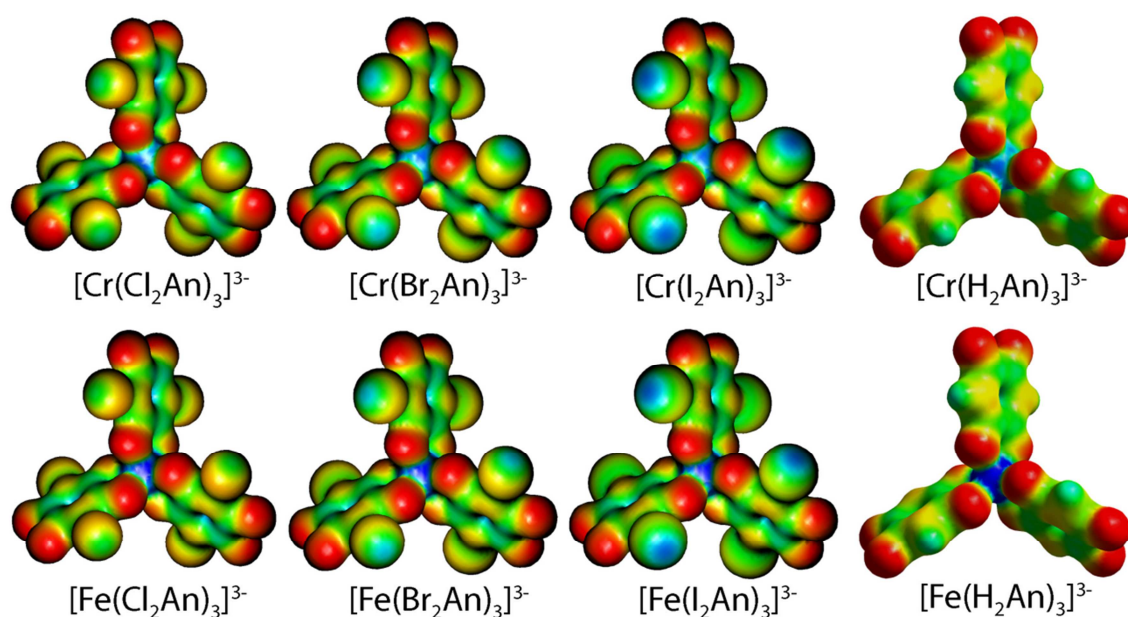


Figure 2.18. Electrostatic potential for **C1-8** (B3LYP/6-31+G(d)-lan12dz). Colour codes thresholds: red -0.3 , yellow -0.2 , green -0.15 , light blue -0.1 , blue 0.0 .

The spin distribution on the metals for the Cr^{III} and Fe^{III} complexes is approximately 3 and 4, respectively, pointing to a localized nature of the spin on the chromium centers, but to a less localized spin distribution in the Fe^{III} complexes (Table 2.4).

Table 2.4. Mulliken spin densities of the metal, Mulliken and NPA charges of the metal, and expectation values of the $\langle S^2 \rangle$ operator after annihilation of the first spin contaminant for the **C1-8** anionic complexes.

	Mulliken spin density	Mulliken charges	NPA charges	$\langle S^2 \rangle$
C1	3.098	-0.125	1.379	8.750
C2	4.158	-1.421	1.798	3.750
C3	3.071	$+0.037$	1.380	8.750
C4	4.159	-1.507	1.800	3.750
C5	3.078	-0.098	1.383	8.750
C6	4.167	-1.677	1.805	3.750
C7	3.007	-0.697	1.337	8.750
C8	4.181	-1.812	1.802	3.750

This is also evidenced by inspecting the shape of total spin density, which for the Fe^{III} complexes is significantly distributed over the six oxygen atoms of the coordination sphere. On the other hand, the cubic shape of the total spin density of the Cr^{III} complexes reflects the octahedral t_{2g}^3 configuration (Figure 2.19).³⁷

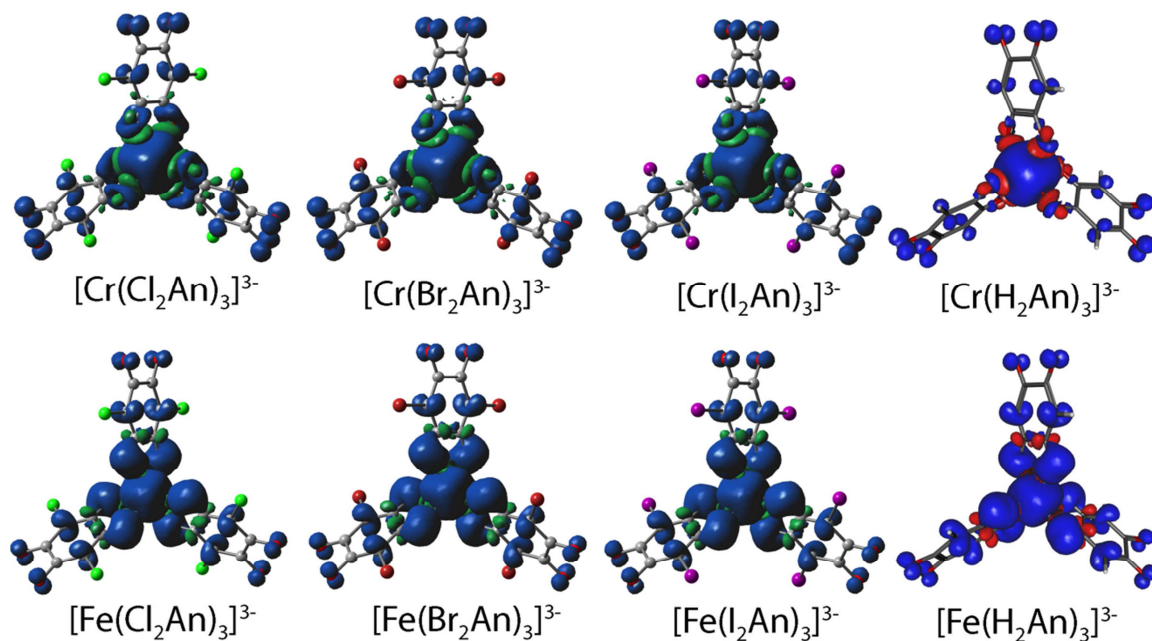


Figure 2.19, Spin density for **C1-8** (B3LYP/6-31+G(d)-lanl2dz). Colours blue and green (or red) refer to α - and β -spin density, respectively (isosurface plot at 0.0008 esu \AA^{-3}).

2.2.5 Spectroscopical Studies

2.2.5.1 Vibrational Spectroscopy

As shown in Table 2.6 and as reported in the Crystal Structure Description Section, compounds **C1-10** crystallize in different space groups even if they are associated to the same counterion (e.g. compounds **C1c** and **C2c**, or **C1b**, **C3b** respect to **C5b**), hampering an evaluation of their molecular isostructurality using X-ray powder diffraction. To overcome this drawback, a detailed spectroscopical study using FT-IR vibrational spectroscopy is particularly helpful in demonstrating that all the components of this family are isostructural from the molecular point of view. For shortness, only the FT-IR spectra of compounds **C1a-10a** ($n\text{-Bu}_4\text{N}^+$ as counterion) are discussed since the FT-IR spectra of compounds **C1b-10b** or **C1c-2c** show the same features, except for the contribution of the different counterion.

The FT-IR of **C1a** and **C2a** show, in the 3000–2800 cm^{-1} region, the typical $\nu(\text{C-H})$ vibrational modes of the $(n\text{-Bu})_4\text{N}^+$ counterion. A comparison between the spectra of **C1a** and **C2a** in the 1850–650 cm^{-1} region (Figure 2.20), showing the same vibrational bands, with similar shape and relative intensity, suggests the same coordination geometry and the same chemical environment for Cr^{III} and Fe^{III} complexes.

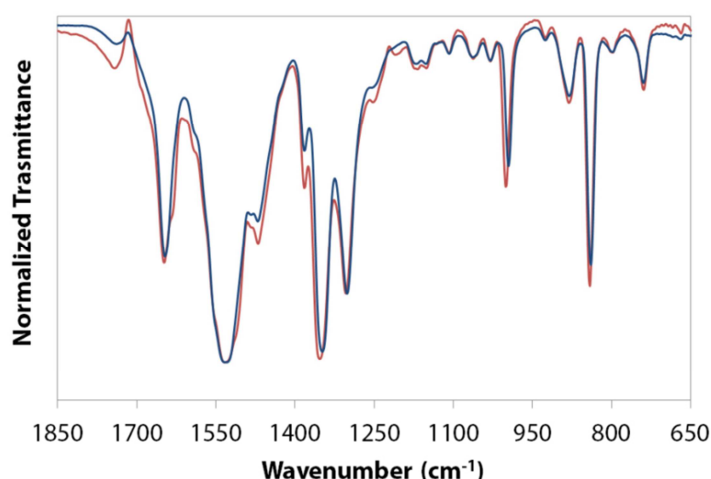


Figure 2.20, FT-IR spectra (1850–650 cm^{-1}) for **C1a** (red line) and **C2a** (blue line).

According to Pawluko \acute{c} *et al.*,³⁸ the band centered at ca. 1650 cm^{-1} is assigned to the $\nu(\text{C}=\text{O})$ vibration mode for the uncoordinated $\text{C}=\text{O}$ groups of the ligands. A downshift of this band with respect to the free ligand (1665 cm^{-1}) is observed and it can be attributed to a weakened double bond character of the terminal $\text{C}=\text{O}$ groups due to the coordination with the metal ion. The strong and broad band centered at ca. 1530 cm^{-1} can be assigned to a $\nu(\text{C}=\text{C}) + \nu(\text{C}=\text{O})$ combination band. The significant downshift observed (1631 cm^{-1} for the free ligand³⁸) could be related, also in this case, to the coordination effect. The two bands present in the 1400–1250 cm^{-1} region are assigned to the $\nu(\text{C}-\text{C}) + \nu(\text{C}-\text{O})$ combination band and $\nu(\text{C}-\text{C})$ vibration, respectively, whereas the two ones centered at ca. 995 cm^{-1} and 840 cm^{-1} for both spectra can be related to the $\nu(\text{C}-\text{C}) + \nu(\text{C}-\text{O}) + \delta(\text{C}-\text{Cl})$, and to the $\delta(\text{C}=\text{O}) + \delta(\text{C}-\text{O}) + \nu(\text{C}-\text{Cl})$, combination bands.³⁸ It is noteworthy that in the 650–400 cm^{-1} region the spectra of the two metal complexes show some differences. Except for the wagging vibrational mode related to the $\text{C}-\text{Cl}$ bond centered at ca. 570 cm^{-1} for both compounds, three bands at ca. 596, 581 and 505 cm^{-1} are present for **C2a** and four bands at ca. 612, 597, 508, 447 cm^{-1} are observed for **C1a** (Figure S2.6). These bands, which are not present in the ligand and counterion spectra, can be related to vibrational modes involving $\text{M}-\text{O}$ bonds.

Vibrational spectra of compounds **C3-6** (bromanilate and iodanilate complexes) show similar features in the whole MIR region (4000–400 cm^{-1}) with respect to the chloranilate complexes described above. A summary of the most significant bands with the corresponding assignments is reported in Table 2.5.

Table 2.5, Selected vibrational frequencies (cm^{-1}) for compounds **C1-6**.

Vibrational mode	C1	C2	C3	C4	C5	C6
$\nu(\text{C}=\text{O})$	1650	1647	1639	1640	1630	1630
$\nu(\text{C}=\text{C}) + \nu(\text{C}=\text{O})$	1530	1530	1521	1521	1513	1515
$\nu(\text{C}-\text{C}) + \nu(\text{C}-\text{O})$	1353	1349	1343	1337	1330	1326
$\nu(\text{C}-\text{C}) + \nu(\text{C}-\text{O}) + \delta(\text{C}-\text{X})$	1000	995	988	978	968	962
$\delta(\text{C}=\text{O}) + \delta(\text{C}-\text{O}) + \nu(\text{C}-\text{X})$	841	839	808	803	779	781
$\gamma(\text{C}-\text{X})$	572	574	558	560	548	551

The IR spectra of **C2a**, **C4a**, and **C6a** show similar features. The only remarkable difference consists in the downward shift of the halogen-sensitive bands as the halogen mass increases (Figure 2.21).

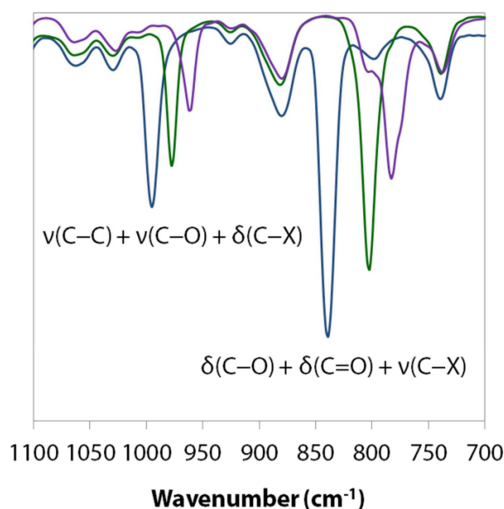


Figure 2.21, FT-IR spectra (1800–400 cm^{-1}) for **C2a** (blue line), **C4a** (green line), **C6a** (violet line).

These spectroscopic findings suggest that the haloanilate ligands exhibit, in all compounds, the same coordination mode, in agreement with structural data.

The FT-IR spectra of **C7b** and **C8b** show, in the 3700–3100 cm^{-1} range, a broad and asymmetric band centered at ca. 3415 cm^{-1} , ascribed to the several $\nu(\text{O–H})$ vibrational modes of the crystallization water molecules present in the structures. In the 3100–2900 cm^{-1} region the typical $\nu(\text{C–H})$ vibrational modes of the $(\text{Ph})_4\text{P}^+$ cation are present, along with the $\nu(\text{C–H})$ vibration of the ligand (3093 cm^{-1}) which is not shifted with respect to the protonated ligand.^{39,40} A comparison between the spectra of **C7b** and **C8b** in the 1700–650 cm^{-1} range (Figure S2.7), where the same vibrational bands with similar shape and relative intensity are observed, suggests the same chemical environment and therefore the same coordination geometry for both Cr^{III} and Fe^{III} complexes, in agreement with PXRD results. The band centered at ca. 1600 cm^{-1} may be assigned to the $\nu(\text{C=O})$ vibrational mode for the uncoordinated C=O groups of the ligands. A downshift of this band with respect to the one of the free ligand (1647 cm^{-1})²⁵ is observed and it can be attributed to a weakened double bond character of these terminal groups due to the coordination with the metal ion, in agreement with structural data. The strong and broad band centered at ca. 1535 cm^{-1} can be assigned to a $\nu(\text{C=C}) + \nu(\text{C=O})$ combination band and the observed significant downshift (1611 cm^{-1} for the free ligand²⁶) could be related, also in this case, to the coordination effect. The strong and broad band centered at ca. 1375 cm^{-1} may be assigned to the $\nu(\text{C–C}) + \nu(\text{C–O}) + \delta(\text{C–H})$ combination band, whereas the band centered at ca. 1245 cm^{-1} can be related to the $\nu(\text{C–O}) + \delta(\text{C–H}) + \text{Ring}_{\text{def}}$ combination band of the ligand.⁴⁰

It is noteworthy that in the 650–400 cm^{-1} region, the spectra of the two metal complexes show some differences. Except for the vibrational mode associated to the $(\text{Ph})_4\text{P}^+$

cation centered at ca. 527 cm^{-1} , three bands at ca. 560, 500 and 483 cm^{-1} are present for **C7b** and four bands at ca. 590, 578, 506, 483 cm^{-1} are observed for **C8b** (Figure S2.8). Also in this case, these bands, which are not present in the ligand and counterion spectra, can be related to vibrational modes involving M–O bonds, as observed for the haloanilate-based complexes.

The FT-IR spectra of **C9a** and **C10a** show very similar features when compared with those of **C1a** and **C2a** due to the presence of one Cl substituent on the ligand. The main differences are, in fact, ascribed to the presence of additional bands associated to vibrational modes involving the CN substituent.

In the 3000–2800 cm^{-1} region, the typical $\nu(\text{C-H})$ vibrational modes of the $(n\text{-Bu})_4\text{N}^+$ counterion are present, whereas the $\nu(\text{C-N})$ vibrational mode related to the CN substituent is present as a sharp band at 2213 cm^{-1} for both **C9a** and **C10a**. The band centered at ca. 1650 cm^{-1} is assigned to the $\nu(\text{C=O})$ vibration mode for the uncoordinated C=O groups of the ligands.³⁸ A downshift of this band with respect to the free ligand (1676 cm^{-1}) is observed and it can be attributed to a weakened double bond character of the terminal C=O groups due to the coordination with the metal ion. The weak band present at 1612 cm^{-1} for both **C9a** and **C10a**, not present for **C1a** and **C2a**, may be related to the coupling commonly occurring between C–O and C–N stretching modes. The strong and broad bands centered at ca. 1560 cm^{-1} and 1530 cm^{-1} can be assigned to a $\nu(\text{C=C}) + \nu(\text{C=O})$ combination band. The band present at 1395 cm^{-1} is assigned to the $\nu(\text{C-C}) + \nu(\text{C-O})$ combination band and the one at ca. 1306 cm^{-1} is assigned to the $\nu(\text{C-C})$ vibration. **C9a** and **C10a** show two additional bands at ca. 1325 cm^{-1} and 1260 cm^{-1} with respect **C1a** and **C2a**, whose origin may be related to vibrational modes involving the CN group. The two bands centered at ca. 1027 cm^{-1} and 860 cm^{-1} for both spectra can be related to the $\nu(\text{C-C}) + \nu(\text{C-O}) + \delta(\text{C-Cl})$, and to the $\delta(\text{C=O}) + \delta(\text{C-O}) + \nu(\text{C-Cl})$, combination bands, respectively.³⁸ Interestingly, a shift of these bands toward higher wavenumbers is observed when compared to the same bands of **C1a** and **C2a** (at ca. 995 cm^{-1} and 840 cm^{-1} , respectively) (Figure S2.9). It is noteworthy that in the 650–400 cm^{-1} region the spectra of the two metal complexes show some differences. Except for the wagging vibrational mode related to the C–Cl bond centered at ca. 610 cm^{-1} for both compounds,³⁸ three bands at ca. 680, 510 and 420 cm^{-1} are present for **C10a** and four bands at ca. 624, 596, 517, 444 cm^{-1} are observed for **C1a**. These bands, that are not present in the ligand and counterion spectra, can be related to vibrational modes involving M–O bonds.

2.2.5.2 UV-Vis Electronic Spectroscopy

UV-Vis absorption spectra for compounds **C1-10** show, in the 200–400 nm range, absorption bands with absorption coefficients in the 15000–30000 $\text{mol}^{-1} \text{dm}^3 \text{cm}^{-1}$ range. These bands are also present in the free ligands spectra, both as protonated and deprotonated forms, and may be ascribed to $\pi \rightarrow \pi^*$ electronic transitions involving the coordinated anilate ligands. They are centered at ca. 225 and 325 nm for all compounds and their position does not change remarkably as a function of the substituents on the anilate ring. As far as the same ligand is concerned, a red-shift of these bands is observed when going from the protonated ligand to

the dianionic and coordinated ligand, as a consequence of a better energetic stabilization of the latter. The absorption bands observed in the 425–525 nm region for the Cr^{III} complexes ($\epsilon = 3000\text{--}7000 \text{ mol}^{-1} \text{ dm}^3 \text{ cm}^{-1}$), and in the 400–500 nm region for the Fe^{III} complexes ($\epsilon = 3000\text{--}8000 \text{ mol}^{-1} \text{ dm}^3 \text{ cm}^{-1}$), are too intense to be ascribed to $d\text{--}d$ transitions and can be related to LMCT processes (Figure 2.22).

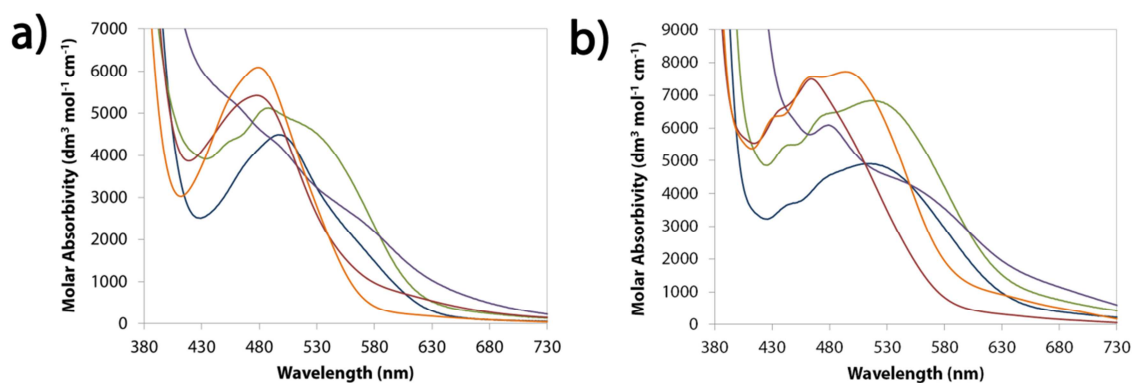


Figure 2.22, UV-Vis spectra (380–730 nm) for a) the Cr^{III} complexes **C1a** (blue line), **C3a** (green line), **C5a** (violet line), **C7a** (red line), **C9a** (orange line), and b) the Fe^{III} complexes **C2a** (blue line), **C4a** (green line), **C6a** (violet line), **C8a** (red line), **C10a** (orange line).

The 460–650 nm range is characterized for both Cr^{III} and Fe^{III} complexes by absorption bands with $\epsilon = 2000\text{--}8000 \text{ mol}^{-1} \text{ dm}^3 \text{ cm}^{-1}$ absorption coefficients. Also in this case, these bands are present in the free ligands spectra, both as protonated and deprotonated forms, and may be related to $n\rightarrow\pi^*$ transitions of the coordinated ligands. Their position follow the order $\lambda_{\text{Cl/CN}} < \lambda_{\text{Cl}} < \lambda_{\text{Br}} < \lambda_{\text{I}}$, in agreement with the electron withdrawing properties of the substituents. The position of this band for the hydranilate derivatives is not well defined, being convoluted with the above described LMCT bands. The same red-shift of these bands when compared with those of the protonated and deprotonated free ligands is observed.

The UV-Vis spectra of compounds **C1b–10b** show similar features to the above described **C1a–10a** compounds, except for the contribution of the different counterion in the UV region.

2.2.6 Electrochemical Studies

Compounds **C1–10** were studied by cyclic voltammetry in order to verify their stability toward electrochemical oxidation. Cyclic voltammograms for **C1a** and **C2a** are reported, as examples, in Figure 2.23.

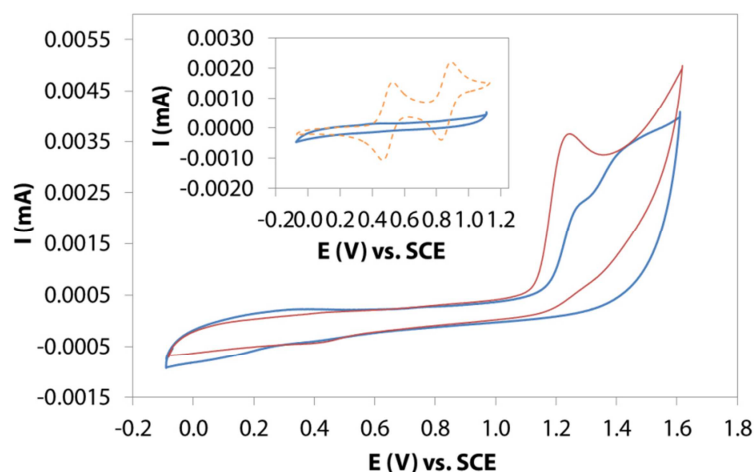


Figure 2.23, Cyclic voltammograms (-0.1–1.6 V) for **C1a** (red line) and **C2a** (blue line). Inset: cyclic voltammogram (-0.1–1.1 V) for **2a** (blue line) superimposed with the cyclic voltammogram for BEDT-TTF (orange dashed line) for comparison.

C1a shows one irreversible oxidation peak at ca. +1.23 V and **C2a** shows two irreversible oxidation peaks at ca. +1.23 and +1.37 V. The same features are observed for all the Cr^{III} and Fe^{III} compounds, and their redox potentials are summarized in Table 2.6.

Table 2.6, Cyclic Voltammetry data for compounds **C1-6**.

Oxidation Peak	C1	C2	C3	C4	C5	C6
1 st Oxidation Peak	+1.23	+1.23	+1.33	+1.31	+1.32	+1.30
2 nd Oxidation Peak	-	+1.37	-	+1.43	-	+1.66

It is noteworthy that in the 0.0–1.1 V range no oxidation peaks are observed. This suggests that these complexes are suitable candidates as counterions toward organic donors such as BEDT-TTF, which shows a monoelectronic reversible oxidation process at ca. +0.5 V (Inset in Figure 2.23).

2.2.7 Magnetic Properties

The thermal variation of the molar magnetic susceptibility per Fe^{III} ion expressed as $\chi_m T$ for compounds **C2b**, **C4b**, and **C6b** is shown in Figure 2.24. These compounds show similar behaviors with $\chi_m T$ values at r.t. of ca. 4.4 cm³ K mol⁻¹, close to the expected value (4.375 cm³ K mol⁻¹) for isolated high spin Fe^{III} ions ($S = 5/2$, $g = 2$). These values remain constant down to ca. 15 K, then the $\chi_m T$ product decreases. The observed behavior in the high temperature region is typical of magnetically isolated $S = 5/2$ ions. The observed decrease at low temperature may be due to weak antiferromagnetic interactions between the Fe^{III} ions and/or to the presence of a ZFS in the $S = 5/2$ ground state of the Fe^{III} complexes. Taking into account the crystallographic data for **C2b**, **C4b**, and **C6b**, which indicate either slightly-distorted octahedral coordination geometries around the Fe^{III} ions (*vide supra*) or Fe^{III} ions quite isolated

in the crystal structure (in particular for **C2b** and **C4b**), it seems reasonable to use a model that considers isolated $S = 5/2$ ions with a ZFS parameter D to fit the $\chi_m T$ vs T magnetic data.⁴¹⁻⁴³

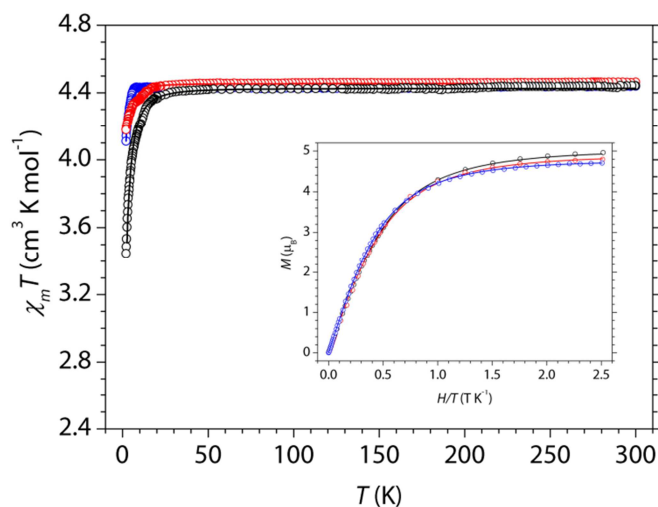


Figure 2.24, Thermal variation of $\chi_m T$ for **C2b** (black circles), **C4b** (red circles), and **C6b** (blue circles). Solid lines are the best fit of the model (see text). Inset shows the isothermal magnetization at 2 K for **C2b**, **C4b**, and **C6b** (same colour codes).

This model satisfactorily reproduces the magnetic properties of compounds **C2b**, **C4b**, and **C6b** in the whole temperature range, with $g = 1.987(1)$, $2.006(1)$, $2.017(1)$, and $|D| = 2.3(1)$, $0.62(1)$, $0.94(1)$ cm^{-1} , for **C2b**, **C4b**, and **C6b** respectively. Unfortunately, since magnetic measurements were performed on polycrystalline samples, the sign of D was not determined. The isothermal magnetization measurements (Inset in Figure 2.24) support the $S = 5/2$ ground spin state of the Fe^{III} ions for all **C2b**, **C4b**, and **C6b**, since they can be well reproduced with a Brillouin function for a $S = 5/2$ spin state.

Thus, compounds **C2b**, **C4b**, and **C6b** present Fe^{III} ions in the high spin configuration with a $S = 5/2$ ground spin state and show a typical paramagnetic behaviour of isolated ions. All the described haloanilate-based Fe^{III} complexes, despite having counterions of different nature, show analogous magnetic behavior. A comparison of the thermal variation of $\chi_m T$ for **C2a**, **C2b**, and **C2c** (same anionic complex with different counterion) is reported in Figure S2.10.

The thermal variation of the molar magnetic susceptibility per Cr^{III} ion expressed as $\chi_m T$ for compounds **C1b**, **C3b**, and **C5b** is shown in Figure 2.25. These compounds show similar behaviors with $\chi_m T$ values at r.t. of ca. $1.9 \text{ cm}^3 \text{ K mol}^{-1}$, close to the expected value ($1.875 \text{ cm}^3 \text{ K mol}^{-1}$) for isolated Cr^{III} ions ($S = 3/2$, $g = 2$). These values remain constant down to ca. 10 K, then the $\chi_m T$ product decreases. The observed behavior in the high temperature region is typical of magnetically isolated $S = 3/2$ ions. As in the Fe^{III} complexes, the observed decrease at low temperature may be due to weak antiferromagnetic interactions between the Cr^{III} ions and/or to the presence of a ZFS in the $S = 3/2$ ground state of the Cr^{III} complexes. Taking into account the same structural considerations, since $(\text{Ph})_4\text{P}^+$ salts of Cr^{III} and Fe^{III} complexes are

isostructural, it seems reasonable to use a model that consider isolated $S = 3/2$ ions with a ZFS parameter D to fit the $\chi_m T$ vs T magnetic data.⁴¹⁻⁴³

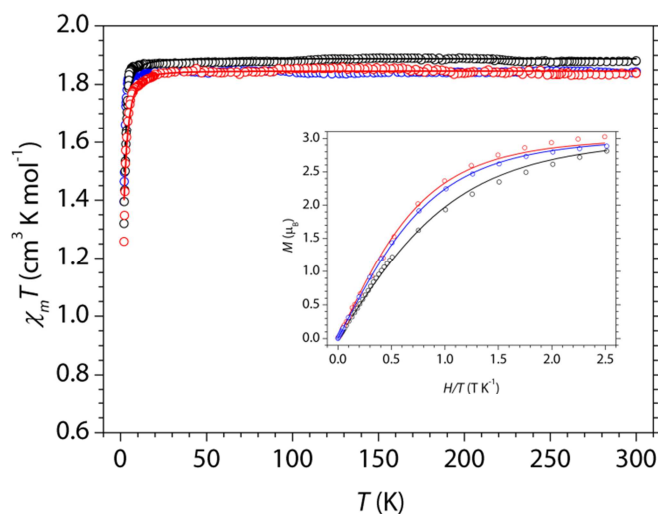


Figure 2.25. Thermal variation of $\chi_m T$ for **C1b** (black circles), **C3b** (red circles), and **C5b** (blue circles). Solid lines are the best fit of the model (see text). Inset shows the isothermal magnetization at 2 K for **C1b**, **C3b**, and **C5b** (same colour codes).

This model satisfactorily reproduces the magnetic properties of compounds **C1b**, **C3b**, and **C5b** in the whole temperature range, with $g = 1.994(1)$, $1.992(1)$, $2.024(1)$, and $|D| = 4.2(1)$, $4.0(1)$, $3.0(1)$ cm^{-1} , for **C1b**, **C3b**, and **C5b** respectively. The isothermal magnetization measurements (Inset in Figure 2.25) support the $S = 3/2$ ground spin state of the Cr^{III} ions for all **C1b**, **C3b**, and **C5b**, since they can be well reproduced with a Brillouin function for a $S = 3/2$ spin state. Thus, compounds **C2b**, **C4b**, and **C6b** present Cr^{III} ions with a $S = 3/2$ ground spin state and show a typical paramagnetic behaviour of isolated ions.

Interestingly, compound **C5a** presents a unique magnetic behavior among these complexes. For this Cr^{III} complex, the thermal trend of the $\chi_m T$ product decreases much more than in the others, *i.e.* decreases from the r.t. expected value of about $1.88 \text{ cm}^3 \text{ K mol}^{-1}$ down to $0.5 \text{ cm}^3 \text{ K mol}^{-1}$ at 2 K (Figure S2.11). This is due to the unique trend of the molar magnetic susceptibility χ_m , which reaches a maximum at $4.1(1)$ K and decreases down to 2 K (Figure 2.26). Moreover, the isothermal magnetization measurements performed on **C5a** (Inset in Figure 2.26) do not show the typical behavior of isolated $S = 3/2$ ions, because it appears quite linear and does not reach the expected saturation value of $3 \mu_B$.

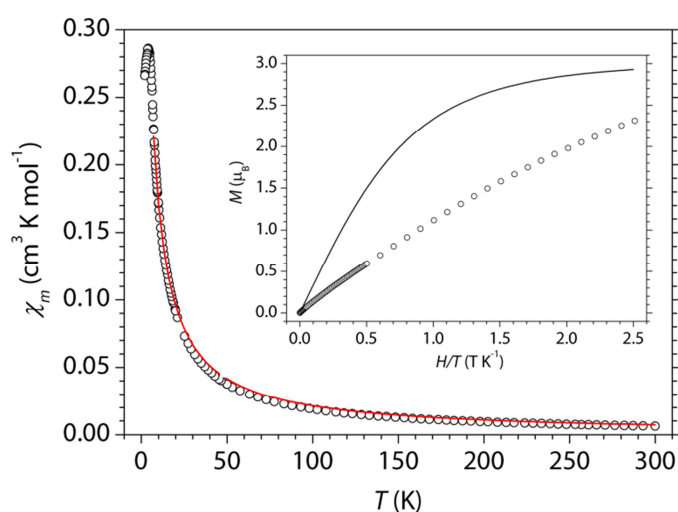


Figure 2.26, Thermal variation of χ_m for **C5a**. Solid line is the best fit to the Curie-Weiss law (see text). Inset shows the isothermal magnetization at 2 K for **C5a**. Solid line represents the Brillouin function for an isolated $S = 3/2$ ion with $g = 2$.

The observed behaviour at low temperature is likely due to magnetic interactions between Cr^{III} ions. This behaviour can be explained considering the crystallographic data for this compound. As described in the Crystal Structure Description Section, the crystal structure for **C5a** shows supramolecular dimers that are held together by two symmetry related I...O interactions (3.092(8) Å) considerably shorter than the sum of iodine and oxygen van der Waals radii (3.50 Å) (Figure 2.4). These XB interactions may be responsible for an antiferromagnetic coupling between different anionic complexes associated in dimers, due to the extended iodine orbitals that can be able to mediate magnetic exchange interactions, as already observed in the literature.⁴⁴⁻⁴⁷ In this case, the simple model that consider isolated $S = 3/2$ ions only with a ZFS parameter does not fit the magnetic data satisfactorily (Figure S2.10), suggesting that a better fit can be obtained by taking into account magnetic interactions between ions. For this reason, the magnetic susceptibility was fitted using the Curie-Weiss law

$$\chi_m(T) = \frac{Np^2\mu_B^2}{[3k(T - \vartheta)]}$$

where N is the number of magnetic ions in a mole, $p = g[S(S+1)]^{1/2}$ is the effective number of Bohr magnetons, μ_B is the Bohr magneton, k is the Boltzmann constant and ϑ is the Weiss constant.⁴¹⁻⁴³ The fit gives an effective Bohr magneton number $p = 4.2(1)$ and a Weiss constant $\vartheta = -2.8(1)$ K. The negative Weiss constant points out that the interactions between Cr^{III} ions are antiferromagnetic. This is confirmed by the low isothermal magnetization and by the maximum of χ_m at 4.1(1) K, which identifies the transition to the antiferromagnetic state.⁴¹⁻⁴³

The other described haloanilate-based Cr^{III} complexes, despite having counterions of different nature, show analogous magnetic behavior. A comparison of the thermal variation of $\chi_m T$ for **C1a**, **C1b**, and **C1c** (same anionic complex with different counterions) is reported in Figure S2.11.

The temperature dependence of the magnetic susceptibility for **C8b** as a $\chi_m T$ vs T plot is shown in Figure 2.27. The $\chi_m T$ value at r.t. of ca. $4.5 \text{ cm}^3 \text{ K mol}^{-1}$ is close to the expected value ($4.375 \text{ cm}^3 \text{ K mol}^{-1}$) for isolated high spin Fe^{III} centres ($S = 5/2$, $g = 2$). This value remain constant down to ca. 20 K, then the $\chi_m T$ product decreases slightly to $4.3 \text{ cm}^3 \text{ K mol}^{-1}$ at 1.85 K. The observed behavior in the high temperature region ($T > 20 \text{ K}$) is typical of magnetically isolated $S = 5/2$ ions, whereas the observed decrease at low temperature is likely due to weak antiferromagnetic interactions between the isotropic Fe^{III} magnetic sites. On the basis of the crystal structure (*vide supra*) that highlights the presence of short contacts in many different directions, the magnetic data have been modelled in the frame of the mean-field approximation using the well-known Curie-Weiss law.

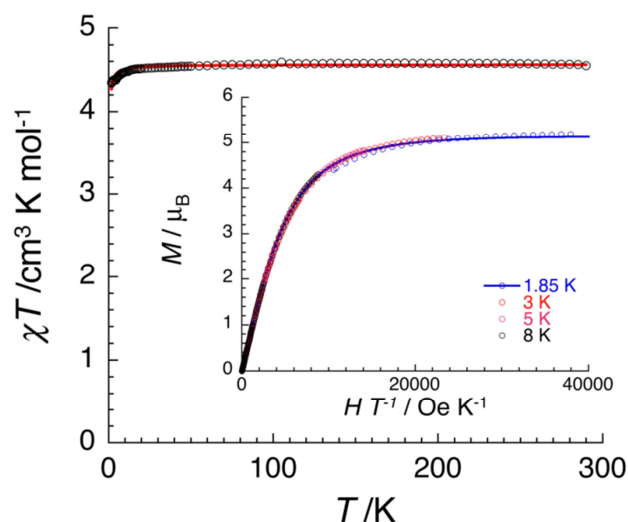


Figure 2.27. Temperature dependence of $\chi_m T$ product at 1000 Oe between 1.85 and 300 K for a polycrystalline sample of **C8b**. The solid line is the best fit obtained using the Curie-Weiss law. Inset: Field dependence of the magnetization for **C8b** between 1.85 and 8 K at magnetic fields between 0 and 7 T. The solid line is the best fit obtained using $S = 5/2$ Brillouin function.

This model satisfactorily reproduces the magnetic properties of compound **C8b** in the whole temperature range, with $g = 2.03(5)$ and $zJ/k_B = -20 \text{ mK}$. The magnitude of the inter-complex magnetic interactions of the order of a few mK falls well in the range expected for dipolar magnetic interactions but this observation does not rule out the possibility to have extremely small coupling also mediated by HB interactions. The field dependence of the magnetization below 8 K supports the $S = 5/2$ ground spin state of the Fe^{III} ions for **C8b** since a Brillouin function for an $S = 5/2$ spin state reproduces well the experimental data with $g = 2.06(3)$ (Inset in Figure 2.27). Thus, compound **C8b** presents a high spin configuration for the Fe^{III} ions with a $S = 5/2$ ground spin state and show a typical paramagnetic behaviour of quasi-isolated ions.

The thermal variation of the magnetic susceptibility per mole of Cr^{III} complex expressed as $\chi_m T$ for compound **C7b** is shown in Figure 2.28. The $\chi_m T$ value at r.t. of ca. $2.0 \text{ cm}^3 \text{ K mol}^{-1}$ is close to the expected value ($1.875 \text{ cm}^3 \text{ K mol}^{-1}$) for isolated Cr^{III} magnetic centres ($S = 3/2$, $g = 2$). This value slowly decreases to reach $1.4 \text{ cm}^3 \text{ K mol}^{-1}$ at ca. 1.85 K with a more marked decrease below 120 K. The observed behavior in the high temperature region is typical of magnetically

isolated $S = 3/2$ ions, whereas the observed decrease below 120 K is not usually seen for Cr^{III} complexes with an $S = 3/2$ ground state (*vide supra*). The field dependence of the magnetization (inset Figure 2.28) is indeed not compatible with an $S = 3/2$ spin state with a magnetization of about $2.5 \mu_{\text{B}}$ at 1.85 K under 7 T, much lower than the expected $3 \mu_{\text{B}}$. Moreover these experimental data cannot be model by a simple $S = 3/2$ Brillouin function with reasonable g factor.

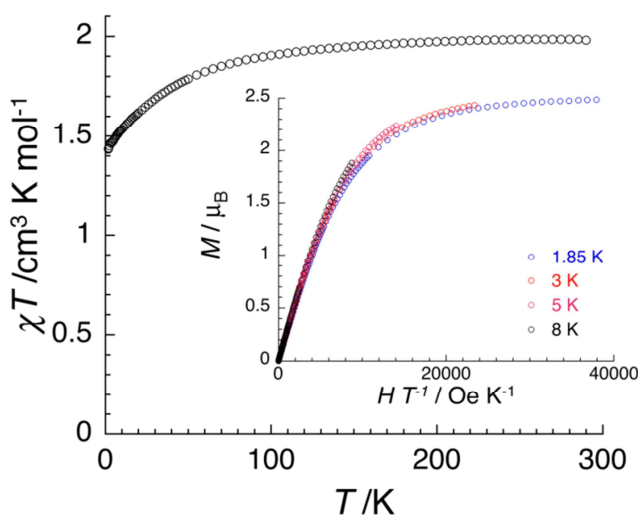


Figure 2.28. Temperature dependence of $\chi_m T$ product at 1000 Oe between 1.85 and 300 K for a polycrystalline sample of **C7b**. Inset: Field dependence of the magnetization for **C7b** between 1.85 and 8 K at magnetic fields between 0 and 7 T.

The magnetic behaviour of **C7b** is not well understood at this point as none of the magnetic models tried was able to reproduce both $\chi_m T$ vs T and M vs H data. The decrease of the $\chi_m T$ product at low temperature is incompatible with the presence of magnetic interactions between magnetic centres as a Curie-Weiss, used for **C8b**, does not reproduce the experimental data. On the other hand, $S = 3/2$ models considering magnetic anisotropy were not more successful. Therefore, in the absence of an X-ray crystal structure, it is only possible to speculate on the origin of this magnetic behaviour, that might be related, for example, to some kind of charge transfer between the $\text{Cr}(\text{III})$ metal ions and the hydranilate ligands.

The temperature dependence of the magnetic susceptibility for **C9a** and **C10a** are shown in Figure 2.29 as $\chi_m T$ vs T plots. The $\chi_m T$ values at r.t., of ca. $1.9 \text{ cm}^3 \text{ K mol}^{-1}$ and $4.4 \text{ cm}^3 \text{ K mol}^{-1}$ for **C9a** and **C10a**, respectively, are close to the expected values ($1.875 \text{ cm}^3 \text{ K mol}^{-1}$ and $4.375 \text{ cm}^3 \text{ K mol}^{-1}$) for isolated Cr^{III} ($S = 3/2$, $g = 2$) and high spin Fe^{III} centres ($S = 5/2$, $g = 2$). These values remain constant in the whole temperature range, and only below 10 K the $\chi_m T$ products of both **C9a** and **C10a** show a slightly increase. The observed behaviours in the high temperature region ($T > 10$ K) are typical of magnetically isolated $S = 3/2$ (**C9a**) or $S = 5/2$ (**C10a**) ions, whereas the observed increases at low temperature are likely due to very weak magnetic interactions between the isotropic magnetic sites. On the basis of the crystal structures (*vide supra*) that highlight the presence of short $\text{Cl}\cdots\text{N}$ contacts between complex anions, the

magnetic data have been modelled in the frame of the mean-field approximation using the Curie-Weiss law.

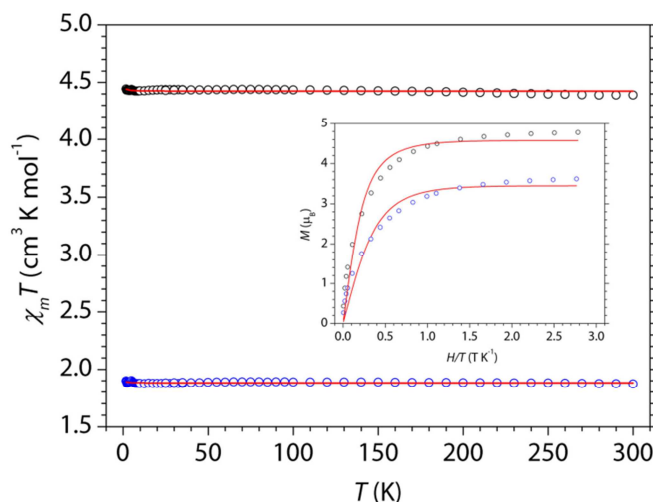


Figure 2.29, Temperature dependence of $\chi_m T$ between 1.80 and 300 K for polycrystalline samples of **C9a** (blue circles) and **C10a** (black circles). The solid red lines are the best fits obtained using the Curie-Weiss law. Inset: Field dependence of the magnetization for **C9a** and **C10a** (same colour codes) at 1.80 K, for magnetic fields between 0 and 5 T. The red solid lines are the best fits obtained using a $S = 3/2$ (**C9a**) or $S = 5/2$ (**C10a**) Brillouin function.

This model satisfactorily reproduces the magnetic properties of compounds **C9a** and **C10a** in the whole temperature range, with $g = 2.00(1)$ and $2.01(1)$, and $zJ/k_B = +11$ mK and $+9$ mK, for **C9a** and **C10a**, respectively. The magnitude of the inter-complex magnetic interactions, of the order of a few mK, falls well in the range expected for dipolar magnetic interactions but this observation does not rule out the possibility to have extremely small coupling also mediated by Cl...N interactions. The field dependence of the magnetization at 1.8 K supports the $S = 3/2$ and $S = 5/2$ ground spin state of the Cr^{III} and Fe^{III} ions since the corresponding Brillouin functions for $S = 3/2$ and $S = 5/2$ spin states, satisfactorily reproduce the experimental data with $g = 2.10(8)$, and $1.93(5)$ for **C9a** and **C10a**, respectively (Inset in Figure 2.29). Thus, **C9a** presents Cr^{III} ions with a $S = 3/2$ ground spin state, **C10a** presents Fe^{III} ions in high spin configuration with a $S = 5/2$ ground spin state, and both compounds show a typical paramagnetic behaviour of isolated ions.

The thermal variation of the magnetic susceptibility for **C9b** and **C10b** are shown in Figure 2.30 as $\chi_m T$ vs T plots. The $\chi_m T$ values at r.t., of ca. $1.9 \text{ cm}^3 \text{ K mol}^{-1}$ and $4.4 \text{ cm}^3 \text{ K mol}^{-1}$ for **C9b** and **C10b**, respectively, are close to the expected values ($1.875 \text{ cm}^3 \text{ K mol}^{-1}$ and $4.375 \text{ cm}^3 \text{ K mol}^{-1}$) for isolated Cr^{III} ($S = 3/2$, $g = 2$) and high spin Fe^{III} centres ($S = 5/2$, $g = 2$). The $\chi_m T$ values remain constant down to ca. 20 K, then, $\chi_m T$ for **C9b** shows a slightly increase to $2.2 \text{ cm}^3 \text{ K mol}^{-1}$ at 1.80 K, whereas that of **C10b** shows a slightly decrease to $4.1 \text{ cm}^3 \text{ K mol}^{-1}$ at 1.80 K. The observed behaviours in the high temperature region ($T > 20$ K) are typical of magnetically isolated $S = 3/2$ (**C9b**) or $S = 5/2$ (**C10b**) ions, whereas the observed increase/decrease at low temperature are likely due to weak magnetic interactions between the isotropic magnetic sites. On the basis of the crystal structures (*vide supra*) that highlight the presence of quite isolated complex anions surrounded by $(\text{Ph})_4\text{P}^+$ cations, the magnetic

data have been modelled in the frame of the mean-field approximation using the Curie-Weiss law to evaluate the strength of these interactions.

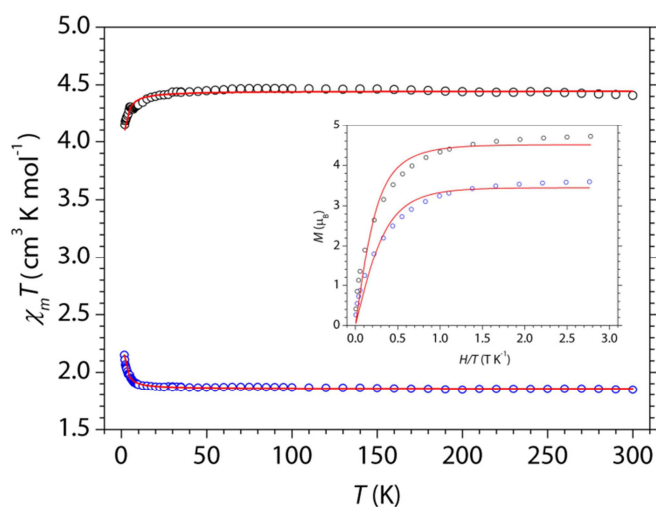


Figure 2.30, Temperature dependence of $\chi_m T$ between 1.80 and 300 K for polycrystalline samples of **C9b** (blue circles) and **C10b** (black circles). The solid red lines are the best fits obtained using the Curie-Weiss law. Inset: Field dependence of the magnetization for **C9b** and **C10b** (same colour codes) at 1.80 K for magnetic fields between 0 and 5 T. The red solid lines are the best fits obtained using a $S = 3/2$ (**C9b**) or $S = 5/2$ (**C10b**) Brillouin function.

This model satisfactorily reproduces the magnetic properties of compounds **C9b** and **C10b** in the whole temperature range, with $g = 1.99(1)$ and $2.02(1)$, and $zJ/k_B = +344$ mK and -237 mK, for **C9b** and **C10b**, respectively. The magnitude of the inter-complex magnetic interactions of the order of mK falls well in the range expected for dipolar magnetic interactions, the only expected type of magnetic interactions for these compounds given the absence of direct intermolecular contacts between magnetic centers. Interestingly, the small magnetic interactions observed in compounds **C9b** and **C10b** have similar magnitude, in agreement with their isostructurality, but different sign, *i.e.* ferromagnetic in **C9b** and antiferromagnetic in **C10b**. The field dependence of the magnetization at 1.8 K supports the $S = 3/2$ and $S = 5/2$ ground spin state of the Cr^{III} and Fe^{III} ions since the respective Brillouin functions for $S = 3/2$ and $S = 5/2$ spin states satisfactorily reproduce the experimental data with $g = 2.13(5)$ and $1.90(5)$, for **C9b** and **C10b**, respectively (Inset in Figure 2.30). Thus, **C9b** presents Cr^{III} ions with a $S = 3/2$ ground spin state, **C10b** presents Fe^{III} ions in high spin configuration with a $S = 5/2$ ground spin state, and both compounds show a typical paramagnetic behaviour of quasi-isolated ions.

2.3 Conclusions

A general and straightforward synthetic strategy has been employed for the preparation of a family of $[M^{III}(X_2An)_3]^{3-}$ ($M^{III} = Cr, Fe$; $X = Cl, Br, I, H, Cl/CN$) tris(anilato)metallate(III) complexes, that have been thoroughly characterized through X-ray crystal structures, spectroscopic studies, DFT calculations, HS analysis and magnetic measurements. These complexes represent a family of challenging anionic molecular building blocks for the rational design of functional and multifunctional molecular materials since the substituents at the 3,6 position of the anilate moiety play a key role in determining the physical properties of the resulting materials, either at the electronic level, by varying the electron density on the anilate ring, or at the supramolecular level, affecting the molecular packing *via* different supramolecular interactions. Especially, compounds **C3-6** represent one of the few examples of metal complexes with bromanilate and iodanilate as ligands reported in the literature, and compounds **C9-10** the first examples with chlorocyananilate. It is noteworthy that the presence of XB interactions in **C5a** are responsible for a unique magnetic behaviour in this family. This complex shows antiferromagnetic interactions, with an antiferromagnetic transition at 4.1(1) K, in agreement with the formation of halogen-bonded supramolecular dimers. The crystal structures of compounds **C7b** and **C8b** are instead dominated by an extensive network of moderate-strong HBs between the peripheral oxygen atoms of the ligands and crystallization water molecules. These interactions are responsible, as clearly shown by the analysis of the Hirshfeld Surface, for the formation of supramolecular layers showing an unprecedented H-bonded 2D supramolecular architecture in the family of anilate-based networks. The magnetic properties of **C7b** are intriguing and might find their origin in some kind of charge transfer between the Cr^{III} metal ions and the hydranilate ligands. The possibility to have magnetic exchange coupling also mediated by HB interactions is not ruled out. Furthermore, as perspective, this family of anionic complexes, can work (i) as molecular building blocks for constructing 2D molecule-based magnets, in analogy with the family of oxalate-based magnets,⁴⁸⁻⁵¹ (ii) as precursors for the preparation of metal-organic frameworks with tunable size which depends, in turn, on the substituent size, (iii) as magnetic components for building up multifunctional molecular materials based on the BEDT-TTF organic donor or its chiral and achiral derivatives, which furnish the pathway for combining electrical conductivity with magnetic properties, in analogy with the relevant class of $[M(ox)_3]^{3-}$ tris-chelated complexes which have produced the first family of molecular paramagnetic superconductors.⁵²⁻⁵⁴ The combined structural/theoretical analysis reported herein also enlarges the general knowledge on the supramolecular interactions shown by the anilate-based metallotectons and provides an effective tool for engineering anilate-based supramolecular architectures showing peculiar physical properties.

2.4 Experimental

2.4.1 Syntheses and Analytical Data

[(*n*-Bu)₄N]₃[Cr(Cl₂An)₃] (C1a). An aqueous solution (5 mL) of CrCl₃·6H₂O (210 mg, 0.80 mmol) was added dropwise to an aqueous solution (50 mL) of H₂Cl₂An (500 mg, 2.4 mmol), NaOH (200 mg, 5.0 mmol) and (*n*-Bu)₄NBr (800 mg, 2.5 mmol). After ca. 30 min at 60 °C, **C1a** starts to precipitate as red-violet solid, partially soluble in water. The mixture was allowed to cool to 25 °C, extracted with CH₂Cl₂ and dried under Na₂SO₄. The solution was filtered, rota-evaporated, and the obtained lacquer-like solid was crystallized in a MeOH/CH₂Cl₂ mixture to give red shiny crystals. Yield: 73%. Elemental anal. Calcd for C₆₆H₁₀₈Cl₆CrN₃O₁₂: C, 56.61; H, 7.77; N, 3.00; Found. C, 56.38; H, 7.71; N, 2.83. FT-IR (ν_{max}/cm⁻¹, KBr pellets): 2962(m), 2933(w), 2875(m), 1649(m), 1531(vs), 1469(w), 1383(w), 1353(s), 1303(m), 1000(m), 880(w), 841(m), 739(vw), 612(m), 597(w), 572(w), 508(w), 447(w). UV-Vis (CH₃CN solution, λ_{max}/nm (ε/dm³ mol⁻¹ cm⁻¹)): 466 sh, 497 (4493), 570 sh. ESI-MS, m/z Found (Calcd) = 1156.27 (1154.26) [[(*n*-Bu)₄N]₂[Cr(Cl₂An)₃]]⁻; 914.99 (915.00) [[(*n*-Bu)₄N][Cr(Cl₂An)₃]-H]⁻; 456.99 (455.99) [[(*n*-Bu)₄N][Cr(Cl₂An)₃]]²⁻.

[(Ph)₄P]₃[Cr(Cl₂An)₃]·H₂O (C1b). An aqueous solution (5 mL) of CrCl₃·6H₂O (210 mg, 0.80 mmol) was added dropwise to an aqueous solution (50 mL) of H₂Cl₂An (500 mg, 2.4 mmol), NaOH (200 mg, 5.0 mmol) and (Ph)₄PBr (1050 mg, 2.5 mmol). **C1b** precipitates as red-violet solid. The mixture was allowed to cool to 25 °C, and then the precipitate was collected by filtration, washed several times with fresh water and dried in desiccator. Yield: 80%. The product was recrystallized from a MeOH/CH₂Cl₂ mixture. Elemental anal. Calcd for C₉₀H₆₂Cl₆CrP₃O₁₃: C, 63.25; H, 3.66; Found. C, 62.88; H, 3.61. FT-IR (ν_{max}/cm⁻¹, KBr pellets): 3059(m), 3023(w), 2993(w), 1646(m), 1587(w), 1531(vs), 1438(s), 1352(vs), 1305(m), 1189(w), 1165(w), 1108(s), 1000(m), 843(m), 816(w), 756(m), 724(s), 690(m), 611(m), 571(w), 528(s), 449(w). UV-Vis (CH₃CN solution, λ_{max}/nm (ε/dm³ mol⁻¹ cm⁻¹)): 466 sh, 497 (3878), 570 sh. ESI-MS, m/z Found (Calcd) = 1349.67 (1351.68) [[(Ph)₄P]₂[Cr(Cl₂An)₃]]⁻; 1013.48 (1013.49) [[(Ph)₄P][Cr(Cl₂An)₃]-H]⁻; 506.15 (505.03) [[(Ph)₄P][Cr(Cl₂An)₃]]²⁻.

[(Et)₃NH]₃[Cr(Cl₂An)₃]·H₂O (C1c). Triethylamine (0.7 mL, 9.5 mmol) was added to a CH₃CN solution (50 mL) of H₂Cl₂An (500 mg, 2.4 mmol), then an aqueous solution (15 mL) of KCr(SO₄)₂·12H₂O (400 mg, 0.80 mmol) was added dropwise to the CH₃CN solution. The resulting mixture was heated up to reflux for 12 hours. **1c** precipitates as red shiny crystals suitable for X-ray analysis after slow evaporation of the mother liquor. Yield: 78%. Elemental anal. Calcd for C₃₆H₅₀Cl₆CrN₃O₁₃: C, 43.35; H, 5.05; N, 4.21; Found. C, 42.89; H, 4.93; N, 4.15. FT-IR (ν_{max}/cm⁻¹, KBr pellet): 3567(m), 3497(m), 3036(m), 2985(w), 2862(w), 1653(m), 1630(s), 1530(vs), 1472(s), 1357(vs), 1325(s), 1264(w), 1159(w), 1059(w), 1003(m), 846(s), 616(s), 573(m), 512(m), 450(m), 404(w). UV-Vis (CH₃CN solution, λ_{max}/nm (ε/dm³ mol⁻¹ cm⁻¹)): 466 sh, 497 (4235), 570 sh. ESI-MS, m/z Found (Calcd) = 1080.10 (1080.18) [[(Et)₃NH]₄[Cr(Cl₂An)₃]]⁺; 978.56 (979.36) [[(Et)₃NH]₃[Cr(Cl₂An)₃]-H]⁺; 878.56 (878.64) [[(Et)₃NH]₂[Cr(Cl₂An)₃]-2H]⁺.

[(*n*-Bu)₄N]₃[Fe(Cl₂An)₃] (C2a). This compound was synthesized as dark-violet shiny crystals according to the procedure described for **C1a**, using FeCl₃ (130 mg, 0.80 mmol), H₂Cl₂An (500 mg, 2.4 mmol), NaOH (200 mg, 5.0 mmol) and (*n*-Bu)₄NBr (800 mg, 2.5 mmol). Yield: 80%. Elemental anal. Calcd for C₆₆H₁₀₈Cl₆FeN₃O₁₂: C, 56.46; H, 7.75; N, 2.99; Found. C, 56.47; H, 7.83; N, 3.03. FT-IR (ν_{max}/cm⁻¹, KBr pellets): 2962(m), 2933(w), 2875(m), 1647(m), 1531(vs), 1469(w), 1383(w), 1349(s), 1300(s), 995(m), 878(w), 839(w), 739(w), 596(m), 574(m), 506(m). UV-Vis (CH₃CN solution, λ_{max}/nm (ε/dm³ mol⁻¹ cm⁻¹)): 444 (3669),

477 (4494), 516 (4910). ESI-MS, m/z Found (Calcd) = 1160.24 (1158.26) $[(n\text{-Bu})_4\text{N}]_2[\text{Fe}(\text{Cl}_2\text{An})_3]^-$; 918.94 (918.99) $[(n\text{-Bu})_4\text{N}][\text{Fe}(\text{Cl}_2\text{An})_3-\text{H}]^-$; 458.98 (457.98) $[(n\text{-Bu})_4\text{N}][\text{Fe}(\text{Cl}_2\text{An})_3]^{2-}$.

[(Ph)₄P]₃[Fe(Cl₂An)₃₂O (C2b). This compound was synthesized as dark-violet shiny crystals according to the procedure described for **C1b**, using FeCl₃ (130 mg, 0.80 mmol), H₂CA (500 mg, 2.4 mmol), NaOH (200 mg, 5.0 mmol) and (Ph)₄PBr (1050 mg, 2.5 mmol). Yield: 85%. Elemental anal. Calcd for C₉₀H₆₂Cl₆FeP₃O₁₃: C, 63.11; H, 3.65; Found. C, 62.75; H, 3.31. FT-IR ($\nu_{\text{max}}/\text{cm}^{-1}$, KBr pellets): 3059(m), 3023(w), 2993(w), 1644(m), 1587(w), 1528(vs), 1438(s), 1350(vs), 1304(m), 1188(w), 1165(w), 1108(s), 996(m), 839(m), 755(m), 724(s), 690(m), 597(m), 573(w), 528(s), 507(w). UV-Vis (CH₃CN solution, $\lambda_{\text{max}}/\text{nm}$ ($\epsilon/\text{dm}^3 \text{ mol}^{-1} \text{ cm}^{-1}$)): 444 (3823), 477 (4617), 516 (5075). ESI-MS, m/z Found (Calcd) = 1353.57 (1355.48) $[(\text{Ph})_4\text{P}]_2[\text{Fe}(\text{Cl}_2\text{An})_3]^-$; 1016.09 (1015.39) $[(\text{Ph})_4\text{P}][\text{Fe}(\text{Cl}_2\text{An})_3-\text{H}]^-$; 507.19 (508.05) $[(\text{Ph})_4\text{P}][\text{Fe}(\text{Cl}_2\text{An})_3]^{2-}$.

[(Et)₃NH]₃[Fe(Cl₂An)₃₂O (C2c). This compound was synthesized as dark-violet crystals according to the procedure described for **C1c**, using Fe(ClO₄)₃·6H₂O (290 mg, 0.80 mmol), H₂Cl₂An (0.5 g, 2.4 mmol) and triethylamine (0.7 mL, 9.5 mmol). Yield: 84%. Elemental anal. Calcd for C₃₆H₅₀Cl₆FeN₃O₁₃: C, 43.18; H, 5.03; N, 4.20; Found. C, 42.78; H, 4.83; N, 4.08. FT-IR ($\nu_{\text{max}}/\text{cm}^{-1}$, KBr pellets): 3567(m), 3497(m), 3039(m), 2985(w), 2866(w), 1651(m), 1633(m), 1530(vs), 1472(s), 1359(vs), 1322(s), 1264(w), 1159(w), 1059(w), 996(m), 841(s), 601(s), 575(m), 512(m), 404(w). UV-Vis (CH₃CN solution, $\lambda_{\text{max}}/\text{nm}$ ($\epsilon/\text{dm}^3 \text{ mol}^{-1} \text{ cm}^{-1}$)): 444 (3750), 477 (4523), 516 (5010). ESI-MS, m/z Found (Calcd) = 1083.98 (1084.03) $[(\text{Et})_3\text{NH}]_4[\text{Fe}(\text{Cl}_2\text{An})_3]^{+}$; 982.63 (983.21) $[(\text{Et})_3\text{NH}]_3[\text{Fe}(\text{Cl}_2\text{An})_3-\text{H}]^+$; 881.51 (882.39) $[(\text{Et})_3\text{NH}]_2[\text{Fe}(\text{Cl}_2\text{An})_3]-2\text{H}^+$.

[(n-Bu)₄N]₃[Cr(Br₂An)₃] (C3a). This compound was synthesized as red shiny crystals according to the procedure described for **C1a**, using CrCl₃·6H₂O (61 mg, 0.22 mmol), H₂Br₂An (194 mg, 0.65 mmol), NaOH (52 mg, 1.3 mmol) and (n-Bu)₄NBr (213 mg, 0.66 mmol). Yield: 70%. Elemental anal. Calcd for C₆₆H₁₀₈Br₆CrN₃O₁₂: C, 47.55; H, 6.53; N, 2.52; Found. C, 47.22; H, 6.43; N, 2.33. FT-IR ($\nu_{\text{max}}/\text{cm}^{-1}$, KBr pellets): 2962(m), 2933(w), 2873(m), 1638(m), 1620(m), 1521(vs), 1343(s), 1310(m), 989(m), 883(w), 813(m), 736(w), 613(m), 594(w), 559(m), 507(m), 472(vw), 413(w). UV-Vis (CH₃CN solution, $\lambda_{\text{max}}/\text{nm}$ ($\epsilon/\text{dm}^3 \text{ mol}^{-1} \text{ cm}^{-1}$)): 455 (4347), 490 (5115), 555 sh. ESI-MS, m/z Found (Calcd) = 1423.92 (1424.55) $[(n\text{-Bu})_4\text{N}]_2[\text{Cr}(\text{Br}_2\text{An})_3]^-$; 1182.66 (1185.10) $[(n\text{-Bu})_4\text{N}][\text{Cr}(\text{Br}_2\text{An})_3-\text{H}]^-$.

[(Ph)₄P]₃[Cr(Br₂An)₃]·H₂O (C3b). This compound was synthesized as red shiny crystals according to the procedure described for **C1b**, using CrCl₃·6H₂O (61 mg, 0.22 mmol), H₂Br₂An (194 mg, 0.65 mmol), NaOH (52 mg, 1.3 mmol) and (Ph)₄PBr (277 mg, 0.66 mmol). Yield: 83%. Elemental anal. Calcd for C₉₀H₆₂Br₆CrP₃O₁₂: C, 54.71; H, 3.16; Found. C, 54.32; H, 3.03. FT-IR ($\nu_{\text{max}}/\text{cm}^{-1}$, KBr pellets): 3059(m), 3023(w), 2993(w), 1639(m), 1586(w), 1521(vs), 1438(s), 1364(m), 1341(vs), 1299(m), 1283(m), 1187(w), 1165(w), 1109(s), 1000(m), 986(m), 812(m), 756(m), 724(s), 690(m), 603(m), 558(w), 527(s), 501(m), 459(w). UV-Vis (CH₃CN solution, $\lambda_{\text{max}}/\text{nm}$ ($\epsilon/\text{dm}^3 \text{ mol}^{-1} \text{ cm}^{-1}$)): 455 (3385), 490 (4403), 555 sh. ESI-MS, m/z Found (Calcd) = 1279.14 (1280.00) $[(\text{Ph})_4\text{P}][\text{Cr}(\text{Br}_2\text{An})_3-\text{H}]^-$; 641.21 (639.50) $[(\text{Ph})_4\text{P}][\text{Cr}(\text{Br}_2\text{An})_3]^{2-}$.

[(n-Bu)₄N]₃[Fe(Br₂An)₃] (C4a). This compound was synthesized as violet shiny crystals according to the procedure described for **C1a**, using FeCl₃ (35 mg, 0.22 mmol), H₂Br₂An (194 mg, 0.65 mmol), NaOH (52 mg, 1.3 mmol) and (n-Bu)₄NBr (213 mg, 0.66 mmol). Yield: 75%. Elemental anal. Calcd for C₆₆H₁₀₈Br₆FeN₃O₁₂: C, 47.44; H, 6.52; N, 2.51; Found. C, 46.98; H, 6.31; N, 2.52. FT-IR ($\nu_{\text{max}}/\text{cm}^{-1}$, KBr pellets): 2962(m), 2933(w), 2875(m), 1640(m), 1620(m), 1521(vs), 1472(m), 1338(s), 1281(m), 978(m), 883(w), 803(m), 739(w), 576(m), 562(m), 500(w). UV-Vis (CH₃CN solution, $\lambda_{\text{max}}/\text{nm}$ ($\epsilon/\text{dm}^3 \text{ mol}^{-1} \text{ cm}^{-1}$)): 443 (5487), 477 (6439), 519 (6841). ESI-MS, m/z Found (Calcd) = 1427.90 (1428.40) $[(n\text{-Bu})_4\text{N}]_2[\text{Fe}(\text{Br}_2\text{An})_3]^-$; 1186.59 (1188.95) $[(n\text{-Bu})_4\text{N}][\text{Fe}(\text{Br}_2\text{An})_3-\text{H}]^-$.

[(Ph)₄P]₃[Fe(Br₂An)₃]·H₂O (C4b). This compound was synthesized as dark-violet shiny crystals according to the procedure described for **C1b**, using FeCl₃ (35 mg, 0.22 mmol), H₂Br₂An (194 mg, 0.65 mmol), NaOH (52 mg, 1.3 mmol) and (Ph)₄PBr (277 mg, 0.66 mmol). Yield: 83%. Elemental anal. Calcd for C₉₀H₆₂Br₆FeP₃O₁₃: C, 54.60; H, 3.16; Found. C, 54.13; H, 2.98. FT-IR (ν_{max}/cm⁻¹, KBr pellets): 3059(m), 3023(w), 2993(w), 1640(m), 1586(w), 1519(vs), 1438(s), 1336(vs), 1281(m), 1188(w), 1164(w), 1109(s), 997(m), 979(m), 804(m), 756(m), 724(s), 690(m), 580(m), 559(w), 530(s), 501(m), 459(w). UV-Vis (CH₃CN solution, λ_{max}/nm (ε/dm³ mol⁻¹ cm⁻¹)): 443 (6323), 477 (6856), 519 (6535). ESI-MS, m/z Found (Calcd) = 1621.29 (1622.23) [(Ph)₄P]₂[Fe(Br₂An)₃]⁻; 1283.09 (1283.84) [(Ph)₄P][Fe(Br₂An)₃]-H⁻; 640.89 (641.42) [(Ph)₄P][Fe(Br₂An)₃]²⁻.

[(n-Bu)₄N]₃[Cr(I₂An)₃] (C5a). This compound was synthesized as dark-red shiny crystals according to the procedure described for **C1a**, using CrCl₃·6H₂O (88 mg, 0.33 mmol), H₂I₂An (392 mg, 1.0 mmol), NaOH (80 mg, 2.0 mmol) and NBu₄Br (387 mg, 1.2 mmol). Yield: 74%. Elemental anal. Calcd for C₆₆H₁₀₈I₆CrN₃O₁₂: C, 40.67; H, 5.59; N, 2.16; Found. C, 40.37; H, 5.59; N, 2.16. FT-IR (ν_{max}/cm⁻¹, KBr pellets): 2962(m), 2933(w), 2873(m), 1630(s), 1513(vs), 1330(s), 1270(m), 968(m), 881(w), 791(m), 778(m), 738(w), 698(m), 549(m), 501(m). UV-Vis (CH₃CN solution, λ_{max}/nm (ε/dm³ mol⁻¹ cm⁻¹)): 463 sh, 502 (5102), 575 sh. ESI-MS, m/z Found (Calcd) = 1705.90 (1705.87) [(n-Bu)₄N]₂[Cr(I₂An)₃]⁻.

[(Ph)₄P]₃[Cr(I₂An)₃]·H₂O (C5b). This compound was synthesized as dark-red shiny crystals according to the procedure described for **C1b**, using CrCl₃·6H₂O (59 mg, 0.22 mmol), H₂I₂An (255 mg, 0.65 mmol), NaOH (52 mg, 1.3 mmol) and (Ph)₄PBr (277 mg, 0.66 mmol). Yield: 84%. Elemental anal. Calcd for C₉₀H₆₂I₆CrP₃O₁₃: C, 47.88; H, 2.77; Found. C, 47.29; H, 2.63. FT-IR (ν_{max}/cm⁻¹, KBr pellets): 3059(m), 3023(w), 2993(w), 1630(m), 1585(w), 1511(vs), 1437(s), 1330(vs), 1274(m), 1188(w), 1164(w), 1108(s), 997(m), 969(m), 790(m), 778(m), 754(m), 723(s), 689(s), 590(m), 548(m), 527(s), 503(m), 456(w). UV-Vis (CH₃CN solution, λ_{max}/nm (ε/dm³ mol⁻¹ cm⁻¹)): 463 sh, 502 (5003), 575 sh. ESI-MS, m/z Found (Calcd) = 1562.76 (1562.00) [(Ph)₄P][Cr(I₂An)₃]-H⁻; 779.86 (780.50) [(Ph)₄P][Cr(I₂An)₃]²⁻.

[(n-Bu)₄N]₃[Fe(I₂An)₃] (C6a). This compound was synthesized as dark-violet shiny crystals according to the procedure described for **C1a**, using FeCl₃ (54 mg, 0.33 mmol), H₂I₂An (390 mg, 1.0 mmol), NaOH (80 mg, 2.0 mmol) and NBu₄Br (330 mg, 1.0 mmol). Yield: 85%. Elemental anal. Calcd for C₆₆H₁₀₈I₆FeN₃O₁₂: C, 40.59; H, 5.57; N, 2.15; Found. C, 39.15; H, 5.03; N, 2.04. FT-IR (ν_{max}/cm⁻¹, KBr pellets): 2962(m), 2932(w), 2872(m), 1630(s), 1515(vs), 1325(s), 1269(m), 962(m), 878(w), 795(m), 781(m), 736(w), 588(m), 551(m), 497(m). UV-Vis (CH₃CN solution, λ_{max}/nm (ε/dm³ mol⁻¹ cm⁻¹)): 450 (6210), 479 (6098), 530 sh. ESI-MS, m/z Found (Calcd) = 1709.81 (1709.87) [(n-Bu)₄N]₂[Fe(I₂An)₃]⁻.

[(Ph)₄P]₃[Fe(I₂An)₃]·4H₂O (C6b). This compound was synthesized as dark-violet shiny crystals according to the procedure described for **C2b**, using FeCl₃ (35 mg, 0.22 mmol), H₂I₂An (255 mg, 0.65 mmol), NaOH (52 mg, 1.3 mmol) and (Ph)₄PBr (277 mg, 0.66 mmol). Yield: 90%. Elemental anal. Calcd for C₉₀H₆₈I₆FeP₃O₁₆: C, 46.68; H, 2.96; Found. C, 46.42; H, 2.81. FT-IR (ν_{max}/cm⁻¹, KBr pellets): 3059(m), 3023(w), 2993(w), 1629(m), 1585(w), 1515(vs), 1436(s), 1325(vs), 1266(m), 1189(w), 1163(w), 1107(s), 996(m), 962(m), 783(m), 757(m), 723(s), 689(m), 578(m), 550(w), 527(s), 499(m). UV-Vis (CH₃CN solution, λ_{max}/nm (ε/dm³ mol⁻¹ cm⁻¹)): 450 (5770), 479 (6088), 530 sh. ESI-MS, m/z Found (Calcd) = 1565.85 (1565.07) [(Ph)₄P][Fe(I₂An)₃]-H⁻; 781.90 (782.42) [(Ph)₄P][Fe(I₂An)₃]²⁻.

[(Ph)₄P]₃[Cr(H₂An)₃]·6H₂O (C7b). An aqueous solution (20 mL) of CrCl₃·6H₂O (330 mg, 1.2 mmol) was added dropwise to an aqueous solution (250 mL) of H₂H₂An (500 mg, 3.6 mmol), NaOH (286 mg, 3.2 mmol) and (Ph)₄PBr (1.50 g, 3.6 mmol). After ca. 30 min at reflux temperature, **C7b** precipitates as a red-brown lacquer-like solid, partially soluble in water. The mixture was allowed to cool to r.t. and the mother liquor was separated. The precipitate was dissolved in the minimum amount of methanol, then

150 mL of boiling water were slowly added to the methanolic solution. A red-brown microcrystalline solid was obtained by removing the residual methanol by rota-evaporation. The solution was filtered, washed with cold water and the precipitate recrystallized in a MeOH-H₂O (9:1) mixture to give **C7b** as red shiny crystals. Crystals of **C7b** were also obtained by slow cooling of the mother liquor. Yield 30%. Elemental anal. calcd for C₉₀H₇₈CrP₃O₁₈: C, 67.88; H, 4.94; Found. C, 67.36; H, 4.25. FT-IR ($\nu_{\max}/\text{cm}^{-1}$, KBr pellets): 3416(s), 3058(w), 2928(w), 1627(w), 1602(m), 1535(vs), 1484(w), 1437(m), 1377(s), 1245(s), 1188(w), 1164(w), 1108(s), 1027(w), 996(m), 835(m), 812(m), 758(m), 723(m), 690(m), 664(w), 578(m), 527(m), 482(w). UV-Vis (CH₃CN solution, λ_{\max}/nm ($\epsilon/\text{dm}^3 \text{ mol}^{-1} \text{ cm}^{-1}$)): 452 sh, 478 (5421), 517 sh. ESI-MS, m/z Found (Calcd) = 1143.88 (1144.19) [[(Ph)₄P]₂[Cr(H₂An)₃]]⁻; 804.67 (805.06) [[(Ph)₄P][Cr(H₂An)₃]-H]⁻; 402.35 (402.53) [[(Ph)₄P][Cr(H₂An)₃]]²⁻; 155.28 (155.31) [[Cr(H₂An)₃]]³⁻.

[(Ph)₄P]₃[Fe(H₂An)₃₂O (C8b). An aqueous solution (10 mL) of FeCl₃ (195 mg, 1.2 mmol) was added dropwise to an aqueous solution (250 mL) of H₂H₂An (500 mg, 3.6 mmol), NaOH (286 mg, 7.2 mmol) and (Ph)₄PBr (1.50 g, 3.6 mmol). After ca. 30 min at 30 °C, **C8b** precipitates slowly as a brown lacquer-like solid, partially soluble in water. The mixture was allowed to cool to r. and the mother liquor was separated. The precipitate was vigorously washed with clean boiling water and the resulting mixture was ultrasonicated. A red-brown microcrystalline solid was obtained by washing several times the lacquer-like solid with fresh boiling water. The solution was filtered, washed with cold water and the precipitate recrystallized in a MeOH-H₂O (9:1) mixture to give **C8b** as red shiny crystals suitable for an X-ray analysis. Yield 40%. Elemental anal. calcd for C₉₀H₇₈FeP₃O₁₈: C, 67.72; H, 4.92. Found. C, 67.28; H, 4.44. FT-IR ($\nu_{\max}/\text{cm}^{-1}$, KBr pellets): 3415(s), 3058(w), 2928(w), 1629(w), 1604(m), 1586(w), 1535(vs), 1484(w), 1437(m), 1370(s), 1247(s), 1188(w), 1164(w), 1108(s), 1027(w), 996(m), 829(m), 814(m), 758(m), 723(m), 690(m), 660(w), 560(m), 527(m), 483(w). UV-Vis (CH₃CN solution, λ_{\max}/nm ($\epsilon/\text{dm}^3 \text{ mol}^{-1} \text{ cm}^{-1}$)): 435 (6514), 464 (7499), 503 sh. ESI-MS, m/z found (calcd) = 1147.91 (1148.18) [[(Ph)₄P]₂[Fe(H₂An)₃]]⁻; 809.64 (810.05) [[(Ph)₄P][Fe(H₂An)₃]-H]⁻; 404.43 (404.53) [[(Ph)₄P][Fe(H₂An)₃]]²⁻; 156.66 (156.64) [[Fe(H₂An)₃]]³⁻.

[(n-Bu)₄N]₃[Cr(CICNAn)₃] (C9a). This compound was synthesized as red shiny crystals according to the procedure described for **C1a**, using CrCl₃·6H₂O (61 mg, 0.22 mmol), KHClCNAn (154 mg, 0.65 mmol), NaOH (26 mg, 0.66 mmol) and (n-Bu)₄NBr (213 mg, 0.66 mmol). Yield: 85%. Elemental anal. Calcd for C₆₉H₁₀₈Cl₃CrN₆O₁₂: C, 60.40; H, 7.93; N, 6.13; Found. C, 60.29; H, 7.92; N, 6.20. FT-IR ($\nu_{\max}/\text{cm}^{-1}$, KBr pellets): 2963(m), 2934(w), 2876(m), 2213(m), 1644(m), 1612(w), 1562(s), 1528(vs), 1480(m), 1395(vs), 1324(m), 1306(m), 1262(m), 1032(m), 882(w), 862(m), 740(w), 624(m), 610(m), 596(m), 517(w), 444(w). UV-Vis (CH₃CN solution, λ_{\max}/nm ($\epsilon/\text{dm}^3 \text{ mol}^{-1} \text{ cm}^{-1}$)): 446 sh, 480 (6099), 530 sh. ESI-MS, m/z Found (Calcd) = 1129.30 (1429.52) [[(n-Bu)₄N]₂[Cr(CICNAn)₃]]⁻; 443.29 (443.53) [[(n-Bu)₄N][Cr(CICNAn)₃]]²⁻.

[(Ph)₄P]₃[Cr(CICNAn)₃]·H₂O (C9b). This compound was synthesized as red shiny crystals according to the procedure described for **C1b**, using CrCl₃·6H₂O (61 mg, 0.22 mmol), KHClCNAn (154 mg, 0.65 mmol), NaOH (26 mg, 0.66 mmol) and (Ph)₄PBr (277 mg, 0.66 mmol). Yield: 79%. Elemental anal. Calcd for C₉₃H₆₂Cl₃CrP₃N₃O₁₃: C, 66.46; H, 3.72; N, 2.50; Found. C, 66.02; H, 3.67; N, 2.47. FT-IR ($\nu_{\max}/\text{cm}^{-1}$, KBr pellets): 3063(w), 2211(s), 1636(m), 1610(w), 1560(s), 1526(vs), 1484(m), 1438(s), 1393(vs), 1306(m), 1263(m), 1188(w), 1165(w), 1108(s), 1031(m), 997(m), 863(m), 755(m), 724(s), 690(s), 625(m), 608(m), 595(m), 527(s), 443(w). UV-Vis (CH₃CN solution, λ_{\max}/nm ($\epsilon/\text{dm}^3 \text{ mol}^{-1} \text{ cm}^{-1}$)): 446 sh, 480 (5614), 530 sh. ESI-MS, m/z Found (Calcd) = 1322.95 (1323.37) [[(Ph)₄P]₂[Cr(CICNAn)₃]]⁻; 982.84 (983.98) [[(Ph)₄P][Cr(CICNAn)₃]-H]⁻; 491.72 (491.99) [[(Ph)₄P][Cr(CICNAn)₃]]²⁻.

[(n-Bu)₄N]₃[Fe(CICNAn)₃] (C10a). This compound was synthesized as dark-red shiny crystals according to the procedure described for **C1a**, using FeCl₃ (35 mg, 0.22 mmol), KHClCNAn (154 mg, 0.65 mmol), NaOH (52 mg, 1.3 mmol) and (n-Bu)₄NBr (213 mg, 0.66 mmol). Yield: 95%. Elemental anal. Calcd for

$C_{69}H_{108}Cl_3FeN_6O_{12}$: C, 60.24; H, 7.91; N, 6.11; Found. C, 60.04; H, 7.90; N, 6.12. FT-IR (ν_{max}/cm^{-1} , KBr pellets): 2963(m), 2934(w), 2876(m), 2213(m), 1653(m), 1612(w), 1560(s), 1529(vs), 1480(m), 1395(vs), 1327(m), 1308(m), 1257(m), 1026(m), 883(w), 859(m), 740(w), 611(m), 577(m), 511(w), 418(w). UV-Vis (CH_3CN solution, λ_{max}/nm ($\epsilon/dm^3 mol^{-1} cm^{-1}$)): 430 (6323), 460 (7518), 495 (7723). ESI-MS, m/z Found (Calcd) = 1133.27 (1133.37) $[(n-Bu)_4N]_2[Fe(CICNAn)_3]^-$; 890.01 (890.90) $[(n-Bu)_4N][Fe(CICNAn)_3-H]^-$; 445.34 (445.34) $[(n-Bu)_4N][Fe(CICN_2An)_3]^{2-}$.

[(Ph)₄P]₃[Fe(CICNAn)₃]-H₂O (C10b). This compound was synthesized as red shiny crystals according to the procedure described for **C1b**, using $FeCl_3$ (35 mg, 0.22 mmol), $KHCICNAn$ (154 mg, 0.65 mmol), $NaOH$ (52 mg, 1.3 mmol) and $(Ph)_4PBr$ (277 mg, 0.66 mmol). Yield: 85%. Elemental anal. Calcd for $C_{93}H_{62}C_3FeP_3N_3O_{13}$: C, 66.31; H, 3.71; N, 2.49; Found. C, 65.76; H, 3.46; N, 2.50. FT-IR (ν_{max}/cm^{-1} , KBr pellets): 3063(w), 2211(s), 1636(m), 1610(w), 1560(s), 1526(vs), 1484(m), 1438(s), 1393(vs), 1306(m), 1263(m), 1188(w), 1165(w), 1108(s), 1026(m), 997(m), 860(m), 756(m), 724(s), 690(s), 610(m), 577(m), 528(s), 419(vw). UV-Vis (CH_3CN solution, λ_{max}/nm ($\epsilon/dm^3 mol^{-1} cm^{-1}$)): 430 (7313), 460 (8310), 495 (8200). ESI-MS, m/z Found (Calcd) = 1326.92 (1327.22) $[(Ph)_4P]_2[Fe(CICNAn)_3]^-$; 988.81 (988.83) $[(Ph)_4P][Fe(CICNAn)_3-H]^-$; 493.67 (493.92) $[(Ph)_4P][Fe(CICNAn)_3]^{2-}$.

2.4.2 Equipment and Measurements Details

Elemental Analyses. C, H, N, and S measurements were performed with a Thermo Electron Analyser CHNS Flash 2000 or with a Carlo Erba EA1108 CHNS analyser.

FT-IR and UV-Vis Spectroscopy. FT-IR spectra were performed on KBr pellets and collected with a Bruker Equinox 55 spectrophotometer. Electronic spectra (1200–200 nm) were recorded on a Varian Cary 5 spectrophotometer.

ESI-MS Analyses. ESI-MS spectra were collected on a Bruker Esquire 3000 Ionic Trap (TOF analyser) in negative and positive ion mode.

Cyclic Voltammetry. Cyclic voltammetry was carried out with a BioLogic potentiostat model SP-150, using a three-electrode cell equipped with a platinum working millielectrode with a surface area of $0.126 cm^2$, an Ag/Ag^+ pseudoreference and a platinum-wire as counterelectrode. The experiments were performed at r.t. (25 °C), in dry and Nitrogen-degassed CH_3CN solution containing $0.1 mol dm^{-3} [(n-Bu)_4N]PF_6$ as supporting electrolyte, at $50 mV s^{-1}$ scan rate. All the voltamograms were corrected for the half-wave potential of the ferrocene-ferrocenium couple as internal standard (0.42 V under these conditions).

Single Crystal X-Ray Crystallography. Single crystal data were collected with a Bruker AXS Smart 1000, or with a Bruker Smart APEXII, or with a Bruker Nonius Kappa CCD area detector diffractometers. All data collection were performed with the $MoK\alpha$ radiation ($\lambda = 0.71073 \text{ \AA}$). The unit cell parameters were obtained using 60 ω -frames of 0.5° width and scanned from three different zone of reciprocal lattice. The intensity data were integrated from several series of exposures frames of 0.3° width covering the sphere of the reciprocal lattice.⁵⁵ Absorption corrections were applied using the program SADABS.⁵⁶ The structures were solved by direct methods (SIR97 and SIR2004^{57,58}) and refined on F^2 with full-matrix least squares (SHELXL-97⁵⁹), using the Wingx software package.⁶⁰ The crystallization water molecules for compounds **C1-6** were refined without hydrogen atoms. The hydrogen atoms of crystallization water molecules for **C8b** were located from the difference Fourier map and they were refined with distance and angle restraints. The crystals of **C2b** and **C4b** were thin plates and diffracted poorly, and only a partial structure determination could be obtained. In **C2b** and **C4b** the carbon atoms of the $(Ph)_4P^+$

cations were refined with isotropic displacement parameters, and one of the ligands was found disordered in two positions that were refined with isotropic thermal parameters and with site occupancy factors of 0.53/0.47 and 0.62/0.38, respectively. The remaining non-hydrogen atoms were refined anisotropically for all compounds, and the hydrogen atoms were placed at their calculated positions. Graphical material was prepared with Mercury CSD 3.3.⁶¹ A summary of the crystallographic data and the structure refinement for **C1c**, **C2c**, **C5a**, **C2b**, **C4b**, **C6b**, **C8b**, **C9a**, **C9b**, **C10a** is reported in Table 2.7.

Table 2.7. Summary of X-ray crystallographic data for **C1c**, **C2c**, **C5a**, **C2b**, **C4b**, **C6b**, **C8b**, **C9a**, **C9b**, **C10a**.

	C1c	C2c	C5a	C2b
Empirical formula	C ₃₆ H ₅₀ Cl ₆ CrN ₃ O ₁₄	C ₃₆ H ₅₀ Cl ₆ FeN ₃ O ₁₄	C ₆₈ H ₁₀₈ l ₆ CrN ₃ O ₁₂	C ₉₀ H ₆₂ Cl ₆ FeP ₃ O ₁₃
Formula weight	997.49	1019.36	1948.95	1712.86
Crystal size, mm	0.27 × 0.15 × 0.10	0.33 × 0.27 × 0.13	0.14 × 0.09 × 0.05	0.19 × 0.03 × 0.03
Crystal system	Monoclinic	Orthorhombic	Orthorhombic	Monoclinic
Space group	<i>P2₁/n</i>	<i>Pbcn</i>	<i>Pbca</i>	<i>P2₁/n</i>
<i>a</i> , Å	16.154(3)	26.340(6)	24.339(1)	13.336(3)
<i>b</i> , Å	10.575(2)	16.510(4)	20.262(1)	18.855(5)
<i>c</i> , Å	26.682(4)	10.564(3)	32.155(2)	32.473(8)
α, deg.	90	90	90	90
β, deg.	92.092(3)	90	90	91.462(3)
γ, deg.	90	90	90	90
<i>V</i> , Å ³	4555(1)	4594(2)	15858(1)	8163(3)
<i>Z</i>	4	4	8	4
<i>T</i> , K	293(2)	293(2)	293(2)	293(2)
ρ (calc), Mg/m ³	1.455	1.474	1.633	1.394
μ, mm ⁻¹	0.655	0.742	2.534	0.504
θ range, deg.	1.4–27.58	1.46–27.08	1.45–24.00	1.25–23.33
Goof	1.007	1.020	1.064	1.015
<i>R</i> 1	0.0834	0.0572	0.0570	0.0887
<i>wR</i> 2	0.1515	0.1562	0.1206	0.1592
	C4b	C6b	C8b	C9a
Empirical formula	C ₉₀ H ₆₂ Br ₆ FeP ₃ O ₁₃	C ₉₀ H ₆₈ l ₆ FeP ₃ O ₁₆	C ₉₀ H ₇₈ FeP ₃ O ₁₃	C ₆₉ H ₁₀₈ Cl ₃ FeN ₆ O ₁₂
Formula weight	1979.62	2311.57	1596.28	1371.96
Crystal size, mm	0.12 × 0.08 × 0.03	0.29 × 0.24 × 0.07	0.32 × 0.10 × 0.03	0.60 × 0.12 × 0.07
Crystal system	Monoclinic	Monoclinic	Triclinic	Monoclinic
Space group	<i>P2₁/n</i>	<i>C2/c</i>	<i>P-1</i>	<i>P2₁/a</i>
<i>a</i> , Å	13.408(2)	35.023(5)	13.704(3)	20.219(2)
<i>b</i> , Å	18.871(2)	12.482(2)	17.106(4)	13.162(3)
<i>c</i> , Å	32.851(4)	46.347(7)	19.923(5)	29.914(5)
α, deg.	90	90	77.007(4)	90
β, deg.	91.198(3)	114.467(2)	84.696(5)	108.729(10)
γ, deg.	90	90	64.123(4)	90
<i>V</i> , Å ³	8310(2)	18441(1)	4094(2)	7539(2)
<i>Z</i>	4	8	2	4
<i>T</i> , K	293(2)	293(2)	293(2)	150(2)
ρ (calc), Mg/m ³	1.582	1.665	1.295	1.209

μ , mm ⁻¹	3.187	2.286	1.291	0.317
θ range, deg.	1.24–22.81	1.75–23.42	1.55–25.70	1.88–24.10
Goof	1.003	1.042	1.010	1.089
R1	0.0735	0.0894	0.0606	0.1062
wR2	0.1123	0.1518	0.1241	0.2104
	C9b	C10a		
Empirical formula	C ₉₃ H ₆₀ Cl ₃ CrN ₃ P ₃ O ₁₃	C ₆₉ H ₁₀₈ Cl ₃ FeN ₆ O ₁₂		
Formula weight	1678.70	1375.81		
Crystal size, mm	0.32 × 0.28 × 0.10	0.80 × 0.60 × 0.10		
Crystal system	Monoclinic	Monoclinic		
Space group	<i>P</i> 2 ₁ / <i>n</i>	<i>P</i> 2 ₁ / <i>a</i>		
<i>a</i> , Å	13.202(2)	20.167(1)		
<i>b</i> , Å	18.819(5)	13.190(3)		
<i>c</i> , Å	32.627(7)	29.964(7)		
α , deg.	90	90		
β , deg.	91.914(14)	108.603(11)		
γ , deg.	90	90		
<i>V</i> , Å ³	8101(3)	7554(2)		
<i>Z</i>	4	4		
<i>T</i> , K	150(2)	150(2)		
ρ (calc), Mg/m ³	1.376	1.210		
μ , mm ⁻¹	0.367	0.365		
θ range, deg.	1.25–26.50	1.88–24.50		
Goof	1.057	1.016		
R1	0.0734	0.0882		
wR2	0.1784	0.2051		

$$R1 = \frac{\sum ||F_o| - |F_c||}{\sum |F_o|}, wR2 = \frac{[\sum (w(F_o^2 - F_c^2)^2)]^{1/2}}{[\sum (wF_o^2)]^{1/2}}, w = 1/[\sigma^2(F_o^2) + (aP)^2 + bP], \text{ where } P = [\max(F_o^2, 0) + 2F_c^2]/3.$$

Powder X-Ray Crystallography. WAPXRD patterns on polycrystalline samples were recorded on a Panalytical Empyrean diffractometer equipped with a graphite monochromator on the diffracted beam, and a X'Celerator linear detector. The scans were collected within the range 5–40° (2 θ) using Cu K α radiation. The simulated patterns were generated from the atomic coordinates of the single-crystal structure solutions using the program Mercury 3.3 (copyright CCDC, <http://www.ccdc.cam.ac.uk/mercury/>) using a FWHM of 0.15 and a 2 θ step of 0.05.

Computational details. Density functional theory calculations were performed on the isolated anions X₂An (X = Cl, Br, I, H) and on the complexes [M^{III}(X₂An)₃]³⁻ (M = Cr, Fe; X = Cl, Br, I, H). The geometries of the anions were optimized with the B3LYP^{62,63} hybrid density functional and the SDD basis set with Stuttgart-Dresden effective core potential for bromine and iodine atoms.⁶⁴⁻⁶⁶ The geometries of the metal complexes were optimized with the B3LYP density functional and the LANL2DZ basis set with Hay and Wadt effective core potential (ECP)^{67,68} for iron, chromium and halogen atoms and the 6-31G basis set^{69,70} for the C and O atoms. Single point calculations were performed on the complexes by using the B3LYP density functional and the LANL2DZ basis set with Hay and Wadt ECP for the metal ions and halogen atoms, whereas C and O atoms were treated with the 6-31+G(d) basis set. Atomic charges derived by the NPA were obtained with the NBO 3.1 program⁷¹ incorporated in the Gaussian03 package. Molecular orbital diagrams and electrostatic potential diagrams were generated with the MOLDEN⁷² or Gabedit⁷³ program. All the calculations have been performed with the Gaussian03 program suite.⁷⁴

Hirshfeld surface analysis. The HS surface and its properties were calculated with the CrystalExplorer 3.0^{75,76} software.

Magnetic Properties. The magnetic susceptibility measurements were performed with a Quantum Design MPMS-XL-5 SQUID susceptometer in the temperature range 2–300 K with an applied magnetic field of 0.1, 0.5 or 1 T on polycrystalline samples of compounds **C1-10** with masses of 22.04, 15.36, 20.22, 21.52, 20.96, 23.17, 22.48, 15.67, 18.05, 11.66, 24.97, 18.34, 26.00, 11.38, 13.63, 11.64, 11.48, 6.73, 8.98, and 4.11 mg for **C1a, C1b, C1c, C2a, C2b, C2c, C3a, C3b, C4a, C4b, C5a, C5b, C6a, C6b, C7b, C8b, C9a, C10a, C9b,** and **C10b**, respectively. The isothermal magnetization measurements were performed on the same samples at 1.8 or 2 K with magnetic fields up to 5 or 7 T with the same equipment. Susceptibility data were corrected for the sample holder previously measured using the same conditions and for the diamagnetic contributions of the salt using Pascal's constant tables.⁷⁷ PXRD measurements have been performed on the same polycrystalline samples that were measured in the SQUID and they show experimental patterns which correspond to the simulated X-Ray patterns obtained from the single crystal X-Ray structures. PXRD data are reported in Appendix 4 (Figures S2.13-S2.21).

References

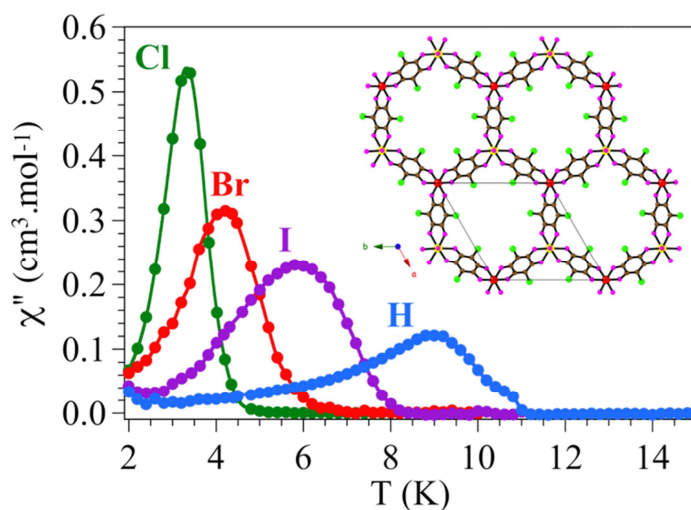
1. Mercuri, M. L.; Deplano, P.; Pilia, L.; Serpe A.; Artizzu F. *Coord. Chem. Rev.* **2010**, *254*, 1419–1433.
2. Steed, J. W.; Atwood, J. L. *Supramolecular Chemistry*, 2nd edition, **2009** John Wiley & Sons.
3. Steed, J.W.; Turner, D. R.; Wallace, K. J. *Core concepts in supramolecular chemistry and nanochemistry* **2007** John Wiley & Sons.
4. Braga, D.; Brammer, L.; Champness, N. R. *Cryst. Eng. Comm.* **2005**, *7*, 1–19;
5. Brammer, L. *Chem. Soc. Rev.* **2004**, *33*, 476–489.
6. Kitagawa, S.; Kawata, S. *Coord. Chem. Rev.* **2002**, *224*, 11–34.
7. Tao, J.; Maruyama, H.; Sato, O. *J. Am. Chem. Soc.* **2006**, *128*, 1790–1791.
8. Schweinfurth, D.; Khusniyarov, M. M.; Bublir, D.; Hohloch, S.; Su, C.-Y.; Sarkar, B. *Inorg. Chem.* **2013**, *52*, 10332–10339.
9. Heinze, K.; Huttner, G.; Zsolnai, L.; Jacobi, A.; Schober, P. *Chem. Eur. J.* **1997**, *3*, 732–743.
10. Casas, J. M.; Falvello, L. R.; Forniés, J.; Mansilla, G.; Martín, A. *Polyhedron* **1998**, *18*, 403–412.
11. Kawahara, M.; Kabir, M. K.; Yamada, K.; Adachi, K.; Kumagai, H.; Narumi, Y.; Kindo, K.; Kitagawa, S.; Kawata, S. *Inorg. Chem.* **2004**, *43*, 92–100.
12. Fujii, C.; Mitsumi, M.; Kodera, M.; Motoda, K.-I.; Ohba, M.; Matsumoto, N.; Okawa, H. *Polyhedron* **1994**, *13*, 933–938.
13. Abrahams, B. F.; Grannas, M. J.; Hudson, T. A.; Hughes, S. A.; Pranoto, N. H.; Robson, R. *Dalton Trans.* **2011**, *40*, 12242–12247.
14. Abrahams, B. F.; Hudson, T. A.; McCormick, L. J.; Robson, R. *Cryst. Growth Des.* **2011**, *11*, 2717–2720.
15. Luo, T.; Liu, Y.; Tsai, H.; Su, C.; Ueng, C.; Lu, K. *Eur. J. Inorg. Chem.* **2004**, *21*, 4253–4258.
16. Abrahams, B. F.; Coleiro, J.; Ha, K.; Hoskins, B. F.; Orchard, S. D.; Robson, R. *J. Chem. Soc. Dalton Trans.* **2002**, 1586–1594.
17. Kawata, S.; Kitagawa, S.; Kumagai, H.; Ishiyama, T.; Honda, K.; Tobita, H.; Adachi, K.; Katada, M. *Chem. Mater.* **1998**, *10*, 3902–3912.
18. Decurtins, S.; Schmalle, H. W.; Zheng, L. M.; Enslin, J. *Inorg. Chim. Acta*, **1996**, *244*, 165–170.
19. Robson, R. *J. Chem. Soc., Dalton Trans.* **2000**, 3735–3744.
20. Abrahams, B. F.; Coleiro, J.; Hoskins, B. F.; Robson, R. *Chem. Comm.* **1996**, 603–604.
21. Kabir, M. K.; Miyazaki, N.; Kawata, S.; Adachi, K.; Kumagai, H.; Inoue, K.; Kitagawa, S.; Iijima, K.; Katada, M. *Coord. Chem. Rev.* **2000**, *198*, 157–169.
22. Molčanov, K.; Jurić, M.; Kojić-Prodić, B. *Dalton Trans.* **2013**, *42*, 15756–15765.
23. Mortl, K. P.; Sutter, J.-P.; Golhen, S.; Ouahab, L.; Kahn, O. *Inorg. Chem.* **2000**, *39*, 1626–1627.
24. Imaz, I.; Mouchaham, G.; Roques, N.; Brandès, S.; Sutter, J.-P. *Inorg. Chem.* **2013**, *52*, 11237–11243.
25. K. S. Min, A. L. Rhinegold, J. S. Miller, *J. Am. Chem. Soc.* **2006**, *128*, 40–41.
26. Hunter, C. A.; Sanders, J. K. M. *J. Am. Chem. Soc.* **1990**, *112*, 5525–5534.
27. Hunter, C. A. *Angew. Chem., Int. Ed. Engl.* **1993**, *32*, 1584–1586.
28. Hunter, C. A. *Chem. Soc. Rev.* **1994**, *23*, 101–109.
29. Głowka, M. L.; Martynowski, D.; Kozłowska, K. *J. Mol. Struct.* **1999**, *474*, 81–89.

30. Janiak, C. *J. Chem. Soc., Dalton Trans.* **2000**, 3885–3896.
31. Mayer, E. A.; Castellano, R. K.; Diedrich, F. *Angew. Chem., Int. Ed.* **2003**, *42*, 1210–1250.
32. Dance, I.; Scudder, M. *Chem. Eur. J.* **1996**, *2*, 481–486.
33. Molcanov, K.; Kojic-Prodic, B.; Babic, D.; Stare, J. *CrystEngComm* **2013**, *15*, 135–143.
34. Spackman, M. A.; Jayatilaka, D. *CrystEngComm* **2009**, *11*, 19–32.
35. Cramer, C.J. *Essentials of Computational Chemistry. Theories and Models*, 2nd ed., **2004**, John Wiley & Sons, Chichester, UK.
36. Scrocco, E.; Tomasi, J. *Top. Curr. Chem.* **1973**, *42*, 95–170.
37. Ruiz, E.; Cirera, J.; Alvarez, S. *Coord. Chem. Rev.* **2005**, *249*, 2649–2660.
38. Pawlukojć, A.; Bator, G.; Sobczyk, L.; Grech, E.; Nowicka-Scheibe, J. *J. Phys. Org. Chem.* **2003**, *16*, 709.
39. Pawlukojć, A.; Natkaniec, I.; Nowicka-Scheibe, J.; Grech, E.; Sobczyk, L. *Spectrochim. Acta, Part A* **2003**, *59*, 537–542.
40. Szabó, A.; Kovács, A. *J. Mol. Struct.* **1999**, *510*, 215–225
41. O'Connor, C. J. *Prog. Inorg. Chem.* **1982**, *29*, 203.
42. Kahn, O. *Molecular Magnetism* **1993**, VCH Publishers, Cambridge, UK.
43. Morrish, A. H. *The Physical Principles of Magnetism* **2001**, IEEE Press, New York, US.
44. Fourmigué, M. *Structure and Bonding*, Springer-Verlag: Berlin, **2008**, *126*, 181–207.
45. Pang, X.; Zhao, X. R.; Wang, H.; Sun, H.L.; Jun Jin, W. *Cryst. Growth Des.* **2013**, *13*, 3739–3745
46. Butcher, T. R.; Novoa, J. J.; Ribas-Ariño, J.; Sandvik, A. W.; Turnbull, M. M.; Landee, C. P.; Wells, M. B.; Awwadi, F. F. *Chem. Commun.* **2009**, 1359–1361.
47. Schlueter, J. A.; Park, H.; Halder, G. J.; Armand, W. R.; Dunmars, C.; Chapman, K. W.; Manson, J. L.; Singleton, J.; McDonald, R.; Plonczak, A.; Kang, J.; Lee, C.; Whangbo, M. H.; Lancaster, T.; Steele, A. J.; Franke, I.; Wright, J. D.; Blundell, S. J.; Pratt, F. L.; de George, J.; Turnbull, M. M.; Landee, C. P. *Inorg. Chem.* **2012**, *51*, 2121–2129.
48. Tamaki, H.; Zhong, Z. J.; Matsumoto, N.; Kida, S.; Koikawa, M.; Achiwa, N.; Hashimoto, Y.; Okawa, H. *J. Am. Chem. Soc.* **1992**, *114*, 6974–6979.
49. Atovmyan, L. O.; Shilov, G. V.; Lyubovskaya, R. N.; Zhilyaeva, E. I.; Ovanesyan, N. S.; Pirumova, S. I.; Gusakovskaya, I. G.; Morozov, Y. G. *JETP Lett.* **1993**, *58*, 766–769.
50. Decurtins, S.; Schmalte, H. W.; Oswald, H. R.; Linden, A.; Enslin, J.; Gu. tlich, P.; Hauser, A. *Inorg. Chim. Acta* **1994**, *216*, 65–73.
51. Mathoniere, C.; Nuttall, C. J.; Carling, S. G.; Day, P. *Inorg. Chem.* **1996**, *35*, 1201–1206.
52. Kurmoo, M.; Graham, A. W.; Day, P.; Coles, S. J.; Hursthouse, M.B.; Caulfield, J. M.; Singleton, J.; Ducasse, L.; Guionneau, P. *J. Am. Chem. Soc.* **1995**, *117*, 12209–12217.
53. Coronado, E.; Day, P. *Chem. Rev.* **2004**, *104*, 5419–5448;
54. Mercuri, M. L.; Deplano, P.; Serpe, A.; Artizzu, F. *Multifunctional Materials of interest in Molecular Electronics, Chapter in Handbook of Multifunctional Molecular Materials*, Ouahab, L., ed.; Pan Stanford Publishing, **2011**.
55. SMART (control) and SAINT (integration) software for CCD systems, Bruker AXS, Madison, WI, USA, **1994**.
56. Area-Detector Absorption Correction, Siemens Industrial Automation Inc., Madison, WI, **1996**.

57. Altomare, A.; Burla, M. C.; Camalli, M.; Cascarano, G. L.; Giacovazzo, C.; Guagliardi, A.; Moliterni, A. G. G.; Polidori, G.; Spagna, R. *J. App. Cryst.* **1999**, *32*, 115–119.
58. Burla, M. C.; Caliendo, R.; Camalli, M.; Carrozzin, B.; Cascarano, G. L.; De Caro, L.; Giacovazzo, C.; Polidori, G.; Spagna, R. *J. App. Cryst.* **2005**, *38*, 381–388.
59. Sheldrick, G. M. *SHELX97. Programs for Crystal Structure Analysis (1997)* (Release 97-2). University of Göttingen, Germany.
60. Farrugia, L. J. *J. App. Cryst.* **1999**, *32*, 837–838.
61. Macrae, C. F.; Edgington, P. R.; McCabe, P.; Pidcock, E.; Shields, G. P.; Taylor, R.; Towler, M.; van de Streek, J. *J. Appl. Crystallogr.* **2006**, *39*, 453–457.
62. Becke, A. D. *Phys. Rev. A* **1988**, *38*, 3098–3100. 25
63. Becke, A. D. *J. Chem. Phys.* **1993**, *98*, 5648–5652. 26
64. Fuentealba, P.; Preuss, H.; Stoll, H.; Szentpaly, L. v. *Chem. Phys. Lett.* **1989**, *89*, 418.
65. Cao, X. Y.; Dolg, M. *J. Mol. Struct. (Theochem)*, **2002**, *81*, 139.
66. Schwerdtfeger, P.; Dolg, M.; Schwarz, W. H. E.; Bowmaker, G. A.; Boyd, P. D. W. *J. Chem. Phys.*, **1989**, *91*, 1762.
67. Hay, P. J.; Wadt, W. R. *J. Chem. Phys.* **1985**, *82*, 299–310.
68. Wadt, W. R.; Hay, P. J. *J. Chem. Phys.* **1985**, *82*, 284–298.
69. Ditchfield, R.; Hehre, W. J.; Pople, J. A. *J. Chem. Phys.* **1971**, *54*, 724–728.
70. Rassolov, V. A.; Ratner, M. A.; Pople, J. A.; Redfern, P. C.; Curtiss, L. A. *J. Comp. Chem.* **2001**, *22*, 976–984.
71. Glendening, E.D.; Reed, A.E.; Carpenter, J.E.; Weinhold, F. *NBO version 3.1*.
72. Schaftenaar, G.; Noordik, J.H. *J. Comput.-Aided Mol. Design* **2000**, *14*, 123–134.
73. Allouche, A. R. *J. Comp. Chem.* **2011**, *32*, 174–182.
74. Gaussian 03, Revision C.02, Frisch, M. J.; Trucks, G. W.; Schlegel, H. B.; Scuseria, G. E.; Robb, M. A.; Cheeseman, J. R.; Montgomery, Jr. J. A.; Vreven, T.; Kudin, K. N.; Burant, J. C.; Millam, J. M.; Iyengar, S. S.; Tomasi, J.; Barone, V.; Mennucci, B.; Cossi, M.; Scalmani, G.; Rega, N.; Petersson, G. A.; Nakatsuji, H.; Hada, M.; Ehara, M.; Toyota, K.; Fukuda, R.; Hasegawa, J.; Ishida, M.; Nakajima, T.; Honda, Y.; Kitao, O.; Nakai, H.; Klene, M.; Li, X.; Knox, J. E.; Hratchian, H. P.; Cross, J. B.; Bakken, V.; Adamo, C.; Jaramillo, J.; Gomperts, R.; Stratmann, R. E.; Yazyev, O.; Austin, A. J.; Cammi, R.; Pomelli, C.; Ochterski, J. W.; Ayala, P. Y.; Morokuma, K.; Voth, G. A.; Salvador, P.; Dannenberg, J. J.; Zakrzewski, V. G.; Dapprich, S.; Daniels, A. D.; Strain, M. C.; Farkas, O.; Malick, D. K.; Rabuck, A. D.; Raghavachari, K.; Foresman, J. B.; Ortiz, J. V.; Cui, Q.; Baboul, A. G.; Clifford, S.; Cioslowski, J.; Stefanov, B. B.; Liu, G.; Liashenko, A.; Piskorz, P.; Komaromi, I.; Martin, R. L.; Fox, D. J.; Keith, T.; Al-Laham, M. A.; Peng, C. Y.; Nanayakkara, A.; Challacombe, M.; Gill, P. M.; Johnson, W.; Chen, B. W.; Wong, M. W.; Gonzalez, C.; Pople, J. A. *Gaussian, Inc.*, Wallingford CT, **2004**.
75. McKinnon, J.J.; Jayatilaka, D.; Spackman, M.A. *Chem Commun.* **2007**, 3814–3816.
76. CrystalExplorer, Wolff, S. K.; Grimwood, D.J.; McKinnon, J.J.; Turner, M.J.; Jayatilaka, D.; Spackman, M.A. University of Western Australia, **2012**.
77. Bain, G. A.; Berry, J. F. *J. Chem. Educ.* **2008**, *85*, 532.

Chapter 3

Molecule-based Magnets



This Chapter reports on a general synthetic strategy used to obtain a novel family of molecule-based ferrimagnets, formulated as $[\text{Mn}^{\text{II}}\text{Cr}^{\text{III}}(\text{X}_2\text{An})_3]^-$ ($\text{X} = \text{Cl}, \text{Br}, \text{I}, \text{H}$), which show tunable magnetic properties. The crystal structures and the magnetic properties of the components of this family are reported herein.

3.1 Introduction

The search for new molecule-based magnets is a very active area in molecular magnetism because these materials provide unique opportunities to design, from a wise selection of molecular building blocks, molecular architectures exhibiting cooperative magnetism and even combination of magnetism with a second property of interest.¹⁻⁷

A breakthrough in this area is represented by the preparation in 1992 by Okawa *et al.*⁸ of the family of layered bimetallic oxalate-based magnets formulated as $[(n\text{-Bu})_4\text{N}][\text{M}^{\text{II}}\text{M}^{\text{III}}(\text{C}_2\text{O}_4)_3]$ ($\text{M}^{\text{III}} = \text{Cr}, \text{Fe}$; $\text{M}^{\text{II}} = \text{Mn}, \text{Fe}, \text{Co}, \text{Ni}$ and Cu) showing the well-known 2D hexagonal honeycomb structure.^{9,10} These systems show ferromagnetic order ($\text{M}^{\text{III}} = \text{Cr}$) with ordering temperatures ranging from 6 to 14 K, or ferrimagnetic order ($\text{M}^{\text{III}} = \text{Fe}$) with T_c ranging from 19 to 48 K.¹¹⁻¹⁵ In these compounds the A^+ cations play a crucial role in tailoring the molecular building blocks assembly and therefore the dimensionality of the resulting bimetallic framework. In addition, the substitution of electronically innocent cations with functional ones can increase the complexity of these systems and confer novel properties to the final material. In fact, in the last 20 years, many efforts have been devoted to incorporate more sophisticated functionalities in these materials by playing with the A^+ cations located between the bimetallic layers. With this strategy, a large series of advanced multifunctional molecular materials where the magnetic ordering of the bimetallic layer coexists or even interacts with other properties arising from the cationic layers, such as paramagnetism,¹²⁻¹⁶ non-linear optical properties,^{17,18} metal-like conductivity,^{19,20} photochromism,^{18,21,22} photoisomerism,²³ spin crossover,²⁴⁻²⁹ chirality,³⁰⁻³³ or proton conductivity^{34,35} have been obtained.

In these layered magnets the ordering temperatures are insensitive to the layer separation determined by the inserted cations, which slightly affects the magnetic properties of the resulting hybrid material, emphasizing their 2D magnetic character.^{11-16,30,36,37} The most effective way to tune the magnetic properties of such systems is to act directly on the exchange pathways within the bimetallic layers. This can be achieved either by varying M^{II} and M^{III} or by modifying the bridging ligand. So far, only the first possibility has been explored, except for a few attempts at replacing the bridging oxalate ligand with the dithioxalate one, leading to small variations of the ordering temperatures.³⁸⁻⁴¹

To overcome this drawback, larger bis-bidentate bridging ligands as the dianion of 2,5-dihydroxy-1,4-benzoquinone ($\text{H}_2\text{C}_6\text{O}_4^{2-}$) and its derivatives ($\text{X}_2\text{C}_6\text{O}_4^{2-} = \text{X}_2\text{An}^{2-}$) can be employed. The coordination modes of these ligands are similar to the oxalate ligand, and it is well-known that they are able to provide an effective pathway for magnetic exchange interactions.⁴² Moreover, they present three additional advantages (i) they are easy to modify or functionalize in order to tune the magnetic exchange coupling between coordinated metals by simply changing the X substituent ($\text{X} = \text{H}, \text{F}, \text{Cl}, \text{Br}, \text{I}, \text{NO}_2, \text{OH}, \text{CN}, \text{Me}, \text{Et}, \text{etc.}$),⁴² (ii) their functionalization does not affect their coordination mode, (iii) the different nature of the substituent can affect the intermolecular interactions in the resulting material, and then, the physical properties.

The ligand H_2An^{2-} and its derivatives, mainly with $X = \text{Cl}$, have been extensively studied, alone or in combination with other ligands, to prepare several compounds with different dimensionalities and structures, spanning from isolated monomers, dimers and oligomers to extended 1D, 2D and 3D structures.⁴² Their coordination modes and ability to act as bridging ligands to afford different coordination frameworks have been summarized by Kitagawa and Kawata.⁴² The most interesting structures obtained so far are the honeycomb layers formed with H_2An^{2-} and $\text{Cl}_2\text{An}^{2-}$.⁴³⁻⁴⁸ In these 2D compounds the structure is similar to that of the oxalate honeycomb layers, but all the systems reported to date are homometallic (*i.e.*, they contain two M^{II} or two M^{III} ions of the same type). The layers formed with two M^{II} ions contain a 2- charge per formula, $[\text{M}^{\text{II}}_2(\text{X}_2\text{An})_3]^{2-}$ ($X = \text{Cl}, \text{H}$), and, accordingly, two monocations are needed to balance the charge. The only known examples of this $[\text{M}^{\text{II}}_2\text{L}_3]^{2-}$ series are the $[\text{M}_2(\text{H}_2\text{An})_3]^{2-}$ ($\text{M} = \text{Mn}$ and Cd)⁴³ and $[\text{M}_2(\text{Cl}_2\text{An})_3]^{2-}$ ($\text{M} = \text{Cu}, \text{Co}, \text{Cd}$ and Zn) systems.⁴⁴ The layers formed with two M^{III} ions are neutral, and the reported examples include the $[\text{M}_2(\text{H}_2\text{An})_3] \cdot 24\text{H}_2\text{O}$ ($\text{M}^{\text{III}} = \text{Y}, \text{La}, \text{Ce}, \text{Gd}, \text{Yb}$ and Lu),^{45,46} $[\text{M}_2(\text{Cl}_2\text{An})_3] \cdot 12\text{H}_2\text{O}$ ($\text{M}^{\text{III}} = \text{Sc}, \text{Y}, \text{La}, \text{Pr}, \text{Nd}, \text{Gd}, \text{Tb}, \text{Yb}, \text{Lu}$)^{46,47}, and $[\text{Y}_2(\text{Br}_2\text{An})_3] \cdot 12\text{H}_2\text{O}$ systems.⁴⁷

A further interest for the anilate ligands is related to their ability to form 3D structures with the (10,3)-*a* topology, similar to the one observed with the oxalate.⁴⁹ These structures are afforded when all the ML_3 units show the same chirality, in contrast with the 2D honeycomb layer, which requires alternating $\Lambda\text{-ML}_3$ and $\Delta\text{-ML}_3$ units. This 3D structure with a (10,3)-*a* topology has been recently reported for the $[(n\text{-Bu})_4\text{N}]_2[\text{M}^{\text{II}}_2(\text{H}_2\text{An})_3]$ ($\text{M}^{\text{II}} = \text{Mn}, \text{Fe}, \text{Ni}, \text{Co}, \text{Zn}$ and Cd) and $[(n\text{-Bu})_4\text{N}]_2[\text{Mn}_2(\text{Cl}_2\text{An})_3]$ systems,⁵⁰ showing a double interpenetrating (10,3)-*a* lattice with opposite stereochemical configuration that yields to an overall achiral structure. The final proof of the versatility of the anilate-based derivatives is the formation of a 3D adamantane-like network in the compounds $[\text{Ag}_2(\text{Cl}_2\text{An})]$,⁵¹ $[\text{H}_3\text{O}][\text{Y}(\text{Cl}_2\text{An})_3] \cdot 8\text{CH}_3\text{OH}$ and $[\text{Th}(\text{Cl}_2\text{An})_2] \cdot 6\text{H}_2\text{O}$.⁴⁶

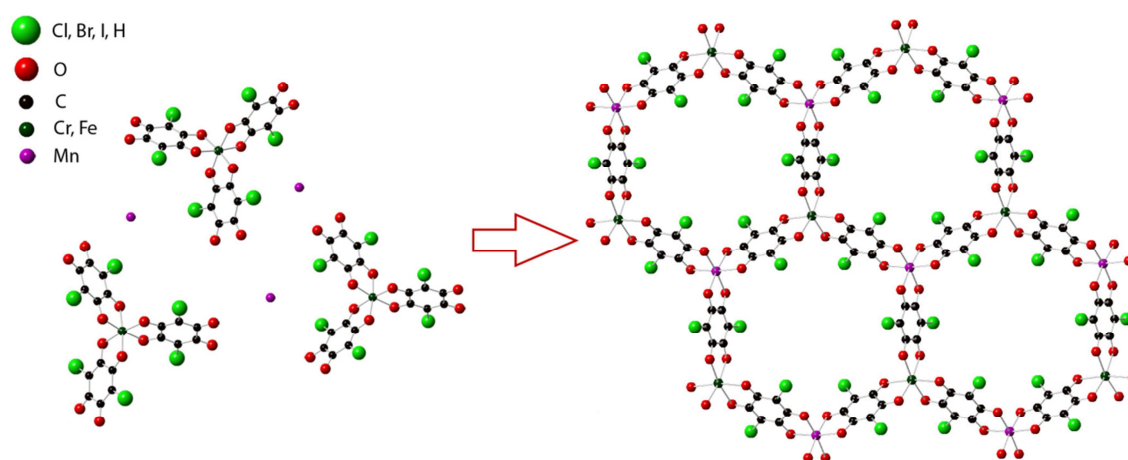
Because these ligands are able to mediate antiferromagnetic exchange interactions, it should be expected that 2D heterometallic lattices of $[\text{M}^{\text{II}}\text{M}^{\text{III}}(\text{X}_2\text{An})_3]^-$ type would afford ferrimagnetic coupling and ordering. Furthermore, if the magnetic coupling depends on the substituent groups X on the ligand, a change of X should modify the magnetic coupling and the T_c . This is probably the most interesting and appealing aspect of the anilate ligands since they can act as the oxalate ligands, but they can also be functionalized with different X groups. This should lead to a modulation of the electronic density in the benzoquinone ring, which, in turn, should result in an easy tuning of the magnetic exchange coupling and, therefore, the magnetic properties (ordering temperatures and coercive fields) in the resulting 2D or 3D magnets. It should be highlighted that among the ligands used to produce the majority of known molecule-based magnets, such as oxalate, azido, or cyano ligands, only anilates can be functionalized.

To investigate these appealing properties, a series of molecule-based magnets formulated as $[\text{A}][\text{Mn}^{\text{II}}\text{M}^{\text{III}}(\text{X}_2\text{An})_3]$ ($\text{A} = [\text{H}_3\text{O}(\text{phz})_3]^+$, $(n\text{-Bu})_4\text{N}^+$; $\text{M}^{\text{III}} = \text{Cr}, \text{Fe}$; $X = \text{Cl}, \text{Br}, \text{I}, \text{H}$), namely $[(\text{H}_3\text{O})(\text{phz})_3][\text{Mn}^{\text{II}}\text{M}^{\text{III}}(\text{X}_2\text{An})_3] \cdot \text{H}_2\text{O}$, with $\text{M}^{\text{III}}/\text{X} = \text{Cr}/\text{Cl}$ (**M1**), Cr/Br (**M2**) and Fe/Br (**M3**) and $[(n\text{-Bu}_4\text{N})][\text{Mn}^{\text{II}}\text{Cr}^{\text{III}}(\text{X}_2\text{An})_3]$, with $X = \text{Cl}$ (**M4**), Br (**M5**), I (**M6**) and H (**M7**) have been synthesized and characterized. The crystal structures and magnetic properties are herein discussed.

3.2 Results and Discussion

3.2.1 Synthetic Strategy

The anilate-based molecular magnets here reported were obtained by following the so-called “complex-as-ligand” approach. In this synthetic strategy, a molecular building block, the homoleptic $[M^{III}(X_2An)_3]^{3-}$ tris(anilato)metallate octahedral complex ($M^{III} = Cr, Fe; X = Cl, Br, I, H$), is used as a ligand towards the divalent paramagnetic metal ion Mn^{II} . Their combination results in the formation of 2D anionic complexes which precipitate in the presence of the $(n-Bu)_4N^+$ bulky organic cation or the $[H_3O(phz)_3]^+$ chiral adduct (Scheme 3.1).



Scheme 3.1, Graphic representation of the “complex-as-ligand” approach used for obtaining compounds **M1-7**.

In these compounds, the monovalent cations act not only as charge-compensating counterions but also as templating agents controlling the dimensionality of the final system. In particular, the chiral cation $[(H_3O)(phz)_3]^+$ obtained *in situ* by the interaction between phenazine molecules and hydronium cations appears to template and favor the crystallization process. In fact, most of the attempts to obtain single crystals from a mixture of the $(n-Bu)_4N^+$ salts of the $[M^{III}(X_2An)_3]^{3-}$ precursors and Mn^{II} chloride yielded poorly crystalline products, and only the crystal structure for the system $[(n-Bu)_4N][MnCr(Cl_2An)_3]$ (**M4**) was obtained by slow diffusion of the two components.

3.2.2 Crystal Structure Description

Compounds $[(H_3O)(phz)_3][MnCr(Cl_2An)_3(H_2O)]$ (**M1**), $[(H_3O)(phz)_3][MnCr(Br_2An)_3] \cdot H_2O$ (**M2**) and $[(H_3O)(phz)_3][MnFe(Br_2An)_3] \cdot H_2O$ (**M3**) are isostructural and present a layered structure with alternating cationic and anionic layers (Figure 3.1). The only differences between compounds **M1-3**, besides the change of Cl_2An^{2-} (**M1**) with Br_2An^{2-} (**M2**), or Cr^{III} (**M2**) with Fe^{III} (**M3**), are (i) the presence of an inversion center in compounds **M2** and **M3** (not present in **M1**) resulting in a statistical distribution of the M^{III} and Mn^{II} ions in the anionic layers (see Experimental Section),

(ii) the presence of a water molecule coordinated to the Mn^{II} ions in **M1** (Mn–O1w 2.38(1) Å), in contrast with compounds **M2** and **M3** where this water molecule is not directly coordinated (Mn···O1w 3.123(3) and 4.587(6) Å, in **M2** and **M3**, respectively).

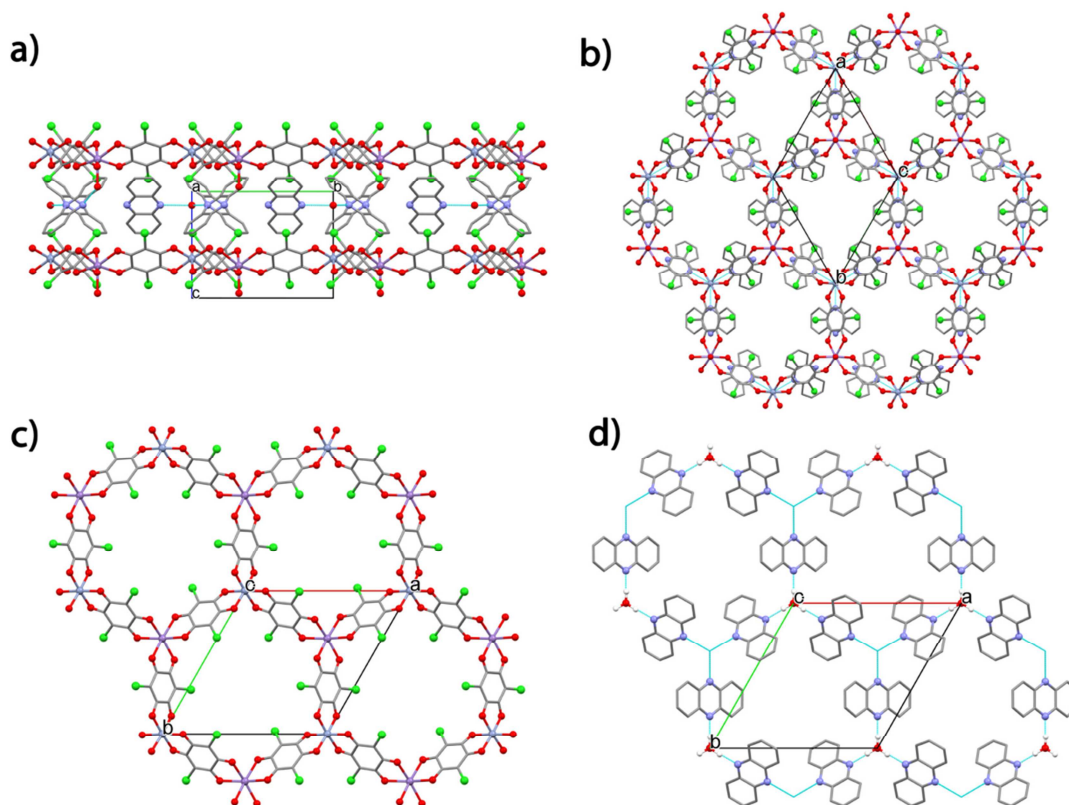


Figure 3.1. View of the crystal structure of **M1**: a) Side view of the alternating cationic and anionic layers, b) Top view of the two layers, c) Top view of the anionic layer, (d) Top view of the cationic layer showing the positions of the metal centers in the anionic layer (blue dashed hexagon).

The structure of **M1** is formed by cationic and anionic layers parallel to the *ab* plane alternating along the *c* direction (Figure 3.1). The anionic layer is formulated as $[\text{MnCr}(\text{Cl}_2\text{An})_3(\text{H}_2\text{O})]^-$ ($[\text{MnCr}(\text{Br}_2\text{An})_3]^-$ in **M2** and $[\text{MnFe}(\text{Br}_2\text{An})_3]^-$ in **M3**) and shows hexagonal honeycomb layer where the Cr^{III} and Mn^{II} ions, connected through the anilate bis-bidentate ligands, occupy alternating vertices of the hexagons (Figure 3.1). Each Mn^{II} ion is connected to three Cr^{III} ions and *vice versa* (Figure 3.2). The metal-oxygen bond distances for Cr^{III}, Mn^{II}, and Fe^{III} are in agreement with the high spin character of these systems (*vide infra*) (Table 3.1).

Table 3.1. M–O bond distances (Å) for compounds **M1-4**.

Bonds	M1	M2	M3	M4
M–O(2)	2.013(10)	2.102(13)	2.119(4)	2.140(9)
M–O(3)	1.944(14)	-	-	2.115(8)
M–O(5)	2.281(9)	-	-	2.011(7)
M–O(6)	2.185(8)	-	-	1.982(8)

The C–O bond distances of the ligand are influenced by the coordination to the metal centers. The oxygen atoms coordinated to the metal ions have C–O distances in the 1.254(6)–1.305(12) Å range, which corresponds to a C–O single bond character, and no significant difference as a function of the nature of the coordinated metal ions are observed. Accordingly, the electronic structure of the ligand can be represented by the delocalized form already reported and described in Scheme 1.4 (Chapter 1).

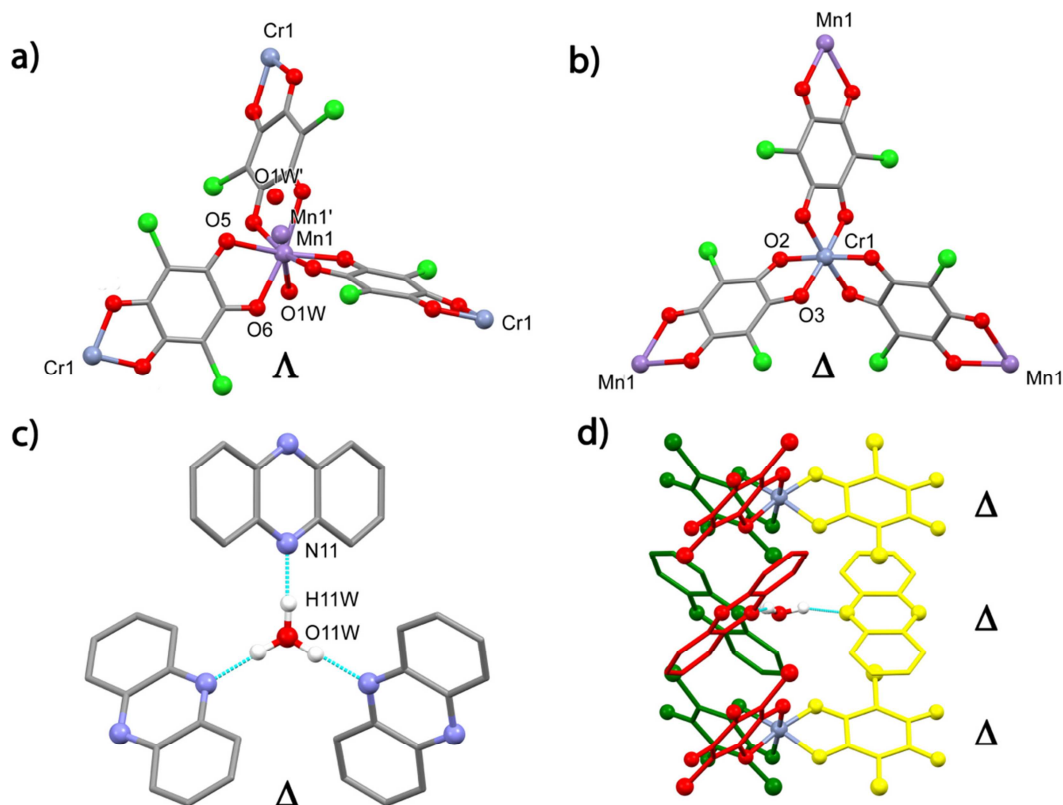


Figure 3.2. Structural building units of **M1**: a) Δ -[Mn(Cl₂An)₃(H₂O)]⁴⁻ unit connected to three Cr^{III} ions showing the two disordered positions of the H₂O molecule and the Mn^{II} ion, b) Δ -[Cr(Cl₂An)₃]³⁻ unit connected to three Mn^{II} ions, c) Δ -[(H₃O)(phz)₃]⁺ cation showing the O–H...N bonds as light blue dotted lines, d) Side view of two anionic and one cationic layers showing the Δ -[Cr(Cl₂An)₃]³⁻ units located above and below a Δ -[(H₃O)(phz)₃]⁺ adduct. Stacked phenazine and anilate rings are displayed with the same colour.

Although this structure is similar to that of the homometallic [M₂(X₂An)₃]ⁿ⁻ ($n = 0$ or 2) derivatives reported in the literature,⁴³⁻⁴⁸ there are three significant differences (i) compounds **M1-3** are heterometallic and monoanionic (*i.e.*, contain two different metal ions with two different oxidation states, M^{III} and Mn^{II}, resulting in a charge of 1- per formula unit, (ii) in **M1** the metal ions are perfectly ordered (in contrast to **M2**, **M3**, and almost all of the heterometallic oxalate-based magnets) because of the absence of an inversion center in the center of the hexagon as a result of the chirality of this structure, (iii) in **M1** the Mn^{II} ions (but not the Cr^{III} ones) present an additional coordinated water molecule perpendicular to the layers, either above or below, (Figure 3.2a) generating a displacement of the Mn^{II} ions of 0.59 Å with respect to the average plane defined by the Cr^{III} ions. Since the water molecules are

statistically distributed over two possible positions, the Mn^{II} ions are also disordered on two close positions with a Mn–Mn distance of 1.18 Å. The presence of a water molecule coordinated to the Mn^{II} ion in **M1** implies that the H₃O⁺ cation is located closer to the Cr^{III} than to the Mn^{II} ion. The extra difference in the repulsion energies between the Cr^{III}...H₃O⁺ and the Mn^{II}...H₃O⁺ dispositions has to be overcome by the extra Mn–OH₂ bond. This idea agrees with the assumption that all the Mn^{II} ions are coordinated to a water molecule and, therefore, that the disorder affects both the Mn^{II} and water positions simultaneously. The opposite distribution, where the Cr^{III} ions are hypothetically heptacoordinated and the Mn^{II} ions are hexacoordinated, has to be excluded given the smaller size of Cr^{III} compared to Mn^{II} and the fact that typical Mn^{II}–O and Cr^{III}–O distances are present. In fact, any attempt to change the metal ions led to significantly worse structural refinements.

The cationic layer is formed by chiral cations Δ -[(H₃O)(phz)₃]⁺ (Figure 3.2c) resulting from the association of three phenazine molecules around a central H₃O⁺ cation through three equivalent strong O–H...N hydrogen bonds (O–H 0.97(2) Å, H...N 1.73(3) Å, O...N 2.663(4) Å, and O–N...H = 160(7)°), generating a propeller-like structure. These Δ -[(H₃O)(phz)₃]⁺ cations are always located below and above the Δ -[Cr(Cl₂An)₃]³⁻ units, because they present the same chirality, allowing a parallel orientation of the phenazine and chloranilate rings (Figure 3.2d). This disposition leads to an unexpected situation where the more highly charged cation Cr^{III} is located closer to the hydronium cation while the less charged cation Mn^{II} is located closer to the water molecule. As indicated above, this extra repulsion is overcome by the Mn–OH₂ bond energy.

Additional interest for compounds **M1–3** is related to the presence of hexagonal channels resulting from the eclipsed packing of the cationic and anionic layers (Figure 3.3) that may contain solvent molecules. The X-ray analysis shows in **M2** (and in a lesser extent in **M3**) the presence of electron density in the channels distributed in a centered planar hexagon (Figure 3.3a) located in the center of both layers (Figure 3.3b). This density can be attributed to the presence of two acetone molecules per formula unit with two different orientations related by a 2-fold axis (Figures 3.3c and 3.3d). Once assigned the electron density corresponding to the two acetone molecules, there is a small residual density that may be assigned to ½ water molecule per formula unit, in agreement with the TGA (*vide infra*). Interestingly, the presence of two acetone and two water molecules was also observed in some homometallic [M₂(Cl₂An)₃]²⁻ lattices.⁴⁴

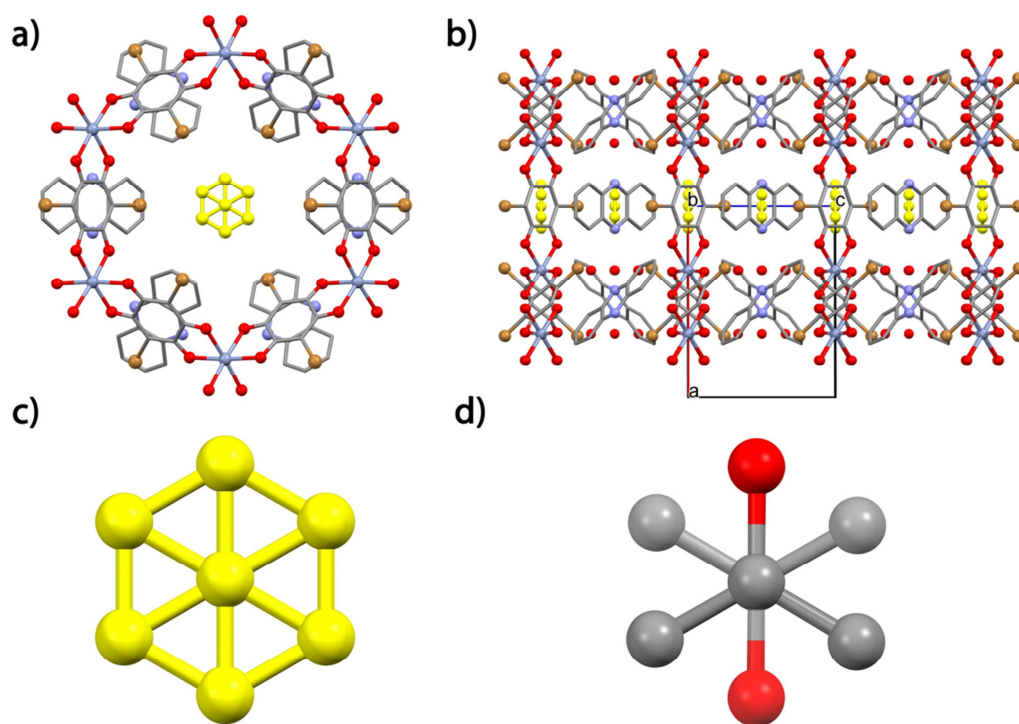


Figure 3.3. View of the structure of **M2**: a) Perspective view of one hexagonal channel running along the *c* direction with the solvent molecules in the center (in yellow); b) Side view of the same hexagonal channel showing the location of the solvent molecules in the center of the anionic and cationic layers; c) Disordered solvent molecules as observed in the center of the hexagonal channels; d) View of two of the possible orientations of the CH₃COCH₃ molecules in the channels.

The only compound with the $(n\text{-Bu})_4\text{N}^+$ as counterion whose structure has been solved, $[(n\text{-Bu})_4\text{N}][\text{MnCr}(\text{Cl}_2\text{An})_3]$ (**M4**), shows a similar layered structure where $[\text{MnCr}(\text{Cl}_2\text{An})_3]^-$ hexagonal anionic layers alternate with cationic layers containing disordered $(n\text{-Bu})_4\text{N}^+$ cations. The main differences between **M4** and **M1-3** is the absence of the water molecule coordinated/located close to the Mn^{II} ion, and the absence of hexagonal channels, since in **M4** the honeycomb layers are not eclipsed but alternated (Figure 3.4).

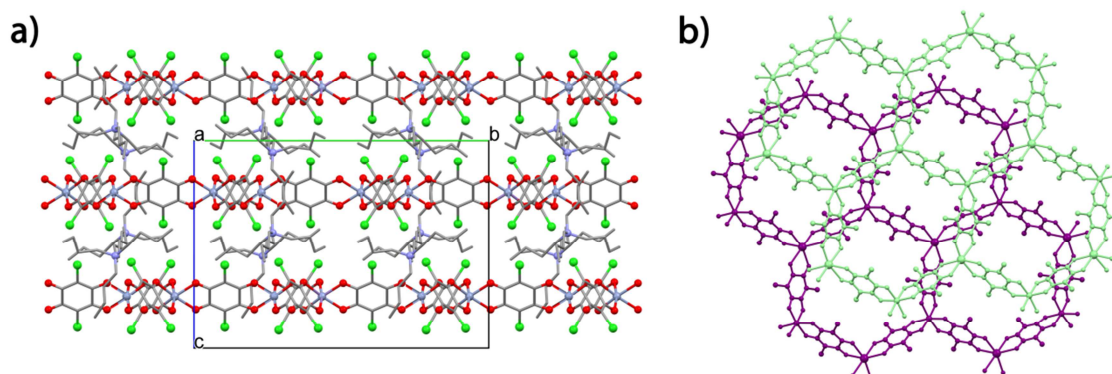


Figure 3.4. View of the crystal structure of **M4**: a) Side view of the alternating anionic and cationic layers; b) Projection, perpendicular to the layers, of two consecutive anionic layers showing their alternate packing.

3.2.3 Thermogravimetric Analysis

The TGA of a polycrystalline sample of **M1** shows a total weight loss of ca. 8.7% in the temperature range 25–130 °C with a plateau above ca. 125 °C (Figure S3.1). This weight loss corresponds to the release of two acetone molecules and half water molecule per formula unit (calcd value 8.7%), in good agreement with the X-ray data of **M2**. It must be noted that although the single crystal used for the structure determination of **M1** did not show any electron density in the hexagonal channels, the corresponding polycrystalline sample contains solvent molecules, as demonstrated by the TGA. This difference can be due to the different synthetic methods used to prepare the single crystals (slow diffusion in a layering tube) and the polycrystalline sample (immediate precipitation in a one-pot reaction).

3.2.4 Vibrational Spectroscopy

The FT-IR spectrum of **C1a**, the mononuclear precursor of **M1** and **M4**, shows two bands, centered at ca. 1000 cm^{-1} and 841 cm^{-1} which are assigned to the $\nu(\text{C}-\text{C})$, $\nu(\text{C}-\text{O})$, $\delta(\text{C}-\text{Cl})$ and $\delta(\text{C}=\text{O})$, $\delta(\text{C}-\text{O})$, $\nu(\text{C}-\text{Cl})$ combination bands (see Chapter 2, Section 2.25).⁵² These bands are typical of the chloranilate ligand and are affected by the coordination with metal ions since they involve the vibrational modes of the chelating group. In fact, the FT-IR spectrum of the heterometallic compound **M4** shows a clear shift to higher wavenumbers of these two bands with respect to **C1a**, which are now at ca. 1007 and 857 cm^{-1} upon coordination of the $\text{Cl}_2\text{An}^{2-}$ ligand to the Mn^{II} centers (Figure 3.5).

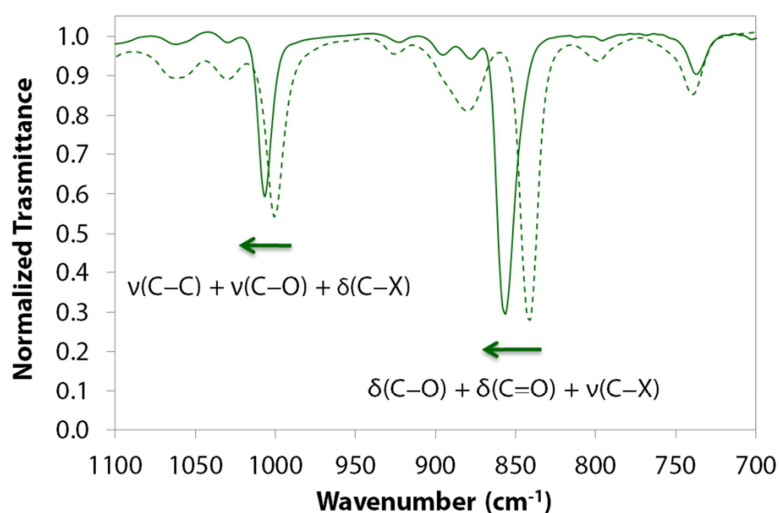


Figure 3.5. FT-IR spectra in the 1100–700 cm^{-1} range for **C1a** (green dashed line) and **M4** (green continuous line).

This suggests a stronger structural rigidity of the anilate ring when acting as a bridging ligand, as already observed in the related heterometallic oxalate-based layered compounds.⁸ The IR spectra of compounds **M5** and **M6** show a similar downshift upon coordination of the corresponding anilate derivative to the Mn^{II} centers. Furthermore, as expected, the IR spectra of compounds **M4–6** show a downshift of these bands as the mass of X increases (Figure 3.6).

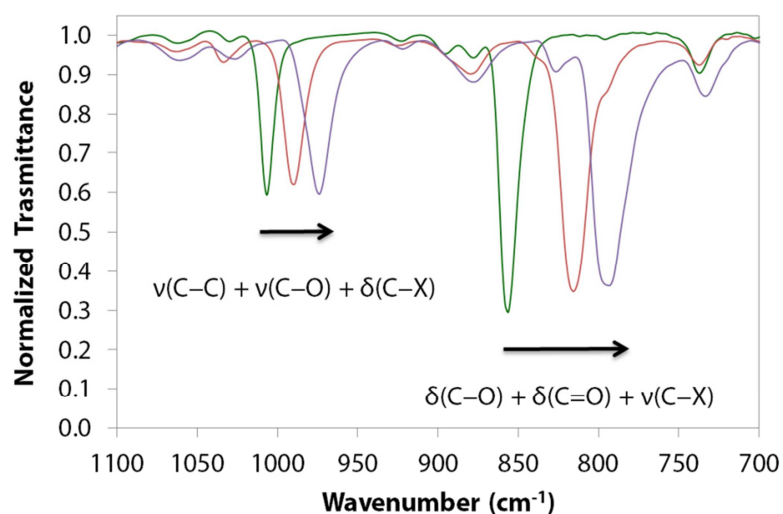


Figure 3.6, FT-IR spectra in the 1100–700 cm^{-1} range for **M4** (green line), **M5** (red line), and **M6** (violet line).

These observations suggest that the X_2An^{2-} ligands ($\text{X} = \text{Cl}, \text{Br}, \text{I}$) exhibit the same coordination mode and support the idea that compounds **M4–6** are isostructural, in agreement with magnetic measurements (*vide infra*).

3.2.5 Magnetic Properties

The thermal variation of the molar magnetic susceptibility expressed as $\chi_m T$ for compounds **M1** and **M2** show the presence of antiferromagnetic $\text{Mn}^{\text{II}}\text{–Cr}^{\text{III}}$ interactions mediated by the anilate ligands (Figure 3.7a). Since the ground spin states of Cr^{III} and Mn^{II} are different ($S = 3/2$ and $5/2$, respectively) this antiferromagnetic interaction leads to a ferrimagnetic coupling that results in an overall long-range ferrimagnetic ordering at low temperatures.

At r.t., $\chi_m T$ shows values of ca. 6.20 and 6.24 $\text{cm}^3 \text{K mol}^{-1}$, for **M1** and **M2**, respectively, close to the expected value (6.25 $\text{cm}^3 \text{K mol}^{-1}$) for a non-interacting couple of Mn^{II} and Cr^{III} ions having $g = 2$. When the temperature is lowered, $\chi_m T$ shows a continuous decrease (since the magnetic coupling is antiferromagnetic and the total magnetic moment is reduced as the temperature decreases), reaching a minimum at ca. 10 K (since the two ground spin states are not fully cancelled), followed by a sharp increase at lower temperatures and a maximum at ca. 5 K, indicating the presence of a long-range ferrimagnetic ordering (Figure 3.7a).

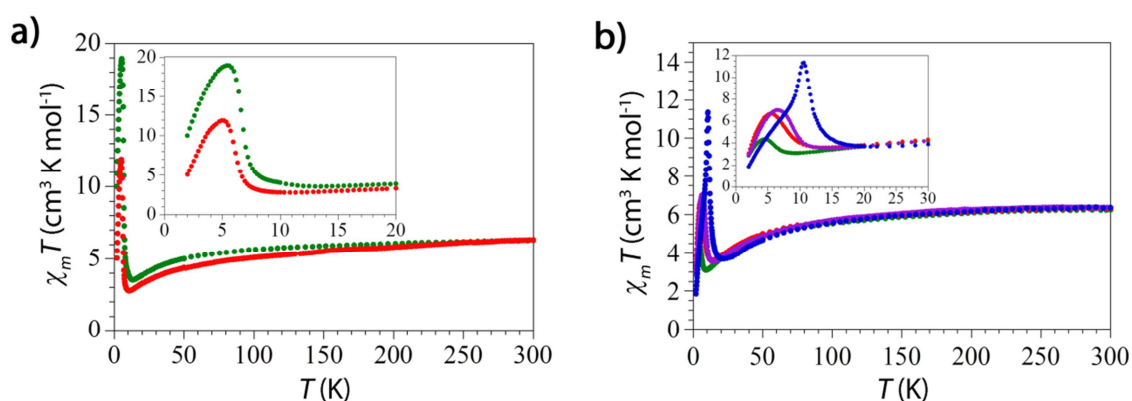


Figure 3.7. Thermal variation of $\chi_m T$ for a) **M1-2** and b) **M4-7**. Insets show the low temperature regions.

This behaviour is very similar to that of the $(n\text{-Bu})_4\text{N}^+$ salts containing the $[\text{MnCr}(\text{X}_2\text{An})_3]^-$ heterometallic layers ($\text{X} = \text{Cl}$ (**M4**), Br (**M5**), I (**M6**) and H (**M7**), Figure 3.7b). In fact, compounds **M4-7** show $\chi_m T$ values at r.t. of ca. $6.2 \text{ cm}^3 \text{ K mol}^{-1}$ that decrease when the temperature is lowered to reach minima at ca. 9.3, 13.5, 14.3 and 21.5 K, followed by a sudden increase with maximum slopes at ca. 5.7, 7.0, 8.6 and 11.2 K and maxima at ca. 4.5, 5.5, 6.5 and 10.5 K for $\text{X} = \text{Cl}$, Br , I and H , respectively (inset in Figure 3.7b). This behaviour confirms the presence of $\text{Mn}^{\text{II}}\text{-Cr}^{\text{III}}$ ferrimagnetic interactions associated to long-range ferrimagnetic orderings at ca. 5.7, 7.0, 8.6, and 11.2 K for **M4-7**, respectively. The shift of the T_c as the X group varies from Cl to Br, I and H, suggests that T_c increases as the electronegativity of X decreases (*vide infra*).

To confirm the long-range order and obtain a more accurate values of T_c , susceptibility measurements with an oscillating magnetic field at different frequencies in the 1–1000 Hz range (AC susceptibility) were performed. These measurements show frequency-independent peaks for all compounds in both in-phase (χ_m') and out-of-phase (χ_m'') susceptibilities, confirming the presence of the long-range ordering (Figure 3.8).

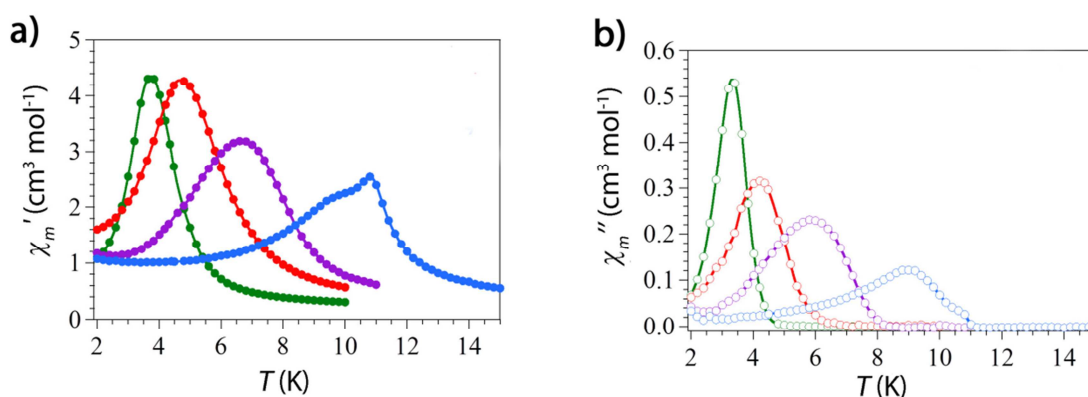


Figure 3.8. Thermal variation of a) the in-phase (χ_m') and b) the out-of-phase (χ_m'') AC susceptibility at 1 Hz for **M4** (green line), **M5** (red line), **M6** (violet line) and **M7** (blue line).

Furthermore, compounds **M1** and **M4**, and **M2** and **M5**, present similar AC susceptibility behaviour, confirming that both compounds contain the same magnetic $[\text{MnCr}(\text{Cl}_2\text{An})_3]^-$ (**M1** and **M4**) or $[\text{MnCr}(\text{Br}_2\text{An})_3]^-$ (**M2** and **M5**) heterometallic layers (Figure 3.9).

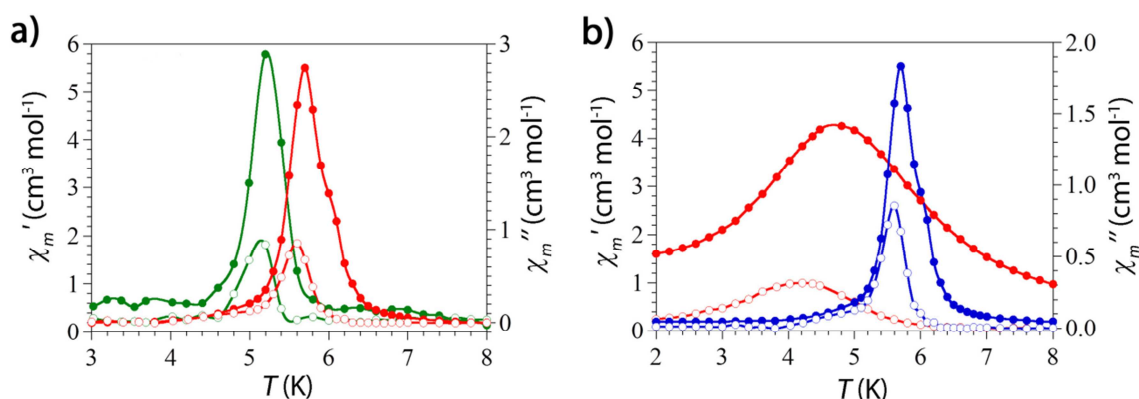


Figure 3.9, a) Thermal variation of the in-phase (χ_m' filled circles, left scale) and out of phase (χ_m'' , empty circles, right scale) AC susceptibility at 1 Hz of **M1** (green line) and **M2** (red line), b) Comparison of the in-phase (χ_m' , filled circles, left scale) and out-of-phase (χ_m'' , empty circles, right scale) AC susceptibilities at 1 Hz for **M2** (red line) and **M5** (blue line).

The peaks observed in the more crystalline samples **M1** and **M2** are narrower than those observed for the $(n\text{-Bu})_4\text{N}^+$ salts **M4** and **M5**, suggesting the presence of a larger structural and occupational disorder and a larger number of vacancies in the metal ion positions in the less crystalline samples.

Although all the compounds show similar AC susceptibility behaviors, the positions of the peaks change with X , as also observed in the DC susceptibility measurements. Thus, for compounds **M4-7** the peaks in the in-phase susceptibility appear at ca. 3.7, 4.7, 6.6 and 10.8 K (Figure 3.8a) and in the out-of-phase susceptibility they appear at ca. 3.3, 4.2, 5.9 and 9.1 K (Figure 3.8b), respectively. The T_c , determined as the temperature at which χ_m'' becomes non-zero, is ca. 5.5, 6.3, 8.2 and 11.0 K for **M4-7**, respectively.

The ferrimagnetic nature of the coupling in all the $\text{Mn}^{\text{II}}\text{-Cr}^{\text{III}}$ compounds is further confirmed by the isothermal magnetization measurements at 2 K that show a smooth increase of the magnetization as the field increases, and no saturation even at high fields (Figure 3.10). These measurements also provide an additional proof of the magnetic ordering presented by these layered materials since all compounds present hysteresis below the ordering temperatures with coercive fields of ca. 11.8, 27.0, 4.5 and 92.0 mT for **M4-7**, respectively (Figure 3.10).

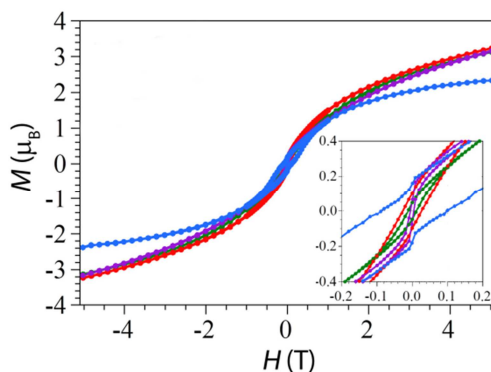


Figure 3.10, Hysteresis cycles at 2 K for the **M4** (green line), **M5** (red line), **M6** (violet line), and **M7** (blue line). The inset shows the low-field region of the hysteresis cycles.

The hysteresis measurements performed at 2 K on **M1** and **M2** show coercive fields of ca. 19.4 and 34.0 mT, respectively, (Figure 3.11) slightly higher than those of the corresponding polycrystalline $(n\text{-Bu})_4\text{N}^+$ salts (11.8 and 27.0 mT for **M4** and **M5**, respectively). A similar effect was observed in the oxalate-based analogous compounds and was attributed to the different packing of the anionic layers (eclipsed vs alternated).¹⁴

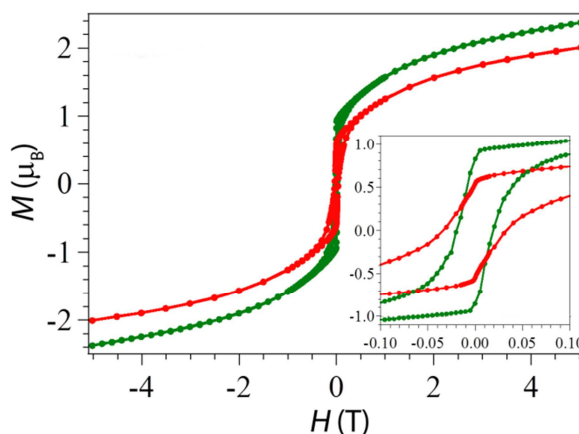


Figure 3.11, Hysteresis cycles at 2 K for **M1** and **M2**. The inset shows the low field region.

Magnetic susceptibility measurement for **M3**, the only Fe^{III} derivative whose structure has been solved, show a $\chi_m T$ value at r.t. of ca. $8.8 \text{ cm}^3 \text{ K mol}^{-1}$, close to the expected value ($8.75 \text{ cm}^3 \text{ K mol}^{-1}$) for a couple of non-interacting Fe^{III} and Mn^{II} ions with $g = 2$, and antiferromagnetic coupling between the $\text{Mn}^{\text{II}}\text{--Fe}^{\text{III}}$ ions, as evidenced by the continuous decrease of $\chi_m T$ as the temperature is lowered to 2 K (Figure 3.12a).

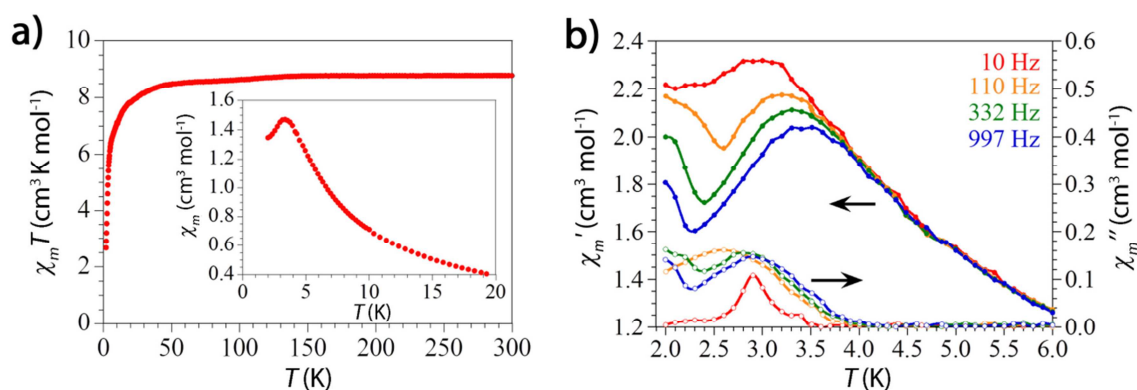


Figure 3.12, a) Thermal variation of $\chi_m T$ for **M3**. Insets show the low temperature region for χ_m , b) Thermal variation of the in phase (χ_m' , left scale, filled symbols) and out-of phase (χ_m'' , right scale, empty symbols) AC susceptibility at different frequencies for **M3**.

A close inspection at the low-temperature data of the χ_m vs T plot (inset in Figure 3.12a) shows a sharp maximum at ca. 4 K, suggesting the presence of a long-range antiferromagnetic ordering. AC susceptibility measurements performed on **M3** show a weak peak in the in-phase (χ_m') and out-of-phase (χ_m'') susceptibilities at ca. 3.5 K, suggesting the presence of a long-range antiferromagnetic ordering associated to spin canting (Figure 3.12b). This situation, already observed in the related oxalate-based $\text{Mn}^{\text{II}}\text{--Fe}^{\text{III}}$ derivatives,^{11, 53} is due to the presence

of a canting angle between the spin of both ions that prevents a perfect antiparallel alignment of the corresponding spins. This canting leads to an incomplete cancellation of the magnetic moments, resulting in a weak ferromagnetic ordering of the non-cancelled components.

As already stated, a very interesting result observed in the Cr-Mn series is the modulation of the T_c as X changes. The order observed in T_c (**M4** < **M5** < **M6** < **M7**, i.e., Cl < Br < I < H) suggests that the electronegativity of X may play a key role in determining T_c . Actually, a plot of T_c vs the electronegativity of X shows clearly a linear correlation (Figure 3.13) that can be easily explained with the electron withdrawing effect of X; as the electronegativity of X increases, the electron density in the anilate ring decreases, resulting in a weaker coupling and, therefore, in a lower T_c . Indeed, the fit of the molar susceptibility of compounds **M4-7** with the Curie-Weiss law ($\chi_m = C/(T-\theta)$, Figure S3.2) shows a linear increase in the absolute value of the Weiss temperature (θ , corresponding to the magnitude to the magnetic coupling) as the electronegativity of X decreases. Thus, the strength of the ferrimagnetic coupling increases as the electronegativity of X decreases, with $\theta = -16.7(2)$, $-17.4(1)$, $-19.7(2)$ and $-23.5(2)$ K for **M4-7**, respectively (Figure 3.13). This demonstrates that in these series, it is possible to tune the T_c by simply changing the X group in the anilate ligand.

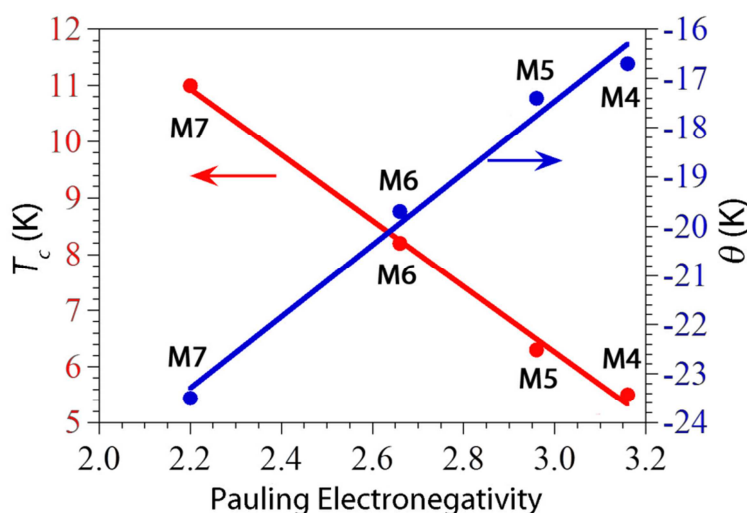


Figure 3.13. Linear dependence of the ordering temperature (T_c , left scale, red) and the Weiss constant (θ , right scale, blue) as a function of the Pauling electronegativity of the X substituent in **M4**, **M5**, **M6**, and **M7**. Solid lines are the corresponding linear fits.

3.3 Conclusions

A synthetic strategy based on the “complex-as-ligand” approach has been fruitfully employed for rationally designing a family of molecule-based magnets whose magnetic properties can be easily modulated. In particular, the predesigned mononuclear building blocks described in Chapter 2 are used as ligands towards the Mn^{II} metal ion to achieve heterometallic 2D compounds (**M1-7**) exhibiting ferrimagnetic ordering. The crystal structure topology and the magnetic properties of these compounds were predicted on the basis of the coordination chemistry and the electronic features of the employed molecular building blocks. In particular,

the key role played by the substituent on the ligand in modulating the T_c value has been demonstrated. In fact, the T_c varies linearly with the electronegativity of the X group, increasing from ca. 5.5, 6.3, 8.2 to 11.0 K for compounds **M4-7**, respectively. The possibility of tailoring the magnetic properties by changing also the M^{III} and M^{II} ions is shown by compound **M3**. Moreover, an unexpected interesting feature exhibited by these compounds is the unusual ordered arrangement of the metal ions and the eclipsed disposition of the layers induced by the presence of the $[(H_3O)(phz)_3]^+$ cation in **M1-3**. This disposition generates hexagonal channels that can be filled with different guest molecules. In fact, compounds **M1-3** present a void volume of ca. 291 \AA^3 (ca. 20% of the unit cell volume) where solvent molecules can be reversibly absorbed, opening the way to the synthesis of new porous magnets which can work as metal-organic frameworks for gas uptake. As perspective, these layered compounds represent suitable building blocks for the preparation of multifunctional molecular materials where functional cations bearing additional properties can be introduced between the layers.

3.4 Experimental

3.4.1 General Remarks

Phz, H_2Cl_2An , H_2H_2An and the metal chloride salts are commercially available and were used as received. H_2Br_2An and H_2I_2An were synthesized according to the literature methods.^{54,55}

3.4.2 Syntheses and Analytical Data

$[(H_3O)(phz)_3][MnCr(Cl_2An)_3(H_2O)]$ (M1). Compound **M1** was obtained as single crystals by carefully layering at r.t. a solution of **C1a** (14 mg, 0.01 mmol) in acetone (2 mL) on top of a solution of phz (54 mg, 0.3 mmol) in THF (2 mL) and a solution of $MnCl_2 \cdot 4H_2O$ (28 mg, 0.14 mmol) in H_2O (2.5 mL). The solution was allowed to stand for about three months to obtain dark-purple/brown hexagonal prismatic crystals together with a purple powder. Crystals suitable for X-ray diffraction were filtered and air dried. Elemental anal. Calcd for $C_{54}H_{29}N_6O_{14}Cl_6CrMn$: C, 49.68; H, 2.24; N, 6.44; Found: C, 49.31; H, 2.12; N, 6.30.

$[(H_3O)(phz)_3][MnCr(Br_2An)_3] \cdot H_2O \cdot 2CH_3COCH_3$ (M2). This compound was prepared as reported for **M1** by using **C3a** (16.7 mg, 0.01 mmol) and phz (108 mg, 0.6 mmol). Crystals suitable for X-ray diffraction were obtained after ca. 6 weeks. Elemental anal. Calcd for $C_{60}H_{41}N_6O_{16}Br_6CrMn$: C, 42.68; H, 2.45; N, 4.98; Found: C, 42.41; H, 2.40; N, 5.03.

$[(H_3O)(phz)_3][MnFe(Br_2An)_3] \cdot H_2O$ (M3). This compound was prepared as reported for **M1** by using **C4a** (16.7, 0.01 mmol) and phz (108 mg, 0.6 mmol). Crystals suitable for X-ray diffraction were obtained after ca. 6 weeks. Elemental anal. Calcd for $C_{54}H_{29}N_6O_{14}Br_6FeMn$: C, 41.15; H, 1.86; N, 5.33; Found: C, 40.91; H, 1.80; N, 5.40.

$[(n-Bu)_4N][MnCr(Cl_2An)_3]$ (M4). This compound was prepared by adding drop-wise a solution of $MnCl_2 \cdot 4H_2O$ (22 mg, 0.11 mmol) in MeOH (5 mL) to a solution of **C1a** (150 mg, 0.11 mmol) in CH_2Cl_2 (25 mL). Compound **M4** precipitates immediately as a microcrystalline violet solid. The product was filtered, washed with CH_2Cl_2 and dried in oven at 60 °C (yield: 80%). Single crystals of this compound were

prepared by carefully layering a solution of **C1a** (42 mg, 0.03 mmol) in acetonitrile (3 mL) on top of a solution of $\text{MnCl}_2 \cdot 4\text{H}_2\text{O}$ (6 mg, 0.03 mmol) in 3 mL of a 9:1 dichloromethane/methanol mixture. The solution was allowed to stand for about three weeks to obtain dark-purple prismatic single crystals. Elemental anal. Calcd for $\text{C}_{34}\text{H}_{36}\text{Cl}_6\text{MnCrNO}_{12}$: C, 42.09; H, 3.74; N, 1.44; Found: C, 41.23; H, 4.43; N, 1.44. FT-IR ($\nu_{\text{max}}/\text{cm}^{-1}$, KBr pellet): 2962(m), 2936(w), 2874(m), 1616(m), 1516(vs), 1360(s), 1310(w), 1006(s), 882(w), 856(s), 736(m), 624(m), 578(m), 511(m), 454(m).

[(*n*-Bu)₄N][MnCr(Br₂An)₃] (M5). This compound was synthesized according to the procedure described above for **M4**, using 16 mg (0.08 mmol) of $\text{MnCl}_2 \cdot 4\text{H}_2\text{O}$ and 133 mg (0.08 mmol) of **C3a** (yield: 60%). Elemental anal. Calcd for $\text{C}_{34}\text{H}_{36}\text{Br}_6\text{MnCrNO}_{12}$: C, 33.01; H, 2.93; N, 1.13; Found: C, 32.23; H, 2.78; N, 1.06. FT-IR ($\nu_{\text{max}}/\text{cm}^{-1}$, KBr pellet): 2962(m), 2936(w), 2874(m), 1621(m), 1521(vs), 1487(vs), 1347(s), 990(w), 816(m), 610(m), 563(m), 507(m), 458(w), 407(w).

[(*n*-Bu)₄N][MnCr(I₂An)₃] (M6). This compound was synthesized according to the procedure described above for **M4**, using 16 mg (0.08 mmol) of $\text{MnCl}_2 \cdot 6\text{H}_2\text{O}$ and 156 mg (0.08 mmol) of **C5a**. (yield: 60%). Elemental anal. Calcd for $\text{C}_{34}\text{H}_{36}\text{I}_6\text{MnCrNO}_{12}$: C, 26.88; H, 2.39; N, 0.92; Found: C, 26.12; H, 2.15; N, 0.75. FT-IR ($\nu_{\text{max}}/\text{cm}^{-1}$, KBr pellet): 2959(m), 2931(w), 2871(w), 1621(m), 1495(vs), 1335(s), 974(m), 794(m), 609(m), 553(m), 506(m), 458(m).

[(*n*-Bu)₄N][MnCr(X₂An)₃] (M7). An aqueous solution (5 mL) of $\text{CrCl}_3 \cdot 6\text{H}_2\text{O}$ (320 mg, 1.2 mmol) was added drop-wise to a hot aqueous solution (50 mL) of $\text{H}_2\text{H}_2\text{An}$ (500 mg, 3.6 mmol), NaOH (290 mg, 7.2 mmol) and (*n*-Bu)₄NBr (1160 mg, 3.6 mmol). After ca. 30 min at 60 °C a red-brown solid, partially soluble in water, precipitates. The mixture was allowed to cool down until r.t., extracted with CH_2Cl_2 and dried under Na_2SO_4 . Na_2SO_4 was removed by filtration, and a solution of $\text{MnCl}_2 \cdot 6\text{H}_2\text{O}$ (22 mg, 0.12 mmol) in MeOH (5 mL) was added drop-wise to the CH_2Cl_2 solution. Compound **M7** precipitates immediately as a microcrystalline violet solid. The product was filtered and washed with CH_2Cl_2 and dried in oven at 60 °C (yield: 75%). Elemental anal. Calcd for $\text{C}_{34}\text{H}_{42}\text{MnCrNO}_{12}$: C, 53.48; H, 5.54; N, 1.83; Found: C, 52.87; H, 5.32; N, 1.78. FT-IR ($\nu_{\text{max}}/\text{cm}^{-1}$, KBr pellet): 2963(m), 2931(w), 2874(w), 1589(w), 1580(w), 1510(vs), 1424(m), 1396(s), 1365(s), 1251(s), 833(m), 823(m), 766(w), 720(w), 680(w), 587(m), 557(w), 543(w), 492(m), 442(w).

3.4.3 Equipment and Measurements Details

Elemental Analyses. C, H, N, and S measurements were performed with a Thermo Electron Analyser CHNS Flash 2000 or with a Carlo Erba mod. EA1108 CHNS analyser.

FT-IR and UV-Vis Spectroscopy. FT-IR spectra were performed on KBr pellets and collected with a Bruker Equinox 55 spectrophotometer. Electronic spectra (1200–200 nm) were recorded on a Varian Cary 5 spectrophotometer.

Thermogravimetric analysis. TGA was done on a polycrystalline sample ($m = 6.24$ mg) of compound **M1** crystallized from an acetone/water/THF mixture using a Mettler-Toledo TGA/SDTA 851e analyzer with a sensibility of 10^{-7} g.

Single Crystal X-Ray Crystallography. X-ray data were collected at 130 K (**M1**) or 120 K (**M2-4**) on a Supernova diffractometer equipped with a graphite-monochromated Enhance (Mo) X-ray Source ($\lambda = 0.71073$ Å). The program CrysAlisPro, Oxford Diffraction Ltd., was used for unit cell determinations and data reduction. Empirical absorption correction was performed using spherical harmonics, implemented in the SCALE3 ABSPACK scaling algorithm. **M1** crystallizes in the trigonal chiral $P3$ space group, whereas **M2** and **M3** crystallize in the centrosymmetric $P-31m$ space group and **M4** in the

centrosymmetric $C2/c$ space group. Crystal structures of **M1**, **M2** and **M3** have been solved in both, $P3$ and $P-31m$ space groups, but no suitable models have been found except as reported here. In addition, different datasets on different single crystals have been collected for each compound and the results are consistent. Crystal structures were solved and refined against all F^2 values using the SHELXTL suite of programs.⁵⁶ Non-hydrogen atoms were refined anisotropically (when no disorder was present) and hydrogen atoms were assigned fixed isotropic displacement parameters. Hydrogen atoms of the phenazine ligand were placed in calculated positions that were refined using idealized geometries (riding model) and hydrogen atoms associated with oxygen atoms were located from the difference map and the O–H distance fixed at 0.86 Å. In **M1**, the chloranilate ligand, the Mn^{II} center and the coordinated water molecule are disordered over two sites and have been modelled with a 49.8(8):50.2(2) ratio. In **M2** and **M3** the increase of symmetry from $P3$ to $P-31m$ don not allow a differentiation between the Mn^{III} and the Mn^{II} centers and have been refined in the same position with a 50:50 ratio. In **M2** there is a disorder between H₂O and the H₃O⁺ molecules, which have been refined with a common thermal parameter, whereas in **M3** the H₂O and the H₃O⁺ lie in the same position and, thus, cannot be differentiated. The presence of solvent molecules in the structure voids has been analyzed with PLATON/SQUEEZE⁵⁷ when a suitable model has not been found (**M1** and **M3**). In **M1**, no electron density is found in the voids, while in **M3** 12 electrons per void are found, possibly due to the presence of a small amount of disordered acetone molecules. In **M2**, the voids are filled with two acetone molecules, which have been modelled with a disorder over six orientations each, with the carbon atoms of the C=O groups lying at a C3 axis. One thermal parameter has been used for each acetone molecule, and their hydrogen atoms were not modelled. A summary of the data collection and structure refinements is provided in Table 3.2. In compound **M4** the small size of the crystals gave rise to very weak scattering and to a low number of reflections, precluding an anisotropic refinement of all the atoms, which was only applied to the heavy ones. Thus, carbon, nitrogen and oxygen atoms could only be modelled isotropically. This caused high R1 and wR2 values. The tetrabutylammonium cation is disordered over two positions and required restraints and exclusion of the hydrogen atoms.. Nevertheless, although the disorder in the butyl chains of the cations precludes a very precise resolution of the structure, the presence of a layered structure where the anionic layer is identical to that of **M1** is clearly established.

Table 3.2. Summary of X-ray crystallographic data for compounds **M1-4**.

	M1	M2	M3	M4
Empirical formula	C ₅₄ H ₂₉ Cl ₆ MnCrN ₆ O ₁₄	C ₆₀ H ₄₁ Br ₆ MnCrN ₆ O ₁₆	C ₅₄ H ₂₉ N ₆ O ₁₄ Br ₆ FeMn	C ₃₄ H ₃₆ Cl ₆ MnCrNO ₁₂
Formula weight	1305.47	1688.39	1576.08	970.28
Crystal size, mm	0.05 × 0.05 × 0.04	0.10 × 0.07 × 0.05	0.11 × 0.03 × 0.03	0.09 × 0.06 × 0.03
Crystal system	Trigonal	Trigonal	Trigonal	Monoclinic
Space group	$P3$	$P-31m$	$P-31m$	$C2/c$
<i>a</i> , Å	13.7991(2)	13.7999(5)	13.9147(2)	13.776(5)
<i>b</i> , Å	13.7991(2)	13.7999(5)	13.9147(2)	23.339(5)
<i>c</i> , Å	9.0281(3)	9.2118(6)	9.1747(4)	16.833(5)
α, deg.	90	90	90	90
β, deg.	90	90	90	101.476(5)
γ, deg.	120	120	120	90
<i>V</i> , Å ³	1489(1)	1519(1)	1538(1)	5304(3)
<i>Z</i>	1	1	1	4
<i>T</i> , K	130(2)	120(2)	120(2)	120(2)

ρ (calc), Mg/m ³	1.456	1.845	1.701	1.215
μ , mm ⁻¹	0.731	4.407	4.402	0.791
θ range, deg.	3.4–25.05	1.70–25.00	2.93–27.50	3.0–25.13
Goof	1.110	1.240	1.153	1.302
R1	0.0559	0.1352	0.0557	0.1584
wR2	0.1763	0.3272	0.2157	0.4721

$$R1 = \frac{\sum |F_o| - |F_c|}{\sum |F_o|}, wR2 = \frac{[\sum (w(F_o^2 - F_c^2)^2)] / \sum (w(F_o^2)^2)]^{1/2}}, w = 1 / [\sigma^2(F_o^2) + (aP)^2 + bP], \text{ where } P = [\max(F_o^2, 0) + 2F_c^2] / 3.$$

Powder X-Ray Crystallography. The X-ray powder diffractometer was collected for a polycrystalline sample of **M4** filled into a 0.3 mm glass capillary that was mounted and aligned on a Empyrean PANalytical powder diffractometer, using CuK α radiation ($\lambda = 1.54177 \text{ \AA}$). A total of 2 scans were collected at r.t. in the 2θ range 2–60°.

Magnetic Properties. Magnetic measurements were performed with a Quantum Design MPMS-XL-5 SQUID magnetometer in the 2 to 300 K temperature range with an applied magnetic field of 0.1 T on polycrystalline samples with masses of 0.23, 1.77, 3.18 and 0.79 mg for the single crystalline phases **M1-4**, respectively, and 14.21, 4.23, 16.00 and 15.07 mg for the powder samples **M4-7**, respectively. **M4** was measured as single crystals and as microcrystalline powder to confirm that both samples present the same magnetic properties. The hysteresis measurements were done with fields from –5 to +5 T at different temperatures below T_c after cooling the samples in zero field. AC susceptibility measurements were performed on the same samples with an oscillating magnetic field of 0.395 mT at low temperatures in the frequency range 1–1000 Hz. Susceptibility data were corrected for the sample holder and for the diamagnetic contribution of the salts using Pascal's constants.⁵⁸

References

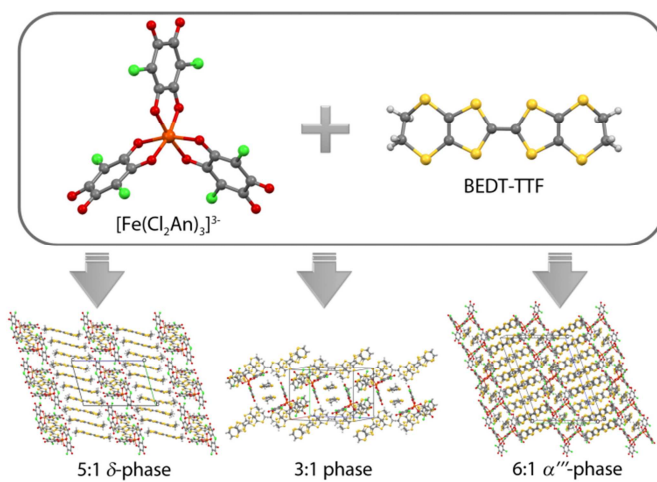
1. Miller, J. S.; Gatteschi, D. *Chem. Soc. Rev.* **2011**, *40*, 3065–3066.
2. Sorace, L.; Benelli, C.; Gatteschi, D. *Chem. Soc. Rev.* **2011**, *40*, 3092–3104.
3. Sugawara, T.; Komatsu, H.; Suzuki, K. *Chem. Soc. Rev.* **2011**, *40*, 3105–3118.
4. Coronado, E.; Minguez Espallargas, G. *Chem. Soc. Rev.* **2013**, *42*, 1525–1539.
5. Coronado, E.; Giménez-Marqués, M.; Mínguez Espallargas, G.; Brammer, L. *Nat. Commun.* **2012**, *3*, 828.
6. Mercuri, M. L.; Deplano, P.; Serpe, A.; Artizzu, F. Chapter 7 In *Handbook of Multifunctional Molecular Materials, Multifunctional Nanomaterials of interest in Electronics*, 219–280; Ouahab, L., Ed.; Pan Stanford Publishing: Singapore, **2013**.
7. Pilia, L.; Sessini, E.; Artizzu, F.; Yamashita, M.; Serpe, A.; Kubo, K.; Ito, H.; Tanaka, H.; Kuroda, S.; Yamada, J.; Deplano, P.; Gómez-García, C. J.; Mercuri, M. L. *Inorg. Chem.* **2012**, *52*, 423–430.
8. Tamaki, H.; Zhong, Z. J.; Matsumoto, N.; Kida, S.; Koikawa, M.; Achiwa, N.; Hashimoto, Y.; Okawa, H. *J. Am. Chem. Soc.* **1992**, *114*, 6974–6979.
9. Atovmyan, L. O.; Shilov, G. V.; Lyubovskaya, R. N.; Zhilyaeva, E. I.; Ovanesyan, N. S.; Pirumova, S. I.; Gusakovskaya, I. G.; Morozov, Y. G. *JETP Lett.* **1993**, *58*, 766–769.
10. Decurtins, S.; Schmalle, H. W.; Oswald, H. R.; Linden, A.; Ensling, J.; Gutlich, P.; Hauser, A. *Inorg. Chim. Acta* **1994**, *216*, 65–73.
11. Mathoniere, C.; Nuttall, C. J.; Carling, S. G.; Day, P. *Inorg. Chem.* **1996**, *35*, 1201–1206.
12. Clemente-Leon, M.; Coronado, E.; Galan-Mascaros, J. R.; Gómez-García, C. J. *Chem. Commun.* **1997**, 1727–1728.
13. Coronado, E.; Clemente-Leon, M.; Galan-Mascaros, J. R.; Gimenez-Saiz, C.; Gómez-García, C. J.; Martínez-Ferrero, E. *J. Chem. Soc., Dalton Trans.* **2000**, 3955–3961.
14. Coronado, E.; Galan-Mascaros, J. R.; Gómez-García, C. J.; Ensling, J.; Gutlich, P. *Eur. J. Inorg. Chem.* **2000**, *6*, 552–563.
15. Coronado, E.; Galan-Mascaros, J. R.; Gómez-García, C. J.; Martínez-Agudo, J. M. *Adv. Mater.* **1999**, *11*, 558–561.
16. Coronado, E.; Galan-Mascaros, J. R.; Gómez-García, C. J.; Martínez-Agudo, J. M.; Martínez-Ferrero, E.; Waerenborgh, J. C.; Almeida, M. J. *Solid State Chem.* **2001**, *159*, 391–402.
17. Benard, S.; Riviere, E.; Yu, P.; Nakatani, K.; Delouis, J. F. *Chem. Mater.* **2001**, *13*, 159–162.
18. Bénard, S.; Yu, P.; Audièrre, J. P.; Rivière, E.; Clément, R.; Guilhem, J.; Tchertanov, L.; Nakatani, K. *J. Am. Chem. Soc.* **2000**, *122*, 9444–9454.
19. Coronado, E.; Galan-Mascaros, J. R.; Gómez-García, C. J.; Laukhin, V. *Nature* **2000**, *408*, 447–449.
20. Alberola, A.; Coronado, E.; Galan-Mascaros, J. R.; Gimenez-Saiz, C.; Gómez-García, C. J. *J. Am. Chem. Soc.* **2003**, *125*, 10774–10775.
21. Aldoshin, S. M.; Nikonova, L. A.; Shilov, G. V.; Bikanina, E. A.; Artemova, N. K.; Smirnov, V. A. *J. Mol. Struct.* **2006**, *794*, 103–109.
22. Aldoshin, S. M.; Sanina, N. A.; Minkin, V. I.; Voloshin, N. A.; Ikorskii, V. N.; Oveharenko, V. I.; Smirnov, V. A.; Nagaeva, N. K. *J. Mol. Struct.* **2007**, *826*, 69–74.

23. Kida, N.; Hikita, M.; Kashima, I.; Okubo, M.; Itoi, M.; Enomoto, M.; Kato, K.; Takata, M.; Kojima, N. *J. Am. Chem. Soc.* **2008**, *131*, 212–220.
24. Clemente-Leon, M.; Coronado, E.; Giménez-Lopez, M. C.; Soriano-Portillo, A.; Waerenborgh, J. C.; Delgado, F. S.; Ruiz-Perez, C. *Inorg. Chem.* **2008**, *47*, 9111–9120.
25. Sieber, R.; Decurtins, S.; Stoeckli-Evans, H.; Wilson, C.; Yufit, D.; Howard, J. A. K.; Capelli, S. C.; Hauser, A. *Chem. –Eur. J.* **2000**, *6*, 361–368.
26. Clemente-Leon, M.; Coronado, E.; Lopez-Jorda, M.; Minguez Espallargas, G.; Soriano-Portillo, A.; Waerenborgh, J. C. *Chem. –Eur. J.* **2010**, *16*, 2207–2219.
27. Clemente-Leon, M.; Coronado, E.; Lopez-Jorda, M. *Dalton Trans.* **2010**, *39*, 4903–4910.
28. Clemente-Leon, M.; Coronado, E.; Lopez-Jorda, M.; Waerenborgh, J. C. *Inorg. Chem.* **2011**, *50*, 9122–9130.
29. Clemente-Leon, M.; Coronado, E.; Lopez-Jorda, M.; Desplanches, C.; Asthana, S.; Wang, H.; Letard, J. *Chem. Sci.* **2011**, *2*, 1121–1127.
30. Gruselle, M.; Train, C.; Boubekour, K.; Gredin, P.; Ovanesyan, N. *Coord. Chem. Rev.* **2006**, *250*, 2491–2500.
31. Brissard, M.; Gruselle, M.; Malezieux, B.; Thouvenot, R.; Guyard-Duhayon, C.; Convert, O. *Eur. J. Inorg. Chem.* **2001**, 1745–1751.
32. Train, C.; Gheorghe, R.; Krstic, V.; Chamoreau, L.; Ovanesyan, N. S.; Rikken, G. L. J. A.; Gruselle, M.; Verdaguer, M. *Nat. Mater.* **2008**, *7*, 729–734.
33. Clemente-Leon, M.; Coronado, E.; Dias, J. C.; Soriano-Portillo, A.; Willett, R. D. *Inorg. Chem.* **2008**, *47*, 6458–6463.
34. Sadakiyo, M.; Okawa, H.; Shigematsu, A.; Ohba, M.; Yamada, T.; Kitagawa, H. *J. Am. Chem. Soc.* **2012**, *134*, 5472–5475.
35. Okawa, H.; Shigematsu, A.; Sadakiyo, M.; Miyagawa, T.; Yoneda, K.; Ohba, M.; Kitagawa, H. *J. Am. Chem. Soc.* **2009**, *131*, 13516–13522.
36. Clement, R.; Decurtins, S.; Gruselle, M.; Train, C. *Monatsh. Chem.* **2003**, *134*, 117–135.
37. Fishman, R. S.; Clemente-Leon, M.; Coronado, E. *Inorg. Chem.* **2009**, *48*, 3039–3046.
38. Carling, S. G.; Bradley, J. M.; Visser, D.; Day, P. *Polyhedron* **2003**, *22*, 2317–2324.
39. Bradley, J. M.; Carling, S. G.; Visser, D.; Day, P.; Hautot, D.; Long, G. J. *Inorg. Chem.* **2003**, *42*, 986–996.
40. Kojima, N.; Aoki, W.; Itoi, M.; Ono, Y.; Seto, M.; Kobayashi, Y.; Maeda, Y. *Solid State Commun.* **2001**, *120*, 165–170.
41. Okawa, H.; Mitsumi, M.; Ohba, M.; Kodera, M.; Matsumoto, N. *Bull. Chem. Soc. Jpn.* **1994**, *67*, 2139–2144.
42. Kitagawa, S.; Kawata, S. *Coord. Chem. Rev.* **2002**, *224*, 11–34.
43. Weiss, A.; Riegler, E.; Robl, C. *Z. Naturforsch., B: J. Chem. Sci.* **1986**, *41*, 1501–1505.
44. Luo, T.; Liu, Y.; Tsai, H.; Su, C.; Ueng, C.; Lu, K. *Eur. J. Inorg. Chem.* **2004**, 4253–4258.
45. Abrahams, B. F.; Coleiro, J.; Hoskins, B. F.; Robson, R. *Chem. Commun.* **1996**, 603–604.
46. Abrahams, B. F.; Coleiro, J.; Ha, K.; Hoskins, B. F.; Orchard, S. D.; Robson, R. *J. Chem. Soc., Dalton Trans.* **2002**, 1586–1594.
47. Christian, R. *Mater. Res. Bull.* **1987**, *22*, 1483–1491.

48. Shilov, G. V.; Nikitina, Z. K.; Ovanesyan, N. S.; Aldoshin, S. M.; Makhaev, V. D. *Russ. Chem. Bull.* **2011**, *60*, 1209–1219.
49. Coronado, E.; Galán-Mascarós, J. R.; Gómez-García, C. J.; Martínez-Agudo, J. M. *Inorg. Chem.* **2001**, *40*, 113–120.
50. Abrahams, B. F.; Hudson, T. A.; McCormick, L. J.; Robson, R. *Cryst. Growth Des.* **2011**, *11*, 2717–2720.
51. Frenzer, W.; Wartchow, R.; Bode, H. Z. *Kristallogr.* **1997**, *212*, 237–237.
52. Pawlukojs, A.; Bator, G.; Sobczyk, L.; Grech, E.; Nowicka-Scheibe, J. *J. Phys. Org. Chem.* **2003**, *16*, 709–714
53. Carling, S. G.; Mathoniere, C.; Day, P.; Malik, K. M. A.; Coles, S. J.; Hursthouse, M. B. *J. Chem. Soc., Dalton Trans.* **1996**, 1839–1843.
54. Torrey, H. A.; Hunter, W. H. *J. Am. Chem. Soc.* **1912**, *34*, 702–716.
55. Stenhouse, J. *J. Chem. Soc.* **1870**, *23*, 6–14.
56. Sheldrick, G. M. *Acta Crystallogr., Sect. A* **2008**, *64*, 112–122.
57. Spek, A. *J. Appl. Crystallogr.* **2003**, *36*, 7–13.
58. Bain, G. A.; Berry, J. F. *J. Chem. Educ.* **2008**, *85*, 532–536.

Chapter 4

Magnetic Molecular Conductors



This Chapter reports on the structural diversity and the physical properties of three paramagnetic molecular conductors obtained by combining the BEDT-TTF organic donor and the tris(chloranilato)ferrate(III) metal complex as conducting and magnetic building blocks, respectively.

4.1 Introduction

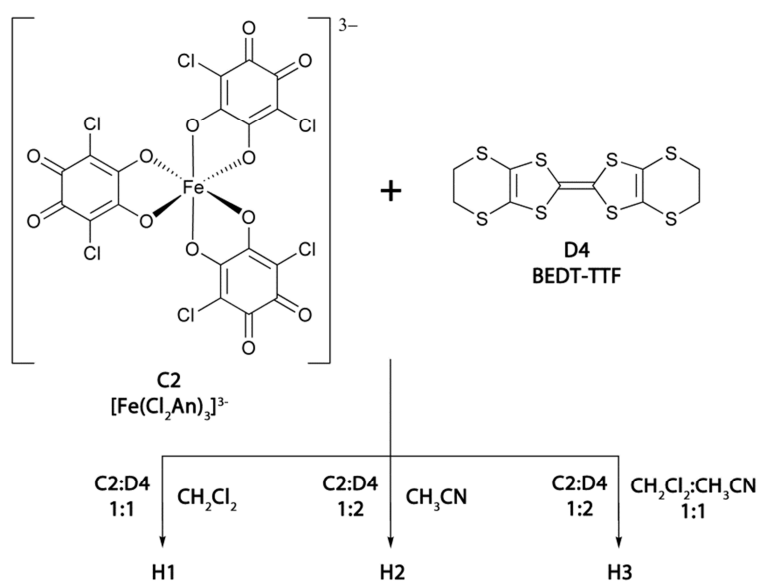
Molecular materials combining conducting (delocalized π -electrons) and magnetic (localized d -electrons) properties have attracted major interest in molecular science since they can exhibit coexistence of two distinct physical properties, furnished by two networks, or novel and improved properties due to the interactions established between them.¹⁻¹⁷ The development of these π - d systems as multifunctional materials represents one of the main targets in current materials science for their potential applications in molecular electronics.¹⁻⁸ Important milestones in the field of magnetic molecular conductors have been achieved using as molecular building blocks the BEDT-TTF organic donor⁹⁻¹² or its selenium derivatives, and charge-compensating anions ranging from simple mononuclear complexes $[MX_4]^{n-}$ ($M = Fe^{II}$, Cu^{II} ; $X = Cl, Br$)^{13,14,17} and $[M(ox)_3]^{3-}$ ^{1,9-12,18-21} with tetrahedral and octahedral geometries, to layered structures such as the bimetallic oxalate-based layers of the type $[M^II M^III(ox)_3]^-$ ($M^II = Mn, Co, Ni, Fe, Cu$; $M^III = Fe, Cr$).²²⁻²⁷ In these systems the shape of the anion and the arrangement of intermolecular contacts, especially hydrogen-bonding, between the anionic and cationic layers influence the packing motif of the BEDT-TTF radical cations, and therefore the physical properties of the obtained charge-transfer salt.²⁸ Tris-chelated metal complexes with octahedral geometry are among the most successful counterions for favoring enhanced intermolecular interactions between donor molecules, and hence good transport properties, thanks to their capability to provide organic-inorganic segregation, compared to square-planar complexes, such as d^8 metal dithiolenes, which favor instead mixed organic-inorganic stacks and thus semiconducting or insulating states. In addition, tris-chelated metal complexes have the possibility of a specific assembly order of Λ and Δ chirality that may influence the packing and thus the physical properties of the material, as well as to introduce functionalities such as magnetic properties. Typically, the structure of these multifunctional materials is formed by segregated stacks of the organic donors and the inorganic counterions which add the second functionality to the conducting material. The intermolecular interactions, in particular $S \cdots S$, $Se \cdots Se$, contacts shorter than the sum of the van der Waals radii, π - π , halogen-bonding, H-bonding *etc.*, play a crucial role in self-assembling these pre-designed molecular units. Therefore, the packing of the organic network and the corresponding conducting properties can be influenced by playing with the size, shape, symmetry and charge of the inorganic counterions. In this respect, anilate-based metal complexes²⁹⁻³⁴ are very interesting molecular building blocks to be used as paramagnetic counterions, also because they offer the opportunity of exchange coupling at great distance through the anilate bridge (see Chapter 3), being therefore extremely versatile in the construction of the above mentioned conducting/magnetic molecule-based materials. With the aim of studying new multifunctional materials whose physical properties may be tuned by changes on the molecular structures of their building units, the combination of the tris(chloranilato)ferrate(III) $[Fe(Cl_2An)_3]^{3-}$ complex anion as paramagnetic building block with the BEDT-TTF organic donor as conducting building block is reported in this Chapter. By varying the stoichiometric ratio of the components and the solvent mixture, three different hybrid systems formulated as $[BEDT-TTF]_3[Fe(Cl_2An)_3] \cdot 3CH_2Cl_2 \cdot H_2O$ (**H1**), δ - $[BEDT-TTF]_5 [Fe(Cl_2An)_3] \cdot 4H_2O$ (**H2**), and α'' - $[BEDT-$

TTF]₁₈[Fe(Cl₂An)₃]₃·3CH₂Cl₂·6H₂O (**H3**) were obtained. The synthesis, crystal structures, physical properties, and tight-binding band structure calculations of compounds **H1-3**, that represent the first examples of radical cation salts with the tris(chloranilato)ferrate(III) metal complex as counterion, are described herein, and the correlation between crystal structure and conducting behavior is also investigated.

4.2 Results and Discussion

4.2.1 Synthetic Strategy

The tris(chloranilato)ferrate(III) complex **C2** and the BEDT-TTF donor were combined in electrocrystallization experiments using the same current density but different reagents stoichiometric ratios and solvent mixtures. Three different hybrid systems formulated as [BEDT-TTF]₃[Fe(Cl₂An)₃]₃·3CH₂Cl₂·H₂O (**H1**), δ-[BEDT-TTF]₅[Fe(Cl₂An)₃]₃·4H₂O (**H2**) and α''-[BEDT-TTF]₁₈[Fe(Cl₂An)₃]₃·3CH₂Cl₂·6H₂O (**H3**) were obtained as reported in Scheme 4.1.



Scheme 4.1. Molecular structures for the complex anion [Fe(Cl₂An)₃]³⁻ and the BEDT-TTF organic donor, and experimental conditions used for obtaining compounds **H1-3**.

These systems mainly differ in the donor/anion ratio: 3:1, 5:1 and 6:1, for **H1**, **H2** and **H3** respectively, which, along with the different crystallization solvent molecules present in the structures, influences the crystal packing motif exhibited by the BEDT-TTF molecules in the organic layer and the resulting physical properties (*vide infra*).

4.2.2 Crystal Structure Description

The crystal structures of the three reported hybrid systems consist of homoleptic tris-chelated complex anions and BEDT-TTF radical cations. In each system, the metal complexes exhibit octahedral coordination geometry, with the Fe^{III} ion surrounded by six oxygen atoms of three chloranilate chelating ligands. These complexes are chiral according to the metal coordination, but both Λ and Δ enantiomers are present in the crystal lattices. The intramolecular Fe...Fe distances are of ca. 13.5 Å, and do not allow for a magnetic exchange interaction between metal centers (*vide infra*). The molecular structure of the complex anion for **H1** is reported in Figure 4.1.

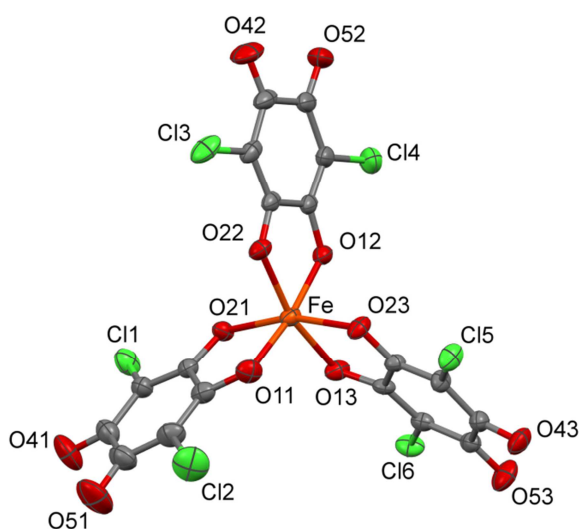


Figure 4.1. ORTEP drawing for the tris(chloranilato)ferrate(III) anionic complex (Δ enantiomer) for **H1** with thermal ellipsoids at the 30% probability level.

The metal-oxygen bond distances in compounds **H1-3** vary in the 1.994(7)–2.037(4) Å range and are very close to those observed for the precursor **C2b** (Table 4.1), suggesting the high spin character of the Fe^{III} ions.

Table 4.1. Fe–O bond distances (Å) for the anionic complex in compounds **H1-3** compared with those of **C2b**.

Bonds	H1	H2	H3	C2b
Fe–O(11)	1.996(5)	2.008(6)	2.020(6)	2.002(6)
Fe–O(21)	2.002(4)	2.022(6)	2.028(6)	2.008(6)
Fe–O(12)	2.018(4)	2.019(5)	1.994(7)	2.001(6)
Fe–O(22)	1.998(4)	1.999(6)	2.028(6)	2.017(6)
Fe–O(13)	2.026(4)	2.039(6)	2.018(6)	2.013(6)
Fe–O(23)	2.037(4)	2.014(6)	1.989(7)	1.999(6)
Fe–O average	2.013	2.017	2.013	2.007

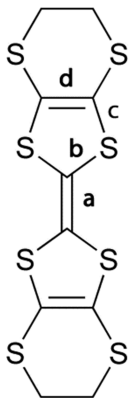
The C–O bond distances are influenced by the coordination to the metal center. The oxygen atoms coordinated to the metal have C–O distances, on average, 0.06 Å longer than those of the peripheral oxygen atoms, which show a major double bond character (Table 4.2).

Table 4.2. C–O bond distances (Å) for the anionic complex in compounds **H1-3** compared with those of **C2b**.

Bonds	H1	H2	H3	C2b
C(11)–O(11)	1.307(8)	1.295(9)	1.286(9)	1.28(1)
C(21)–O(21)	1.295(7)	1.299(9)	1.284(8)	1.29(1)
C(41)–O(41)	1.216(9)	1.219(9)	1.224(10)	1.20(1)
C(51)–O(51)	1.214(9)	1.227(9)	1.239(10)	1.22(1)
C(12)–O(12)	1.295(6)	1.287(9)	1.283(10)	1.29(1)
C(22)–O(22)	1.282(7)	1.291(9)	1.273(9)	1.29(1)
C(42)–O(42)	1.218(7)	1.221(10)	1.220(8)	1.23(1)
C(52)–O(52)	1.227(8)	1.224(10)	1.235(10)	1.21(1)
C(13)–O(13)	1.281(7)	1.302(10)	1.280(9)	1.25(2)
C(23)–O(23)	1.268(6)	1.282(10)	1.289(8)	1.31(2)
C(43)–O(43)	1.229(7)	1.237(9)	1.229(9)	1.23(2)
C(53)–O(53)	1.211(7)	1.221(10)	1.223(9)	1.24(2)

The X-ray analysis shows that **H1** crystallizes in the triclinic centrosymmetric space group *P*–1 with three independent BEDT-TTF molecules (indicated as **A**, **B**, **C**) and one complex anion $[\text{Fe}(\text{Cl}_2\text{An})_3]^{3-}$ in the asymmetric unit. The analysis of the bond distances for each crystallographically independent BEDT-TTF molecule, according to the procedure described by Day *et al.*,³⁵ reveals that each of the three donor molecules bear a charge of 1.0 ± 0.1 , in agreement with the +3 value expected for this salt (Table 4.3).

Table 4.3. Bond distances analysis and selected bond distances (Å) for the BEDT-TTF donor molecules in **H1**.

	A	B	C	
	a	1.391(8)	1.388(8)	1.400(8)
	b	1.723(6)	1.716(6)	1.716(6)
		1.716(6)	1.725(6)	1.716(6)
		1.713(6)	1.716(6)	1.715(6)
c	1.718(5)	1.719(6)	1.723(6)	
	1.741(7)	1.744(6)	1.742(7)	
	1.753(7)	1.735(6)	1.747(7)	
d	1.741(6)	1.747(7)	1.735(7)	
	1.736(7)	1.744(7)	1.741(6)	
	1.335(10)	1.338(10)	1.356(9)	
$\delta = (b+c)-(a+d)$	1.355(9)	1.342(8)	1.351(9)	
	δ	0.724	0.734	0.704
$Q = 6.347 - 7.4638 \cdot \delta$	Q	0.9(1)	0.9(1)	1.1(1)

The crystal packing of **H1** is unusual and consists of two perpendicularly interpenetrated sublattices, one formed by dimers of **C** molecules separated by complex anions along the *ac* plane, and the other formed by **B-A-A-B** tetramers of **A** and **B** molecules along the *bc* plane (Figures 4.2).

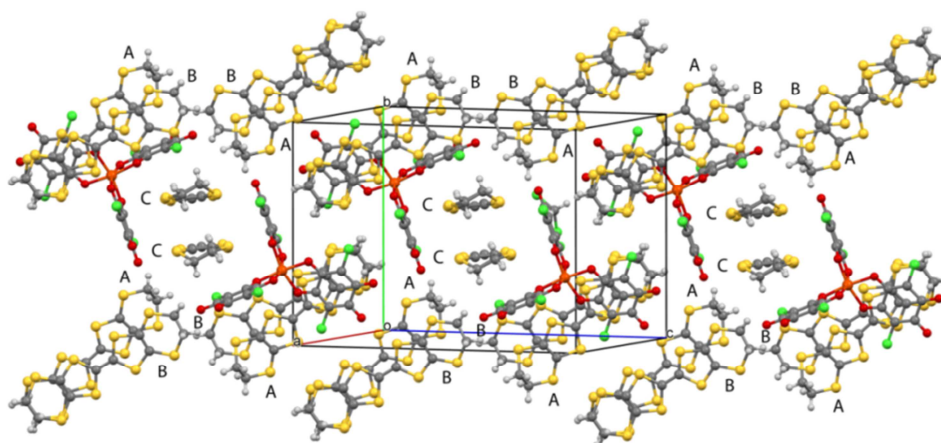


Figure 4.2. View of the crystal packing of **H1** along the *bc* plane with labelled **A**, **B** and **C** BEDT-TTF molecules. Crystallization water and CH_2Cl_2 molecules are omitted for clarity.

The role of the intermolecular interactions is crucial in determining the packing of the building blocks. Thus, in the **CC** dimers, planar BEDT-TTF molecules are disposed in a face-to-face manner,³⁶⁻³⁹ forming isolated dimers that are surrounded by two metal complexes of opposite chirality establishing $\text{Cl}\cdots\text{S}$ interactions (Figure 4.3). This arrangement is similar to the one observed in the $[\text{BEDT-TTF}][\text{P}(\text{C}_6\text{O}_2\text{Cl}_4)_3]\cdot\text{CH}_2\text{Cl}_2\cdot\text{CH}_3\text{CN}$ ^{40,41} salt formed with the shape-related $[\text{P}(\text{C}_6\text{O}_2\text{Cl}_4)_3]^-$ anion (trisphat), which presents the same tris-chelated chiral structure of $[\text{Fe}(\text{Cl}_2\text{An})_3]^{3-}$ with tetrachlorinated phenyl rings.

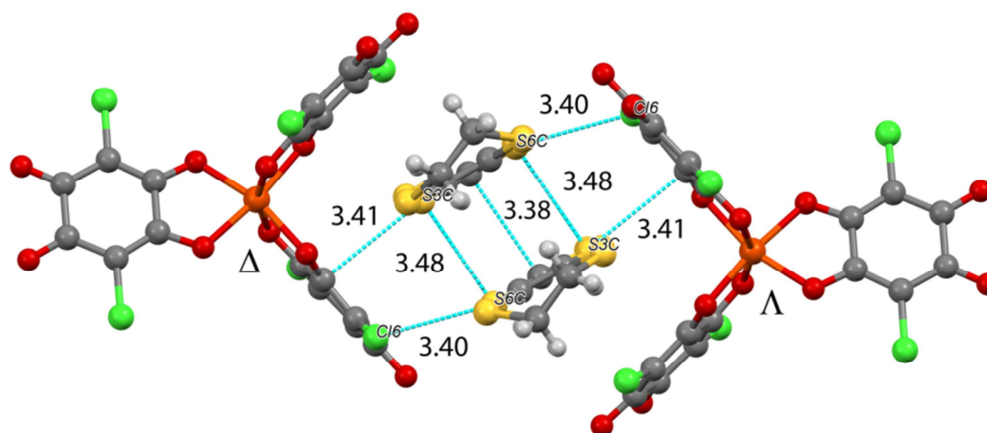


Figure 4.3. **C-C** dimer surrounded by two metal complexes of opposite chirality in **H1**. Symmetry related $\text{S}\cdots\text{S}$ contacts and intermolecular interactions lower than the sum of the van der Waals radii between the BEDT-TTF molecules and the chloranilate ligands are highlighted. (Å): $\text{S}(3\text{C})\cdots\text{S}(6\text{C})$ 3.48, $\text{S}(4\text{C})\cdots\text{S}(5\text{C})$ 3.57, $\text{Cl}(6)\cdots\text{S}(6\text{C})$ 3.40, $\text{C}(13\text{C})\cdots\text{S}(6\text{C})$ 3.41.

The **A** and **B** molecules interact through $\text{S}\cdots\text{S}$ interactions forming dimers where the BEDT-TTF molecules are tilted 11° along the $\text{C}=\text{C}$ double bond direction (torsion angle $\text{C}(5\text{A})-\text{C}(6\text{A})-\text{C}(6\text{B})-\text{C}(5\text{B})$). This molecular arrangement might be due to the lateral interactions between two **A** molecules of two consecutive **AB** dimers, giving rise to a **B-A-A-B** tetramer (Figure 4.4).

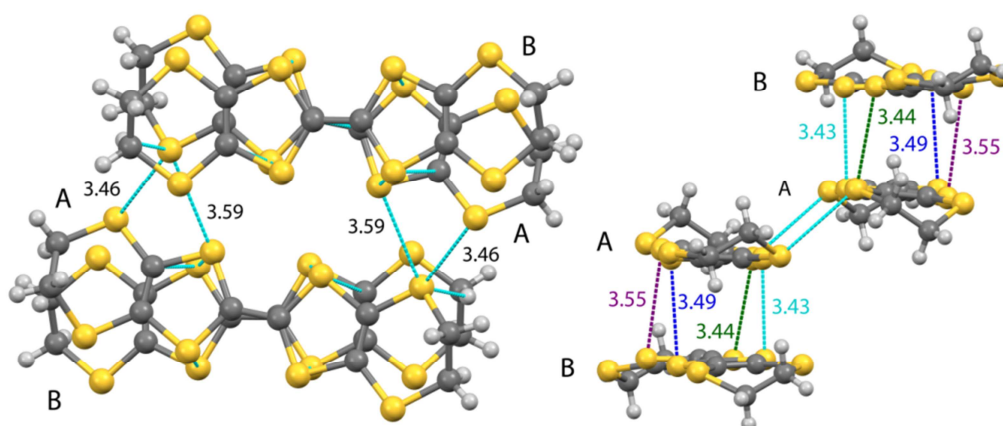


Figure 4.4. S...S contacts shorter than the sum of the van der Waals radii for the **B-A-A-B** tetramer in **1**. (Å): S(1A)...S(7A) 3.46, S(3A)...S(7A) 3.59, S(3A)...S(3B) 3.44, S(4A)...S(4B) 3.55, S(5A)...S(5B) 3.43, S(6A)...S(6B) 3.49.

The donor molecules arrangement in compound **H1** (*i.e.* association in noninteracting dimers and tetramers), along with the fact that all the BEDT-TTF molecules bear a charge of +1, precludes a charge delocalization along the organic layers, in agreement with the semiconducting behavior and the low conductivity at r.t. observed for this salt (*vide infra*).

Compound **H2** crystallizes in the triclinic centrosymmetric space group $P\bar{1}$ with five independent BEDT-TTF molecules (indicated as **A–E**) and one complex anion $[\text{Fe}(\text{Cl}_2\text{An})_3]^{3-}$ in the asymmetric unit. The crystal packing of **H2** shows organic-inorganic layer segregation. The hybrid inorganic layer consists of BEDT-TTF dimers (**EE**) surrounded by metal complexes as observed in compound **H1** for the **CC** type dimer (*vide supra*). The purely-organic layer is formed by the other four BEDT-TTF molecules (Figure 4.5).

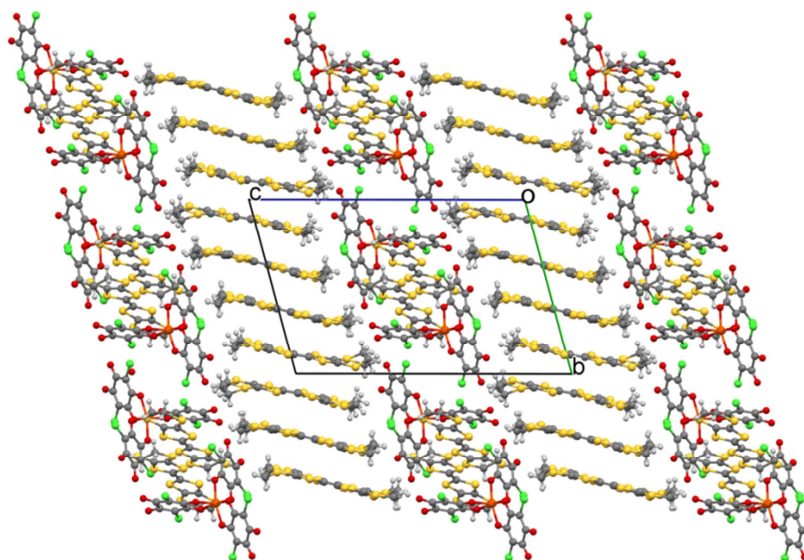


Figure 4.5. View of the crystal packing of **H2** along the *bc* plane showing the organic-inorganic layer segregation. Crystallization water molecules are omitted for clarity.

The organic layer shows the **A–D** donor molecules arranged in the exotic δ -phase packing motif, which contains stacks of twisted BEDT-TTF dimer units.^{36–39} The **A** and **C** molecules interact laterally along *a*, showing alternated **AA** and **CC** dimer units, with S...S interdimer contacts (3.41–3.56 Å) shorter than the intradimer ones, that are longer than the sum of the van der Waals radii (3.65 Å). The **B** and **D** molecules are, instead, alternated in a **BD–DB** sequence (Figure 4.6).

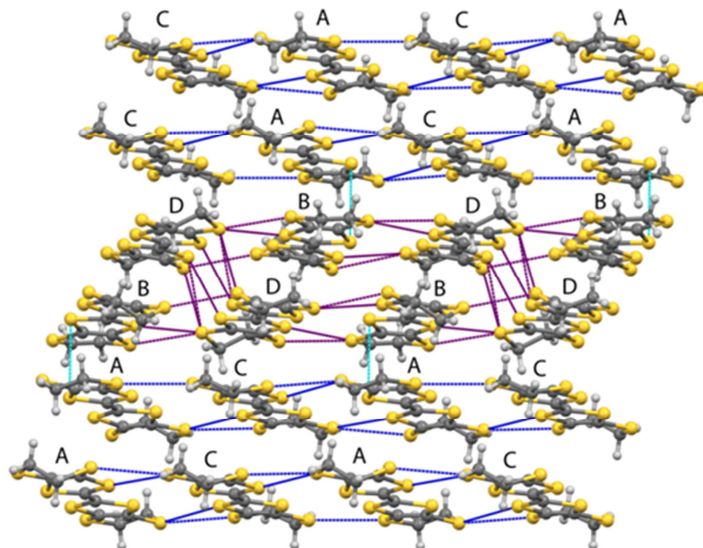


Figure 4.6. View of the δ -phase packing for **H2** where the short intermolecular contacts for the **AA–CC** and **BD–DB** sublayers are highlighted. Blue, contacts on the **AA–CC** layer; purple, contacts on the **BD–DB** layer; light blue, contacts between sublayers. (Å): S(1A)...S(2C) 3.44, S(6C)...S(7A) 3.39, S(7A)...S(8C) 3.41, S(1C)...S(2A) 3.41, S(2A)...S(3C) 3.44, S(6A)...S(7C) 3.43, S(7C)...S(8A) 3.56, S(1B)...S(2A) 3.46, S(5B)...S(8D) 3.43, S(8D)...S(7B) 3.43, S(2B)...S(1D) 3.54, S(1D)...S(4B) 3.58, S(5D)...S(8B) 3.46, S(8B)...S(7D) 3.47.

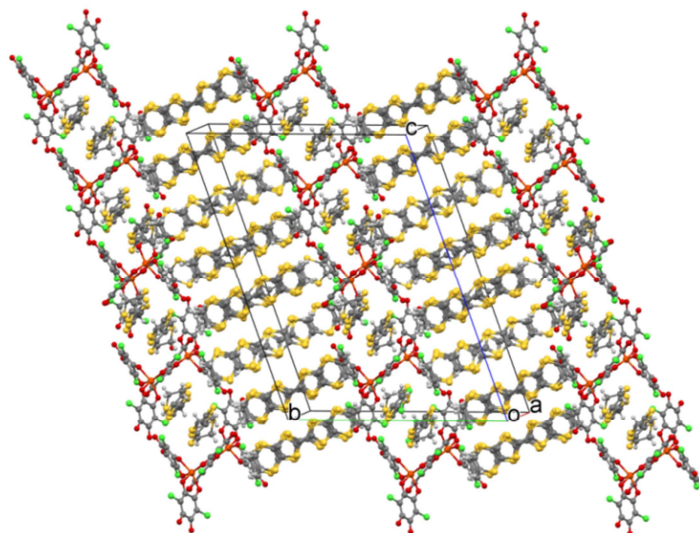
In this layer the shortest S...S contacts are found for the lateral interactions between the **B** and **D** molecules (3.43–3.46 Å). The oblique distances between the **D–D** molecules range from 3.57 to 3.60 Å, whereas those between the **B–B** molecules (3.62 Å) are longer. Between the two sublayers quite long S...S interactions are observed. These interactions are due to the typical twisted overlap mode of the δ -phases, characterized, in the present case, by $\omega = 30.6^\circ$ and $D = 2.6$ Å, where ω and D are the angle and the displacement between the molecular long axes, respectively.^{36–39}

The analysis of the central C=C and internal C–S bond lengths³⁵ confirms that **E**, the molecule associated in dimers surrounded by the metal complexes, bears a charge of +1, whereas the molecules arranged in the organic-layer (**A–D**) are present in a mixed-valence state. The longer C=C and shorter C–S bonds for **A** and **D** when compared to **B** and **C** indicates that the former bear a more positive charge than the latter, but a certain degree of charge delocalization occurs, since **B** and **C** are not in their neutral form either (Table 4.4).

Table 4.4. Bond distances analysis and selected bond distances (Å) for the BEDT-TTF donor molecules in **H2**.

	A	B	C	D	E	F
a	1.372(10)	1.373(10)	1.343(10)	1.365(10)	1.390(11)	1.372(10)
	1.737(7)	1.750(7)	1.749(7)	1.724(7)	1.718(9)	1.737(7)
b	1.734(7)	1.745(7)	1.749(8)	1.747(7)	1.755(8)	1.734(7)
	1.721(7)	1.745(7)	1.739(8)	1.742(7)	1.735(9)	1.721(7)
c	1.740(7)	1.745(7)	1.764(7)	1.744(7)	1.727(9)	1.740(7)
	1.736(7)	1.749(7)	1.749(7)	1.724(7)	1.718(9)	1.736(7)
d	1.738(7)	1.748(8)	1.749(8)	1.747(7)	1.755(8)	1.738(7)
	1.738(7)	1.748(7)	1.743(8)	1.742(7)	1.735(9)	1.738(7)
δ	1.765(7)	1.755(8)	1.764(7)	1.744(7)	1.727(9)	1.765(7)
	1.375(10)	1.348(10)	1.340(10)	1.360(10)	1.390(12)	1.375(10)
Q	1.355(10)	1.343(10)	1.338(11)	1.370(10)	1.360(13)	1.355(10)
	0.740	0.778	0.820	0.748	0.703	0.740
	0.8(1)	0.5(1)	0.2(1)	0.8(1)	1.0(1)	0.8(1)

Compound **H3** crystallizes in the triclinic centrosymmetric space group $P\bar{1}$ with 18 independent BEDT-TTF molecules (indicated as **A1**, **A2**, **A3**, ..., **F1**, **F2**, **F3**) and three complex anions $[\text{Fe}(\text{Cl}_2\text{An})_3]^{3-}$ in the asymmetric unit. This compound is isostructural to a solvate formulated as $\theta^1\text{-[BEDT-TTF]}_6[\text{Fe}(\text{Cl}_2\text{An})_3]\cdot(\text{H}_2\text{O})_{1.5}\cdot(\text{CH}_2\text{Cl}_2)_{0.5}$ (**H3'**), reported during our investigations.⁴² In Figure 4.7 the crystal packing of **H3** is shown with an emphasis on the organic-inorganic layer segregation as observed in **H2**.

**Figure 4.7.** Crystal packing of **H3** along the bc plane showing the organic-inorganic layer segregation. Crystallization water and CH_2Cl_2 molecules are omitted for clarity.

The hybrid inorganic layer of **H3** shows alternated anionic complexes of opposite chirality that surround dimers of mono-oxidized BEDT-TTF radical cations (**F**-type molecules). This packing motif, observed also in **H1** and **H2**, points out the templating influence of the intermolecular interactions between the chloranilate ligand and the dimerized BEDT-TTF molecules.

The organic layer contains donor molecules stacked in the unusual and peculiar α''' structural packing motif.^{20,39-39} In fact, the BEDT-TTF molecules stack in columns with an arrangement reminiscent of the α structural packing,³⁹⁻³⁹ but with a 2:1:2:1 alternation of the relative disposition of the molecules, instead of the classical 1:1:1:1 sequence (Figure 4.8). The α''' phase can be regarded as 1:2 hybrid of θ and β'' phases.

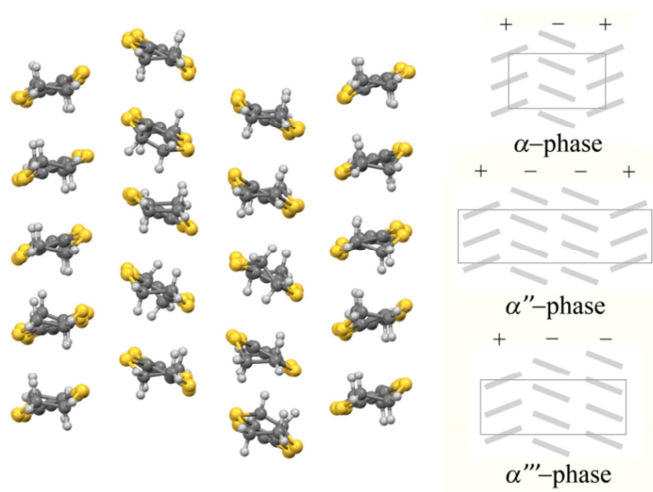


Figure 4.8. View of α''' packing of **H3** along the ac plane (left); schematic representation of the BEDT-TTF molecules arranged in the α , α'' and α''' packing motifs (right).

The donors show two different types of interstack S...S contacts; one type (depicted in blue in Figure 4.9) between columns of BEDT-TTF having the same orientation, in the 3.14–3.48 Å range, and another type (depicted in light blue in Figure 4.9) between columns of BEDT-TTF having opposite orientation, in the 3.30–3.58 Å range. The former are the strongest in the structure, whereas the intrastack S...S distances are longer than the sum of the van der Waals radii.

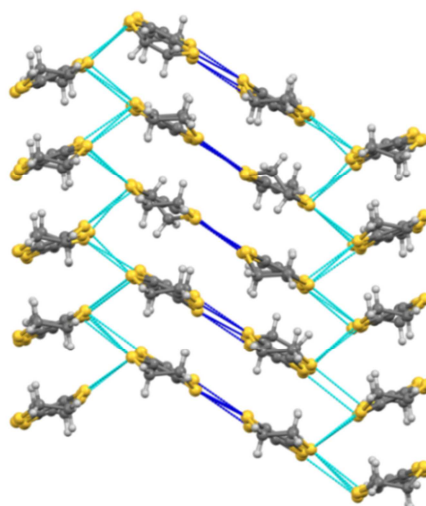
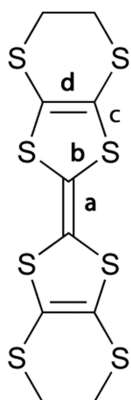


Figure 4.9. View of the BEDT-TTF packing of **H3** along the ac plane where the short intermolecular S...S contacts are highlighted. Some short contacts (Å): S(1D1)...S(7A1) 3.40, S(7A1)...S(3D1) 3.31, S(3A1)...S(7D1) 3.40, S(7D1)...S(1A1) 3.39, S(1B1)...S(5C1) 3.48, S(1D2)...S(2D1) 3.30, S(1D2)...S(2C1) 3.49, S(1D2)...S(4D1) 3.57, S(5D5)...S(8D1) 3.52, S(8D1)...S(7D2) 3.42.

The analysis of the central C=C and internal C–S bond lengths³⁵ confirms that the **F**-type molecules, associated in dimers and surrounded by the metal complexes, bear a charge of +1, as observed for **H1**, **H2** and also for **H3'**. The molecules arranged in the organic-layer (**A1**, **A2**, **A3**, ..., **E1**, **E2**, **E3**) are, instead, present in a mixed-valence state, with similar values in bond lengths and positive charge associated with each molecule, confirming a certain degree of charge delocalization, as expected for such type of molecular packing (Table 4.5).

Table 4.5. Bond distances analysis and selected bond distances (Å) for the BEDT-TTF donor molecules in **H3**.¹

	A	B	C	D	E	F
a	1.380(12)	1.393(12)	1.350(12)	1.390(11)	1.355(8)	1.395(9)
	1.732(9)	1.710(8)	1.737(8)	1.708(9)	1.728(8)	1.713(8)
b	1.755(9)	1.747(8)	1.772(8)	1.753(8)	1.759(8)	1.735(8)
	1.745(9)	1.726(8)	1.746(9)	1.747(8)	1.744(8)	1.720(9)
c	1.735(9)	1.731(8)	1.747(9)	1.729(8)	1.743(8)	1.736(9)
	1.748(8)	1.740(9)	1.738(8)	1.754(9)	1.756(7)	1.729(9)
d	1.754(9)	1.741(8)	1.754(9)	1.745(9)	1.748(9)	1.742(9)
	1.769(8)	1.751(8)	1.755(8)	1.752(8)	1.748(8)	1.720(9)
δ	1.758(9)	1.756(8)	1.785(8)	1.791(8)	1.760(8)	1.736(9)
	1.356(13)	1.363(12)	1.379(12)	1.335(13)	1.347(13)	1.372(11)
Q	1.333(13)	1.340(12)	1.337(12)	1.335(13)	1.353(12)	1.375(12)
	0.775	0.731	0.801	0.770	0.792	0.689
Q = 6.347-7.4638·δ	0.6(1)	0.7(1)	0.4(1)	0.6(1)	0.4(1)	1.1(1)



$$\delta = (b+c)-(a+d)$$

$$Q = 6.347 - 7.4638 \cdot \delta$$

4.2.3 Conducting Properties

The DC conductivity measurements of **H1** show a r.t conductivity of ca. $3 \times 10^{-4} \text{ S cm}^{-1}$ that decreases in a semiconducting way as the sample is cooled (Figure 4.10). The Arrhenius plot ($\ln(\rho)$ vs $1/T$) shows a linear behavior that can be fitted to an Arrhenius law ($\ln(\rho) = \ln(\rho_0) + E_a/kT$) with an activation energy of ca. 200 meV (inset in Figure 4.10).

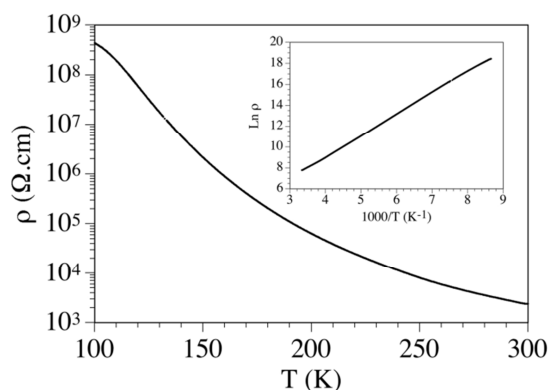


Figure 4.10. Thermal variation of the electrical resistivity ρ of compound **H1**. Inset shows the Arrhenius plot.

¹ The analyses were performed on 6 out of 18 crystallographically independent molecules, and the obtained values must be considered as average values.

This behavior indicates that compound **H1** is a semiconductor with low r.t. conductivity and high activation energy, in agreement with the structural data that show that in this compound all the BEDT-TTF molecules bear a charge of +1, precluding a charge delocalization along the organic layers.

Compounds **H2** and **H3** show a much higher r.t. conductivity, between 1 and 10 S cm⁻¹ with average values of ca. 2 S cm⁻¹ (**H2**) and 8 S cm⁻¹ (**H3**), and a semiconducting behavior as shown by the increase of the resistivity as the temperature is decreased (Figure 4.11). The Arrhenius plot shows that both salts have low activation energies of ca. 700 K (60 meV) and 740 K (64 meV) for **H2** and **H3**, respectively (inset of Figure 4.11). The high r.t. conductivity and low activation energy values for **H3** are similar to those found in compound **H3'**.⁴²

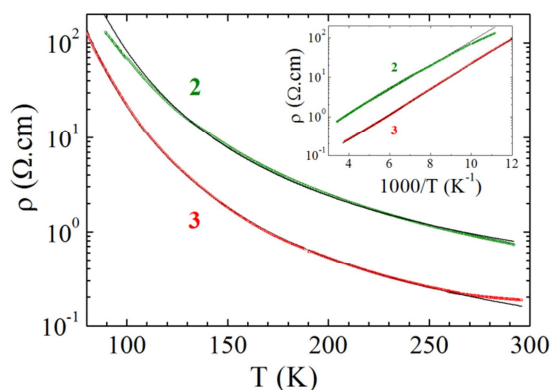


Figure 4.11, Temperature dependence of the electrical resistivity ρ for single crystals of compounds **H2** and **H3**. The inset shows the Arrhenius plot. The black lines are the fit to the data with the law $\rho = \rho_0 \exp(E_a/T)$ giving the activation energy E_a .

Resistivity measurements were also performed on compound **H3** under high hydrostatic pressure. The pressure dependence of the electrical conductivity, $\sigma(P)$, at r.t. is linear, with a slope of $(\sigma(P) - \sigma(1 \text{ bar}))/\sigma(1 \text{ bar}) = 28\% (\text{kbar})^{-1}$ (Figure 4.12b), in agreement with the low resistivity value and the low activation energy measured at ambient pressure.

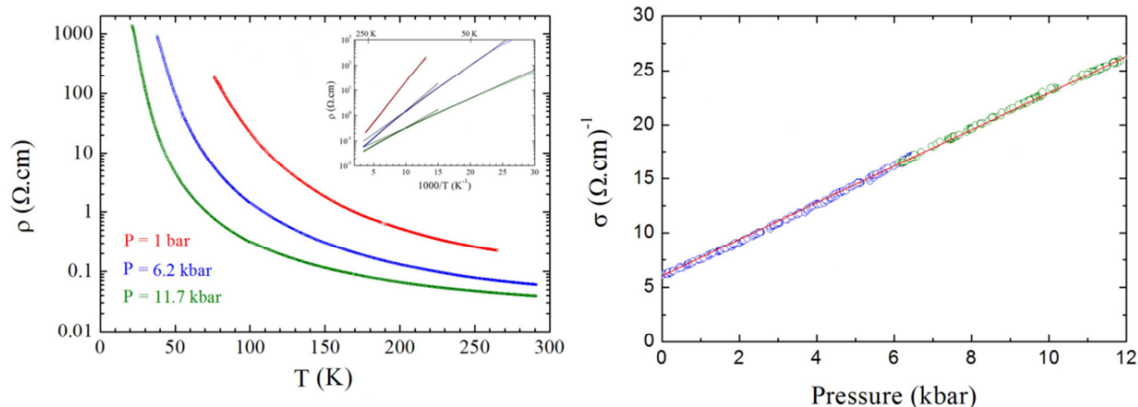


Figure 4.12, Left, Temperature dependence of the electrical resistivity, ρ , for a single crystal of compound **H3** at indicated pressures. Inset shows the Arrhenius plot. The black lines are the fit to the data with the law $\rho = \rho_0 \exp(E_a/T)$ giving the activation energy E_a . Right, Pressure dependence of the electrical conductivity, $\sigma(P)$, at r.t. for a single crystal of compound **H3**.

Moreover, the temperature dependence of the resistivity (Figure 4.12a) shows that the activation energy decreases with the pressure. The E_a reaches a value of the order of the room temperature (ca. 300 K) at 12 kbar, indicating that the gap is no more significant.

4.2.4 Band Structure Calculations

Band Structure calculation were performed in order to get insight on the intermolecular contacts responsible for the conducting properties of compounds **H2** and **H3**, and to support the observed transport properties.

As mentioned in the structural discussion, there are two different types of BEDT-TTF molecules in the structure of **H2**: those leading to the donor layers (**A–D**) and those outside the layers (**E**). Before proceeding to the analysis of the electronic structure, the role of these **E** type BEDT-TTF donors must be considered. They are found as dimers in between the $[\text{Fe}(\text{Cl}_2\text{An})_3]^{3-}$ anions. Both the S...S distances, which are quite short, and the overlap mode, with sulfur atoms almost on top of each other lead to a strong σ type HOMO...HOMO interaction, suggesting that these dimers must be considered as $[(\text{BEDT-TTF})_2]^{2+}$. This is consistent with the central C=C bond length of donor **E**, 1.381 Å, which is the largest of the system and the very large splitting (1.29 eV) between the bonding and antibonding combinations of the HOMOs. Consequently, the repeating unit of the donor layer contains four different types of BEDT-TTF donors (Figure 4.13), and the average charge of these donors is $(2/4)^+$.

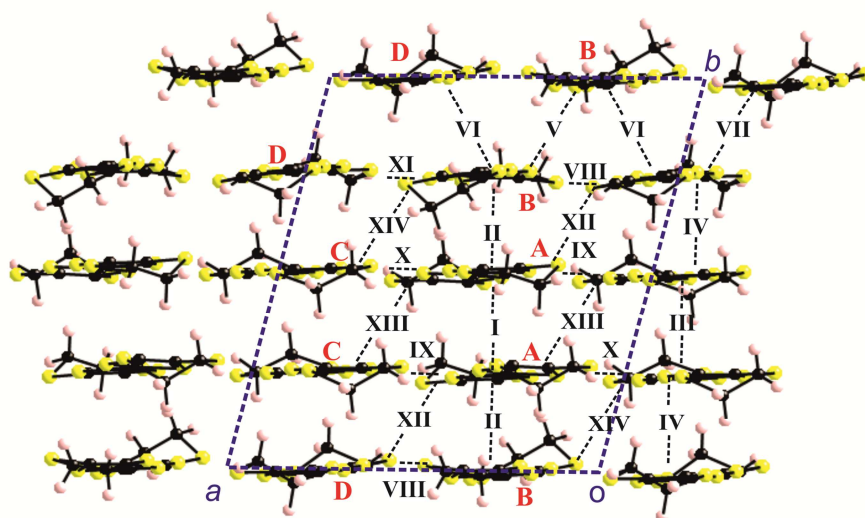


Figure 4.13, Donor layer of compound **H2** where the four different donors and 14 intermolecular interactions are shown.

Since the layers contain eight BEDT-TTF donors, the band structure near the Fermi level will contain eight HOMO-based bands. Because of the stoichiometry these bands must contain four holes so that the equivalent of two of these bands must be empty. The calculated band structure for **H2** is shown in Figure 4.14. There is a band gap of around 35 meV separating the

two upper bands from the lower ones so that the conductivity must exhibit an activated behavior, in agreement with the transport measurements.

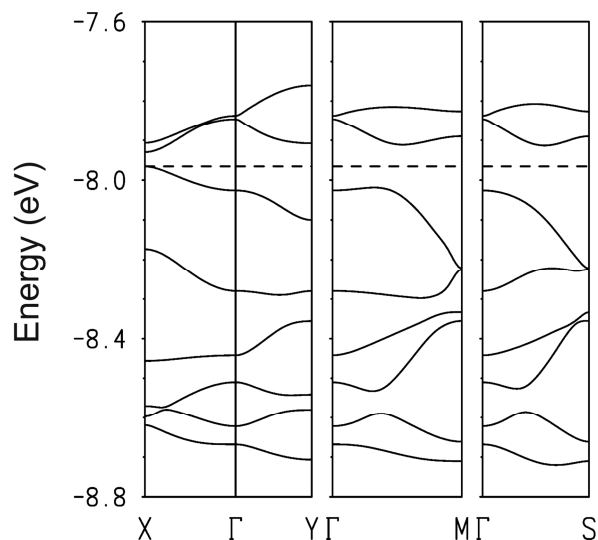


Figure 4.14, Calculated band structure for the donor layers of compound **H2** where $\Gamma = (0, 0)$, $X = (a^*/2, 0)$, $Y = (0, b^*/2)$, $M = (a^*/2, b^*/2)$ and $S = (-a^*/2, b^*/2)$. The dashed line refers to the highest occupied level.

By analyzing the density of states of this compound, it is possible to explain what is the origin of the activated conductivity. The density of states of **H2** shows that the two upper bands are strongly based on the HOMO levels of donors **A** and **D** whereas the upper filled level is strongly based on those of **B** type. In order to understand this observation which is at the origin of the gap occurrence, we must have a hint as to the strength of the different HOMO-HOMO interactions which ultimately dictate the composition and shape of the HOMO bands. The repeating unit of the layers contains 14 different intermolecular interactions (see Figure 4.13 for the labeling). The strength of the HOMO-HOMO interactions associated with the different intermolecular interactions may be quantified from their associated $|\beta_{\text{HOMO-HOMO}}|$ interaction energies.⁴³ The calculated values for compound **H2** are reported in Table 4.5. An important observation is that all the values corresponding to lateral interactions (VIII to XI) as well as XII-XIV and VI are smaller (between 0.0635 and 0.1640 eV) than those from I to IV as well as V and VII (between 0.2016 and 0.3587 eV). This means that the HOMO-HOMO interactions within the chains **-B-A-A-B-B-A-A-B-** and **-D-C-C-D-D-C-C-D-** along the *b*-direction play the leading role in building the band structure. As far as the second chain is concerned, the **D-D** interaction (VII) is by far the strongest. This means that the antibonding combination of the two HOMOs of the **D** type BEDT-TTFs will provide the highest lying levels of this chain and thus will be the major building blocks of one of the empty bands. In the first chain, the **A-A** interaction (I) is still the strongest but the difference with interaction **A-B** (II) is smaller. Consequently, although the higher lying levels associated with this chain, that is the second lower empty band, will be based on the antibonding combination of the HOMOs of the **A** type BEDT-TTFs, they will also contain substantial contributions from the **B** type ones. However, if the coupling interactions between the chains are considered, those associated with the **A**

donors (0.1640, 0.1593, 0.1499 and 0.0608 eV) are stronger than those associated with the **B** ones (0.1212, 0.1153, 0.0849 and 0.0635 eV). This means that the antibonding interchain interactions affect more strongly the HOMO-**A** levels and, as a result, the levels of the second empty band are localized on the **AA** dimers.

Table 4.5. $|\beta_{\text{HOMO-HOMO}}|$ interaction energies (eV) for the donor...donor interactions defined in Figure 12.

Interaction		$ \beta_{\text{HOMO-HOMO}} $	Interaction		$ \beta_{\text{HOMO-HOMO}} $
I	(A-A)	0.3587	II	(A-B)	0.3296
III	(C-C)	0.2383	IV	(C-D)	0.2016
V	(B-B)	0.3094	VI	(B-D)	0.0849
VII	(D-D)	0.3282	VIII	(B-D)	0.1153
IX	(A-C)	0.1593	X	(A-C)	0.1499
XI	(B-D)	0.1212	XII	(A-D)	0.0608
XIII	(C-A)	0.1640	XIV	(B-C)	0.0635

Thus, the **AA** and **DD** dimerizations, by leading to high energy lying antibonding combinations of the HOMOs located on these dimers, provide the main driving force for the occurrence of a band gap in **H2**. Since the dimerization is already strong in the **-D-C-C-D-D-C-C-D-** chain and thus leads to the upper empty band, it is the **-B-A-A-B-B-A-A-B-** chain which mostly controls the magnitude of the gap. There are two ways to increase/(decrease) the dimerization and thus the band gap (i) decreasing/(increasing) the intrachain **A-B** interaction, and (ii) increasing/(decreasing) the strength of the HOMO...HOMO interchain interactions associated with donors **A** with respect those affecting donors **B**.

The repeating unit of compound **H3** contains 18 different types of BEDT-TTF donors. Fifteen of them (**A1**, **A2**, **A3**,... **E1**, **E2**, **E3**) lead to the donor layers and three of them (**F1**, **F2**, **F3**) are found in between these donor layers in the vicinity of the anions. The repeating unit of the layers contains 30 BEDT-TTF donors and there are 45 different intermolecular interactions. Thus, calculating and understanding the band structure of this material is a truly challenging task. Before trying to solve this problem, the role of the **F** type BEDT-TTF donors must be considered. These donors are found as dimers in between the $[\text{Fe}(\text{Cl}_2\text{An})_3]^{3-}$ anions. Both the S...S distances, which are short, and the $|\beta_{\text{HOMO-HOMO}}|$ interaction energies, which are by far the largest ones (0.6390 and 0.5060 eV) of the system (*vide infra*), suggest that these dimers are really $[(\text{BEDT-TTF})_2]^{2+}$, as found for **H2**. Thus, in terms of electron counting, the **F** type donors should be considered as bearing a positive charge so that the average charge of the 15 crystallographically independent BEDT-TTF donors of the layer is $(6/15)^+$.

The numerous intermolecular interactions in the layer can be divided into three different groups: (i) those within the chains along *a*, (ii) those between pairs of chains of donors with the same inclination with respect to the *a*-direction, and (iii) those between pairs of chains of donors with opposite inclination with respect to the *a*-direction. The shortest S...S contacts are associated to the second ones. However, most of the physical properties of molecular conductors are determined by the band structure near the Fermi level and thus, by the strength of the HOMO...HOMO interactions. The calculated values of the $|\beta_{\text{HOMO-HOMO}}|$ interaction energies for **H3** occur in a range between 0.05 and 0.17 eV for the interactions (i) and between 0.03 and 0.18 eV for those of type (iii). The strongest interactions are those

between pairs of chains with the same inclination with respect to a . However, among them, the interactions between pairs of donors approximately in the same plane (*i.e.* those associated with the dark blue interactions in Figure 4.9) which are associated with the shortest S...S contacts in the structure, are only associated with $|\beta_{\text{HOMO-HOMO}}|$ values of ~ 0.15 eV, whereas those not highlighted in Figure 4.9 are the largest in the layer, ca. 0.30–0.35 eV. The reason why the first are smaller is that the contacts are lateral with π type overlaps which are generally weak. In contrast, the latter have a strong σ type component because of the favorable orientation of the Sp_z orbitals. Globally, the strongest interactions in the layer are those between the pairs of donors with the same inclination that form a continuous zigzag path along the a direction. However, these zigzag chains are connected through the numerous interactions of type (ii) which even if smaller, are not negligible. This means that **H3** should be a 2D conductor although with somewhat better conductivity along a , that is, the chain direction.

The donor layers of **H3** contain 30 BEDT-TTF donors and consequently, the band structure near the Fermi level will contain 30 HOMO-based bands. Taking into account the above-mentioned average charge of the donors in the layers, these bands must contain 12 holes so that the equivalent of six of these bands must be empty. From the viewpoint of the correlation between the electronic structure and conductivity of the system there are two different possibilities (*i*) there is a band gap separating the six upper HOMO-based bands from the lower ones so that the system will exhibit an activated conductivity, (*ii*) there is no band gap separating the six upper bands from the lower ones and then the system is either metallic or semiconducting when disorder is strong enough to localize the carriers. Thus, it is very important to establish if a band gap really occurs for the appropriate electron count in the band structure. The band structure for this system with fifteen upper HOMO bands is shown in Figure 4.15. The most important observation is that the top of the upper filled band, depicted as a dashed line in Figure 4.15, is separated by an indirect band gap of approximately 10 meV from the bottom of the next band. Inspection of the full Brillouin zone confirms this observation. Consequently, as is the case for **H2**, compound **H3** is a regular semiconductor with a small band gap and thus with a relatively high, though activated, conductivity. Analysis of the topology of the calculated band structure does not provide a better insight than that provided by consideration of the different $|\beta_{\text{HOMO-HOMO}}|$ values (*vide infra*). The large number of bands and crystallographically independent molecules, along with the low symmetry of the lattice, lead to a plethora of avoided crossings between bands. The band structure thus appears as a large series of quite flat bands, most of them being separated from each other with relatively small gaps. This is likely the case for most of the molecular conducting salts with such large number of crystallographically independent donors, which most likely will exhibit a semiconducting behavior.

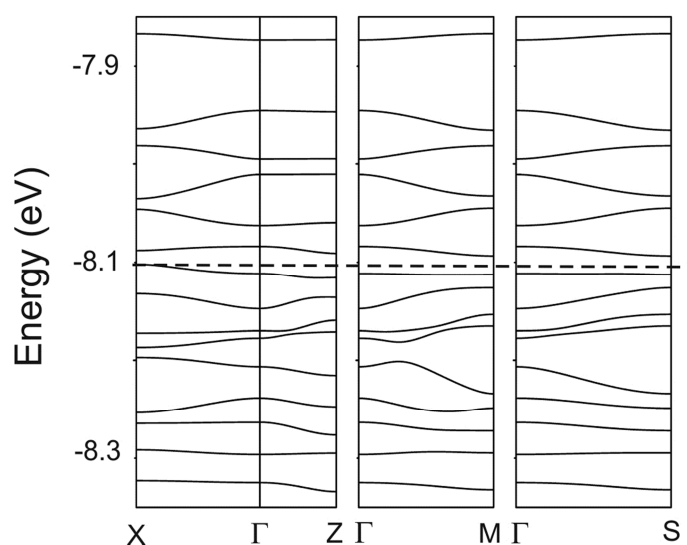


Figure 4.15, Upper 15 HOMO-based bands calculated for the donor layers of compound **H3** where $\Gamma = (0, 0)$, $X = (a^*/2, 0)$, $Z = (0, c^*/2)$, $M = (a^*/2, c^*/2)$, and $S = (-a^*/2, c^*/2)$. The dashed line refers to the upper filled level.

4.2.5 Magnetic Properties

The thermal variation of the magnetic susceptibility, expressed as $\chi_m T$, for compound **H1** shows a r.t. value of ca. $4.75 \text{ cm}^3 \text{ K mol}^{-1}$, slightly above the expected value for one isolated $S = 5/2 \text{ Fe}^{\text{III}}$ ion ($4.375 \text{ cm}^3 \text{ K mol}^{-1}$). When the temperature is decreased, $\chi_m T$ shows a smooth decrease and reaches a plateau of ca. $4.45 \text{ cm}^3 \text{ K mol}^{-1}$ below ca. 60 K. Below ca. 10 K $\chi_m T$ shows a more abrupt decrease and reaches a value of ca. $3.95 \text{ cm}^3 \text{ K mol}^{-1}$ at 2 K (Figure 4.16). This behavior indicates that besides the expected contribution from the $[\text{Fe}(\text{Cl}_2\text{An})_3]^{3-}$ anions, at high temperature there is an extra contribution from the BEDT-TTF sublattice of ca. $0.3 \text{ cm}^3 \text{ K mol}^{-1}$, which is close to the expected contribution of one unpaired localized electron. Since there are three BEDT-TTF⁺ radical cations per formula unit, we can assume that two of the three radicals are strongly antiferromagnetically coupled and, therefore, do not present any contribution to the magnetic moment. A close look at the S...S intermolecular contacts indicates that most probably the dimer **AB** is the one presenting a strong antiferromagnetic coupling, since it shows several intermolecular S...S interactions in the range of 3.43–3.49 Å, much shorter than the sum of the van der Waals radii (3.65 Å). The other dimer (**CC**) presents larger intermolecular S...S contacts (in the range of 3.48–3.57 Å) and, therefore, it would be responsible for the extra contribution and the observed antiferromagnetic coupling. This assumption agrees with the fact that there is half **CC** dimer (*i.e.* one electron) and one **AB** dimer per formula unit. The abrupt decrease observed at very low temperatures is attributed to the presence of a ZFS of the $S = 5/2 \text{ Fe}^{\text{III}}$ ion. Accordingly, we have fitted the magnetic properties of compound **H1** with a model including the contribution of an isolated $S = 5/2$ ion with a ZFS and that of a half $S = 1/2$ dimer with an antiferromagnetic coupling. To reduce the number of adjustable parameters, we have fixed the g value of the BEDT-TTF radicals to 2.0. This model reproduces very satisfactorily the magnetic properties of compound **H1** (solid line in Figure 4.16) with $g_{\text{Fe}} = 2.026$, $|D| = 1.2 \text{ cm}^{-1}$, $g_{\text{BEDT-TTF}} = 2.0$ (fixed) and $J_{\text{CC}} = -180 \text{ cm}^{-1}$ (J_{CC} is the

intradimer coupling constant. The Hamiltonian is written as $H = -JS_1S_2$. It should be pointed out that it was not possible to determine the sign of D since the measurements were performed on a polycrystalline sample and that the obtained D value could also contain a very weak antiferromagnetic contribution.

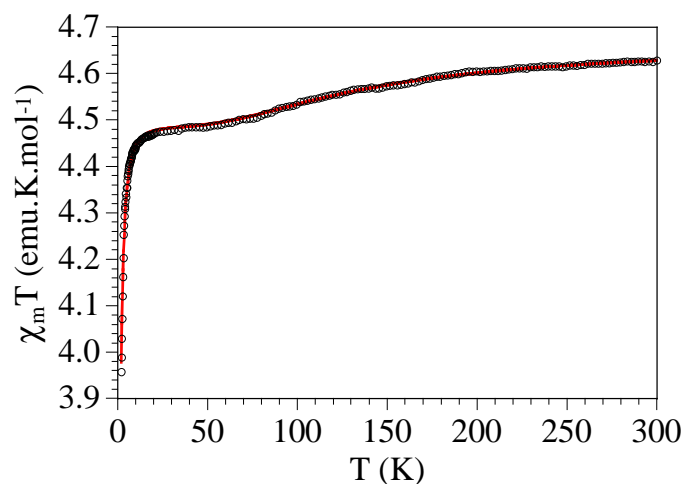


Figure 4.16, Thermal variation of $\chi_m T$ for compound **H1**. Solid line is the best fit to the model.

The D value is in good agreement with the value for **C1b** and within the normal range found in Fe^{III} complexes with similar structures.⁴⁵

4.2.6 Electron Paramagnetic Resonance

The EPR spectra of a single crystal of compound **H3** for any orientation shows a single line with a line-width of 26 G when the magnetic field is perpendicular to the plane of the BEDT-TTF molecules in the organic layer and 33 G when the field is parallel to the BEDT-TTF molecular plane (Figure 4.17a).

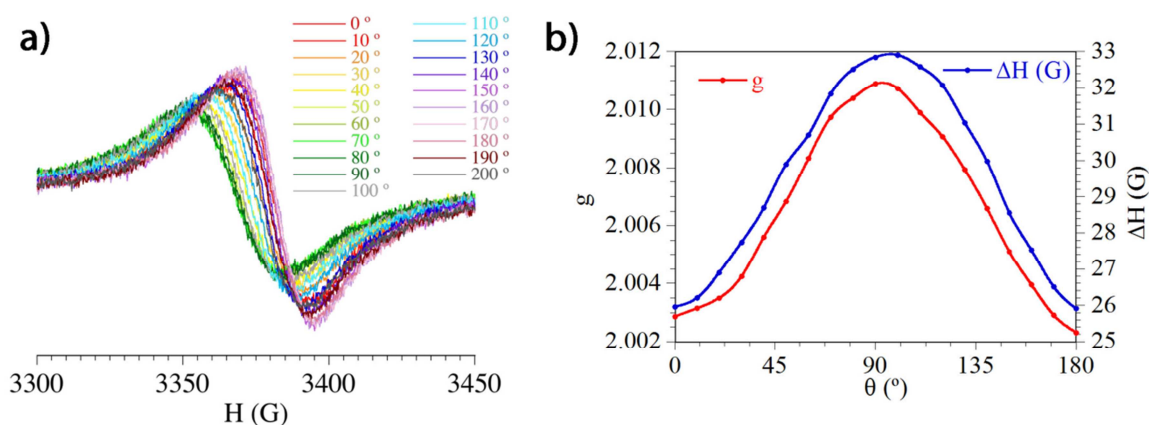


Figure 4.17, a) X-band EPR spectra of **H3** at r.t. at different orientations of the single crystal, b) Angular dependence of the g factor and line width (ΔH) of the X-band EPR signal.

The g values oscillate between 2.003 and 2.011 for the perpendicular and parallel orientations, respectively (Figure 4.17b). These values are within the normal range found in many other

BEDT-TTF salts.⁶ The intensity of this signal slightly decreases when the temperature is decreased for both orientations of the magnetic field: parallel ($\theta = 0^\circ$, Figure 4.18a) or perpendicular to the layers ($\theta = 90^\circ$, Figure 4.18b), suggesting the presence of an antiferromagnetic coupling between the BEDT-TTF radicals.

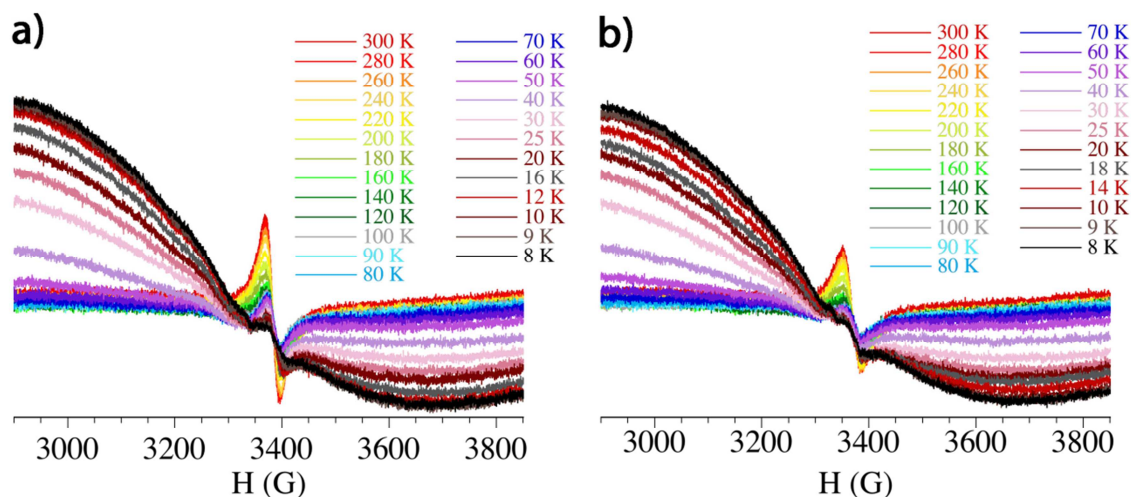


Figure 4.18. X-band EPR spectra of a single crystal of compound **H3** at different temperature when the magnetic field is parallel a) ($\theta = 0^\circ$) and perpendicular b) ($\theta = 90^\circ$) to the BEDT-TTF layers.

In fact, the thermal variation of the normalized product of the spin susceptibility (proportional to the area of the signal) times the temperature ($\chi_s T$) shows a continuous decrease when the temperature is lowered, and approaches to zero at very low temperatures, confirming the AF coupling in the cationic lattice (Figure 4.19).

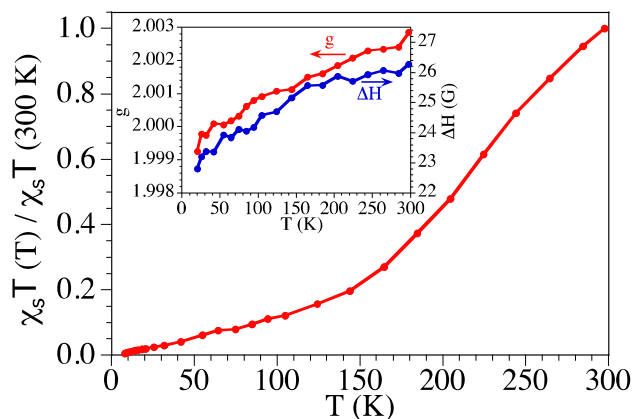


Figure 4.19. Thermal variation of the normalized $\chi_s T$ product of the X-band EPR signal of compound **H3** when the magnetic field is parallel to the layers ($\theta = 0^\circ$). Inset shows the thermal variation of the g value (left scale) and line width (ΔH , right scale) in the same experiment.

The g and ΔH values also decrease when the sample is cooled down (inset in Figure 4.19), although at very low temperatures it is very difficult to measure the signal since it is hidden by a large signal arising from the Fe^{III} anions whose intensity increases as the sample is cooled down, as expected for a paramagnetic Fe^{III} anion.

4.3 Conclusions

Three different crystalline radical cation salts based on the BEDT-TTF donor and the tris(chloranilato)ferrate(III) anion were prepared *via* electrocrystallization by slightly changing the donor/anion stoichiometry and the solvents. As a common structural feature for the three phases one can disclose the presence of dimerized oxidized BEDT-TTF units in the inorganic layer, very likely due to the establishment of intermolecular S...Cl contacts and also electrostatic interactions. While in compound **H1**, of 3:1 stoichiometry, the three BEDT-TTF molecules are fully oxidized in radical cations, in the salts **H2** and **H3**, of 5:1 and 6:1 stoichiometry, respectively, only the donors located in the inorganic layers are fully oxidized, while those forming the organic layers are in mixed valence state. The packing motif found in the organic layers is of δ type in **H2** and α'' type in **H3**. Single crystal conductivity measurements show semiconducting behavior for the three materials, but with low r.t. conductivity and high activation energy for **H1**, as expected from the structural analysis, and high r.t. conductivity of 1–10 S cm⁻¹ for **H2** and **H3**, with low activation energies of 60–65 meV. Band structure calculations for **H2** and **H3** are in agreement with an activated conductivity with low band gaps. A detailed analysis of the density of states and HOMO...HOMO interactions in **H2** explains the origin of the gap as a consequence of a dimerization in one of the donor chains, whereas the challenging calculation of **H3**, due to the presence of 18 crystallographically independent BEDT-TTF molecules, represents a milestone in the band structure calculations of such relatively rare and complex crystal structures. Magnetic susceptibility measurements for **H1** clearly indicate the presence of isolated high spin $S = 5/2$ Fe^{III} ions, with a contribution at high temperatures from BEDT-TTF radical cations. These latter are evidenced also by EPR variable-temperature measurements on single crystals of **H3**. This first family of conducting radical cation salts based on the magnetic tris(chloranilato)ferrate(III) complex demonstrates the versatility of this type of anions for the preparation of multifunctional molecular materials. Currently, a topic of special interest is the introduction of chirality in the organic layer,⁴⁶⁻⁵² thus allowing for the preparation of multifunctional materials in which the chirality may influence the conducting properties.

4.4 Experimental

4.4.1 General Remarks

BEDT-TTF (Aldrich) was used as received. Crystals were grown by the electrocrystallization technique (see Appendix 3).⁵³⁻⁵⁵ Solvents used for electrocrystallization experiments (HPLC grade) were dried under basic alumina and degassed with argon prior to use.

4.4.2 Syntheses

[BEDT-TTF]₃[Fe(Cl₂An)₃]·3CH₂Cl₂·H₂O (H1). C2b (22 mg) was dissolved in 8 mL of CH₂Cl₂ and placed in the cathode chamber of an H-shape electrocrystallization cell. BEDT-TTF (5 mg) was dissolved in 8 mL of CH₂Cl₂ and placed in the anode chamber of the cell. A current density of 1.0 $\mu\text{A cm}^{-2}$ was applied. Black prismatic single crystals of **H1** were grown at 20 °C on the anode surface of a platinum wire electrode over one month.

δ -[BEDT-TTF]₅[Fe(Cl₂An)₃]·4H₂O (H2). C2b (6 mg) was dissolved in 8 mL of CH₃CN and placed in the cathode chamber of an H-shape electrocrystallization cell. BEDT-TTF (3 mg) was dissolved in 8 mL of CH₃CN and placed in the anode chamber of the cell. A current density of 1.0 $\mu\text{A cm}^{-2}$ was applied. Single crystals of **H2** as black thin plates were grown at 20 °C on the anode surface of a platinum wire electrode over three weeks.

α' -[BEDT-TTF]₁₈[Fe(Cl₂An)₃]·3CH₂Cl₂·6H₂O (H3). C2b (6 mg) was dissolved in 8 mL of a 1:1 CH₂Cl₂:CH₃CN mixture and placed in the cathode chamber of an H-shape electrocrystallization cell. BEDT-TTF (3 mg) was dissolved in 8 mL of a 1:1 CH₂Cl₂/CH₃CN solution and placed in the anode chamber of the cell. A current density of 1.0 $\mu\text{A cm}^{-2}$ was applied. Single crystals of **H3** as black elongated prisms were grown at 20 °C on the anode surface of a platinum wire electrode over one week.

4.4.3 Equipment and Measurements Details

Single Crystal X-Ray Crystallography. X-ray diffraction measurements were performed on a Nonius Kappa CCD diffractometer, using graphite-monochromated MoK α radiation ($\lambda = 0.71073 \text{ \AA}$). The structures were solved by direct methods (SHELXS-97) and refined on F^2 with full-matrix least squares (SHELXL-97),⁵⁶ using the Wingx software package.⁵⁷ The non-H atoms were refined with anisotropic displacement parameters. The crystallization water molecules were refined without the hydrogen atoms. A summary of the crystallographic data and the structure refinement for **H1-3** is reported in Table 4.6.

Table 4.6. Summary of X-ray crystallographic data for **H1-3**.

	H1	H2	H3
Empirical formula	C ₅₁ H ₃₀ Cl ₁₂ FeO ₁₃ S ₂₄	C ₆₈ H ₄₀ Cl ₆ FeO ₁₆ S ₄₀	C ₂₃₇ H ₁₅₀ Cl ₂₄ Fe ₃ O ₄₂ S ₁₄₄
Formula weight	2101.44	2663.95	9304.56
Crystal size, mm	0.40 × 0.20 × 0.05	0.33 × 0.27 × 0.13	0.14 × 0.09 × 0.05
Crystal system	Triclinic	Triclinic	Triclinic
Space group	<i>P</i> -1	<i>P</i> -1	<i>P</i> -1
<i>a</i> , Å	13.177(1)	13.382(1)	20.944(1)
<i>b</i> , Å	15.356(2)	16.152(2)	26.679(1)
<i>c</i> , Å	19.795(2)	24.269(2)	33.931(1)
α , deg.	92.030(7)	104.052(8)	68.231(2)
β , deg.	106.571(6)	93.403(7)	80.742(2)
γ , deg.	96.654(7)	101.751(7)	71.238(2)
<i>V</i> , Å ³	3803(1)	4949(1)	16654(1)
<i>Z</i>	2	2	2
<i>T</i> , K	293(2)	150(2)	293(2)
ρ (calc), Mg/m ³	1.835	1.788	1.856

μ , mm ⁻¹	1.337	1.219	1.291
θ range, deg.	1.66 to 27.01	1.56 to 26.50	1.55 to 26.00
GooF	1.037	1.079	1.041
R1	0.0700	0.1065	0.1202
wR2	0.1772	0.2738	0.2970

$$R1 = \sum |F_o| - |F_c| / \sum |F_o|, wR2 = [\sum [w(F_o^2 - F_c^2)^2] / \sum [w(F_o^2)^2]]^{1/2}, w = 1 / [\sigma^2(F_o^2) + (aP)^2 + bP], \text{ where } P = [\max(F_o^2, 0) + 2F_c^2] / 3.$$

Single crystal conductivity measurements. The single crystal conductivity measurements were carried out with the four or two contacts methods (depending on the size of the single crystals) on six different single crystals of compound **H1** in the temperature range 300–2 K (although the resistance was above the detection limit below ca. 110 K). The results were identical in the cooling and warming scans. The contacts were made with Pt wires (25 μ m diameter) using graphite paste. The samples were measured in a Quantum Design PPMS-9 equipment connected to an external voltage source (Keithley model 2400 source-meter) and amperometer (Keithley model 6514 electrometer). The samples were measured by applying a constant voltage of 1 V and measuring the intensity. All the conductivity quoted values were measured in the voltage range where the crystals are Ohmic conductors. The cooling and warming rates were 0.5 K/min in all cases. For compounds **H2** and **H3** electrical resistivity was measured on platelet-shaped single crystals using a four point method. Four gold contacts were evaporated on both faces of the crystals and gold wires (17 μ m diameter) were glued with silver paste on those contacts. A low frequency (<100 Hz) lock-in technique was used with a measuring current $I_{ac} = 0.1 \mu$ A. Low temperature, in the range 15–300 K, was provided by a cryocooler equipment. Experiments under high hydrostatic pressure were performed in a CuBe clamped cell up to 12 kbar with silicon oil (Daphne 7373) as pressure transmitting medium. The pressure at r.t. was extracted from the resistance of a manganin gauge in the pressure cell and it is this value that is indicated in the figures. However, the loss of pressure during cooling is estimated to 2 kbar. A copper-constantan thermocouple inside the pressure cell was used as the thermometer.

EPR measurements. The EPR spectra were recorded on a single crystal of compound **H3** from 2900 to 3900 G in the temperature range of 300–5 K with a X-band (9.48 GHz) Bruker ELEXSYS E580 Spectrometer equipped with a helium cryostat. The crystal was rotated along the longitudinal axis so that the field was parallel or perpendicular to the layers for θ values of 0° or 90°, respectively.

Band structure calculations. The tight-binding band structure calculations were of the extended Hückel type.⁵⁸ A modified Wolfsberg-Helmholtz formula⁵⁹ was used to calculate the non-diagonal $H_{\mu\nu}$ values. All valence electrons were taken into account in the calculations and the basis set consisted of Slater-type orbitals of double- ζ quality for C 2s and 2p, S 3s and 3p and of single- ζ quality for H. The ionization potentials, contraction coefficients and exponents were taken from previous work.⁶⁰

Magnetic measurements. Susceptibility measurements were carried out in the temperature range of 2–300 K with an applied magnetic field of 0.1 T on a polycrystalline sample of compound **H1** (mass = 16.03 mg) with a Quantum Design MPMS-XL-5 SQUID susceptometer. The susceptibility data were corrected for the sample holders previously measured using the same conditions and for the diamagnetic contributions of the salt as deduced by using Pascal's constant tables ($\chi_{dia} = -1077 \times 10^{-6} \text{ cm}^3 \text{ mol}^{-1}$).⁶¹

References

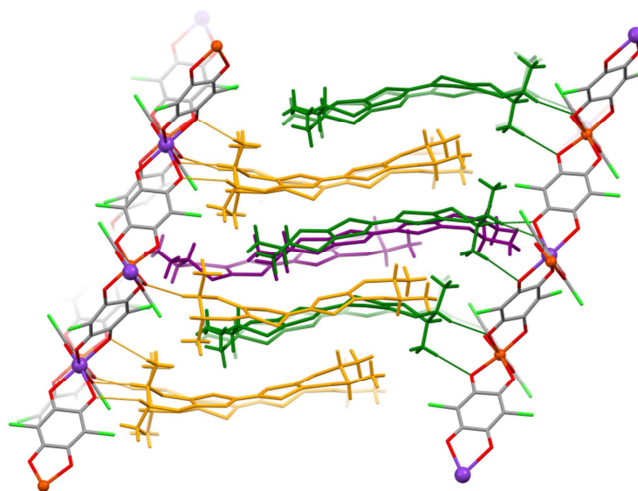
1. Coronado, E.; Day, P. *Chem. Rev.* **2004**, *104*, 5419–5448.
2. Enoki, T.; Miyazaki, A. *Chem. Rev.* **2004**, *104*, 5449–5478.
3. Kobayashi, H.; Cui, H. B.; Kobayashi, A. *Chem. Rev.* **2004**, *104*, 5265–5288.
4. Mercuri, M. L.; Deplano, P.; Serpe, A.; Artizzu, F. Chapter 7 in *Handbook of Multifunctional Molecular Materials, Multifunctional Nanomaterials of interest in Electronics*, 219–280; Ouahab, L., Ed.; Pan Stanford Publishing: Singapore, **2013**.
5. Focused Issue on Molecular Electronics, *Nature Nanotech.* **2013**, *8*, 377–467.
6. Williams, J. M.; Ferraro, J. R.; Thorn, R. J.; Carlson, K. D.; Geiger, U.; Wang, H. H.; Kini, A. M.; Whangbo, M. H. *Organic Superconductors: Synthesis, Structure, Properties and Theory*; Grimes, R. N., Ed.; Prentice Hall: Englewood Cliffs, NJ, **1992**.
7. Coronado, E.; Giménez-Saiz, C.; Gómez-García, C. J. *Coord. Chem. Rev.* **2005**, *249*, 1776–1796.
8. Coronado, E.; Clemente-León, M.; Galán-Mascarós, J. R.; Giménez-Saiz, C.; Gómez-García, C. J.; Martínez-Ferrero, E. *J. Chem. Soc., Dalton Trans.* **2000**, 3955–3961.
9. Kurmoo, M.; Graham, A. W.; Day, P.; Coles, S. J.; Hursthouse, M. B.; Caulfield, J. L.; Singleton, J.; Pratt, F. L.; Hayes, W.; Ducasse, L.; Guionneau, P. *J. Am. Chem. Soc.* **1995**, *117*, 12209–12217.
10. Martin, L.; Turner, S. S.; Day, P.; Mabbs, F. E.; McInnes, E. J. L. *Chem. Commun.* **1997**, *15*, 1367–1368.
11. Rashid, S.; Turner, S. S.; Day, P.; Howard, J. A. K.; Guionneau, P.; McInnes, E. J. L.; Mabbs, F. E.; Clark, R. J. H.; Firth, S.; Biggs, T. *J. Mater. Chem.* **2001**, *11*, 209–2101.
12. Schlueter, J. A.; Geiser, U.; Whited, M. A.; Driehko, N.; Salameh, B.; Petukhov, K.; Dressel M. *Dalton Trans.* **2007**, 2580–2588 and references therein.
13. Uji, S.; Shinagawa, H.; Terashima, T.; Yakabe, T.; Terai, Y.; Tokumoto, M.; Kobayashi, A.; Tanaka, H.; Kobayashi, H.; *Nature* **2001**, *410*, 908–910.
14. Fujiwara, H.; Fujiwara, E.; Nakazawa, Y.; Narymbetov, B. Zh.; Kato, K.; Kobayashi, H.; Kobayashi, A.; Tokumoto, M. and Cassoux, P. *J. Am. Chem. Soc.* **2001**, *123*, 306–314.
15. Coronado, E.; Falvello, L. R.; Galán-Mascarós, J. R.; Giménez-Saiz, C.; Gómez-García, C. J.; Lauhkin, V. N.; Pérez-Benítez, A.; Rovira, C.; Veciana, *Adv. Mater.* **1997**, *9*, 984–987.
16. Yamaguchi, K.; Kitagawa, Y.; Onishi, T.; Isobe, H.; Kawakami, T.; Nagao, H.; Takamizawa, S. *Coord. Chem. Rev.* **2002**, *226*, 235–249 and references therein.
17. Day, P.; Kurmoo, M.; Mallah, T.; Marsden, I. R.; Friend, R. H.; Pratt, F. L.; Hayes, W.; Chasseau, D.; Gaultier, *J. Am. Chem. Soc.* **1992**, *114*, 10722–10729.
18. Coronado, E.; Curreli, S.; Giménez-Saiz, C.; Gómez-García, C. J. *J. Mater. Chem.* **2005**, *15*, 1429–1436.
19. Coronado, E.; Curreli, S.; Giménez-Saiz, C.; Gómez-García, C. J. *Inorg. Chem.* **2012**, *51*, 1111–1126.
20. Martin, L.; Day, P.; Clegg, W.; Harrington, R. W.; Horton, P. N.; Bingham, A.; Hursthouse, M. B.; McMilland P.; Firth S.; *J. Mater. Chem.* **2007**, *17*, 3324–3329.
21. Coronado, E.; Curreli, S.; Giménez-Saiz, C.; Gómez-García, C. J.; Alberola, A. *Inorg. Chem.* **2006**, *45*, 10815–10824.
22. Tamaki, H.; Zhong, Z. J.; Matsumoto, N.; Kida, S.; Koikawa, M.; Achiwa, N.; Hashimoto, Y.; Okawa, H. *J. Am. Chem. Soc.* **1992**, *114*, 6974–6979.
23. Mathonière, C.; Nuttall, C. J.; Carling, S. G.; Day, P. *Inorg. Chem.* **1996**, *35*, 1201–1206.

24. Coronado, E.; Galan-Mascaros, J. R.; Gomez-Garcia, C. J.; Laukhin, V. *Nature* **2000**, *408*, 447–449.
25. Alberola, A.; Coronado, E.; Galán-Mascarós, J. R.; Giménez-Saiz, C.; Gómez-García, C. J. *J. Am. Chem. Soc.* **2003**, *125*, 10774–10775.
26. Coronado, E.; Galán-Mascarós, J. R.; Gómez-García, C. J.; Martínez-Ferrero, E.; van Smaalen, S. *Inorg. Chem.* **2004**, *43*, 4808–4810.
27. Alberola, A.; Coronado, E.; Galán-Mascarós, J. R.; Giménez-Saiz, C.; Gómez-García, C. J.; Martínez-Ferrero, E.; Murcia-Martínez, A. *Synth. Met.* **2003**, *135*, 687–689.
28. Fourmigué, M.; Batail, P. *Chem. Rev.* **2004**, *104*, 5379–5418.
29. Kitagawa, S.; Kawata, S. *Coord. Chem. Rev.* **2002**, *224*, 11–34, and references therein.
30. Tinti, F.; Verdagner, M.; Kahn, O.; Savariault, J. M. *Inorg. Chem.* **1987**, *26*, 2380–2384.
31. Min, K. S.; Rhinegold, A. L.; Miller, J. S. *J. Am. Chem. Soc.* **2005**, *128*, 40–41.
32. Min, K. S.; Rheingold, A. L.; DiPasquale, A.; Miller, J. S. *Inorg. Chem.* **2006**, *45*, 6135–6137.
33. Min, K. S.; DiPasquale, A. G.; Golen, J. A.; Rheingold, A. L.; Miller, J. S. *J. Am. Chem. Soc.* **2007**, *129*, 2360–2368.
34. Nagayoshi, K.; Kabir, M. K.; Tobita, H.; Honda, K.; Kawahara, M.; Katada, M.; Adachi, K.; Nishikawa, H.; Ikemoto, I.; Kumagai, H.; Hosokoshi, Y.; Inoue, K.; Kitagawa, S.; Kawata, S. *J. Am. Chem. Soc.* **2003**, *125*, 221–232.
35. Guionneau, P.; Kepert, C. J.; Bravic, G.; Chasseau, D.; Truter, M. R.; Kurmoo, M.; Day, P. *Synth. Met.* **1997**, *86*, 1973–1974.
36. Mori, T. *Bull. Chem. Soc. Jpn.* **1998**, *71*, 2509–2526.
37. Mori, T. *Bull. Chem. Soc. Jpn.* **1999**, *72*, 2011–2027.
38. Mori, T.; Mori, H.; Tanaka, S. *Bull. Chem. Soc. Jpn.* **1999**, *72*, 179–197.
39. Shibaeva, R. P.; Yagubskii E. B. *Chem. Rev.* **2004**, *104*, 5347–5378.
40. Clemente-León, M.; Coronado, E.; Gómez-García, C. J.; Soriano-Portillo, A.; Constant, S.; Frantz, R.; Lacour, J. *Inorg. Chim. Acta* **2007**, *360*, 955–960.
41. Riobé, F.; Piron, F.; Réthoré, C.; Madalan, A. M.; Gómez-García, C. J.; Lacour, J.; Wallis, J. D.; Avarvari, N. *New J. Chem.* **2011**, *35*, 2279–2286.
42. Benmansour, S.; Coronado, E.; Giménez-Saiz, C.; Gómez-García, C. J.; Röhlér, C. *Eur. J. Inorg. Chem.* **2014**, *24*, 3949–3959.
43. Whangbo, M.-H.; Williams, J. M.; Leung, P. C. W.; Beno, M. A.; Emge, T. J.; Wang, H. H. *Inorg. Chem.* **1985**, *24*, 3500–3502.
44. Mori, H.; Tanaka, S.; Oshima, G.; Saito, G.; Mori, T.; Maruyama, Y.; Inokuchi, H. *Bull. Chem. Soc. Jpn.* **1990**, *63*, 2183–2190.
45. Boca, R. *Coord. Chem. Rev.* **2004**, *248*, 757–902.
46. Avarvari, N.; Wallis, J. D. *J. Mater. Chem.* **2009**, *19*, 4061–4076.
47. Galán-Mascarós, J. R.; Coronado, E.; Goddard, P. A.; Singleton, J.; Coldea, A. I.; Wallis, J. D.; Coles, S. J.; Alberola, A. *J. Am. Chem. Soc.* **2010**, *132*, 9271–9273.
48. Pop, F.; Auban-Senzier, P.; Frąckowiak, A.; Ptaszyński, K.; Olejniczak, I.; Wallis, J. D.; Canadell, E.; Avarvari, N. *J. Am. Chem. Soc.* **2013**, *135*, 17176–17186.

49. Pop, F.; Laroussi, S.; Cauchy, T.; Gómez-García, C. J.; Wallis, J. D.; Avarvari, N. *Chirality* **2013**, *25*, 466–474.
50. Yang, S.; Pop, F.; Melan, C.; Brooks, A. C.; Martin, L.; Horton, P.; Auban-Senzier, P.; Rikken, G. L. J. A.; Avarvari, N.; Wallis, J. D. *CrystEngComm* **2014**, *16*, 3906–3916.
51. Pop, F.; Allain, M.; Auban-Senzier, P.; Martínez-Lillo, J.; Lloret, F.; Julve, M.; Canadell, E.; Avarvari, N. *Eur. J. Inorg. Chem.* **2014**, *24*, 3855–3862.
52. Pop, F.; Auban-Senzier, P.; Canadell, E.; Rikken, G. L. J. A.; Avarvari, N. *Nat. Commun.* **2014**, *5*, 3757.
53. Emge, T. J.; Wang, H. H.; Beno, M. A.; Williams, J. M.; Whangbo M. H.; Evain, M.; *J. Am. Chem. Soc.* **1986**, *108*, 8215–8223.
54. Stephens, D. A.; Rehan, A. E.; Compton, S. J.; Barkhau R. A.; Williams, J. M. *Inorg. Synth.* **1986**, *24*, 130–143.
55. Batail, P.; Boubekeur, K.; Fourmigué, M.; Gabriel, J.-C. P. *Chem. Mater.* **1998**, *10*, 3005–3015.
56. Sheldrick, G. M. *Programs for the Refinement of Crystal Structures*, University of Göttingen: Göttingen, Germany, **1996**.
57. Farrugia, L. J. *J. Appl. Crystallogr.* **1999**, *32*, 837–838.
58. Whangbo, M.-H.; Hoffmann, R. *J. Am. Chem. Soc.* **1978**, *100*, 6093–6098.
59. Ammeter, J. H.; Bürgi, H.-B.; Thibeault, J.; Hoffmann, R. *J. Am. Chem. Soc.* **1978**, *100*, 3686–3692.
60. Pénicaud, A.; Boubekeur, K.; Batail, P.; Canadell, E.; Auban-Senzier, P.; Jérôme, D. *J. Am. Chem. Soc.* **1993**, *115*, 4101–4112.
61. Bain, G. A.; Berry, J. F. *J. Chem. Educ.* **2008**, *85*, 532–536.

Chapter 5

Chiral Molecular Conductors



*This Chapter reports on the crystal structure and the physical properties of a complete series of isostructural chiral molecular conductors obtained by combining the TM-BEDT-TTF organic donor as (*S,S,S,S*) and (*R,R,R,R*) enantiopure forms, or as racemic mixture (*rac*), with 2D heterobimetallic anionic layers obtained “in situ” by the self-assembling of tris(chloranilato)ferrate(III) metal complexes and potassium cations.*

5.1 Introduction

The introduction of chirality in the field of tetrathiafulvalene-based molecular conductors represents one of the most recent advances¹ in the search for multifunctional molecular materials where properties such as charge transport, magnetism, spin crossover, chirality, and so on, coexist or interplay in the same material.²⁻⁴ One of the milestones in this field is the first observation of the electrical magneto-chiral anisotropy (eMChA) effect in a bulk crystalline chiral conductor,⁵ as a synergy between chirality and conductivity.⁶⁻⁸ However, the combination of chirality with electroactivity in chiral TTF precursors afforded several other recent important results such as *i*) the modulation of the structural disorder in the solid state, and hence a difference in conductivity between the enantiopure and racemic forms as observed in conducting salts based on ethylenedithio-TTF-oxazolines (EDT-TTF-Ox),⁹⁻¹² *ii*) the tuning of the chiroptical properties through electrochemical or chemical oxidation as observed for example in TTF-allenes¹³ or TTF-helicenes,¹⁴ *iii*) the control of the supramolecular chirality in electroactive helical aggregates,¹⁵⁻¹⁸ *iv*) the induction of different packing patterns and crystalline space groups in mixed valence salts of dimethyl-ethylenedithio-tetrathiafulvalene (DM-EDT-TTF) (**D6**, Chart 2) showing semiconducting (enantiopure forms) or metallic (racemic form) behavior.¹⁹ Although the first example of an enantiopure TTF derivative, namely the tetramethyl-bis(ethylenedithio)-tetrathiafulvalene (TM-BEDT-TTF) (**D4**, Chart 2), was described almost 30 years ago as the (*S,S,S,S*) enantiomer,^{20,21} the number of TM-BEDT-TTF based conducting radical cation salts is rather limited. They range from the semiconducting salts [**D4**]₂X₂F₆ (X = As, Sb)²² or [**D4**]₃²³ as complete series of both enantiomers and racemic forms, to the ferromagnetic metal [**D4**]_x[MnCr(ox)]₃²⁴ described only as (*S,S,S,S*) enantiomer. As far as the π -*d* systems are concerned, *i.e.* system where delocalized π -electrons of the organic donor are combined with localized *d*-electrons of magnetic counterions (see Chapter 4), the number of conducting systems based on enantiopure TTF precursors is even scarcer.^{24,25} These π -*d* systems offer, with respect to the radical cation salts obtained with diamagnetic anions, the additional opportunity to investigate the interplay between the magnetic contribution of the anion and the conducting properties of the cation in the presence of chiral elements. In this respect, anilate-based metal complexes²⁶⁻³¹ are very interesting molecular building blocks to be used as paramagnetic components for obtaining conducting radical cation salts (see Chapter 4), also because they offer the opportunity of providing magnetic exchange coupling through the anilate bridge (see Chapter 3).

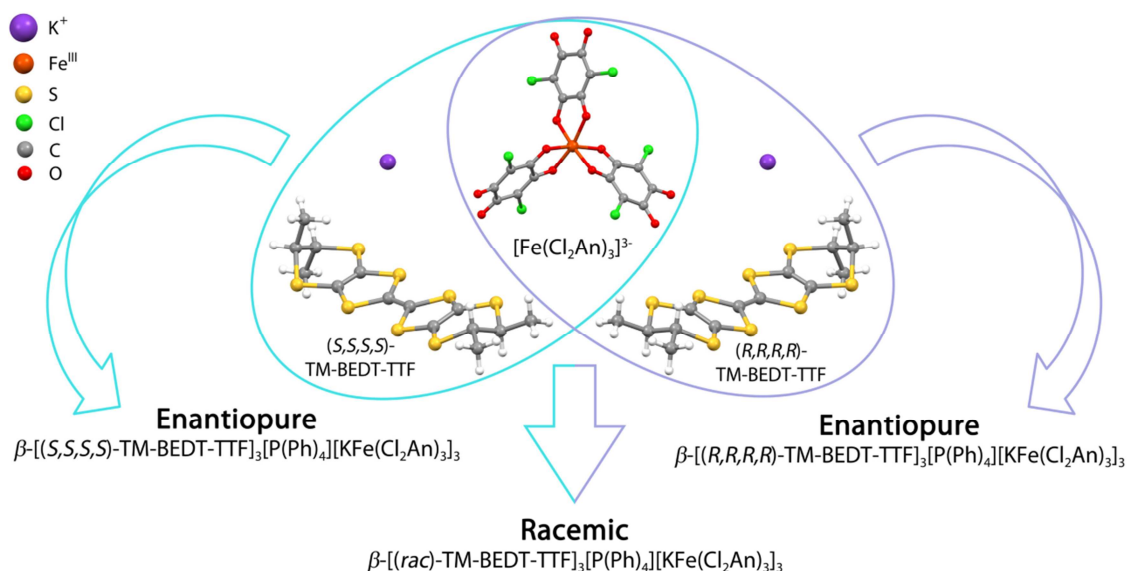
With the aim to explore the potential of both anilate-based molecular building blocks and chiral TTF derivatives in the construction of π -*d* multifunctional materials where chirality can influence the conducting/magnetic properties, the tris(chloranilato)ferrate(III) [Fe(Cl₂An)₃]³⁻ complex anion has been combined, in the presence of potassium cations, with the TM-BEDT-TTF organic donor as (*S,S,S,S*) and (*R,R,R,R*) enantiopure forms or as racemic mixture (*rac*). A complete series of chiral hybrid systems, formulated as β -[TM-BEDT-TTF]₃[P(Ph)₄][K^{III}Fe^{III}(Cl₂An)₃] \cdot 3H₂O have been obtained, representing the first family of chiral radical cation salts with chloranilate-bridged heterobimetallic honeycomb layers. Their synthesis, crystal structures, physical properties, and tight-binding band structure calculations

are thoroughly investigated in this Chapter along with the correlation between the crystal structure and the conducting behavior.

5.2 Results and Discussion

5.2.1 Synthetic Strategy

Electrocrystallization of enantiopure (*S,S,S,S*)-, (*R,R,R,R*)- or (*rac*)-TM-BEDT-TTF, the latter obtained by mixing equimolar amounts of pure enantiomers, in the presence of potassium cations and the tris(chloranilato)ferrate(III) $[\text{Fe}(\text{Cl}_2\text{An})_3]^{3-}$ paramagnetic chiral anion (**C2**) afforded a complete series of isostructural radical cation salts formulated as β - $[(S,S,S,S)\text{-TM-BEDT-TTF}]_3[\text{P}(\text{Ph})_4][\text{KFe}^{\text{III}}(\text{Cl}_2\text{An})_3] \cdot 3\text{H}_2\text{O}$ (**H4**), β - $[(R,R,R,R)\text{-TM-BEDT-TTF}]_3[\text{P}(\text{Ph})_4][\text{KFe}^{\text{III}}(\text{Cl}_2\text{An})_3] \cdot 3\text{H}_2\text{O}$ (**H5**) and β - $[(rac)\text{-TM-BEDT-TTF}]_3[\text{P}(\text{Ph})_4][\text{KFe}^{\text{III}}(\text{Cl}_2\text{An})_3] \cdot 3\text{H}_2\text{O}$ (**H6**) (Scheme 5.1).



Scheme 5.1, Graphical representation of $[\text{Fe}(\text{Cl}_2\text{An})_3]^{3-}$ (**C2**) and the TM-BEDT-TTF chiral donor (**D4**) combined via electrocrystallization for obtaining the **H4-6** hybrid systems.

The successful synthetic strategy for obtaining these systems consists in combining the so-called “complex-as-ligand” approach with a classical electrocrystallization experiment. More specifically, the tris(chloranilato)ferrate(III) $[\text{Fe}(\text{Cl}_2\text{An})_3]^{3-}$ octahedral complex was used as ligand towards potassium cations, thus affording, in a first step, dianionic 2D heterobimetallic layers, which, subsequently, has combined with oxidized donors and $(\text{Ph})\text{P}^+$ cations to provide a segregated organic-inorganic crystal structure.

5.2.2 Crystal Structure Description

The three hybrid systems **H4-6** are isostructural and present a crystal structure formed by alternating heterobimetallic chloranilate-based honeycomb double-layers and layers of TM-BEDT-TTF radical cations. Compounds **H4** and **H5** crystallize in the non-centrosymmetric triclinic space group *P1* with six crystallographically independent TM-BEDT-TTF chiral donors ((*S,S,S,S*) configuration for **H4** and (*R,R,R,R*) configuration for **H5**), two $[K^I\text{Fe}^{\text{III}}(\text{Cl}_2\text{An})_3]^-$ units, whose metal centers exhibit opposite stereochemical configuration ($[\Lambda\text{-}K^I\Delta\text{-Fe}^{\text{III}}(\text{Cl}_2\text{An})_3]^{2-}$ and $[\Delta\text{-}K^I\Lambda\text{-Fe}^{\text{III}}(\text{Cl}_2\text{An})_3]^{2-}$), and two charge-compensating $(\text{Ph})_4\text{P}^+$ cations in the unit cell. Compound **H6** crystallizes in the centrosymmetric triclinic space group *P-1* and contains half of the content of **H4** and **H5** in the asymmetric unit, since the stereochemically opposite content is generated by the inversion center.

In each system, the Fe^{III} complexes retain the octahedral coordination geometry of the starting building block **C2b**, with the Fe^{III} ion surrounded by six oxygen atoms of three chloranilate chelating ligands. The iron-oxygen bond distances in compounds **H4-6** vary in the 1.987(8)–2.030(5) Å range and are close to those observed for **C2b** and for its BEDT-TTF radical cation salts **H1-3** (Table 5.1). These data are in accordance with a high spin character of the Fe^{III} ions (*vide infra*).

Table 5.1, Fe–O bond distances (Å) for the Fe^{III} complex subunit in compounds **H4-6** compared with the observed values for **C2b** and for its BEDT-TTF radical cation salts **H1-3**.

Bonds	H4	H5	H6	C2b	H1	H2	H3
Fe–O(11)	2.025(8)	2.007(6)	2.009(6)	2.002(6)	1.996(5)	2.008(6)	2.020(6)
Fe–O(21)	2.002(8)	2.045(5)	2.020(6)	2.008(6)	2.002(4)	2.022(6)	2.028(6)
Fe–O(12)	1.994(8)	1.988(5)	2.017(6)	2.001(6)	2.018(4)	2.019(5)	1.994(7)
Fe–O(22)	2.001(7)	2.018(5)	1.999(6)	2.017(6)	1.998(4)	1.999(6)	2.028(6)
Fe–O(13)	2.019(8)	2.030(5)	2.010(6)	2.013(6)	2.026(4)	2.039(6)	2.018(6)
Fe–O(23)	1.987(8)	2.000(5)	2.041(6)	1.999(6)	2.037(4)	2.014(6)	1.989(7)
Fe–O average	2.005(8)	2.014(5)	2.016(6)	2.007	2.013	2.017	2.013

The six peripheral oxygen atoms of each $[\text{Fe}(\text{Cl}_2\text{An})_3]^{3-}$ unit act as additional 1,2-bidentate coordinating sites toward three potassium cations (Figure 5.1a), so that each K^I is coordinated by three different $[\text{Fe}(\text{Cl}_2\text{An})_3]^{3-}$ units in a slightly distorted octahedral coordination geometry (Figure 5.1b).

The potassium-oxygen bond distances in compounds **H4-6**, ranging from 2.259(8) to 2.382(9) Å (Table 5.2), are very short if compared to the sum of the K and O ionic radii (ca. 2.9 Å), or the already observed $K^+\cdots O$ interactions involving potassium cations and mononuclear chloranilate-based complexes (shortest distance of ca. 2.9 Å in a secondary interaction)³² or hydrogen chloranilate (HCl_2An^-) (shortest distance of ca. 2.7 Å in a tri-capped trigonal prismatic geometry).³³

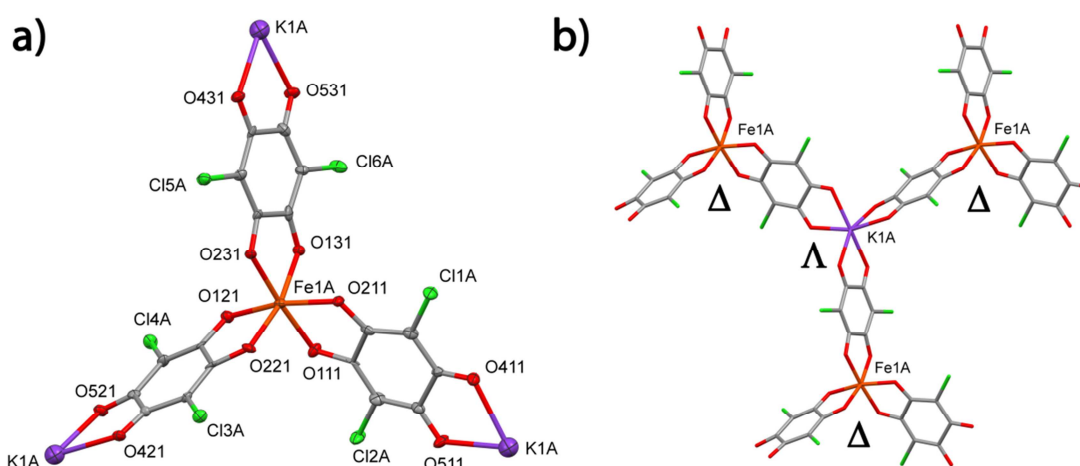


Figure 5.1. a) ORTEP drawing for the tris(chloranilato)ferrate(III) unit (Δ enantiomer) connected to three K^+ cations for **H5** (thermal ellipsoids at the 30% probability level); b) Schematic view of the K^+ cation coordinated by three $[Fe(Cl_2An)_3]^{3-}$ units.

Table 5.2. K–O bond distances (\AA) for compounds **H4–6**.

Bonds	H4	H5	H6
K–O(41)	2.382(9)	2.356(6)	2.338(7)
K–O(51)	2.364(9)	2.346(7)	2.357(7)
K–O(42)	2.408(9)	2.311(7)	2.303(7)
K–O(52)	2.259(8)	2.367(6)	2.392(8)
K–O(43)	2.394(9)	2.372(6)	2.332(7)
K–O(53)	2.347(9)	2.375(7)	2.378(7)
average K–O	2.359(9)	2.354(7)	2.350(7)

It is noteworthy that an octahedral coordination geometry exhibited by an alkali metal ion having anilates as ligands was never observed, whereas coordination geometries with higher coordination numbers are already known.³⁴

The C–O bond distances of the ligand are influenced by the coordination to the metal centers. The oxygen atoms coordinated to the Fe^{III} have C–O distances on average 0.05 \AA longer than those of the oxygen atoms coordinated to the K^+ , which show a major double bond character (Table 5.3).

Table 5.3. C–O bond distances (\AA) for the anionic complex in compounds **H4–6**.

Coordinated Metal	Bonds	H4	H5	H6
Fe^{III}	C(11)–O(11)	1.311(13)	1.310(10)	1.304(10)
	C(21)–O(21)	1.238(17)	1.277(9)	1.291(10)
	C(12)–O(12)	1.242(16)	1.281(10)	1.291(10)
	C(22)–O(22)	1.323(13)	1.292(10)	1.283(10)
	C(13)–O(13)	1.246(18)	1.257(10)	1.289(10)
	C(23)–O(23)	1.312(15)	1.261(9)	1.288(10)
	average C–O	1.278(16)	1.280(10)	1.291(10)

K ^I	C(41)–O(41)	1.254(15)	1.212(10)	1.252(10)
	C(51)–O(51)	1.225(15)	1.245(9)	1.251(10)
	C(42)–O(42)	1.232(15)	1.206(9)	1.217(11)
	C(52)–O(52)	1.274(14)	1.235(9)	1.231(11)
	C(43)–O(43)	1.260(14)	1.226(9)	1.242(10)
	C(53)–O(53)	1.248(16)	1.213(10)	1.219(10)
	average C–O	1.249(15)	1.223(9)	1.235(10)

The Fe^{III} complexes combined with potassium cations in the electrocrystallization medium generate anionic 2D heterobimetallic layers formulated as [K^IFe^{III}(Cl₂An)₃]²⁻, showing the hexagonal honeycomb topology³⁵ where the Fe^{III} and K^I ions, connected through the 1,2-bis-bidentate chloranilate ligand, alternate on the vertexes of a hexagon (Figure 5.2), as already observed in the analogues heterometallic systems reported in Chapter 3.

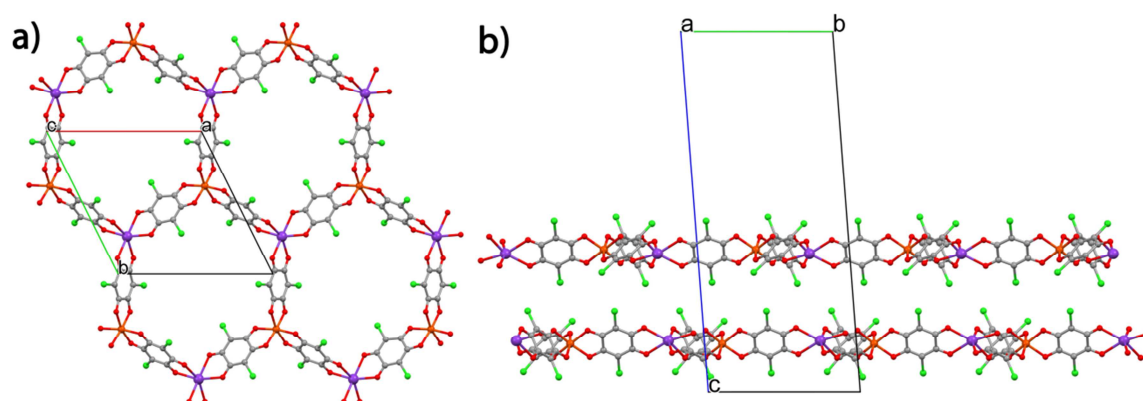


Figure 5.2. a) Top view of the 2D anionic layers parallel to the *ab* plane showing the connection and alternation of Fe^{III} and K^I ions through the chloranilate ligand; b) Side view of the 2D anionic layers.

It should be highlighted that in each layer, all the [Fe(Cl₂An)₃]³⁻ units have the same stereochemical configuration and, consequently, the K^I centers have the opposite one (e.g. [Δ -Fe^{III} Λ -K^I(Cl₂An)₃]²⁻ or *vice versa*) (Figure 5.1b and Figure S5.1).

Another peculiarity of the structure of these salts is the double-layers association of the heterobimetallic coordination polymers. This is likely due to the establishment of two predominant intermolecular interactions: Cl...Cl interactions lower than the sum of the van der Waals radii (3.50 Å) between the chlorine atoms on the ligands of adjacent layers, and π - π stacking interactions between the chloranilate ligands and the phenyl rings of the (Ph)₄P⁺ molecules that are present between the layers as charge-compensating cations (Figure 5.3).

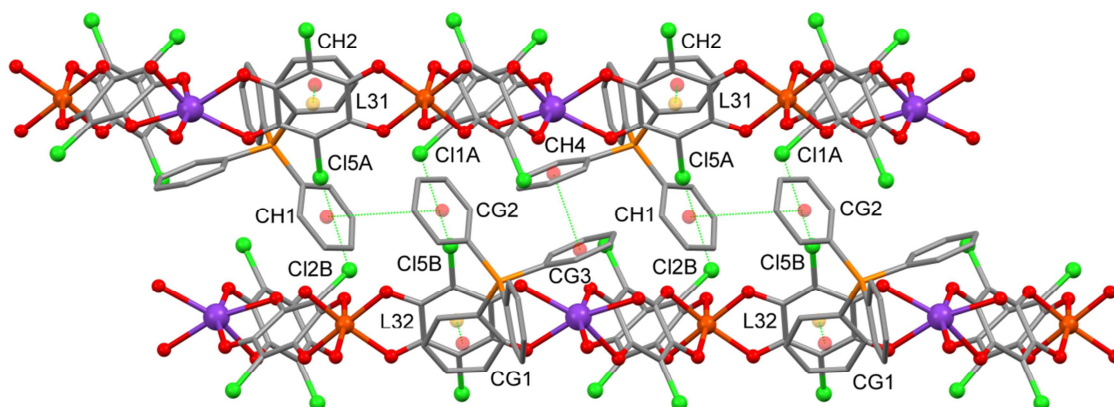


Figure 5.3, Side view of the inorganic anionic layers arranged in double-layers due to the establishment of intermolecular non-covalent interactions. Selected short contacts (Å): Cl(5A)···Cl(2B) 3.42, Cl(1A)···Cl(5B) 3.42, CH1···CG2 4.54, CH4···CG3 6.24, L31···CH2 4.00, L32···CG1 3.85. Legend: CH1, CH2, CG1, CG2 indicate calculated centroids on phenyl rings CXH1, CXH2, CXG1, CXG2 (X = 1-6), respectively; L31, L32 indicate calculated centroids on chloranilate rings CX31 and CX32 (X = 1-6), respectively.

It should be highlighted that the Cl···Cl interactions (Cl(5A)···Cl(2B) 3.42 Å, Cl(1A)···Cl(5B) 3.42 Å) directly connect two adjacent layers, whereas those mediated by the $(\text{Ph})_4\text{P}^+$ cations involve multiple π - π stacking interactions either between the chloranilate ligand and the phenyl rings (L31···CH2 4.00 Å, L32···CG1 3.85 Å) or between phenyl rings of adjacent $(\text{Ph})_4\text{P}^+$ molecules (CH1···CG2 4.54 Å, CH4···CG3 6.24 Å), as already observed in other supramolecular architectures involving tris(anilate)metallate(III) complexes and $(\text{Ph})_4\text{P}^+$ cations (see Chapter 2, Section 2.2.2). These interactions force the anionic layers in an alternate disposition (Figure 5.4) instead of an eclipsed one (see Chapter 3, Section 3.2.2).

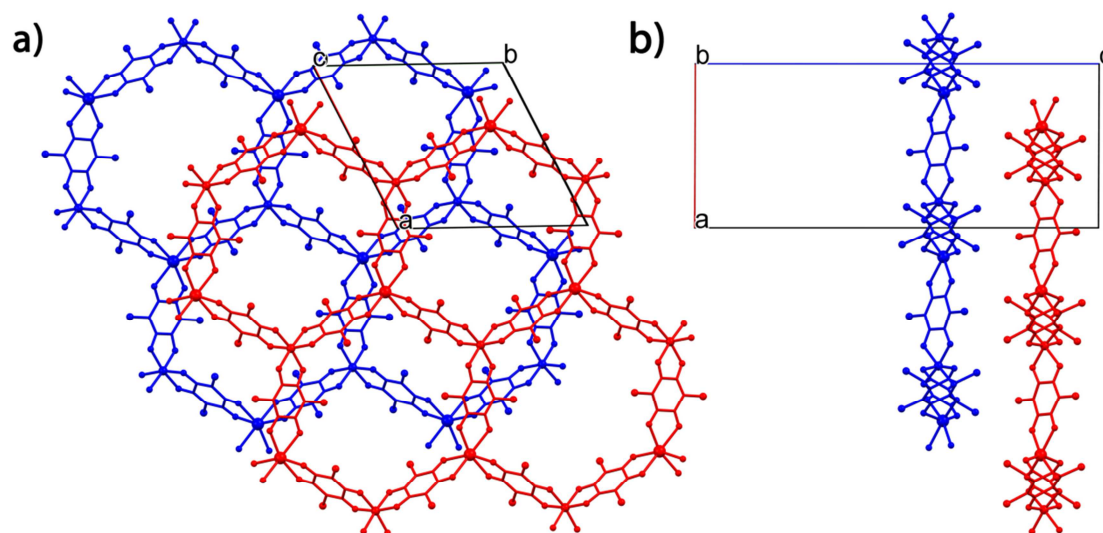


Figure 5.4, a) Top view of the 2D anionic layers parallel to the ab plane showing the anionic double-layers in the alternate disposition; b) Side view of the layers. $(\text{Ph})_4\text{P}^+$ cations and crystallization water molecules between the layers are omitted for clarity.

In the crystal structure of compounds **H4-6**, these inorganic layers alternate with cationic layers formed by the chiral donor TM-BEDT-TTF ((*S,S,S,S*)-enantiomer for **H4**, (*R,R,R,R*)-enantiomer for **H5**, and their racemic mixture for **H6**) (Figure 5.5).

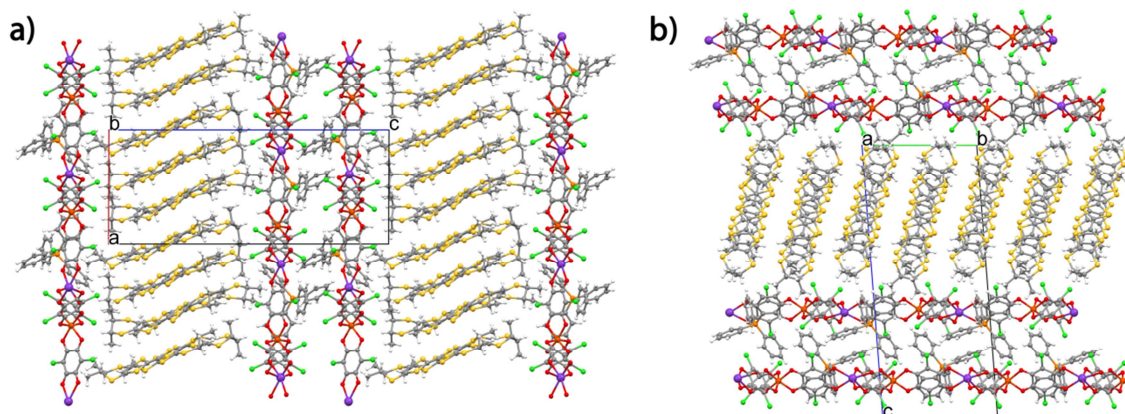


Figure 5.5. Crystal packing of **H5** a) in the *ac* plane, and b) in the *bc* plane, showing the organic–inorganic layer segregation. Crystallization water molecules are omitted for clarity.

The organic layer shows **A–F** donor molecules arranged in the classical β -phase packing motif,³⁶ alternating along *a* in a **-B-E-C-** and a **-A-D-F-** sequence (Figure 5.6).

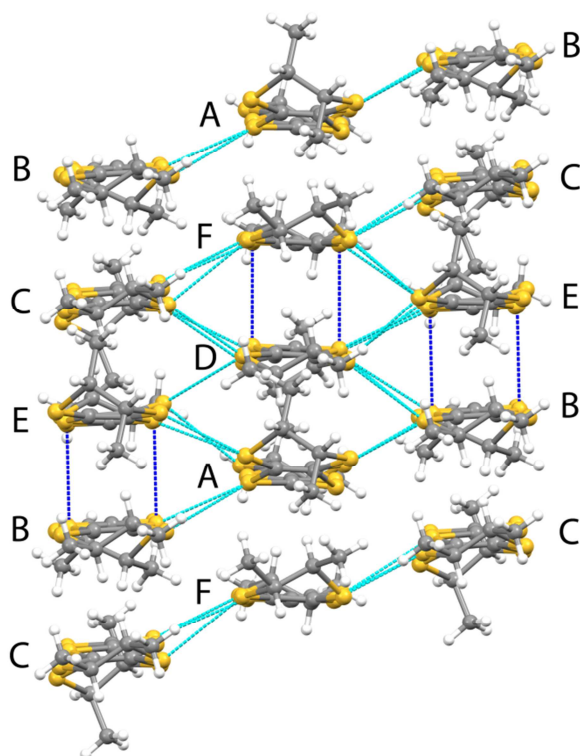
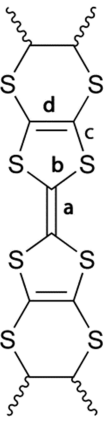


Figure 5.6. View of the TM-BEDT-TTF packing of **H5** along the *ab* plane where the short intermolecular S...S contacts are highlighted. Some short contacts (Å): S(3F)...S(5D) 3.57, S(4F)...S(6D) 3.62, S(3E)...S(5B) 3.58, S(4E)...S(6B) 3.57, S(1F)...S(4C) 3.67, S(4C)...S(3F) 3.66, S(1D)...S(2C) 3.55, S(2C)...S(3D) 3.52, S(7F)...S(8C) 3.66, S(8D)...S(7D) 3.48, S(7D)...S(2E) 3.65, S(1B)...S(2D) 3.44, S(7E)...S(8F) 3.41.

The analysis of the S...S short contacts reveals that lateral interstack interactions between donor molecules (represented in light blue in Figure 5.6) in the 3.41–3.66 Å range, are, on average, shorter than the intrastack ones, of 3.57–3.62 Å (represented in blue in Figure 5.6). Note that no S...S interactions lower than the sum of the van der Waals radii (ca. 3.70 Å) are observed between **BC** and **AF** molecules (3.90–4.03 Å), so that the organic layer can be considered divided in three molecules height sublayers.

The analysis of the central C=C and internal C–S bond lengths for each crystallographically independent molecule for **H5** (Table 5.3),³⁷ indicates that **B**, **D**, **E** and **F** molecules bear a more positive charge than **A** and **C**, in agreement with their planar or bent shapes (Figure S5.2).

Table 5.3, Bond distances analysis and selected bond distances (Å) for the TM-BEDT-TTF donor molecules in **H5**.

	A	B	C	D	E	F	
	a	1.337(13)	1.354(12)	1.335(11)	1.370(12)	1.380(12)	1.367(12)
		1.765(8)	1.769(9)	1.780(6)	1.776(8)	1.770(7)	1.753(8)
	b	1.763(9)	1.700(10)	1.749(6)	1.753(9)	1.727(8)	1.748(9)
		1.784(9)	1.737(9)	1.762(8)	1.743(8)	1.758(7)	1.813(8)
		1.737(8)	1.744(8)	1.728(8)	1.736(9)	1.725(7)	1.711(7)
		1.790(7)	1.789(10)	1.722(8)	1.834(6)	1.724(8)	1.730(8)
	c	1.796(6)	1.765(7)	1.774(7)	1.785(6)	1.741(6)	1.724(8)
		1.769(7)	1.753(8)	1.774(6)	1.749(8)	1.782(6)	1.749(9)
		1.716(7)	1.771(8)	1.791(7)	1.751(6)	1.806(9)	1.732(9)
	d	1.269(12)	1.316(12)	1.347(11)	1.306(11)	1.394(13)	1.328(12)
		1.363(12)	1.400(11)	1.319(13)	1.413(13)	1.321(12)	1.400(14)
$\delta = (b+c)-(a+d)$	δ	0.877	0.795	0.852	0.802	0.771	0.759
$Q = 6.347 - 7.4638 \cdot \delta$	Q	0.0(1)	0.4(1)	0.0(1)	0.4(1)	0.6(1)	0.7(1)

The structural features reported for **H5** ((*R,R,R,R*)-enantiomer) are also valid for **H4** ((*S,S,S,S*)-enantiomer) (Table S5.1) and **H6** (racemic form) (Table S5.2). The only difference for the racemic system **H6**, when compared with **H4** and **H5**, consists in the presence of an **-A-C-B-** sequence of 2:1 alternate (*S,S,S,S*)- and (*R,R,R,R*)-TM-BEDT-TTF donors in the organic layer (Figure S5.3). The S...S interstack (3.40–3.66 Å) and intrastack (3.59–3.60 Å) contacts (represented in light blue and blue, respectively in Figure S5.3) have similar values to those of **H4** and **H5**.

Interestingly, in the crystal packing of the organic layer, the pairs of molecules where no S...S contacts lower than the sum of the van der Waals radii were observed, *i.e.* **BC** and **AF**, always involve a less positive charged molecule (**A** or **C**) (Figure 5.6). This can be likely responsible for the weaker intermolecular interactions observed between such sublayers.

It is noteworthy that the TM-BEDT-TTF organic donor in compounds **H4-6** adopts two different conformations in the crystal packing. Two donor molecules per formula unit present the usual all-equatorial (eq) conformation for the four terminal methyl groups (Figure 5.7), encountered in most of the radical cation salts of this donor,^{21,22,23} and also in its neutral form,²³

although this conformer is slightly less stable in the gas phase than the all-axial (ax) one.²³ Note that the later was also described in the solid state.²² The other four donor molecules per formula unit present, instead, an unusual mixed conformation where methyl groups adopt eq orientations on one ethylene bridge, but ax orientations on the other ethylene bridge (Figure 5.7).

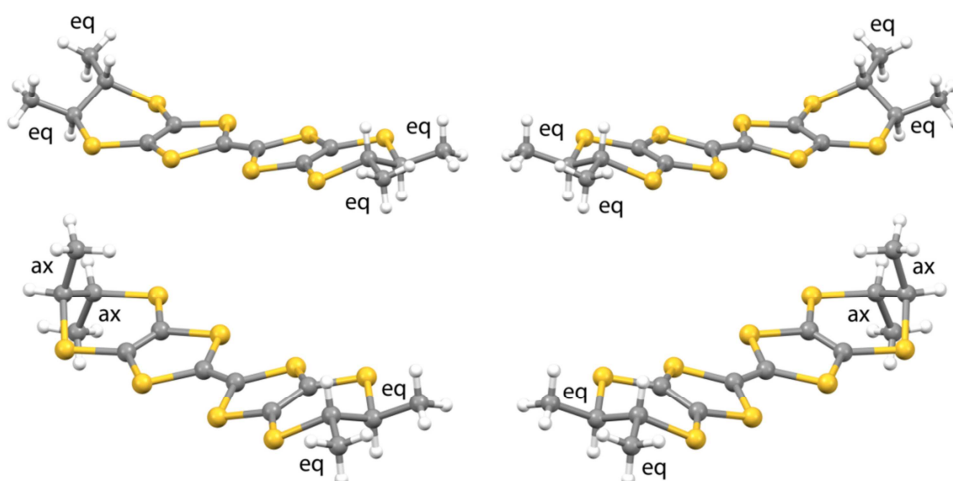


Figure 5.7, Molecular structure of the TM-BEDT-TTF organic donor in the all-eq conformation (top left (*S,S,S,S*) enantiomer, top right (*R,R,R,R*) enantiomer) and in the mixed (ax,ax,eq,eq) conformation (bottom left (*S,S,S,S*) enantiomer, bottom right (*R,R,R,R*) enantiomer).

This (ax,ax,eq,eq) mixed conformation of the TM-BEDT-TTF was recently observed for some charge transfer salts of the (*S,S,S,S*)-enantiomer with TCNQ.³⁸

Finally, it should be pointed out which interactions are involved between the inorganic and organic layers. The position of the TM-BEDT-TTF donor molecules in the organic layers with respect to the vertexes of the hexagons occupied by alternate Fe^{III}/K^I metal centers is strongly determined by the hexagonal symmetry of the honeycomb inorganic layers (Figure 5.8 and S5.4).

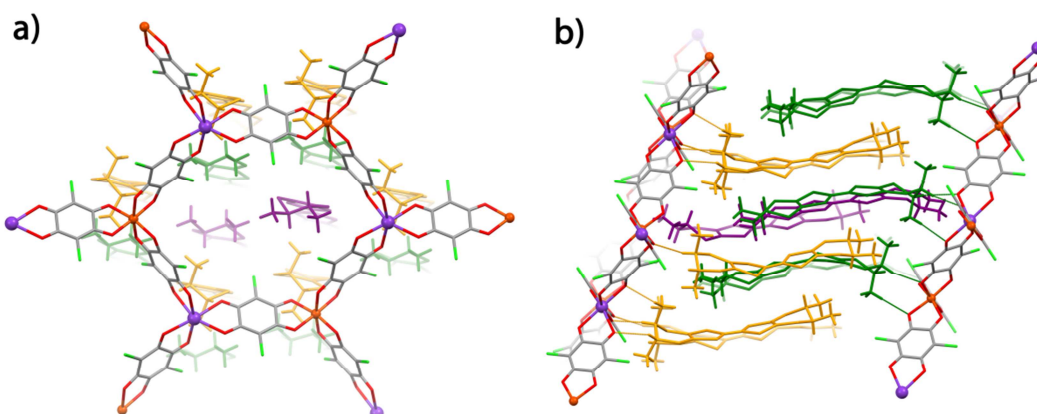


Figure 5.8, a) Top view of the 2D anionic layers parallel to the *ab* plane of **H5** showing the specific position of the TM-BEDT-TTF organic donors with respect to the vertexes of the hexagons occupied by alternate metal centers; b) Side view of the layers showing the short C–H...O contacts.

For each pair of hexagons encompassing the organic layers, six donor molecules showing (ax,ax,eq,eq) conformation (represented in yellow in Figure 5.8) interact with the coordinated oxygen atoms of the same inorganic layer through short C–H...O contacts (2.20–2.66 Å) involving their axial methyl groups and the equatorial C–H of the ethylene bridge (Figure 5.8). Other six donor molecules having the same conformation (represented in green in Figure 5.8) interact, in the same way, with oxygen atoms of the inorganic layer located on the other side of the organic layer (Figure 5.8). Two donor molecules having the all-ax conformation (represented in purple in Figure 5.8) occupy, instead, the centre of the hexagon without interacting with the complexes. Thus, it is clear that the chloranilate-based honeycomb layers strongly influence the disposition and conformation of the organic donors in the crystal structure, which, in turn, ultimately influence the resulting physical properties.

5.2.3 Conducting Properties

The two points conductivity measurements for compounds **H4** and **H6** show r.t. conductivity values of ca. $3 \times 10^{-4} \text{ S cm}^{-1}$ that decrease in a semiconducting way as the samples are cooled (Figure 5.9). The Arrhenius plot, $\ln(\rho)$ vs $1/T$ (inset in Figure 5.9) shows a linear behavior that can be fitted to the law $\ln(\rho) = \ln(\rho_0) + E_a/kT$ with an activation energy E_a of ca. 1300–1400 K corresponding to ca. 110–120 meV.

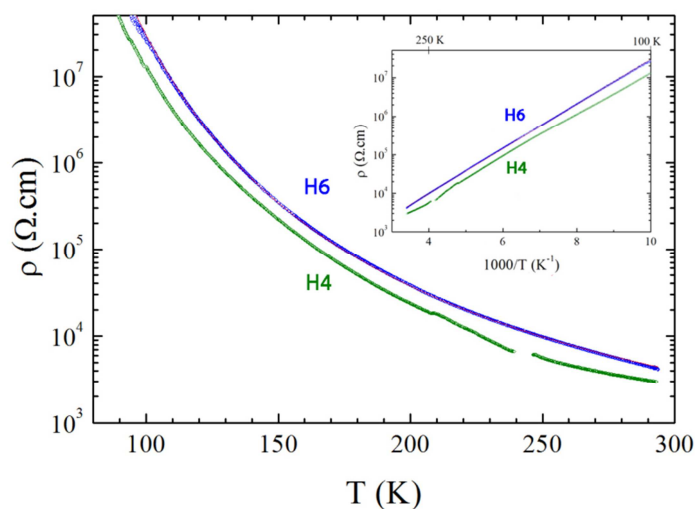


Figure 5.9. Thermal variation of the electrical resistivity for compounds **H4** and **H6**. Inset shows the Arrhenius plot. The red line is the Arrhenius fit to the data for compound **H6**.

This behavior indicates that compounds **H4-6** are semiconductors with low r.t. conductivity and a medium value of activation energy. No significant difference between the enantiopure and the racemic systems is observed. These results are in agreement with the structural data showing the presence of a neutral TM-BEDT-TTF molecule out of three in the crystal packing, thus precluding an efficient charge delocalization along the organic layers, and also with the band structure calculations (*vide infra*).

5.2.4 Band Structure Calculations

In order to get insight on the origin of the activated conductivity of these systems, band structure calculations were performed on compound **H4**. The repeating unit of the donor layers of **H4** contains six crystallographically independent donor molecules with an average charge of +1/3. Consequently, the calculated band structure near the Fermi level for this salt contains six bands mostly based on the HOMOs of the different TM-BEDT-TTF donors (Figure 5.10). Because of the stoichiometry, these bands must contain two holes so that the equivalent of one of these bands must be empty. Since there is a band gap separating the upper band from the lower ones, the upper band is completely empty. This salt is thus predicted to be a regular (band gap) semiconductor in agreement with the transport measurements.

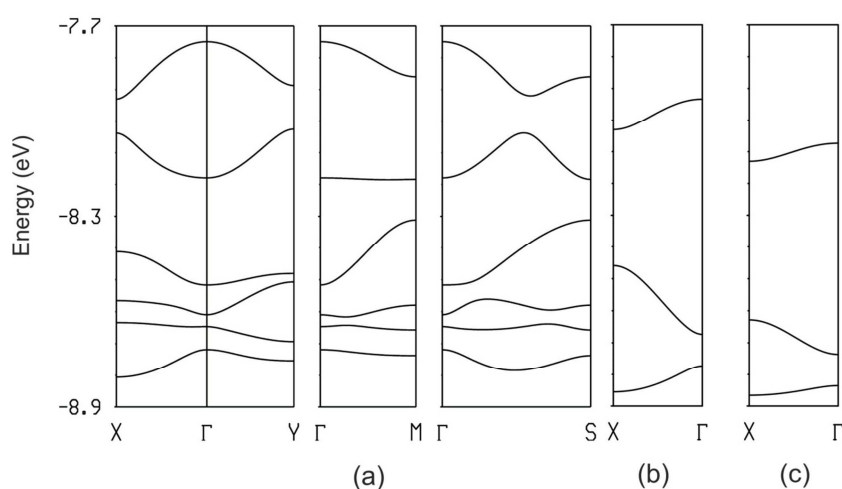


Figure 5.10, Electronic structure for **H4**. Calculated band structure of: (a) the $[(\text{TM-BEDT-TTF})_6]^{2+}$ donor layers, (b) the isolated **-B-E-C-** chains and (c) the isolated **-A-D-F-** chains, where $\Gamma = (0, 0)$, $X = (a^*/2, 0)$, $Y = (0, b^*/2)$, $M = (a^*/2, b^*/2)$ and $S = (-a^*/2, b^*/2)$.

The donor layers of **H4** can be described as a series of parallel stacks along the a -direction; they contain six different donors (labeled **A**, **B**, ..., **F**) and there are eighteen different types of interactions between the HOMOs of these molecules (labeled I, II, ..., XVIII) (Figure 5.11). The HOMO energies of the six donors are found within a relatively broad energy range: -8.806 eV (**A**), -8.698 eV (**C**), -8.660 eV (**D**), -8.528 eV (**E**), -8.514 eV (**F**) and -8.478 eV (**B**). There are three donors (**B**, **E** and **F**) with relatively high energy HOMOs but only two holes to be placed in the upper HOMO band. It is thus not clear where these holes are located, so that they will be most likely delocalized.

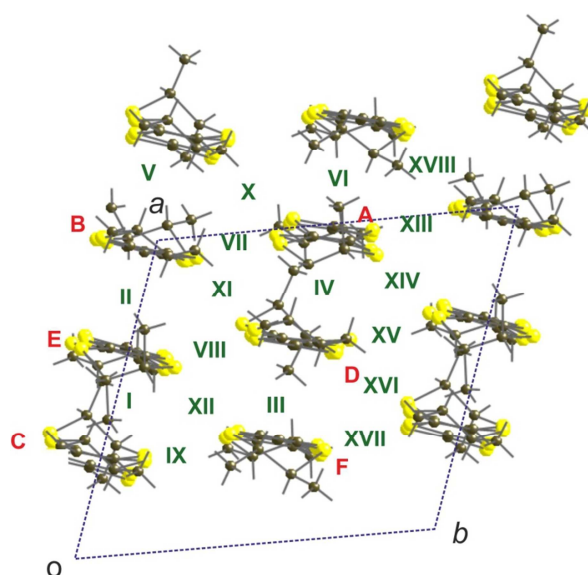


Figure 5.11, Donor layer of **H4** where the six different donors and eighteen different HOMO...HOMO interactions are shown.

To explain what is the origin of the activated conductivity in these compounds, it is essential have an idea of the strength of the different HOMO...HOMO interactions in the donor layers. The eighteen interactions in Figure 5.11 can be classified into three different classes: (a) interactions within the stacks along the *a*-direction (I, II, ...,VI), (b) lateral interactions along the *b*-direction (VII, VIII, IX, XIII, XV, and XVII) mostly of π -type, and (c) interactions along the step-chains **-B-D-C-A-E-C-** (X, XI, XII, XIV, XVI, and XVIII). The strength of these HOMO...HOMO interactions may be quantified from the absolute value of the HOMO...HOMO interaction energy, $|\beta_{\text{HOMO-HOMO}}|$, associated with each interaction.³⁹ The calculated values for the eighteen interactions are reported in Table 5.4.

Table 5.4, $|\beta_{\text{HOMO-HOMO}}|$ interaction energies (eV) for the donor...donor interactions defined in Figure 5.11.

Interaction	$ \beta_{\text{HOMO-HOMO}} $	Interaction	$ \beta_{\text{HOMO-HOMO}} $
I (E-C)	0.2178	II (E-B)	0.5355
III (D-F)	0.4783	IV (A-D)	0.1231
V (B-C)	0.3684	VI (A-F)	0.3054
VII (B-A)	0.0022	VIII (E-D)	0.0138
IX (C-F)	0.0028	X (A-C)	0.0918
XI (B-D)	0.1163	XII (E-F)	0.0910
XIII (A-B)	0.0004	XIV (A-E)	0.0911
XV (D-E)	0.0154	XVI (D-C)	0.0714
XVII (C-F)	0.0143	XVIII (B-F)	0.8710

Consideration of these results lead to the following observations. First, the interactions along the stacks in the *a*-direction are by far the stronger ones. Second, the lateral π -type interactions along the *b*-direction are negligible. Third, the interactions along the step-chains are quite sizeable even if weaker than those along the stacks. Consequently, as far as the HOMO...HOMO interactions are concerned, the donor layers of the present salt should be described as a series of substantially coupled parallel stacks along *a*.

Thus, a useful way to understand the electronic features of the donor layers is to consider the two different chains as the building blocks. The calculated band structures for the isolated **-B-E-C-** and **-A-D-F-** chains are shown in Figure 5.10b and Figure 5.10c, respectively. In both cases the upper band is strongly separated from the two lower ones. The upper well-separated bands mostly originate from the antibonding combination of the HOMOs of donors **B** and **E** (Figure 5.10b) and the antibonding combination of the HOMOs of donors **D** and **F** (Figure 5.10c), because II (**B-E**) and III (**D-F**) are by far the stronger interactions within each chain. Since all interactions are stronger for the **-B-E-C-** chain, the upper band of this chain is the highest in energy. When the interactions along the step-chains are switched on, the bands of the isolated chains communicate and acquire additional dispersion both along the chain and interchain directions. However, the initial separation and the strength of the interactions are larger enough to ensure that the two bands remain well separated all along the Brillouin zone. If the two chains had been more similar in terms of the strength of the HOMO...HOMO interactions, it is quite possible that a semimetallic type overlap of the two bands had occurred and the conductivity could have been non-activated.

With these results in mind we have analyzed the composition of the upper empty bands in Figure 5.10. We have found that the upper band is delocalized among the two different chains though more strongly based on the **-B-E-C-** one: around three-quarters of the electron density associated with this band originates from the levels of the **-B-E-C-** chains and one-quarter from the levels of the **-A-D-F-** chains. However, the participation of the donors of a given chain is very different: 67% of the electron density originates from the **BE** dimer, 7% from donor **C**, 23% from the **DF** dimer and 3% from donor **A**. Thus, two of the donors, **A** and **C**, have a very small participation in this band and can be considered as essentially neutral, in agreement with the structural findings. All these results are in agreement with the previous analysis. Thus the picture emerging from this study is that the two holes in the band structure are delocalized among the antibonding combination of the HOMO levels of both the **BE** and **DF** dimers, which are coupled through the interactions along the step-chains (depicted in blue in Figure 5.6), although with a larger weight in the **BE** dimers. The composition of the upper filled band in Figure 5.10a is the counterpart of the upper empty band, *i.e.* it is delocalized between the antibonding combination of the HOMO levels of both the **BE** and **DF** dimers but with a larger weight on the **DF** dimers.

The transport in an intrinsic semiconducting way is due to the holes created in the upper filled band and the electrons filling the lower empty band because of the thermal excitation. Thus the conductivity carriers in this salt are both delocalized among the two types of dimers of the layer (though the holes and electrons are more strongly tight to the **DF** and **BE** dimers, respectively) whereas donors **A** and **C** practically do not contribute to the conductivity.

Given the similar conductivity behavior, electrical conductivity at room temperature, and activation energy values for the three components of this series, along with their isostructurality, the band structure calculation and the explanation of the origin of the activated conductivity for **H4** can be reasonably extended to **H5** and **H6**.

5.2.5 Magnetic Properties

The temperature dependence of the magnetic susceptibility for **H6** is shown in Figure 5.12 as a $\chi_m T$ vs T plot. The $\chi_m T$ value at r.t. of ca. $4.4 \text{ cm}^3 \text{ K mol}^{-1}$ is close to the expected value ($4.375 \text{ cm}^3 \text{ mol}^{-1} \text{ K}$) for isolated high spin Fe^{III} centres ($S = 5/2, g = 2$). This value remains constant down to ca. 20 K, then the $\chi_m T$ product decreases slightly to $4.3 \text{ cm}^3 \text{ K mol}^{-1}$ at 1.85 K. The observed behavior in the high temperature region ($T > 20 \text{ K}$) is typical of magnetically isolated $S = 5/2$ ions, whereas the observed decrease at low temperature is likely due to weak antiferromagnetic interactions between the isotropic Fe^{III} magnetic sites. On the basis of the crystal structure (*vide supra*), which highlights the presence of Fe^{III} ions connected through chloranilate bridging ligands but separated by diamagnetic K^{I} ions, the magnetic data have been modelled in the frame of the mean-field approximation using the well-known Curie-Weiss law.

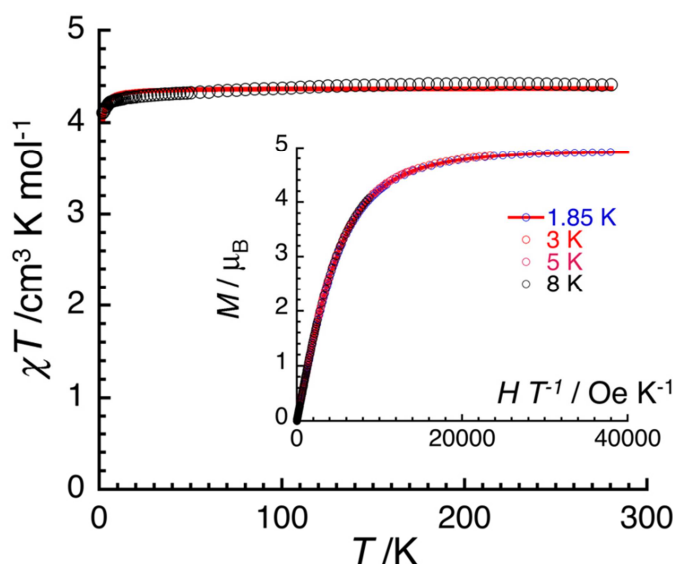


Figure 5.12. Temperature dependence of $\chi_m T$ product at 1000 Oe between 1.85 and 280 K for a polycrystalline sample of **H6**. The solid line is the best fit obtained using the Curie-Weiss law. Inset: Field dependence of the magnetization for **H6** between 1.85 and 8 K at magnetic fields between 0 and 7 T. The solid line is the best fit obtained using $S = 5/2$ Brillouin function.

This model satisfactorily reproduces the magnetic properties of compound **H6** in the whole temperature range, with $g = 2.01(5)$ and $zJ/k_B = -84 \text{ mK}$. The magnitude of the magnetic interactions of the order of a few mK falls well in the range expected for dipolar magnetic interactions. The field dependence of the magnetization below 8 K supports the $S = 5/2$ ground spin state of the Fe^{III} ions for **H6** since a Brillouin function for an $S = 5/2$ spin state reproduces well the experimental data with $g = 1.99(2)$ (Inset in Figure 5.12). Thus, compound **H6** exhibits a high spin configuration for the Fe^{III} ions with a $S = 5/2$ ground spin state and shows a typical paramagnetic behaviour of quasi-isolated ions, since the $\text{M}\cdots\text{M}$ distances between paramagnetic metal centers (ca. 13.6 \AA through-space and ca. 16.2 \AA through the bridging ligands) are too large to permit significant magnetic interactions.

As far as the contribution of the TM-BEDT-TTF donors is concerned, the expected contribution of the paramagnetic radical cations is not well visible in the $\chi_m T$ vs T plot. A slight decrease of the $\chi_m T$ value associated to the Fe^{III} contribution is observed in the whole temperature range, indicating that the contribution of the donors seems mainly hidden. This is not surprising given the +1/2 charge of two out of three donor molecules per formula unit, *i.e.* half unpaired delocalized electron per partially oxidized donor molecule, when compared to the $S = 5/2$ contribution of the Fe^{III} centers, *i.e.* five unpaired localized electrons per ion. However, the structural analysis reveals the presence of short contacts between pairs of charged donor molecules (**BE** and **DF**) (depicted in blue in Figure 5.6) that can be at the origin of an antiferromagnetic coupling. Therefore, it seems reasonable to consider the unpaired delocalized electrons of the organic donors as antiferromagnetically coupled in the whole temperature range, in order to explain their low contribution to the overall magnetic susceptibility of this system. The establishment of strong contacts between **BE** and **DF** molecules pairs is further confirmed by the band structure calculations that predict a partial degree of dimerization for the electrons of these molecules.

5.3 Conclusions

A complete series of isostructural crystalline mixed valence radical cation salts based on the TM-BEDT-TTF chiral donor and chloranilate-bridged heterobimetallic honeycomb layers were prepared *via* electrocrystallization. The use of the “complex-as-ligand” approach during an electrocrystallization experiment has been successful for obtaining these systems where the self-assembling of the tris(chloranilato)ferrate(III) anion with potassium cations afforded 2D anionic layers, that further template the structure in segregated organic and inorganic layers. As a common structural feature for the three systems one can disclose the presence of inorganic layers associated in double-layers, as a result of two major intermolecular interactions, Cl...Cl and π - π stacking interactions between the chloranilate ligands and the $(\text{Ph})_4\text{P}^+$ charge-compensating cations, and the simultaneous presence of two different conformations of the TM-BEDT-TTF donor in the crystal packing, very likely due to the diverse interactions of the terminal methyl groups with the oxygen atoms of the chloranilate ligands. The structural analyses and band structure calculations are in agreement with the single crystal conductivity measurements showing semiconducting behavior for the three materials, with low r.t. conductivity and a medium value of the activation energy, as expected from the presence of one neutral TM-BEDT-TTF donor in the crystal packing and the presence of a slight dimerization of the partially oxidized molecules. Magnetic susceptibility measurements for **H6** indicate the presence of isolated high spin $S = 5/2$ Fe^{III} ions, with a very low contribution at high temperatures from the TM-BEDT-TTF radical cations. This first family of isostructural chiral conducting radical cation salts based on magnetic chloranilate-bridged heterobimetallic honeycomb layers demonstrates the versatility of these anions for the preparation of π - d multifunctional molecular materials where properties such as charge transport, magnetism and chirality coexist in the same crystal lattice. Currently, a topic of special interest is to include chiral donors within the ferrimagnetic anionic layers presented in Chapter 3 with the aim to

further investigate the potential of these building blocks in the preparation of new multifunctional materials with improved physical properties.

5.4 Experimental

5.4.1 General Remarks

(*S,S,S,S*)-TM-BEDT-TTF and (*R,R,R,R*)-TM-BEDT-TTF were synthesized according to the literature procedures.^{19,20} Crystals were grown by the electrocrystallization technique (see Appendix 3).⁴⁰⁻⁴² Solvents used for electrocrystallization experiments (HPLC grade) were dried under basic alumina and degassed with argon prior to use.

5.4.2 Synthesis

β [(*S,S,S,S*)-TM-BEDT-TTF]₃[P(Ph)₄][K^IFe^{III}(Cl₂An)₃·3H₂O (H4). C2b (8 mg) was dissolved in 7 mL of CH₃CN and placed in the cathode chamber of an H-shape electrocrystallization cell together with 2 mg of KCl. (*S,S,S,S*)-TM-BEDT-TTF (3 mg) was dissolved in 7 mL of CH₃CN and placed in the anode chamber of the cell. A current density of 1.0 $\mu\text{A cm}^{-2}$ was applied. Black prismatic single crystals of **H4** were grown at 20 °C on the anode surface of a platinum wire electrode over 2 weeks.

β [(*R,R,R,R*)-TM-BEDT-TTF]₃[P(Ph)₄][K^IFe^{III}(Cl₂An)₃·3H₂O (H5). C2b (8 mg) was dissolved in 7 mL of CH₃CN and placed in the cathode chamber of an H-shape electrocrystallization cell together with 2 mg of KCl. (*R,R,R,R*)-TM-BEDT-TTF (3 mg) was dissolved in 7 mL of CH₃CN and placed in the anode chamber of the cell. A current density of 1.0 $\mu\text{A cm}^{-2}$ was applied. Black prismatic single crystals of **H5** were grown at 20 °C on the anode surface of a platinum wire electrode over 2 weeks.

β [(*rac*)-TM-BEDT-TTF]₃[P(Ph)₄][K^IFe^{III}(Cl₂An)₃·3H₂O (H6). C2b (8 mg) was dissolved in 7 mL of CH₃CN and placed in the cathode chamber of an H-shape electrocrystallization cell together with 2 mg of KCl. (*rac*)-TM-BEDT-TTF (3 mg), obtained by mixing 1.5 mg of (*S,S,S,S*)-TM-BEDT-TTF and 1.5 mg of (*R,R,R,R*)-TM-BEDT-TTF, was dissolved in 7 mL of CH₃CN and placed in the anode chamber of the cell. A current density of 1.0 $\mu\text{A cm}^{-2}$ was applied. Black elongated prismatic single crystals of **H6** were grown at 20 °C on the anode surface of a platinum wire electrode over 1 week.

5.4.3 Equipment and Measurements Details

Single Crystal X-Ray Crystallography. X-ray diffraction measurements were performed on a Nonius Kappa CCD diffractometer, using graphite-monochromated MoK α radiation ($\lambda = 0.71073 \text{ \AA}$). The structures were solved by direct methods (SHELXS-97) and refined on F^2 with full-matrix least squares (SHELXL-97),⁴³ using the Wingx software package.⁴⁴ The non-H atoms were refined with anisotropic displacement parameters. The crystallization water molecules were refined without the hydrogen atoms. A summary of the crystallographic data and the structure refinement for **H4-6** is reported in Table 5.5.

Table 5.5. Summary of X-ray crystallographic data for **H4**, **H5**, and **H6**.

	H4	H5	H6
Empirical formula	C ₁₆₈ H ₁₃₆ Cl ₁₂ Fe ₂ K ₂ O ₃₀ P ₂ S ₄₈	C ₁₆₈ H ₁₃₆ Cl ₁₂ Fe ₂ K ₂ O ₃₀ P ₂ S ₄₈	C ₈₄ H ₆₈ Cl ₆ FeKO ₁₅ PS ₂₄
Formula weight	4850.89	4850.89	2417.44
Crystal size, mm	0.50 × 0.27 × 0.04	0.60 × 0.60 × 0.40	0.11 × 0.06 × 0.02
Crystal system	Triclinic	Triclinic	Triclinic
Space group	<i>P</i> 1	<i>P</i> 1	<i>P</i> -1
<i>a</i> , Å	13.629(1)	13.635(1)	13.598(3)
<i>b</i> , Å	14.174(2)	14.148(2)	14.171(2)
<i>c</i> , Å	30.143(8)	30.122(5)	30.107(7)
α, deg.	85.370(15)	85.210(13)	85.659(12)
β, deg.	88.106(10)	88.033(10)	88.219(17)
γ, deg.	63.346(9)	63.419(8)	63.378(12)
<i>V</i> , Å ³	5187(1)	5178(1)	5172(2)
<i>Z</i>	1	1	2
<i>T</i> , K	150(2)	150(2)	150(2)
ρ (calc), Mg/m ³	1.553	1.556	1.552
μ, mm ⁻¹	0.898	0.899	0.900
θ range, deg.	1.61–26.00	1.61–27.50	1.61–25.25
GooF	1.005	1.032	1.000
Flack Parameter	0.15(4)	0.09(3)	–
<i>R</i> 1	0.0883	0.0742	0.1078
<i>wR</i> 2	0.2118	0.1904	0.2531

$$R1 = \sum ||F_o| - |F_c|| / \sum |F_o|, wR2 = [\sum [w(F_o^2 - F_c^2)^2] / \sum [w(F_o^2)^2]]^{1/2}, w = 1 / [\sigma^2(F_o^2) + (aP)^2 + bP], \text{ where } P = [\max(F_o^2, 0) + 2F_c^2] / 3.$$

Single crystal conductivity measurements. Electrical transport measurements were performed on platelet-shaped single crystals. Gold contacts were evaporated on both faces of the crystals and gold wires (17 μm diameter) were glued with silver paste on those contacts. Two-probe DC measurements were performed applying a constant voltage in the range 0.5–1V and measuring the current using a Keithley 6487 Picoammeter/Voltage Source. Low temperature was provided by a homemade cryostat equipped with a 4K pulse-tube.

Band structure calculations. The tight-binding band structure calculations were of the extended Hückel type.⁴⁵ A modified Wolfsberg-Helmholtz formula was used to calculate the non-diagonal $H_{\mu\nu}$ values.⁴⁶ All valence electrons were taken into account in the calculations and the basis set consisted of Slater-type orbitals of double-ζ quality for C 2s and 2p, S 3s and 3p and of single-ζ quality for H. The ionization potentials, contraction coefficients and exponents were taken from previous work.⁴⁷

Magnetic measurements. The magnetic susceptibility measurements were obtained with the use of MPMS-XL Quantum Design SQUID magnetometer that works between 1.8 and 400 K for DC applied fields ranging from -7 to +7 T. Measurements were performed on a polycrystalline sample of 3.6 mg for **H6**, introduced in a polyethylene sample holder (3 × 0.5 × 0.02 cm). *M* vs *H* measurements have been performed at 100 K to check for the presence of ferromagnetic impurities that has been found absent. The magnetic data were corrected for the sample holder and the diamagnetic contribution.⁴⁸

References

1. Avarvari, N.; Wallis, J. D. *J. Mater. Chem.* **2009**, *19*, 4061–4076.
2. Coronado, E.; Day, P. *Chem. Rev.* **2004**, *104*, 5419–5448.
3. Coronado, E.; Galán-Mascarós, J. R. *J. Mater. Chem.* **2005**, *15*, 66–74.
4. Lorcy, D.; Bellec, N.; Fourmigué, M.; Avarvari, N. *Coord. Chem. Rev.* **2009**, *253*, 1398–1438.
5. Pop, F.; Auban-Senzier, P.; Canadell, E.; Rikken, G. L. J. A.; Avarvari, N. *Nat. Commun.* **2014**, *5*:3757, DOI:10.1038/ncomms4757.
6. Rikken, G. L. J. A.; Fölling, J.; Wyder, P. *Phys. Rev. Lett.* **2001**, *87*, 236602-1–4.
7. Krstić, V.; Roth, S.; Burghard, M.; Kern, K.; Rikken, G. L. J. A. *J. Chem. Phys.* **2002**, *117*, 11315–11319.
8. De Martino, A.; Egger, R.; Tselik, A. M. *Phys. Rev. Lett.* **2006**, *97*, 076402-1–4.
9. Réthoré, C.; Fourmigué, M.; Avarvari, N. *Chem. Commun.* **2004**, 1384–1385.
10. Réthoré, C.; Avarvari, N.; Canadell, E.; Auban-Senzier, P.; Fourmigué, M. *J. Am. Chem. Soc.* **2005**, *127*, 5748–5749.
11. Madalan, A. M.; Réthoré, C.; Fourmigué, M.; Canadell, E.; Lopes, E. B.; Almeida, M.; Auban-Senzier, P.; Avarvari, N. *Chem. Eur. J.* **2010**, *16*, 528–537.
12. Olejniczak, I.; Frąckowiak, A.; Matysiak, J.; Madalan, A.; Pop, F.; Avarvari, N. *Cent. Eur. J. Phys.* **2014**, *12*, 215–220.
13. Hasegawa, M.; Sone, Y.; Iwata, S.; Matsuzawa, H.; Mazaki, Y. *Org. Lett.* **2011**, *13*, 4688–4691.
14. Biet, T.; Fihey, A.; Cauchy, T.; Vanthuynne, N.; Roussel, C.; Crassous, J.; Avarvari, N. *Chem. Eur. J.* **2013**, *19*, 13160–13167.
15. Danila, I.; Riobé, F.; Puigmartí-Luis, J.; Pérez del Pino, Á.; Wallis, J. D.; Amabilino, D. B.; Avarvari, N. *J. Mater. Chem.* **2009**, *19*, 4495–4504.
16. Danila, I.; Riobé, F.; Piron, F.; Puigmartí-Luis, J.; Wallis, J. D.; Linares, M.; Ågren, H.; Beljonne, D.; Amabilino, D. B.; Avarvari, N. *J. Am. Chem. Soc.* **2011**, *133*, 8344–8353.
17. Danila, I.; Pop, F.; Escudero, C.; Feldborg, L. N.; Puigmartí-Luis, J.; Riobé, F.; Avarvari, N.; Amabilino, D. B. *Chem. Commun.* **2012**, *48*, 4552–4554.
18. Pop, F.; Melan, C.; Danila, I.; Linares, M.; Beljonne, D.; Amabilino, D. B.; Avarvari, N. *Chem. Eur. J.* **2014**, *20*, 17443–17453.
19. Pop, F.; Auban-Senzier, P.; Frąckowiak, A.; Ptaszyński, K.; Olejniczak, I.; Wallis, J. D.; Canadell, E.; Avarvari, N. *J. Am. Chem. Soc.* **2013**, *135*, 17176–17186.
20. Dunitz, J. D.; Karrer, A.; Wallis, J. D. *Helv. Chim. Acta* **1986**, *69*, 69–70.
21. Karrer, A.; Wallis, J. D.; Dunitz, J. D.; Hilti, B.; Mayer, C. W.; Bürkle, M.; Pfeiffer, J. *Helv. Chim. Acta* **1987**, *70*, 942–953.
22. Yang, S.; Pop, F.; Melan, C.; Brooks, A. C.; Martin, L.; Horton, P.; Auban-Senzier, P.; Rikken, G. L. J. A.; Avarvari, N.; Wallis, J. D. *CrystEngComm* **2014**, *16*, 3906–3916.
23. Pop, F.; Laroussi, S.; Cauchy, T.; Gómez-García, C. J.; Wallis, J. D.; Avarvari, N. *Chirality* **2013**, *25*, 466–474.
24. Galán-Mascarós, J. R.; Coronado, E.; Goddard, P. A.; Singleton, J.; Coldea, A. I.; Wallis, J. D.; Coles, S. J.; Alberola, A. *J. Am. Chem. Soc.* **2010**, *132*, 9271–9273.

25. Pop, F.; Allain, M.; Auban-Senzier, P.; Martínez-Lillo, J.; Lloret, F.; Julve, M.; Canadell, E.; Avarvari N. *Eur. J. Inorg. Chem.* 2014, 3855–3862.
26. Kitagawa, S.; Kawata, S. *Coord. Chem. Rev.* **2002**, 224, 11–34, and references therein.
27. Tinti, F.; Verdaguer, M.; Kahn, O.; Savariault, J. M. *Inorg. Chem.* **1987**, 26, 2380–2384.
28. Min, K. S.; Rhinegold, A. L.; Miller, J. S. *J. Am. Chem. Soc.* **2005**, 128, 40–41.
29. Min, K. S.; Rheingold, A. L.; DiPasquale, A.; Miller, J. S. *Inorg. Chem.* **2006**, 45, 6135–6137.
30. Min, K. S.; DiPasquale, A. G.; Golen, J. A.; Rheingold, A. L.; Miller, J. S. *J. Am. Chem. Soc.* **2007**, 129, 2360–2368.
31. Nagayoshi, K.; Kabir, M. K.; Tobita, H.; Honda, K.; Kawahara, M.; Katada, M.; Adachi, K.; Nishikawa, H.; Ikemoto, I.; Kumagai, H.; Hosokoshi, Y.; Inoue, K.; Kitagawa, S.; Kawata, S. *J. Am. Chem. Soc.* **2003**, 125, 221–232.
32. Mouchaham, G.; Roques, N.; Duhayon, C.; Imaz, I.; Sutter, J.-P. *New J. of Chem.* **2013**, 37, 3476–3487.
33. Molčanov, K.; Kojic-Prodic, B.; Meden, A. *CrystEngComm* **2009**, 11, 1407–1415.
34. Abrahams, B. F.; Grannas, M. J.; Hudson, T. A.; Hughes, S. A.; Pranoto, N. H.; Robson, R. *Dalton Trans.* **2011**, 40, 12242–12247.
35. Luo, T.-T.; Liu, Y.-H.; Tsai, H.-L.; Su, C.-C.; Ueng, C.-H.; Lu, K.-L. *Eur. J. Inorg. Chem.* **2004**, 4253–4258.
36. Mori, T.; *Bull. Chem. Soc. Jpn.* **1998**, 71, 2509–2546.
37. Guionneau, P.; Kepert, C. J.; Bravic, G.; Chasseau, D.; Truter, M. R.; Kurmoo, M.; Day, P. *Synth. Met.* **1997**, 86, 1973–1974.
38. Yang, S.; Pop, F.; Melan, C.; Brooks, A. C.; Martin, L.; Horton, P.; Auban-Senzier, P.; Rikken, G. L. J. A.; Avarvari, N.; Wallis, J. D. *CrystEngComm* **2014**, 16, 3906–3916.
39. Whangbo, M.-H.; Williams, J. M.; Leung, P. C. W.; Beno, M. A.; Emge, T. J.; Wang, H. H., *Inorg. Chem.* **1985**, 24, 3500–3502.
40. Emge, T. J.; Wang, H. H.; Beno, M. A.; Williams, J. M.; Whangbo M. H.; Evain, M.; *J. Am. Chem. Soc.* **1986**, 108, 8215–8223.
41. Stephens, D. A.; Rehan, A. E.; Compton, S. J.; Barkhau R. A.; Williams, J. M. *Inorg. Synth.* **1986**, 24, 130–143.
42. Batail, P.; Boubekour, K.; Fourmigué, M.; Gabriel, J.-C. P. *Chem. Mater.* **1998**, 10, 3005–3015.
43. Sheldrick, G. M. *Programs for the Refinement of Crystal Structures*, University of Göttingen: Göttingen, Germany, **1996**.
44. Farrugia, L. J. *J. Appl. Crystallogr.* **1999**, 32, 837–838.
45. Whangbo, M.-H.; Hoffmann, R. *J. Am. Chem. Soc.* **1978**, 100, 6093–6098.
46. Ammeter, J. H.; Bürgi, H.-B.; Thibeault, J.; Hoffmann, R. *J. Am. Chem. Soc.* **1978**, 100, 3686–3692.
47. Pénicaud, A.; Boubekour, K.; Batail, P.; Canadell, E.; Auban-Senzier, P.; Jérôme, D., *J. Am. Chem. Soc.* **1993**, 115, 4101–4112.
48. Bain, G. A.; Berry, J. F. *J. Chem. Educ.* **2008**, 85, 532–536.

Part III

Conclusions and Perspectives

1.1 Conclusions

In this work the rational design and the synthesis of novel versatile molecular building blocks based on the family of anilate ligands have been explored. The potential of these anilate-based molecular building blocks to act as suitable precursors for the preparation of functional and multifunctional molecular materials with conducting and/or magnetic properties has been investigated.

Among the anilate ligands known in the literature, the derivatives with Cl, Br, I, H, and Cl/CN substituents at the 3,6 positions have been selected for obtaining, through a general and straightforward synthetic strategy, a novel family of paramagnetic octahedral mononuclear complexes. These molecular building blocks, which have been thoroughly characterized through X-ray diffraction analysis, spectroscopic studies, DFT calculations, and magnetic measurements, show electronic and structural features suitable for obtaining diverse functional and multifunctional molecular materials.

By reacting these complexes with Mn^{II} paramagnetic metal ions through the "complex-as-ligand approach", a family of molecule-based magnets showing tunable magnetic properties have been prepared and fully characterized. In this family, subtle changes in the nature of the substituents (X = Cl, Br, I, H) on the anilate moiety have been rationally employed as "adjusting screws" in tuning the magnitude of the magnetic interaction between the metals, and thus, the magnetic properties. In fact, their key role is highlighted by the observed linear correlation between their electronegativity, *i.e.* their electron withdrawing properties, and the critical temperature values of the resulting molecular magnets.

Moreover, the ability of these mononuclear building blocks to work as components of hybrid paramagnetic molecular conductors has been demonstrated through the synthesis, *via* electrocrystallization, of three different crystalline radical cation salts based on the BEDT-TTF donor, as conductivity carrier, and the tris(chloranilato)ferrate(III) anion, showing magnetic/conducting properties and peculiar molecular arrangements of the BEDT-TTF molecules.

To explore the possibility of modulating the conducting properties of such multifunctional materials by introducing chirality in the organic donors, a complete series of radical cation salts obtained by combining the TM-BEDT-TTF organic donor in its (*S,S,S,S*) and (*R,R,R,R*) enantiopure forms, or their racemic mixture (*rac*), with 2D heterobimetallic anionic layers obtained "*in situ*" by combining the tris(chloranilato)ferrate(III) metal complexes and potassium cations has been prepared and structurally and physically characterized.

Finally, the ability of the anilate moiety to be functionalized with various substituents bearing selected physical properties has been proved through the synthesis of novel derivatives having Th, EDOT and Cl/CN substituents, showing electroactive and luminescent properties, respectively.

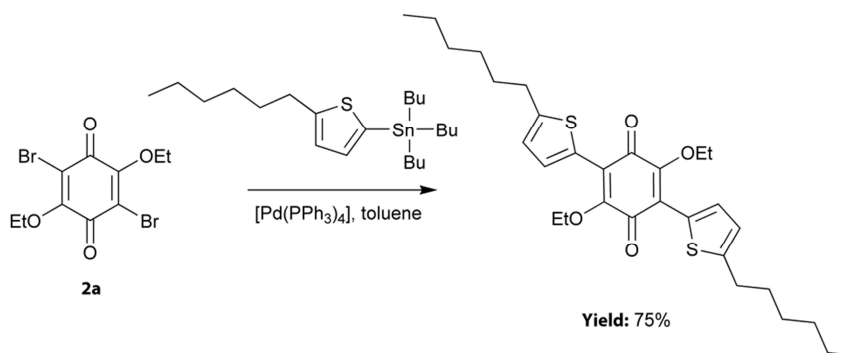
The combined structural/theoretical analysis reported herein also enlarges the general knowledge on the supramolecular interactions shown by the anilate-based molecular building blocks, and provides an effective tool for engineering novel anilate-based supramolecular architectures showing peculiar and improved physical properties.

1.2 Perspectives

On the basis of the obtained results, the following perspectives can be envisaged:

- I. As far as the functionalization of the anilate moiety is concerned, the Stille coupling strategy presented in Chapter 1 is very challenging and opens the way to the synthesis of several novel anilate derivatives, where a rational selection of the functional groups connected to the anilate moiety may afford new properties on the ligands and on the resulting metal complexes.

With the aim to prepare and structurally characterize octahedral tris-chelated metal complexes with the Th and EDOT substituted ligands (**L6** and **L7**, respectively), in analogy to those reported in Chapter 2, preliminary studies have been performed to increase the solubility of these ligands without altering the functionality of the substituent group. In particular, the Stille coupling reaction between the *para*-substituted protected precursor **2a** and a 5-hexyl-thiophenyl Sn derivative (Scheme 1.1) was performed to achieve the 5-hexyl-thiophene-anilate derivative where the solubility of the ligand and the corresponding metal complexes can be improved by the presence of the flexible alkyl chain.



Scheme 1.1, Synthesis of the *para* 5-hexyl-thiophenyl derivative of 1,4-benzoquinone.

In fact, although the reaction of **L6** and **L7** with Cr^{III} and Fe^{III} gives the corresponding octahedral tris-chelated metal complexes, their low solubility did not allow for a structural characterization.

The same Stille coupling synthetic strategy can be reasonably extended to several derivatives bearing various substituents, such as alkyl chains having various chain lengths, aromatic groups, *etc.* and the introduction of chiral functional groups can also be envisaged. This will allow for the preparation of enantiopure ligands that may influence the chirality of the metal centers, the solid-state crystal packing, and thus, the physical properties of the obtained material.

- II. As far as the octahedral metal complexes are concerned, their molecular geometry allows for the preparation of heteroleptic complexes where one anilate ligand is replaced by a N,N-donating one (*e.g.* bipyridine or phenantroline). These mononuclear metal complexes can be used as potential magnetic molecular building blocks for the preparation of functional molecular materials. Preliminary experiments have been

performed in this direction, and a molecular structure of one of such heteroleptic complexes of general formula $[M^{III}(X_2An)_2(bpy)]^-$ ($M^{III} = Cr, Fe; X = Cl, Br, I$) is reported in Figure 1.1.

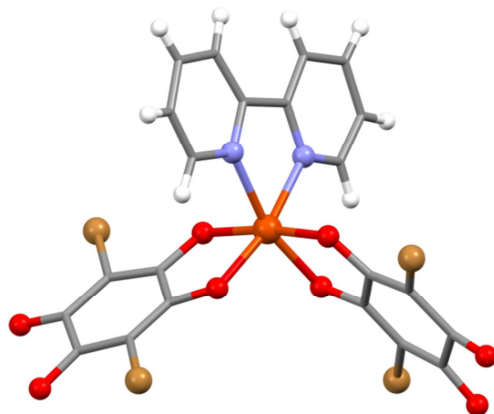


Figure 1.1, Molecular structure for the complex anion $[Fe(Br_2An)_2(bpy)]^-$ (Δ enantiomer).

- III. As far as the molecule-based magnets are concerned, the results presented here are still in their infancy. In fact, (i) the investigation of the magnetic properties of different pairs of metal ions (e.g. Cr^{III} or Fe^{III} with Co^{II}), (ii) the preparation of new derivatives with electron-rich substituents in order to increase the electron density on the anilate framework and then, the ordering temperature, (iii) the introduction of functional cations between the layers, such as spin crossover and luminescent cations, etc. will be explored as future work with the goal of improving the properties of the molecule-based magnets herein studied and to build new multifunctional (magnetic/luminescent) materials. In particular the latter have been partially studied during this work.
- IV. Particular attention will be devoted to the design and the synthesis of new ligands for potential cationic spin crossover complexes. Derivatives of the *N*-(8-quinolyl) salicylaldimine ligand with halogen substituents (Cl, Br, I) on the 5,7 positions of the quinoline group have been prepared and fully characterized during this work with this purpose. The molecular structure of the iodo derivative is reported in Figure 1.2.

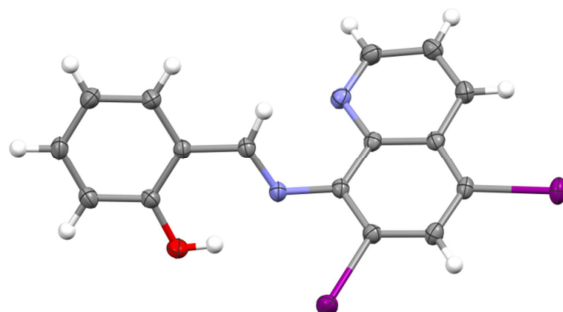


Figure 1.2, ORTEP drawing of the *N*-(5,7-diiodo-8-quinolyl)salicylaldimine ligand with thermal ellipsoids at the 30% probability level.

These ligands, where the substituted *N*-(8-quinolyl)salicylaldehyde moiety can induce spin crossover properties in the coordinated Fe^{III} metal ion, are currently under investigation in order to check the ability of the substituent groups the modulation of the spin crossover transition temperature. Furthermore, they can also be included between the layers of the anilate-based magnets with the aim to study the influence and the occurrence of potential halogen-bonding interactions between the halogen substituent of the two systems. This could be a challenging tool for inducing interplay between the ferrimagnetic properties of the anionic layer and the spin crossover properties of the cationic layer.

- V. As far as the magnetic molecular conductors are concerned, new systems where the tris(chloranilato)ferrate(III) anion is replaced by its Br or I analogues will be prepared. This could allow for a systematic study on the influence of the nature and strength of the intermolecular interaction, due to the different substituent, in affecting the crystal packing and then, the conducting properties of the obtained materials. In this context, the α'' -[BEDT-TTF]₁₈[Fe(Br₂An)₃]₃·3CH₂Cl₂·6H₂O system (Figure 1.3), that shows isostructurality with respect to the **H3** system described in Chapter 4, has been prepared and its physical properties are currently under investigation.

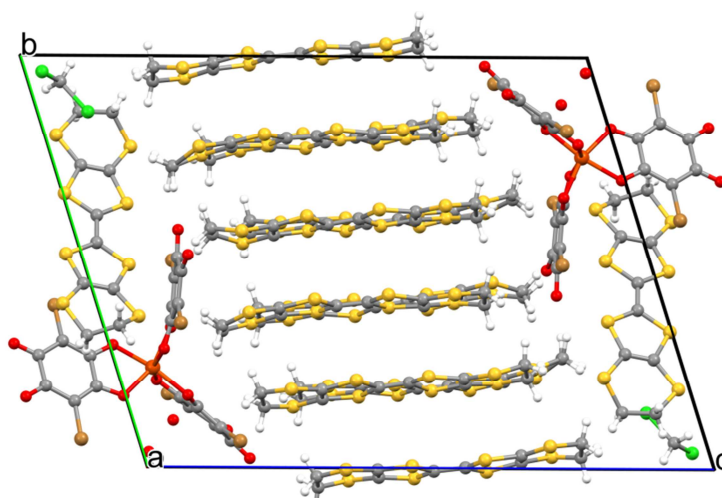


Figure 1.3, View of the unit cell content for the α'' -[BEDT-TTF]₁₈[Fe(Br₂An)₃]₃·3CH₂Cl₂·6H₂O system.

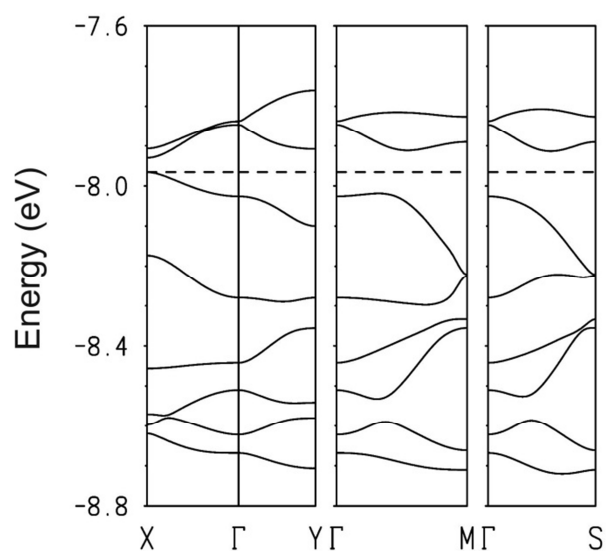
- VI. Finally, other chiral derivatives of the TTF organic donor (e.g. **D6** and **D7**, see Chart 2) will be combined with both paramagnetic and ferrimagnetic systems presented in this work to further investigate the influence of the chirality on the conducting properties and, as a topic of special current interest, to explore the effect of the magnetic contribution of the obtained material on the electrical magneto-chiral anisotropy effect.

Part IV

Appendices

Appendix 1

Electrical Conductivity of Molecular Materials



The basic physical principles of electrical conductivity in molecular materials are reported in this Appendix. The main structural and electronic features shown by the class of conducting molecular materials discussed in this thesis are also herein summarized.

1.1 Electrical Conductivity of Molecular Materials

Electrical conductivity, σ , is the physical property that quantifies the ability of a given material to transport charge carriers when it is subjected to the action of an electric potential.

When a conducting material is subjected to an electric potential denoted as ΔV , an electrical current of intensity i flows through it. The intensity value depends on the applied electric potential and the material resistance R as stated by the **I Ohm's Law**

$$i = \frac{\Delta V}{R}$$

The resistance value is connected to the intrinsic nature of the material, *i.e.* its atomic and electronic structure, and to geometrical factors not correlated to its composition such as its length l and its section s , as stated by the **II Ohm's Law**

$$R = \rho \frac{l}{s}$$

where ρ is the **resistivity** or **specific resistance** and quantifies the resistance of a certain material independently from its geometrical features.

Conductivity or **specific conductance**, expressed in $S\text{ cm}^{-1}$, is the reciprocal of the resistivity, as stated by the following expression

$$\sigma = \frac{1}{\rho} = \frac{l}{R s} = \frac{i l}{\Delta V s}$$

The value of the conductivity allows to classify materials in insulators ($\sigma < 10^{-6} S\text{ cm}^{-1}$), semiconductors ($10^{-6} < \sigma < 10 S\text{ cm}^{-1}$), metals ($10 < \sigma < 10^7 S\text{ cm}^{-1}$) or superconductors ($\sigma > 10^7 S\text{ cm}^{-1}$).¹

The electrical conductivity in molecular conductors can be explained by means of the band theory of solids, as for the case of traditional conductors, considering the interactions between molecular orbitals instead of atomic orbitals.²

From a general point of view, the combination of two different orbitals leads to a bonding and an antibonding orbital having lower and higher energy values, respectively, than the non-interacting starting orbitals. This means that the combination of N orbitals lead to the formation of $N/2$ bonding orbitals and $N/2$ antibonding orbitals. The combination of N orbitals do not allow for well-separated energy levels but a continuous of energy levels described as an energy band (Figure A1.1).²

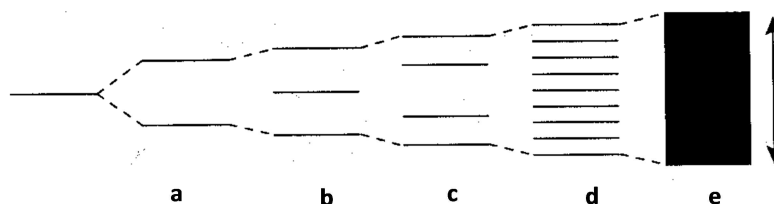


Figure A1.1. Origin of the energy bands for a certain solid material; orbitals for a) a single molecule, b) c) d) different interacting molecules, e) energy band for a solid.

The band width, *i.e.* the energy difference between the highest and the lowest energy levels, depends on the interactions between the involved orbitals. The equation that quantitatively describes the band width is $W_{\alpha} = 4t_{\alpha}$, where t_{α} is the overlapping integral between the orbitals. In a molecular conductor, the intermolecular interactions are weaker than the interactions between atoms as found in a classical conductor. This is due to an orbital overlap that involves molecular, instead of atomic, orbitals, resulting, in most of cases, in a lower conductivity for the molecular systems when compared with the atom-based materials.

An energy gap (E_g) can be also found between the band formed by the bonding orbitals and the band formed by the antibonding ones, representing forbidden energy values for the electrons in the electronic structure of the material. The conducting properties of a material are strongly dependent on the filled energy bands levels and the energy gap between two bands, where the Fermi energy level represents the highest occupied level at 0 K. (Figure A1.2).

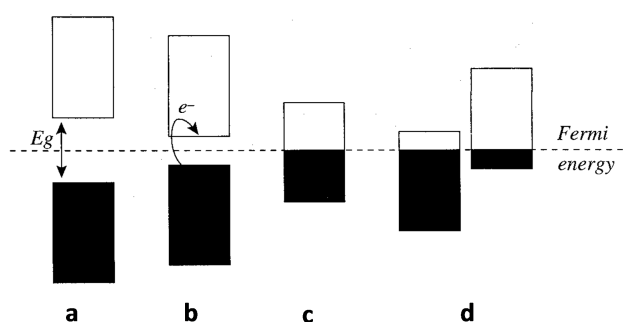


Figure A1.2, Energy bands for an insulator (a), a semiconductor (b), a metal (c), a semimetal (d).

When the material has a big E_g value (> 5 eV), no electrons have enough energy to be promoted in the empty band at higher energy values, and the material behaves as an insulator. If the E_g value has an energy value comparable with the thermal energy ($3/2k_B T$), a certain number of electrons have enough energy to pass from the lower energy band, the valence band, to the higher energy band, the conducting band, that will be partially occupied. In this case, the electrical conductivity is thermally activated and the material behaves as a semiconductor. If no E_g is present between the valence and conducting bands, they are bordering, and a small amount of thermal energy will be sufficient to promote the electrons from the valence band to the conducting band. In this case the material behaves as a metal-like conductor. If the bands are bordering and are 10% or 90% occupied (see Figure 1.2d) the material behaves as a semimetal.²

The electrical conductivity σ of a certain material depends also on the number of charge carriers n , and their mobility μ . The relation between these quantities is

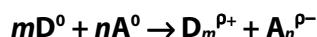
$$\sigma = n \mu e$$

where e is the charge of a carrier.² For a metal-like conductor, n does not change as a function of the temperature, whereas μ decreases as the temperature increases due to diffusing phenomena acting on the carriers, essentially due to reticular vibrations. For this reason, the conductivity of a metal increases as the temperature decreases. For a semiconductor, μ varies

as for a metal, but the carriers number n increases as the temperature increases (for the reasons explained above), therefore, the conductivity is thermally activated. A semimetal shows a conducting behaviour at room temperature similar to that shown by the semiconductors, but n remains almost constant as the temperature change, as for the metals.

The conducting properties of molecular conductors are also strongly dependent on their structural anisotropy. In fact, these materials are characterized by mono-dimensional or bi-dimensional stacks along with the conductivity has the maximum value, due to the favorable overlap between the molecular orbitals of the building units. The interactions between different stacks are instead weaker, resulting in a lower conductivity in the direction perpendicular to the stacks. They are also subject to the "Peierls distortion", *i.e.* dimerization phenomena at low temperature responsible for an increased energy gap between the valence and conducting bands, giving rise to lower conductivity values.^{3,4} The conducting properties of such materials are in fact often characterized by metal-insulator or metal-semiconducting transitions due to these phenomena. The experimental evidence suggest that to reduce or avoid the Peierls distortion the material dimensionality should be increased by favoring the interactions between different stacks. This leads to less deviation from the metal-like behaviour and favors the conducting and superconducting properties. The most successful strategy to reach this goal is based on the introduction of highly polarizable atoms on the molecular building units.

Many of the molecular conductors known in the literature are charge transfer salts. These systems are characterized by one or more molecular building units obtained through the following equation:



where **D**, the donor, is the electron donating species, and **A**, the acceptor, is the electron acceptor species.¹

In Figure A1.3 are reported some of the most important molecular donors and acceptors.

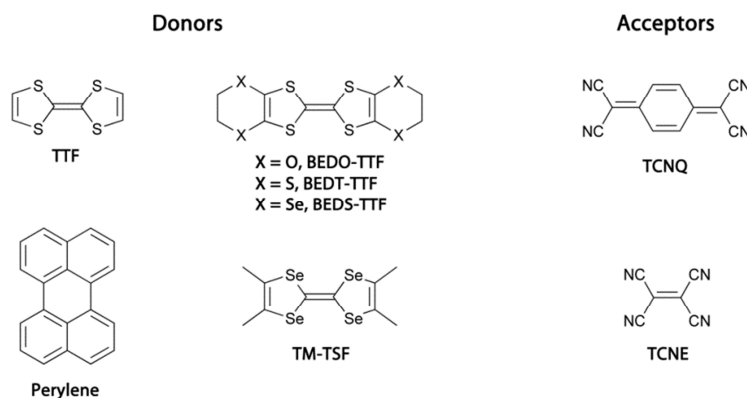


Figure A1.3. Molecular structures for some of the most important molecular donors and acceptors.

The exponent p quantifies the charge transfer degree between the two molecules and can be complete ($p = 1$) or partial ($0 < p < 1$). The p value depends on the difference between the oxidation potential of the donor and the reduction potential of the acceptor.¹

Generally, donors and acceptors are planar molecules with an extended π delocalization. These are fundamental features for the formation of stacked columns and for the stabilization of different and/or fractional oxidation states. One of the most known example of such compounds is the TTF-TCNQ system (Figure A1.4), where molecules of the TTF donor and molecules of the TCNQ acceptor are arranged in segregated stacks along which the conductivity reaches its maximum value.^{5,6}

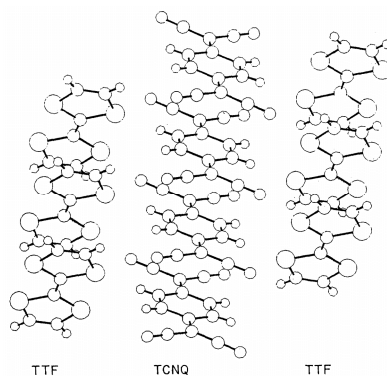


Figure A1.4, Segregated stacks of TTF and TCNQ molecules for the compound TTF-TCNQ.

Generally, two types of stacks can be observed:

- Mixed stacks, where the donors and the acceptors alternate in a **-D-A-D-A-D-** sequence;
- Segregated stacks, where the donors and the acceptors form separated **-D-D-D-D-D-** and **-A-A-A-A-A-** stacks.

The concept of charge transfer salts has been extended also to those systems where one of the components is a simple cationic or anionic species that acts as a counterion of the donor or the acceptor bearing a fractional charge.¹ This is the case of the $[\text{TM-TSF}]_2[\text{ClO}_4]$ system (Figure A1.5).⁷

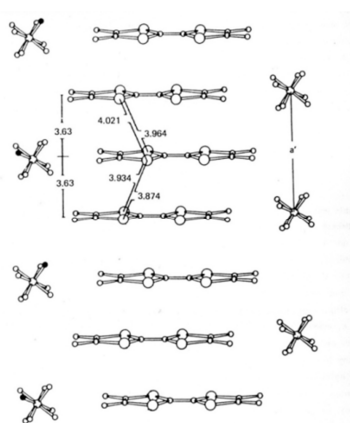


Figure A1.5, View of the crystal structure of $[\text{TMTSF}]_2[\text{ClO}_4]$, showing segregated stacks of the TM-TSF donor separated by ClO_4^- counteranions.

With this view, the electronic and structural features that a good donor molecule should have are:

- high degree of π delocalization, that allows for a charge stabilization and reduces the electrostatic repulsions between molecules, leading to a more efficient overlap between molecular orbitals;
- the presence of polarizable atoms at the molecule periphery, which play a key role in promoting inter- and intra-stack contacts responsible for an increased dimensionality of the resulting material;
- good planarity, that allows for an effective π superposition of the molecular orbitals, and thereby, good conducting properties.

Tetrathiafulvalene and its derivatives represents the most important family of organic donors showing these features. In particular, TTF led to conducting salt that, even if characterized by high r.t. conductivity values, are commonly affected by Peierls distortion due to the low efficiency of this donor to establish short contacts between the stacks. To avoid or reduce the Peierls distortion, various structural modification of this molecule have been considered and investigated. Specifically, the following have been studied:

- the extension of the donor periphery by introducing O, S and Se-based substituent able to maintain a good planarity and favor interstack contacts through non-covalent interactions; among the various TTF derivatives, the most successful donors which have produced the majority of known molecular superconductors and metals are the BEDT-TTF, the BEDS-TTF, and the BEDO-TTF;
- the substitution of the S atoms with atoms having more extended and polarizable orbitals, such as Se and Te, as in the case of the TM-TSF, which has produced the first molecular superconductor.

The physical properties of molecular materials are strongly dependent on the nature of their building units as well as on the way these molecular bricks self-assemble in the crystal lattice. In fact, radical cation salts built with the same building units but showing completely different physical properties are well-known in the literature. This is mainly due to the different packing motifs exhibited by the donor molecules.^{8,9} Some of the most common molecular packing exhibited by the TTF and its derivatives are reported in Figure A1.6.¹⁰⁻¹²

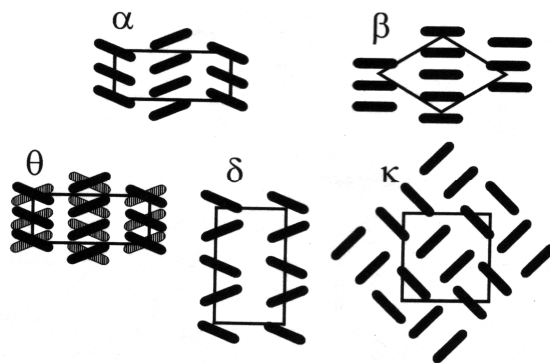


Figure A1.6, Schematic representation of the structural phases exhibited by the TTF and its derivatives with classification symbols.

The molecular packing of the donor molecules is driven by several factors, and hence is difficult to predict. Moreover, it is not commonly easy to understand the reason why a specific packing is favorite respect to the others, if specific supramolecular interactions are not observed between the donors and the counterions.

In the case of radical cation salts where only one species undergoes partial oxidation or reduction process, the role of the counterion is of fundamental importance because it can influence the arrangement of the electroactive donor molecules in the crystal lattice, and thus the physical properties of the material, depending on:

- its molecular geometry;
- its redox potential;
- its ability to give intermolecular interactions with the electroactive donor molecules.

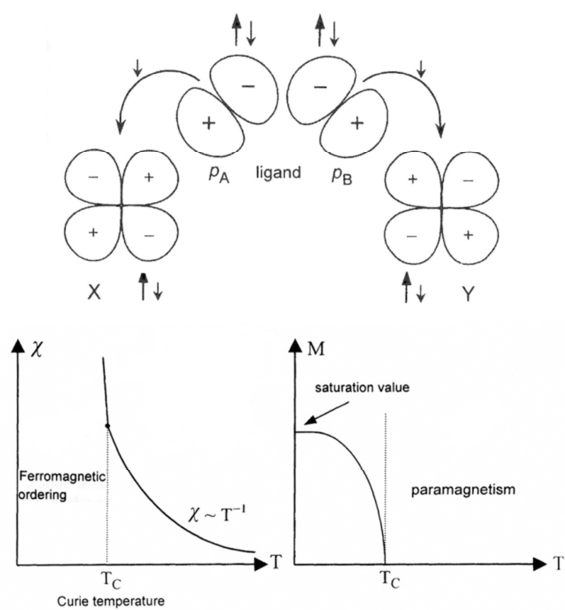
The counterion can also be a carrier of an additional physical property, such as magnetic or optical properties, leading to a multifunctional material where more physical properties coexist or interact in the same crystal lattice. The search for multifunctionality in a molecular material is of relevant scientific and technological interest because the coexistence or interplay of different physical properties it is difficult to achieve in classical inorganic materials.

References

1. Launay, J.-P.; Verdaguer, M. *Electrons in Molecules, From Basic Principles to Molecular Electronics.*, Oxford University Press, Oxford, **2013**.
2. Kittel, C. *Introduzione alla fisica dello stato solido*, Bollati Boringhieri editore, **1998**.
3. Peierls, R. E. *Quantum Theory of Solids*, Oxford University Press, **1995**.
4. Hoffmann, R. *Solid and Surfaces: A Chemist's View of Bonding in Extended Structures*, Wiley-VCH, **1989**, 58
5. Coleman, L. B.; Cohen, M. J.; Sandman, D. J.; Yamagishi, F. G.; Garito, A. F.; Ferris, A. J. *Solid State Commun.*, **1973**, 12, 1125–1202.
6. Farris, A. J.; Cowan, D. O.; Walatka, V.; Perlstein, J. H. *J. Am. Chem. Soc.*, **1973**, 95, 948–949.
7. Jerome, D.; Mazaud, M.; Ribault, M.; Bechgaard, K. *J. Phys. Lett.*, **1980**, L95, 1416.
8. Kobayashi, A.; Udagawa, T.; Tomita, H.; Naito, T.; Kobayashi, H. *Chem. Lett.*, **1993**, 2179–2182.
9. Kobayashi, H.; Tomita, H.; Naito, T.; Kobayashi, A.; Sakai, F.; Watanabe, T.; Cassoux, P. *J. Am. Chem. Soc.*, **1996**, 118, 368–377.
10. Mori, T. *Bull. Chem. Soc. Jpn.*, **1998**, 71, 2509–2526.
11. Mori, T. *Bull. Chem. Soc. Jpn.* **1999**, 72, 2011–2027.
12. Mori, T.; Mori, H.; Tanaka, S. *Bull. Chem. Soc. Jpn.* **1999**, 72, 179–197.

Appendix 2

Fundamentals of Magnetism and Magnetochemistry



An overview of the basic principles of magnetism and magnetochemistry required for understanding and discussing the magnetic properties of the molecular materials reported in this thesis is given in this Appendix.

2.1 Introduction

Magnetism is the field of physics dealing with the study of magnetic properties of matter by analysing the behaviour of materials when they are subjected to the action of a magnetic field. It is one of the oldest scientific subjects and one of the most difficult to understand. Closely connected with magnetism is the magnetochemistry, a field of chemical-physics whose origin is much more recent than magnetism. **Magnetochemistry** deals with the description and understanding of magnetic properties of chemical compounds. Its final goal is being a tool for the design and synthesis of new materials with expected magnetic properties. It is clear that for a chemist or a material scientist a deep knowledge of magnetism and magnetochemistry is fundamental for obtaining new materials with desired magnetic properties. The following is addressed to the description of their fundamental principles with particular attention for the classes of materials that are subject of this thesis.

2.2 Principles and fundamental quantities

2.2.1 The magnetic field

One of the fundamental principles in magnetism is the concept of **magnetic field**. When a magnetic field is generated in a certain volume of space, an energy gradient is generated so that a force is produced. This force can be detected by:

- the acceleration of a charge moving in the field;
- the force on a current-carrying conductor;
- the torque on a magnetic dipole;
- electronic spin reorientation in certain types of atoms or ions.

A magnetic field is produced whenever there is a charge in motion. This can be due to an electrical current flowing in a conductor, as it was first discovered by Oersted in 1819, or it can be generated by a permanent magnet. In the latter case there is no conventional electrical current, but the orbital and spin motions of the electrons forming the permanent magnet lead to a magnetization within the material and to a magnetic field generation.

The force of a magnetic field **H** generated by an electrical current can be calculated through the **Biot-Savart law**. In its usual form the law gives the value of the field generated by the current flowing in an elementary length of conductor

$$\delta\mathbf{H} = \frac{1}{4\pi r^2} i \delta\mathbf{l} \times \mathbf{u}$$

where i is the current flowing in a $\delta\mathbf{l}$ elemental length of a conductor, r is the radial distance, \mathbf{u} is a unit vector along the radial direction and $\delta\mathbf{H}$ is the contribution to the magnetic field at r distance due to the current element $i\delta\mathbf{l}$.

The Biot-Savart law can also be used for determining the magnetic field \mathbf{H} generated at the center of a circular coil with radius of a meters, carrying a current of i amperes. It is possible to divide the coil into $\delta\mathbf{l}$ elements each one contributing $\delta\mathbf{H}$ to the total \mathbf{H} field at the center of the coil. From the Biot-Savart law

$$\mathbf{H} = \sum \frac{1}{4\pi r^2} i \delta\mathbf{l} \sin \theta$$

and because $\Sigma\delta\mathbf{l} = 2\pi a$, $r = a$, $\delta\mathbf{l}$ is perpendicular to \mathbf{u} , so $\theta = 90^\circ$ and $\sin \theta = 1$

$$\mathbf{H} = \frac{i}{2a} [A m^{-1}]$$

2.2.2 The magnetic induction

When a magnetic field \mathbf{H} is generated in a medium by a current, the response of the medium to this force is the **magnetic induction \mathbf{B}** , also called **flux density**. The physical quantity which allow to correlate the magnetic field and the magnetic induction is called **magnetic permeability of the medium μ** .

Whenever a magnetic field is present, there will be a **magnetic flux Φ** . The rate of changing of the flux can be measured since it generates an **electromotive force, e.m.f.**, in a closed circuit of a conducting material where the flux passes through. It is possible to consider the magnetic flux to be caused by the presence of the magnetic field in a certain medium. The amount of flux generated by a magnetic field depends on the properties of the medium and varies from one medium to another.

The magnetic induction \mathbf{B} or flux density represents the amount of magnetic flux per unit area and is measured in Wb m^{-2} . Consequently, a flux density of 1 Wb m^{-2} corresponds to a magnetic induction of 1 tesla, T.

It should be highlighted that in several media the magnetic induction \mathbf{B} is a linear function of the magnetic field \mathbf{H} . In particular, in the free space

$$\mathbf{B} = \mu_0 \mathbf{H}$$

where μ_0 is the **magnetic permeability of the free space** which is an universal constant. The magnetic permeability represents the tendency of a medium to be magnetized. In other words, if μ is small, \mathbf{B} will be slightly different from \mathbf{H} and the magnetic field will have a strong influence on the material, whereas, if μ is big, \mathbf{B} will be quite different from \mathbf{H} and the magnetic field will not have a strong influence on the material. The magnetic permeability unit is the Henry per meter, H m^{-1} . However, in other media and in particular on ferromagnets and ferrimagnets, \mathbf{B} is no longer a linear function of \mathbf{H} , nor it is a single-valued function of \mathbf{H} . In these cases, \mathbf{B} and \mathbf{H} are still related by the equation

$$\mathbf{B} = \mu \mathbf{H}$$

but μ is not necessarily a constant. With reference to the classes of magnetic materials, μ is constant over a wide range of H for paramagnets and diamagnets, whereas it varies remarkably with H in ferromagnets and ferrimagnets.

2.2.3 The magnetic dipole

The most elementary units in magnetism are:

- a closed circuit of a conductor carrying an electric current
- a magnetic dipole

With the term **magnetic dipole** two **magnetic monopoles** of different sign separated by a distance l are considered (Figure A2.1).

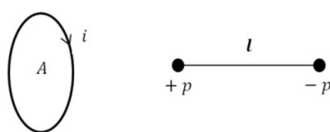


Figure A2.1. Schematic representation of the most elemental units in magnetism: left, a closed circuit carrying an electric current; right, a linear magnetic dipole.

In each case, a **magnetic moment m** associated with the elementary unit of magnetism is present. In the closed circuit case the magnetic moment is equal to the product of the current i and the area of the loop A

$$m = i A$$

In the dipole moment case, instead, the magnetic moment is equal to the product of the pole strength p and the distance between them l

$$m = p l$$

The torque on a magnetic dipole moment m immerse in a magnetic field associated to a magnetic induction B is given by the cross product

$$\tau = m \times B$$

and in the free space is

$$\tau = \mu_0 m \times H$$

This means that the magnetic induction B tries to align the magnetic dipole so that the moment m lies parallel to the magnetic induction. If no frictional forces are operating, the work done by the turning force will be conserved. This gives rise to the following expression for defining the energy associated to the dipole moment m in the presence of a magnetic induction B

$$E = -m \cdot B = -m B \cos\theta$$

It is clear that for θ values of 0° and 180° the energy assumes its minimum values.

2.2.4 Magnetization and magnetic moment

On going to consider magnetic materials, it is first necessary to define the physical quantities that represent the response of these materials to the field. These quantities are the **magnetic moment** and **magnetization**. Another important property that must be considered is the **susceptibility**, which is closely related to the **permeability**.

- **Magnetic Moment**

The magnetic moment can be expressed as the maximum torque on a magnetic dipole moment τ_{\max} divided by B

$$m = \frac{\tau_{\max}}{B}$$

and hence in the free space

$$m = \frac{\tau_{\max}}{\mu_0 H}$$

The magnetic moment vector m associated to the dipole moment tends to align itself along B under the action of the torque as shown in Figure A2.2.

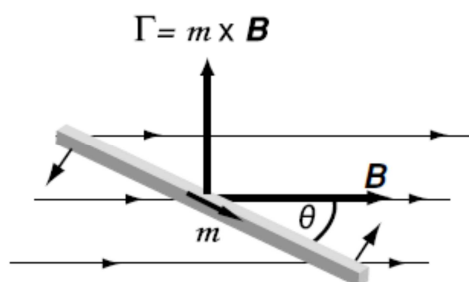


Figure A2.2, The torque on a bar magnet in an external magnetic field. The magnetic moment vector tends to align itself along the B direction.

The energy associated to a conductor coil carrying an electrical current in a magnetic field depends on the product of the current i and the magnetic flux Φ . It is reasonable therefore to classify the “strength” of a permanent magnets in terms of magnetic flux that it produces. From the expression of the magnetic flux, the strength of a dipole p in A m units can be defined as

$$p = \frac{\Phi}{\mu_0}$$

that allows to define the magnetic moment of a magnetic dipole as a function of its strength p .

In a dipole moment consisting in two opposite poles, each of strength p , separated by a distance l , the dipole magnetic moment is

$$m = p l$$

where m is in A m² units, and consequently

$$\mathbf{m} = \frac{\Phi l}{\mu_0}$$

Comparing this equation with the previous expression for the magnetic moment of a current loop ($\mathbf{m} = i A$), it is possible compare the magnetic properties of these two units.

$$\frac{\Phi l}{\mu_0} = iA$$

This relation allow to understand the limitation of describing magnetic materials either solely in terms of currents loops or magnetic dipoles. This is due to the fact that a circuit has no effective length while the dipole has no effective area.

- **Magnetization**

The concept of **magnetization** describes the correlation between the magnetic properties of a certain material and the magnetic induction \mathbf{B} . The magnetization \mathbf{M} can be defined as the magnetic moment per volume unit of a solid

$$\mathbf{M} = \frac{\mathbf{m}}{V}$$

From the relationship between the magnetic moment \mathbf{m} and the flux Φ , $\mathbf{m} = (\Phi l)/\mu_0$, a simple relationship between \mathbf{M} and \mathbf{B} can be found.

$$\mathbf{M} = \frac{\mathbf{B}}{\mu_0}$$

It is noteworthy that \mathbf{B} and \mathbf{M} are correlated as \mathbf{B} and \mathbf{H} ($\mathbf{B} = \mu_0 \mathbf{H}$) are. This means that both magnetization \mathbf{M} and magnetic field \mathbf{H} contribute to the magnetic induction \mathbf{B} in a similar way. If both magnetization and magnetic field are present, their contributions can be added up for giving the global value of the magnetic induction.

- **Relation between \mathbf{H} , \mathbf{M} and \mathbf{B}**

The magnetic induction in the free space is $\mathbf{B} = \mu_0 \mathbf{H}$, while the contribution from the magnetization of the material is $\mathbf{B} = \mu_0 \mathbf{M}$. Thus the magnetic induction is simply the vector sum of the two contributions

$$\mathbf{B} = \mu_0 (\mathbf{H} + \mathbf{M})$$

where \mathbf{B} is given in T and \mathbf{M} and \mathbf{H} in A m^{-1} .

- **Magnetic permeability and susceptibility**

It is possible to define the physical quantities called **magnetic permeability** μ and **magnetic susceptibility** χ .

The magnetic permeability is defined as

$$\mu = \frac{\mathbf{B}}{\mathbf{H}}$$

and the magnetic susceptibility as

$$\chi = \frac{M}{H}$$

Since B and M may be or not linear functions of H , depending on the type of material or medium, it should be noted that permeability and susceptibility may be or not constant.

It is also defined the relative permeability of a medium μ_r as

$$\mu_r = \frac{\mu}{\mu_0}$$

where μ_0 is the permeability of the free space.

The relative permeability is closely related to the susceptibility in agreement with the following equation, that is always true

$$\mu_r = \chi + 1$$

In experimental practice the magnetic susceptibility is not defined as the dimensionless unit χ , but as magnetic susceptibility per mass unit χ_m ($\text{cm}^3 \text{g}^{-1}$), or as molar magnetic susceptibility χ_{mol} ($\text{cm}^3 \text{mol}^{-1}$).

2.3 Magnetic materials

2.3.1 Classification of magnetic materials

The various types of magnetic materials are traditionally classified according to their bulk susceptibility. Materials having χ small and negative, $\chi \approx -10^{-5}$, are called **diamagnets**, and their magnetic response opposes the magnetic field. Superconductors are a special group of diamagnets for which $\chi \approx -1$. Materials having χ small and positive, typically $\chi \approx 10^{-3}$ – 10^{-5} , are the **paramagnets**. The magnetization of paramagnets is weak but aligned parallel with the direction of the applied magnetic field. A third group of magnetic materials are the **ferromagnets** for which the susceptibility is positive and much greater than 1; typical χ values are found in the 50–10000 range.

At constant temperature and for relatively low values of magnetic field H , the magnetic susceptibility of diamagnets and paramagnets is constant. Under this condition the materials are called "linear", *i.e.* M is proportional to H . Consequently, the following can be written

$$\begin{aligned} M &= \chi H \\ B &= \mu_0 (1 + \chi) H \\ &= \mu_0 \mu_r H \\ &= \mu H \end{aligned}$$

μ_r is slightly greater than one in paramagnets and slightly less than one in diamagnets. At the same time χ is slightly more than zero in paramagnets and slightly less than zero in diamagnets. In ferromagnets neither χ nor μ_r have a constant value. Both permeability and susceptibility are strongly affected by the applied magnetic field H .

There are some other types of magnetic materials apart from the three classes presented. These other materials are closely related to ferromagnets because they are magnetically ordered. They are **ferrimagnets** and **antiferromagnets**. In particular, ferrimagnets are of great importance because their magnetic properties are very similar to the ones observed in ferromagnets.

2.3.2 Magnetic properties of ferromagnets

To date the most important classes of magnetic materials are ferromagnets and ferrimagnets due to their relevant technological interest. In engineering applications ferromagnets are used because of their high permeability which enables high magnetic inductions applying only modest magnetic fields, their ability to retain magnetization and thereby act as a field source.

The most important property of ferromagnets is their high relative permeability. The permeability of a ferromagnet is not constant as a function of magnetic field in the way that permeability of paramagnets is. For this reason, in order to characterize the properties of a ferromagnetic material it is necessary to measure the magnetic induction B as a function of the magnetic field H over a continuous range of values to obtain a **hysteresis curve**. Alternatively it is possible to plot the magnetization M as a function of the field H . This gives the same information since $B = \mu_0 (H + M)$.

It is well known that ferromagnets can be magnetized, *i.e.* once exposed to a magnetic field they retain their magnetization even when the field is removed. The retention of magnetization distinguishes ferromagnets from paramagnets which although they acquire a magnetization in an applied magnetic field, cannot maintain the magnetization after the field is removed.

The feasibility of ferromagnetic materials for technological applications is determined essentially from their hysteresis loops. For example, materials for transformer applications require high permeability and low hysteresis losses for an efficient energy conversion, instead, permanent magnet materials require high **remanence** and **coercivity** in order to retain the magnetization as soon as possible (Figure A2.3).

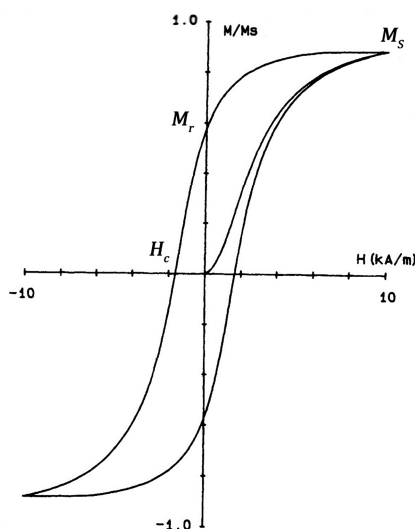


Figure A2.3. A typical hysteresis loop for a ferromagnetic material: M_S = saturation magnetization, M_r = remanent magnetization, H_c = coercive field.

From magnetization measurements as a function of the applied field it can be seen that a ferromagnet in its initial state is not magnetized. Application of an external magnetic field H causes a magnetization increase in the field direction. If H is increased indefinitely, magnetization reaches saturation at a value designate as M_0 or M_S . This value represents a state where all the magnetic dipoles within the material are aligned in the direction of the magnetic field. The saturation magnetization is dependent only on the magnitude of the atomic magnetic moments m and the number of atoms per unit volume n .

$$M_0 = n m$$

M_0 is dependent only on the type of material and is not structure sensitive.

When a ferromagnet is subjected to the action of an external magnetic field, once magnetized and the field is reduced to zero, the value of the magnetization does not assume the initial zero value but assume a certain nonzero value represented by the **remanent magnetization** M_r . The remanent magnetization is correlated with the **remanent magnetic induction** B_r according to the expression

$$B_r = \mu_0 M_r$$

The remanent magnetization can be reduced to zero by applying a reverse magnetic field of strength H_c called **coercive field**. This value is strongly correlated with the thermal history of the sample.

All ferromagnets when heated to sufficiently high temperatures become paramagnets. The transition temperature from ferromagnetic and paramagnetic behaviour is called **Curie temperature** T_C . At this temperature the permeability of the material drops suddenly and both coercivity and remanence become zero.

2.3.3 Magnetic properties of paramagnets

Paramagnets do not find as many applications as ferro- and ferrimagnets, but the description of paramagnetism is, however, very important in the understanding of magnetism since paramagnetism is a much simpler phenomenon to describe than ferromagnetism. Reasonable theories of paramagnetism have been developed on the basis of very simple models and these simple theories give good agreement with the experimental observation. The study of paramagnetism allows for investigating the atomic magnetic moments of almost isolated atoms, since unlike ferromagnetism, paramagnetism is not a cooperative phenomenon.

Materials exhibiting paramagnetism are atoms, ions or molecules with an odd number of electrons so that there is an unpaired electron spin which gives rise to a net magnetic moment. This includes atoms and ions of transition elements or lanthanides with partially filled *d* and *f* inner orbitals, respectively.

In many paramagnets the magnetic susceptibility is inversely correlated to the temperature as established by the **Curie Law**

$$\chi = \frac{C}{T}$$

where *T* is the temperature in kelvin and *C* is a constant known as the **Curie constant**. In other types of paramagnets the susceptibility is temperature independent. Two theories have been developed to describe these behaviours (i) the localized moment model which leads to the Curie law (**Curie paramagnetism**), and (ii) the conduction band electron model of Pauli which leads to the temperature-independent susceptibility (**Pauli paramagnetism**).

The dependence of the susceptibility χ and its reciprocal χ^{-1} as a function of the temperature for a typical Curie paramagnet are reported in Figure A2.4.

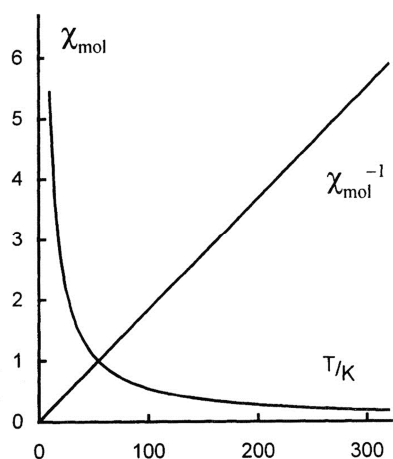


Figure A2.4. Variation of χ and χ^{-1} as a function of *T* for a Curie paramagnet.

In paramagnets subjected to magnetic fields, other than very high fields, the magnetization **M** is proportional to the field **H**. In other words the susceptibility is virtually constant and assumes values in the 10^{-3} – 10^{-5} range. In most cases the magnetic moments are not coupled or

are only weakly coupled so that they can be considered independent to a good approximation. The reason for this is the thermal energy is sufficiently great to cause random alignment of the moment in zero field. When a field is applied the magnetic moment being aligned, but the fraction deflected into the field direction remains small for all practical field strengths. The variation of the magnetization of a typical paramagnet with temperature and field is shown in Figure A2.5.

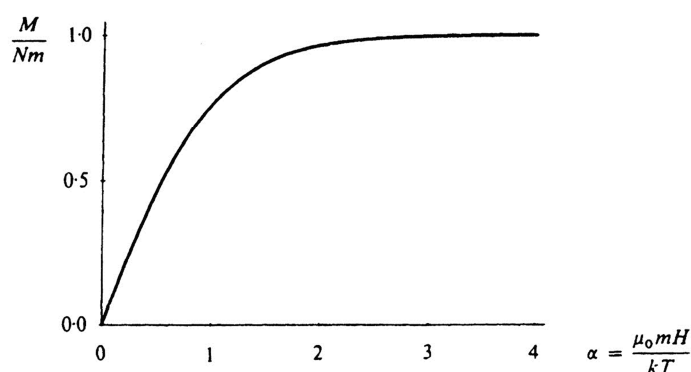


Figure A2.5, Variation of the magnetization as a function of the temperature and the field for a Curie paramagnet in accordance to the classical Langevin function.

At moderate and strong fields the susceptibility is still constant and saturation only occurs at very high field strengths. The dependence can be expressed by using the classical **Langevin function**

$$\frac{M}{nm} = \coth\left(\frac{\mu_0 m H}{k_B T}\right) - \left(\frac{k_B T}{\mu_0 m H}\right)$$

where n is the number of atoms per unit volume, m is the atomic magnetic moment, k_B is the Boltzmann constant and T is the temperature in kelvin. This leads to the following approximate expression for susceptibility which is verified at high T

$$\chi = \frac{\mu_0 n m^2}{3 k_B T}$$

Note that $\mu_0 n m^2 / 3 k_B$ is the Curie constant C . A more accurate expression can be obtained using the **Brillouin function** which is the quantum mechanics analogue of the **Langevin function**.

2.3.4 Magnetic properties of diamagnets

Elements without permanent electronic magnetic moment are unable to exhibit magnetic behaviours like paramagnetism and ferromagnetism. If subjected to magnetic fields **diamagnets** induce a magnetization that opposes the applied field according to the **Lenz law**, and then they assume negative susceptibility values. The dependence of the magnetization on the applied field, *i.e.* the susceptibility, according with **classical Langevin theory of diamagnetism** is expressed by the following equation

$$\chi = -\frac{\mu_0 n Z e^2 \langle r^2 \rangle}{6 m_e}$$

where n is the number of atoms per unit volume, Z is the number of electrons per atom, e is the electronic charge, m_e is the electronic mass and $\langle r^2 \rangle$ the root mean square of the atomic radius. The **diamagnetic susceptibility** is substantially temperature independent.

2.4 Magnetic behaviours

Theories based on phenomenological models used for describing magnetic behaviours of materials and particularly the magnetic ordering phenomena will be discuss here. These theories well describe order-disorder magnetic transitions occurring at the critical temperature for certain classes of materials. These models are based on the assumption that each atom has a fixed magnetic moment but make no assumptions about its origin. This will be discuss in paragraph 2.5.

2.4.1 Diamagnetism

The magnetic moments associated with atoms in magnetic materials can have three origins:

- The electronic spin motion causes a spin magnetic moment;
- The electronic orbital motion causes an orbital magnetic moment;
- The change in orbital motion of electrons caused by an applied magnetic field.

Since diamagnets only have atoms with no permanent net magnetic moment, their diamagnetic susceptibility is necessarily given by the change in orbital motion of electrons caused by the influence of an external magnetic field. Although all materials exhibit diamagnetic susceptibility, not all are classified as diamagnets. Some materials have a net magnetic moment per atom due to an unpaired electron spin which leads to paramagnetism or even to ordered magnetic states as ferromagnetism. In either case the paramagnetic or ferromagnetic susceptibility is much greater than diamagnetic susceptibility and paramagnetism or ferromagnetism will be the dominant effects.

The diamagnetic susceptibility was first explained by Langevin by applying some of the earlier ideas of Ampère, Weber and Lenz on the effect of a magnetic field on a current-carrying conductor to the motion of an electron within an atom.

An electron in orbit around an atomic nucleus can be compared with an electrical current passing through a loop of conductor. Therefore it will have an orbital magnetic moment m_o since, as already explained, an electrical charge moving in a closed loop generates a magnetic moment.

In the case of a conventional current loop the magnetic moment m_o is

$$m_o = i A$$

where i is the current and A is the area of the loop. For an electron in orbital motion is

$$m_o = \frac{eA}{\tau}$$

where e is the electronic charge and τ is the orbital period. If the electronic motion is circular the area will be $A = \pi r^2$ and $\tau = 2\pi r/v$, where v is instantaneous tangential velocity of the electron and r is the orbital radius. This gives rise to the following equation

$$m_o = \frac{evr}{2}$$

which leads to the magnetic moment associated to the orbital motion of the electron. In the absence of a magnetic field the orbital moments of paired electrons within an atom are cancelled because they will have same magnitude but opposite direction. An applied magnetic field \mathbf{H} can, instead, accelerate or decelerate the orbital motion and contribute to a change in the orbital magnetic moment. The change in magnetic moment arising from this for one electron is

$$\Delta m_o = -\frac{\mu_0 e^2 r^2 \mathbf{H}}{6m_e}$$

If Z outer electrons are considered, the change in orbital magnetic moment per atom is

$$\Delta m_o = -\frac{\mu_0 Z e^2 r^2 \mathbf{H}}{6m_e}$$

that can be converted in magnetization change $\Delta \mathbf{M}$

$$\Delta \mathbf{M} = -\left(\frac{N_A \rho}{W_a}\right) \left(\frac{\mu_0 Z e^2 r^2 \mathbf{H}}{6m_e}\right)$$

where N_A is the Avogadro's number, ρ is the density and W_a the relative atomic mass.

Since $\chi = \mathbf{M}/\mathbf{H}$

$$\chi = -\left(\frac{N_A \rho}{W_a}\right) \frac{(\mu_0 Z e^2 r^2)}{6m_e}$$

This relation explains why in the case of diamagnetic materials, which have no net atomic magnetic moment in the absence of a field, the action of a magnetic field causes changes in the velocity of electrons in a way that the induced moment opposes the applied field. It is also clear that the expression of the diamagnetic susceptibility is temperature independent.

2.4.2 Paramagnetism

Paramagnetism is observed in all materials having a permanent net magnetic moment per atom at high temperature. The atomic magnetic moments of a paramagnetic material are randomly orientated as a result of their thermal energy, but can be aligned by an external magnetic field.



Both spin and orbital magnetic moments give contributions to the magnetization which lead to positive susceptibility values for paramagnets. The susceptibilities of paramagnets have typically values of the order 10^{-3} – 10^{-5} and at low fields M is proportional to H , although deviations from proportionality occur at very high fields where the magnetization begins to saturate. The paramagnetic behaviour of materials can be explained using different models. These range from the localized moments model of Langevin, in which the noninteracting electronic magnetic moments on the atomic sites are randomly orientated as a result of their thermal energy, to the Van Vleck model of localized paramagnetic moment, which leads to a temperature-independent susceptibility under certain circumstances. Finally, there is the Pauli model of paramagnetism which depends on the weak spin paramagnetism of the delocalized conduction-band electrons in metals. The Pauli model also leads to a temperature-independent paramagnetic susceptibility.

- The Curie law

The susceptibilities of a number of paramagnetic solids were measured over a wide temperature range by Curie. He found that the susceptibility varied inversely with temperature, as shown in Figure A2.6. This dependence can be described using the well-known **Curie law**

$$\chi = \frac{C}{T}$$

where C is the **Curie constant**.

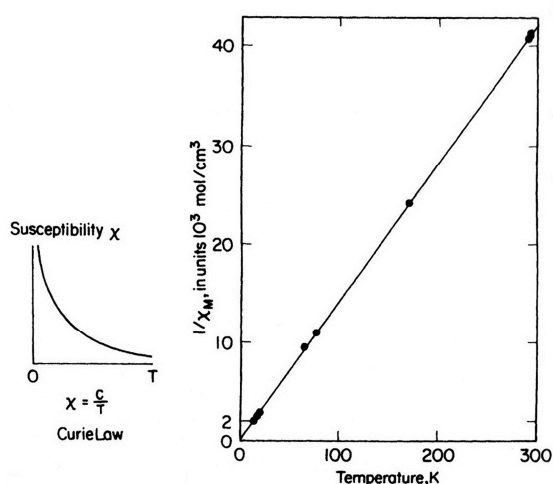


Figure A2.6, Temperature dependence of paramagnetic susceptibility for a Curie paramagnet.

The materials which obey this law are those in which the magnetic moments are localized at the atomic or ionic sites. These can be considered to be “diluted” magnetic materials, in which the magnetic atoms are surrounded by a number of nonmagnetic atoms, like transition metal complexes.

- **Langevin theory of paramagnetism**

In materials with unpaired electrons, and consequently in which the orbital magnetic moments are not balanced, there is a net permanent magnetic moment per atom. If this net magnetic moment \mathbf{m} , obtained as the vector sum of the spin \mathbf{m}_s and orbital \mathbf{m}_o components, were put under a magnetic field \mathbf{H} , its energy will be

$$E = -\mu_0 \mathbf{m} \cdot \mathbf{H}$$

Thermal energy tends to randomize the alignment of the magnetic moments. Langevin supposed that the moments are noninteracting so that the classical Boltzmann statistic can be used to express the probability of any given electron occupying an energy state E . If $k_B T$ is the thermal energy, the probability function which describe the distribution of the magnetic moments in the energy levels is

$$p(E) = e^{\left(-\frac{E}{k_B T}\right)}$$

An expression for evaluating the number of magnetic moment per unit area of the material can be obtained using the levels occupation probability function and integrating this expression over the entire range of possible direction. This gives the total number of magnetic moments per unit volume N

$$N = 2\pi C \int_0^\pi \sin \theta \exp\left(\frac{\mu_0 m H}{k_B T}\right) d\theta$$

$$C = \frac{N}{2\pi \int_0^\pi \sin \theta \exp\left(\frac{\mu_0 m H}{k_B T}\right) d\theta}$$

from which the Langevin expression for the magnetization of a paramagnet can be obtained.

$$\mathbf{M} = \frac{N\mu_0 m^2 \mathbf{H}}{3k_B T}$$

which immediately leads to the **Curie law**

$$\chi = \frac{\mathbf{M}}{\mathbf{H}} = \frac{N\mu_0 m^2}{3k_B T} = \frac{C}{T}$$

This demonstrates that the Langevin model leads to a paramagnetic susceptibility which varies inversely with the temperature, in agreement with the experimental observations of Curie.

- **The Curie-Weiss law**

It was found that the susceptibilities of a number of paramagnetic metals obey a modified or generalized version of the Curie law, **Curie-Weiss law**. The susceptibility of these materials was found to vary as shown in Figure A2.7 and it can be represented in the paramagnetic region by the following equation

$$\chi = \frac{C}{(T - T_c)}$$

where C is again the Curie constant and T_c is another constant with dimensions of temperature.

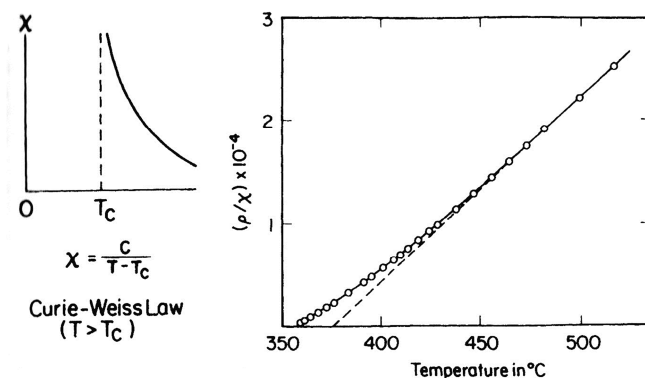


Figure A2.7. Variation of susceptibility as a function of temperature for a paramagnetic material which undergo a transition to ferromagnetism at the Curie temperature T_c .

T_c can be either positive, negative or zero. $T_c = 0$ corresponds, obviously, to the Curie law. Materials having $T_c > 0$ undergo a paramagnetic to ferromagnetic transition and are called ferromagnets, whereas materials having $T_c < 0$ undergo a paramagnetic to antiferromagnetic transition and are called antiferromagnets. The T_c constant is also indicated with the symbol θ and assumes the name of **Weiss constant** (Figure A2.8).

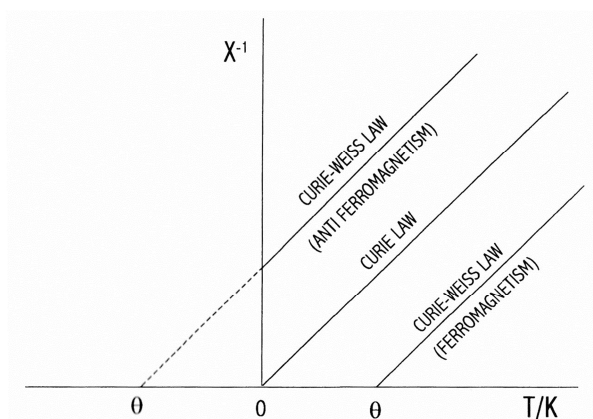


Figure A2.8. Variation of the reciprocal susceptibility as a function of the temperature for: a paramagnet which follow the Curie law ($\theta = 0$), a paramagnet that undergo a paramagnetic to ferromagnetic transition which follows the Curie-Weiss law ($\theta > 0$), a paramagnet that undergo a paramagnetic to antiferromagnetic transition which follows the Curie-Weiss law ($\theta < 0$); the slope of each line is C^{-1} .

The real transition temperatures from a paramagnetic to ferromagnetic or antiferromagnetic state are both positive and are called **Curie temperature** and **Néel temperature** respectively. It should be remembered that the susceptibility of ferromagnets and antiferromagnets only follows the Curie-Weiss law in the paramagnetic region. For lower temperatures, once the material becomes ordered, the susceptibility behaves in a more complicated way and no longer has a unique value for a given field strength.

- **Weiss theory of paramagnetism**

Weiss showed that the variation of paramagnetic susceptibility with temperature of materials which obeyed the Curie-Weiss law could be explained if the individual magnetic moment interacted with each other via an atomic interaction field H_e .

Since in paramagnets the magnetization is locally homogeneous, the magnetic moment per unit volume will be everywhere equal to the bulk magnetization M . Therefore interactions between individual magnetic moments within a localized volume can be expressed as an interaction between a given magnetic moment and the bulk magnetization M .

This can be represented by an interaction field H_e written as

$$H_e = \alpha M$$

The total magnetic field experienced by a magnetic moment then becomes

$$H_{tot} = H + H_e$$

and hence

$$H_{tot} = H + \alpha M$$

Considering the magnetic susceptibility of a material in which such a field operates, this can be view as a perturbation of the Langevin model. A modified Curie law can be obtained assuming that the orientation of magnetic moments is in thermal equilibrium and obeys to the Boltzmann statistics.

$$\frac{M}{H_{tot}} = \frac{C}{T}$$

Since susceptibility is still given as

$$\chi = \frac{M}{H}$$

substituting H with $H_{tot} = H + \alpha M$ the following expression is obtained

$$\chi = \frac{C}{T - \alpha C}$$

$$\chi = \frac{C}{T - T_C}$$

which is the **Curie-Weiss law**.

In conclusion a paramagnetic material with localized but interacting magnetic moments obeys the Curie-Weiss law. The critical temperature T_C defines the boundary between the paramagnetic (disordered) and ferromagnetic or antiferromagnetic (ordered) states of magnetic materials.

2.4.3 Ferromagnetism

In ferromagnetic solids, at temperatures well below the Curie temperature, the magnetic moments within microscopic portions of material called **magnetic domains** are parallel-aligned.



This behaviour can be explained in a phenomenological way by the Weiss field interaction which was originally suggested in order to explain the dependence of paramagnetic susceptibility on temperature in certain materials. As the temperature of a ferromagnet is increased the thermal energy increases while the interaction energy between the magnetic moments is unaffected. At a critical temperature the randomizing effect of thermal energy overcomes the aligning effect of the interaction energy and above this temperature the magnetic state becomes disordered. The variation of susceptibility and magnetization as a function of the temperature for a ferromagnet are reported in Figure A2.9.

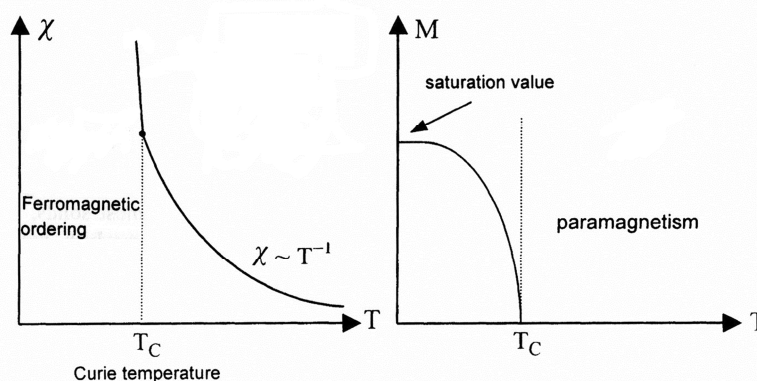


Figure A2.9, Variation of χ and M as a function of T for a typical ferromagnet.

- Weiss theory of ferromagnetism

If electronic magnetic moments, which are responsible for the magnetic properties, are localized on the atomic sites the interaction between magnetic moments can be considered in the same form discussed above for the Weiss theory of paramagnetism. This interaction, introduced by Weiss to explain the variation of the paramagnetic susceptibility of certain materials, leads to the existence of a critical temperature less than the thermal energy of the electronic moments is not enough to cause the random paramagnetic alignment. This means that the effective field H_e can be used to explain the alignment of magnetic moments within magnetic domains for temperatures below T_c .

Supposed that any magnetic moment m_i experiences an effective field H_{eij} due to the presence of another moment m_j and vice versa, the effective field can be written as

$$H_{eij} = J_{ij}m_j$$

The total **field interaction** or **exchange interaction** on the moment \mathbf{m}_i will be the vector sum of all interactions with the other moments of the magnets domain

$$\mathbf{H}_{ei} = \sum_{allj} \mathcal{J}_{ij} \mathbf{m}_j$$

where \mathcal{J}_{ij} it's the interaction constant, also known as **exchange constant**.

In the case of a zero external magnetic field, the only field operating within a domain will be the **Weiss field**

$$\mathbf{H}_{tot} = \mathbf{H}_e$$

When considering the magnetic moments within a domain and the mean-field model, the field interaction, identified with a constant α , will be proportional to the spontaneous magnetization \mathbf{M}_S within a domain. Following an analogous assumption to that given by Langevin for paramagnetism, the following expression can be obtained

$$\frac{\mathbf{M}_S}{\mathbf{M}_0} = \coth\left(\frac{\mu_0 \mathbf{m} \alpha \mathbf{M}_S}{k_B T}\right) - \left(\frac{k_B T}{\mu_0 \mathbf{m} \alpha \mathbf{M}_S}\right)$$

The solution of this equation leads to a perfect alignment of magnetic moments within a domain for temperatures approaching the absolute zero. As the temperature increases the spontaneous magnetization \mathbf{M}_S decreases as shown in Figure A2.10.

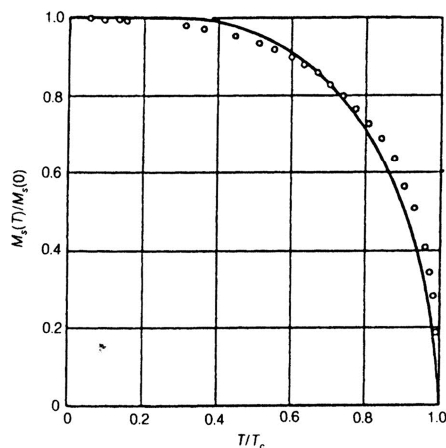


Figure A2.10, Variation of spontaneous magnetization as a function of the temperature for a typical ferromagnet.

At a certain temperature, which corresponds to the T_C , \mathbf{M}_S assumes rapidly the 0 values and this represents the transition between the ordered ferromagnetic state to the disordered paramagnetic state.

From the Curie-Weiss law

$$\chi = \frac{C}{T - T_C}$$

where the Curie constant is

$$C = \frac{N\mu_0 m^2}{3k_B}$$

it is possible to obtain, from the relation $T_C = \alpha C$, the following expression for T_C

$$T_C = \frac{N\mu_0 m^2}{3k_B}$$

From this expression it is possible to determine the mean-field exchange coupling constant α if the value of the magnetic moment per atom m is known.

2.4.4 Antiferromagnetism

Antiferromagnetic order, in which nearest-neighbour moments in a magnetic structure are antiparallel aligned, can be interpreted on the basis of the Weiss model.



There are two ways to explain this behaviour. One consists in considering the magnetic material as divided in two magnetic sublattices A and B, with the magnetic moments of each sublattice interacting with a positive coupling coefficient, whereas the interactions between the two sublattices have a negative coefficient. This ensures that the magnetic moments of the two sublattices point in different directions leading to an overall antiferromagnetic order. Another way is to describe the system with a negative interaction between nearest neighbors.

Considering the simplified situation of a linear chain of magnetic moments, as depicted in the previous scheme, the exchange interaction energy between nearest neighbors with a negative coefficient $-\alpha$ associated to a parallel alignment of spins is

$$E_{\text{paral}} = 10m^2\mu_0\alpha$$

while for an antiparallel alignment

$$E_{\text{anti}} = -10m^2\mu_0\alpha$$

which shows that for a negative nearest-neighbour interaction coefficient an antiparallel alignment is energetically favoured.

The Curie-Weiss also applies to antiferromagnets for T values above the ordering temperature, the **Néel temperature** T_N . Since the exchange coefficient α assumes a negative value, the Curie Weiss law becomes

$$\chi = \frac{C}{T + T_C}$$

For antiferromagnets the T_C appears as a negative temperature below the absolute zero. In fact the plot of $1/\chi$ against T intercepts the temperature axis in the negative region at $-T_C$. At the corresponding positive value of temperature, the Néel temperature, these materials undergo a transition from the ordered antiferromagnetic state to the disordered paramagnetic

state. For T values lower than the Néel temperature, the susceptibility does not follow the Curie-Weiss anymore and behaves in a more complex way. The variation of the susceptibility as a function of the temperature is shown in Figure A2.11.

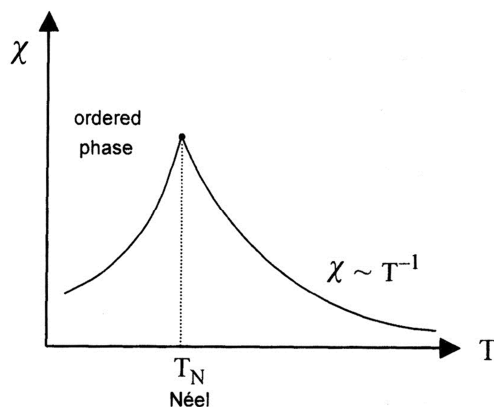


Figure A2.11, Variation of χ as a function of the T for an antiferromagnet; usually the maximum of the susceptibility, corresponding to the T_N , is not that sharp and defined as shown in the figure.

The Néel temperature of antiferromagnets is the analogous of the Curie temperature of ferromagnets. Both mark the borderline temperature above which the material is disordered and above which it is ordered. In both cases the thermal energy is the same as the coupling energy at these transition temperatures. However, it should be pointed out that these two definitions of T_C and T_N are not somewhat equivalent. Some materials, in fact, can be antiferromagnetic and ferromagnetic ordered in different temperature regions and they can have both Curie and Néel temperatures.

2.4.5 Ferrimagnetism

Ferromagnetism can be considered as a particular case of antiferromagnetism in which the magnetic moments of two A and B sublattices are aligned in an antiparallel way, but having a different magnitude give rise to an overall nonzero magnetization.



Ferrimagnetic order was first proposed by Néel to explain the magnetic behaviour of ferrites. Ferrimagnets behave on a macroscopic scale as ferromagnets so that it was not realized for many years that there was a distinction. They have a spontaneous magnetization below the critical temperature and are organized in domains, and they also exhibit hysteresis and a saturation magnetization. The general model used for the description of the ferrimagnetic order consists in considering the magnetic structure divided in two sublattices with magnetic moment of different magnitude. The magnetic moments are parallel coupled on the same sublattice, but are antiparallel coupled respect the magnetic moments of the other sublattice. The superexchange interactions responsible for the coupling of the magnetic moments give rise to an overall ferrimagnetic order that can be also view as a non-compensated antiferromagnetism.

Since the exchange interlattice constant J_{AB} is generally stronger than the intralattice constants J_{AA} and J_{BB} , this leads to the following expression for the temperature dependence of susceptibility which is more complicated than the Curie-Weiss law, but is nevertheless similar

$$\chi = \frac{(C_A + C_B)T - 2\alpha C_A C_B}{T^2 - \alpha^2 C_A C_B}$$

where T is the temperature, α is the interlattice coupling coefficient, and C_A and C_B are the Curie constants for the respective sublattices. In this expression the Curie temperature T_C is given by

$$T_C = \alpha \sqrt{C_A C_B}$$

From the above equations it can be seen that, unlike ferromagnets, the reciprocal susceptibility of ferrimagnets shows a considerable curvature as a function of the temperature as T_C is approached.

2.4.6 Magnetic exchange coupling

The cooperative magnetic phenomena which lead to a magnetically ordered state have been discussed as a consequence of exchange interactions between atomic magnetic moments. The mechanisms responsible for these interactions will be describe now, with the aim of understand and predict the magnetic properties of new magnetic compounds on the basis of their electronic configuration and their molecular structure.

Magnetic moments can interact through-space *via dipolar interactions*, but these interactions are too weak to justify the relatively strong interactions observed in magnetic materials where magnetic centers are quite far with respect each other. On the other hand, magnetic moments can interact through **exchange interactions** based on orbital overlapping characterized by an exchange constant J_{ij} that quantifies the strength of the interaction. These interactions can occur through a direct overlap between the magnetic orbitals of the two magnetic ions, in the so-called **direct exchange coupling**, which is involved in those systems where magnetic atoms are very close to each other. Anyway, since most of magnetic materials, for example transition metal oxides or transition metal complexes, have magnetic ions separated by non-magnetic ions, a mechanism based on an **indirect exchange coupling** must be required to describe these interactions. This mechanism implies the presence of an ion or a molecule bound to the metal centers, a ligand, that is responsible for the interactions between magnetic centers in a so-called **superexchange interaction**.

Considering two metal ions M^{n+} connected in a linear way through a covalent bond with an O^{2-} oxide ion acting as a ligand, the overlap between each metal d -orbitals containing the unpaired electrons responsible for the magnetic properties and the ligand p -orbitals containing paired electrons, leads to a partial donation of the electron density to the metal sites. Supposing that the unpaired electron of the X metal ion has spin $+\frac{1}{2}$ (\uparrow), then, on the basis of the Pauli exclusion principle, the electron density transferred from the ligand p -orbital

must have opposite spin, $-\frac{1}{2}$ (\downarrow). To preserve the spin neutrality of the ligand p -orbital, 0 ($\uparrow\downarrow$), the electron density donated simultaneously to the other metal center Y must have opposite spin sign, $+\frac{1}{2}$ (\uparrow). This induced the unpaired electron on the Y metal site to have spin $-\frac{1}{2}$ (\downarrow), that is opposite to the one associated to the X metal center, as depicted in Figure A2.12.

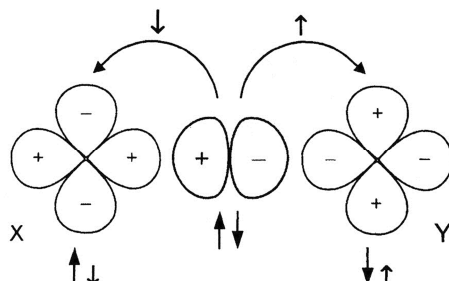


Figure A2.12, Superexchange interactions between two metal ions connected in a linear way through a ligand.

The final result of such superexchange interaction of metal ions connected in a linear way through a ligand, is an antiferromagnetic coupling between them. It should be noted that if metal ions have different magnetic moments the interaction will be ferrimagnetic.

If magnetic ions are connected through the same type of ligand but in a 90° angled spatial configuration, as shown in Figure A2.13, the magnetic interaction will be different.

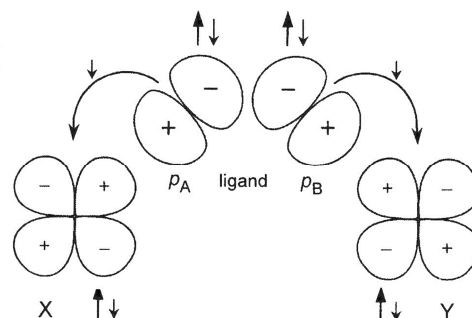


Figure A2.13, Superexchange interactions between two metal ions connected through a ligand in an angular way.

In this case the d -orbitals overlap with different p -orbitals of the same ligand. Spin correlation within the ligand, which always favours the parallel alignment of spins in different orbitals, allow that the electron density given to the metal ions will be of the same sign. The Pauli exclusion principle, as in the previous case, force the spin orientation of the unpaired electrons on the metal centers to be antiparallel with respect to the electron density given by the ligand. This gives rise to a parallel alignment of the spins on the metal centers and a ferromagnetic coupling will be favoured.

It should be noted that the superexchange interaction can lead to different types of magnetic couplings as a function of the M-L-M geometry and, especially, the symmetry of the interacting ligand and metals orbitals. The type of superexchange interaction, ferromagnetic or antiferromagnetic, can be predicted on the basis of the symmetry of the interacting magnetic orbitals and their occupancy following the so-called Goodenough-Kanamori rules. Briefly, an antiferromagnetic coupling is expected if the interacting metal ions have partially

occupied orbitals having the same symmetry (e.g. $\text{Cr}^{\text{III}} t_{2g}^3$, $\text{V}^{\text{II}} t_{2g}^3$), whereas a ferromagnetic coupling is expected for the interaction between metal ions having partially occupied orbitals with different symmetry (e.g. $\text{Cr}^{\text{III}} t_{2g}^3$, $\text{Ni}^{\text{II}} t_{2g}^6 e_g^2$). If a certain metal ion has more than one type of partially occupied orbitals having different symmetry (e.g. $\text{Mn}^{\text{II}} t_{2g}^3 e_g^2$), the interaction with another metal ion whose orbitals are partially occupied for a certain symmetry and empty for the other type of symmetry (e.g. $\text{Cr}^{\text{III}} t_{2g}^3 e_g^0$), can be ferromagnetic or antiferromagnetic as a consequence of the competition between antiferromagnetic interactions between partially occupied orbitals having the same symmetry (t_{2g}^3) and ferromagnetic interactions between partially occupied orbitals having different symmetry (e.g. $\text{Mn}^{\text{II}} e_g^2$, $\text{Cr}^{\text{III}} t_{2g}^3$).

It must be highlighted that these are semi-empirical rules that are not always proved since other factors, such as the bond geometry and the ligand orbitals symmetry, contribute to the overall sign of the interaction.

2.5 Electronic magnetic moments

The magnetic properties of electrons are of fundamental importance in magnetism because the different energy states that an atom can assume in the presence of a magnetic field are connected with their properties, and because the combination of electronic magnetic moments, originated from their angular momentum, gives the so-called atomic magnetic moment.

2.5.1 The classical model of magnetic moments

In the classical model the **angular momentum of electrons** can be used to describe the **electronic magnetic moment** by invoking the concept of electrical charge in motion. The electronic magnetic moment is given as a vector sum of two contributions:

- the orbital magnetic moment due to the orbital angular momentum;
- the spin magnetic moment due to the electronic spin angular momentum.
- **Electronic orbital magnetic moment**

Assuming that an electron moves in an orbit around an atomic nucleus having area A and period τ . This would then be equivalent to a current i given by

$$i = \frac{e}{\tau}$$

From the basis of the previously described definitions, this system will be associated to an orbital magnetic moment m_o given as

$$m_o = i A = -\frac{e A}{\tau}$$

The angular momentum of such electron in orbital motion is $\mathbf{p}_O = I\boldsymbol{\omega}$, where I is the moment of inertia of the particle of mass m_e orbiting the nucleus and $\boldsymbol{\omega}$ is the angular velocity. Since $I = m_e r^2$ then

$$\mathbf{p}_O = m_e r^2 \boldsymbol{\omega}$$

where r is the orbit radius. The area of the orbit will be

$$A = \left(\frac{1}{2}\right) \mathbf{p}_O \frac{\tau}{m_e}$$

At this point an equation for describing the orbital magnetic moment \mathbf{m}_O of the electron in terms of orbital angular momentum \mathbf{p}_O can be written as follow

$$\mathbf{m}_O = -\left(\frac{e}{2m_e}\right) \mathbf{p}_O$$

remembering that the magnetic moment vector points in the opposite direction to the angular moment vector because the electron has negative charge.

- **Electronic spin magnetic moment**

The **electronic spin angular momentum** \mathbf{p}_S generates an **electronic spin magnetic moment** \mathbf{m}_S . In this case the relation between \mathbf{m}_S and \mathbf{p}_S is

$$\mathbf{m}_S = -\left(\frac{e}{m_e}\right) \mathbf{p}_S$$

It should be noted that for a given angular momentum the spin gives twice the magnetic moment of orbital moment. This results can be justified classically relating this system to a rotating disk of mass m_e whose charge is localized on the circumference. The spin angular momentum is then $\mathbf{p}_S = I\boldsymbol{\omega}$, where $I = \frac{1}{2} m_e r^2$, so that $\mathbf{p}_S = \frac{1}{2} m_e r^2 \boldsymbol{\omega}$ and the magnetic moment is

$$\mathbf{m}_S = i A = -\frac{e \boldsymbol{\omega} r^2}{2}$$

- **Total electronic magnetic moment**

The **total magnetic moment** per electron can be described as the vector sum of the spin and orbital magnetic moments

$$\begin{aligned} \mathbf{m}_{tot} &= \mathbf{m}_O + \mathbf{m}_S \\ \mathbf{m}_{tot} &= -\left(\frac{e}{2m_e}\right) 2\mathbf{p}_O - \left(\frac{e}{2m_e}\right) \mathbf{p}_S \end{aligned}$$

The terms on the right-hand side can be combined to give the following expression

$$\mathbf{m}_{tot} = -g \left(\frac{e}{2m_e}\right) \mathbf{p}_{tot}$$

where \mathbf{p}_{tot} is the **total angular momentum** of the electron. The term g is called the **Landè splitting factor**, which assumes the value of $g = 2$ for the spin component and $g = 1$ for the orbital component.

Although this equation relating the angular momentum to the magnetic moment of an electron works quite well, allowing for a variable splitting factors g , the classical interpretation of the magnetic moment of the electron in terms of a spinning charge leads to unreasonable tangential velocities. Therefore, the classical interpretation in terms of an effective or "Ampèrian" current has to be abandoned in favour of a quantum mechanical approach.

2.5.2 Quantum mechanical model of magnetic moments

In the classical model the angular momenta \mathbf{p}_O and \mathbf{p}_S can assume any values. Actually this is not realistic since the possible values of electronic angular momentum are restricted by quantum mechanics. Consequently, the magnetic moments are also quantized.

- **Electronic orbital magnetic moment**

If the **orbital angular momentum** is expressed in $h/2\pi$ units, its expression becomes

$$\mathbf{m}_O = -\left(\frac{eh}{4\pi m_e}\right)\left(\frac{2\pi\mathbf{p}_O}{h}\right)$$

and since $\mathbf{p}_O = \mathbf{l}(h/2\pi)$

$$\mathbf{m}_O = -\left(\frac{eh}{4\pi m_e}\right)\mathbf{l}$$

where \mathbf{l} is the **orbital angular momentum quantum number**.

From quantum theory, the electronic orbital angular momentum \mathbf{p}_O is an integral multiple of $h/2\pi$, so that the contribution to the magnetic moment of the orbital angular momentum is an integral multiple of $eh/4\pi m_e$. This quantity is known as the **Bohr magneton** μ_B , which has the value of $9.27 \times 10^{-24} \text{ A m}^2$.

$$\mathbf{m}_O = -\mu_B \mathbf{l}$$

- **Electronic spin magnetic moment**

The electronic spin is always $1/2$, then assuming that the spin angular momentum \mathbf{p}_S is an integer multiple of $h/2\pi$, $\mathbf{p}_S = \mathbf{s}(h/2\pi)$ where \mathbf{s} is the **spin quantum number**. The magnetic moment \mathbf{m}_S due to the spin is then

$$\mathbf{m}_S = -\left(\frac{eh}{2\pi m_e}\right)\left(\frac{2\pi\mathbf{p}_S}{h}\right)$$

Replacing $(2\pi\mathbf{p}_S/h)$ by the spin quantum number \mathbf{s}

$$\mathbf{m}_S = -2\left(\frac{eh}{4\pi m_e}\right)\mathbf{s}$$

Here it is found that, for a given angular momentum, the spin gives twice the magnetic moment with respect to the orbital contribution to the total electronic moment, as found with

the classical model. The difference in the relations between the spin and orbital magnetic moments and their respective angular momenta is attributed to relativistic effects.

Replacing the quantity $eh/4\pi m_e$ with the Bohr magneton μ_B

$$\mathbf{m}_S = -2\mu_B \mathbf{s}$$

where $2\mathbf{s} = 4\pi\mathbf{p}_s/h$ as a consequence of the quantization of the angular momentum. Since s must be $+1/2$ or $-1/2$, the spin magnetic moment of one electron corresponds to one Bohr magneton.

- Total electronic magnetic moment

The **total magnetic moment** of an electron can be expressed in terms of multiples of the **total angular momentum** $(h/2\pi)\mathbf{j}$.

$$\begin{aligned}\mathbf{m}_{tot} &= -g \left(\frac{eh}{4\pi m_e} \right) \left(\frac{2\pi\mathbf{p}_{tot}}{h} \right) \\ &= -g\mu_B \left(\frac{2\pi\mathbf{p}_{tot}}{h} \right) \\ &= -g\mu_B \mathbf{j}\end{aligned}$$

where \mathbf{j} is the **total angular momentum quantum number**.

For an electron the total magnetic moment can be written as

$$\begin{aligned}\mathbf{m}_{tot} &= \mathbf{m}_O + \mathbf{m}_S \\ \mathbf{m}_{tot} &= -(\mu_B \mathbf{l} + 2\mu_B \mathbf{s})\end{aligned}$$

For completeness, it shall be taken into account that the assumption that the angular momenta are integral multiples of the quantum numbers l and s is not quite valid. Precisely, the values according to wave mechanics are $\mathbf{p}_O^2 = (h/2\pi)^2 l(l+1)$ and $\mathbf{p}_S^2 = (h/2\pi)^2 s(s+1)$, and the corresponding magnetic moments become $\mathbf{m}_O = \mu_B \sqrt{|l(l+1)|}$ and $\mathbf{m}_S = \mu_B \sqrt{|s(s+1)|}$. The total magnetic moment \mathbf{m}_{tot} needs an analogous correction since $\mathbf{p}_{tot} = (h/2\pi)\sqrt{|j(j+1)|}$.

2.5.3 Magnetic properties of free atoms

The magnetic properties of an atom are principally determined by the magnetic moments of its electrons which can be calculated as sum of spin and angular contributions. Since the net magnetic moment of a filled electron shell is zero, only the unfilled shell needs to be considered.

The angular momentum of an atom can be found summing vectorially the spin and orbital angular momenta of its electrons. This can be done in two ways. The \mathbf{j} value can be found for each electron and the sum of these values gives the value of the **total angular momentum \mathbf{J}** . Alternatively the orbital angular momenta of all electrons within an atom can be vectorially summed giving the **total angular momentum \mathbf{L}** , and in a similar way, the spin angular

momenta can be vectorially summed giving the **total spin angular momentum S** . L and S can then be added vectorially to provide the J for an atom. These two methods do not give identical results when the spin and orbit moments are coupled.

- **Atomic magnetic moment**

The atomic magnetic moment can be determined from the value of its total angular momentum. A semi-classical vector model allows to calculate the J value using L and S . The model is semi-classic because J is calculated as classical vector sum of quantum mechanics values L and S .

An electron has a total angular momentum j which arises from its orbital angular momentum l and its spin angular momentum s . In the vector model j is simply the vector sum of l and s .

$$j = l + s$$

For any given value of l , j can only have two possible values, $j = l \pm s$, depending on whether s is parallel or antiparallel to l , except for $l = 0$ where $j = \pm \frac{1}{2}$. For an atom with a single electron in an outer unfilled shell, these values determine the angular momentum of the atom, then its total magnetic moment. For a multielectron atom, that is one with more than one electron in an unfilled shell, the values of J , L and S need to be determined for obtaining the atomic magnetic moment.

It should be mentioned that a very small contribution to the total angular momentum of an atom is due to the nuclear spin magnetic moment. This contribution is about 10^{-3} smaller than the electronic spin. The nuclear magnetic moment is measured in nuclear magnetons μ_N units. The value of μ_N is $5,05 \times 10^{-27} A m^2$, compared to $9,27 \times 10^{-24} A m^2$ for the Bohr magneton.

- **Atomic orbital angular momentum L**

The atomic orbital angular momentum, denoted by the quantum number L is the vector sum of the orbital angular momenta of electrons within an atom.

$$L = \sum l_i$$

The magnitude of the orbital angular momentum L , $|L|$, is

$$|L| = \sqrt{[L(L + 1)]}$$

which is identical in form to the relation of $|l|$ for a single electron.

- **Atomic spin angular momentum S**

The atomic spin angular momentum S and its magnitude $|S|$ can be obtained in a similar way as described for L

$$S = \sum s_i$$
$$|S| = \sqrt{[S(S + 1)]}$$

- **Hund's rules: occupancy of available electron states**

A set of empirical rules allow for determine the occupancy of the available electronic states within an atom. These rules identify how the possible electronics states are filled and can be used therefore to calculate L , S and J for an atom from the electron configuration of its unfilled shell.

The **Hund's rules** can be applied to electrons in a particular shell to determine the ground state of the atom. The three rules apply to determine S , L and J respectively:

- the maximum value of the total atomic spin angular momentum $S = \sum m_s$ is obtained without violating the Pauli exclusion principle;
- the maximum value of the total atomic spin angular momentum $L = \sum m_l$ in as a function of the state occupancy determined by S ;
- the value of the total atomic angular momentum J is equal to $|L - S|$ when the shell is less than half full, and is equal to $|L + S|$ when the shell is more than half full. When the shell is exactly half full $L = 0$ so that $J = S$.

This means that the electrons will occupy states with all spins parallel within a shell as far as is possible. The electronic configuration obtained following the Hund's rules is associated to an energy state of the system identified by a **term symbol**.

$$^{2S+1}L_J$$

where $2S + 1$ is the spin multiplicity, and $L = 0, 1, 2, 3, \dots$, assume the symbols S, P, D, F, \dots , respectively.

- **Total atomic angular momentum J**

The coupling between the orbital angular momentum of an atom L and the spin angular momentum S gives the total atomic angular momentum J . This sum can be obtained in two ways.

- by independently summing the orbital and spin angular momenta of the unpaired electrons

$$J = \sum l_i + \sum s_i$$

This method is known as **Russell-Saunders coupling**. In this case the l vectors of the electrons are coupled together ($l - l$), and the s vectors are coupled together ($s - s$). These couplings are stronger than the coupling between the resultant L and S vectors.

- by summing the total angular momenta of the electrons, which are obtained for each electron individually by summing its l and s values

$$J = \sum j_i = \sum (l_i + s_i)$$

This method is known as ***j-j coupling*** and occurs if there is a strong ***spin-orbit coupling*** ($l - s$) for each electron. In this case the coupling between l and s within an electron is stronger than the coupling between the various l and s values for different electrons.

In practice, the most common way of describing the coupling is the Russel-Saunders method. This method is the most appropriate for describing magnetic properties of first transition elements whereas the ***j-j*** coupling applies better for describing heavier atoms, especially lanthanides.

- Quenching of the orbital angular momentum L

For $3d$ elements it has been found experimentally that $J = S$ as shown in Table A2.1. This implies that $L = 0$ and we say that the orbital angular momentum is "quenched".

Table A2.1. Calculated magnetic moments for $L \neq 0$ and $L = 0$, and experimental magnetic moments m for $3d$ ions.

Ion	Configuration	$m = g\sqrt{J(J+1)}$	$m = g\sqrt{S(S+1)}$	m
Ti(III), V(IV)	$3d^1$	1.55	1.73	1.8
V(III)	$3d^2$	1.63	2.83	2.8
Cr(III), V(II)	$3d^3$	0.77	3.87	3.8
Mn(III), Cr(II)	$3d^4$	0	4.90	4.9
Fe(III), Mn(II)	$3d^5$	5.92	5.92	5.9
Fe(II)	$3d^6$	6.70	4.90	5.4
Co(II)	$3d^7$	6.63	3.87	4.8
Ni(II)	$3d^8$	5.59	2.83	3.2
Cu(II)	$3d^9$	3.55	1.73	1.9

Under certain conditions the plane associated to the orbit motion of the electron can move frequently, so that the orbital angular momentum contribution is averaged to zero. It should be highlighted that this phenomenon does not occur for those elements having unpaired electrons on $4f$ orbitals or for heavy transition metals.

Since in these elements $J = S$ and $L = 0$, the total atomic magnetic moment is given by the following equation

$$m = 2\mu_B\sqrt{S(S+1)}$$

the so-called ***spin-only magnetic moment***.

For example, the magnetic moment for a Fe^{II} (d^6) ion calculated with the spin-only formula corresponds to $4,9 \mu_B$. This agrees reasonably well with the observed value of $5,36 \mu_B$ whereas the calculated value without quenching of the orbital contribution is $6,7 \mu_B$, which clearly disagree with the experimental value.

It should be highlighted that these calculations apply only to the isolated paramagnetic (non-interacting) atoms or ions. When a large number of atoms are present within a solid, the electron energy levels are drastically altered and the magnetic moment per atom in most cases significantly different from the isolated atoms values.

- Effective magnetic moment and χT value

By associating the spin-only moment expression to the Curie law, an expression for describing the paramagnetic susceptibility variation as a function of the temperature can be obtained

$$\chi = \frac{N_A \mu_B^2}{3k_B T} [g^2 S(S+1)]$$

which can be written in terms of χT as follow

$$\chi T = \frac{N_A \mu_B^2}{3k_B} [g^2 S(S+1)]$$

where the $N_A \mu_B^2 / 3k_B$ constant assumes the $0.125048612 \text{ cm}^3 \text{ mol}^{-1}$ value. The χT product has great importance in experimental susceptibility measurements. For a Curie paramagnet the variation of χT as a function of the temperature is constant and appears in the whole temperature range as a straight line, except at very low temperature where zero field splitting effects, *i.e.* the separation of the degenerate energy states associated to different values of the spin quantum number, can be observed. For those systems which undergo magnetic phase transition the variation of χT as a function of the temperature is not constant and deviations from the linearity can be observed. An increase in χT as the temperature decreases is associated to a ferromagnetic coupling, *i.e.* a positive Weiss constant θ , whereas a decrease of χT as the temperature decreases is associated to an antiferromagnetic coupling, *i.e.* a negative Weiss constant θ .

The χT product is associated to another relevant quantity used in the experimental practice, the effective magnetic moment μ_{eff} , defined as

$$\mu_{eff} = g \sqrt{|S(S+1)|} = \sqrt{8\chi T}$$

and expressed as Bohr magnetons units; the factor 8 arises from a combination of the various constants. In Table A2.2 the calculated μ_{eff} and χT values are reported for different numbers of unpaired electrons in the case of spin-only approximation.

Table A2.2. Calculated values for χT and μ_{eff} for different numbers of unpaired electrons in the case of spin-only approximation.

e	$\mu_{eff} (\mu_B)$	$\chi T (\text{cm}^3 \text{K mol}^{-1})$
1	1.73	0.375
2	2.83	1.000
3	3.87	1.875
4	4.90	3.000
5	5.92	4.375

It should be highlighted that this values are associated to high temperatures states, *i.e.* around r.t., where the thermal energy is higher than the coupling interactions and the system behaves as a pure paramagnet. The χT product can also be summed up whereas μ_{eff} is not additive: if a molecule has two spin centers, the calculated value of χT is simply the sum of the contributions furnished by the two metal ions

$$\chi T = \frac{N_A \mu_B^2}{3k_B} [(g_A^2 S_A(S_A + 1)) + (g_B^2 S_B(S_B + 1))]$$

where g_A and g_B are the Landé splitting factors for the two different metal ions (the Landé factors can be considered equal to 2 in first approximation). The μ_{eff} value, instead, is not additive due to its dependence on $\sqrt{\chi}$.

A plot of χT as a function of T (Figure A2.14) is very useful because:

- deviations from linearity are associated to magnetic ordering phenomena that can be described as a function of the increased or decreased χT value with respect of the value at high temperature;
- the χT value at high temperature is associated to the magnetic moment per mole of the system.

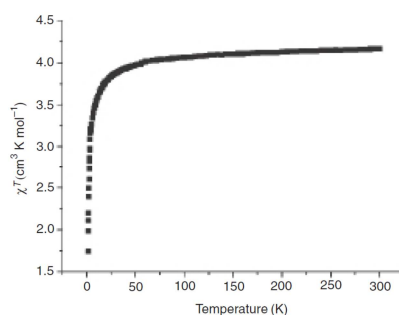


Figure A2.14, Thermal variation of χT for a Mn^{II} complex. The r.t. value of χT ($4,17 \text{ cm}^3 \text{ K mol}^{-1}$) is in agreement with the calculated value for a d^5 metal ion in the only-spin approximation ($S = 5/2$) $4,375 \text{ cm}^3 \text{ K mol}^{-1}$. The decrement of χT at low temperature is associate to antiferromagnetic coupling interactions between magnetic centers.

The expression of the saturation magnetization M_S

$$M_S = N_A g S \mu_B$$

it is also of great importance for the magnetic materials characterization and in particular for molecular systems.

This equation allows for determining the spin state of a system when subjected to the action of a magnetic field strong enough to orientate all magnetic moments in the same direction (Figure A2.15). If magnetization is expressed as μ_B units, its value is simply given by the gS product.

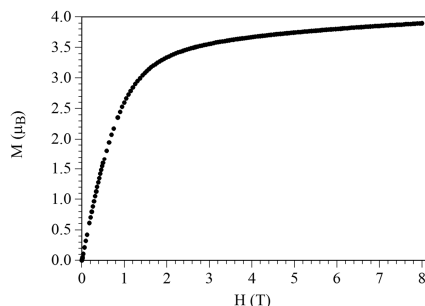


Figure A2.15, Variation of M as a function of the field for an Fe^{2+} ($S = 2$) complex; it can be seen that the magnetization values at high fields tends to the calculate value for M_S of $4\mu_B$.

References

This Appendix has been written with the support of the following textbooks:

- Jiles, D. *Introduction to Magnetism and Magnetic Materials*, **1998**, Chapman & Hall;
- Orchard, A. F. *Magnetochemistry*, **2003**, Oxford University Press;
- Carlin, R. L. *Magnetochemistry*, **1986**, Springer;
- Kahn, O. *Molecular Magnetism*, **1993**, VCH, New York.
- Coey, J. M. D. *Magnetism and Magnetic Materials*, **2010**, Cambridge University Press;
- *Magnetism, Molecules to Materials II: Molecule-Based Materials*, Edited by Miller, J. S. and Drillon, M., **2002**, Wiley-VCH;
- Robertson, N. and Yee, G.T. *Molecular Materials, Chapter III: Magnetic Molecular Materials*, Edited by Bruce, D. W.; O'Hare, D.; Walton, R. I., **2010**, Wiley.

Appendix 3

The Electrocrystallization Technique



A short description of the experimental technique commonly employed for the preparation of crystalline radical cation salts is reported herein. Examples of such systems are reported in Chapters 4 and 5 of this thesis.

3.1 The Electrocrystallization Technique

To fully characterize a molecular conductor, high-quality single crystals are required for X-ray diffraction studies and four-probes conductivity measurements.

Molecular conductors can be obtained by chemical or electrochemical oxidation of the organic donor. The first method yields, in most cases, powdered materials (due to their low solubility), whereas, the second one, commonly called electrocrystallization, allows for a controlled and slow oxidation of the organic donor on the surface of a platinum wire electrode. Once the experimental conditions are optimized, high quality single crystals suitable for the desired chemical and physical characterization can be obtained.

A synthesis *via* electrocrystallization is commonly performed in a special H-shape glass cell where two chambers are connected through a porous septum (Figure A3.1). The two chambers are called anodic and cathodic compartments. In the anodic compartment usually is placed a solution of the organic donor mixed with the counterion, whereas in the cathodic compartment there is a solution of the counterion only. Usually the solutions were degassed before the experiments. The septum allows for a slow diffusion of the two solutions, and, in the same time, permits ion-based electrical conductivity in solution due to the presence of the counterion that works also as electrolyte. The electrodes, usually two platinum wires, are placed in the two compartments, and are connected to a potentiostat/galvanostat, depending if the experiment is performed in potentiostatic or galvanostatic conditions. Two valves can be connected to the cell if inert atmosphere is needed.

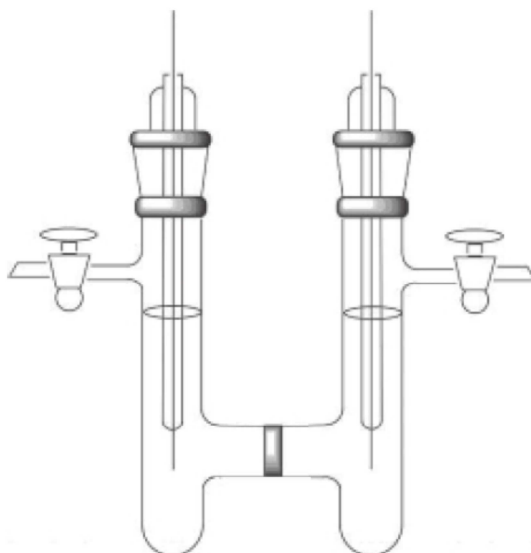


Figure A3.1. Schematic picture of a generic H-shape electrocrystallization cell equipped with a pair of electrodes.

An electrosynthesis usually lasts from few days to several weeks and is performed in a thermostatic free of vibrations dark ambient.

During an electrocrystallization experiment, the following parameters have to be controlled and taken into account:

- the solvent; it can be a pure compound or a mixture. It plays an important role on the solubility of the starting materials and the final product, on the redox potentials of the species in solution, and on the electrode/solution and crystal/solution surface tension, affecting the crystals quality and, in some cases, the crystal phase;
- the temperature; same as above although to a different extent;
- the current intensity; the rate of the crystal growing, and hence, the quality of the crystals depends on its value. Galvanostatic conditions are usually preferred to potentiostatic conditions to promote a regular crystal growing. To ensure reproducible experimental conditions, the value of current density (the current intensity/electrode surface ratio) should be taken into account rather than the current intensity.

Moreover, the experiment is affected by the following factors:

- electrochemical properties of the counterion;
- purity and concentration of the reagents ;
- solvents purity;
- stability of the applied current intensity.

Due to the high number of parameters involved in the outcome of an electrosynthesis, several experiments are often required to optimize the experimental conditions for obtaining high quality single crystals.

Moreover, the electrical properties of a material can be strongly dependent on the type and amount of its impurities. For this reason, in order to have reproducible results, great attention must be given to clean the equipment, with particular attention to the electrodes surface.

The electrodes cleaning consists in the following steps:

- chemical cleaning, by using *aqua regia* (HNO_3/HCl 1:3 v/v) or *piranha solution* (H_2SO_4 95-98%/ H_2O_2 30% 3:1 v/v);
- electrochemical cleaning (or depolarization); it consists in placing the electrodes in a aqueous solution of diluted sulfuric acid (~1M) and connecting them to a DC generator. By periodically inverting the polarity of the electrodes, H_2 and O_2 are alternatively generated on their surface, allowing for the elimination by reduction or oxidation of all undesired impurities.
- washings with distilled water and methanol.

Electrocrystallization is the most employed technique for the preparation of crystalline conducting molecular materials. It presents some disadvantages, such as the meticulous preparation of the experiments, their duration in time, and the small quantity of obtained products (often few milligrams). Nevertheless, it allows to obtaining the desired materials as high-quality single crystals, the morphological form suitable for their full structural and physical characterization.

Appendix 4

Supplementary Material

4.1 Chapter 1 Supplementary Material

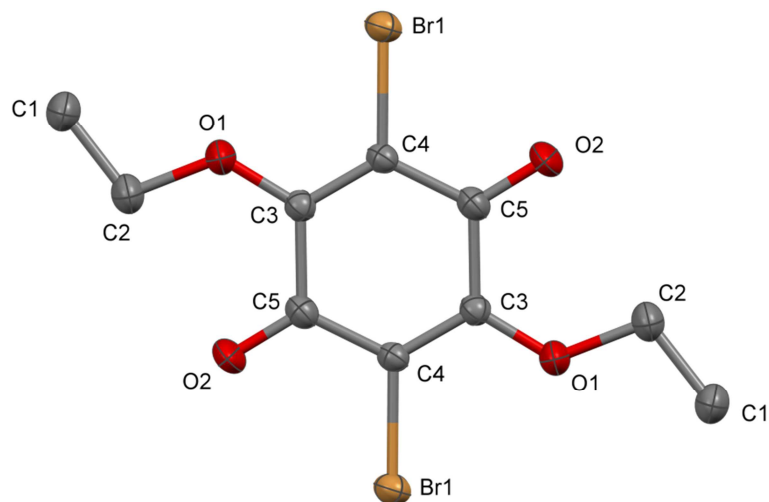


Figure S1.1. Ortep drawing of **2a** with thermal ellipsoids at 30% probability level.

Table S1.1. Summary of X-ray crystallographic data for **2a**.

2a	
Empirical formula	C ₁₀ H ₁₀ Br ₂ O ₂
Formula weight	354.00
Crystal size, mm	0.20 × 0.05 × 0.025
Crystal system	Monoclinic
Space group	<i>P</i> 2 ₁ / <i>a</i>
<i>a</i> , Å	8.937(1)
<i>b</i> , Å	5.0321(2)
<i>c</i> , Å	13.314(1)
α, deg.	90
β, deg.	96.958(8)
γ, deg.	90
<i>V</i> , Å ³	594.34(9)
<i>Z</i>	2
<i>T</i> , K	293(2)
ρ (calc), Mg/m ³	1.978
μ, mm ⁻¹	6.815
θ range, deg.	4.33–26.98
GooF	1.091
<i>R</i> 1	0.0357
<i>wR</i> 2	0.0568

$$R1 = \sum ||F_o| - |F_c|| / \sum |F_o|, wR2 = [\sum [w(F_o^2 - F_c^2)^2] / \sum [w(F_o^2)^2]]^{1/2}, w = 1 / [\sigma^2(F_o^2) + (aP)^2 + bP], \text{ where } P = [\max(F_o^2, 0) + 2F_c^2] / 3.$$

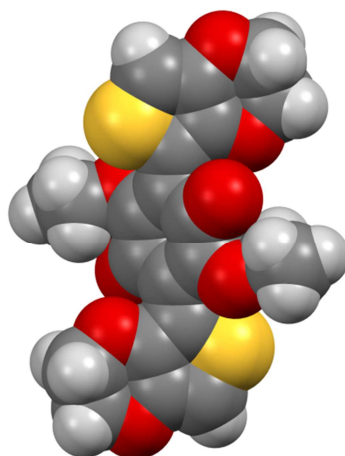


Figure S1.2, Molecular structure for compound **4a** in space filling model; the steric hindrance between the 3,4-ethylenedioxy group and the benzoquinone moiety is highlighted.

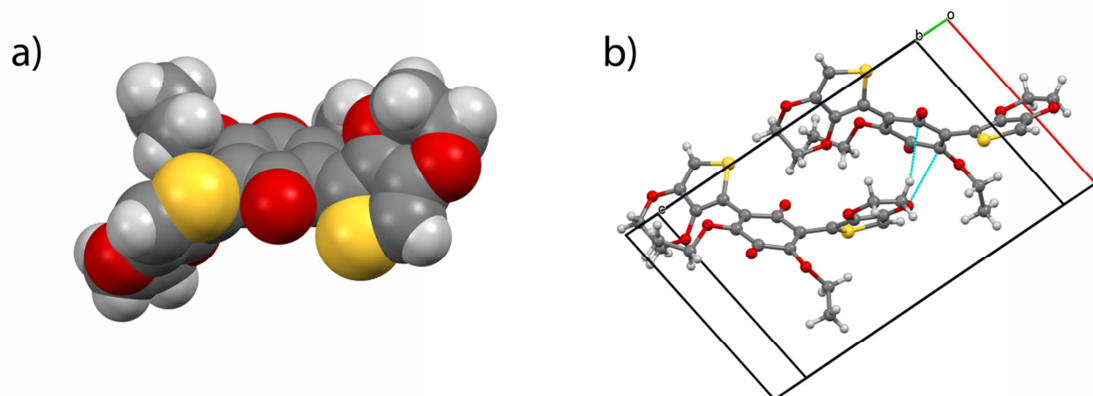


Figure S1.3, a) Molecular structure for compound **4b** in space filling model; b) Stacking interactions between the 3,4-ethylenedioxy fragment and the benzoquinone ring: O(7)...C(3) 3.19 Å; C(18)-H...C(1) 2.86 Å.

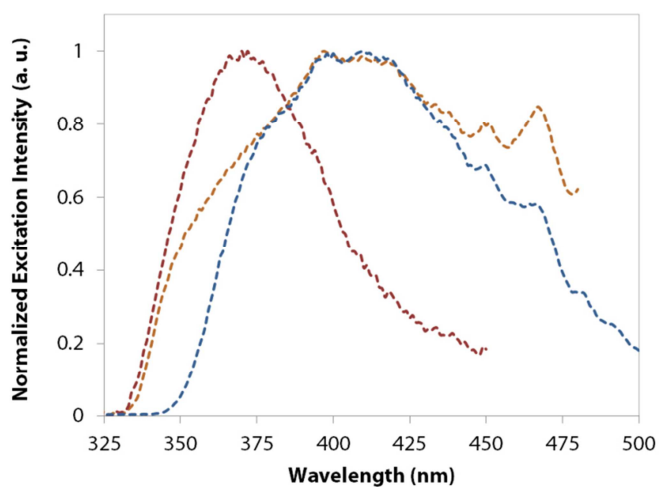


Figure S1.4, Excitation spectra (325–500 nm) for **9** in CH₃CN solution (orange line), and **8** in H₂O solution in its protonated (red line) and dianionic (blue line) forms.

Table S1.2. Selected bond distances (Å) of the benzoquinone ring for compounds **3a**, **3b**, **4a**, and **4b**.

	3a	3b		4a	4b
C=O	1.223(4)	1.218(4) 1.227(4)	1.223(4) 1.219(4)	1.222(2)	1.226(5) 1.223(4)
C=C	1.359(4)	1.352(5) 1.346(5)	1.368(5) 1.347(5)	1.359(2)	1.345(5) 1.343(5)
C–O	1.334(4)	1.361(4) 1.344(4)	1.361(4) 1.342(4)	1.342(2)	1.342(4) 1.352(4)
C–C	1.479(4)	1.482(5) 1.500(5)	1.489(5) 1.471(5)	1.475(2)	1.484(5) 1.495(5)
	1.501(4)	1.481(5) 1.500(5)	1.505(5) 1.488(5)	1.499(2)	1.481(5) 1.489(5)

Table S1.3. Frontier orbitals plots for **3a** and **3b** with an isovalue chosen to represent 35% of the function.

MO	3a	3b
LUMO+1		
LUMO		
HOMO		
HOMO-1		

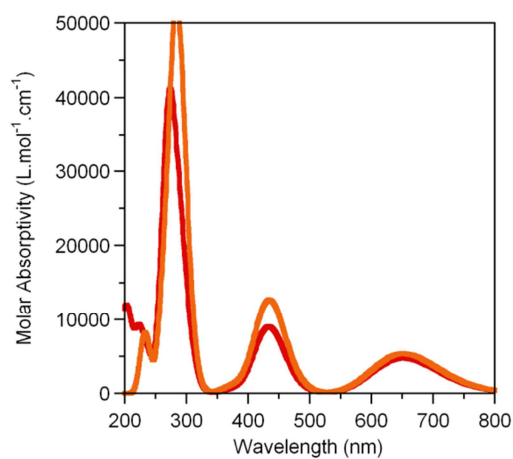
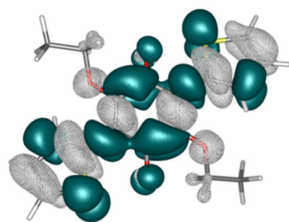


Figure S1.5. Comparison between simulated absorption spectra of **3b** in solution (non-equilibrium LR-PCM) (orange line) and in gas phase (red line).

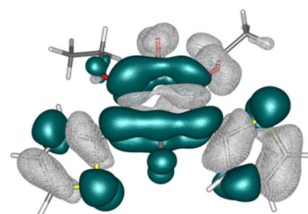
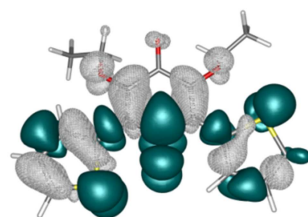
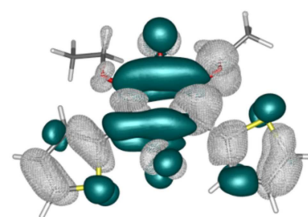
Table S1.4. One-electron density difference between the ES and GS. The isocontour value is set to represent 75% of the electron. The solid turquoise (white grid) zones indicate increase (decrease) of density upon electronic transition.

Excitation (Osc. Str.)	3a	Excitation (Osc. Str.)	3b
$S_0 \rightarrow S_1$ (0.000)		$S_0 \rightarrow S_1$ (0.066)	
$S_0 \rightarrow S_2$ (0.122)		$S_0 \rightarrow S_2$ (0.050) + $S_0 \rightarrow S_4$ (0.050)	

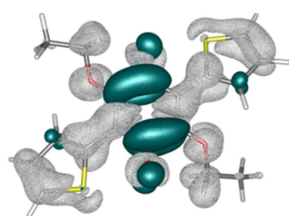
$S_0 \rightarrow S_8$
(0.612)



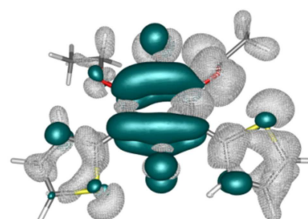
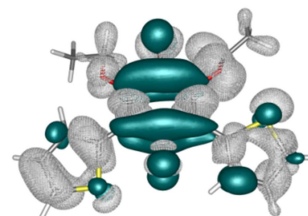
$S_0 \rightarrow S_8$
(0.088)
+
 $S_0 \rightarrow S_{10}$
(0.410)
+
 $S_0 \rightarrow S_{12}$
(0.071)



$S_0 \rightarrow S_9$
(0.308)



$S_0 \rightarrow S_9$
(0.161)
+
 $S_0 \rightarrow S_{11}$
(0.122)



4.2 Chapter 2 Supplementary Material

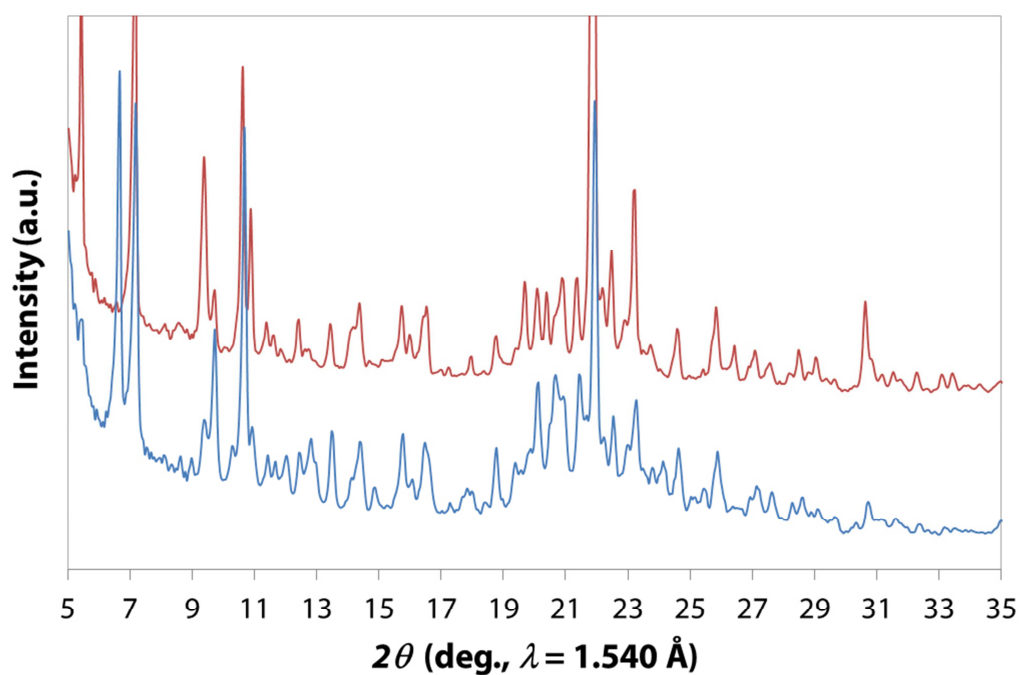


Figure S2.1, Comparison between experimental PXRD patterns (5–35°, 2θ) for **C1b** (blue line) and **C2b** (red line).

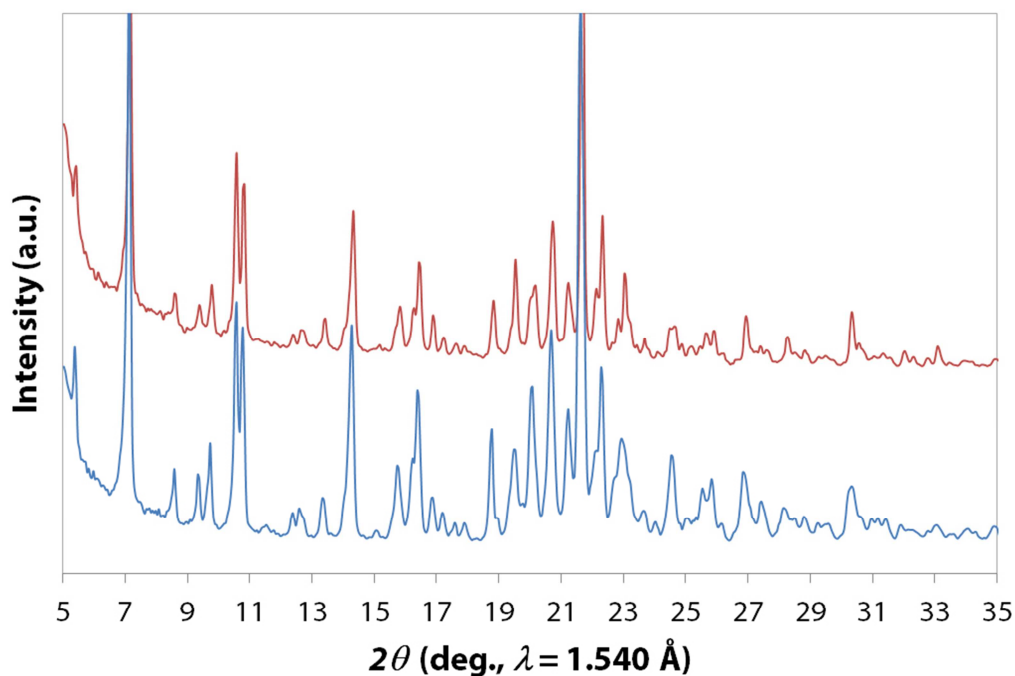


Figure S2.2, Comparison between experimental PXRD patterns (5–35°, 2θ) for **C3b** (blue line) and **C4b** (red line).

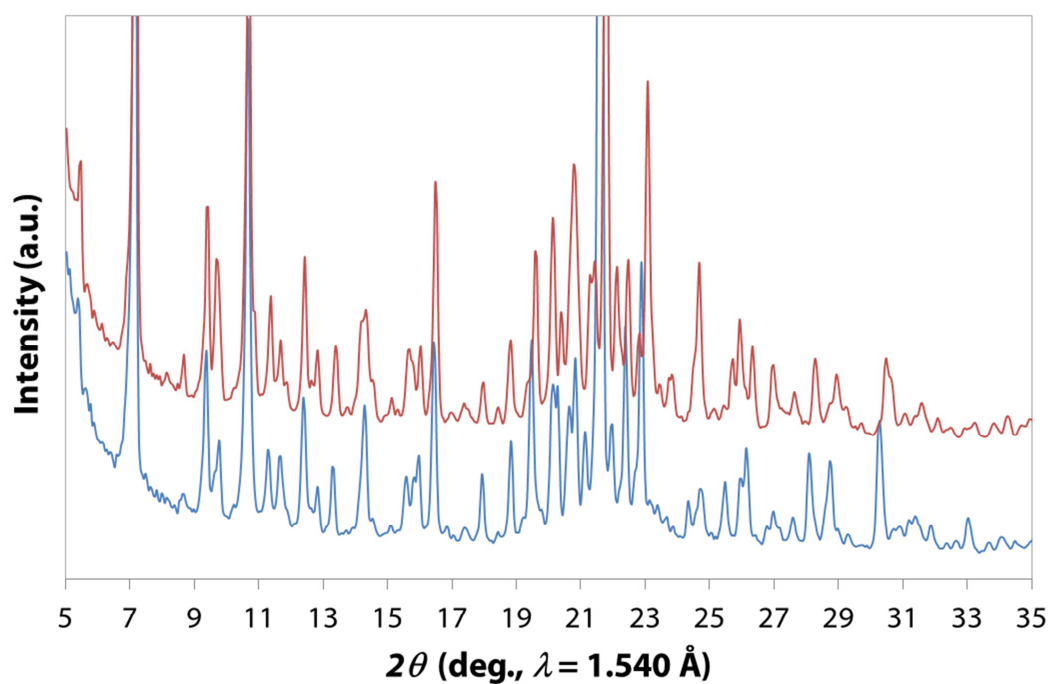


Figure S2.3, Comparison between experimental PXRD patterns (5–35°, 2θ) for **C10b** (blue line) and **C9b** (red line).

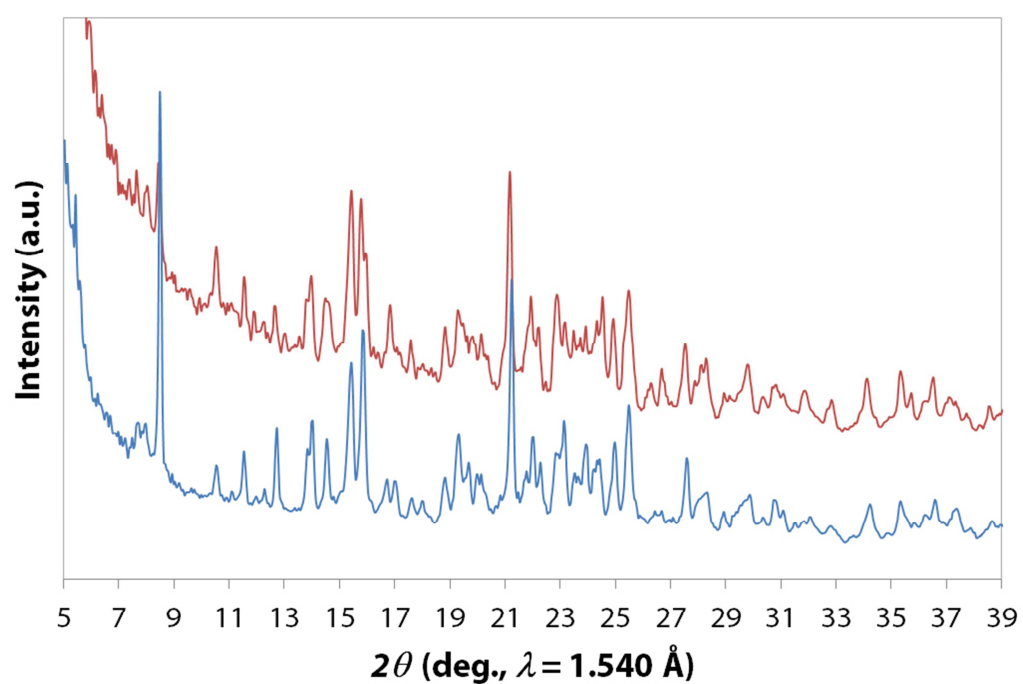


Figure S2.4, Comparison between experimental PXRD patterns (5–39°, 2θ) for **C5b** (blue line) and **C6b** (red line).

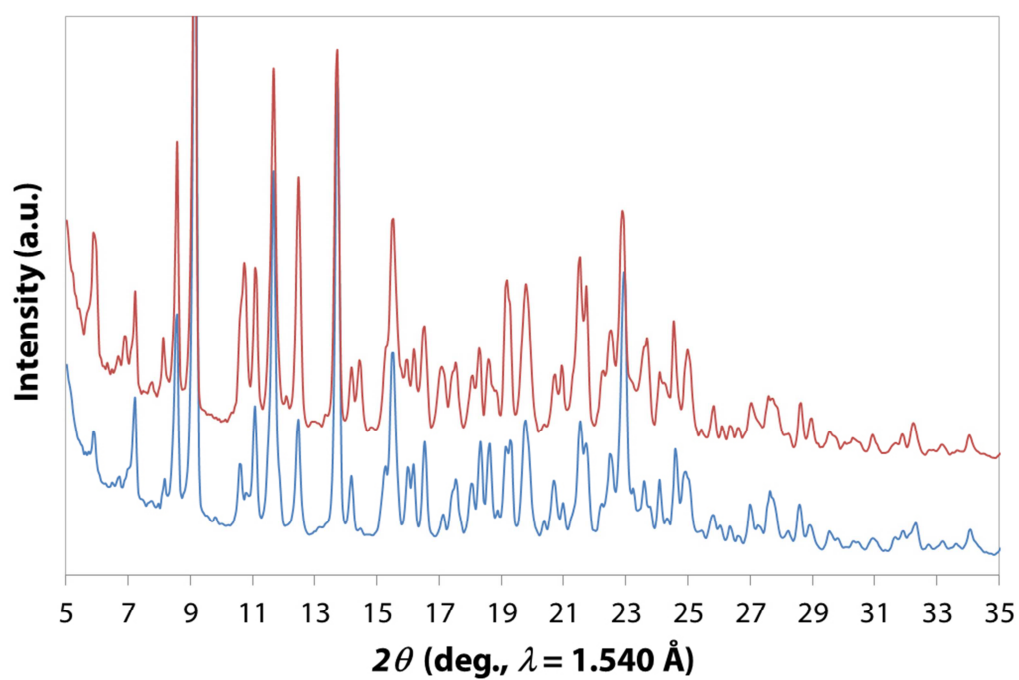


Figure S2.5, Comparison between experimental PXRD patterns (5–35°, 2θ) for **C7b** (blue line) and **C8b** (red line).

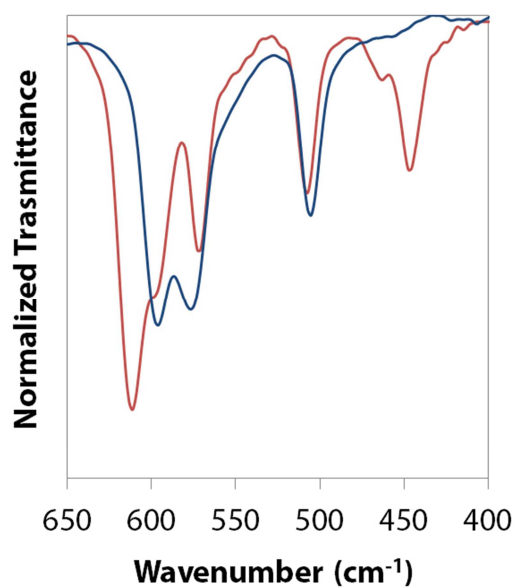


Figure S2.6, FT-IR spectra (650–400 cm⁻¹) for **C1a** (red line) and **C2a** (blue line).

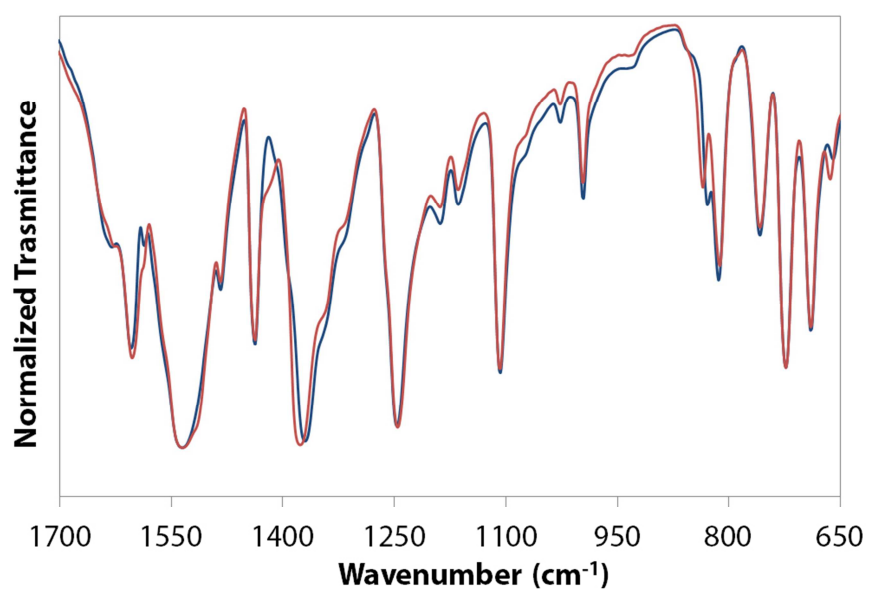


Figure S2.7, FT-IR spectra (1100–650 cm⁻¹) for **C7b** (red line) and **C8b** (blue line).

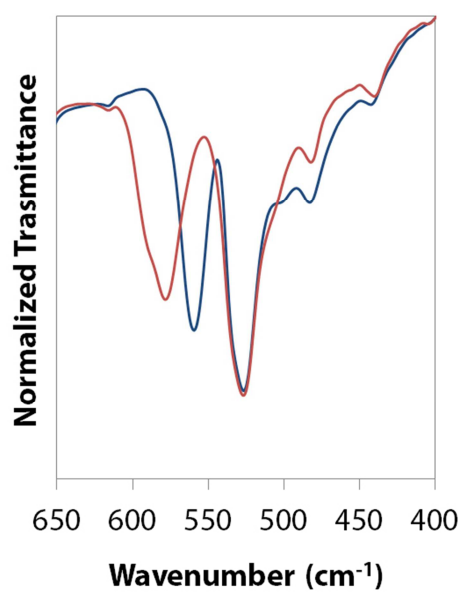


Figure S2.8, FT-IR spectra (640–400 cm⁻¹) for **C7b** (red line) and **C8b** (blue line).

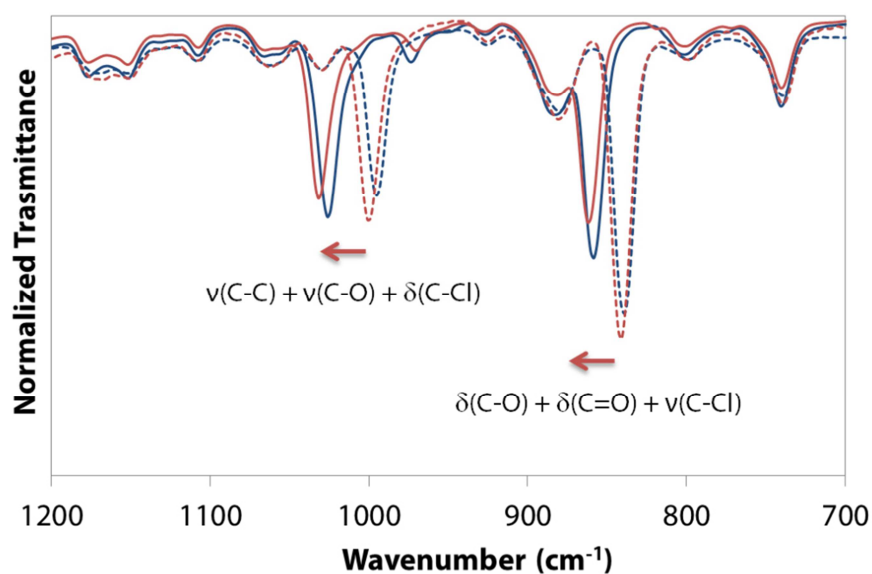


Figure S2.9, FT-IR spectra (1200–700 cm^{-1}) for **C9a** (red line) and **C10a** (blue line) compared with **C1a** (red dashed line) and **C2a** (blue dashed line).

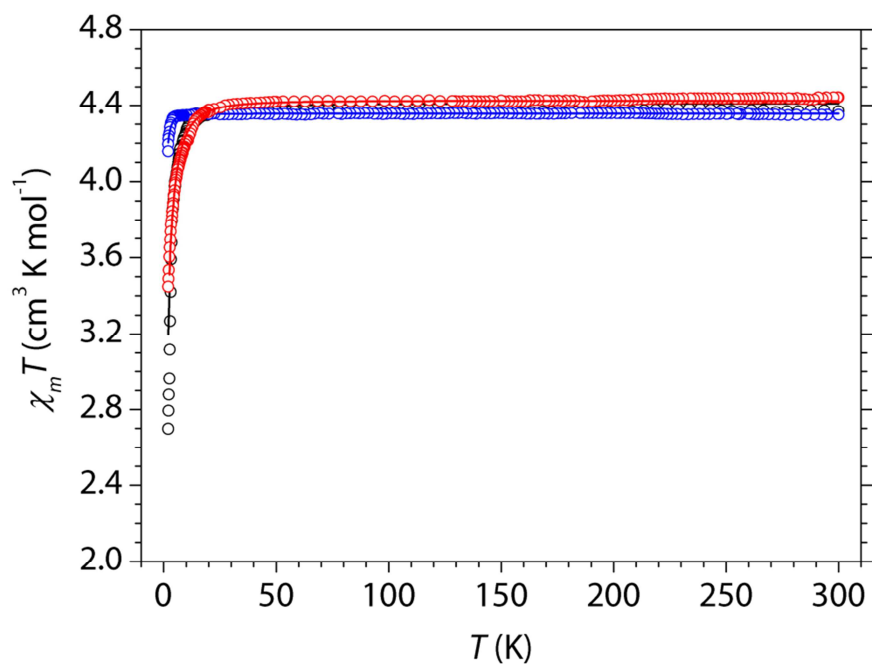


Figure S2.10, Thermal variation of $\chi_m T$ for **C2a** (black circles), **C2b** (red circles), and **C2c** (blue circles). Solid lines are the best fit of the model (see text).

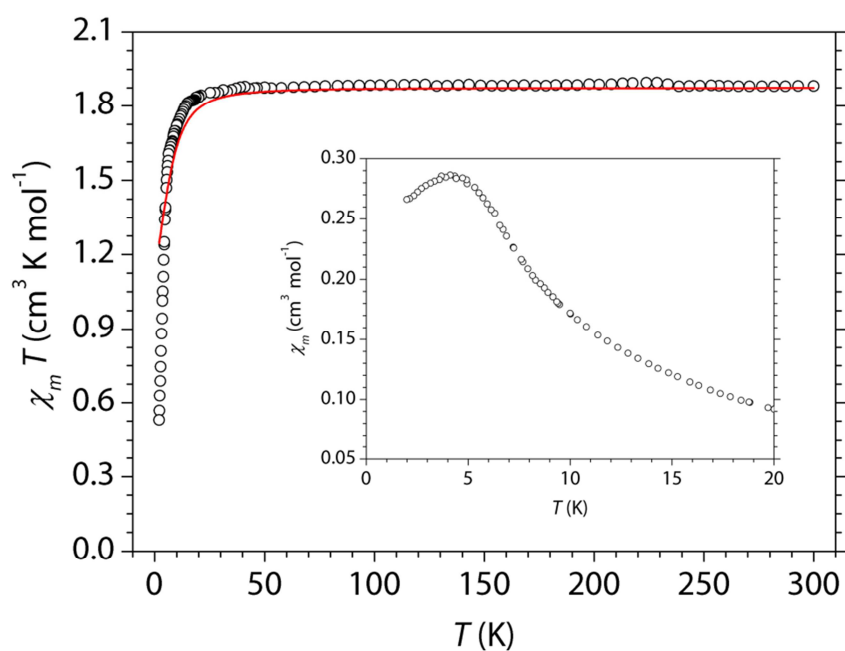


Figure S2.11, Thermal variation of $\chi_m T$ for **C5a**. Solid line is the best fit of the model which takes into account the zero field splitting (see text). The inset shows the maximum of the susceptibility.

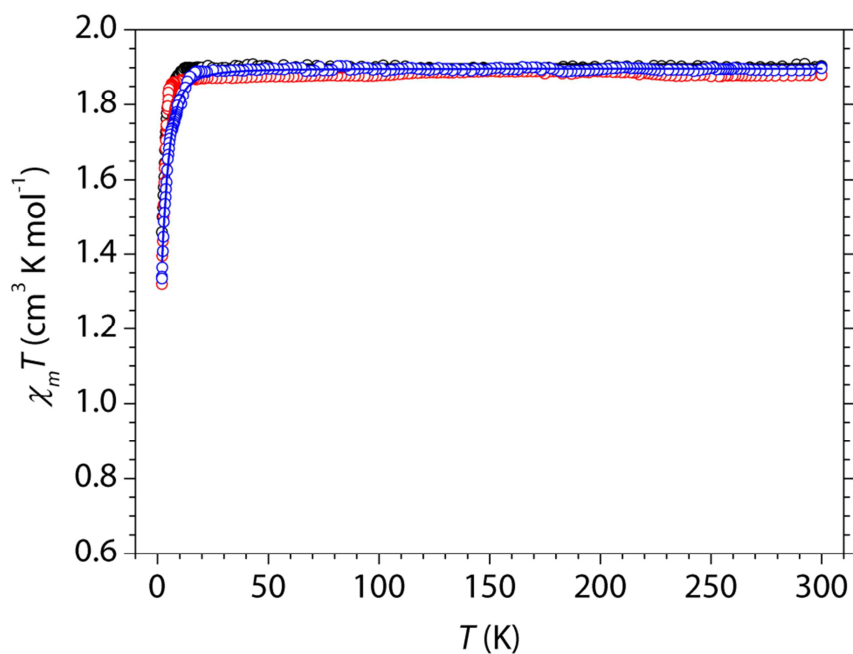


Figure S2.12, Thermal variation of $\chi_m T$ for **C1a** (black circles), **C1b** (red circles), and **C1c** (blue circles). Solid lines are the best fit of the model (see text).

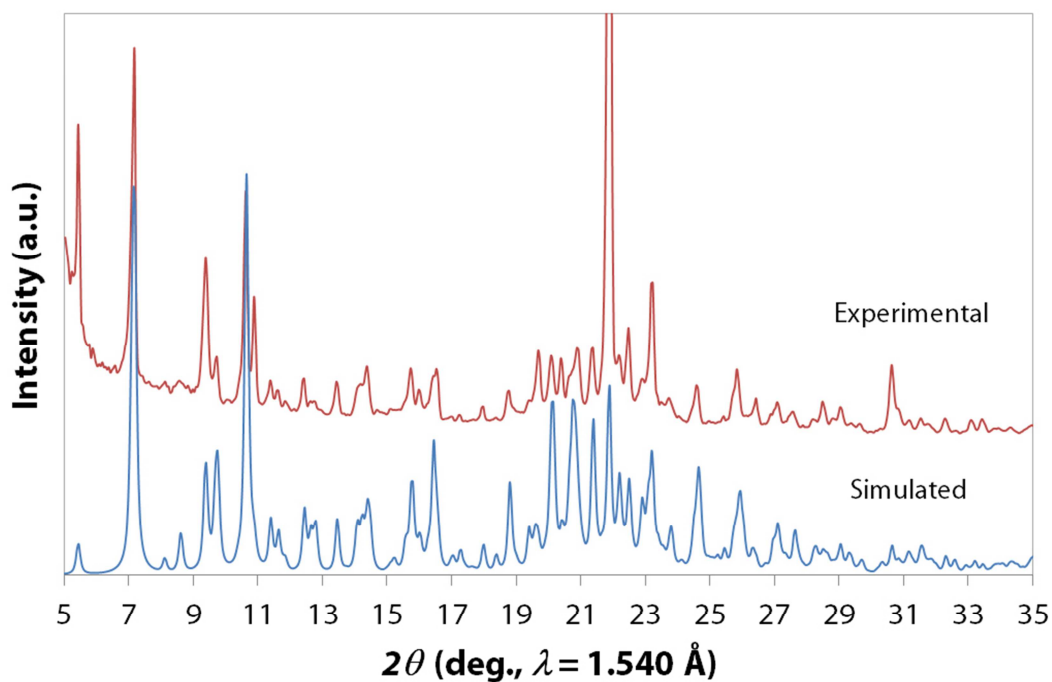


Figure S2.13, Comparison between experimental (red line) and simulated (blue line) PXRD patterns (5–35°, 2θ) for C2b.

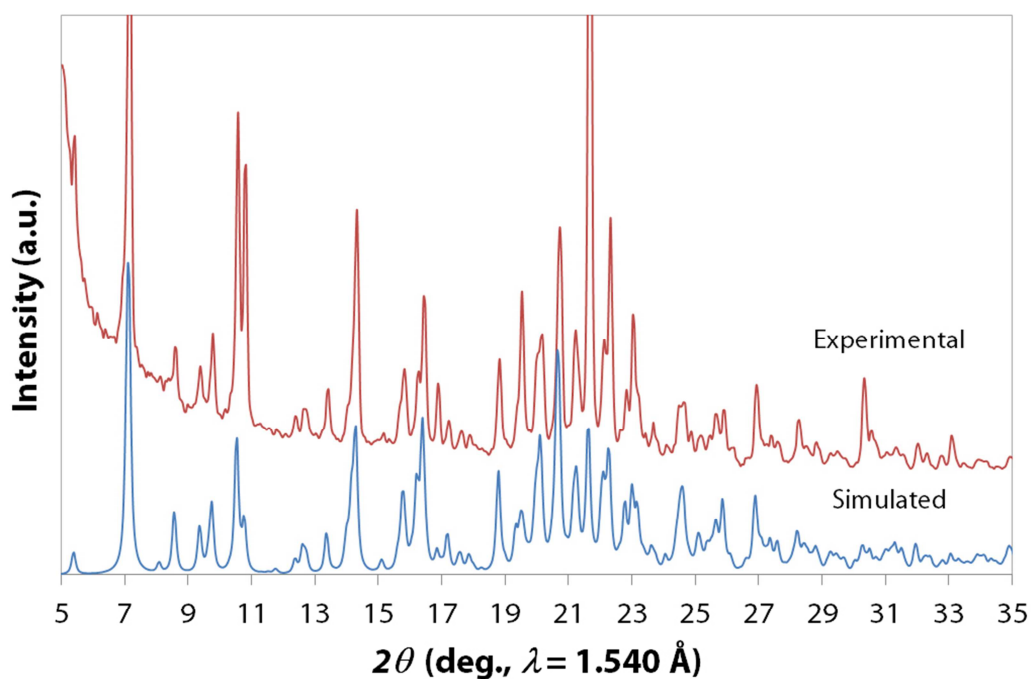


Figure S2.14, Comparison between experimental (red line) and simulated (blue line) PXRD patterns (5–35°, 2θ) for C4b.

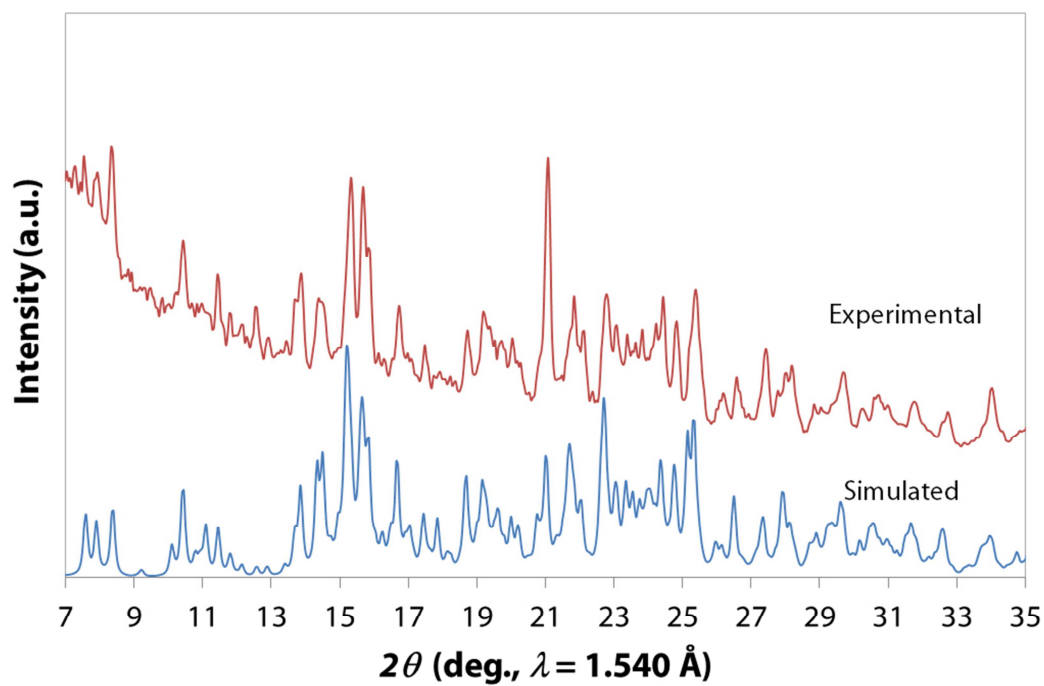


Figure S2.15, Comparison between experimental (red line) and simulated (blue line) PXRD patterns (5–35°, 2θ) for C6b.

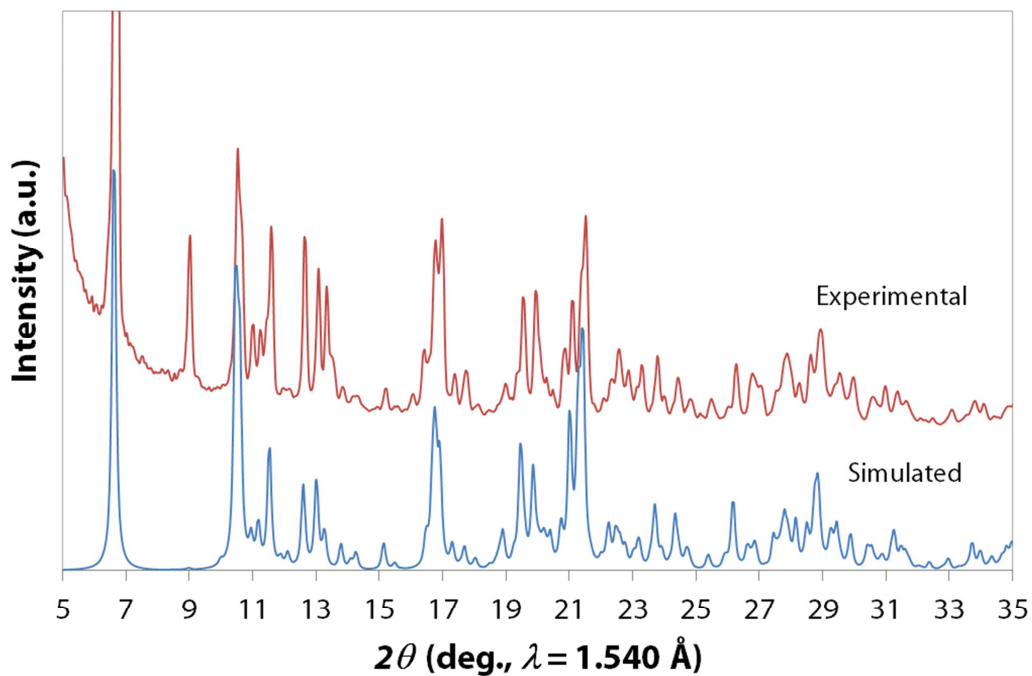


Figure S2.16, Comparison between experimental (red line) and simulated (blue line) PXRD patterns (5–35°, 2θ) for C1c.

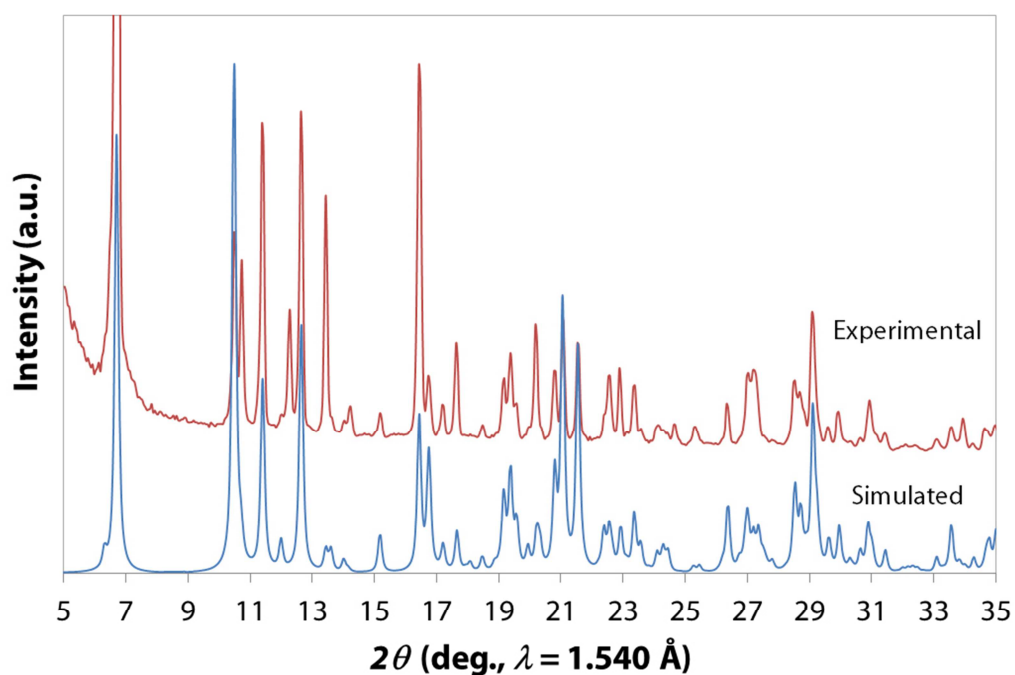


Figure S2.17, Comparison between experimental (red line) and simulated (blue line) PXRD patterns (5–35°, 2θ) for C2c.

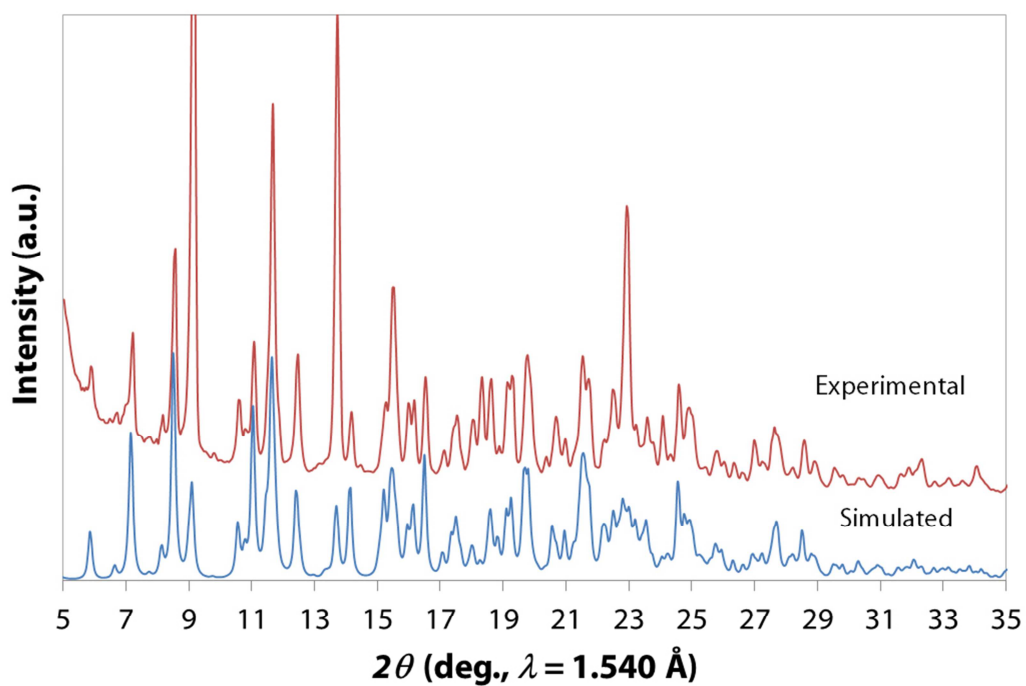


Figure S2.18, Comparison between experimental (red line) and simulated (blue line) PXRD patterns (5–35°, 2θ) for C8b.

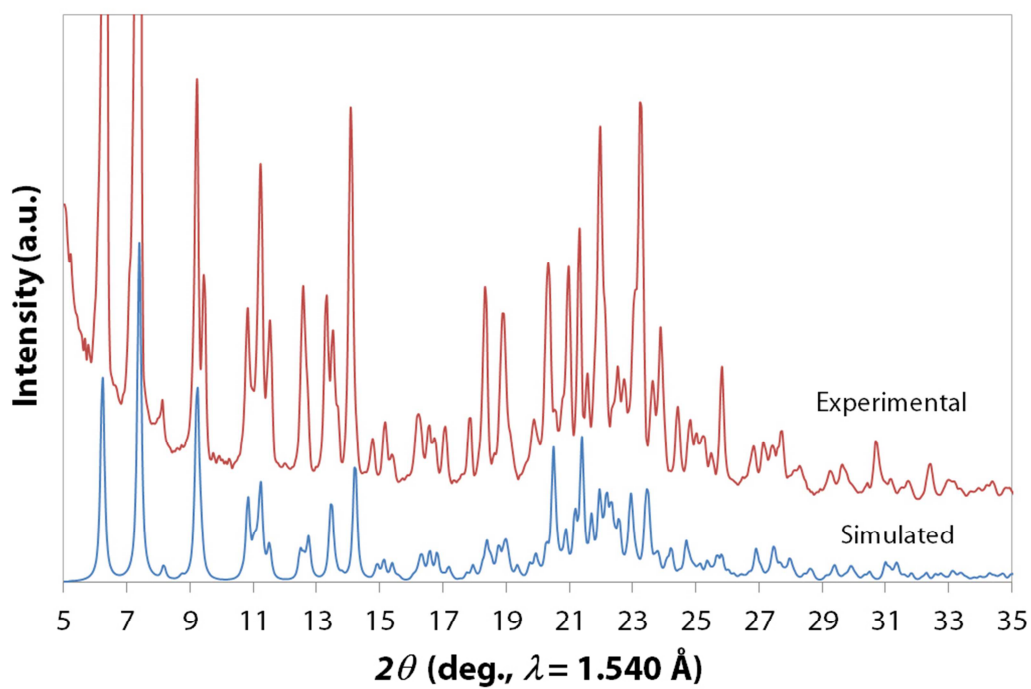


Figure S2.19, Comparison between experimental (red line) and simulated (blue line) PXRD patterns (5–35°, 2θ) for C9a.

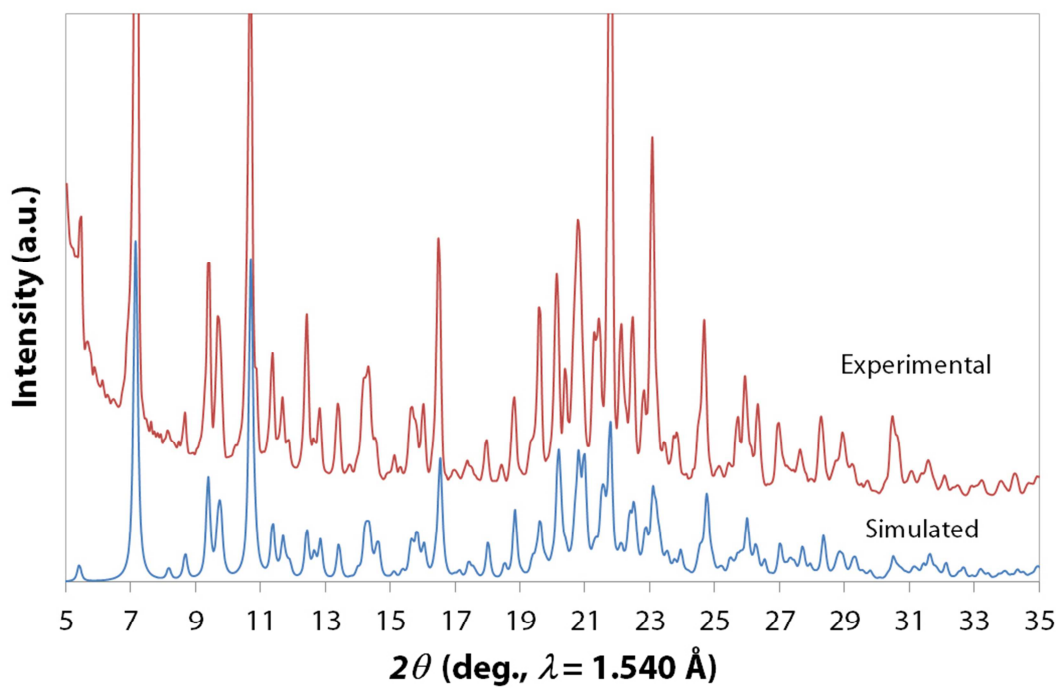


Figure S2.20, Comparison between experimental (red line) and simulated (blue line) PXRD patterns (5–35°, 2θ) for C9b.

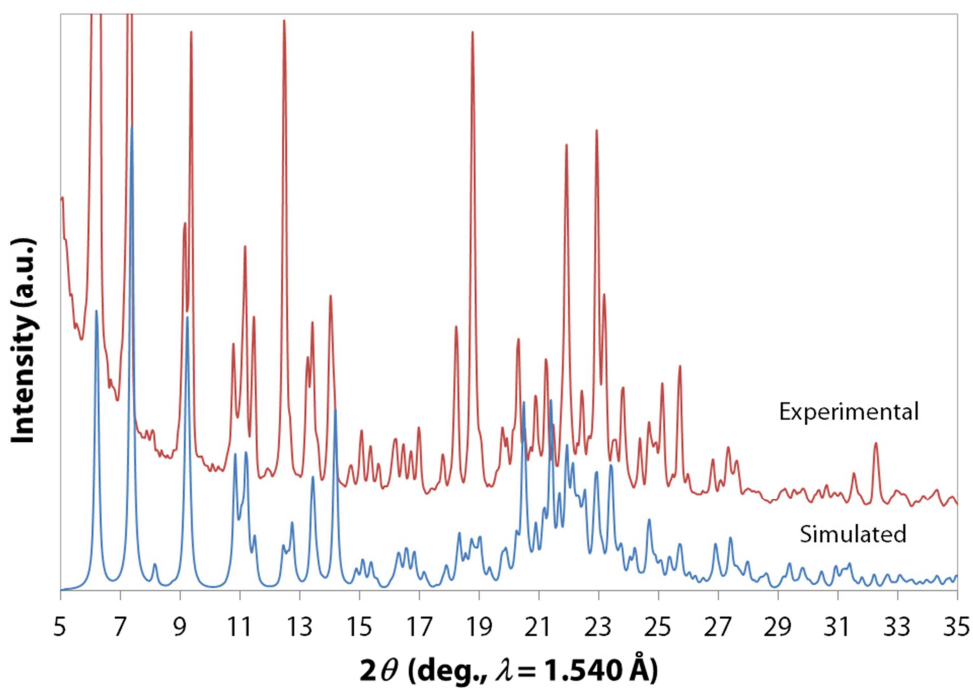


Figure S2.21, Comparison between experimental (red line) and simulated (blue line) PXRD patterns (5–35°, 2θ) for C10a.

4.3 Chapter 3 Supplementary Material

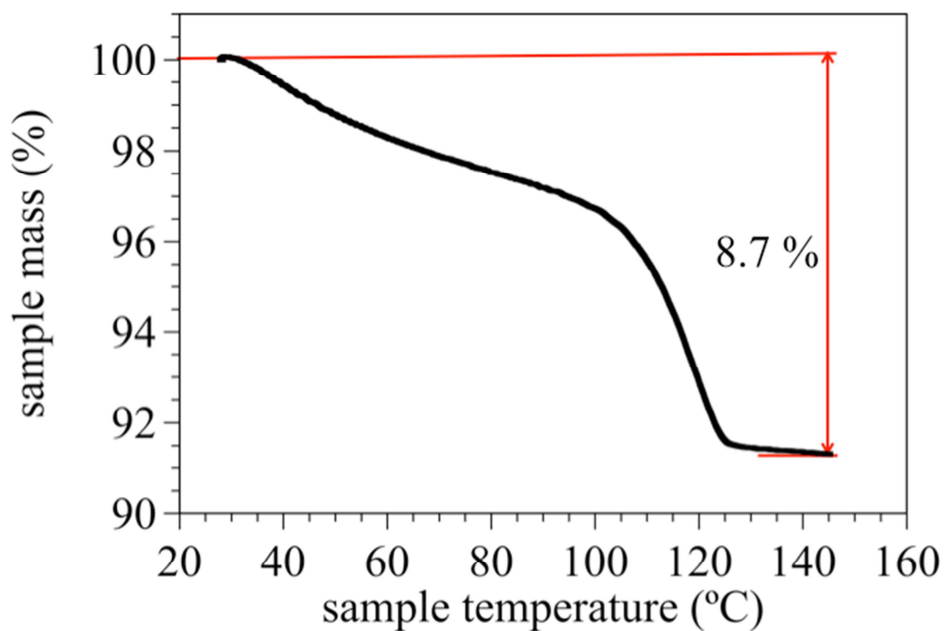


Figure S3.1, TGA of M1.

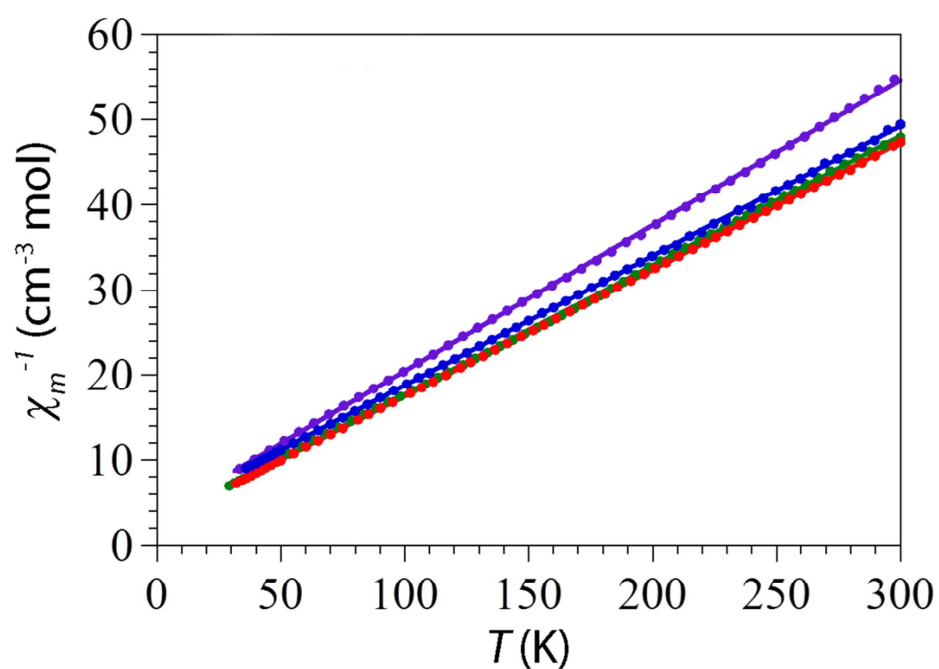


Figure S3.2, Curie-Weiss plot of **M4** (green line), **M5** (red line), **M6** (violet line), and **M7** (blue line). Solid lines are the best fit to the Curie-Weiss law ($\chi_m = C/(T-\theta)$).

4.4 Chapter 5 Supplementary Material

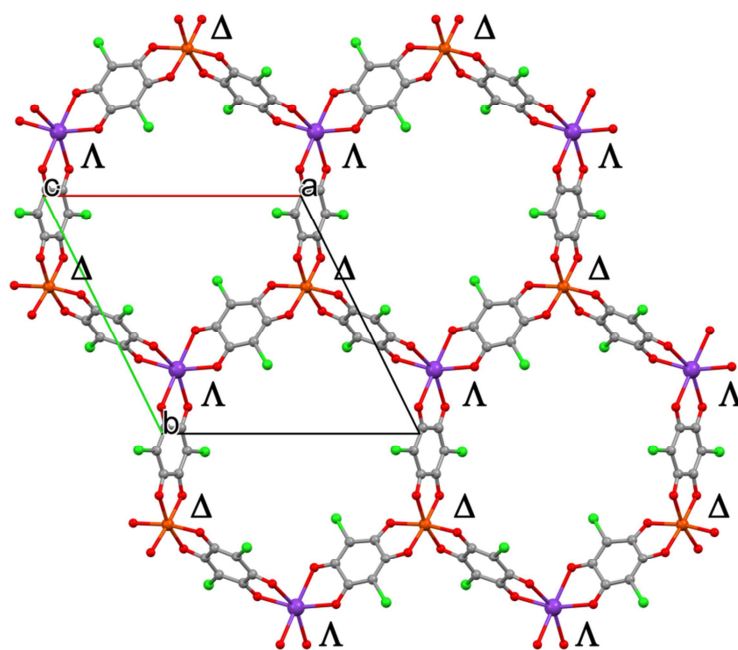


Figure S5.1, Top view of the 2D anionic layers of **H4** where the stereochemical configuration of each metal centre is highlighted.

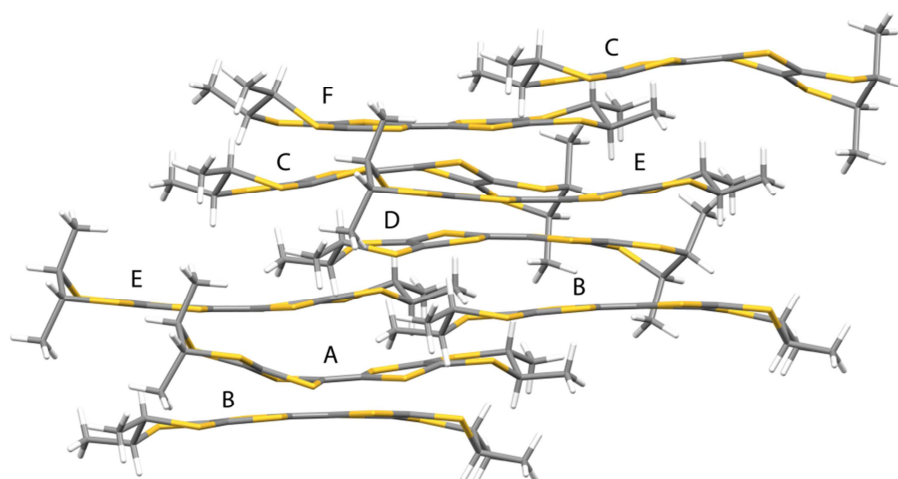


Figure S5.2, View of the crystal structure of **H4** where the bent or planar conformation of the donor molecules is highlighted.

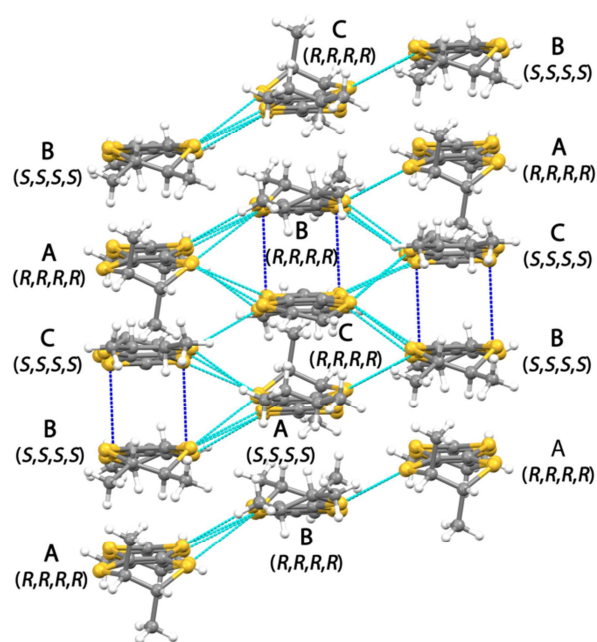


Figure S5.3, View of the TM-BEDT-TTF packing of **H6** along the *ab* plane where the short intermolecular S...S contacts are highlighted. Some short contacts (Å): S(7C)...S(7C') 3.60, S(7C)...S(8A) 3.61, S(1C)...S(2A) 3.64, S(2A)...S(3C) 3.66, S(2C)...S(8B) 3.40.

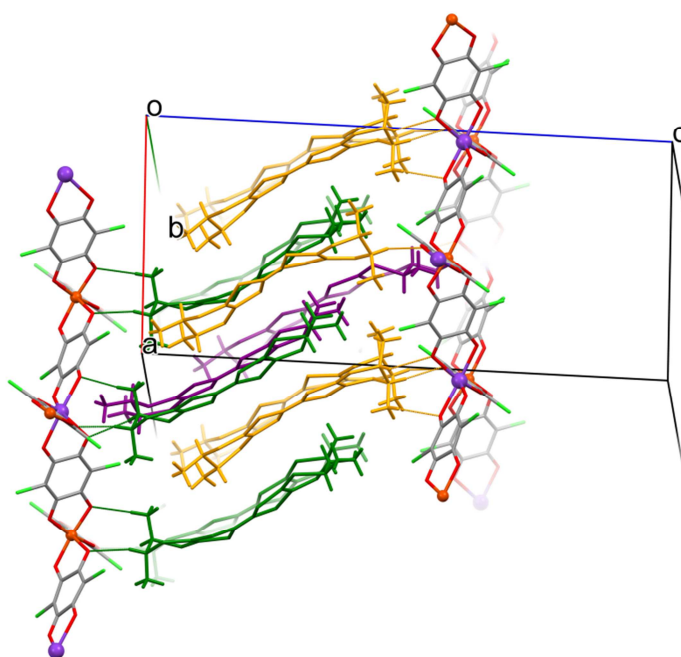
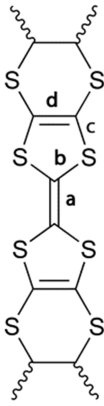


Figure S5.4. Side view of the crystal structure of **H5** where the orientations of the donor molecules and their interactions with the inorganic layer are highlighted.

Table S5.1. Bond distance analysis and selected bond distances (Å) for the TM-BEDT-TTF donor molecules in **H4**.

	A	B	C	D	E	F
a	1.337(13)	1.354(12)	1.335(11)	1.370(12)	1.380(12)	1.367(12)
	1.765(8)	1.769(9)	1.780(6)	1.776(8)	1.770(7)	1.753(8)
b	1.763(9)	1.700(10)	1.749(6)	1.753(9)	1.727(8)	1.748(9)
	1.784(9)	1.737(9)	1.762(8)	1.743(8)	1.758(7)	1.813(8)
c	1.737(8)	1.744(8)	1.728(8)	1.736(9)	1.725(7)	1.711(7)
	1.790(7)	1.789(10)	1.722(8)	1.834(6)	1.724(8)	1.730(8)
d	1.796(6)	1.765(7)	1.774(7)	1.785(6)	1.741(6)	1.724(8)
	1.769(7)	1.753(8)	1.774(6)	1.749(8)	1.782(6)	1.749(9)
δ	1.716(7)	1.771(8)	1.791(7)	1.751(6)	1.806(9)	1.732(9)
	1.269(12)	1.316(12)	1.347(11)	1.306(11)	1.394(13)	1.328(12)
Q	1.363(12)	1.400(11)	1.319(13)	1.413(13)	1.321(12)	1.400(14)
	0.877	0.795	0.852	0.802	0.771	0.759
Q = 6.347-7.4638•δ	0.0(1)	0.4(1)	0.0(1)	0.4(1)	0.6(1)	0.7(1)

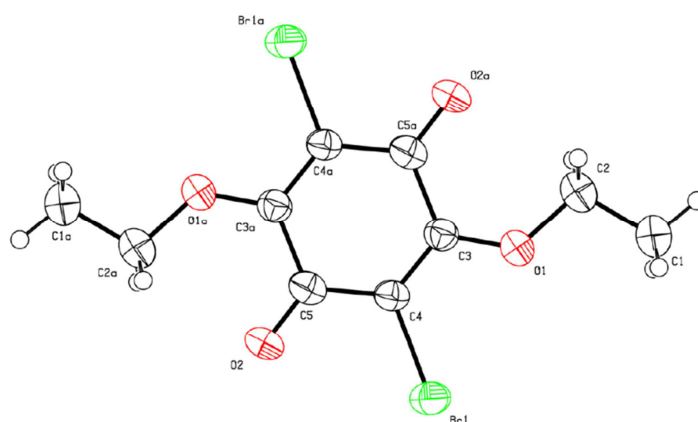
Table S5.2. Bond distance analysis and selected bond distances (Å) for the TM-BEDT-TTF donor molecules in **H6**.

	A	B	C	
 <p>$\delta = (\mathbf{b+c})-(\mathbf{a+d})$ $\mathbf{Q} = 6.347-7.4638 \cdot \delta$</p>	a	1.340(14)	1.350(14)	1.355(13)
	b	1.773(10)	1.729(10)	1.761(9)
		1.757(9)	1.763(9)	1.739(9)
		1.753(9)	1.756(10)	1.746(9)
		1.752(10)	1.748(10)	1.752(9)
	c	1.769(10)	1.737(10)	1.763(9)
		1.771(11)	1.759(10)	1.756(9)
		1.764(11)	1.759(10)	1.765(9)
		1.769(10)	1.736(10)	1.750(9)
	d	1.337(13)	1.367(13)	1.354(13)
		1.338(13)	1.359(14)	1.350(12)
	δ	0.850	0.784	0.801
Q	0.0(1)	0.5(1)	0.4(1)	

Appendix 5

Supplementary Crystallographic Data

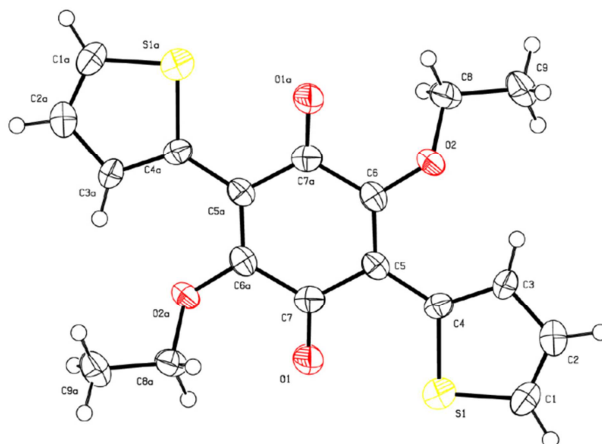
2,5-dibromo-3,6-diethoxy-1,4-benzoquinone (2a)



Selected bond lengths and angles.

Bonds	Å	Bonds	Å	Angles	°	Angles	°
Br(1)-C(4)	1.884(4)	C(2)-C(1)	1.488(5)	C(3)-O(1)-O(1)	127.0(3)	C(3)-C(4)-Br(1)	120.4(3)
O(2)-C(5)	1.213(4)	C(4)-C(5)	1.499(5)	O(1)-C(3)-C(4)	118.9(3)	C(5)-C(4)-Br(1)	115.7(2)
O(1)-C(3)	1.323(4)	C(5)-C(3)	1.521(5)	O(1)-C(3)-C(5)	122.1(3)	O(2)-C(5)-C(4)	122.5(4)
O(1)-C(2)	1.437(4)	-	-	C(4)-C(3)-C(5)	119.0(3)	O(2)-C(5)-C(3)	120.4(3)
C(3)-C(4)	1.348(5)	-	-	O(1)-C(2)-C(1)	106.8(3)	C(4)-C(5)-C(3)	117.1(3)
C(3)-C(5)	1.521(5)	-	-	C(3)-C(4)-C(5)	123.9(3)	-	-

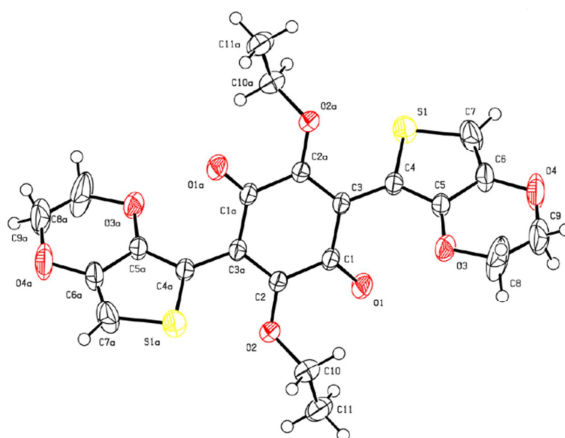
2,5-di(thiophen-2-yl)-3,6-diethoxy-1,4-benzoquinone (3a)



Selected bond lengths and angles.

Bonds	Å	Bonds	Å	Angles	°	Angles	°
S(1)-C(1)	1.696(3)	C(5)-C(6)	1.359(4)	C(1)-S(1)-C(4)	92.41(2)	C(6)-C(5)-C(7)	116.7(3)
S(2)-C(4)	1.738(3)	C(5)-C(7)	1.479(4)	C(6)-O(2)-C(8)	121.7(2)	C(4)-C(5)-C(7)	119.3(3)
O(1)-C(7)	1.223(4)	C(6)-C(7)	1.501(4)	C(2)-C(1)-S(1)	112.3(3)	O(2)-C(6)-C(5)	120.3(3)
O(2)-C(6)	1.344(4)	C(8)-C(9)	1.489(4)	C(1)-C(2)-C(3)	113.8(3)	O(2)-C(6)-C(7)	117.5(3)
O(2)-C(8)	1.465(4)	-	-	C(4)-C(3)-C(2)	112.1(3)	C(5)-C(6)-C(7)	121.9(3)
C(1)-C(2)	1.355(5)	-	-	C(3)-C(4)-C(5)	128.4(3)	O(1)-C(7)-C(5)	120.7(3)
C(2)-C(3)	1.414(5)	-	-	C(3)-C(4)-S(1)	109.4(2)	O(1)-C(7)-C(6)	118.0(3)
C(3)-C(4)	1.394(4)	-	-	C(5)-C(4)-S(1)	122.2(2)	C(5)-C(7)-C(6)	121.2(3)
C(4)-C(5)	1.465(4)	-	-	C(6)-C(5)-C(4)	124.0(3)	O(2)-C(8)-C(9)	107.9(3)

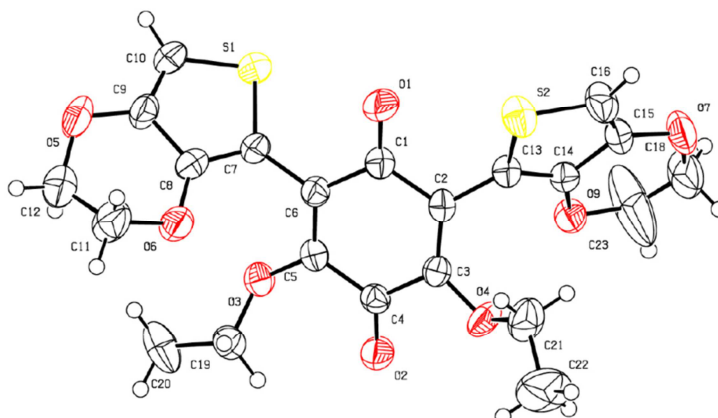
2,5-di(3,4-ethylenedioxythiophen-2-yl)-3,6-diethoxy-1,4-benzoquinone (4a)



Selected bond lengths and angles.

Bonds	Å	Bonds	Å	Angles	°	Angles	°
C(1)-O(1)	1.222(2)	C(8)-C(9)	1.350(5)	O(1)-C(1)-C(3)	121.0(2)	C(4)-C(5)-C(6)	113.1(2)
C(1)-C(3)	1.475(2)	C(8)-C(3)	1.416(3)	O(1)-C(1)-C(2)	119.5(2)	C(7)-C(6)-O(4)	124.7(2)
C(1)-C(2)	1.499(2)	C(9)-O(4)	1.374(4)	C(3)-C(1)-C(2)	119.2(2)	C(7)-C(6)-C(5)	113.0(2)
C(2)-O(2)	1.342(2)	C(10)-O(2)	1.467(2)	O(2)-C(2)-C(3)	118.3(2)	O(4)-C(6)-C(5)	122.3(2)
C(2)-C(3)	1.359(2)	C(10)-C(11)	1.488(3)	C(3)-C(2)-C(1)	112.5(2)	C(6)-C(7)-S(1)	111.1(2)
C(3)-C(4)	1.467(2)	-	-	C(2)-C(3)-C(4)	123.5(2)	C(9)-C(8)-O(3)	121.8(3)
C(4)-C(5)	1.370(2)	-	-	C(2)-C(3)-C(1)	118.4(2)	C(8)-C(9)-O(4)	124.0(2)
C(4)-S(1)	1.732(2)	-	-	C(4)-C(3)-C(1)	117.6(2)	O(2)-C(10)-C(11)	108.3(2)
C(5)-O(3)	1.361(2)	-	-	C(5)-C(4)-C(3)	127.6(2)	C(2)-O(2)-C(10)	119.9(2)
C(2)-C(6)	1.425(2)	-	-	C(5)-C(4)-S(1)	109.9(2)	C(5)-O(3)-C(8)	113.0(2)
C(6)-C(7)	1.359(2)	-	-	C(3)-C(4)-S(1)	122.4(2)	C(6)-O(4)-C(9)	113.5(2)
C(6)-O(4)	1.370(2)	-	-	O(3)-C(5)-C(4)	124.0(2)	C(7)-S(1)-C(4)	92.87(1)
C(7)-S(1)	1.710(2)	-	-	O(3)-C(5)-C(6)	122.9(2)	-	-

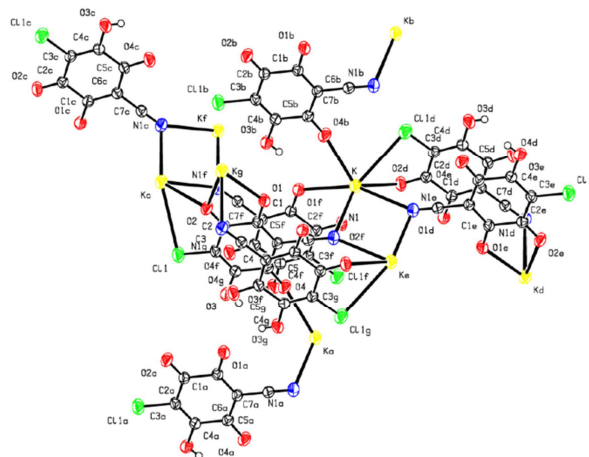
2,6-di(3,4-ethylenedioxythiophen-2-yl)-3,5-diethoxy-1,4-benzoquinone (4b)



Selected bond lengths and angles.

Bonds	Å	Bonds	Å	Angles	°	Angles	°
C(20)-C(19)	1.480(6)	O(7)-C(15)	1.374(4)	O(10)-S(1)-C(7)	92.28(2)	C(14)-C(13)-S(2)	110.2(3)
C(22)-C(21)	1.457(7)	O(7)-C(18)	1.390(6)	C(16)-S(2)-C(13)	92.30(2)	C(2)-C(13)-S(2)	124.4(2)
S(1)-C(10)	1.704(4)	O(5)-C(9)	1.387(5)	C(5)-O(3)-C(19)	120.2(3)	O(4)-C(3)-C(2)	127.7(3)
S(1)-C(7)	1.727(4)	O(5)-C(12)	1.429(6)	C(3)-O(4)-C(21)	119.1(3)	O(4)-C(3)-C(4)	110.9(3)
S(2)-C(16)	1.709(4)	C(15)-C(16)	1.346(6)	O(2)-C(4)-C(5)	121.5(3)	C(2)-C(3)-C(4)	121.2(3)
S(2)-C(13)	1.726(4)	C(7)-C(8)	1.366(5)	O(2)-C(4)-C(3)	120.6(3)	C(9)-O(5)-C(12)	111.2(3)
O(3)-C(5)	1.352(4)	C(8)-C(9)	1.414(5)	C(5)-C(4)-C(3)	117.8(3)	C(16)-C(15)-O(7)	125.3(3)
O(3)-C(19)	1.442(4)	C(9)-C(10)	1.337(5)	C(14)-O(9)-C(23)	112.2(3)	C(16)-C(15)-C(14)	112.6(3)
O(4)-C(3)	1.342(4)	C(18)-C(23)	1.321(8)	C(5)-C(6)-C(7)	121.6(3)	O(7)-C(15)-C(14)	122.2(3)
O(4)-C(21)	1.456(5)	C(12)-C(11)	1.486(7)	C(5)-C(6)-C(1)	119.3(3)	C(8)-C(7)-C(6)	127.6(3)
C(4)-O(2)	1.223(4)	-	-	C(7)-C(6)-C(1)	119.1(3)	C(8)-C(7)-S(1)	109.7(3)
C(4)-C(5)	1.481(5)	-	-	C(3)-C(2)-C(13)	123.7(3)	C(6)-C(7)-S(1)	122.8(3)
C(4)-C(3)	1.495(5)	-	-	C(3)-C(2)-C(1)	118.2(3)	O(3)-C(19)-C(20)	107.4(4)
O(9)-C(14)	1.357(4)	-	-	C(13)-C(2)-C(1)	118.0(3)	O(6)-C(8)-C(7)	123.5(3)
O(9)-C(23)	1.398(6)	-	-	C(8)-O(6)-C(11)	112.4(3)	O(6)-C(8)-C(9)	123.2(3)
C(6)-C(5)	1.343(5)	-	-	O(9)-C(14)-C(13)	123.7(3)	C(7)-C(8)-C(9)	113.3(3)
C(6)-C(7)	1.458(5)	-	-	O(9)-C(14)-C(15)	123.2(3)	C(15)-C(16)-S(2)	111.9(3)
C(6)-C(1)	1.489(5)	-	-	C(13)-C(14)-C(15)	113.1(3)	C(10)-C(9)-O(5)	125.3(4)
C(2)-C(3)	1.345(5)	-	-	O(1)-C(1)-C(2)	119.5(3)	C(10)-C(9)-C(8)	112.9(4)
C(2)-C(13)	1.473(5)	-	-	O(1)-C(1)-C(6)	119.8(3)	O(5)-C(9)-C(8)	121.8(4)
C(2)-C(1)	1.484(5)	-	-	C(2)-C(1)-C(6)	120.6(3)	C(9)-C(10)-S(1)	111.8(3)
O(6)-C(8)	1.365(4)	-	-	C(6)-C(5)-O(3)	120.5(3)	O(4)-C(21)-C(22)	107.5(4)
O(6)-C(11)	1.446(5)	-	-	C(6)-C(5)-C(4)	121.3(3)	C(23)-C(18)-O(7)	123.9(4)
C(14)-C(13)	1.366(5)	-	-	O(3)-C(5)-C(4)	117.8(3)	O(5)-C(12)-C(11)	111.4(4)
C(14)-C(15)	1.424(5)	-	-	C(17)-O(7)-O(18)	112.8(3)	O(6)-C(11)-C(12)	111.3(4)
C(1)-O(1)	1.226(5)	-	-	C(14)-C(13)-C(2)	125.4(3)	C(18)-C(23)-O(9)	124.2(5)

KHCICNAn (8)

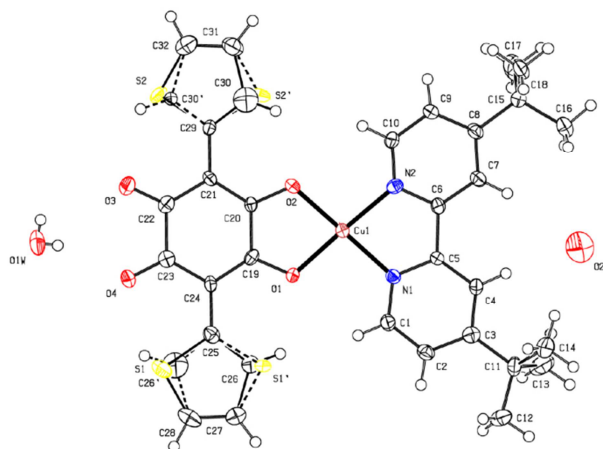


Selected bond lengths and angles.

Bonds	Å	Bonds	Å	Angles	°	Angles	°
K-O(4) ⁱ	2.722(2)	C(4)-C(5)	1.507(4)	O(4) ⁱⁱⁱ -K-O(2) ⁱⁱ	115.92(7)	O(4) ⁱⁱⁱ -K-Cl(1) ⁱⁱⁱ	56.26(4)
K-O(2) ⁱⁱ	2.807(2)	C(5)-C(6)	1.426(4)	O(4) ⁱ -K-O(1) ⁱⁱ	66.54(6)	N(1) ^{iv} -K-Cl(3) ⁱⁱⁱ	146.79(6)
K-O(1) ⁱⁱ	2.807(2)	C(6)-C(1)	1.403(4)	O(2) ⁱⁱ -K-O(1) ⁱⁱ	56.96(6)	N(1)-K-Cl(3) ⁱⁱⁱ	73.30(6)
K-O(2) ⁱⁱⁱ	2.860(2)	C(6)-C(7)	1.435(4)	O(4) ⁱ -K-O(2) ⁱⁱⁱ	111.55(7)	O(3) ^v -K-Cl(1) ⁱⁱⁱ	106.78(5)
K-N(1)	2.973(3)	C(1)-C(2)	1.548(4)	O(2) ⁱⁱ -K-O(2) ⁱⁱⁱ	69.10(7)	O(4) ⁱ -K-Cl(1) ^v	83.74(6)
K-N(1) ^{iv}	3.014(3)	C(7)-N(1)	1.146(4)	O(1) ⁱⁱ -K-O(2) ⁱⁱⁱ	112.22(7)	O(2) ⁱⁱ -K-Cl(1) ^v	159.05(6)
K-O(3) ^v	3.311(3)	N(1)-K ^{iv}	3.014(6)	O(4) ⁱ -K-N(1)	118.46(8)	O(1) ⁱⁱ -K-Cl(1) ^v	133.29(5)
K-Cl(1) ⁱⁱⁱ	3.369(1)	-	-	O(2) ⁱⁱ -K-N(1)	82.22(8)	O(2) ⁱⁱⁱ -K-Cl(1) ^v	111.93(5)
K-Cl(1) ^v	3.449(1)	-	-	O(1) ⁱⁱ -K-N(1)	82.02(7)	N(1)-K-Cl(1) ^v	81.80(6)
Cl(1)-C(3)	1.736(3)	-	-	O(2) ⁱⁱ -K-N(1)	129.36(7)	N(1) ^{iv} -K-Cl(1) ^v	59.34(6)
Cl(1)-K ^{vii}	3.369(1)	-	-	O(4) ⁱ -K-N(1) ^{iv}	137.21(7)	O(3) ^v -K-Cl(1) ^v	51.24(5)
Cl(1)-K ^{viii}	3.449(1)	-	-	O(2) ⁱⁱ -K-N(1) ^{iv}	104.33(7)	Cl(1) ⁱⁱⁱ -K-Cl(1) ^v	68.18(3)
O(2)-C(2)	1.216(3)	-	-	O(1) ⁱⁱ -K-N(1) ^{iv}	155.43(7)	C(3)-Cl(1)-K ^{vii}	97.60(9)
O(2)-K ^{ix}	2.807(2)	-	-	O(2) ⁱⁱ -K-N(1) ^{iv}	69.09(7)	C(3)-Cl(1)-K ^{viii}	104.78(9)
O(2)-K ^{vii}	2.860(2)	-	-	N(1) ⁱⁱⁱ -K-N(1) ^{iv}	79.46(8)	K ^{vii} -Cl(1)-K ^{viii}	111.82(3)
O(1)-C(1)	1.247(3)	-	-	O(4) ⁱ -K-O(3) ^v	64.09(7)	C(2)-O(2)-K ^{ix}	121.18(7)
O(1)-K ^{ix}	2.807(2)	-	-	O(2) ⁱⁱ -K-O(3) ^v	128.93(6)	C(2)-O(2)-K ^{vii}	123.00(7)
O(3)-C(4)	1.327(3)	-	-	O(1) ⁱⁱ -K-O(3) ^v	82.81(6)	K ^{ix} -O(2)-K ^{vii}	110.90(7)
O(3)-K ^{viii}	3.311(3)	-	-	O(2) ⁱⁱⁱ -K-O(3) ^v	161.94(6)	C(1)-O(1)-K ^{ix}	122.07(7)
O(3)-H(3)	0.71(3)	-	-	N(1)-K-O(3) ^v	60.42(7)	C(4)-O(3)-K ^{viii}	119.11(7)
O(4)-C(5)	1.234(3)	-	-	N(1) ^{iv} -K-O(3) ^v	101.64(8)	C(4)-O(3)-H(3)	109(3)
O(4)-K ^x	2.722(2)	-	-	O(4) ⁱ -K-Cl(1) ⁱⁱⁱ	73.28(5)	C(5)-O(4)-K ^x	156.6(2)
C(3)-C(4)	1.345(4)	-	-	O(4) ⁱⁱ -K-Cl(1) ⁱⁱⁱ	122.48(5)	C(4)-C(3)-Cl(1)	120.5(2)
C(3)-C(2)	1.454(4)	-	-	O(4) ⁱⁱⁱ -K-Cl(1) ⁱⁱⁱ	129.00(5)	C(2)-C(3)-Cl(1)	117.7(2)

Symmetry transformations: i) $x, y, z+1$; ii) $x-1/2, -y+3/2, z$; iii) $-x+3/2, y+1/2, -z+3$; iv) $-x+2, -y+2, -z+3$; v) $x+1/2, -y+3/2, z+1$; vi) $-x+1, -y+2, -z+3$; vii) $-x+3/2, y-1/2, -z+3$; viii) $x-1/2, -y+3/2, z-1$; ix) $x+1/2, -y+3/2, z$; x) $x, y, z-1$.

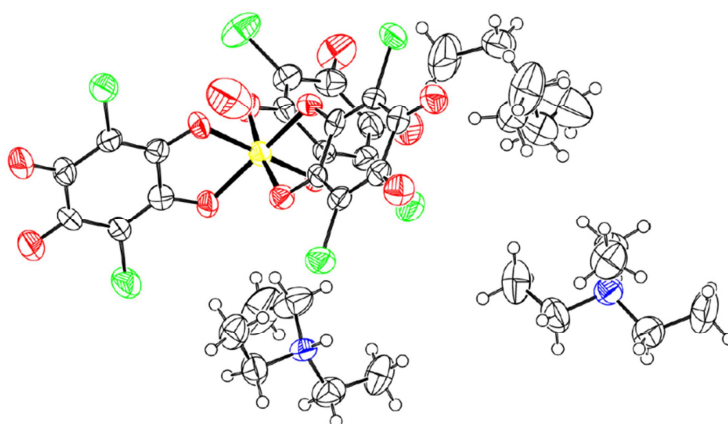
[Cu(Th₂An)(tbbpy)]·2H₂O (C11)



Selected bond lengths and angles.

Bonds	Å	Bonds	Å	Angles	°	Angles	°
S(2)-C(32)	1.615(7)	C(29)-C(21)	1.474(6)	C(32)-S(2)-C(29)	91.7(3)	N(2)-C(6)-C(5)	113.3(4)
S(2)-C(29)	1.749(6)	C(23)-C(22)	1.557(7)	C(28)-S(1)-C(25)	93.1(4)	C(7)-C(6)-C(5)	125.1(4)
S(1)-C(28)	1.604(7)	C(22)-C(21)	1.447(6)	C(25)-C(26)-C(27)	109.5(12)	N(1)-C(1)-C(2)	121.7(4)
S(1)-C(25)	1.729(7)	C(3)-C(2)	1.392(6)	C(29)-C(30)-C(31)	112.2(14)	C(30)-C(29)-C(21)	126.1(10)
C(26)-C(25)	1.427(18)	C(3)-C(4)	1.402(6)	C(20)-O(2)-Cu(1)	113.9(3)	C(30)-C(29)-S(2)	111.3(10)
C(26)-C(27)	1.52(2)	C(3)-C(11)	1.524(7)	C(19)-O(1)-Cu(1)	113.9(3)	C(21)-C(29)-S(2)	122.6(4)
C(30)-C(29)	1.326(19)	C(9)-C(8)	1.386(6)	O(1)-Cu(1)-O(2)	84.06(12)	O(4)-C(23)-C(24)	123.2(4)
C(30)-C(31)	1.55(2)	C(5)-C(4)	1.379(6)	O(1)-Cu(1)-N(1)	95.69(14)	O(4)-C(23)-C(22)	116.8(4)
O(2)-C(20)	1.302(5)	C(7)-C(8)	1.385(6)	O(2)-Cu(1)-N(1)	176.92(15)	C(24)-C(23)-C(22)	120.0(4)
O(2)-Cu(1)	1.914(3)	C(8)-C(15)	1.531(6)	O(1)-Cu(1)-N(2)	176.98(14)	C(26)-C(25)-C(24)	127.5(4)
O(1)-C(19)	1.285(5)	C(11)-C(12)	1.532(7)	O(2)-Cu(1)-N(2)	98.10(14)	C(26)-C(25)-S(1)	109.9(4)
O(1)-Cu(1)	1.912(3)	C(11)-C(13)	1.538(7)	N(1)-Cu(1)-N(2)	82.26(16)	C(24)-C(25)-S(1)	122.6(4)
N(1)-Cu(1)	1.953(4)	C(11)-C(14)	1.546(7)	C(10)-N(2)-C(6)	118.3(4)	O(3)-C(22)-C(21)	124.0(4)
N(2)-Cu(1)	1.961(4)	C(15)-C(16)	1.528(7)	C(10)-N(2)-Cu(1)	126.3(3)	O(3)-C(22)-C(23)	115.6(4)
N(2)-C(10)	1.346(6)	C(15)-C(17)	1.528(7)	C(6)-N(2)-Cu(1)	115.3(3)	C(21)-C(22)-C(21)	120.0(4)
N(2)-C(6)	1.358(6)	C(15)-C(18)	1.532(7)	C(1)-N(1)-C(5)	118.5(4)	C(10)-C(9)-C(8)	121.2(4)
O(3)-C(22)	1.235(5)	C(27)-C(28)	1.334(7)	C(1)-N(1)-Cu(1)	125.9(3)	N(1)-C(5)-C(4)	121.7(4)
O(4)-C(23)	1.238(5)	C(32)-C(31)	1.346(7)	C(5)-N(1)-Cu(1)	115.5(3)	N(1)-C(5)-C(6)	113.4(4)
N(1)-C(1)	1.349(6)	O(1W)-H(1W)	0.59(6)	O(2)-C(20)-C(21)	123.7(4)	C(4)-C(5)-C(6)	124.8(4)
N(2)-C(5)	1.358(5)	O(1W)-H(2W)	0.76(7)	O(2)-C(20)-C(19)	113.3(4)	C(6)-C(7)-C(8)	120.50(4)
C(20)-C(21)	1.387(6)	-	-	C(21)-C(20)-C(19)	123.0(4)	C(7)-C(8)-C(9)	116.7(4)
C(20)-C(19)	1.509(6)	-	-	O(1)-C(19)-C(24)	123.1(4)	C(7)-C(8)-C(15)	122.7(4)
C(19)-C(24)	1.401(6)	-	-	O(1)-C(19)-C(20)	114.7(4)	C(9)-C(8)-C(15)	120.6(4)
C(24)-C(23)	1.445(6)	-	-	C(24)-C(19)-C(20)	122.2(4)	C(20)-C(21)-C(22)	117.1(4)
C(24)-C(25)	1.472(6)	-	-	C(19)-C(24)-C(23)	117.1(4)	C(20)-C(21)-C(29)	122.7(4)
C(10)-C(9)	1.370(6)	-	-	C(19)-C(24)-C(25)	122.0(4)	C(22)-C(21)-C(29)	120.2(4)
C(6)-C(7)	1.381(6)	-	-	C(23)-C(24)-C(25)	120.8(4)	C(3)-C(11)-C(12)	112.0(4)
C(6)-C(5)	1.494(6)	-	-	N(2)-C(10)-C(9)	121.7(4)	C(3)-C(11)-C(13)	108.6(4)
C(1)-C(2)	1.371(6)	-	-	N(2)-C(6)-C(7)	121.6(4)	H(1W)-O(1W)-H(2W)	89.8(8)

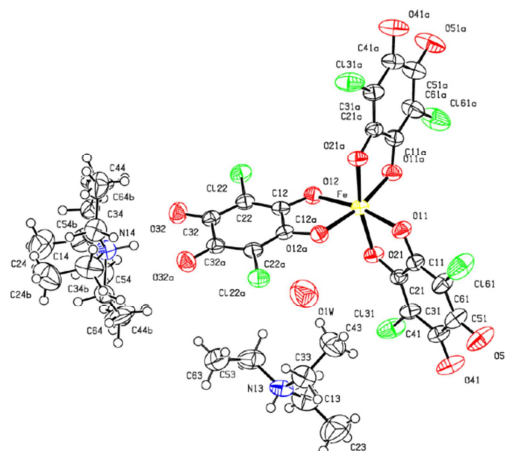
[(Et)₃NH]₃[Cr(Cl₂An)₃]·H₂O (C1c)



Selected bond lengths (Å) and angles (°).

Bonds	Å	Bonds	Å	Angles	°	Angles	°
Cr-O(11)	1.951(4)	N(15)-C(55)	1.489(7)	O(11)-Cr-O(23)	92.17(17)	O(23)-C(23)-C(13)	113.6(5)
Cr-O(23)	1.959(4)	N(15)-C(35)	1.534(7)	O(11)-Cr-O(13)	89.19(16)	O(13)-C(13)-C(63)	124.9(6)
Cr-O(13)	1.968(4)	O(43)-C(53)	1.250(7)	O(23)-Cr-O(13)	82.11(17)	O(13)-C(13)-C(31)	115.2(6)
Cr-O(21)	1.972(4)	O(52)-O(42)	1.224(7)	O(11)-Cr-O(21)	82.24(17)	O(33)-C(43)-C(61)	125.9(6)
Cr-O(12)	1.974(4)	-	-	O(23)-Cr-O(21)	172.67(17)	O(33)-C(43)-C(33)	122.5(7)
Cr-O(22)	1.987(4)	-	-	O(13)-Cr-O(21)	93.03(16)	O(21)-C(21)-C(53)	119.4(6)
Cl(21)-C(61)	1.763(6)	-	-	O(11)-Cr-O(12)	173.31(17)	C(23)-C(33)-Cl(13)	120.5(5)
Cl(12)-C(32)	1.745(6)	-	-	O(23)-Cr-O(12)	93.15(17)	C(43)-C(33)-Cl(13)	120.0(5)
Cl(11)-C(31)	1.748(6)	-	-	O(13)-Cr-O(12)	95.56(16)	C(21)-C(31)-Cl(11)	120.7(5)
Cl(22)-C(62)	1.733(6)	-	-	O(21)-Cr-O(12)	92.78(17)	C(41)-C(31)-Cl(11)	117.7(5)
Cl(23)-C(63)	1.726(7)	-	-	O(11)-Cr-O(22)	94.44(16)	C(22)-C(32)-Cl(12)	119.6(5)
Cl(13)-C(33)	1.724(6)	-	-	O(23)-Cr-O(22)	92.65(16)	C(42)-C(32)-Cl(12)	118.4(5)
O(21)-C(21)	1.307(4)	-	-	O(13)-Cr-O(22)	173.74(17)	O(12)-C(12)-C(62)	124.7(6)
O(41)-C(51)	1.228(7)	-	-	O(21)-Cr-O(22)	92.52(16)	O(12)-C(12)-C(22)	113.7(5)
O(11)-C(11)	1.296(6)	-	-	O(12)-Cr-O(22)	81.27(16)	C(13)-C(63)-Cl(23)	119.7(5)
O(22)-C(22)	1.280(6)	-	-	C(21)-O(21)-Cr	113.6(4)	C(53)-C(63)-Cl(23)	119.6(5)
O(13)-C(13)	1.288(6)	-	-	C(11)-O(11)-Cr	114.8(4)	O(41)-C(51)-C(61)	125.7(6)
O(23)-C(23)	1.324(6)	-	-	C(22)-O(22)-Cr	114.5(4)	O(41)-C(51)-C(41)	116.5(6)
O(12)-C(12)	1.295(6)	-	-	C(13)-O(13)-Cr	113.9(4)	C(11)-C(61)-Cl(21)	118.8(5)
N(16)-C(16)	1.484(8)	-	-	C(23)-O(23)-Cr	113.8(4)	C(51)-C(61)-Cl(21)	118.2(5)
N(16)-C(36)	1.503(9)	-	-	O(21)-C(21)-C(31)	124.6(6)	O(32)-C(42)-C(32)	124.7(7)
N(16)-C(56)	1.520(10)	-	-	O(11)-C(11)-C(61)	125.9(6)	O(32)-C(42)-C(52)	116.8(6)
C(41)-O(31)	1.223(7)	-	-	O(11)-C(11)-C(21)	114.4(6)	O(42)-C(52)-C(62)	124.4(6)
O(32)-C(42)	1.230(7)	-	-	C(12)-O(12)-Cr	115.2(4)	O(42)-C(52)-C(42)	117.4(5)
C(43)-O(33)	1.236(7)	-	-	O(31)-C(41)-C(31)	125.7(6)	C(12)-C(62)-Cl(22)	120.8(5)
N(14)-C(54)	1.495(8)	-	-	O(31)-C(41)-C(51)	117.1(6)	C(52)-C(62)-Cl(22)	118.8(5)
N(14)-C(34)	1.500(8)	-	-	O(22)-C(22)-C(32)	126.2(6)	O(43)-C(53)-C(63)	125.5(6)
N(14)-C(14)	1.513(8)	-	-	O(22)-C(22)-C(12)	115.2(6)	O(43)-C(53)-C(43)	114.8(6)
N(15)-C(15)	1.465(8)	-	-	O(23)-C(23)-C(33)	124.3(6)	-	-

[(Et)₃NH]₃[Fe(Cl₂An)₃]·H₂O (C2c)

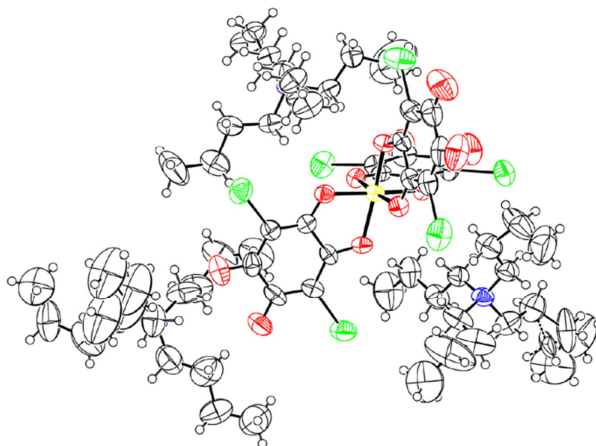


Selected bond lengths (Å) and angles (°).

Bonds	Å	Bonds	Å	Angles	°	Angles	°
Fe-O(11)	1.999(2)	N(14)-C(34)	1.498(7)	O(11)-Fe-O(11) ⁱ	99.00(13)	O(22)-C(22)-C(32)	126.2(6)
Fe-O(12)	2.003(2)	N(14)-C(54)	1.552(7)	O(11)-Fe-O(12) ⁱ	90.96(9)	O(22)-C(22)-C(12)	115.2(6)
Fe-O(21)	2.013(2)	-	-	O(11)-Fe-O(12)	168.36(8)	O(23)-C(23)-C(33)	124.3(6)
Cl(22)-C(22)	1.729(3)	-	-	O(11)-Fe-O(21)	79.58(8)	C(21)-C(31)-Cl(31)	120.4(2)
Cl(31)-C(31)	1.724(3)	-	-	O(12)-Fe-O(21)	94.02(8)	C(41)-C(31)-Cl(31)	117.8(2)
Cl(61)-C(61)	1.725(4)	-	-	O(12)-Fe-O(21) ⁱ	95.02(9)	O(11)-C(11)-C(61)	125.0(3)
O(12)-C(12)	1.280(3)	-	-	O(21)-Fe-O(21)	168.20(13)	O(11)-C(11)-C(21)	114.3(2)
O(21)-C(21)	1.279(3)	-	-	C(12)-O(12)-Fe	115.62(18)	C(11)-C(61)-Cl(61)	120.1(3)
O(11)-C(11)	1.275(3)	-	-	C(21)-O(21)-Fe	115.60(18)	C(51)-C(61)-Cl(61)	118.6(3)
O(32)-C(32)	1.227(4)	-	-	C(11)-O(11)-Fe	116.13(19)	O(32)-C(32)-C(22)	125.2(3)
N(13)-C(13)	1.482(5)	-	-	C(12)-C(22)-Cl(22)	119.3(2)	O(32)-C(32)-C(32) ⁱ	116.96(18)
N(13)-C(53)	1.492(5)	-	-	C(32)-C(22)-Cl(22)	118.7(2)	O(41)-C(41)-C(31)	125.2(3)
N(13)-C(33)	1.506(5)	-	-	O(21)-C(21)-C(31)	126.0(3)	O(41)-C(41)-C(51)	116.7(3)
O(51)-C(51)	1.229(4)	-	-	O(21)-C(21)-C(11)	114.1(2)	O(51)-C(51)-C(61)	124.6(4)
O(41)-C(41)	1.216(4)	-	-	O(12)-C(12)-C(22)	125.6(3)	O(51)-C(51)-C(41)	117.1(3)
N(14)-C(14)	1.443(7)	-	-	O(12)-C(12)-C(12) ⁱ	114.40(15)	-	-

Symmetry transformations: i) -x,y,-z+1/2.

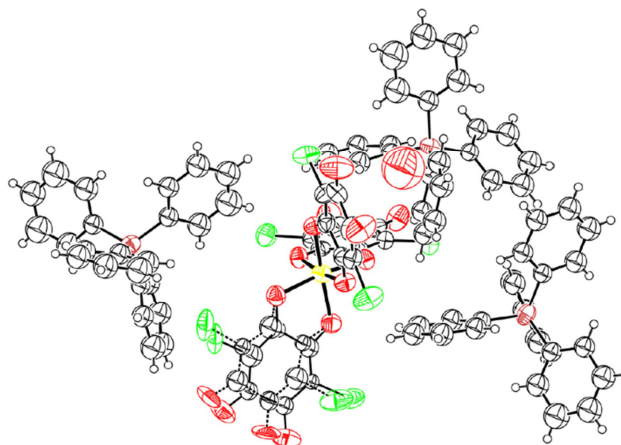
[(*n*-Bu)₄N]₃[Cr(I₂An)₃] (C5a)



Selected bond lengths (Å) and angles (°).

Bonds	Å	Bonds	Å	Angles	°	Angles	°
I(31)-C(31)	2.058(7)	O(41)-C(41)	1.226(8)	O(23)-Cr-O(13)	81.0(2)	O(23)-C(23)-C(33)	126.1(7)
I(61)-C(61)	2.088(7)	C(13)-C(63)	1.354(10)	O(23)-Cr-O(11)	89.24(19)	O(23)-C(23)-C(13)	114.3(6)
I(62)-C(62)	2.074(7)	O(43)-C(43)	1.239(10)	O(13)-Cr-O(11)	92.9(2)	O(13)-C(13)-C(63)	123.8(8)
I(32)-C(32)	2.068(8)	C(14)-N(14)	1.519(9)	O(23)-Cr-O(22)	92.2(2)	O(13)-C(13)-C(23)	114.3(6)
I(63)-C(63)	2.078(9)	C(14)-C(24)	1.524(11)	O(13)-Cr-O(22)	93.6(2)	O(11)-C(11)-C(61)	125.3(7)
I(33)-C(33)	2.053(9)	C(11)-C(61)	1.356(10)	O(11)-Cr-O(22)	173.5(2)	O(11)-C(11)-C(21)	113.8(6)
Cr-O(23)	1.962(5)	C(61)-C(51)	1.409(11)	O(23)-Cr-O(21)	97.6(2)	C(11)-C(61)-I(61)	122.0(6)
Cr-O(13)	1.966(5)	C(31)-C(41)	1.411(10)	O(13)-Cr-O(21)	174.3(2)	C(51)-C(61)-I(61)	115.9(6)
Cr-O(11)	1.968(5)	C(41)-C(51)	1.571(12)	O(11)-Cr-O(21)	81.52(19)	C(21)-C(31)-I(31)	121.6(6)
Cr-O(22)	1.971(5)	O(53)-C(53)	1.245(9)	O(22)-Cr-O(21)	91.98(19)	C(41)-C(31)-I(31)	117.1(5)
Cr-O(21)	1.971(4)	C(62)-C(12)	1.371(10)	O(23)-Cr-O(12)	170.0(2)	O(41)-C(41)-C(31)	125.0(8)
Cr-O(12)	1.978(5)	C(62)-C(52)	1.415(11)	O(13)-Cr-O(12)	92.3(2)	O(41)-C(41)-C(51)	116.8(7)
O(23)-C(23)	1.284(8)	C(54)-C(64)	1.496(11)	O(11)-Cr-O(12)	98.4(2)	C(12)-C(62)-I(62)	120.3(6)
O(12)-C(12)	1.284(8)	C(15)-C(25)	1.503(11)	O(22)-Cr-O(12)	80.9(2)	C(52)-C(62)-I(62)	118.4(6)
O(11)-C(11)	1.298(8)	C(33)-C(43)	1.431(12)	O(21)-Cr-O(12)	89.85(19)	O(12)-C(12)-C(62)	126.4(7)
O(21)-C(21)	1.292(8)	C(53)-C(63)	1.428(12)	C(23)-O(23)-Cr	115.1(4)	O(12)-C(12)-C(22)	113.7(6)
O(13)-C(13)	1.279(8)	C(53)-C(43)	1.542(13)	C(12)-O(12)-Cr	115.4(4)	C(23)-C(33)-I(33)	120.8(6)
O(22)-C(22)	1.280(8)	-	-	C(11)-O(11)-Cr	114.7(4)	C(43)-C(33)-I(33)	117.9(7)
O(51)-C(51)	1.222(9)	-	-	C(21)-O(21)-Cr	114.7(4)	O(51)-C(51)-C(61)	126.7(9)
C(32)-C(22)	1.363(10)	-	-	C(13)-O(13)-Cr	115.2(5)	O(51)-C(51)-C(41)	115.9(7)
C(32)-C(42)	1.428(11)	-	-	C(22)-O(22)-Cr	115.4(4)	O(53)-C(53)-C(63)	125.2(10)
O(52)-C(52)	1.207(9)	-	-	C(22)-C(32)-I(32)	121.5(6)	O(53)-C(53)-C(43)	117.1(9)
C(22)-C(12)	1.519(10)	-	-	C(42)-C(32)-I(32)	116.8(6)	O(52)-C(52)-C(62)	123.6(9)
O(42)-C(42)	1.225(9)	-	-	O(22)-C(22)-C(32)	125.7(7)	O(52)-C(52)-C(42)	117.2(8)
C(42)-C(52)	1.532(12)	-	-	O(22)-C(22)-C(12)	114.3(6)	C(13)-C(63)-I(63)	121.9(6)
C(21)-C(31)	1.378(9)	-	-	O(42)-C(42)-C(32)	124.8(8)	C(53)-C(63)-I(63)	116.9(6)
C(21)-C(11)	1.505(10)	-	-	O(42)-C(42)-C(52)	117.3(8)	O(43)-C(43)-C(33)	123.5(10)
C(23)-C(33)	1.371(10)	-	-	O(21)-C(21)-C(31)	125.9(7)	O(43)-C(43)-C(53)	118.2(9)
C(23)-C(13)	1.495(10)	-	-	O(21)-C(21)-C(11)	114.5(6)	-	-

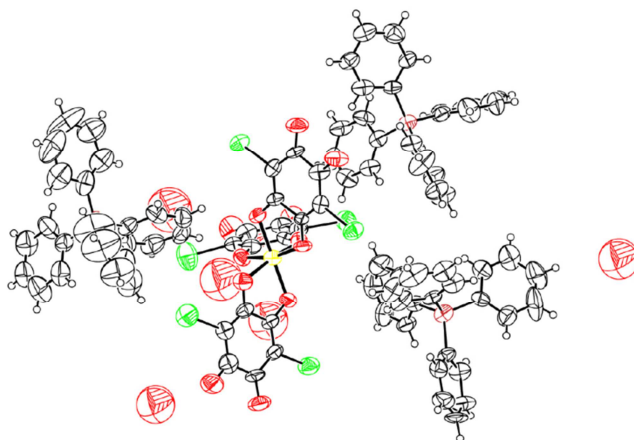
[(Ph)₄P]₃[Fe(Cl₂An)₃]·H₂O (C2b)



Selected bond lengths (Å) and angles (°).

Bonds	Å	Bonds	Å	Angles	°	Angles	°
Cl(32)-C(32)	1.728(9)	C(22)-C(32)	1.373(11)	O(23)-Fe-O(12)	90.3(2)	O(22)-C(22)-C(32)	124.9(8)
Cl(31)-C(31)	1.736(9)	C(22)-C(12)	1.500(11)	O(23)-Fe-O(11)	92.7(2)	O(22)-C(22)-C(12)	114.1(9)
Fe-O(23)	1.999(6)	C(13)-C(63)	1.320(16)	O(12)-Fe-O(11)	172.0(3)	C(22)-C(32)-Cl(32)	120.8(8)
Fe-O(12)	2.001(6)	C(13)-C(23)	1.515(18)	O(23)-Fe-O(21)	97.4(2)	C(42)-C(32)-Cl(32)	118.2(8)
Fe-O(11)	2.002(6)	C(23)-C(33)	1.397(16)	O(12)-Fe-O(21)	92.6(2)	O(12)-C(12)-C(62)	124.6(9)
Fe-O(21)	2.008(6)	C(33)-C(43)	1.406(17)	O(11)-Fe-O(21)	79.6(2)	O(12)-C(12)-C(22)	115.8(8)
Fe-O(13)	2.013(6)	C(33)-Cl(33)	1.810(16)	O(23)-Fe-O(13)	80.3(3)	O(52)-C(52)-C(62)	124.5(9)
Fe-O(22)	2.017(6)	C(43)-O(43)	1.233(16)	O(12)-Fe-O(13)	97.0(2)	O(52)-C(52)-C(42)	118.4(10)
Cl(62)-C(62)	1.729(9)	C(43)-C(53)	1.538(18)	O(11)-Fe-O(13)	90.9(2)	C(12)-C(62)-Cl(62)	120.2(8)
Cl(61)-C(61)	1.744(9)	C(53)-O(53)	1.240(16)	O(21)-Fe-O(13)	170.1(2)	C(52)-C(62)-Cl(62)	117.4(7)
O(21)-C(21)	1.286(10)	C(53)-C(63)	1.377(16)	O(23)-Fe-O(22)	163.6(2)	O(42)-C(42)-C(32)	124.0(10)
O(13)-C(13)	1.245(15)	C(63)-Cl(63)	1.799(16)	O(12)-Fe-O(22)	80.1(2)	O(42)-C(42)-C(52)	117.1(9)
O(22)-C(22)	1.290(9)	Cl(6A)-C(63A)	1.840(18)	O(11)-Fe-O(22)	98.6(2)	O(11)-C(11)-C(61)	125.1(9)
O(11)-C(11)	1.279(10)	Cl(3A)-C(33A)	1.809(17)	O(21)-Fe-O(22)	96.4(2)	O(11)-C(11)-C(21)	115.6(9)
O(42)-C(42)	1.233(10)	C(53A)-O(53A)	1.233(17)	O(13)-Fe-O(22)	87.6(2)	C(11)-C(61)-Cl(61)	118.6(8)
O(23)-C(23)	1.312(15)	C(53A)-C(63A)	1.379(17)	C(21)-O(21)-Fe	116.2(6)	C(51)-C(61)-Cl(61)	119.4(8)
O(52)-C(52)	1.214(9)	C(53A)-C(43A)	1.533(18)	C(13)-O(13)-Fe	121.4(12)	C(13)-C(63)-Cl(63)	120.1(16)
O(12)-C(12)	1.286(10)	O(43A)-C(43A)	1.229(18)	C(22)-O(22)-Fe	115.0(6)	C(53)-C(63)-Cl(63)	116.1(14)
C(51)-O(51)	1.220(10)	C(33A)-C(23A)	1.340(17)	C(11)-O(11)-Fe	115.1(6)	O(53A)-C(53A)-C(63A)	125(3)
C(51)-C(61)	1.400(12)	C(33A)-C(43A)	1.370(17)	C(23)-O(23)-Fe	108.6(11)	O(53A)-C(53A)-C(43A)	121(3)
C(51)-C(41)	1.557(13)	C(23A)-C(13A)	1.524(18)	C(12)-O(12)-Fe	114.7(6)	C(23A)-C(33A)-Cl(3A)	120.9(19)
C(14)-C(24)	1.383(11)	C(63A)-C(13A)	1.370(17)	O(51)-C(51)-C(61)	124.0(10)	C(43A)-C(33A)-Cl(3A)	116.0(17)
C(14)-C(64)	1.396(11)	-	-	O(51)-C(51)-C(41)	117.0(10)	O(43A)-C(43A)-C(33A)	124(3)
C(31)-C(21)	1.366(12)	-	-	C(21)-C(31)-Cl(31)	119.0(8)	O(43A)-C(43A)-C(53A)	119(2)
C(31)-C(41)	1.415(12)	-	-	C(41)-C(31)-Cl(31)	116.9(8)	O(23)-C(23A)-C(33A)	127(2)
C(16)-C(26)	1.378(11)	-	-	O(21)-C(21)-C(31)	127.6(9)	O(23)-C(23A)-C(13A)	107(2)
C(16)-C(66)	1.387(11)	-	-	O(21)-C(21)-C(11)	113.1(9)	C(13A)-C(63A)-Cl(6A)	111(2)
C(21)-C(11)	1.508(12)	-	-	O(41)-C(41)-C(31)	126.7(10)	C(53A)-C(63A)-Cl(6A)	115.4(19)
C(41)-O(41)	1.204(10)	-	-	O(41)-C(41)-C(51)	117.3(10)	O(13)-C(13A)-C(63A)	130(2)

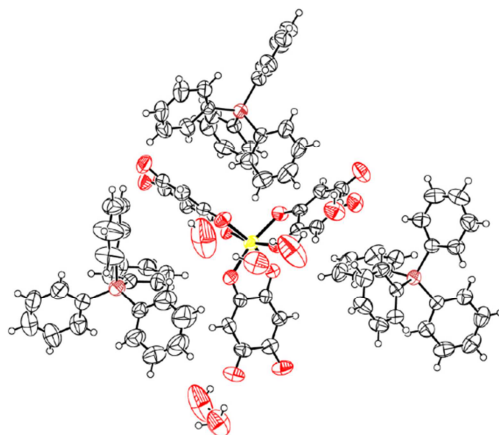
[(Ph)₄P]₃[Fe(I₂An)₃]·H₂O (C6b)



Selected bond lengths (Å) and angles (°).

Bonds	Å	Bonds	Å	Angles	°	Angles	°
I(31)-C(31)	2.088(14)	C(63)-C(13)	1.39(2)	O(22)-Fe-O(12)	81.0(4)	O(11)-C(11)-C(21)	112.4(12)
I(61)-C(61)	2.050(14)	C(42)-C(32)	1.48(2)	O(22)-Fe-O(21)	97.9(4)	O(23)-C(23)-C(33)	125.8(15)
I(32)-C(32)	2.072(15)	C(42)-C(52)	1.55(2)	O(12)-Fe-O(21)	98.3(4)	O(23)-C(23)-C(13)	114.0(14)
I(33)-C(33)	2.094(16)	C(11)-C(61)	1.356(19)	O(22)-Fe-O(11)	176.3(4)	C(23)-C(33)-I(33)	120.8(12)
I(62)-C(62)	2.085(16)	C(24)-C(34)	1.38(3)	O(12)-Fe-O(11)	97.2(4)	C(43)-C(33)-I(33)	117.2(12)
I(63)-C(63)	2.070(16)	C(24)-C(14)	1.39(2)	O(21)-Fe-O(11)	79.2(4)	C(22)-O(22)-Fe	114.6(9)
Fe-O(22)	1.994(10)	C(23)-C(33)	1.35(2)	O(22)-Fe-O(23)	89.6(4)	C(11)-C(61)-I(61)	122.2(12)
Fe-O(12)	1.999(10)	C(23)-C(13)	1.51(2)	O(12)-Fe-O(23)	165.4(5)	C(51)-C(61)-I(61)	116.8(11)
Fe-O(21)	2.006(9)	C(25)-C(15)	1.339(19)	O(21)-Fe-O(23)	94.0(4)	C(12)-C(62)-I(62)	121.0(13)
Fe-O(11)	2.007(10)	C(25)-C(35)	1.383(19)	O(11)-Fe-O(23)	92.8(4)	C(52)-C(62)-I(62)	117.1(12)
Fe-O(23)	2.010(10)	C(33)-C(43)	1.43(2)	O(22)-Fe-O(13)	94.8(4)	O(12)-C(12)-C(62)	124.8(15)
Fe-O(13)	2.038(10)	C(35)-C(45)	1.36(2)	O(12)-Fe-O(13)	90.2(4)	O(12)-C(12)-C(22)	115.3(14)
O(13)-C(13)	1.264(16)	O(22)-C(22)	1.331(16)	O(21)-Fe-O(13)	165.7(4)	O(51)-C(51)-C(61)	126.5(15)
O(21)-C(21)	1.290(16)	C(61)-C(51)	1.44(2)	O(11)-Fe-O(13)	88.4(4)	O(51)-C(51)-C(41)	116.9(15)
O(51)-C(51)	1.195(16)	C(62)-C(12)	1.35(2)	O(23)-Fe-O(13)	79.5(4)	O(22)-C(22)-C(32)	123.7(14)
O(23)-C(23)	1.328(17)	C(62)-C(52)	1.45(2)	C(13)-O(13)-Fe	116.2(10)	O(22)-C(22)-C(12)	113.4(13)
O(12)-C(12)	1.296(16)	C(16)-C(66)	1.39(2)	C(21)-O(21)-Fe	117.5(9)	O(43)-C(43)-C(33)	125.3(17)
O(42)-C(42)	1.227(17)	C(16)-C(26)	1.40(2)	C(23)-O(23)-Fe	115.2(9)	O(43)-C(43)-C(53)	118.0(16)
C(21)-C(31)	1.376(19)	C(12)-C(22)	1.510(19)	C(12)-O(12)-Fe	114.9(10)	O(13)-C(13)-C(63)	124.0(15)
C(21)-C(11)	1.556(18)	C(75)-C(85)	1.39(2)	O(21)-C(21)-C(31)	129.4(13)	O(13)-C(13)-C(23)	114.8(14)
O(11)-C(11)	1.301(15)	C(51)-C(41)	1.60(2)	O(21)-C(21)-C(11)	112.9(13)	C(22)-C(32)-I(32)	120.4(11)
O(41)-C(41)	1.223(17)	C(26)-C(36)	1.42(2)	C(11)-O(11)-Fe	116.8(9)	C(42)-C(32)-I(32)	120.3(12)
C(44)-C(54)	1.35(3)	C(22)-C(32)	1.364(19)	C(21)-C(31)-I(31)	118.5(11)	O(41)-C(41)-C(31)	124.5(15)
C(44)-C(34)	1.35(3)	O(52)-C(52)	1.225(19)	C(41)-C(31)-I(31)	118.4(11)	O(41)-C(41)-C(51)	117.0(14)
C(31)-C(41)	1.41(2)	C(43)-C(53)	1.55(2)	C(53)-C(63)-I(63)	120.3(13)	O(53)-C(53)-C(63)	125.2(18)
O(53)-C(53)	1.261(18)	C(56)-C(66)	1.42(2)	C(13)-C(63)-I(63)	120.5(13)	O(53)-C(53)-C(43)	113.7(17)
O(43)-C(43)	1.238(17)	C(54)-C(64)	1.37(2)	O(42)-C(42)-C(32)	121.0(16)	O(52)-C(52)-C(62)	126.7(18)
C(55)-C(45)	1.40(2)	C(64)-C(14)	1.35(2)	O(42)-C(42)-C(52)	121.6(16)	O(52)-C(52)-C(42)	114.8(17)
C(63)-C(53)	1.39(2)	-	-	O(11)-C(11)-C(61)	125.3(13)	C(62)-C(52)-C(42)	118.5(15)

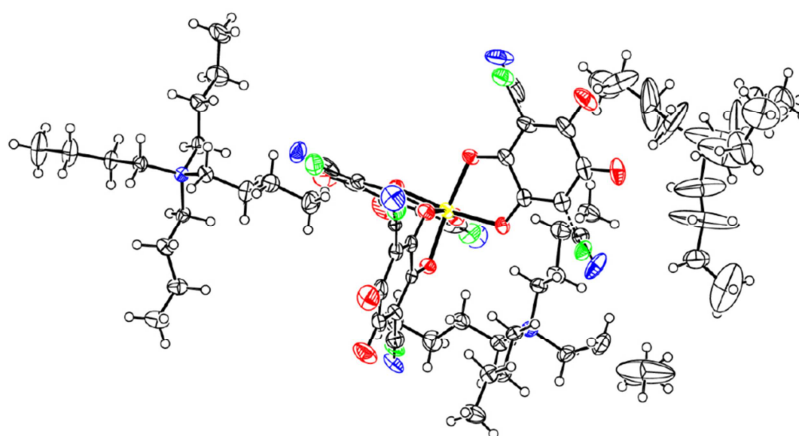
[(Ph)₄P]₃[Fe(H₂An)₃]-6H₂O (C8b)



Selected bond lengths (Å) and angles (°).

Bonds	Å	Bonds	Å	Angles	°	Angles	°
Fe-O(23)	1.990(2)	O(43)-C(43)	1.228(3)	O(11)-Fe-O(21)	80.56(6)	O(22)-C(22)-C(32)	125.67(6)
Fe-O(13)	2.036(3)	O(51)-C(51)	1.234(3)	O(11)-Fe-O(22)	98.12(7)	O(23)-C(23)-C(13)	113.73(5)
Fe-O(11)	1.997(2)	O(52)-C(52)	1.231(3)	O(11)-Fe-O(23)	167.09(6)	O(53)-C(53)-C(63)	124.69(6)
Fe-O(12)	1.997(3)	O(53)-C(53)	1.244(3)	O(12)-Fe-O(13)	92.35(5)	Fe-O(11)-C(11)	115.04(7)
Fe-O(21)	1.994(3)	O(1W)-H(2)	1.02(1)	O(12)-Fe-O(21)	166.92(7)	Fe-O(12)-C(12)	115.09(6)
Fe-O(22)	2.000(2)	O(1W)-H(1)	0.98(1)	O(12)-Fe-O(22)	80.16(6)	Fe-O(13)-C(13)	115.38(5)
P(14)-C(74)	1.792(3)	O(2W)-H(3)	1.15(1)	O(12)-Fe-O(23)	100.5(8)	Fe-O(21)-C(21)	115.05(6)
P(14)-C(14)	1.787(2)	O(2W)-H(4)	0.98(1)	O(13)-Fe-O(21)	95.99(6)	Fe-O(22)-C(22)	116.13(6)
P(14)-C(194)	1.785(3)	O(3W)-H(6)	0.99(1)	O(13)-Fe-O(22)	167.51(6)	Fe-O(23)-C(23)	116.99(7)
P(14)-C(134)	1.786(3)	O(3W)-H(5)	0.94(1)	O(13)-Fe-O(23)	79.46(7)	H(1)-O(1W)-H(2)	99.0(5)
P(15)-C(75)	1.789(4)	O(4W)-H(7)	0.98(1)	O(21)-Fe-O(22)	93.23(6)	H(3)-O(2W)-H(4)	110.0(5)
P(15)-C(195)	1.778(3)	O(4W)-H(8)	0.97(1)	O(21)-Fe-O(23)	90.94(5)	H(5)-O(3W)-H(6)	105.0(5)
P(15)-C(135)	1.794(3)	O(5W)-H(9)	0.97(1)	O(22)-Fe-O(23)	92.00(6)	H(7)-O(4W)-H(8)	104.0(5)
P(15)-C(15)	1.793(3)	O(5W)-H(10)	0.98(1)	O(11)-Fe-O(12)	89.15(6)	H(9)-O(5W)-H(10)	102.0(5)
P(16)-C(196)	1.790(3)	O(6W)-H(11)	0.98(1)	O(11)-Fe-O(13)	91.70(7)	H(11)-O(6W)-H(12)	101.0(5)
P(16)-C(136)	1.780(4)	O(6W)-H(12)	1.11(1)	O(11)-C(11)-C(21)	114.31(6)	O(41)-C(41)-C(31)	123.85(6)
P(16)-C(16)	1.780(3)	-	-	O(11)-C(11)-C(61)	125.19(5)	O(41)-C(41)-C(51)	117.72(5)
P(16)-C(76)	1.792(4)	-	-	O(12)-C(12)-C(22)	115.13(6)	O(42)-C(42)-C(52)	117.83(6)
O(11)-C(11)	1.299(3)	-	-	C(22)-C(12)-C(62)	120.17(6)	O(42)-C(42)-C(32)	124.23(6)
O(12)-C(12)	1.297(3)	-	-	O(12)-C(12)-C(62)	124.70(5)	O(43)-C(43)-C(33)	124.06(4)
O(13)-C(13)	1.288(3)	-	-	O(13)-C(13)-C(23)	114.40(6)	O(43)-C(43)-C(53)	118.12(6)
O(21)-C(21)	1.294(3)	-	-	O(13)-C(13)-C(63)	125.23(6)	O(51)-C(51)-C(61)	123.21(6)
O(22)-C(22)	1.293(3)	-	-	C(23)-C(13)-C(63)	120.36(5)	O(51)-C(51)-C(41)	117.6(6)
O(23)-C(23)	1.296(3)	-	-	O(21)-C(21)-C(11)	114.57(6)	O(52)-C(52)-C(42)	118.1(7)
O(41)-C(41)	1.227(3)	-	-	O(21)-C(21)-C(31)	124.67(6)	O(52)-C(52)-C(62)	123.41(6)
O(42)-C(42)	1.231(3)	-	-	O(22)-C(22)-C(12)	113.49(6)	O(53)-C(53)-C(43)	116.28(6)

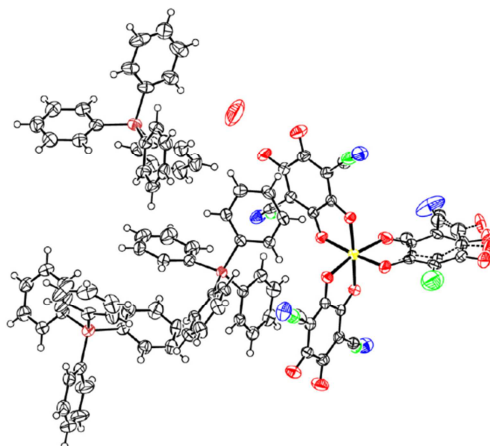
[(*n*-Bu)₄N]₃[Cr(ClCNA)₃] (C9a)



Selected bond lengths (Å) and angles (°).

Bonds	Å	Bonds	Å	Angles	°	Angles	°
Cl(31)-C(31)	1.863(8)	C(63)-C(53)	1.450(9)	O(11)-Cr-O(21)	82.08(16)	C(73)-C(63)-Cl(63)	119.3(2)
Cl(32)-C(32)	1.877(9)	C(21)-C(31)	1.378(8)	O(11)-Cr-O(12)	92.59(17)	C(13)-C(63)-Cl(63)	119.3(6)
Cl(33)-C(33)	1.826(8)	C(21)-C(11)	1.520(8)	O(21)-Cr-O(12)	91.78(16)	C(53)-C(63)-Cl(63)	119.9(6)
Cl(61)-C(61)	1.912(9)	O(53)-C(53)	1.231(7)	O(11)-Cr-O(13)	92.20(16)	O(21)-C(21)-C(31)	125.9(6)
Cl(62)-C(62)	1.921(9)	C(13)-C(23)	1.500(8)	O(21)-Cr-O(13)	171.88(16)	O(21)-C(21)-C(11)	114.5(5)
Cl(63)-C(63)	1.847(10)	C(22)-C(32)	1.389(8)	O(12)-Cr-O(13)	94.25(17)	O(13)-C(13)-C(63)	124.3(6)
Cr-O(11)	1.961(4)	C(22)-C(12)	1.507(9)	O(11)-Cr-O(22)	170.66(16)	O(13)-C(13)-C(23)	114.6(5)
Cr-O(21)	1.966(4)	C(31)-C(41)	1.438(10)	O(21)-Cr-O(22)	90.61(16)	O(22)-C(22)-C(32)	125.3(6)
Cr-O(12)	1.975(4)	O(42)-C(42)	1.232(8)	O(12)-Cr-O(22)	81.76(16)	O(22)-C(22)-C(12)	114.7(5)
Cr-O(13)	1.975(4)	C(32)-C(42)	1.447(9)	O(13)-Cr-O(22)	95.63(16)	O(23)-C(23)-C(33)	124.7(6)
Cr-O(22)	1.977(4)	C(41)-C(51)	1.541(10)	O(11)-Cr-O(23)	92.04(16)	O(23)-C(23)-C(13)	115.2(5)
Cr-O(23)	1.978(4)	C(43)-C(53)	1.542(10)	O(21)-Cr-O(23)	92.55(16)	O(41)-C(41)-C(31)	124.1(7)
O(21)-C(21)	1.293(7)	C(12)-C(62)	1.383(8)	O(12)-Cr-O(23)	174.05(17)	O(41)-C(41)-C(51)	118.4(6)
O(23)-C(23)	1.287(7)	C(52)-C(62)	1.434(10)	O(13)-Cr-O(23)	81.84(16)	O(43)-C(43)-C(33)	123.5(7)
O(22)-C(22)	1.279(7)	C(52)-C(42)	1.546(11)	O(22)-Cr-O(23)	94.11(16)	O(43)-C(43)-C(53)	118.5(6)
O(11)-C(11)	1.292(7)	C(71)-N(71)	1.26(3)	C(21)-O(21)-Cr	114.5(4)	O(12)-C(12)-C(62)	124.8(6)
O(13)-C(13)	1.296(7)	C(72)-N(72)	1.24(4)	C(23)-O(23)-Cr	113.7(4)	O(12)-C(12)-C(22)	115.2(5)
O(12)-C(12)	1.281(7)	C(73)-N(73)	1.16(4)	C(22)-O(22)-Cr	114.0(4)	O(51)-C(51)-C(61)	122.6(7)
O(43)-C(43)	1.230(7)	C(81)-N(81)	1.14(5)	C(11)-O(11)-Cr	115.1(4)	O(51)-C(51)-C(41)	119.1(6)
O(51)-C(51)	1.227(8)	C(82)-N(82)	1.15(4)	C(13)-O(13)-Cr	113.7(4)	O(11)-C(11)-C(61)	125.6(6)
O(41)-C(41)	1.222(8)	C(83)-N(83)	1.12(3)	C(12)-O(12)-Cr	113.8(4)	O(11)-C(11)-C(21)	113.8(5)
C(33)-C(23)	1.389(8)	-	-	C(83)-C(33)-Cl(33)	6.7(9)	O(52)-C(52)-C(62)	123.5(8)
C(33)-C(43)	1.440(9)	-	-	C(23)-C(33)-Cl(33)	118.4(5)	O(52)-C(52)-C(42)	118.9(7)
C(61)-C(11)	1.366(8)	-	-	C(43)-C(33)-Cl(33)	120.1(5)	O(53)-C(53)-C(63)	123.7(7)
C(61)-C(51)	1.453(9)	-	-	C(71)-C(61)-Cl(61)	4.3(8)	O(53)-C(53)-C(43)	117.8(6)
O(52)-C(52)	1.220(8)	-	-	C(11)-C(61)-Cl(61)	117.2(5)	O(42)-C(42)-C(32)	123.7(8)
C(63)-C(13)	1.382(8)	-	-	C(51)-C(61)-Cl(61)	121.4(5)	O(42)-C(42)-C(52)	118.1(7)

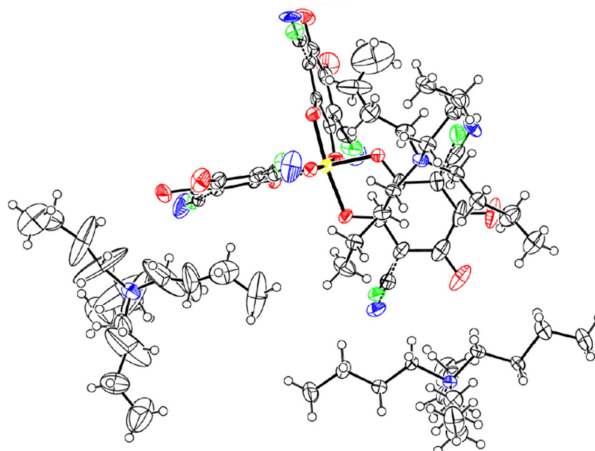
[(Ph)₄P]₃[Cr(CICNAn)₃·H₂O (C9b)



Selected bond lengths (Å) and angles (°).

Bonds	Å	Bonds	Å	Angles	°	Angles	°
C(11)-C(61)	1.366(7)	C(53)-O(53)	1.222(5)	C(61)-C(11)-O(11)	121.7(7)	O(43)-C(43)-C(53)	117.2(4)
C(11)-O(11)	1.375(7)	C(53)-C(63)	1.442(5)	C(61)-C(11)-C(21)	122.6(6)	C(33)-C(43)-C(53)	118.2(3)
C(11)-C(21)	1.511(8)	Cr(1)-O(11)	1.966(3)	O(11)-C(11)-C(21)	115.7(4)	O(52)-C(52)-C(62)	124.4(4)
C(21)-O(21)	1.215(6)	Cr(1)-O(21)	1.968(3)	O(21)-C(21)-C(31)	126.0(6)	O(52)-C(52)-C(42)	117.8(4)
C(21)-C(31)	1.437(8)	Cr(1)-O(12)	1.968(3)	O(21)-C(21)-C(11)	112.6(5)	C(62)-C(52)-C(42)	117.7(3)
C(31)-C(41)	1.437(9)	Cr(1)-O(23)	1.973(3)	C(31)-C(21)-C(11)	121.4(5)	O(53)-C(53)-C(63)	124.3(4)
C(31)-Cl(3)	1.644(7)	Cr(1)-O(22)	1.977(3)	C(21)-C(31)-C(41)	117.4(6)	O(53)-C(53)-C(43)	117.7(4)
C(41)-O(41)	1.229(8)	Cr(1)-O(13)	1.982(3)	C(21)-C(31)-Cl(3)	122.2(5)	C(63)-C(53)-C(43)	118.0(3)
C(41)-C(51)	1.566(13)	C(71)-N(71)	0.986(7)	C(41)-C(31)-Cl(3)	120.4(5)	C(12)-C(62)-C(52)	121.4(3)
C(51)-O(51)	1.204(9)	-	-	O(41)-C(41)-C(31)	121.2(8)	C(12)-C(62)-Cl(1)	121.8(3)
C(51)-C(61)	1.481(11)	-	-	O(41)-C(41)-C(51)	117.9(6)	C(52)-C(62)-Cl(1)	116.7(3)
C(61)-C(71)	1.596(8)	-	-	C(31)-C(41)-C(51)	120.9(6)	C(13)-C(63)-C(53)	121.6(3)
Cl(1)-C(62)	1.792(5)	-	-	O(51)-C(51)-C(61)	124.3(10)	C(13)-C(63)-Cl(2)	118.3(4)
N(72)-C(72)	1.15(4)	-	-	O(51)-C(51)-C(41)	118.1(8)	C(53)-C(63)-Cl(2)	119.8(4)
C(72)-C(32)	1.48(4)	-	-	C(61)-C(51)-C(41)	117.5(6)	O(11)-Cr(1)-O(21)	81.91(14)
C(73)-N(73)	1.19(2)	-	-	C(11)-C(61)-C(51)	119.1(7)	O(11)-Cr(1)-O(12)	91.48(12)
C(73)-C(33)	1.42(2)	-	-	C(11)-C(61)-C(71)	124.0(6)	O(21)-Cr(1)-O(12)	93.03(11)
Cl(2)-C(63)	1.766(9)	-	-	C(51)-C(61)-C(71)	116.9(5)	O(11)-Cr(1)-O(23)	89.28(12)
C(12)-O(12)	1.287(4)	-	-	N(72)-C(72)-C(32)	166(4)	O(21)-Cr(1)-O(23)	91.56(11)
C(12)-C(62)	1.376(5)	-	-	N(73)-C(73)-C(33)	178(2)	O(12)-Cr(1)-O(23)	175.40(11)
C(12)-C(22)	1.509(5)	-	-	O(12)-C(12)-C(62)	124.7(3)	O(11)-Cr(1)-O(22)	167.90(13)
C(13)-O(13)	1.290(4)	-	-	O(12)-C(12)-C(22)	114.5(3)	O(21)-Cr(1)-O(22)	88.32(12)
C(13)-C(63)	1.368(5)	-	-	C(62)-C(12)-C(22)	120.9(3)	O(12)-Cr(1)-O(22)	81.88(11)
C(13)-C(23)	1.512(5)	-	-	O(13)-C(13)-C(63)	125.9(3)	O(23)-Cr(1)-O(22)	98.15(11)
C(22)-O(22)	1.286(4)	-	-	O(13)-C(13)-C(23)	113.8(3)	O(11)-Cr(1)-O(13)	98.63(13)
C(22)-C(32)	1.378(5)	-	-	C(63)-C(13)-C(23)	120.3(3)	O(21)-Cr(1)-O(13)	172.68(11)
C(23)-O(23)	1.280(4)	-	-	O(22)-C(22)-C(32)	125.6(3)	O(12)-Cr(1)-O(13)	94.25(11)
C(23)-C(33)	1.384(5)	-	-	O(22)-C(22)-C(12)	114.9(3)	O(23)-Cr(1)-O(13)	81.16(11)
C(32)-C(42)	1.424(5)	-	-	C(32)-C(22)-C(12)	119.5(3)	O(22)-Cr(1)-O(13)	91.97(11)
C(33)-C(43)	1.430(6)	-	-	O(23)-C(23)-C(33)	124.9(3)	C(11)-O(11)-Cr(1)	110.7(4)
C(42)-O(42)	1.233(5)	-	-	O(23)-C(23)-C(13)	114.7(3)	C(12)-O(12)-Cr(1)	114.5(2)
C(42)-C(52)	1.553(6)	-	-	C(33)-C(23)-C(13)	120.4(3)	C(13)-O(13)-Cr(1)	114.9(2)
C(43)-O(43)	1.229(5)	-	-	C(22)-C(32)-C(42)	122.1(4)	C(21)-O(21)-Cr(1)	118.9(4)
C(43)-C(53)	1.553(6)	-	-	C(23)-C(33)-C(43)	121.3(4)	C(22)-O(22)-Cr(1)	113.8(2)
C(52)-O(52)	1.222(5)	-	-	O(42)-C(42)-C(32)	124.5(4)	C(23)-O(23)-Cr(1)	115.1(2)
C(52)-C(62)	1.435(6)	-	-	O(42)-C(42)-C(52)	117.2(3)	N(71)-C(71)-C(61)	149.0(7)

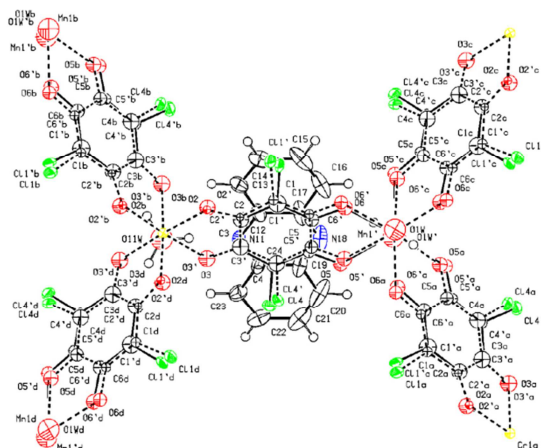
[(*n*-Bu)₄N]₃[Fe(CICNAn)₃] (C10a)



Selected bond lengths (Å) and angles (°).

Bonds	Å	Bonds	Å	Angles	°	Angles	°
Cl(31)-C(31)	1.861(7)	O(42)-C(42)	1.242(7)	C(33)-C(73)-N(73)	176.2(16)	O(12)-C(12)-C(62)	124.8(5)
Cl(32)-C(32)	1.824(8)	O(51)-C(51)	1.226(7)	O(11)-Fe(1)-O(12)	91.37(14)	O(12)-C(12)-C(22)	114.7(4)
Cl(33)-C(63)	1.893(10)	C(61)-C(11)	1.375(7)	O(11)-Fe(1)-O(22)	96.52(14)	C(12)-C(62)-Cl(62)	118.8(7)
C(71)-N(71)	1.26(3)	C(61)-C(51)	1.448(8)	O(12)-Fe(1)-O(22)	79.70(14)	C(52)-C(62)-Cl(62)	119.3(7)
C(71)-C(61)	1.293(17)	O(41)-C(41)	1.226(7)	O(11)-Fe(1)-O(21)	79.97(14)	O(41)-C(41)-C(31)	124.2(6)
C(72)-N(72)	1.10(6)	C(32)-C(22)	1.381(7)	O(12)-Fe(1)-O(21)	167.54(14)	O(41)-C(41)-C(51)	118.3(6)
C(72)-C(62)	1.40(6)	C(32)-C(42)	1.446(8)	O(22)-Fe(1)-O(21)	92.31(14)	O(13)-C(13)-C(63)	126.3(6)
C(73)-C(33)	1.22(3)	C(21)-C(31)	1.384(7)	O(11)-Fe(1)-O(23)	92.51(15)	O(13)-C(13)-C(23)	114.2(4)
C(73)-N(73)	1.26(4)	C(21)-C(11)	1.522(7)	O(12)-Fe(1)-O(23)	93.43(14)	O(22)-C(22)-C(32)	125.2(5)
Cl(61)-C(61)	1.911(8)	O(53)-C(53)	1.229(7)	O(22)-Fe(1)-O(23)	168.75(15)	O(22)-C(22)-C(12)	114.8(4)
Cl(62)-C(62)	1.809(12)	O(43)-C(43)	1.216(7)	O(21)-Fe(1)-O(23)	95.86(14)	O(11)-C(11)-C(61)	125.7(5)
Cl(63)-C(33)	1.928(8)	O(52)-C(52)	1.234(7)	O(11)-Fe(1)-O(13)	165.93(14)	O(11)-C(11)-C(21)	114.0(5)
C(81)-N(81)	1.13(3)	C(23)-C(33)	1.377(7)	O(12)-Fe(1)-O(13)	100.59(14)	C(21)-C(31)-Cl(31)	116.4(5)
C(81)-C(31)	1.29(2)	C(23)-C(13)	1.516(8)	O(22)-Fe(1)-O(13)	92.92(14)	C(41)-C(31)-Cl(31)	120.7(5)
C(82)-N(82)	1.13(3)	C(12)-C(62)	1.375(8)	O(21)-Fe(1)-O(13)	89.27(14)	O(42)-C(42)-C(32)	122.6(6)
C(82)-C(32)	1.35(2)	C(12)-C(22)	1.501(7)	O(23)-Fe(1)-O(13)	79.50(14)	O(42)-C(42)-C(52)	119.4(5)
C(83)-N(83)	1.06(5)	C(62)-C(52)	1.440(8)	C(11)-O(11)-Fe(1)	116.2(3)	C(13)-C(63)-Cl(33)	116.2(6)
C(83)-C(63)	1.29(4)	C(41)-C(31)	1.437(8)	C(21)-O(21)-Fe(1)	115.0(3)	C(53)-C(63)-Cl(33)	120.5(6)
Fe(1)-O(11)	1.998(4)	C(41)-C(51)	1.545(9)	C(22)-O(22)-Fe(1)	115.0(3)	O(43)-C(43)-C(33)	124.2(7)
Fe(1)-O(12)	2.008(3)	C(13)-C(63)	1.373(8)	C(13)-O(13)-Fe(1)	115.6(3)	O(43)-C(43)-C(53)	118.4(6)
Fe(1)-O(22)	2.017(3)	C(42)-C(52)	1.534(9)	C(23)-O(23)-Fe(1)	115.2(3)	C(73)-C(33)-Cl(63)	12.6(8)
Fe(1)-O(21)	2.018(3)	C(63)-C(53)	1.436(9)	C(12)-O(12)-Fe(1)	114.8(3)	C(23)-C(33)-Cl(63)	115.8(5)
Fe(1)-O(23)	2.019(3)	C(43)-C(33)	1.432(9)	C(11)-C(61)-Cl(61)	116.9(4)	C(43)-C(33)-Cl(63)	121.0(5)
Fe(1)-O(13)	2.021(3)	C(43)-C(53)	1.551(10)	C(51)-C(61)-Cl(61)	121.2(4)	O(52)-C(52)-C(62)	124.1(6)
O(11)-C(11)	1.282(6)	-	-	C(22)-C(32)-Cl(32)	118.5(4)	O(52)-C(52)-C(42)	117.9(5)
O(21)-C(21)	1.282(6)	-	-	C(42)-C(32)-Cl(32)	119.9(5)	C(62)-C(52)-C(42)	118.0(5)
O(22)-C(22)	1.281(6)	-	-	O(21)-C(21)-C(31)	126.1(5)	O(51)-C(51)-C(61)	123.5(6)
O(13)-C(13)	1.281(6)	-	-	O(21)-C(21)-C(11)	114.8(4)	O(51)-C(51)-C(41)	118.3(6)
O(23)-C(23)	1.281(6)	-	-	O(23)-C(23)-C(33)	125.5(6)	O(53)-C(53)-C(63)	124.9(7)
O(12)-C(12)	1.293(6)	-	-	O(23)-C(23)-C(13)	115.0(4)	O(53)-C(53)-C(43)	117.7(6)

[(H₃O)(phz)₃][MnCr(Cl₂An)₃(H₂O)] (M1)

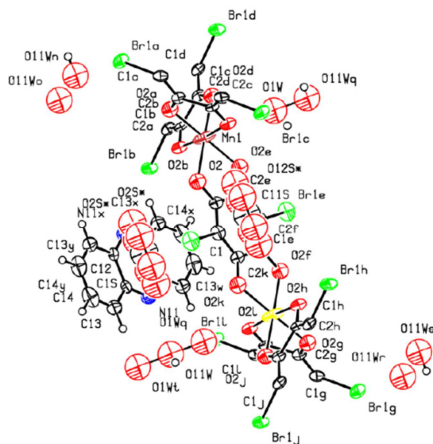


Selected bond lengths (Å) and angles (°).

Bonds	Å	Bonds	Å	Angles	°	Angles	°
Cr(1)-O(3)	1.944(14)	C(15)-C(16)	1.354(12)	O(3)-Cr(1)-O(3) ⁱ	101.3(5)	O(6) ^{iv} -Mn(1)-O(1W)	73.8(3)
Cr(1)-O(3) ⁱ	1.944(14)	C(16)-C(17)	1.427(10)	O(3)-Cr(1)-O(3) ⁱⁱ	101.3(5)	O(5) ⁱⁱⁱ -Mn(1)-O(1W)	123.2(2)
Cr(1)-O(3) ⁱⁱ	1.944(14)	C(17)-N(18)	1.326(9)	O(3) ⁱ -Cr(1)-O(3) ⁱⁱ	101.3(5)	O(5) ^{iv} -Mn(1)-O(1W)	123.2(2)
Cr(1)-O(2) ⁱⁱ	2.013(10)	N(18)-C(19)	1.340(10)	O(3)-Cr(1)-O(2) ⁱⁱ	172.3(5)	O(5)-Mn(1)-O(1W)	123.2(2)
Cr(1)-O(2)	2.013(10)	C(19)-C(20)	1.420(10)	O(3) ⁱ -Cr(1)-O(2) ⁱⁱ	85.7(4)	Mn(1)-O(1W)-H(1W)	119(3)
Cr(1)-O(2) ⁱ	2.013(10)	C(19)-C(24)	1.438(8)	O(3) ⁱⁱ -Cr(1)-O(2) ⁱⁱ	80.1(5)	C(2)-C(1)-Cl(1)	118.4(11)
Mn(1)-O(6) ⁱⁱⁱ	2.185(8)	C(20)-C(21)	1.341(12)	O(3)-Cr(1)-O(2)	80.1(5)	C(6)-C(1)-Cl(1)	120.4(9)
Mn(1)-O(6)	2.185(8)	C(21)-C(22)	1.409(12)	O(3) ⁱ -Cr(1)-O(2)	172.3(5)	O(2)-C(2)-C(1)	124.6(13)
Mn(1)-O(6) ^{iv}	2.185(8)	C(22)-C(23)	1.361(9)	O(3) ⁱⁱ -Cr(1)-O(2)	85.7(4)	O(2)-C(2)-C(3)	114.4(13)
Mn(1)-O(5) ⁱⁱⁱ	2.281(9)	C(23)-C(24)	1.428(9)	O(2) ⁱⁱ -Cr(1)-O(2)	92.5(4)	C(2)-O(2)-Cr(1)	114.1(9)
Mn(1)-O(5) ^{iv}	2.281(9)	O(11W)-H(11W)	0.97(2)	O(3)-Cr(1)-O(2) ⁱ	85.7(4)	O(3)-C(3)-C(4)	124.8(18)
Mn(1)-O(5)	2.281(9)	-	-	O(3) ⁱ -Cr(1)-O(2) ⁱ	80.1(5)	O(3)-C(3)-C(2)	115.8(17)
Mn(1)-O(1W)	2.379(17)	-	-	O(3) ⁱⁱ -Cr(1)-O(2) ⁱ	172.3(5)	C(4)-C(3)-C(2)	119.1(16)
O(1W)-H(1W)	0.96(2)	-	-	O(2) ⁱⁱ -Cr(1)-O(2) ⁱ	92.5(4)	C(3)-O(3)-Cr(1)	114.5(13)
C(1)-C(2)	1.367(19)	-	-	O(2)-Cr(1)-O(2) ⁱ	92.5(4)	C(5)-C(4)-Cl(4)	120.2(13)
C(1)-C(6)	1.380(16)	-	-	O(6) ⁱⁱⁱ -Mn(1)-O(6)	112.5(2)	C(3)-C(4)-Cl(4)	119.7(14)
C(1)-Cl(1)	1.739(18)	-	-	O(6) ⁱⁱⁱ -Mn(1)-O(6) ^{iv}	112.5(2)	O(5)-C(5)-C(4)	123.8(14)
C(2)-O(2)	1.260(17)	-	-	O(6)-Mn(1)-O(6) ^{iv}	112.5(2)	O(5)-C(5)-C(6)	117.3(11)
C(2)-C(3)	1.46(2)	-	-	O(6) ⁱⁱⁱ -Mn(1)-O(5) ⁱⁱⁱ	72.2(3)	C(5)-O(5)-Mn(1)	114.9(9)
C(3)-O(3)	1.30(2)	-	-	O(6)-Mn(1)-O(5) ⁱⁱⁱ	79.1(3)	O(6)-C(6)-C(1)	124.4(11)
C(3)-C(4)	1.43(3)	-	-	O(6) ^{iv} -Mn(1)-O(5) ⁱⁱⁱ	162.5(4)	O(6)-C(6)-C(5)	116.1(9)
C(4)-C(5)	1.40(2)	-	-	O(6) ⁱⁱⁱ -Mn(1)-O(5) ^{iv}	79.1(3)	C(6)-O(6)-Mn(1)	118.9(7)
C(4)-Cl(4)	1.80(2)	-	-	O(6)-Mn(1)-O(5) ^{iv}	162.5(4)	C(24)-N(11)-C(12)	118.4(5)
C(5)-O(5)	1.249(14)	-	-	O(6) ^{iv} -Mn(1)-O(5) ^{iv}	72.2(3)	N(11)-C(12)-C(13)	120.1(5)
C(5)-C(6)	1.506(16)	-	-	O(5) ⁱⁱⁱ -Mn(1)-O(5) ^{iv}	92.9(3)	N(11)-C(12)-C(17)	120.6(5)
C(6)-O(6)	1.255(12)	-	-	O(6) ⁱⁱⁱ -Mn(1)-O(5)	162.5(4)	N(18)-C(17)-C(16)	119.1(6)
N(11)-C(24)	1.329(7)	-	-	O(6)-Mn(1)-O(5)	72.2(3)	N(18)-C(17)-C(12)	121.9(6)
N(11)-C(12)	1.332(7)	-	-	O(6) ^{iv} -Mn(1)-O(5)	79.1(3)	C(17)-N(18)-C(19)	117.1(5)
C(12)-C(13)	1.427(9)	-	-	O(5) ⁱⁱⁱ -Mn(1)-O(5)	92.9(3)	N(18)-C(19)-C(20)	120.0(6)
C(12)-C(17)	1.433(8)	-	-	O(5) ^{iv} -Mn(1)-O(5)	92.9(3)	N(18)-C(19)-C(24)	121.4(6)
C(13)-C(14)	1.383(9)	-	-	O(6) ⁱⁱⁱ -Mn(1)-O(1W)	73.8(3)	N(11)-C(24)-C(23)	120.6(5)
C(14)-C(15)	1.400(12)	-	-	O(6)-Mn(1)-O(1W)	73.8(3)	N(11)-C(24)-C(19)	120.6(6)

Symmetry transformations: i) -x+y+1,-x+2,z; ii) -y+2,x-y+1,z; iii) -x+y+1,-x+1,z; iv) -y+1,x-y,z.

[(H₃O)(phz)₃][MnCr(Br₂An)₃]·H₂O·2CH₃COCH₃ (M2)

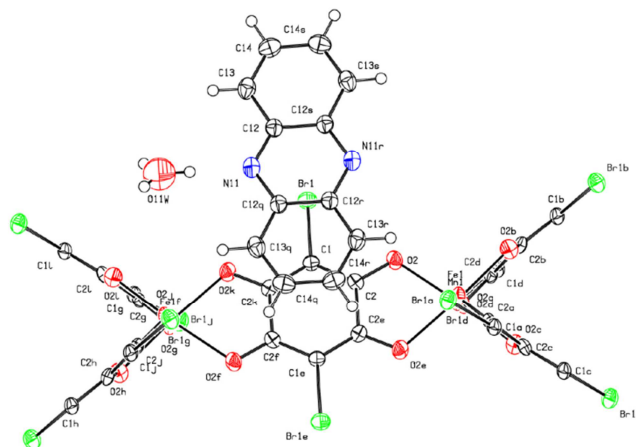


Selected bond lengths (Å) and angles (°).

Bonds	Å	Bonds	Å	Angles	°	Angles	°
Mn(1)-O(2)	2.102(13)	C(12)-O(12) ^{xv}	1.37(9)	O(2)-Mn(1)-O(2) ⁱ	84.1(7)	C(2)-C(1)-O(2) ^x	120.000(4)
Mn(1)-O(2) ⁱ	2.102(13)	-	-	O(2)-Mn(1)-O(2) ⁱⁱ	77.0(7)	C(2) ^{ix} -C(1)-O(2) ^x	60.000(17)
Mn(1)-O(2) ⁱⁱ	2.102(13)	-	-	O(2) ^j -Mn(1)-O(2) ⁱⁱ	99.5(4)	O(2) ^{viii} -C(1)-O(2) ^{ix}	120.000(2)
Mn(1)-O(2) ⁱⁱⁱ	2.102(13)	-	-	O(2)-Mn(1)-O(2) ⁱⁱⁱ	99.5(4)	C(2)-C(1)-O(2) ^{ix}	180.000(12)
Mn(1)-O(2) ^{iv}	2.102(13)	-	-	O(2) ^j -Mn(1)-O(2) ⁱⁱⁱ	77.0(7)	O(2) ^x -C(1)-O(2) ^{ix}	60.000(18)
Mn(1)-O(2) ^v	2.102(13)	-	-	O(2) ⁱⁱ -Mn(1)-O(2) ⁱⁱⁱ	175.4(7)	O(2) ^{viii} -C(1)-C(2) ^x	180(5)
C(1)-Br(1)	1.90(3)	-	-	O(2)-Mn(1)-O(2) ^{iv}	99.5(4)	O(2) ^{ix} -C(1)-C(2) ^x	60.000(17)
C(2)-O(2)	1.219(19)	-	-	O(2) ^j -Mn(1)-O(2) ^{iv}	175.4(7)	O(2) ^x -C(1)-C(2) ^{viii}	180.000(8)
N(11)-C(12) ^{vii}	1.33(2)	-	-	O(2) ⁱⁱ -Mn(1)-O(2) ^{iv}	84.1(7)	O(2) ^{ix} -C(1)-C(2) ^{viii}	120.000(11)
N(11)-C(12)	1.33(2)	-	-	O(2) ⁱⁱⁱ -Mn(1)-O(2) ^{iv}	99.5(4)	O(2) ^{viii} -C(1)-C(2) ^{xi}	60.000(5)
O(11W)-H(11W)	0.850(10)	-	-	O(2)-Mn(1)-O(2) ^v	175.4(7)	O(2) ^x -C(1)-C(2) ^{xi}	120.000(14)
O(1W)-H(1W)	0.860(10)	-	-	O(2) ^j -Mn(1)-O(2) ^v	99.5(4)	O(2) ^{ix} -C(1)-C(2) ^{xi}	60.000(2)
C(1)-O(2) ⁱⁱⁱ	1.36(9)	-	-	O(2) ⁱⁱ -Mn(1)-O(2) ^v	99.5(4)	O(2) ^{viii} -C(1)-O(2) ^{xi}	60.000(5)
C(1)-O(2) ^x	1.36(9)	-	-	O(2) ⁱⁱⁱ -Mn(1)-O(2) ^v	84.1(7)	O(2) ^x -C(1)-O(2) ^{xi}	120.000(14)
C(1)-O(2) ^{ix}	1.36(9)	-	-	O(2) ^{iv} -Mn(1)-O(2) ^v	77.0(7)	O(2) ^{ix} -C(1)-O(2) ^{xi}	60.000(2)
C(1)-O(2) ^{xi}	1.36(9)	-	-	C(2) ^{vi} -C(1)-Br(1)	118.3(11)	O(2) ^{viii} -C(1)-O(2) ^{xii}	120.000(5)
C(1)-O(2) ^{xii}	1.36(9)	-	-	C(2)-C(1)-Br(1)	118.3(11)	O(2) ^x -C(1)-O(2) ^{xii}	60.000(4)
C(2)-O(2) ^{xii}	1.36(9)	-	-	O(2)-C(2)-C(1)	125.8(16)	O(2) ^{ix} -C(1)-O(2) ^{xii}	120.000(12)
C(2)-O(2) ^{viii}	1.36(9)	-	-	O(2)-C(2)-C(2) ⁱⁱ	116.1(9)	O(2) ^{xi} -C(1)-O(2) ^j	180.000(10)
C(11)-O(12) ^{xiii}	1.37(9)	-	-	C(2)-O(2)-Mn(1)	115.3(10)	O(2) ^{viii} -C(1)-C(2) ^{xii}	120.000(5)
C(11)-O(12) ^{xiv}	1.37(9)	-	-	C(12) ^{vii} -N(11)-C(12)	118(2)	O(2) ^x -C(1)-C(2) ^{xii}	60.000(4)
C(11)-O(12) ^x	1.37(9)	-	-	N(11)-C(12)-C(13)	120.8(17)	O(2) ^{ix} -C(1)-C(2) ^{xii}	120.000(12)
C(11)-C(12)	1.37(9)	-	-	N(11)-C(12)-C(12) ^{vi}	120.8(11)	O(2) ^{xi} -C(1)-C(2) ^{xi}	180.000(10)
C(11)-O(12) ^{xi}	1.37(9)	-	-	O(2) ^{viii} -C(1)-C(2)	60.000(2)	O(2) ^{xii} -C(2)-O(2) ^{viii}	120.00(4)
C(11)-O(12) ^{xv}	1.37(9)	-	-	O(2) ^{viii} -C(1)-C(2) ^{ix}	120.000(2)	O(2) ^{xii} -C(2)-C(2) ^{viii}	120.00(4)
C(12)-O(12) ^{xiv}	1.37(9)	-	-	O(2) ^{viii} -C(1)-O(2) ^x	180.0(5)	-	-

Symmetry transformations: i) -y+1,-x+1,-z; ii) -x+y+1,y,-z; iii) -y+1,x-y,z; iv) -x+y+1,-x+1,z; v) x,x-y,-z; vi) x-y,-y,z; vii) -x+y+1,y,-z+1; viii) x-y,x-1,-z+1; ix) -x+2,-y,-z+1; x) 10 -x+y+2,-x+1,z; xi) -y+1,x-y-1,z; xii) y+1,-x+y+1,-z+1; xiii) -x+2,-y,-z; xiv) x-y,x-1,-z; xv) y+1,-x+y+1,-z.

[(H₃O)(phz)₃][MnFe(Br₂An)₃]·H₂O (M3)

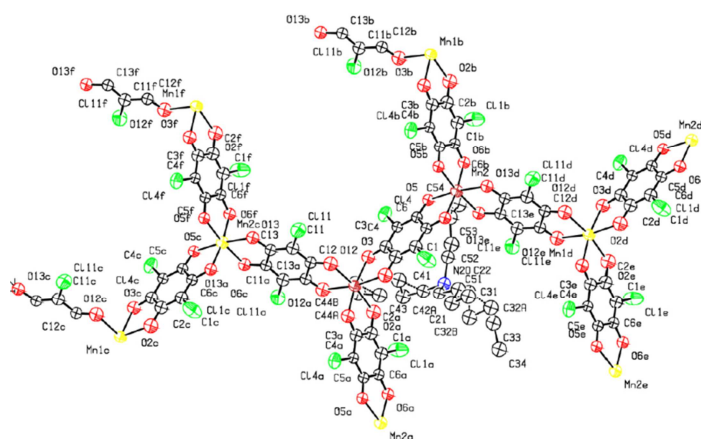


Selected bond lengths (Å) and angles (°).

Bonds	Å	Bonds	Å	Angles	°	Angles	°
Mn(1)-O(2) ⁱ	2.119(4)	C(12)-C(12) ^{vi}	1.437(10)	O(2) ⁱ -Mn(1)-O(2) ⁱⁱ	85.2(2)	O(2) ^{iv} -Mn(1)-O(2) ^v	76.26(19)
Mn(1)-O(2) ⁱⁱ	2.119(4)	C(13)-C(14)	1.365(8)	O(2) ^j -Mn(1)-O(2)	76.26(19)	C(2)-C(1)-C(2) ^{vi}	121.8(6)
Mn(1)-O(2)	2.119(4)	C(14)-C(14) ^{vi}	1.410(14)	O(2) ⁱⁱ -Mn(1)-O(2)	99.39(14)	C(2)-C(1)-Br(1)	119.1(3)
Mn(1)-O(2) ⁱⁱⁱ	2.119(4)	O(11W)-H(11W)	0.8574	O(2) ⁱ -Mn(1)-O(2) ⁱⁱⁱ	99.39(14)	C(2) ^{vi} -C(1)-Br(1)	119.1(3)
Mn(1)-O(2) ^{iv}	2.119(4)	-	-	O(2) ⁱⁱ -Mn(1)-O(2) ⁱⁱⁱ	76.26(19)	O(2)-C(2)-C(1)	126.0(4)
Mn(1)-O(2) ^v	2.119(4)	-	-	O(2)-Mn(1)-O(2) ⁱⁱⁱ	174.20(17)	O(2)-C(2)-C(2) ⁱ	115.2(3)
C(1)-C(2)	1.393(6)	-	-	O(2) ⁱ -Mn(1)-O(2) ^{iv}	99.39(14)	C(1)-C(2)-C(2) ⁱ	118.8(3)
C(1)-C(2) ^{vi}	1.393(6)	-	-	O(2) ⁱⁱ -Mn(1)-O(2) ^{iv}	174.20(18)	C(2)-O(2)-Mn(1)	116.5(3)
C(1)-Br(1)	1.889(7)	-	-	O(2)-Mn(1)-O(2) ^{iv}	85.2(2)	C(12) ^{vii} -N(11)-C(12)	118.0(6)
C(2)-O(2)	1.254(6)	-	-	O(2) ⁱⁱⁱ -Mn(1)-O(2) ^{iv}	99.39(14)	N(11)-C(12)-C(13)	119.5(5)
C(2)-C(2) ⁱ	1.546(9)	-	-	O(2) ⁱ -Mn(1)-O(2) ^v	174.20(18)	N(11)-C(12)-C(12) ^{vi}	121.0(3)
N(11)-C(12) ^{vii}	1.358(6)	-	-	O(2) ⁱⁱ -Mn(1)-O(2) ^v	99.39(14)	C(13)-C(12)-C(12) ^{vi}	119.5(3)
N(11)-C(12)	1.358(6)	-	-	O(2)-Mn(1)-O(2) ^v	99.39(14)	C(14)-C(13)-C(12)	119.0(6)
C(12)-C(13)	1.416(7)	-	-	O(2) ⁱⁱⁱ -Mn(1)-O(2) ^v	85.2(2)	C(13)-C(14)-C(14) ^{vi}	121.4(4)

Symmetry transformations: i) -x+y+1,y,-z+2; ii) -y+1,x-y,z; iii) -y+1,-x+1,-z+2; iv) x,x-y,-z+2; v) -x+y+1,-x+1,z; vi) x-y,-y,z; vii) -x+y+1,y,-z+3.

$[(n\text{-Bu})_4\text{N}][\text{MnCr}(\text{Cl}_2\text{An})_3]$ (M4)

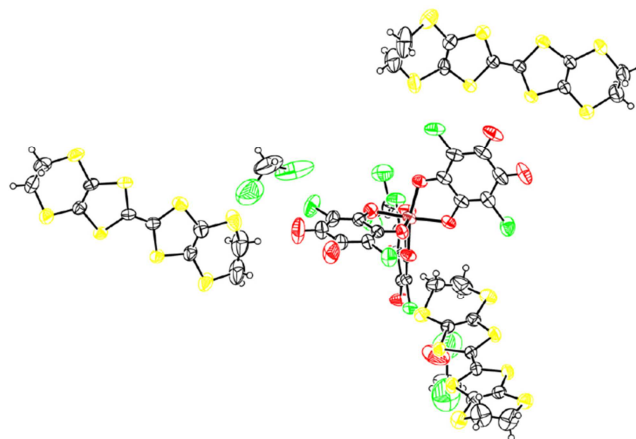


Selected bond lengths (Å) and angles (°).

Bonds	Å	Bonds	Å	Angles	°	Angles	°
Mn(1)-O(3)	2.115(8)	C(12)-C(12) ⁱ	1.54(2)	O(3)-Mn(1)-O(3) ⁱ	169.6(5)	O(5)-Mn(2)-O(13) ^{iv}	172.9(3)
Mn(1)-O(3) ⁱ	2.115(8)	O(13)-C(13)	1.285(13)	O(3)-Mn(1)-O(12)	91.6(3)	O(13) ⁱⁱⁱ -Mn(2)-O(13) ^{iv}	80.3(5)
Mn(1)-O(12)	2.116(9)	O(13)-Cr(2) ^v	2.034(8)	O(3)-Mn(1)-O(12)	96.6(3)	C(6)-C(1)-Cl(1)	123.1(10)
Mn(1)-O(12) ^j	2.116(9)	O(13)-Mn(2) ^v	2.034(8)	O(3)-Mn(1)-O(12) ⁱ	96.6(3)	C(2)-C(1)-Cl(1)	116.6(10)
Mn(1)-O(2) ⁱ	2.140(9)	-	-	O(3) ⁱ -Mn(1)-O(12) ⁱ	91.6(3)	O(2)-C(2)-C(1)	126.7(12)
Mn(1)-O(2)	2.140(9)	-	-	O(12)-Mn(1)-O(12) ⁱ	75.2(5)	O(2)-C(2)-C(3)	114.5(11)
Mn(2)-O(6) ⁱⁱ	1.982(8)	-	-	O(3)-Mn(1)-O(2) ⁱ	96.1(3)	C(2)-O(2)-Mn(1)	116.2(8)
Mn(2)-O(6)	1.982(8)	-	-	O(3) ⁱ -Mn(1)-O(2) ⁱ	76.7(3)	C(3)-O(3)-Mn(1)	115.9(7)
Mn(2)-O(5) ⁱⁱ	2.011(7)	-	-	O(12)-Mn(1)-O(2) ⁱ	168.8(3)	O(3)-C(3)-C(4)	125.6(11)
Mn(2)-O(5)	2.011(7)	-	-	O(12) ^j -Mn(1)-O(2) ⁱ	95.8(3)	O(3)-C(3)-C(2)	116.4(11)
Mn(2)-O(13) ⁱⁱⁱ	2.034(8)	-	-	O(3)-Mn(1)-O(2)	76.7(3)	C(3)-C(4)-Cl(4)	118.3(8)
Mn(2)-O(13) ^{iv}	2.034(8)	-	-	O(3) ⁱ -Mn(1)-O(2)	96.1(3)	C(5)-C(4)-Cl(4)	120.1(8)
Cl(1)-C(1)	1.761(13)	-	-	O(12)-Mn(1)-O(2)	95.8(3)	C(5)-O(5)-Mn(2)	114.1(7)
C(1)-C(6)	1.342(15)	-	-	O(12) ^j -Mn(1)-O(2)	168.8(4)	O(5)-C(5)-C(4)	124.7(10)
C(1)-C(2)	1.384(17)	-	-	O(2) ^j -Mn(1)-O(2)	93.9(5)	O(5)-C(5)-C(6)	116.7(10)
C(2)-O(2)	1.258(14)	-	-	O(6) ⁱⁱ -Mn(2)-O(6)	172.1(4)	C(6)-O(6)-Mn(2)	114.2(7)
C(2)-C(3)	1.558(16)	-	-	O(6) ⁱⁱ -Mn(2)-O(5) ⁱⁱ	80.6(3)	O(6)-C(6)-C(1)	122.5(10)
O(3)-C(3)	1.261(14)	-	-	O(6)-Mn(2)-O(5) ⁱⁱ	93.9(3)	O(6)-C(6)-C(5)	114.4(10)
C(3)-C(4)	1.392(15)	-	-	O(6) ⁱⁱ -Mn(2)-O(5)	93.9(3)	C(13)-C(11)-Cl(11)	120.7(10)
Cl(4)-C(4)	1.728(11)	-	-	O(6)-Mn(2)-O(5)	80.6(3)	C(12)-C(11)-Cl(11)	119.3(9)
C(4)-C(5)	1.374(14)	-	-	O(5) ⁱⁱ -Mn(2)-O(5)	92.2(4)	C(12)-O(12)-Mn(1)	117.2(8)
O(5)-C(5)	1.252(12)	-	-	O(6) ⁱⁱ -Mn(2)-O(13) ⁱⁱⁱ	95.4(3)	O(12)-C(12)-C(11)	125.2(11)
C(5)-C(6)	1.481(14)	-	-	O(6)-Mn(2)-O(13) ⁱⁱⁱ	90.7(3)	O(12)-C(12)-C(12) ^j	115.1(7)
O(6)-C(6)	1.305(12)	-	-	O(5) ⁱⁱ -Mn(2)-O(13) ⁱⁱⁱ	172.9(3)	C(13)-O(13)-Cr(2) ^v	115.1(7)
Cl(11)-C(11)	1.716(12)	-	-	O(5)-Mn(2)-O(13) ⁱⁱⁱ	93.9(3)	C(13)-O(13)-Mn(2) ^v	115.1(7)
C(11)-C(13)	1.353(15)	-	-	O(6) ⁱⁱ -Mn(2)-O(13) ^{iv}	90.7(3)	O(13)-C(13)-C(11)	124.8(11)
C(11)-C(12)	1.387(16)	-	-	O(6)-Mn(2)-O(13) ^{iv}	95.4(3)	O(13)-C(13)-C(13) ⁱ	114.7(6)
O(12)-C(12)	1.218(13)	-	-	O(5) ⁱⁱ -Mn(2)-O(13) ^{iv}	93.9(3)	-	-

Symmetry transformations: i) $-x+3,y,-z+3/2$; ii) $-x+4,y,-z+3/2$; iii) $-x+7/2,y-1/2,-z+3/2$; iv) $x+1/2,y-1/2,z$; v) $x-1/2,y+1/2,z$; vi) $-x+7/2,-y+1/2,-z+1$.

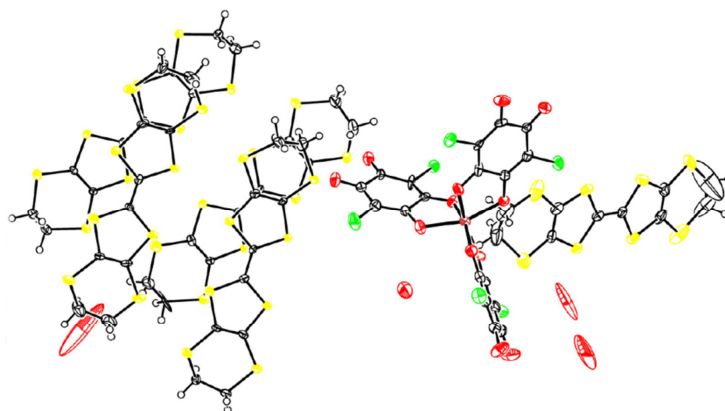
[BEDT-TTF]₃[Fe(Cl₂An)₃]·3CH₂Cl₂·H₂O (H1)



Selected bond lengths (Å) and angles (°).

Bonds	Å	Bonds	Å	Angles	°	Angles	°
C(11)-O(11)	1.307(8)	C(52)-C(62)	1.432(9)	O(11)-C(11)-C(61)	125.4(6)	C(51)-C(61)-Cl(2)	118.9(6)
C(11)-C(61)	1.365(10)	C(53)-O(53)	1.211(7)	O(11)-C(11)-C(21)	113.9(5)	C(12)-C(62)-Cl(4)	120.1(5)
C(11)-C(21)	1.503(8)	C(53)-C(63)	1.419(8)	O(12)-C(12)-C(62)	125.3(6)	C(52)-C(62)-Cl(4)	118.3(5)
C(12)-O(12)	1.295(6)	C(61)-Cl(2)	1.719(7)	O(12)-C(12)-C(22)	113.9(5)	C(13)-C(63)-Cl(6)	118.3(4)
C(12)-C(62)	1.360(9)	C(62)-Cl(4)	1.732(7)	O(13)-C(13)-C(63)	126.3(5)	C(53)-C(63)-Cl(6)	118.6(4)
C(12)-C(22)	1.512(9)	C(63)-Cl(6)	1.742(5)	O(13)-C(13)-C(23)	114.2(5)	O(11)-Fe-O(22)	94.17(19)
C(13)-O(13)	1.281(7)	Fe-O(11)	1.996(5)	O(21)-C(21)-C(11)	114.2(5)	O(11)-Fe-O(21)	79.73(17)
C(13)-C(63)	1.362(8)	Fe-O(22)	1.998(4)	O(22)-C(22)-C(32)	125.0(6)	O(22)-Fe-O(21)	97.09(17)
C(13)-C(23)	1.524(7)	Fe-O(21)	2.002(4)	O(22)-C(22)-C(12)	115.0(5)	O(11)-Fe-O(12)	172.00(18)
C(21)-O(21)	1.295(7)	Fe-O(12)	2.018(4)	O(23)-C(23)-C(33)	125.8(5)	O(22)-Fe-O(12)	79.92(17)
C(21)-C(31)	1.359(8)	Fe-O(13)	2.026(4)	O(23)-C(23)-C(13)	114.6(5)	O(21)-Fe-O(12)	95.56(16)
C(22)-O(22)	1.282(7)	Fe-O(23)	2.037(4)	C(21)-C(31)-Cl(1)	120.2(5)	O(11)-Fe-O(13)	99.58(19)
C(22)-C(32)	1.368(8)	C(3)-Cl(23)	1.666(17)	C(41)-C(31)-Cl(1)	118.0(5)	O(22)-Fe-O(13)	165.13(18)
C(23)-O(23)	1.268(6)	C(3)-Cl(13)	1.73(2)	C(22)-C(32)-Cl(3)	119.8(6)	O(21)-Fe-O(13)	90.97(16)
C(23)-C(33)	1.371(8)	C(2)-Cl(22)	1.737(9)	C(42)-C(32)-Cl(3)	118.4(5)	O(12)-Fe-O(13)	86.89(17)
C(31)-C(41)	1.428(9)	C(2)-Cl(12)	1.747(9)	C(23)-C(33)-Cl(5)	119.2(4)	O(11)-Fe-O(23)	88.54(19)
C(31)-Cl(1)	1.727(6)	C(1)-Cl(11)	1.533(9)	C(43)-C(33)-Cl(5)	118.4(4)	O(22)-Fe-O(23)	96.03(16)
C(32)-C(42)	1.435(10)	C(1)-Cl(21)	1.886(10)	O(41)-C(41)-C(31)	123.7(7)	O(21)-Fe-O(23)	162.97(16)
C(32)-Cl(3)	1.734(7)	-	-	O(41)-C(41)-C(51)	117.8(7)	O(12)-Fe-O(23)	97.39(18)
C(33)-C(43)	1.413(8)	-	-	O(42)-C(42)-C(32)	124.5(8)	O(13)-Fe-O(23)	78.77(15)
C(33)-Cl(5)	1.736(5)	-	-	O(42)-C(42)-C(52)	117.6(7)	C(11)-O(11)-Fe	115.9(4)
C(41)-O(41)	1.216(9)	-	-	O(43)-C(43)-C(33)	124.5(6)	C(12)-O(12)-Fe	115.3(4)
C(41)-C(51)	1.539(11)	-	-	O(43)-C(43)-C(53)	117.5(5)	C(13)-O(13)-Fe	116.2(3)
C(42)-O(42)	1.218(7)	-	-	O(51)-C(51)-C(61)	123.7(8)	C(21)-O(21)-Fe	116.1(3)
C(42)-C(52)	1.548(11)	-	-	O(51)-C(51)-C(41)	118.7(8)	C(22)-O(22)-Fe	115.7(4)
C(43)-O(43)	1.229(7)	-	-	O(52)-C(52)-C(62)	123.8(8)	C(23)-O(23)-Fe	115.9(3)
C(43)-C(53)	1.567(8)	-	-	O(52)-C(52)-C(42)	118.2(6)	Cl(23)-C(3)-Cl(13)	108.6(9)
C(51)-O(51)	1.214(9)	-	-	O(53)-C(53)-C(63)	125.5(6)	Cl(22)-C(2)-Cl(12)	112.1(4)
C(51)-C(61)	1.441(12)	-	-	O(53)-C(53)-C(43)	117.4(6)	Cl(11)-C(1)-Cl(21)	109.0(5)
C(52)-O(52)	1.227(8)	-	-	C(11)-C(61)-Cl(2)	119.7(6)	-	-

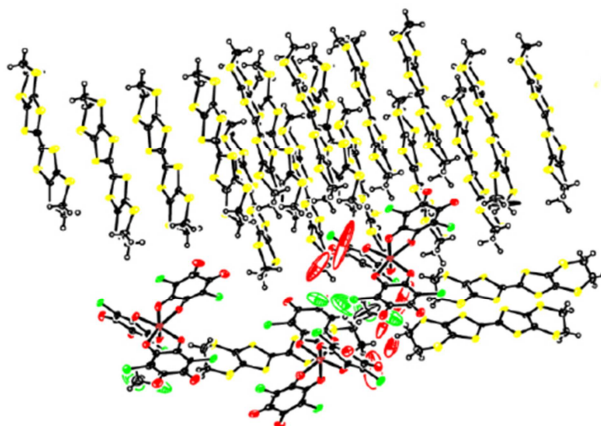
δ [BEDT-TTF]₅[Fe(Cl₂An)₃]₄·4H₂O (H2)



Selected bond lengths (Å) and angles (°).

Bonds	Å	Bonds	Å	Angles	°	Angles	°
C(11)-O(11)	1.295(9)	C(52)-O(52)	1.224(10)	O(11)-C(11)-C(61)	125.1(7)	O(53)-C(53)-C(43)	116.8(8)
C(11)-C(61)	1.370(11)	C(52)-C(62)	1.422(12)	O(11)-C(11)-C(21)	114.9(7)	C(11)-C(61)-Cl(2)	120.1(6)
C(11)-C(21)	1.493(10)	C(53)-O(53)	1.221(10)	O(12)-C(12)-C(62)	126.5(7)	C(51)-C(61)-Cl(2)	117.9(6)
C(12)-O(12)	1.287(9)	C(53)-C(63)	1.427(12)	O(12)-C(12)-C(22)	114.2(7)	C(12)-C(62)-Cl(4)	119.2(7)
C(12)-C(62)	1.351(11)	C(61)-Cl(2)	1.739(8)	O(13)-C(13)-C(63)	125.8(8)	C(52)-C(62)-Cl(4)	117.8(7)
C(12)-C(22)	1.530(11)	C(62)-Cl(4)	1.738(9)	O(13)-C(13)-C(23)	113.4(7)	C(13)-C(63)-Cl(6)	119.3(7)
C(13)-O(13)	1.302(10)	C(63)-Cl(6)	1.725(8)	O(21)-C(21)-C(31)	124.7(7)	C(53)-C(63)-Cl(6)	118.5(6)
C(13)-C(63)	1.369(11)	Fe-O(22)	1.999(6)	O(21)-C(21)-C(11)	114.9(7)	O(22)-Fe-O(11)	103.3(2)
C(13)-C(23)	1.534(11)	Fe-O(11)	2.008(6)	O(22)-C(22)-C(32)	125.1(7)	O(22)-Fe-O(23)	165.4(2)
C(21)-O(21)	1.299(9)	Fe-O(23)	2.014(6)	O(22)-C(22)-C(12)	114.5(7)	O(11)-Fe-O(23)	88.0(2)
C(21)-C(31)	1.362(11)	Fe-O(12)	2.019(5)	O(23)-C(23)-C(33)	128.3(8)	O(22)-Fe-O(12)	80.4(2)
C(22)-O(22)	1.291(9)	Fe-O(21)	2.022(6)	O(23)-C(23)-C(13)	114.2(7)	O(11)-Fe-O(12)	94.9(2)
C(22)-C(32)	1.352(11)	Fe-O(13)	2.039(6)	C(21)-C(31)-Cl(1)	120.0(6)	O(23)-Fe-O(12)	89.7(2)
C(23)-O(23)	1.282(10)	-	-	C(41)-C(31)-Cl(1)	117.6(6)	O(22)-Fe-O(21)	91.0(2)
C(23)-C(33)	1.319(12)	-	-	C(22)-C(32)-Cl(3)	118.9(6)	O(11)-Fe-O(21)	79.8(2)
C(31)-C(41)	1.421(11)	-	-	C(42)-C(32)-Cl(3)	118.5(6)	O(23)-Fe-O(21)	100.1(2)
C(31)-Cl(1)	1.751(8)	-	-	C(23)-C(33)-Cl(5)	117.7(6)	O(12)-Fe-O(21)	168.6(2)
C(32)-C(42)	1.423(12)	-	-	C(43)-C(33)-Cl(5)	115.8(6)	O(22)-Fe-O(13)	92.5(2)
C(32)-Cl(3)	1.735(8)	-	-	O(41)-C(41)-C(31)	125.6(8)	O(11)-Fe-O(13)	158.6(2)
C(33)-C(43)	1.427(10)	-	-	O(41)-C(41)-C(51)	117.1(7)	O(23)-Fe-O(13)	79.1(2)
C(33)-Cl(5)	1.788(8)	-	-	O(42)-C(42)-C(32)	125.7(8)	O(12)-Fe-O(13)	102.0(2)
C(41)-O(41)	1.219(9)	-	-	O(42)-C(42)-C(52)	117.3(8)	O(21)-Fe-O(13)	85.6(2)
C(41)-C(51)	1.557(11)	-	-	O(43)-C(43)-C(33)	125.7(7)	C(11)-O(11)-Fe	114.9(5)
C(42)-O(42)	1.221(10)	-	-	O(43)-C(43)-C(53)	118.2(7)	C(12)-O(12)-Fe	115.3(5)
C(42)-C(52)	1.567(12)	-	-	O(51)-C(51)-C(61)	124.3(7)	C(13)-O(13)-Fe	114.6(5)
C(43)-O(43)	1.237(9)	-	-	O(51)-C(51)-C(41)	118.4(7)	C(21)-O(21)-Fe	114.5(5)
C(43)-C(53)	1.573(11)	-	-	O(52)-C(52)-C(62)	124.7(9)	C(22)-O(22)-Fe	115.6(5)
C(51)-O(51)	1.227(9)	-	-	O(52)-C(52)-C(42)	117.7(8)	C(23)-O(23)-Fe	116.3(5)
C(51)-C(61)	1.428(10)	-	-	O(53)-C(53)-C(63)	126.4(8)	-	-

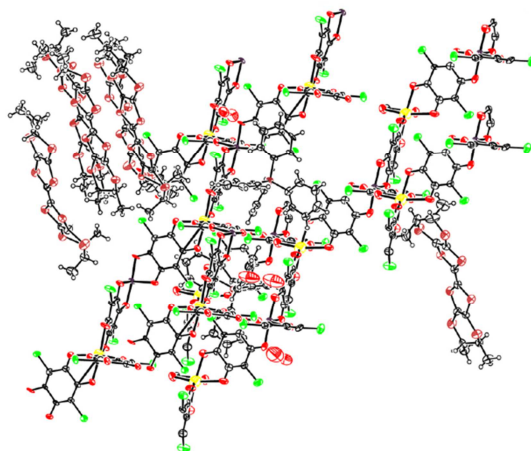
α'' -[BEDT-TTF]₁₈[Fe(Cl₂An)₃]₃·3CH₂Cl₂·6H₂O (H3)



Selected bond lengths (Å) and angles (°).

Bonds	Å	Bonds	Å	Angles	°	Angles	°
C(11A)-O(11A)	1.286(9)	C(43A)-O(43A)	1.229(9)	C(13C)-C(18C)-Cl(6C)	120.1(7)	O(11A)-Fe(1A)-O(21A)	79.3(3)
C(11B)-O(11B)	1.294(9)	C(43B)-O(61B)	1.220(9)	C(22C)-C(23C)-Cl(3C)	120.9(7)	O(23A)-Fe(1A)-O(22A)	95.1(3)
C(11C)-O(11C)	1.277(8)	C(51A)-O(51A)	1.239(10)	C(24C)-C(23C)-Cl(3C)	118.6(7)	O(12A)-Fe(1A)-O(22A)	79.2(3)
C(12A)-O(12A)	1.283(10)	C(51B)-O(51B)	1.238(9)	C(12C)-C(26C)-Cl(4C)	119.6(7)	O(13A)-Fe(1A)-O(22A)	97.3(3)
C(12C)-O(12C)	1.296(10)	C(51C)-O(51C)	1.236(9)	C(25C)-C(26C)-Cl(4C)	118.4(7)	O(11A)-Fe(1A)-O(22A)	90.6(3)
C(13A)-O(13A)	1.263(9)	C(52A)-O(52A)	1.235(10)	C(21A)-C(31A)-Cl(1A)	119.0(7)	O(21A)-Fe(1A)-O(22A)	161.0(3)
C(13B)-O(13B)	1.280(9)	C(52B)-O(52B)	1.230(9)	C(41A)-C(31A)-Cl(1A)	118.2(8)	O(23B)-Fe(1B)-O(21B)	104.5(3)
C(13C)-O(13C)	1.276(8)	C(53A)-O(53A)	1.208(9)	C(21B)-C(31B)-Cl(1B)	119.2(7)	O(23B)-Fe(1B)-O(12B)	159.2(3)
C(14C)-O(14C)	1.287(9)	C(53B)-O(71B)	1.223(9)	C(41B)-C(31B)-Cl(1B)	118.4(8)	O(21B)-Fe(1B)-O(12B)	88.4(3)
C(15C)-Cl(5C)	1.722(8)	C(61A)-Cl(2A)	1.729(9)	C(21C)-C(31C)-Cl(1C)	119.5(8)	O(23B)-Fe(1B)-O(13B)	78.6(3)
C(16C)-O(16C)	1.238(8)	C(61B)-Cl(2B)	1.729(9)	C(41C)-C(31C)-Cl(1C)	118.0(7)	O(21B)-Fe(1B)-O(13B)	96.1(3)
C(17C)-O(17C)	1.228(10)	C(61C)-Cl(2C)	1.735(8)	C(22A)-C(32A)-Cl(3A)	119.3(7)	O(12B)-Fe(1B)-O(13B)	84.0(3)
C(18C)-Cl(6C)	1.722(9)	C(62A)-Cl(4A)	1.730(9)	C(42A)-C(32A)-Cl(3A)	119.3(7)	O(23B)-Fe(1B)-O(11B)	91.5(3)
C(21A)-O(21A)	1.284(8)	C(62B)-Cl(4B)	1.737(8)	C(22B)-C(32B)-Cl(3B)	120.7(6)	O(21B)-Fe(1B)-O(11B)	79.7(2)
C(21B)-O(21B)	1.284(9)	C(63A)-Cl(6A)	1.734(9)	C(42B)-C(32B)-Cl(3B)	118.9(6)	O(12B)-Fe(1B)-O(11B)	107.1(3)
C(21C)-O(21C)	1.290(8)	C(63B)-Cl(6B)	1.749(9)	C(23A)-C(33A)-Cl(5A)	119.6(7)	O(13B)-Fe(1B)-O(11B)	167.9(3)
C(22A)-O(22A)	1.273(9)	O(11A)-Fe(1A)	2.020(6)	C(43A)-C(33A)-Cl(5A)	119.3(7)	O(23B)-Fe(1B)-O(22B)	92.4(3)
C(22C)-O(22C)	1.279(9)	O(11B)-Fe(1B)	2.020(6)	C(23B)-C(33B)-Cl(5B)	120.6(7)	O(21B)-Fe(1B)-O(22B)	159.7(3)
C(23A)-O(23A)	1.289(8)	O(11C)-Fe(1C)	2.012(6)	C(11A)-C(61A)-Cl(2A)	119.1(8)	O(12B)-Fe(1B)-O(22B)	78.9(2)
C(23B)-O(23B)	1.294(8)	O(12A)-Fe(1A)	1.994(7)	C(11C)-C(61C)-Cl(2C)	119.4(7)	O(13B)-Fe(1B)-O(22B)	98.2(3)
C(23C)-Cl(3C)	1.725(8)	O(12C)-Fe(1C)	1.984(7)	C(51C)-C(61C)-Cl(2C)	119.2(7)	O(11B)-Fe(1B)-O(22B)	88.9(2)
C(24C)-O(24C)	1.222(10)	O(13A)-Fe(1A)	2.018(6)	C(12B)-C(62B)-Cl(4B)	119.5(6)	O(21C)-Fe(1C)-O(12C)	159.7(3)
C(25C)-O(25C)	1.240(9)	O(13B)-Fe(1B)	2.011(6)	C(52B)-C(62B)-Cl(4B)	118.4(7)	O(21C)-Fe(1C)-O(13C)	103.7(3)
C(26C)-Cl(4C)	1.737(8)	O(13C)-Fe(1C)	2.007(6)	C(13A)-C(63A)-Cl(6A)	119.8(7)	O(12C)-Fe(1C)-O(13C)	88.7(3)
C(31A)-Cl(1A)	1.755(10)	O(14C)-Fe(1C)	2.010(6)	C(53A)-C(63A)-Cl(6A)	117.7(7)	O(21C)-Fe(1C)-O(14C)	93.1(3)
C(31B)-Cl(1B)	1.741(10)	O(21A)-Fe(1A)	2.024(7)	C(13B)-C(63B)-Cl(6B)	120.2(7)	O(12C)-Fe(1C)-O(14C)	105.2(3)
C(31C)-Cl(1C)	1.726(10)	O(21B)-Fe(1B)	2.006(6)	C(53B)-C(63B)-Cl(6B)	117.7(6)	O(13C)-Fe(1C)-O(14C)	79.5(2)
C(32A)-Cl(3A)	1.720(9)	O(21C)-Fe(1C)	1.981(7)	O(23A)-Fe(1A)-O(12A)	160.6(3)	O(21C)-Fe(1C)-O(11C)	79.6(3)
C(32B)-Cl(3B)	1.725(9)	O(22A)-Fe(1A)	2.028(6)	O(23A)-Fe(1A)-O(13A)	78.8(3)	O(12C)-Fe(1C)-O(11C)	83.0(3)
C(33A)-Cl(5A)	1.734(9)	O(22C)-Fe(1C)	2.032(6)	O(12A)-Fe(1A)-O(13A)	83.5(3)	O(13C)-Fe(1C)-O(11C)	96.7(3)
C(33B)-Cl(5B)	1.725(10)	O(23A)-Fe(1A)	1.989(7)	O(23A)-Fe(1A)-O(11A)	91.9(3)	O(14C)-Fe(1C)-O(11C)	170.8(3)
C(41A)-O(41A)	1.256(11)	O(23B)-Fe(1B)	1.994(6)	O(12A)-Fe(1A)-O(11A)	106.5(3)	O(21C)-Fe(1C)-O(22C)	92.5(3)
C(41B)-O(41B)	1.241(10)	O(12B)-C(12B)	1.291(11)	O(13A)-Fe(1A)-O(11A)	168.3(3)	O(12C)-Fe(1C)-O(22C)	79.1(3)
C(41C)-O(41C)	1.224(10)	O(12B)-Fe(1B)	2.009(6)	O(23A)-Fe(1A)-O(21A)	101.3(3)	O(13C)-Fe(1C)-O(22C)	160.6(3)
C(42A)-O(42A)	1.197(9)	O(22B)-C(22B)	1.285(11)	O(12A)-Fe(1A)-O(21A)	88.1(3)	O(14C)-Fe(1C)-O(22C)	89.2(2)
C(42B)-O(42B)	1.220(8)	O(22B)-Fe(1B)	2.028(6)	O(13A)-Fe(1A)-O(21A)	95.3(3)	O(11C)-Fe(1C)-O(22C)	96.6(3)

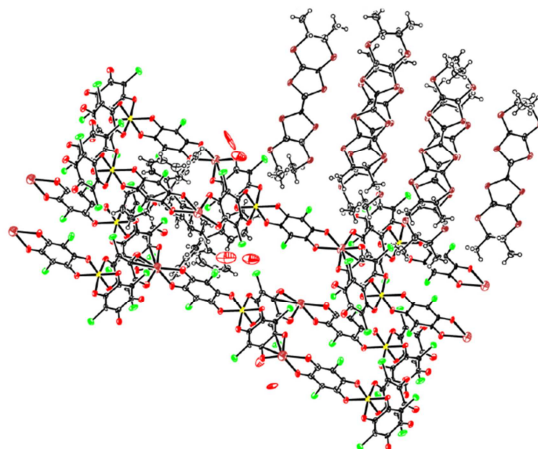
β -[(S,S,S)-TM-BEDT-TTF]₃[P(Ph)₄]₄[K⁺Fe^{III}(Cl₂An)₃]₃·3H₂O (H4)



Selected bond lengths (Å) and angles (°).

Bonds	Å	Bonds	Å	Angles	°	Angles	°
K(1A)-O(131)	2.311(11)	C(311)-Cl(1A)	1.748(14)	O(131)-K(1A)-O(231)	70.0(3)	O(412)-K(1B)-O(422)	83.6(3)
K(1A)-O(231)	2.355(10)	C(312)-Cl(1B)	1.733(13)	O(131)-K(1A)-O(511)	94.8(4)	O(432)-K(1B)-O(422)	155.2(3)
K(1A)-O(511)	2.361(11)	C(322)-Cl(3B)	1.742(14)	O(231)-K(1A)-O(511)	122.3(4)	C(112)-C(612)-Cl(2B)	120.6(9)
K(1A)-O(221)	2.367(10)	C(331)-Cl(6A)	1.721(13)	O(131)-K(1A)-O(221)	160.6(4)	C(512)-C(612)-Cl(2B)	119.7(9)
K(1A)-O(121)	2.366(11)	C(332)-Cl(5B)	1.712(13)	O(231)-K(1A)-O(221)	92.2(3)	C(121)-C(621)-Cl(4A)	122.1(11)
K(1A)-O(411)	2.372(10)	C(411)-O(411)	1.254(15)	O(511)-K(1A)-O(221)	101.5(4)	C(521)-C(621)-Cl(4A)	115.4(10)
K(1B)-O(522)	2.259(8)	C(412)-O(412)	1.250(16)	O(131)-K(1A)-O(121)	99.8(4)	C(122)-C(622)-Cl(4B)	117.7(8)
K(1B)-O(532)	2.347(9)	C(422)-O(422)	1.232(15)	O(231)-K(1A)-O(121)	82.8(4)	C(522)-C(622)-Cl(4B)	115.7(8)
K(1B)-O(512)	2.364(9)	C(432)-O(432)	1.260(14)	O(511)-K(1A)-O(121)	154.2(4)	C(131)-C(631)-Cl(5A)	118.2(12)
K(1B)-O(412)	2.382(10)	C(511)-O(511)	1.201(16)	O(221)-K(1A)-O(121)	69.3(3)	C(532)-C(632)-Cl(6B)	121.8(10)
K(1B)-O(432)	2.394(9)	C(512)-O(512)	1.225(15)	O(131)-K(1A)-O(411)	102.6(4)	C(132)-C(632)-Cl(6B)	118.9(9)
K(1B)-O(422)	2.408(9)	C(522)-O(522)	1.274(14)	O(231)-K(1A)-O(411)	166.0(4)	O(431)-Fe(1A)-O(421)	98.0(4)
O(421)-Fe(1A)	2.019(9)	C(532)-O(532)	1.248(16)	O(511)-K(1A)-O(411)	69.2(3)	O(431)-Fe(1A)-O(111)	96.2(4)
O(431)-Fe(1A)	2.011(9)	C(611)-Cl(2A)	1.760(13)	O(221)-K(1A)-O(411)	93.1(4)	O(421)-Fe(1A)-O(111)	89.6(4)
O(521)-Fe(1A)	2.044(10)	C(612)-Cl(2B)	1.729(12)	O(121)-K(1A)-O(411)	86.9(4)	O(431)-Fe(1A)-O(521)	168.1(4)
O(531)-Fe(1A)	2.045(9)	C(621)-Cl(4A)	1.742(15)	O(522)-K(1B)-O(532)	91.3(3)	O(421)-Fe(1A)-O(521)	80.1(3)
C(111)-O(111)	1.268(16)	C(622)-Cl(4B)	1.793(11)	O(522)-K(1B)-O(512)	162.5(4)	O(111)-Fe(1A)-O(521)	95.5(4)
C(112)-O(112)	1.311(13)	C(631)-Cl(5A)	1.754(16)	O(532)-K(1B)-O(512)	102.8(3)	O(431)-Fe(1A)-O(531)	79.8(4)
C(121)-O(121)	1.242(16)	C(632)-Cl(6B)	1.716(12)	O(522)-K(1B)-O(412)	95.7(3)	O(421)-Fe(1A)-O(531)	92.6(4)
C(122)-O(122)	1.277(12)	Fe(1A)-O(111)	2.031(10)	O(532)-K(1B)-O(412)	166.1(4)	O(111)-Fe(1A)-O(531)	175.7(4)
C(131)-O(131)	1.246(18)	Fe(1A)-O(211)	2.053(9)	O(512)-K(1B)-O(412)	68.4(3)	O(521)-Fe(1A)-O(531)	88.5(4)
C(132)-O(132)	1.320(13)	Fe(1B)-O(212)	2.002(8)	O(522)-K(1B)-O(432)	99.9(3)	O(431)-Fe(1A)-O(211)	90.4(4)
C(211)-O(211)	1.238(17)	Fe(1B)-O(112)	2.025(8)	O(532)-K(1B)-O(432)	69.3(3)	O(421)-Fe(1A)-O(211)	167.7(3)
C(212)-O(212)	1.247(13)	-	-	O(512)-K(1B)-O(432)	94.8(3)	O(111)-Fe(1A)-O(211)	80.5(4)
C(221)-O(221)	1.179(15)	-	-	O(412)-K(1B)-O(432)	120.9(4)	O(521)-Fe(1A)-O(211)	93.5(3)
C(222)-O(222)	1.323(13)	-	-	O(522)-K(1B)-O(422)	71.4(3)	O(531)-Fe(1A)-O(211)	97.7(4)
C(231)-O(231)	1.210(16)	-	-	O(532)-K(1B)-O(422)	87.3(3)	O(212)-Fe(1B)-O(112)	79.1(3)
C(232)-O(232)	1.342(15)	-	-	O(512)-K(1B)-O(422)	98.6(4)	-	-

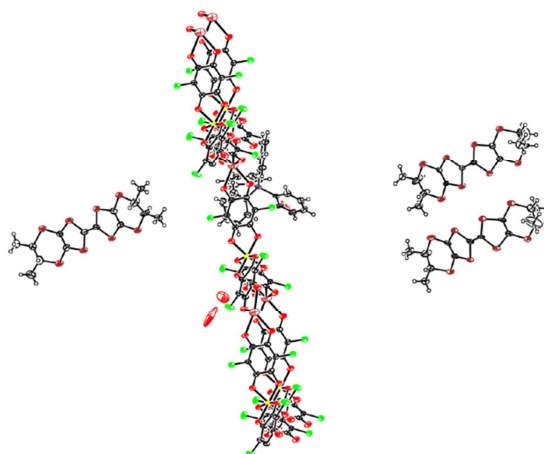
β -[(*R,R,R,R*)-TM-BEDT-TTF]₃[P(Ph)₄]₄[K^IFe^{III}(Cl₂An)₃·3H₂O (H5)



Selected bond lengths (Å) and angles (°).

Bonds	Å	Bonds	Å	Angles	°	Angles	°
C(111)-O(111)	1.310(10)	C(632)-Cl(6B)	1.727(7)	C(211)-C(311)-Cl(1A)	119.6(6)	O(122)-Fe(1B)-O(212)	92.9(2)
C(112)-O(112)	1.284(8)	Fe(1A)-O(231)	2.002(5)	C(212)-C(312)-Cl(1B)	120.2(6)	O(232)-Fe(1B)-O(212)	174.3(2)
C(121)-O(121)	1.281(10)	Fe(1A)-O(211)	2.005(5)	C(221)-C(321)-Cl(3A)	120.2(6)	O(112)-Fe(1B)-O(212)	79.4(2)
C(122)-O(122)	1.288(9)	Fe(1A)-O(111)	2.016(6)	C(222)-C(322)-Cl(3B)	119.4(6)	O(132)-Fe(1B)-O(212)	97.5(2)
C(131)-O(131)	1.257(10)	Fe(1A)-O(121)	2.016(6)	C(231)-C(331)-Cl(5A)	118.0(6)	O(222)-Fe(1B)-O(212)	88.8(2)
C(132)-O(132)	1.298(8)	Fe(1A)-O(221)	2.018(5)	C(232)-C(332)-Cl(5B)	121.8(6)	O(421)-K(1A)-O(511)	61.7(2)
C(211)-O(211)	1.286(9)	Fe(1A)-O(131)	2.030(5)	C(111)-C(611)-Cl(2A)	119.6(7)	O(421)-K(1A)-O(411)	93.5(2)
C(212)-O(212)	1.277(9)	Fe(1B)-O(122)	1.988(5)	C(112)-C(612)-Cl(2B)	120.9(5)	O(511)-K(1A)-O(411)	69.7(2)
C(221)-O(221)	1.292(10)	Fe(1B)-O(232)	2.000(5)	C(121)-C(621)-Cl(4A)	119.9(6)	O(421)-K(1A)-O(521)	70.4(2)
C(222)-O(222)	1.296(9)	Fe(1B)-O(112)	2.007(6)	C(122)-C(622)-Cl(4B)	119.1(6)	O(511)-K(1A)-O(521)	99.5(2)
C(231)-O(231)	1.261(9)	Fe(1B)-O(132)	2.026(5)	C(131)-C(631)-Cl(6A)	119.3(6)	O(411)-K(1A)-O(521)	83.7(2)
C(232)-O(232)	1.315(8)	Fe(1B)-O(222)	2.030(6)	C(132)-C(632)-Cl(6B)	121.2(5)	O(421)-K(1A)-O(431)	102.2(2)
C(311)-Cl(1A)	1.726(8)	Fe(1B)-O(212)	2.045(5)	O(231)-Fe(1A)-O(211)	96.1(2)	O(511)-K(1A)-O(431)	93.3(2)
C(312)-Cl(1B)	1.730(8)	K(1A)-O(431)	2.372(6)	O(211)-Fe(1A)-O(111)	79.6(2)	O(411)-K(1A)-O(431)	121.9(2)
C(321)-Cl(3A)	1.704(7)	K(1A)-O(531)	2.375(7)	O(231)-Fe(1A)-O(121)	95.6(2)	O(521)-K(1A)-O(431)	154.2(2)
C(322)-Cl(3B)	1.724(7)	K(1B)-O(532)	2.339(6)	O(111)-Fe(1A)-O(121)	88.6(2)	O(421)-K(1A)-O(531)	93.8(2)
C(331)-Cl(5A)	1.729(8)	K(1B)-O(432)	2.366(6)	O(231)-Fe(1A)-O(221)	89.7(2)	O(511)-K(1A)-O(531)	101.0(2)
C(332)-Cl(5B)	1.722(7)	-	-	O(211)-Fe(1A)-O(221)	98.3(2)	O(411)-K(1A)-O(531)	165.6(3)
C(411)-O(411)	1.212(10)	-	-	O(111)-Fe(1A)-O(221)	92.6(2)	O(521)-K(1A)-O(531)	87.2(2)
C(412)-O(412)	1.228(9)	-	-	O(121)-Fe(1A)-O(221)	80.5(2)	O(431)-K(1A)-O(531)	68.3(2)
C(421)-O(421)	1.206(9)	-	-	O(231)-Fe(1A)-O(131)	80.2(2)	O(522)-K(1B)-O(532)	90.4(2)
C(422)-O(422)	1.208(10)	-	-	O(211)-Fe(1A)-O(131)	90.6(2)	O(522)-K(1B)-O(412)	61.9(2)
C(431)-O(431)	1.226(9)	-	-	O(111)-Fe(1A)-O(131)	98.1(2)	O(532)-K(1B)-O(412)	103.9(2)
C(432)-O(432)	1.243(9)	-	-	O(121)-Fe(1A)-O(131)	92.6(2)	O(522)-K(1B)-O(432)	100.0(2)
C(511)-O(511)	1.236(10)	-	-	O(221)-Fe(1A)-O(131)	167.2(2)	O(532)-K(1B)-O(432)	69.7(2)
C(512)-O(512)	1.245(9)	-	-	O(122)-Fe(1B)-O(232)	90.5(2)	O(412)-K(1B)-O(432)	95.5(2)
C(521)-O(521)	1.248(10)	-	-	O(122)-Fe(1B)-O(112)	97.6(2)	O(522)-K(1B)-O(512)	94.8(2)
C(522)-O(522)	1.235(9)	-	-	O(232)-Fe(1B)-O(112)	95.6(2)	O(532)-K(1B)-O(512)	166.4(2)
C(531)-O(531)	1.213(10)	-	-	O(122)-Fe(1B)-O(132)	167.5(2)	O(412)-K(1B)-O(512)	68.9(2)
C(532)-O(532)	1.267(9)	-	-	O(232)-Fe(1B)-O(132)	79.8(2)	O(432)-K(1B)-O(512)	121.4(2)
C(611)-Cl(2A)	1.756(8)	-	-	O(112)-Fe(1B)-O(132)	91.2(2)	O(522)-K(1B)-O(422)	69.9(2)
C(612)-Cl(2B)	1.737(8)	-	-	O(122)-Fe(1B)-O(222)	81.1(2)	O(532)-K(1B)-O(422)	86.8(2)
C(621)-Cl(4A)	1.763(8)	-	-	O(232)-Fe(1B)-O(222)	96.2(2)	O(412)-K(1B)-O(422)	99.3(2)
C(622)-Cl(4B)	1.764(8)	-	-	O(112)-Fe(1B)-O(222)	168.1(2)	O(432)-K(1B)-O(422)	154.7(2)
C(631)-Cl(6A)	1.738(8)	-	-	O(132)-Fe(1B)-O(222)	92.1(2)	O(512)-K(1B)-O(422)	83.2(2)

β -[(*rac*)-TM-BEDT-TTF]₃[P(Ph)₄][K^{III}(Cl₂An)₃] \cdot 3H₂O (H6)



Selected bond lengths (Å) and angles (°).

Bonds	Å	Bonds	Å	Angles	°	Angles	°
C(11)-O(11)	1.304(10)	Fe(1)-O(12)	2.017(6)	C(11)-C(61)-Cl(61)	120.5(7)	O(42) ⁱⁱⁱ -K(1)-O(43)	161.2(3)
C(12)-O(12)	1.291(10)	Fe(1)-O(21)	2.020(6)	C(51)-C(61)-Cl(61)	118.7(7)	O(42) ⁱⁱⁱ -K(1)-O(41)	92.6(2)
C(13)-O(13)	1.289(10)	Fe(1)-O(23)	2.041(6)	C(12)-C(62)-Cl(62)	120.2(7)	O(43)-K(1)-O(41)	102.7(2)
C(21)-O(21)	1.286(10)	K(1)-O(42) ⁱⁱⁱ	2.303(7)	C(52)-C(62)-Cl(62)	116.6(7)	O(42) ⁱⁱⁱ -K(1)-O(51)	100.6(3)
C(22)-O(22)	1.283(10)	K(1)-O(43)	2.332(7)	C(13)-C(63)-Cl(63)	120.7(7)	O(43)-K(1)-O(51)	94.9(3)
C(23)-O(23)	1.288(10)	K(1)-O(41)	2.338(7)	C(53)-C(63)-Cl(63)	117.4(7)	O(41)-K(1)-O(51)	69.5(2)
C(31)-Cl(31)	1.738(9)	K(1)-O(51)	2.357(7)	O(22)-Fe(1)-O(13)	99.0(2)	O(42) ⁱⁱⁱ -K(1)-O(53) ^{iv}	93.5(2)
C(32)-Cl(32)	1.735(8)	K(1)-O(53) ^{iv}	2.378(7)	O(22)-Fe(1)-O(11)	90.4(2)	O(43)-K(1)-O(53) ^{iv}	69.2(2)
C(33)-Cl(33)	1.748(8)	K(1)-O(52) ⁱⁱⁱ	2.392(8)	O(13)-Fe(1)-O(11)	95.6(2)	O(41)-K(1)-O(53) ^{iv}	165.9(3)
C(41)-O(41)	1.252(10)	-	-	O(22)-Fe(1)-O(12)	80.2(2)	O(51)-K(1)-O(53) ^{iv}	121.6(3)
C(42)-O(42)	1.217(11)	-	-	O(13)-Fe(1)-O(12)	167.8(2)	O(42) ⁱⁱⁱ -K(1)-O(52) ⁱⁱⁱ	70.5(2)
C(51)-O(51)	1.251(10)	-	-	O(11)-Fe(1)-O(12)	96.6(3)	O(43)-K(1)-O(52) ⁱⁱⁱ	99.3(3)
C(52)-O(52)	1.231(11)	-	-	O(22)-Fe(1)-O(21)	166.9(2)	O(41)-K(1)-O(52) ⁱⁱⁱ	87.2(2)
C(53)-O(53)	1.219(10)	-	-	O(13)-Fe(1)-O(21)	90.4(2)	O(51)-K(1)-O(52) ⁱⁱⁱ	154.9(3)
C(53)-C(63)	1.435(13)	-	-	O(11)-Fe(1)-O(21)	79.7(2)	O(53) ^{iv} -K(1)-O(52) ⁱⁱⁱ	82.9(3)
C(61)-Cl(61)	1.736(9)	-	-	O(12)-Fe(1)-O(21)	92.5(2)	C(11)-O(11)-Fe(1)	115.7(6)
C(62)-Cl(62)	1.751(9)	-	-	O(22)-Fe(1)-O(23)	92.1(2)	C(12)-O(12)-Fe(1)	115.4(5)
C(63)-Cl(63)	1.739(9)	-	-	O(13)-Fe(1)-O(23)	79.5(2)	C(13)-O(13)-Fe(1)	116.1(5)
Fe(1)-O(22)	1.999(6)	-	-	O(11)-Fe(1)-O(23)	174.9(3)	C(21)-O(21)-Fe(1)	115.3(6)
Fe(1)-O(13)	2.010(6)	-	-	O(12)-Fe(1)-O(23)	88.3(2)	C(22)-O(22)-Fe(1)	115.7(5)
Fe(1)-O(11)	2.009(6)	-	-	O(21)-Fe(1)-O(23)	98.5(2)	C(23)-O(23)-Fe(1)	114.2(5)

Symmetry transformations: i) $x, y-1, z$; ii) $x+1, y-1, z$; iii) $x, y+1, z$; iv) $x-1, y+1, z$.

Acknowledgements

First of all, I wish to thank my supervisors, Prof. Maria Laura Mercuri and Dr. Narcis Avarvari, for their precious guide and the continuous support during these years.

Thanks to the Molecular Materials research group of the Department of Chemical and Geological Sciences (Cagliari University), Prof. Paola Deplano, Prof. Emanuele Trogu, Dr. Angela Serpe, Dr. Flavia Artizzu, Dr. Elisa Sessini, Dr. Davide Espa, Dr. Americo Rigoldi and Mr. Salah Attar, for the valuable advices.

Thanks to the équipe Chimie Inorganique, Matériaux et Interfaces of the Moltech-Anjou Laboratory (Angers University), Prof. Nicolas Mercier, Dr. Magali Allain, Dr. Cécile Mézière, Dr. Flavia Pop, Dr. Thomas Cauchy, Ms. Caroline Melan and Mrs. Oksana Toma, for the agreeable months spent during my stay in Angers.

Dr. Flavia Artizzu and Dr. Flavia Pop deserve a special thank for the support and the time spent in fruitful discussions on several aspects of this work.

Dr. Luciano Marchiò (Parma University) is gratefully acknowledged for DFT calculations and crystal structure resolution of some compounds, whereas Dr. Danilo Loche (Cagliari University) is kindly acknowledged for the assistance in performing PXRD measurements.

Dr. Thomas Cauchy (Angers University) and Prof. Enric Canadell (Barcelona University) are gratefully acknowledged for TD-DFT and Band Structure calculations, respectively.

Dr. Rodolphe Clérac (Bordeaux University), Prof. Carlos Gómez-García (Valencia University), Prof. Giorgio Concas (Cagliari University), and Prof. Andrea Caneschi (Firenze University) are kindly acknowledged for magnetic measurements and the contribution to their discussion.

Dr. Pascale Auban-Senzier (Paris-Sud University) is kindly acknowledged for conductivity measurements.

Dr. Valerie Bonin (Angers University) is acknowledged for elemental analyses, Dr. Ingrid Freuze (Angers University) and Dr. Cécile Mézière (Angers University) are acknowledged for MS analyses, whereas Dr. Magali Allain is acknowledged for the assistance during single-crystal XRD measurements.

This work would not have been possible without the financial support from the Italian Ministero dell'Istruzione e della Ricerca (MIUR), which has financed my PhD grant, and the Regione Autonoma della Sardegna, Cagliari and Angers Universities, INSTM, CNRS and Fondazione Banco di Sardegna.

Finally, I wish to thank all the people of the Department of Chemical and Geological Sciences and the Moltech-Anjou Laboratory for the great time spent during these years.

Thèse de Doctorat

Matteo ATZORI

Anilate-based Functional Molecular Materials with Conducting and Magnetic Properties

Résumé

Ce travail de thèse explore la capacité des ligands anilates d'être employés pour la préparation de nouveaux matériaux moléculaires fonctionnels avec des propriétés magnétiques et de conduction électrique.

Les anilates, qui sont les dérivés du 2,5-dihydroxy-1,4-benzoquinone substitués sur les positions 3 et 6, ont été sélectionnés comme ligands puisque leurs caractéristiques électroniques et structurales, leurs modalités de coordination et leur capacité de médiation des interactions de superéchange magnétique en font d'excellents ligands pour la préparation de ces matériaux. Plusieurs ligands anilates ont été utilisés pour le design et la préparation d'une nouvelle classe de complexes paramagnétiques octaédriques tris-chélatés de formule générale $[M^{III}(X_2An)_3]^{3-}$ ($M^{III} = Cr, Fe$; $X = Cl, Br, I, H, Cl/CN$, $An = C_6O_4^{2-} = anilate$). Ces complexes métalliques paramagnétiques ont été complètement caractérisés et utilisés comme briques moléculaires pour la préparation de *i*) une nouvelle classe de ferriaimants moléculaires, dans laquelle la modification des substituants sur le ligand permet de modifier les interactions entre les centres métalliques, et, par conséquent, les propriétés magnétiques, *ii*) des conducteurs paramagnétiques moléculaires obtenus par combinaison avec le donneur organique BEDT-TTF, *iii*) une série de conducteurs moléculaires chiraux obtenus par combinaison du donneur organique TM-BEDT-TTF avec des couches hétérobimétalliques anioniques obtenues par association *in situ* de complexes tris(chloranilate)ferrate(III) et des ions potassium.

En outre, ont été synthétisés de nouveaux dérivés anilates avec des propriétés électroactives et de luminescence, afin de démontrer la capacité du motif anilate d'être fonctionnalisé avec différents substituants comme porteurs de propriétés physiques spécifiques.

Mots clés

Matériaux Moléculaires, Aimants Moléculaires, Anilates, Conducteurs Moléculaires, Magnétisme, Conductivité, Chiralité.

Abstract

This work explores the potential of anilate-based ligands in the synthesis of new rational designed functional molecular materials exhibiting improved magnetic and conducting properties.

Anilates, namely 3,6-disubstitued 2,5-dihydroxy-1,4-benzoquinones in their dianionic form, have been selected as ligands since their electronic/structural features, coordination modes and ability to mediate magnetic exchange interactions between coordinated metal centers make them potential candidates for the preparation of the above-mentioned materials.

Various anilate derivatives have been used for the preparation of a family of rationally designed tris-chelated octahedral paramagnetic metal complexes of general formula $[M^{III}(X_2An)_3]^{3-}$ ($M^{III} = Cr, Fe$; $X = Cl, Br, I, H, Cl/CN$, $An = C_6O_4^{2-} = anilate$). These paramagnetic metal complexes have been thoroughly characterized and used, in turn, as molecular building blocks for the preparation of *i*) a family of molecule-based magnets, where subtle changes in the nature of the substituents on the anilate moiety were employed as "adjusting screws" in tuning the magnitude of the magnetic interaction between the metals, and thus, the magnetic properties, *ii*) hybrid paramagnetic molecular conductors in combination with the BEDT-TTF organic donor, *iii*) a complete series of isostructural chiral molecular conductors obtained by combining the TM-BEDT-TTF chiral donor with 2D heterobimetallic anionic layers obtained *in situ* by the self-assembling of tris(chloranilate)ferrate(III) metal complexes and potassium cations.

Moreover, novel anilate derivatives showing electroactive and luminescent properties have been further synthesized, highlighting the versatility of the anilate moiety to be functionalized with suitable substituents carrying selected physical properties.

Key Words

Molecular Materials, Molecule-based Magnets, Anilates, Molecular Conductors, Magnetism, Conductivity, Chirality.